

CHIMIKA CHRONIKA

NEW SERIES

AN INTERNATIONAL EDITION
OF THE ASSOCIATION OF GREEK CHEMISTS

Proceedings of the
**INTERNATIONAL SYMPOSIUM
ON GLASS SCIENCE AND TECHNOLOGY**

Hellenikos Hyalourgikos Syndesmos
Athens, 6-8 October 1993

Editors: G. D. Chryssikos and E. I. Kamitsos



2-3/94

CMCRCZ 23(2-3), (1994)

ISSN 0366-693X

Volume 23, No 2-3 – Special Edition 1994

CHIMIKA CHRONIKA

NEW SERIES

AN INTERNATIONAL EDITION

Published by the Association of Greek Chemists (A.G.C.)
27 Kaningos str. Athens 106 82 Greece

Journals Managing Committee, A.G.C.:

A. Cosmatos, P.N. Dimotakis, D. Hadjigeorgiou-Giannakaki, M. Kazanis,
M. Petropoulou-Oschsenkühn

Editor-in-chief: P.N. Dimotakis

Editors: N. Alexandrou, A. Cosmatos, A. Evangelopoulos, M.P. Georgiadis, N. Hadjiliadis, N. Hadjichristidis, M.I. Karayannis, N. Katsanos, J. Petropoulos, D. Tassios.

Foreign Advisors: P. Bontchev (Sofia), H. Işçi (Ankara), G.M. Milanovic (Belgrade), K.C. Nikolaou (Cyprus), E. Plasari (Tirana).

Correspondence, submission of papers, subscriptions, renewals and changes of address should be sent to Chimika Chronika-New Series, 27 Kaningos street, Athens 106 82, Greece. The Guide to Authors is published in the first issue of each volume, or sent by request. Subscriptions are taken by volume at 2000 drachms for Corporations in Greece and 50 U.S. dollars to all other countries except Cyprus, where subscriptions are made on request.

Phototypesetted and Printed in Greece by EPTALOFOS S.A.

12, Ardittou Str. 116 36 ATHENS Tel. 9217.513

Υπεύθυνος σύμφωνα με το νόμο: Ν. Κατσαρός, Κάνιγγος 27, Αθήνα 106 82.

Responsible under law: N. Katsaros, 27 Kaningos St., Athens 106 82, Greece.

Proceedings of the
**INTERNATIONAL SYMPOSIUM
ON GLASS SCIENCE AND TECHNOLOGY**

Athens, 6-8 October 1993

Editors: G. D. Chryssikos and E. I. Kamitsos

II

Hellenikos Hyalourgikos Syndesmos, (Greek Glass Federation) **International Symposium on Glass Science and Technology** under the auspices of the International Commission on Glass (ICG), 6-8 October 1993, Athens, GREECE

SPONSORS

YOULA GLASSWORKS S.A.
VALAVANIS Bros GLASSWORKS S.A.
BIOKEF S.A.
E. TSANTALIS S.A.
A. CAMBAS S.A.
S. & E. & A. METAXA S.A.
D. KOURTAKIS S. A.
INTERACTIVE Ltd
Ms. Marianna Dimitriades

GENERAL SECRETARIAT FOR RESEARCH AND TECHNOLOGY
NATIONAL HELLENIC RESEARCH FOUNDATION (Theoretical
and Physical Chemistry Institute)
NCSR "DEMOKRITOS" (Institute of Materials Science)
UNITED STATES AIR FORCE (European Office of
Aerospace Research and Technology)
INTERNATIONAL SCIENCE FOUNDATION
GREEK NATIONAL TOURIST ORGANIZATION

Chairman: John Chatzis - HHS President, **Co-Chairmen:** G. Kordas and E. I. Kamitsos, **International Advisory Committee:** M. D. Ingram, F. Nicoletti, M. Prassas, H. A. Schaeffer, N. Soga, R. A. Weeks and A. Yaraman, **Local Organizing Committee:** G. D. Chryssikos, Th. Kakkos, N. Kartis, S. Orphanos, G. Priftis, B. Stamelos, P. Tsaoussoglou and N. Valavanis.

CONTENTS

| | |
|----------------------|-----|
| <i>Preface</i> | vii |
|----------------------|-----|

VITTORIO GOTTARDI LECTURE

| | |
|--|---|
| Crystallization of glass: A ten year perspective <i>E. D. Zanotto</i> | 3 |
|--|---|

PART I, GLASS MANUFACTURING

| | |
|--|-----|
| Recycling of cullet and filter dust: Challenges for the melting of glass <i>H. A. Schaeffer</i> | 21 |
| Cullet treatment equipment for the glass industry <i>J. Rosenthal</i> | 31 |
| Recycling in the glass industry - An overall view <i>H. Moser</i> | 39 |
| Environmental legislation and glass technology <i>G. J. Copley</i> | 45 |
| Some factors governing improvements in glass melting <i>M. Cable</i> | 53 |
| Modern glass conditioning from throat to orifice <i>R. Sims</i> | 63 |
| Operational experiences with several FlexMelter ^R furnaces <i>H. Pieper</i> | 71 |
| The distribution of electrodes and its influence on the flow of glass <i>S. Kasa and A. Lisý</i> | 81 |
| Spectral element method for thermoconvection in a glass melt <i>N. Vanandruel</i> | 89 |
| Simulation of glass processes with Polyflow, a finite element program <i>N. Vanandruel</i> | 95 |
| Laboratory simulations of bubble defects in glass <i>M. Oran</i> | 101 |
| Mechanical strength of original and corroded float glass <i>J. Matousek and M. Maryska</i> | 107 |
| New lead-free crystal glasses <i>M. Rada, L. Sasek and M. Mika</i> | 113 |
| Surface treatment: An alternative to improve properties of hollow glass <i>F. Hubert</i> | 119 |
| Ion-Exchange of glass surface and salt melt: Understanding the influence of process-parameters better through computer modelling and adequate measurements <i>Yu. K. Startsev</i> | 125 |
| Silica sand of northeastern Bulgaria <i>M. Mochev</i> | 131 |

PART II, SOL-GEL PROCESSING

| | |
|--|-----|
| Rheology of sols in the sol-gel processing <i>S. Sakka and H. Kozuka</i> | 137 |
| Molecular design and processing effects on sol-gel derived thin films <i>B. E. Yoldas</i> | 147 |
| Preparation of SiO ₂ -TiO ₂ -ZrO ₂ gel compositions by means of a liquid crystal approach <i>G. Mezinskis and G. H. Frischat</i> | 157 |
| Original synthesis of II-VI semiconductor nanocrystallites embedded in a sodium borosilicate glass <i>L. Boudes, J. L. Marc, W. Granier, A. Pradel, M. Ribes, J. Allegre and P. Lefebvre</i> | 163 |
| Photophysical properties of dyes incorporated into SiO ₂ matrices by the sol-gel method <i>P. Lianos</i> | 169 |
| An organic-inorganic hybrid glass hosting photochromic dyes <i>L. Hou, M. Mennig and H. Schmidt</i> | 175 |
| Preparation of composite Cu-CuO-SiO ₂ coatings on glass starting from amine-containing solutions <i>N. Maliavski, O. Dushkin, E. Tchekounova, P. Innocenzi, G. Scarcini and M. Guglielmi</i> | 181 |
| Coating of glass powders by sol-gel route <i>M. Bouchnafa, B. Soulestin, R. Guinebretiere, A. Lecomte and A. Dauger</i> | 187 |
| Zircon containing ceramic pigments by sol-gel method <i>C. C. Trapalis, M. A. Karakassides, K. Golematis and G. Kordas</i> | 193 |
| Sol-gel processing and crystallization of alkali germanate glasses <i>A. Marotta, M. Catauro, A. Aronne and P. Pernice</i> | 199 |
| Calcium Hydroxyapatite formation by sol-gel route <i>C. C. Trapalis, A. Koufoudakis, I. Dounis, M. A. Karakassides, G. Kordas</i> | 205 |

PART III, GLASS STRUCTURE AND PROPERTIES

| | |
|---|-----|
| Sub-ambient T _g glasses for ionic rubbers and new generation solid electrolytes <i>C. Liu, E. Sanchez and C. A. Angell</i> | 211 |
| Ion mobility and structural relaxation in glass <i>M. D. Ingram, P. Maass and A. Bunde</i> | 221 |
| Ionic conductivity and structure of superionic glasses containing silver and cuprous halides <i>T. Minami, M. Tatsumisago and N. Maehida</i> | 227 |
| Vitreous ionic conductors with Cu ⁺ <i>M. Mika, L. Sasek and M. Rada</i> | 239 |
| Structural aspects of the mixed alkali effect <i>E. I. Kamitsos, A. P. Patsis, G. D. Chryssikos and J. A. Kapoutsis</i> | 245 |
| Thermal transport by localized and extended phonons in glass <i>G. S. Dixon, T. Doyle, P. A. Watson, W. P. Allen, B. D. Gault, S. Shi,</i> | |

| | |
|--|-----|
| <i>P. G. Dixon, R. Snider and E. T. Knobbe</i> | 251 |
| Dynamic properties of zinc halide glasses and melts | |
| <i>S. N. Yannopoulos and E. A. Pavlatou</i> | 257 |
| Structural properties of ZnCl ₂ -ZnBr ₂ glasses and melts | |
| <i>E. A. Pavlatou</i> | 265 |
| Fragility and decoupling in glass: A chemical perspective | |
| <i>G. D. Chryssikos, E. I. Kamitsos, J. A. Kapoutsis and A. P. Patsis</i> | 271 |
| Vibrational spectra of silicate glasses modelled on the basis of SiO ₄ -ring structures | |
| <i>B. D. Mihailova, N. S. Zotov, M. S. Marinov and L. L. Konstantinov</i> | 277 |
| Calculation of Raman spectra of glasses | |
| <i>M. S. Marinov, N. S. Zotov, B. D. Mihailova and L. L. Konstantinov</i> | 283 |
| Medium range order in silicate glasses | |
| <i>K. H. Karlsson and K. Fröberg</i> | 289 |
| Glass formation and structure of non-oxide glasses | |
| <i>Fuxi Gan</i> | 295 |
| Velocity of ultrasound and elastic properties of lithium borate glasses | |
| <i>M. Kodama, K. Yamakawa and T. Matsushita</i> | 303 |
| Physical properties and spectroscopy of rubidium and caesium borate glasses with exceptionally high alkali content | |
| <i>S. Feller, S. Nijhawan, M. Royle, J. Mackenzie, J. Taylor, M. Sharma, E. I. Kamitsos, G. D. Chryssikos, A. P. Patsis, P. J. Bray and P. E. Stallworth</i> | 309 |
| Physical properties of alkali borosilicate glasses related to atomic arrangements | |
| <i>S. Feller, R. Boekenhauer, H. Zhang, D. Bain, D. Feil, C. Parameswar, K. Budhwani, S. Ghosh, S. Nijhawan and J. Mackenzie</i> | 315 |
| Analysis of X-ray diffraction patterns of crystallized and amorphous Fe borate glasses | |
| <i>M. R. P. Correia and S. K. Mendiratta</i> | 323 |
| Influence of alkaline earth on dynamic response in silicate glasses by IR reflectivity and Brillouin scattering | |
| <i>Y. Vaills, Y. Luspain, G. Hauret and T. Parot-Rajaona</i> | 329 |
| Raman and far-infrared study of aluminum and boron substituted sodium trisilicate glass | |
| <i>E. I. Kamitsos, J. A. Kapoutsis, H. Jain and C. H. Hsieh</i> | 335 |
| Alkali sites in silicate glasses | |
| <i>J. A. Kapoutsis, E. I. Kamitsos, G. D. Chryssikos, Y. D. Yannopoulos, A. P. Patsis and M. Prassas</i> | 341 |
| ³¹ P and ²⁷ Al NMR spectroscopy of Glasses: determination of the structure, of reactions in the batches and of crystallisation phenomena | |
| <i>C. Jäger, D. Ehrhart and G. Kunath</i> | 347 |
| Cross-checking of vibrational and NMR information in glasses | |
| <i>T. Parot-Rajaona, B. Cote, C. Bessada, D. Massiot and F. Gervais</i> | 351 |
| Dissolution studies of phosphate glasses and relationships to structure | |
| <i>J. E. Dickinson</i> | 355 |
| Glass formation and structural models on tellurite glasses | |
| <i>Y. Dimitriev</i> | 361 |
| Structure of vanadate glasses | |
| <i>V. Dimitrov</i> | 367 |
| Induced crystallization of glasses | |
| <i>I. Gutzow and A. Dobrev</i> | 373 |

VI

Non steady state effects in the kinetics of crystallization of glass forming melts
A. Dobrevá and I. Gutzow.....379
 Crystallization kinetics of a $\text{Li}_2\text{O} \cdot 2\text{SiO}_2$ melt based on a liquid model
R. Ota, N. Mishima, T. Wakasugi and J. Fukunaga385
 Phase transitions in mixed network glasses: crystallochemical and structural aspects
L. Stoch.....391
 Multistage crystallization of amorphized solids and glass - A comparative study
I. Waclawska and L. Stoch397
 Crystallization of cordierite-type glass nucleated by Ag
M. Rappensberger and I. Szabó403
 A microwave study of charged defects in glasses
I. Ciccarello, M. Cuccione and M. Li Vigni.....411
 High quality polysilicon films for flat panel displays formed on glass above the strain point
J. Stoemenos, B. Kalaitzidis and N. A. Economou417
 Electrochromic properties of Chemically Vapour Deposited (CVD) WO_3 polycrystalline thin films
D. Davazoglou423

Author Index429

List of Participants431

PREFACE

On the occasion of the annual meetings of the International Commission on Glass (ICG), the Hellenikos Hyalourgikós Syndesmos (Greek Glass Federation) organized an International Symposium on Glass Science and Technology. The Symposium was held on October 6-8, 1993, in Astir Palace Hotel, on the picturesque Vouliagmeni coast, 15 km off Athens.

The main goal of the organizers was to bring together technologists and researchers working on glass. Thus, the topics included recent developments on furnace design and control, environmental aspects of glass manufacturing, as well as advances in fundamental research such as those concerning the sol-gel processing and the establishment of structure-property relationships. Each main topic was introduced by invited speakers and covered by a number of oral and poster presentations. To ensure the maximum interaction between the participants no parallel sessions were held.

The agenda of the Symposium attracted some 160 participants from 26 countries. All together, 30 oral and 45 poster contributions were presented and discussed. Professor E. D. Zanotto was awarded the 1993 ICG Vittorio Gottardi Prize and delivered a plenary lecture on glass crystallization. The authors could submit camera-ready copies of their papers. All papers, but the technical reports, were thoroughly reviewed and 63 of them are included in these Proceedings.

The editors of this volume are thankful to the Chairman and co-chairmen of the Symposium, the members of the International Advisory and Local Organizing Committees, the International Commission on Glass and the sponsors who made the Symposium possible. We also wish to thank our secretary Ms. Sonja Seizova for her assistance, and the officers of the Association of Greek Chemists for publishing these proceedings in the international edition of *Chimika Chronika*. Last but not least, we are indebted to all the authors and the referees for their efforts to make this volume a valuable reference for future advancements in glass science and technology.

*G. D. Chryssikos
E. I. Kamitsos*

Vittorio Gottardi Lecture

CRYSTALLIZATION OF GLASS: A TEN YEAR PERSPECTIVE
1993 "Vittorio Gottardi Prize" Lecture

Edgar Dutra Zanotto
DEPARTMENT OF MATERIALS ENGINEERING
FEDERAL UNIVERSITY OF SAO CARLOS
13565-905, São Carlos, SP- Brazil

This paper reviews four aspects of glass crystallization: i) the effects of liquid-liquid phase separation on crystal nucleation and growth; ii) the validity of the classical nucleation theory; iii) some trends observed on homogeneous and heterogeneous nucleation in oxide glasses and; iv) the state-of-art on surface crystallization kinetics.

INTRODUCTION

First of all I should say that it is a distinct pleasure to deliver this review lecture to such knowledgeable audience, looking at the magnificent scenery of the Greek sea (it can be seen from the lecture theater!). In this occasion, I decided to review my own work, carried out jointly with several colleges and graduate students in the past ten years, because this is a unique opportunity. However, I would like to point out that most of the research described here has been inspired in the earlier work of Russian scientists (V. Fokin, A. Kalinina and V. Filipovich), the Bulgarian group (I. Gutsow and co-workers), the Sheffield group (P. James and students), the Arizona team (M. Weinberg and D. Uhlmann) and my Brazilian colleagues (A. Craievich and E. Meyer).

I **dedicate** this talk to these distinguished scientists. I learned much from them. Throughout the years I discovered how one can be mentally "in phase", at least in our restricted research field, just by carefully reading a few of their papers in chronological order, listening to some of their talks and occasionally talking to them. Sometimes I try to predict what these persons are thinking or which experimental or theoretical problems they are planning to attack next. Surprisingly, I succeed several times! I guess that is how science develops. I see it (science) as a long standing game, played internationally and being **slowly** solved, piece by piece, year after year.

In the next sessions I will show some of the pieces I have put together in the past decade, in chronological order. I will also describe a little the history and motivation behind each research topic. Thus, this review does not cover many other important developments on crystal nucleation and growth in glass. The reader is urged to refer to the above mentioned authors if he intends to be "in phase" in the field.

This paper discusses the effects of liquid-liquid phase separation on crystal nucleation, the applicability of the classical nucleation theory to glass crystallization, some remarkable trends observed on homogeneous and heterogeneous

nucleation in oxide glasses and, finally, the state-of-art on surface crystallization. It does not review the relevant theories nor the experimental procedures due to space limitations. Here instead, I present solely a minimum of relevant equations, necessary to follow the article.

1. THE EFFECTS OF LIQUID PHASE SEPARATION ON CRYSTAL NUCLEATION

In the seventies there was a tremendous scientific excitement and research activity on liquid-liquid phase separation (LLPS) as well as on crystal nucleation and growth (CNG) in glasses, mainly due to the potential development of glass-ceramics having unusual properties and applications. Of special interest were the possible relationships between the two phenomena. Several authors speculated that LLPS occurred before CNG and was a necessary step for the production of fine grained glass-ceramics. A strong **controversy** on how LLPS could affect CNG existed, as shown in a meeting on "The Vitreous State" held at The University of Bristol-UK [1]. Thus, some authors defended that **compositional changes** induced by liquid phase separation could affect CNG, while others believed that the **interfaces** between the glassy phases should play an important role on crystallization, by providing favorable sites for heterogeneous nucleation.

I started working on this specific subject, as a MSc student of physics, with Aldo Craievich, in Sao Carlos, Brazil, in 1977. At the same time, Peter James had a PhD student, Anthony Ramsdem, working on the same topic in Sheffield. We exchanged some information, and after finishing my MSc dissertation in 1979, I received a grant from the Brazilian government and decided to apply to the 'Glass Mecca' at the time, Sheffield University, and there I stayed for three years as a PhD candidate. I continued working on the same topic initiated in Sao Carlos, using the excellent library and glass laboratories of Sheffield, under Peter's guidance.

We did a systematic, detailed, work with $\text{Li}_2\text{O-SiO}_2$ and BaO-SiO_2 glasses, having compositions inside and outside the spinodal and binodal areas of the respective phase diagrams. We used controlled thermal treatments to induce the simultaneous development of LLPS and CNG. The kinetics of these processes could be decoupled with SAXS, TEM and optical microscopy. The experimental details are described in [2-4]. Please note that the actual problem was raised in 1970, our research work started in 1977 and the first publication with conclusive results only came out in 1983!

1.1 Main Results

1.1.1.a. BaO-SiO_2 Glasses:

Figure 1 shows the partial phase diagram of the baria-silica system, with the miscibility gap, glass compositions and thermal treatment temperatures used (black dots). Figure 2

shows the number of crystals nucleated at 743 C (after a development treatment at $T_d \sim 815$ C for ~ 20 min), obtained by optical microscopy associated with stereological techniques, for two glass compositions inside the miscibility gap, but outside the spinodal region. The crystal nucleation rate (curve slope) of glass 27.0 (27.0 mole % BaO) **increases** up to approximately 2 hours, which is shorter than the 7 hours period required for glasses with 28.3 mole % BaO to reach steady-state at the same temperature. The steady-state nucleation rates of the two glasses are equal, spite of their different modifier content.

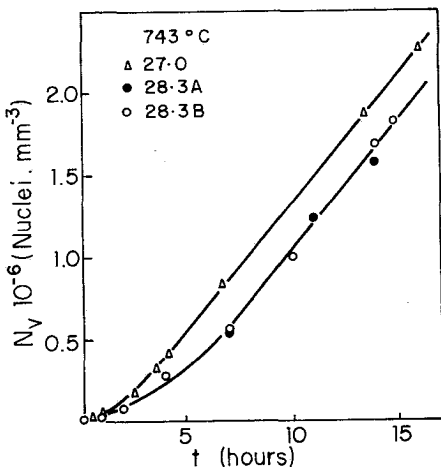
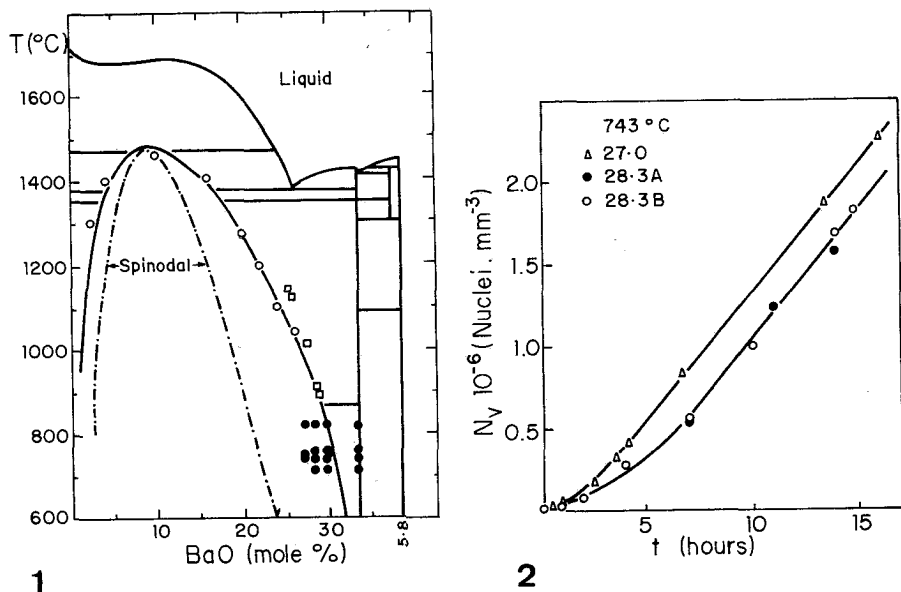


Figure 1. Partial phase diagram of the baria-silica system showing the miscibility gap (O, \square) with the treatments used (\bullet).

Figure 2. Number of crystals nucleated at 743 C in glasses with 27.0 and 28.3% BaO (A and B refer to different glasses).

The liquid-phase separation kinetics in these glasses were followed by SAXS. The scattering of X-rays was mainly due to the amorphous droplets (and not due to the crystal nuclei) because their number and electronic contrast were many orders of magnitude higher than that of the crystals. Figure 3 shows the total integrated SAXS intensity, Q , which is proportional to the electronic density contrast between the two liquid phases. Thus, when the phase separation process reaches the coarsening stage, the matrix composition reaches the equilibrium value dictated by the binodal line and Q remains invariable. The striking feature of that study is that the time required for LLPS be completed (Figure 3) coincides with

that for the establishment of steady-state crystal nucleation rates (Figure 2). Thus, the compositional effects are clear: as LLPS develops, the amorphous matrix phase gets progressively richer in Ba, and the crystal nucleation rates increase till a constant matrix composition is reached (the nucleation rate of a glass with 33.3 mole% BaO, outside the miscibility gap, is much higher). Additionally, there is **no** correlation between the number and surface area of the amorphous droplets and the number of crystals nucleated for all glass compositions and treatments tested. This finding eliminates the possibility that droplet interfaces play an important role on crystallization.

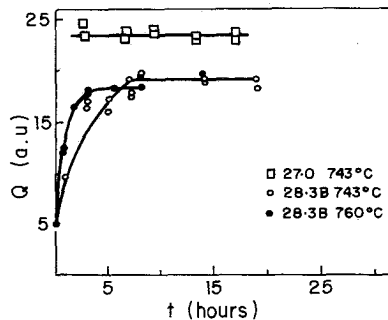


Figure 3. Total integrated SAXS intensity, Q , for the same glasses of Figure 2.

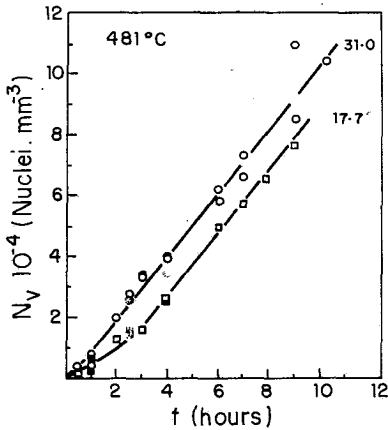
Several other experiments confirmed the overall picture shown above [4]. A limited, but conclusive, number of experiments were carried out to test the effects of LLPS on the crystal **growth** rates. The results were quite similar to those of the crystal nucleation experiments, being explained by the compositional effects of LLPS.

1.1.1.b. $\text{Li}_2\text{O-SiO}_2$ Glasses

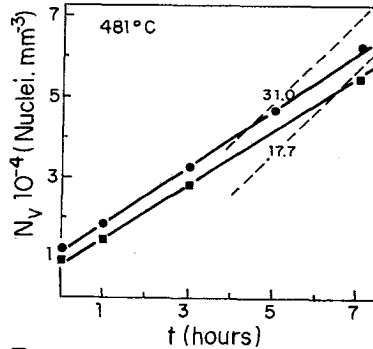
Very similar findings emerged from the study carried out with $\text{Li}_2\text{O-SiO}_2$ glasses. The crystal nucleation rates for compositions having widely different modifier content, a glass with 31.0 mole% Li_2O (in the nucleation and growth region of the miscibility gap) and other with 17.7 mole% Li_2O (well inside the spinodal region) initially increased and then became **identical** when the steady-state regime was reached, after about three hours at 481 C (Figure 4). As the glass transition range is about 450 -460 C for these glasses, we concluded that the initial increase in nucleation was due to the compositional change of the amorphous matrix caused by phase separation, as in the case of Ba-glasses. When LLPS was completed, the matrix composition of the two glasses were identical (given by the binodal line) and so were the crystal nucleation rates.

A different experiment was devised to test the effects of the advanced stages of LLPS on crystal nucleation. Specimens

of the two glasses were first heated to 497 C for 5 hours to bring LLPS to the coarsening stage. After that they were nucleated at 481 C and "developed" at 570 C (the standard way to allow crystal growth to optical microscopy sizes). Figure 5 shows that the crystal nucleation rates are constant and equal from the beginning. For comparison we also plot the steady-state nucleation rates of as-quenched glasses (dashed lines). The previous treatment at 497 C eliminates the curvatures observed in the initial stages (Figure 4) and decreases the nucleation rates. The intercepts on the N_v axis are due to nucleation in the initial treatment at 497 C. The smaller nucleation rates are due to the different matrix composition of glasses which had been previously phase separated at 497 C (less Li_2O) compared to those phase separated at 481 C. In this case, secondary phase separation has not been observed.



4



5

Figure 4. Crystal nucleation curves of glasses with 17.7 (spinodal region) and 31.0 mole % Li_2O (binodal region).

Figure 5. Crystal nucleation curves of glasses 17.7 and 31.0 previously phase-separated at 497 C for 5 h (●,■). The dashed lines refer to the same curves shown in Figure 4.

Conclusions

In the two glass families studied, there is a striking correlation between the time for LLPS be completed (to reach the coarsening stage) and the establishment of steady-state crystal nucleation rates. Phase-separated glasses with widely different oxide modifier contents, but with identical glassy matrix compositions induced by phase-separation, show identical nucleation and growth rates. The number and surface area of liquid-phase droplets are many orders of magnitude higher than the numbers and surface areas of crystals for all

compositions and treatments. Therefore, the increase in crystal nucleation and growth rates are mainly due to the compositional shifts caused by LLPS. However, the observed increase in nucleation rates caused by LLPS (2-3 times) is much smaller than that due to nucleating agents (1-5 orders of magnitudes).

2. THE APPLICABILITY OF CLASSICAL NUCLEATION THEORY (CNT) TO GLASS CRYSTALLIZATION

Between 1971 and 1981 a series of articles were published by Kalinina & Filipovich, Matusita & Tashiro, James and co-workers and Neilson & Weinberg, on experimental tests of classical nucleation theory (CNT) using direct measurements of nucleation rates in $\text{Li}_2\text{O} \cdot 2\text{SiO}_2$ and $\text{Na}_2\text{O} \cdot \text{CaO} \cdot \text{SiO}_2$ glasses; and by Uhlmann and co-workers using indirect estimates (via crystal growth rates and overall crystallization) in $\text{Na}_2\text{O} \cdot 2\text{SiO}_2$ and $\text{CaO} \cdot \text{Al}_2\text{O}_3 \cdot 2\text{SiO}_2$ glasses (see [5]).

Again, there was an intense dispute; a team of authors defended the validity of CNT for glass crystallization while others found enormous discrepancies between theoretical and experimental nucleation rates (from 20 to 50 orders of magnitude!). Arguments in favor and contrary included errors associated to the use of nucleation rates from one study and viscosity data from a different one (for the transport term of CNT), the possible occurrence of heterogeneous nucleation rather than homogeneous, the use of unreliable thermodynamic data or approximations for ΔG , the initial nucleation of metastable phases, the questionable validity of the Stokes-Einstein equation for the transport term, the influence of induction periods, the possible temperature dependence of the surface energy, etc.

In 1978 James et al. [6] provided strong evidence that volume nucleation in lithia-silica glasses were predominantly **homogeneous**. In their study, glasses melted with widely different batch materials and crucibles, including platinum (a known nucleating agent for these glasses) yielded similar nucleation rates. Also, the observed maximum nucleation rates occurred at very high undercoolings, $T_{\text{max}} / T_{\text{melt}} \sim 0.55$, which were comparable to the maximum undercooling ever obtained for a pure element, Ga, in droplet experiments [7]. Also, reliable thermodynamic data were available for this system. Thus, Peter James and I decided to carefully remeasure both the nucleation rate curve and the viscosity of a $\text{Li}_2\text{O} \cdot 2\text{SiO}_2$ glass (from the same melt) having a known amount of H_2O and impurities, and retest CNT. We also performed similar experiments with a $\text{BaO} \cdot 2\text{SiO}_2$ glass, because this composition had not been analyzed before [5].

All studies previously described assumed that the molecular rearrangements at the nuclei/matrix interfaces were controlled by viscous flow, and thus, the transport term was calculated using the Stokes-Einstein equation. Additionally, the interfacial energy σ was considered to be independent of nucleus size or temperature, $\sigma = \sigma_0$. In this case, the steady-

state homogeneous nucleation rate I is given by:

$$I = (AT / \eta) \exp(-K \sigma_0^3 / T \Delta G^2) \quad (1)$$

where A is a weakly temperature dependent term, η the viscosity, ΔG the thermodynamic driving force and K a constant. Thus, $\ln(I\eta/T)$ versus $1/(T \Delta G^2)$ plots should be straight lines with A and σ_0 given by the intercept and slope.

The results for the two glasses were very similar. The temperature dependence of the nucleation rates were well described by CNT (good straight lines), with exception of two points at the lowest temperatures, below DTA- T_g , where induction times are significant and probably render underestimated values of the steady-state nucleation rates. However, the absolute values of I were about 30 orders of magnitude higher than the calculated values. Additionally, no agreement between theory and experiment could be found by varying ΔG (even with absurd values of $\Delta G!$). The only way to force agreement was by fitting a weakly temperature dependent σ . Therefore, our research reached similar conclusions as those of James & co-workers and Neilson & Weinberg regarding the absolute values of the nucleation rates, however, with the new viscosity and nucleation data, a better temperature dependence of I was provided by theory, even with a constant σ .

Other stoichiometric glasses (soda-lime-silica, calcium metasilicate, lithium borate, lithium metasilicate) displaying volume homogeneous nucleation, have been tested by a number of authors. The general feeling is that, in its conventional form (with a constant σ_0), CNT does not predict correctly the magnitudes of crystal nucleation rates in glasses. On the other hand, the reduced surface energy or Turnbull ratio, α (gram-atomic interfacial energy / molar heat of fusion) has been obtained from fitting the experimental nucleation rates of a number of glasses, and varies from 0.4 to 0.6. This range of values compares well with that of several elemental liquids, derived from maximum undercooling experiments, $0.4 < \alpha < 0.5$ [7]. Unfortunately, however, α is the unknown parameter of CNT, and has not been independently measured in glass systems so far. Therefore, one can use this range of α to estimate the temperature dependence (but not the magnitude) of nucleation rates in undercooled liquids.

Thus, the most probable causes of discrepancy between theory and experiment are: i) the initial precipitation of metastable phases, a common phenomenon in glass crystallization; ii) the use of viscosity to calculate the transport term of CNT and iii) the assumption that the surface energy is that of a macroscopic crystal, $\sigma = \sigma_0$.

Taken into account that σ comes out from fitting theory and experiment, its value automatically reflects the nucleating phase stability. Additionally, the diffusion process in crystal nucleation is dictated mainly by atomic transport in the glass (matrix) phase, and thus do not depend on the nature of the nucleating phase. Hence, we discarded the

first possibility. We came to this conclusion because even using absurdly large or small values of ΔG (possible associated with the precipitation of metastable phases) would not bring theory and experimental data into accord. Therefore, we decided to check the second possibility, by carrying out a more rigorous test of CNT, using the **induction periods** rather than **viscosity**, to account for the transport term. This eliminates the assumption that viscous flow controls the atomic transport for nucleation because, in principle, whatever diffusional mechanisms are involved in steady-state nucleation, they should be the same that control the induction times in non-steady-state nucleation. Thus, CNT reads:

$$I = (A' / \tau) \exp(-K \sigma_0^3 / T \cdot \Delta G^2) \quad (2)$$

where τ is the temperature dependent induction period and the other parameters were defined before. Thus, one can fit the independently measured values of I , τ and ΔG to Equation (2) to obtain A' and σ_0 [8].

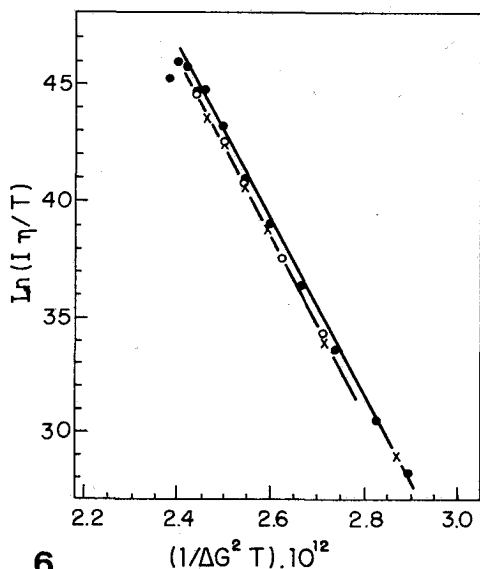
This type of calculation was performed for a number of glasses [8], however, the temperature dependence and magnitudes were not well described by Equation (2). The disagreement was even worse than for the previous tests, using the viscosity (Figures 6 and 7).

The third possibility is to assume a size or temperature dependent surface energy. In three occasions [9-11] we took Tolman's equation for $\sigma(r)$ and rederived CNT with this different view. Tolman's equation reads:

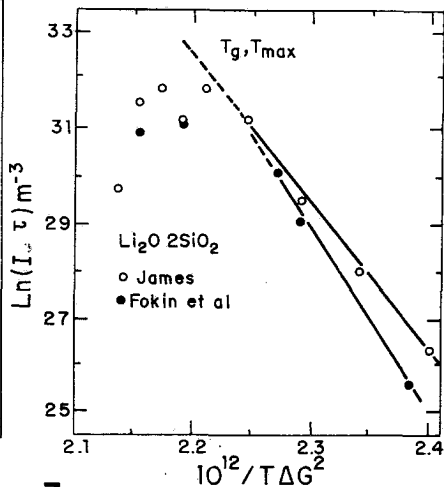
$$\sigma(r) = \sigma_0 / (1 + \lambda/r); \quad \lambda \ll r \quad (3)$$

where λ has the order of a molecular distance. This equation overestimates the surface tension by $\sim 7.5\%$ when $\lambda = r$.

The new form of CNT, denominated curvature dependent classical nucleation theory (CD-CNT), has different pre-exponential and exponential terms from those of Equations (1) and (2) and were described in [9-11]. The problem now is the additional unknown parameter, λ . One may reasonably assume that λ is equal to the lattice parameter of the nucleating crystal, and follow the same procedure used with CNT, i.e. to fit experiment to theory as to make the maximum nucleation temperatures to coincide (CD1) [9]. However, one may instead, leave λ to be adjusted by force fitting CD-CNT to agree with both the magnitude and temperature of maximum experimental nucleation rate (CD2) [10, 11].



6



7

Figure 6. Nucleation plots for $\text{Li}_2\text{O} \cdot 2\text{SiO}_2$ glasses according to Equation (1). Nucleation data from different authors (\bullet , \circ , \times) described in [5]. SI units are employed.

Figure 7. Nucleation plots for $\text{Li}_2\text{O} \cdot 2\text{SiO}_2$ according to Equation (2). Steady-state nucleation rates, I , and induction times, τ , from James and Fokin et al., described in [8].

Figure 8 shows the experimental and theoretical nucleation rates of $\text{Li}_2\text{O} \cdot 2\text{SiO}_2$ calculated by CNT and CD-CNT in the two ways above described. The discrepancies between experiment and theory decreased considerably (from 30 om with CNT to 6 om with CD1). The calculations with CD2 cannot be compared to experiment because both the magnitude and position of the peak were used in the mathematical fitting. Even with this force fitting, the temperature dependence of I is not perfectly described.

Figure 9 shows the variation of σ with temperature, obtained by force fitting the standard form of CNT to experiment (a procedure first used by Turnbull). It also shows the temperature dependence of σ obtained by forcing both the temperature and magnitude of maximum nucleation rate given by CD-CNT to agree with experiment. The size dependence of σ was transformed into temperature dependence. The interesting conclusion is that both methods show a moderate increase in σ with temperature. The challenge now is to devise a way to **measure** σ at a sufficiently high T , where the critical nucleus size is large enough. One possible way, is to find a glass (or polymer) whose crystal growth mechanism is via **2-D secondary nucleation**, to determine σ from the fit to the growth rate curve at low undercoolings and compare that value with the extrapolated ones, obtained from nucleation experiments at much lower temperatures.

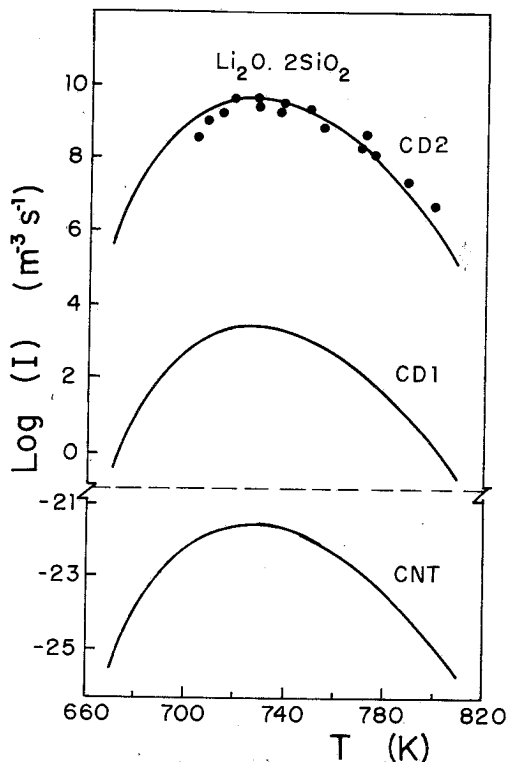


Figure 8. Crystal nucleation rate curves of $\text{Li}_2\text{O} \cdot 2\text{SiO}_2$ calculated by CNT, CD1 and CD2. Experimental data of James (●). Calculations of [10]

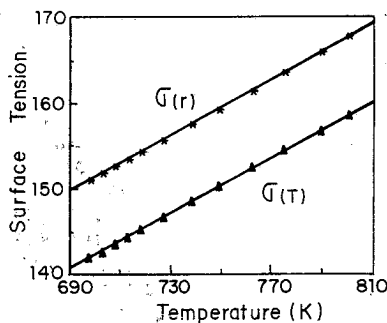


Figure 9. Temperature dependence of surface tension, σ , used by James to fit CNT to the nucleation data of Figure 8, and effective temperature dependence of σ found using a radius dependent surface tension, CD2 [11].

Conclusion

CNT is not capable of quantitatively predicting homogeneous nucleation rates in glasses when a constant surface energy is used. It works much better when a size and/or temperature dependence of σ is taken into account. However, since this parameter cannot be evaluated independently, a main uncertainty still exists concerning the validity of CNT.

3. TRENDS IN CRYSTAL NUCLEATION IN GLASSES

Some reasonably good glass forming systems, even in the absence of nucleating agents, show a remarkable nucleation behavior, ie. volume nucleation is easily detected by optical microscopy at high undercoolings ($T/T_m \sim 0.5-0.6$), and the nucleation rates are only moderately dependent on impurity level. That has been assumed to be a strong sign of homogeneous nucleation. On the other hand, the vast majority of glasses only show surface and catalyzer induced, heterogeneous nucleation. Then, intriguing questions arise: Why some glasses nucleate homogeneously? Do these glasses have any special features?

With that problem in mind, and following a hunch given by James [12], we collected literature data and reported some **trends** observed in the experimental nucleation behavior of stoichiometric oxide glasses [13, 14]. These glasses could be divided in two classes: The first family shows homogeneous nucleation, which has only been observed for compositions having low reduced glass transition temperatures, $T_g/T_m < 0.6$, and whose temperatures of maximum nucleation rates, T_{max} , lie in the vicinity of T_g (DTA T_g). On the other hand, the second family shows only hetero-nucleation, ie. homogeneous nucleation has not been reported for compositions whose T_{max} (predicted by CNT, with reasonable values of α and ΔG) occurs well below the glass transition range. Figure 10 exemplifies the trend, and allows one to distinguish the two families, oxide glasses displaying homo-nucleation (1. $Na_2O.2CaO.3SiO_2$, 2. $Li_2O.2SiO_2$, 3. $BaO.2SiO_2$) from those showing hetero-nucleation (7. $Li_2O.P_2O_5$, 9. $PbO.SiO_2$, 10. SiO_2 , 11. $Na_2O.Al_2O_3.6SiO_2$, 12. B_2O_3). The numbers are the same used in [14], but some data has been omitted for clarity.

Seeking some reasonable explanations for that behavior, we estimated (using the Kaschiev equation and viscosity data) that quite **long induction times** were necessary before nucleation could be detected in all cases of hetero-nucleation, ie glasses having (predicted) T_{max} well below T_g . An additional possibility is that the steady-state homogeneous nucleation rates are very low for this second family, however, this last point cannot be proved due to the insufficient predictive power of CNT.

E. D. Zanotto

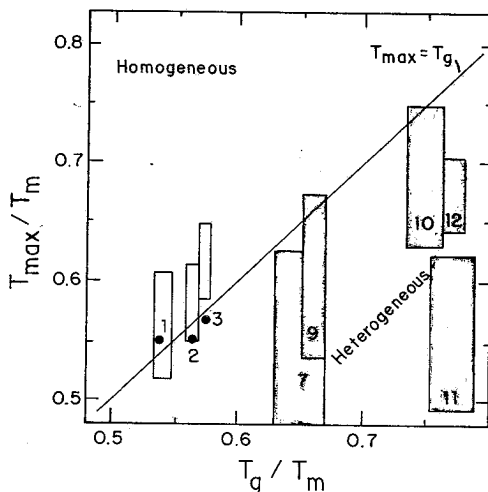


Figure 10. Calculated values of reduced temperature of maximum nucleation frequency against reduced glass transition temperature interval. (•) Experimental data.

Hence, it was clear that two classes of glasses exist. A final point regarding the trends, was provided by two studies aimed to solve the following questions: Are there any relationships between the molecular structure of supercooled liquids and their iso-chemical crystal phases? How could such relationships dictate the nucleation mechanism?

In [15] we looked at the molecular structure of glass and iso-chemical crystal phases, from both **cationic** (short range order around the alkali modifier) and **anionic** (SiO_4 tetrahedra distribution in terms of single-bonded Oxygens) points of view in several stoichiometric silicate glass compositions. We demonstrated that for six glasses belonging to the first family, which nucleate homogeneously, both cationic and anionic arrangements of glass and crystal are quite similar. For five compositions belonging to the second family of glasses, the structures of glass and crystals are different and only hetero-nucleation is observed.

Additional evidence for structural similarity of glass and crystal phases in glasses of the first type was given in [16]. In that paper we demonstrate that the mass densities of glass and crystal do not differ by more than $\sim 8\%$ for those glasses, while the differences can be as high as 33% for the second family of glasses. Thus, we concluded that similar densities of glass and crystal is a necessary, but not sufficient, requirement for structural similarity and inferentially for homo-nucleation.

Conclusion

The questions previously formulated may be answered as follows: Some glasses nucleate homogeneously in laboratory time scales because the short range cationic and anionic arrangements of their glassy and crystal phases are quite similar. Hence, the surface energy (σ) is sufficiently small as to make the nucleation rates measurable at sufficiently low temperatures, but at or above T_g , where the induction periods are not longer than a few minutes. For the other glasses, even the local atomic arrangements of glass and crystal phases are distinct, which make σ large and move the nucleation curve to higher undercoolings, below T_g , where long induction times render the experimental detection of nucleation unfeasible.

5. SURFACE CRYSTALLIZATION OF GLASSES

Surface crystallization is much more frequent than volume crystallization, but much less is known about this phenomenon. Most studies carried out until 1986 were of qualitative character and only (plausible) speculations existed on the mechanisms of surface crystallization.

That year, I decided to attack this problem by giving some of my graduate students the task of measuring nucleation and growth rates at free glass surfaces. By occasion of the International Congress on Glass in Leningrad in 1989, I proposed to the Devitrification Committee of the ICG, TC 7 (now Crystallization Committee) to carry out a systematic study on this subject. The proposal was accepted and the chairman, Wolfgang Pannhorst, prepared specimens of cordierite glasses which were shipped to the committee members: myself, M. Yamane (Japan), I. Mac Donald (UK), I. Szabo (Hungary) and W. Holland and K. Heide (Germany). Wolfgang also sent specimens to Ralf Muller (Germany), who had just finished his PhD Thesis on crystallization kinetics of cordierite glasses [17]. This international group of people is still working on the subject and meet every year to discuss and exchange information. The next meeting is planned to happen in conjunction with the Otto-Schott Colloquium, in Jena (July, 1994).

To my surprise, the first data set obtained by my students in 1986, on the number density of surface crystals N_s (crystals/unit area), in mechanically polished specimens of a diopside glass, a composition which does not show volume nucleation, did **not** vary with time of heat treatment at 820 C ($T_g \sim 730$ C). The scatter in N_s (50%) was much larger than that typical of volume nucleation measurements (10%). The evolution of overall surface area crystallized was quite well described by the Kolmogorov-Avrami equation, without recourse of any adjustable parameter, for the case of **instantaneous nucleation from a constant number of sites**. Hence, surface nucleation reached saturation in the early stages.

Another research was carried out with a microscope slide glass [18], and the effect of the surface condition was tested

by using three types of specimens: as-received, mechanically polished and fire-polished samples treated from 715 to 1000 C ($T_g \sim 550$ C) for time periods of up to 30h. Figure 11 shows the dependence of the number density of devitrite crystals with time, temperature and surface condition. As for diopside, there was a large scatter in the experimental values, specially for the as-received specimens. However, for a given surface treatment these values were insensitive to variations in heat treatment! The effect of surface condition was clearly dominant. Another surprising result was that fire-polished samples did **not** show any crystals at 730 C up to 7.5 hours!

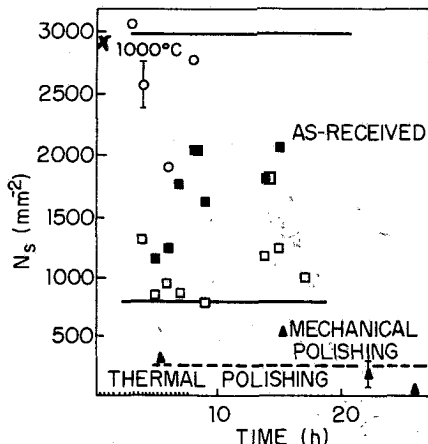


Figure 11. Crystallite density of devitrite on the surface of a microscope slide glass. As-received surfaces 715 C (o), 730 C (■), 735 C (□) and 1000 C (x) [18].

At that time, 1988, I was reluctant to publish the results presented above, mainly due to the unexpected time and temperature insensitivity of N_s . I finally decided to present them at the IV Otto-Schott Colloquium in Jena, in 1990, to a skeptical audience. However, to my surprise, in that same Colloquium, Ralph Muller had a poster showing a very similar behavior of fractured surfaces of cordierite glass. No time or temperature variation in the number of μ -cordierite crystals was observed for a wide range of thermal treatments.

All studies of surface crystallization described so far used single-stage thermal treatments. The final shot came from Kalinina et al. [19], who used the standard double-stage treatments in a cordierite glass, from 140 to 860 C ($T_g = 933$ C for 1.5h) for periods up to 450 h! Again, the number density of μ -cordierite crystals were time and temperature independent, confirming the other studies. However, another phase, x-phase, did show a different temperature dependence, i.e., a bell shaped curve, similar to volume nucleation curves. Thus, in at least one case (x-phase) the surface nucleation rates were sufficiently small to be measured. A summary of the most relevant studies up to 1992 is given in [20].

Conclusions

The surface nucleation sites saturate in the early crystallization stages. Thus N_s appears to be constant. In most cases, the surface nucleation rates are too fast to be measured in wide temperature ranges, from T_g to T_m . This insensitivity to temperature is probably due to the small value of surface energy associated to heterogeneous nucleation. Hence, the Turnbull ratio, α , is expected to be smaller than 0.3, because in this case, the nucleation parabola should be quite flat. No crystallization is observed on pristine, clean, surfaces or internal bubbles, as predicted by simple thermodynamic arguments. Surface nucleation is mainly due to contamination of solid particles, whose number is inversely proportional to the degree of surface perfection and cleanliness. There is scope for further studies of surface crystallization of glasses with well characterized surfaces to determine the active contamination centers and the actual surface nucleation rates. A quantitative evaluation of the Turnbull ratio would be most enlightening.

I deeply thank my students and colleges, the ICG, and the financial support of CNPq, PADCT, FAPESP, CAPES and RHAÉ.

REFERENCES

- [1] D. Uhlmann, J. Zarzycki, S. Shoules and others- Discussions of the Faraday Society (1970)] 50, 220.
- [2] E.D. Zanotto, A.F.Craievich and P.F.James- J.Mat. Science 21(1986)3050.
- [3] E.D. Zanotto and P.F.James- Glastech. Ber. 56K(1983)794.
- [4] A.F.Craievich, E.D.Zanotto and P.F.James- Bull. Soc. Franc. Min. Crist. 106(1983)169.
- [5] E.D.Zanotto and P.F.James- J.Non-Cryst. Solids 74(1985)373.
- [6] P.F.James, B. Scott and P. Armstrong-Phys. Chem. Glasses, 19 (1978)24.
- [7] K.F.Kelton- Sol. State Phys., 45(1991)75.
- [8] M.C.Weinberg and E.D.Zanotto- J. Non-Cryst. Solids 108(1989)99.
- [9] E.D.Zanotto- Proc. 34 Brazilian Congress Cer., v.2(1990)625.
- [10] S.Manrich and E.D.Zanotto- Ceramica (1993) submitted.
- [11] M.C.Weinberg; E.D.Zanotto and S.Manrich- Phys. Chem. Glasses, 32(1992)99.
- [12] P.F.James- J. Non-Cryst. Solids, 73(1985)517.
- [13] E.D.Zanotto- J. Non-Cryst. Solids, 89(1987)361.
- [14] E.D.Zanotto and M.C.Weinberg, Phys. Chem. Glasses, 30(1989)186.
- [15] E.Muller, K.Heide and E.D.Zanotto- J. Non-Cryst. Solids, 155(1993)56.
- [16] E.D.Zanotto and E.Muller- J. Non-Cryst. Solids, 130(1991)220.
- [17] R.Muller- PhD Thesis- University of Berlin (1989).
- [18] E.D.Zanotto- J. Non-Cryst. Solids, 129(1991)183.
- [19] A.M.Kalinina, N.S.Yuritsin, V.M.Fokin and V.N.Filipovich- Proc. Nat. Conf. Vitreous State, Leningrad (1990)235.
- [20] E.D.Zanotto- in Nucleation and Crystallization in Glasses and Liquids, Amer. Ceram. Soc. (1993)65.

Part I, Glass Manufacturing

RECYCLING OF CULLET AND FILTER DUST - CHALLENGES TO THE MELTING OF GLASS

Helmut A. Schaeffer

Hüttentechnische Vereinigung der Deutschen Glasindustrie (HVG)

Deutsche Glastechnische Gesellschaft (DGG)

Frankfurt am Main, Germany

Increasing ecological constraints linked with economic advantages have induced the recycling of cullet predominantly in the container glass industry as well as the recycling of filter dust in various branches of glass production. The recycling of cullet originating from non-returnable glass packaging was introduced more than 20 years ago, whereas the recycling of filter dust originating from waste gas treatment was started only a few years ago. The transition from employing basically constant raw materials to utilizing increasing amounts of recycled glass as the major batch material and the introduction of filter dust as an additive (refining agent) have imposed new challenges on glass melting. Difficulties result from the incorporation and possible enrichment of impurity components such as metals and halogens and furthermore from the unknown and changing contaminations of organic additives and/or reducing agents. Special efforts are required to ensure a reproducible glass quality, e.g. an *in situ* control of the redox state during glass melting by means of electrochemical measurements. Finally, variations of glass properties due to the utilization of recycling glass and filter dust will be discussed.

1. INTRODUCTION

The remelting of glass cullet has been employed very likely since the early days of glass manufacturing. By using cullet in the batch the melting process is facilitated due to the saving of the reaction enthalpies of the primary raw materials when forming the glass melt. Thus an energetic advantage is gained by employing cullet. The melting of glass using 100% cullet would theoretically result in an energy saving in the order of 30% for soda-lime-silica glasses (1).

A further advantage in utilizing cullet consists in reducing the primary raw materials in the batch which is of particular interest for the more expensive raw materials such as the alkali oxides (2).

The recycling of domestic (in-house) cullet is traditional practice in glass melting; the recycling of foreign cullet, however, was started only 20 years ago. Ecological constraints, in particular the limited availability of landfill sites, initiated the large scale recycling of glass packaging products such as bottles and jars. The development of glass recycling is shown in Table 1 for the case of Germany. The recycling rate in Germany has reached a value of 63% (in 1991) corresponding to 2.3×10^6 tons of recycled cullet. In terms of absolute tonnages of recycled glass the German glass industry is leading, but with respect to national recycling rates it is surpassed by The Netherlands (73%) and Switzerland (72%), see Table 2.

As compared to the recycling of cullet, the recycling of filter dust was started only a few years ago. Filter dust is generated as an undesirable by-product as a result of waste gas treatment with the help of an absorption medium and by employing either electrostatic precipitators or bag filters. Utilizing calcium hydroxide as absorption medium the filter dust consists basically of calcium sulphate and unreacted calcium hydroxide. It turned out that the most elegant way

Table 1. Recycling of Packaging Glass in Germany (3)

| year | domestic sale in 10 ⁶ t | recycled glass in 10 ⁶ t | recycling rate % |
|------|---------------------------------------|--|---------------------|
| 1974 | 2.3 | 0.15 | 6.5 |
| 1980 | 2.5 | 0.57 | 23 |
| 1985 | 2.4 | 1.05 | 43.5 |
| 1990 | 3.3 | 1.8 | 54 |
| 1991 | 3.6 | 2.3 | 63 |
| 1992 | 3.8 | 2.5 | 65 |

Table 2. Recycling of Packaging Glass in Europe for 1992 (4)

| country | recycled glass in 10 ³ t | recycling rate % |
|----------------|--|---------------------|
| Germany | 2459 | 65 |
| France | 1100 | 44 |
| Italy | 786 | 53 |
| United Kingdom | 459 | 26 |
| Netherlands | 378 | 73 |
| Spain | 312 | 27 |
| Belgium | 216 | 54 |
| Switzerland | 212 | 72 |
| Austria | 175 | 64 |
| Sweden | 76 | 58 |
| Denmark | 75 | 48 |
| Portugal | 62 | 30 |
| Greece | 30 | 20 |

to disengage from the filter dust is its addition to the glass batch where it can substitute the refining agent. The quantity of filter dust amounts to about 3 kg/t glass, which corresponds e.g. for the German glass industry to about 18×10^3 t of filter dust per year. Therefore the recycling of filter dust is an economical relevant step since it relieves the glass industry from providing high costs for the storage of special waste.

2. UTILIZATION OF RECYCLED CULLET FOR GLASS MELTING

2.1. IMPURITIES IN RECYCLED CULLET

For primary raw materials the specifications are well established and their quality control is assured by various analytical tools. In the case of recycling foreign cullet for the container glass industry the situation is much more complicated. In order to ensure stability in glass homogeneity and coloration the recycled cullet has to be separated from impurities such as ferrous and non-ferrous metals, ceramic materials (porcelain, stones, slags etc.) and organic components

(plastics, paper, food residues etc.) This kind of cullet processing has reached an advanced stage of automation (5).

Furthermore the foreign cullet has to be separated according to colour (flint, green, amber). Unseparated cullet (so-called mixed cullet) can be introduced to green and to a certain extent to amber glass, but not to flint glass. With a typical production of flint container glass in the order of 50% of total packaging glass production in Germany, therefore not even a 50% recycling rate can be attained with unseparated cullet. Thus colour separation of recycled cullet is mandatory in order to achieve high recycling percentages. Various systems with optical detecting devices are now available for the automatic separation of cullet according to colour (6), however, the first and main approach is the collection of non-refillable ("one-way") glass packaging products according to colour.

Table 3. Average Annual Data of Impurities in Processed Foreign Cullet According to Colour (7, 8)

| [g/t] \triangleq ppm | 1981 | 1987 | 1993 | |
|--|------|------|------|-------------|
| cps *) | 115 | 51 | 27 | |
| Al | 54 | 9 | 2 | flint glass |
| Pb | 18 | 2 | 4 | |
| Fe | 1.6 | 0.5 | 1.8 | |
| | | | | |
| cps *) | 197 | 46 | 28 | |
| Al | 234 | 69 | 19 | green glass |
| Pb | 98 | 12 | 18 | |
| Fe | 1.6 | 0.05 | 2.5 | |
| | | | | |
| cps *) | 234 | 57 | 34 | |
| Al | 173 | 36 | 11 | amber glass |
| Pb | 87 | 8 | 14 | |
| Fe | 0.4 | 0.1 | 1.9 | |
| | | | | |
| *)cps \triangleq ceramics, porcelain, stones | | | | |

Table 3 shows that even though remarkable improvements in the elimination of impurities were achieved over a time period of 12 years, yet, no absolute "purification" of the foreign cullet can be realized. Thereby in many cases the achieved level of impurity concentrations determines the percentage of cullet which can be introduced into the batch without affecting the required reproducibility of the melting and forming properties and/or the properties of the final product.

Besides the separable impurities which are listed in Table 3, the recycled foreign cullet contains non-separable impurities which were incorporated during the melt history of recycled cullet due to different origins of the primary glass products, other glasses not based on soda-lime-silica (e.g. opal glasses, lead oxide containing glasses etc.) and due to enrichment effects in the course of recycling (e.g. filter dust recycling, interaction with combustion atmosphere and with refractory materials of the glass tank). Thus recycled cullet can contain various amounts of iron

oxide, chromium oxide, sulphur, fluorine and chlorine, as well as lead oxide, barium oxide, tin oxide.

Table 4. Average Annual Data of Fe₂O₃ and Cr₂O₃ Concentrations in Processed Foreign Cullet (8)

| wt % | 1984 | 1987 | 1990 | 1993 | |
|--------------------------------|-------|-------|--------|--------|-------------|
| Fe ₂ O ₃ | 0.077 | 0.076 | 0.0776 | 0.0723 | flint glass |
| Cr ₂ O ₃ | 0.008 | 0.005 | 0.005 | 0.005 | |
| Fe ₂ O ₃ | - | - | 0.353 | 0.361 | green glass |
| Cr ₂ O ₃ | - | - | 0.196 | 0.216 | |
| Fe ₂ O ₃ | 0.300 | 0.30 | 0.309 | 0.319 | amber glass |
| Cr ₂ O ₃ | 0.026 | 0.033 | 0.043 | 0.044 | |

Table 4 displays data with respect to colouring impurities such as iron oxide and chromium oxide. The requirements for the production of "pure" flint glass are very stringent with respect to the concentrations of iron and chromium oxide. To illustrate this sensitive dependence it can be stated that only 50 g of wrongly coloured glass can be tolerated in 1 t of recycled flint glass (i.e. 50 ppm). Such requirements can probably not be fulfilled with colour-separating technology. The high purity of recycled flint cullet can only be achieved by careful hand sorting or by mechanical negative selection from colour-separated cullet (6).

It was proposed to initiate an international quality standard for recycled cullet (9). However, the outlined variations of the cullet impurities, the different collecting and handling procedures of the cullet represent a technical and economical barrier to assess such an endeavour. Nevertheless, on the company level such quality requirements with respect to separable impurities and grain size do exist.

2.2. CULLET AS MAJOR BATCH COMPONENT

In many glass plants of Western Europe the introduction of 80 to 100 % of recycled cullet for the melting of green container glass is nowadays common practice. Thus recycled cullet has become the major raw material component in the glass batch. This "novel" batch formula gives rise for reinvestigating the various aspects of glass manufacturing as compared to a batch comprised predominantly of primary raw materials.

2.2.1. CHEMICAL COMPOSITION

With increasing amounts of foreign cullet in the batch only few options are left for the realization of particular target compositions. In countries with a high recycling rate the glass composition becomes almost indistinguishable among glass plants. There are interesting consequences to be noted: ingredients added to the glass will be also recycled and remain in the glass composition of the cullet for long periods. A beneficial additive e.g. would be lithium oxide as a flux agent in the melting process ("chemical boosting"), or boron oxide for the im-

provement of chemical resistance. On the other hand lead oxide in the recycled cullet is presently strongly debated. Lead oxide has entered the recycling process either intentionally (by exploiting the melt accelerating effect of lead oxide containing cullet) or unintentionally via the oxidation of lead metal impurities in the recycled cullet. The average lead content in the recycled glass in Western Europe amounts to about 200 ppm. Unexpectedly this low level is in conflict with a regulatory bill passed by the Coalition of North Eastern Governors in the US restricting the sale of packaging materials containing impurities of heavy metals at the ppm level. The regulatory bill foresees limits of less than 100 ppm for the sum of lead, cadmium, mercury and hexavalent chromium (10). Unintelligibly this bill is also used as the basis for the European Community Directive on Packaging which is presently before the Parliament.

This example illustrates the susceptibility of the recycling process to intricate after-effects and it should lead to a more pronounced responsibility to prevent the incorporation of potentially detrimental components.

2.2.2. REDOX STATE

As compared to glass melting with primary raw materials the melting with recycled cullet gives rise to alterations of the redox state of the glass melt due to various amounts of organic materials which are part of the recycled glass products. Whereas a cullet-free batch can be characterized by the redox number or by the chemical oxygen demand of the different components, it is very difficult to assign such characteristics to cullet which fluctuates locally and with time with respect to its organic impurities. Nevertheless, successful attempts for the characterization of the redox state of cullet are reported (11).

The reducing power of the organic impurities lowers the oxidation state of the glass melt and thereby has an impact on the coloration of the glass. In order to maintain the target colours it becomes necessary to provide additives with oxidising power which compensate the reducing organic impurities. Due to the lack of feasible oxidising agents it can become attractive to exploit the higher oxidation state of flint glass cullet in order to adjust the required redox state of green or amber glass. On the other hand, however, the introduction of a mixture of differently coloured recycled cullet gives rise to the release of SO_2 and thus to foam formation. Therefore the oxidation of cullet which is contaminated with organic materials represents a challenge to glass melting and various approaches are being discussed to overcome this problem, e.g. "weathering" of recycled cullet, preheating of the cullet batch and bubbling of the glass melt with oxygen.

3. UTILIZATION OF FILTER DUST IN GLASS MELTING

The dry absorption of gaseous species such as SO_2 , SO_3 , HCl , HF and Se-containing compounds (decolorizing agent for flint glasses) which are present in the waste gas requires the employment of either calcium hydroxide or sodium carbonate (in the form of light soda). The absorption products are collected by means of an electrostatic precipitator (12) or a bag filter (13). They consist of calcium sulphate, calcium carbonate, calcium chloride, calcium fluoride and unreacted calcium hydroxide or of sodium sulphate, sodium chloride, sodium fluoride and unreacted sodium carbonate, respectively.

In the case of high fluorine concentrations in the waste gas it is advantageous to utilize calcium hydroxide as absorption medium which forms calcium fluoride with a high absorption rate of up to 90%, whereas the utilization of soda results only in an absorption rate of 30% in the form of sodium fluoride (calcium fluoride is thermodynamically more stable than sodium fluoride).

On the other hand the opposite holds for high chlorine concentrations in the waste gas: soda is more effective to absorb chlorine as compared to calcium hydroxide, because sodium chloride is more stable than calcium chloride.

For waste gases which contain simultaneously high levels of fluorine and chlorine it is advisable to use a mixture of calcium hydroxide and soda as absorption media or to provide a two stage absorption process, first with calcium hydroxide, then with soda. The practical experience has shown that filter dust can be added to the batch and thus can be recycled provided that respective batch composition corrections are carried out, taking particularly into account that sodium sulphate and calcium sulphate act as refining agents (14). It has been reported that calcium sulphate is a less effective refining agent for glass melts containing more than 90% recycled cullet. This is not surprising because the capability of calcium sulphate to act as refining agent depends on the reaction with soda in the batch to form sodium sulphate. This reaction mechanism disappears with batch compositions consisting of hardly any raw materials. Therefore, the use of light soda as absorption agent is of advantage provided that the fluorine concentration in the waste gas is sufficiently low.

3.1. IMPURITIES IN THE FILTER DUST

The recycling of filter dust requires a careful study of the compositional changes of the filter dust (15). Besides sulphur, especially heavy metals and halogens are incorporated in the filter dust and thus can lead to enrichments of certain elements in the glass (16), see Table 5. Potential candidates are nickel and vanadium in the case of firing with heavy oil, furthermore lead, cadmium, selenium, chlorine, fluorine, titanium and tin from the raw materials and/or recycled cullet; the latter elements can also originate from the hot end treatment using SnCl_4 or TiCl_4 .

Mass balances of the elements being added (via fuel, batch, filter dust) and being released (via emission, filter dust and glass product) have to be performed and discussed with respect to potential enrichment effects. So far no alarming enrichments have been detected which could be attributed to the recycling of the filter dust (12). The filter dust recycling will be jeopardized when the glass melt is saturated with the elements in question. It can not be excluded that this case will occur eventually.

3.2. OXIDATION STATE OF FILTER DUST

Only recently it was recognized that the filter dust originating from electrostatic precipitators (12) or bag filters (13) not necessarily acts as a refining agent, but can possess reducing properties. In terms of the chemical oxygen demand (COD) values for filter dust were reported (17) which correspond to reducing agents such as calumite. This observation has raised the question for the parameters determining the oxidation state of the filter dust, i.e. which are the parameters favouring the formation of sulphites or even sulphides instead of the expected sulphate formation. Which sulphur compound is formed depends e.g. on the type and grain size of the absorbents, the partial pressure of oxygen and water in the waste gas, and on the temperature and time in the reactor of the absorption stage. Presently an investigation is carried out to elucidate the parameters which have an impact on the oxidation state of the filter dust (18).

Table 5. Average sulphur and impurity concentrations with their deviation ranges of filter dust and glass as monitored at a single regeneratively heated flint glass furnace (waste gas treatment: dry absorption with calcium hydroxide, electrostatic precipitator) over a period of 2 years with continuous recycling of filter dust (16)

| Component | Filter Dust | | Glass | |
|--------------------------------|-------------------|--------------|-------|-----------|
| | [mg/kg] \pm ppm | | | |
| TiO ₂ | 7.100 | \pm 4.000 | 497 | \pm 197 |
| V ₂ O ₅ | 580 | \pm 336 | 8 | \pm 5 |
| Cr ₂ O ₃ | 200 | \pm 110 | 45 | \pm 25 |
| MnO | 159 | \pm 87 | 94 | \pm 47 |
| Fe ₂ O ₃ | 1.700 | \pm 600 | 630 | \pm 90 |
| CoO | 96 | \pm 93 | 3 | \pm 1 |
| NiO | 100 | \pm 67 | 6 | \pm 5 |
| CuO | 90 | \pm 83 | 7 | \pm 3 |
| SeO ₂ | 5.100 | \pm 2.063 | 9 | \pm 7 |
| ZrO ₂ | 80 | \pm 78 | 71 | \pm 45 |
| CdO | 60 | \pm 31 | 6 | \pm 5 |
| SnO ₂ | 1.600 | \pm 1.490 | 130 | \pm 127 |
| PbO | 6.300 | \pm 5.270 | 186 | \pm 107 |
| F ⁻ | 7.400 | \pm 2.230 | 315 | \pm 275 |
| Cl ⁻ | 14.500 | \pm 5.370 | 460 | \pm 40 |
| SO ₃ | 261.000 | \pm 86.000 | 1.400 | \pm 100 |

4. REDOX CONTROL IN GLASS MELTS

The varying organic impurities in recycled glass as well as the partially reducing behaviour of filter dust have a negative effect on glass melting and consequently on the homogeneity and reproducibility of the final glass product. Therefore it is desirable - as a first step - to determine continuously by means of in situ measurements the "oxidation state" or the "redox state" of the glass melt.

Electrochemical methods can be exploited in order to monitor the oxygen activity and the quantities of polyvalent ions in the glass melt. The oxygen activity measurements can be carried out with the help of an electrochemical cell based on an oxygen ion - conducting solid electrolyte (yttrium-stabilized zirconia) as reference electrode (19). For some years experience has been gained in the container glass industry by placing the oxygen activity sensor in contact with the glass melt in the forehearth (1200-1250 C), a location of measurement optimally suited to characterize the conditioned glass melt prior to the feeding procedure (20, 21).

For the determination of the quantities of polyvalent ions in situ voltammetric measurements can be utilized. Especially the square-wave voltammetry has proved to be a powerful tool to characterize the glass melt with respect to polyvalent ions (22). First studies have shown that also under industrial conditions polyvalent elements, especially iron, can be detected (23).

Both electrochemical sensors are appropriate to establish an in situ redox control system which provides an early warning for deviations of the oxidation state. Furthermore such sensors can

be used to control batch additions and/or furnace parameters in order to achieve the required redox state and thereby to accomplish those glass properties which depend on the redox state.

5. CORRELATIONS BETWEEN GLASS PROPERTIES AND RECYCLED CULLET

The extensive recycling of glass raises the question whether specific glass properties can be maintained in a reproducible fashion. It is a widespread assumption that high portions of cullet in the batch can result in glasses of poor "workability" or increased "brittleness". So far no evidence was found that such a direct correlation exists. However, as was pointed out, the addition of recycled cullet has an impact on the oxidation state of the glass melt and thus in turn on a variety of glass properties. Therefore indirectly a complex property such as "workability" can become dependent of the amount and type of recycled cullet. It has to be recalled that variations of the oxidation state cause glass property variations in the viscous, viscoelastic and solid region (24). Of special importance are variations of the ferrous/ferric ratio which lead e.g. to variations in viscosity, infrared absorption and emission. These property changes give rise to changes of process properties such as convective flow and heat transfer in the glass melting furnace or heat radiation and heat removal in the glass forming moulds.

It was shown by Hessenkemper and Brückner (25) that soda-lime-silica glass which was melted under reducing conditions possesses lower elastic moduli and a lower relaxation modulus and therefore is less stiff and less brittle, and displays moreover a larger high temperature tensile strength as compared to oxidized glass. This means that a reduced glass (green and especially amber glass) should show a better workability than an oxidized flint glass. However, workability can depend on further parameters which are either redox-dependent (e.g. solubility of gases) or structure-dependent (e.g. phase separation, clustering, microcrystals, inhomogenities) (26). Nevertheless, it can be stated that the major source for property variations is due to unstable redox states of glass melts. Therefore the installation of an in situ redox control system is an important measure to improve the reproducibility of glass melting and glass forming properties as well as glass product properties.

6. CONCLUSIONS AND OUTLOOK

The recycling of foreign cullet and of filter dust represents an evolutionary process in glass manufacturing. The introduction of recycled cullet as a major batch component has caused a new awareness in the melting of glass. New challenges occurred in order to maintain the glass quality requirements. These challenges were and will be met by providing an improved data acquisition of the chemical analyses, by improving computer-aided process control systems combined with a redox control system, and by enlarging the experience in the identification of glass defects and assessing their cause-and-effect relationships. Considering moreover the ecological and energetical optimizations which were accomplished, it becomes obvious that the state-of-the-art of glass melting in the container glass industry has reached a higher level of efficiency.

From the point of view of materials science, glass is an outstanding inorganic packaging material with respect to chemical resistance and inertness when in contact with food or beverages. Glass is optimally suited for recycling not only in the case of returnable and refillable glass containers, but especially for the internal recycling, i.e. remelting of recycled cullet. The material glass is free of any inherent effect of "down-cycling" in the recycling process.

Furthermore, the material glass - as a frozen-in, undercooled silicate liquid - possesses a high solubility for most elements which might be taken up as impurities during the recycling procedure. High solubility means that the impurity elements become part of the glass network structure and thus are protected against chemical attack or leaching phenomena. Nevertheless, enrichment effects of certain elements should be carefully monitored and their increase should be prevented by further improved cullet separation techniques. The existing levels of colouring agents presently limit a further increase of recycled cullet in the melting of flint glass. An increase will depend on a change in the customer attitude to accept also flint glass with a slight tint.

The container glass industry has demonstrated very successfully the realization of the recycling concept and therefore can serve as a model for other branches of the glass industry.

Moreover, the experience which has been gained with the recycling of cullet can be exploited by the glass industry in becoming active in the field of waste glass melting, i.e. vitrification of hazardous and toxic wastes such as fly ashes, filter dusts and slags from incinerators. The glass industry has the expertise also to tackle these novel challenges successfully.

7. REFERENCES

- (1) W. Trier, J. Lauter, L. Schumacher, DGG, FA-Bericht No. 71 (1978)
- (2) A. Reynolds, Proc. First ESG Conf. Sheffield (1991) 247
- (3) BV Glas und Mineralfaser, Düsseldorf, personal communication
- (4) CPIV-INFO, No. 70 (1993) 26
- (5) K.-H. Gitzhofer, Tagungsbd. VDM-Tag. (1992) 209
- (6) K.-H. Gitzhofer, Glastechn. Ber. 64 (1991) 9
- (7) P. Buchmayer, HVG-Fortbildungskurs (1988) 147
- (8) P. Buchmayer, personal communication
- (9) J. H. Edington, Proc. First ESG Conf. Sheffield (1991) 232
- (10) Model Toxics Legislation / CONEG (1989)
- (11) M. Nix, H. P. Williams, Glastechn. Ber. 63 K (1990) 271
- (12) U. Kircher, Glastechn. Ber. 66 (1993), to be published
- (13) B.M. Scalet, C. Ferrero, Proc. 2nd ESG Conf. Venice (1993), to be published
- (14) G. Bachmann, H. Drexler, Glastechn. Ber. 65 (1992) N 61
- (15) W. Trier, Glastechn. Ber. 60 (1987) 225
- (16) J. Kappel, FhG-Berichte 3 (1990) 36
- (17) J. Jansen; personal communication
- (18) HVG/AiF research project
- (19) H. Müller-Simon, K. W. Mergler, Glastechn. Ber. 61 (1988) 293
- (20) H. Müller-Simon, K. W. Mergler, H. A. Schaeffer, Proc. XV. ICG Congress, 1a (1989) 150
- (21) H. Müller-Simon, K. W. Mergler, H. A. Schaeffer, Proc. First ESG Conf. Sheffield (1991) 148
- (22) C. Montel, C. Rüssel, E. Freude, Glastechn. Ber. 61 (1988) 59
- (23) M. Zink, C. Rüssel, H. Müller-Simon, K. W. Mergler, Glastechn. Ber. 65 (1992) 25
- (24) A. Lenhart, H. A. Schaeffer, Proc. XIV. ICG Congress, 1 (1986) 147
- (25) H. Hessenkemper, R. Brückner, Glastechn. Ber. 63 (1990) 244
- (26) F. Geotti-Bianchini, Glastechn. Ber. 65 (1992) 306 & 329

CULLET TREATMENT EQUIPMENT FOR THE GLASS INDUSTRY

Dipl. Ing. (FH) Jens Rosenthal
EME Maschinenfabrik Clasen GmbH

Cullet is one of the most important raw materials in glass melting. The condition of the cullet used has a significant effect on the quality and characteristics of the glass produced. The use of cullet offers advantages in glass melting, and correct handling and suitable treatment equipment help produce high quality factory and foreign cullet.

INTRODUCTION

The production of glass, which can be traced back to 3000 years BC, has been continuously developed and improved throughout its history. The first glass types were the products of chance, but modern glass is a technical material, which is produced with exactly defined properties for specific needs. The raw materials, and the necessary handling and treatment equipment, must be capable of meeting the stringent requirements placed on them.

Used alongside the classic raw materials such as sand, soda ash and limestone, cullet is becoming increasingly important as a raw material. Nowadays cullet is the main raw material for container glass. The reasons for this are well known, but are repeated here for the sake of clarity:

- savings in melting energy and expensive raw materials
- increased life of the melting tanks
- environmental protection, with fewer raw materials being required, lower air pollution and less waste produced.

The trend towards the use of more cullet can be seen in glass factories all over the world. As more good quality cullet is required, so cullet treatment technology is becoming more important.

CULLET TREATMENT

In the glass industry a distinction is made between factory and foreign cullet.

Factory cullet is the production waste from the glass factory itself, which is returned to the melting process. Foreign cullet is used glass, collected regardless of the original manufacturer, and remelted, i.e. recycled.

Methods and equipment for cullet handling can be illustrated using the container industry as an example.

FACTORY CULLET TREATMENT

When glass is manufactured cullet is produced at the forming machines (hot end) and during sorting (cold end). Experience has shown that cullet should be treated and returned directly to the melting process. This method virtually eliminates the risk of contamination by foreign bodies, and uneconomic and unnecessary transport and storage. All melting furnaces should have their own cullet return system to prevent mixing of different types of glass. Figure 1 shows the basic layout of a factory cullet treatment system.

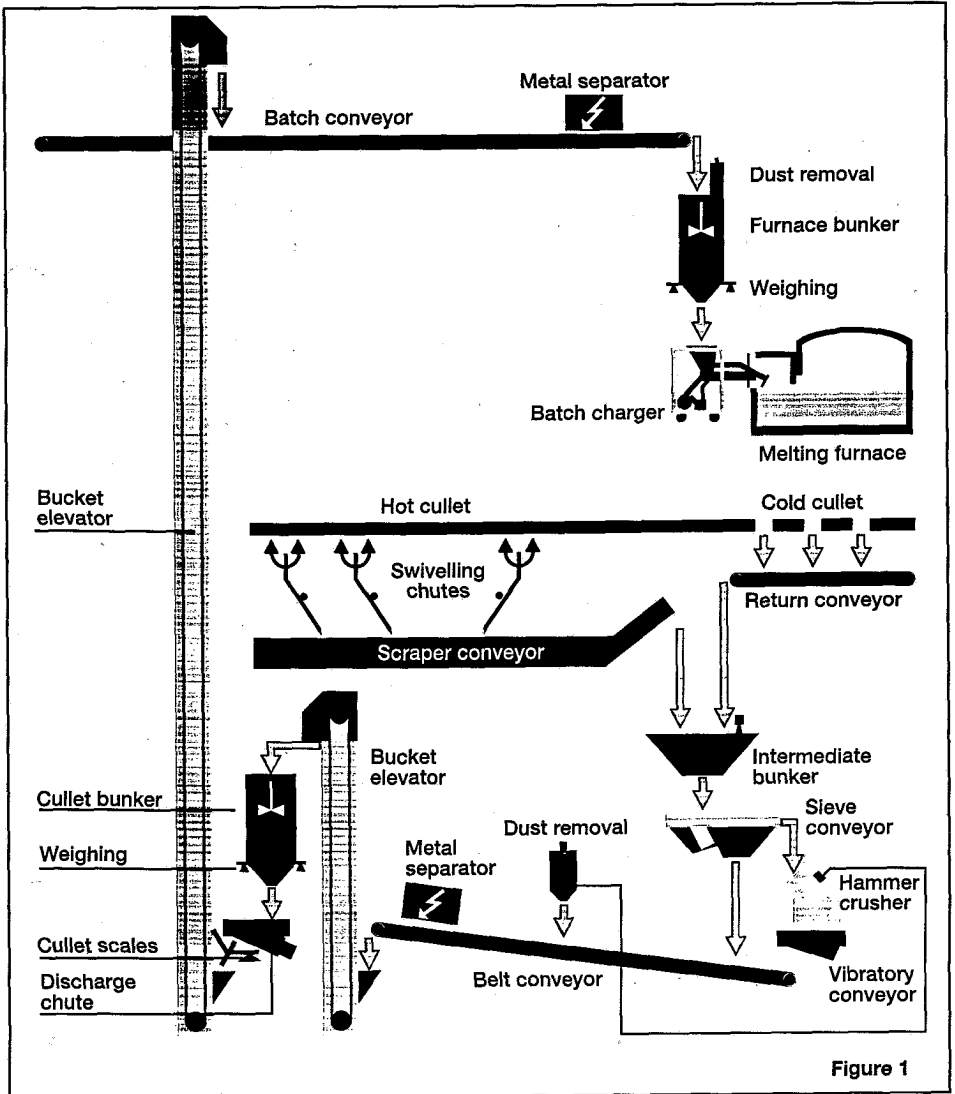


Figure 1

Scraper Conveyor

Glass gobs and hot glass articles pass down chutes into a scraper conveyor, through which cooling water flows. The scraper conveyor must fulfill four functions:

- cooling the hot glass to a temperature suitable for further treatment
- hot glass transport
- draining cooled cullet
- reduction in size of large glass gobs

In order to prevent overflowing of the scraper conveyor and damage to the downstream equipment the chutes are designed to swivel away automatically from the scraper conveyor if a disturbance occurs, and fill waiting transport containers.

Owing to the fact that furnaces now have higher melting capacities, and the necessity to reduce production costs, conventional double-link scraper chains no longer meet the demands of the industry. EME have developed the single link Fortia chain. This special chain has a service life three times longer than that of a standard double link chain, maintenance costs are greatly reduced and it can be used in both single and double-bottomed scraper conveyors.

Double-bottomed scraper conveyors must be installed where the cooling length available is not sufficient to cool the hot glass to the required temperature. Heavy glass gobs are flattened by crushing rollers before they are fed into the scraper conveyor. The larger surface area thus obtained permits faster cooling. Glass articles floating on the water surface can be shattered by a breaker and then discharged.

The transport velocity and the quantity of cooling water introduced are controlled on the basis of the amount of glass entering the conveyor. This ensures that the hot glass entering the conveyor is sufficiently cooled, whilst minimising the water and energy consumptions and the wear.

Modern installations utilise a water circulation system in which the water is cleaned. It is particularly important that the fine glass particles and all oils and fats are removed from the water.

Cullet from both the hot and cold ends is transported along belt conveyors to a hopper. It is essential that an overbelt magnetic separator is installed at a suitable location on the belt conveyor to ensure that all metallic impurities are removed from the cullet before the crusher.

The fact that the wet hot cullet and the dry cullet are brought together before being sorted is advantageous. The dry cullet is moistened which considerably reduces dusting, and the volume of moisture on the wet cullet is also reduced. This prevents the wet, fine glass granules from caking on the conveying equipment and on the walls of the storage bunkers.

Crusher

The mixed cullet is removed from the hopper via a screening chute. Cullet pieces which are too large to be melted are crushed in a hammer crusher.

The type HPB hammer crusher was designed specifically for the difficult conditions encountered in the glass industry, and offers the following advantages:

- very little fine grain cullet is produced
- long service life, because of wear resistant parts, such as rotor, hammers and crushing faces,
- easy maintenance

In order to keep dusting as low as possible the crusher and conveying equipment should be kept under a partial vacuum, and the air sucked off should be passed through a filter.

Storage

After being crushed the treated cullet is stored in a silo. It can then be weighed as required and stored together with the batch in the furnace bunker.

FOREIGN CULLET TREATMENT

As a result of the steadily increasing raw material and energy costs, and growing environmental awareness, the recycling of used glass has become more and more important. The necessity to reduce the level of impurities in the cullet has increased with the rise in the amount of recycled glass added to the melt. Glass from collections always contains impurities, which may cause bubbles or stones, or other faults in the glass. The most common impurities are dirt, ceramics, metal caps, paper and plastic.

The aim of a recycled glass treatment plant must be to maximise the cullet quality and the sorting efficiency whilst minimising the costs. This is the only way in which the use of cullet can be increased up to the theoretical maximum.

Used glass collection

Information provided for consumers, and legislative pressure on industry has led to an increase in glass recycling in many countries in recent years. Success is shown by the high proportion of used glass which is returned by consumers for re-use. In western Europe it amounts to approximately 39 kg per inhabitant per year.

The accuracy and care with which raw cullet is collected, and the condition in which it is supplied to the treatment plant has a major effect on the quality of cullet produced. The quality is much higher and less glass is lost in treatment if the used glass articles fed into the treatment plant are sorted and cleaned, and undamaged.

Process technology (figure 2)

Recycled glass from the storage bunker is fed in controlled quantities into the treatment system by a vibratory chute. A conveyor type weighing scale is used to monitor the amount of cullet fed to the treatment system and control the vibratory chute.

Removal of ferromagnetic materials by an overbelt magnetic separator is followed by the first manual sorting. Coarse impurities such as plastic, wood, refractories, ceramics and similar materials are removed at this stage. The significance of this treatment step should not be underestimated. The following example clearly illustrates this point.

If a stoneware bottle weighing 700 g enters the cullet crusher, it will be broken up into more than 630 pieces⁽¹⁾. As a result of the size of the broken pieces no more than 130 pieces, with a total weight of 540 g, will be removed. The remaining 500 pieces remain in the cullet. A hypothetical calculation based on one day's production with this cullet gives production losses of 14% as a result of ceramic stones.

It is obvious that large, brittle foreign bodies are easier to remove from cullet than numerous fragments. However, if certain technical guidelines are followed the sorting staff are able to recognise and remove impurities.

If only mixed colour cullet is available, and if sufficient complete articles are present, colour sorting is then carried out. The cullet is separated into coarse and fine grain fractions on a bar sieve. The fine grained mixed glass is taken directly to further processing. The coarse grained glass is optically colour sorted and stored in intermediate bunkers. The individual colours are returned for further treatment as and when required.

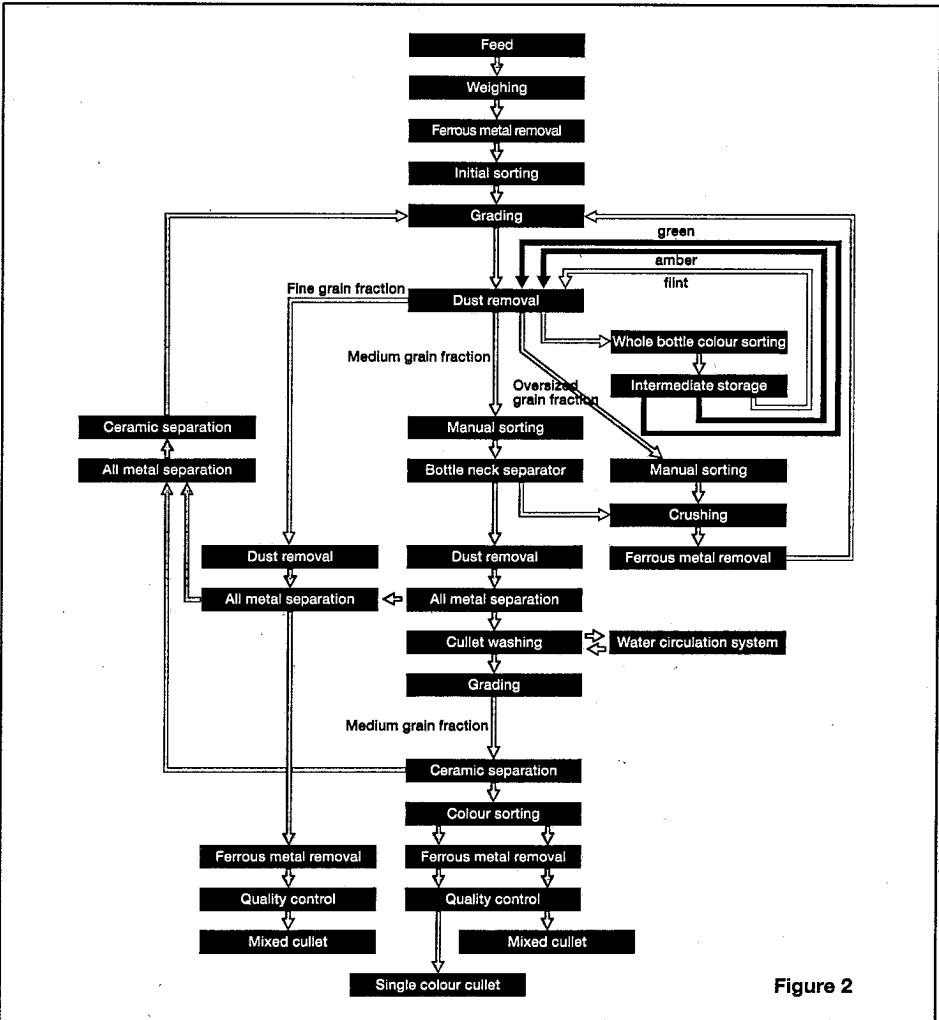


Figure 2

After pre-sorting, the cullet is normally passed through a grading screen, which sorts the different grain size fractions. The number of fractions is partly determined by technical aspects of the treatment process and partly by the capacity of the equipment.

A hammer crusher is used to crush large pieces and bottle necks from the fraction > 20 mm diameter. Therefore only large pieces of cullet or those with attached metal or plastic contamination are broken up. This ensures that the proportion of very fine cullet in the melt is kept as low as possible ⁽²⁾. This process removes the impurities from the glass so that they can be sorted out without glass loss.

A further manual sorting removes large contaminants from coarse and medium cullet fractions prior to crushing. Manual sorting is assisted by the fact that the conveyor belt carries a much lower load - one layer is ideal - and that the grain size range is limited. At this point the example with the ceramic bottle should be recalled to mind.

The crushed material is returned to the grading screen. A suction unit is installed over the grading screen and the subsequent vibratory chutes to remove lightweight substances such as paper, plastic bags and lightweight caps from the cullet flow.

After grading the cullet is passed to a metal separator, which removes all magnetic and especially non-magnetic metals. The metallic impurities are detected either by an electric field and then discarded or are removed by an eddy current separator. These separators have the advantage that the glass loss is very low, but the disadvantage that the degree of separation is less than with separators with permanent magnetic rotors.

There are economic and technical reasons why fine grain fraction cannot be further treated. This cullet is either added to the melt or thrown away, depending on its quality.

The cullet can be washed if high quality requirements must be met. In particular, washing removes organic impurities sticking to the cullet. Washing units have a water recirculation system. If the cullet has a high level of contamination it can be necessary to treat the circulating water. It should be noted that so far no sensible use has been found for the organic sludge produced by the washing process.

The use of washed cullet offers several advantages in the melting process. There is no tendency to foam in the furnace, refining problems and colour streaks are avoided and the glass colour is not affected ⁽³⁾. As only the medium and coarse grained cullet is washed, and mechanical draining is carried out after the washing, the residual moisture in the cullet amounts to only 1%.

Washed cullet is also easier to treat in optical sorting units, where less glass is lost when the cullet is clean. The washed cullet is more transparent and therefore much better quality can be achieved.

The treated cullet is sieved again, drained and fed into the ceramic separator according to grain size. Ceramic separators are optical sorting machines, in which the light transmission of the particles is measured. These particles - ceramics - are removed if the light transmitted by the particles is below a freely selectable level. Cullet washing assists the detection of transparent/opaque particles.

Waste reduction is an important principle of daily life, and is just as valid for used glass treatment. Each treatment stage results in a certain loss of cullet ⁽⁴⁾. This applies in particular to

the metal and ceramic separators. Material sorted out in these machines should therefore be processed again in a second metal and ceramic separating stage. Experience has shown that when the level of contamination in the raw cullet increases more glass is lost and the quality of the product decreases. Therefore metal and ceramics should not be removed in a single unit. If this is done the waste produced is not pure, but is a mixture of metal and ceramics. It is only possible to recycle the waste after a further reprocessing stage.

Increasing use is now being made of colour sorting devices for crushed cullet. This equipment is installed after the ceramic separator and is used to remove cullet of differing colours from the

flow when pure colour is required. Colour separation of crushed mixed colour cullet is not economic at the present time.

The impurity-free cullet can now be returned to the glass melt as a pure raw material.






| Treated cullet | |
|---|---|
| 1. Maximum impurity levels: | |
| Ceramic, mineral, porcelain (CMP) | 1993 < 40 g/t 1994 < 25 g/t |
| Aluminium | < 5 g/t |
| Ferrous metal | < 5 g/t |
| Lead | < 1 g/t |
| Loose organic material | < 500 g/t |
| Moisture | < 2 % |
| 2. Maximum proportion of other colours: | |
| | other colours |
| | flint  amber  green  |
| in flint glass  | - < 0,5 % < 0,1 % |
| in amber glass | < 5,0 % - < 5,0 % |
| in green glass  | < 5,0 % < 5,0 % - |

Figure 3

Figure 3 shows the quality requirements for treated cullet in Germany.

CONCLUSION

Glass is a fascinating material which has been in existence for thousands of years, and which has influenced the development of human civilisation. No other material can be used for such a wide range of applications. However, if glass is to retain its importance, production methods must continue to develop in line with technological advances.

- (1) J.C. Maltha, W.L. Dalmijin, J.V. Houweligen, "Automation in Glass Recycling", Glass, March 1993, Pages 109-112
- (2) Dr. Ir. R. Beerkens, Ir. Enneking, Drs. Faber, "Dutch Goals for Glass Recycling", Glass, August 1992, Pages 324-329
- (3) E. van Fanten, I. van der Hout, C.Q.M. Enneking, "Bewertung von Altglasscherben und Konsequenzen für den Glasschmelzprozeß", 67. Glastechnische Tagung, Königswinter, Mai 1993

RECYCLING IN THE GLASS INDUSTRY
- AN OVERALL VIEW

**BY DIPL. ING. HORST MOSER; SALES DIRECTOR OF
ZIPPE INDUSTRIEANLAGEN GMBH;
WERTHEIM, GERMANY.**

Recycling in the glass industry plays an important role with regards to saving raw materials and energy.

Different methods of recycling are successfully used for the various kinds of waste to produce cullet "ready for remelt".

The sources of raw materials and energies are limited on earth and have to be handled with big care - that fact is well-known to everybody, of course.

Furthermore, it is a fact that the loading capacity of our environment is limited as well.

To steer against those problems and to achieve reasonable remedies, recycling is one of the most effective answers.

Recycling in the glass industry has a reasonable long history.

At the very first beginning the reuse of only own production waste has been acceptable. The furnace operators knew what they had.

The use of waste glass which had been collected externally and which did not come from the own production was considered as being dangerous - at least as long as the treated glass ready for melting did not meet the very stringent purity requirements.

In the meantime, however, recycling plants have been created for all kind of glass waste supplying cullet ready for melting, which means

having the right grain size and the required purity not to affect the furnaces.

So, what are the benefits of recycling glass ?

No. 1 - Production areas and also public waste deposits can be cleared from waste glass.

No. 2 - By remelting cullet expensive batch can be partially replaced. Valuable raw materials are reused.

No. 3 - Cullet are melting with lower energy input. So, each 10% of cullet addition reduces the melting energy by about 2,5% compared to batch melting.

No. 4 - Cullet can be used as a safety melting material stock to feed the furnaces in case batch delivery is interrupted.

Each type of glass waste requires individual treatment facilities.

Hot glass waste arriving directly from the furnaces or the forming machines in the shape of liquid gobs, glass streams or still glowing hot final products is collected, granulated and transported nowadays by scraping conveyors.

Those conveyors located in the basement are designed as water-filled steel plate tanks with rotary chains and mounted scraper bars. They are tailor-made in length concerning the hot glass feeding points position and are ideal modules to be combined with cold waste recycling systems.

Cold glass is collected by belt conveyor systems and crushed after having been mixed with granulated host waste.

The produced cullet ready for melting can be stored and dosed to the batch by using flow meters. The ratio of adding is variable and can go up to 100% in case batch supply will fail.

A big advantage is that furnace hoppers always being considered as safety units can be kept small and all dry-out, segregation and bridging problems of batch and cullet in the furnace can be avoided.

The described system is mainly used in the container glass industry, but can be applied also with minor changes for tableware, crystal glass and even for sheet glass.

Externally collected container glass, so-called ecology glass, has to be treated in this way that all contaminants will be removed within set limits and crushing will be carried out to meet the required cullet grain size.

Big contaminants and non-dominating colour containers are removed by manual sorting, ferrous parts by magnetic separators, light contaminants, so as paper, plastic, wood, aluminium caps, etc., by vacuumizing, non-ferrous metal parts by all-metal-separators with inductive detectors and ceramic parts by ceramic separators with transparency depending laser detection. It is also possible to adapt a colour sorting system.

The operational glass loss will be below 2%.

The purity requirements of less than 5 g/to aluminium, less than 5 g/to iron, less than 1 g/to non-ferrous metals, less than 500 g/to organic materials and less than 25 g/to ceramic, stones, porcelain, etc., can be fulfilled.

The recycling tendency for ecology glass is increasing - in Germany today nearly 60% of used container glass is recycled.

During the production of float glass and also normal sheet glass, waste occurs mainly in form of cut-off edges and faulty sheets. Recycling and crushing has to be carried out "in-line", which means incorporated in the production line.

The waste is crushed firstly in a pre-crusher and after in a main crusher to produce the final grain size.

Fibre glass, say glass wool and continuous filament, is normally collected as a voluminous and light-weight waste material in big containers. That waste has to be charged to the pre-crusher by means of a specially designed vibratory tray feeder. An installed metal detector makes sure that no tramp metal parts will affect the crushers.

The pre-crusher, designed as a shredder, is chopping the waste material to a length of about 4 inches. The main crusher, designed as a hammer mill, is taking that precrushed material and is breaking it to the final grain size with a needle length of max. 5 mm.

In case the waste material has been wet (which is mostly the case), the end grain has to be dried before being added to the batch material for remelting.

In case of glass wool, the coating has to be thermically removed and burned off to make the fibre glass waste acceptable for reuse. Of course, the combustion gases developed by burning the coating have to be cleaned before released into the open air.

For recycling laminated glass the target is to separate glass and plastic foil to produce a grain size of both materials convenient for further use. After precrushing to a size of about 20 x 20 cm a hammer mill beats the glass from the foil and cullet with rice grain size as well as foil fragments as big as half a hand are produced. The separation of both materials is made by using a vibratory screen.

The same plant, slightly modified by installing another crusher grill and by adding a magnetic separating system, is also able to treat wired glass and sheet glass.

The target of all glass recycling activities is to produce a cullet material "ready for remelting".

The plants layed out therefore are designed to operate with a minimum of manpower and maintenance.

The selected materials for the plant equipment have to give a maximum resistance against wearing to achieve long operational periods and to keep expensive interruptions as low as possible.

Crushing glass creates noise.

It is important to keep the noise level down by convenient plant design.

Furthermore, glass crushing creates dust which is dangerous for the operator's health as well as for the plant equipment.

Dust collection and filtering systems with high efficiency have to be incorporated.

Finally I like to draw your attention to a system which allows the direct recycling of energy.

I am speaking of batch and cullet preheating by waste furnace gases.

It is possible today to achieve preheating temperatures of melting material of up to 350° C, which results in a saving of melting energy up to 20%.

In addition to that, furnace life times can be extended due to lower crown temperatures for bottom temperatures are rising by feeding preheated materials. Lower crown temperatures also mean lower NOX-emissions.

The preheating temperature, of course, is depending on the waste gas capacity and temperature level.

New furnace technologies containing oxy-fuel firing will even improve the economy of preheating by supplying waste gases with higher exit temperatures.

ENVIRONMENTAL LEGISLATION AND GLASS TECHNOLOGY

G. J. Copley, British Glass, Sheffield, UK

INTRODUCTION

The purpose of this paper is to illustrate the influence of the law on technology.

During the last ten years there have been important changes in the law in the European Community which regulates the environmental requirements for glass-making plants. During the same period, there have been developments in pollution control technologies.

The glass-maker is now in a position of trying to select pollution control equipment which will meet the law and which will be the best financial choice for the long term.

The theme of this paper is that the choice between pollution control options is by no means straightforward. I will try to indicate some of the possibilities and some of the uncertainties.

ENVIRONMENTAL LEGISLATION

In the early 1980's, three important changes took place in thinking about the environment. There was:

O/H 1 - ENVIRONMENTAL ISSUES - 1980's

- an increased public and political awareness of environmental issues.
- a realisation that pollution has global dimensions.
- increased toxicological evidence that pollution, at much lower levels than previously thought, could have undesirable effects on ecosystems.

O/H 2 - ENVIRONMENTAL STANDARDS - 1980's - 1990's

Ten years ago, glass-makers in Western Europe were required to operate their plant to environmental standards which would:

- safeguard public health, and
- avoid nuisance in the locality.

Now, the law is established:

- to safeguard all ecosystems, and
- to avoid environmental problems locally, regionally and globally.

Manufacturers must now be as much concerned with reducing their contribution to regional problems, such as acid rain, and global problems such as the greenhouse effect, as with being good neighbours in their immediate locality.

This change in emphasis has led to environmental law which is concerned with a wider range of pollutants, with much lower concentrations of pollutants and with the setting of emission limits.

O/H 3 - ENVIRONMENTAL DIRECTIVES

There are over 200 environmental directives and decisions in force in the European Community. I am going to concentrate primarily on one issue, air pollution from large container and flat glass plants, though air pollution cannot be divorced from other issues such as water and waste emissions and energy usage. There is a long list of directives and proposed directives concerned with these issues.

The Framework Directive 84/36/EC has the most direct effect on air pollution legislation. It specifically includes glass manufacturing plants and the common pollutants emitted from these plants. It has been followed in most member states by legislation which in most cases sets emission limits for the principal pollutants and dates for compliance.

There are four proposed directives which will affect air pollution control. Their terms and scope are not yet clear, but at this time when pollution control facilities have to be chosen their presence introduces uncertainty about the demands and emphasis of future legislation. I will return to them.

AIR POLLUTION EMISSION LIMITS

In the early 1980's, acceptable emissions from glassworks chimneys can be judged by reference to the highest emissions at that time.

O/H 4 - MAXIMUM EMISSIONS AND EMISSION LIMITS

| mg/nm ³ | 1980 Maximum emissions | Present national limit values | Future? Limit values - other industries |
|--------------------|------------------------------|-------------------------------------|---|
| Dust | 350 | 50/100 | 5-20 |
| SO _x | 4,000 | 750-1,800 | 250-500 |
| NO _x | 3,500 | 2,700/3,500 | 250-500 |
| HCl | 120 | 30 | |
| HF | 40 | 5 | |

This table shows maximum emissions from uncontrolled glassworks chimneys compared with emission limits which are now set in most European states. Clearly, these emissions are now unacceptable and emission control is necessary.

But there is uncertainty. The table also shows emission limits which have to be met in some other sectors of industry which use combustion processes. If the glass industry had to meet these lower emission limits, then the options for control would be different from those for the present limit values.

IN-FURNACE CONTROL

The first consideration should be emission control by in-furnace methods.

If we consider not maximum emissions, but the typical range of emissions measured on many container and flat glass furnaces, then it can be seen from the lower end of the ranges for gas and oil-fired furnaces that there are some possibilities for in-furnace control.

O/H 5 - RANGE OF EMISSIONS

| mg/nm ³ | Gas-fired | Oil-fired | Limit values |
|--------------------|-----------|-------------|-----------------|
| Dust | 70-260 | 100-350 | 50/100 |
| SO _x | 250-2,000 | 2,000-4,000 | 750(g)/1,800(o) |
| NO _x | 750-3,600 | 530-3,000 | 2,700/3,500 |
| HCl | 6-120 | 6-80 | 30 |
| HF | 4-40 | 4-40 | 5 |

A few furnaces may be able to achieve an emission limit for dust of 100 mg/nm³ by in-furnace methods. For most furnaces, however, secondary pollution control facilities will be needed.

Gas-fired furnaces, with low batch sulphate and high cullet, will be able to meet an emission limit of 1,800 mg SO₂/nm³ and some furnaces may be able to meet 750 mg/nm³ without flue gas desulphurisation. Furnaces using heavy fuel oil will require secondary controls.

The emission limits for dust and SO_x will certainly favour gas firing where gas is available. The availability of fuels will have the greatest effect on the glass-maker's choice of options.

Nitrogen oxides present a particular problem and the statutory emission limits for glass furnaces recognise the difficulty. Good in-furnace combustion control should be capable of meeting an emission limit of 2,700 mg/nm³. However, much lower limit values are being considered and will be imposed when control technology is available.

Chloride and fluoride emissions from container and flat glass manufacture arise from impurities in the raw materials but may exceed the emission limits and control will be needed.

The conclusion from these figures is that to meet the national regulations arising from the Framework Directives most furnaces will require secondary pollution control facilities. The glass-maker should seek to reduce emissions by in-furnace methods to reduce the load on secondary controls, but in most cases this will not be sufficient.

SECONDARY POLLUTION CONTROL

Secondary pollution control facilities are needed now on new furnaces, and in some member states, on rebuilt furnaces.

Clean-up problems associated with glass furnaces arise from:

- the high temperature of the waste gases (400-500°C)
- sub-micron particles (outside the range of mechanical separation)
- the presence of acid gases (SO_x, HCl and HF)
- a high content of nitrogen oxides.

A three stage cleaning process is therefore required.

The glass-maker is required to use the Best Available Technology Not Entailing Excessive Costs - BATNEEC. This follows from Article 13 of the Framework Directive which stipulates that for each plant consideration should be given to:-

O/H 6 - BATNEEC

- the plant's technical characteristics.
- the rate of utilisation and length of its remaining life.
- the nature and volume of polluting emissions from it.
- the desirability of not entailing excessive costs.

BATNEEC is not a generic technology; it must be selected for each plant individually.

FLUE GAS DESULPHURISATION

Emissions of sulphur oxides, HCl and HF may be removed from the waste gases by reaction with an alkali absorbent. There are three available methods, depending upon whether the reaction is carried out wet, dry or semi-dry.

O/H 7 - FLUE GAS DESULPHURISATION

| | Reactant | Waste | SO _x removal % | Exit temperature °C |
|----------|---------------------------|-------|---------------------------|---------------------|
| Dry | Alkali | Dry | 50-65 | 350-450 |
| Semi-dry | Alkali + H ₂ O | Dry | 60-85 | 150-190 |
| Wet | Alkali + H ₂ O | Wet | >85 | <100 |

The dry or semi-dry processes are likely to meet the requirements for most glass-making emissions.

In the dry process, the reaction temperature and the exit gas temperature are between 350 and 450°C. The removal efficiency is 50-65%.

In the semi-dry process, the removal efficiency is higher, 60-85%, but the exit temperature is lower than in the dry process, 150-190°C. This may be a limitation if a subsequent denitrification process is needed. The glass-maker must take into account the fact that not all pollution control methods are compatible with each other.

DUST REMOVAL

The desulphurisation process must be accompanied by a dust removal stage.

O/H 8 - DUST REMOVAL

| | Efficiency % | Temperature °C |
|-----------------------------|--------------|----------------|
| Electrostatic precipitation | 99 | 160-400 |
| Bag filtration | 99 | 160-250 |
| Ceramic filter | | 200-800 |
| Electrified cake scrubber | | 150-500 |
| Electrified granular bed | | 150-500 |

The present methods are electrostatic precipitation and bag filtration. Both have a high filtration efficiency. The bag filter has a lower temperature capability which may be a disadvantage if a subsequent denitrification stage is needed.

But new technologies are being developed. Ceramic filters offer a method of filtering gases at high temperatures, up to 800°C. This is compatible with a de-NO_x process.

Electrified cake filters and electrified beds can be combined particulate filters and de-SO_x systems. Pelletised batch and cullet have been used as the filter bed, thus combining pollution control with batch pre-heating, giving energy savings in the melting process of 10-20%.

Compared with the capital cost of a new furnace, the additional control facilities add 17-33% to the capital cost of a new furnace and may add 10% to the annual operating cost. These are substantial additions for an industry which operates to relatively low profit margins.

To meet emission limits for dust and oxides of sulphur, the glass-maker then has a selection of existing and developing technologies from which to choose. However, the proposed directive on Integrated Pollution Prevention and Control may influence this choice if an optimum control of air, water and waste emissions is needed.

NITROGEN OXIDES

The control of nitrogen oxide emissions is difficult for the glass manufacturer. There is no generally applicable process for the denitrification of glass-making waste gases at this time.

The current emission limits of 2,700 or 3,000 mg/nm³ can generally be met by primary measures of combustion control. More stringent limits have, however, been mentioned and will be imposed if control technology becomes available.

Two denitrification technologies are being developed and are used on certain furnaces. Both use gaseous ammonia to react with nitrogen oxides to produce nitrogen and water. One method uses a catalyst, the other is without a catalyst.

O/H 9 - METHODS FOR CONTROL OF NITROGEN OXIDES

| | Efficiency % | Temperature °C |
|--------|--------------|--------------------------------------|
| SNCR | 50-60 | 850-1,100 700 with H ₂ |
| SCR | 80-90 | 260-400 |
| Staged | 60 | In furnace |
| Oxygen | 90 | In furnace |

Selective non-catalytic reduction SNCR takes place in the temperature range 850 to 1,100°C. The temperature can be reduced to about 700°C by using a combination of ammonia and hydrogen. To use this method, it is necessary to find a location in the flue system to inject ammonia within this temperature range. This is possible with recuperative furnaces, but in regenerative furnaces the temperature range is usually within the regenerator. The reduction in nitrogen oxide emissions with this method is 50-60%.

The selective catalytic reduction process SCR reduces the temperature range to 260-400°C and is capable of higher efficiencies of 80-90%. The process must be used downstream of an efficient desulphurisation and dust removal system, but even so the principal problems at this time are associated with the blocking and poisoning of the catalyst. The required temperature range may not be compatible with the semi-dry de-SO_x process.

Two other, in-furnace, technologies are capable of reducing NO_x emissions. These are staged combustion and oxygen firing.

Staged combustion has, to date, only been used on end-fired furnaces but NO_x reductions of up to 60% can be achieved, with an accompanying reduction in energy used in the furnace of 6%.

Oxygen firing can reduce NO_x emissions by up to 90% and give high savings in the energy used in the glass furnace. A reduction in particulate emissions of 50% (by mass) and a reduction in CO₂ emissions of between 18 and 50% (by mass) have been reported, depending strongly on the thermal efficiency of the furnace before conversion to oxygen. Methods of control which reduce the mass emission of pollutants, but not necessarily the concentration of emissions, throw into question the expression of limit values in terms of concentration rather than mass emissions in environmental legislation regulations.

The developing methods for denitrification are important for the glass-maker. If methods are developed which fall within the requirements of BATNEEC, then regulatory authorities will press for a reduction in the NO_x emission limits for glass-making furnaces. If a method is developed, it may have a strong influence on the choice of the methods used for desulphurisation and dust removal.

Whatever pollution control method is selected, the choice cannot be divorced from the principal objective of making glass and production factors such as throughput, yield, furnace life and quality. The risks of introducing any technology which may upset the high throughput, but sensitive glass manufacturing processes, must first be assessed very carefully.

Of course, the glass-maker could decide to eliminate all the polluting emissions from his plant by turning to electrical melting. This shifts the emissions to the power station if the electricity is generated by fossil fuel. However, the economics of electrical melting do not permit such a radical solution for large furnaces in most of the European member states.

PROPOSED DIRECTIVES

Whatever method the glass manufacturer selects to control emissions to air, he must also take into account the possible future requirements of the proposed directives indicated earlier.

O/H 10 - PROPOSED DIRECTIVES

The proposed directive on integrated pollution prevention and control will require the optimum control of gaseous, water and waste emissions. Pollution control methods which minimise waste, or permit it to be recycled or reused, will in the longer term be preferred. The scope of this proposed directive is not yet clear, but it could replace the Framework Directive.

The CO₂/energy tax, however it emerges, will favour pollution control methods, which will also improve the overall thermal efficiency of the glass-making process. Traditional add-on secondary controls will add 3-5% to the energy bill. Some of the developing methods of control are capable of reducing energy usage while at the same time reducing emissions.

The packaging and waste directive will increase the amount of cullet available to be re-melted in container furnaces. This will reduce waste gas volume and polluting emissions, two of the key factors in the design and cost of pollution control facilities.

An air quality directive may move the emphasis of air pollution law away from emission limits to air quality standards.

CONCLUSIONS

Glass manufacturers are now faced with a requirement to reduce polluting emissions, but the choice of methods is not straightforward.

They must decide what can be achieved by in-furnace methods, without restricting the melting, refining and subsequent glass-making processes.

They must choose between available and developing new methods for flue gas desulphurisation and dust removal. The choice will be strongly influenced by the availability of fuels, the possible need to control NO_x emissions, and the precise regulations on emissions of water, waste and energy.

New methods for de-SO_x and de-NO_x may offer the combined advantages of pollution control, energy saving and a reduction of waste. The ultimate capabilities of the new methods and their rate of development into generally applicable technologies are uncertain.

Alternative methods are not necessarily compatible nor additive in their benefits.

Perhaps, above all, the glass-maker will be uncertain about the future requirements of the law which will govern his options in the longer term.

SOME FACTORS GOVERNING IMPROVEMENTS IN GLASS MELTING

Michael Cable
Glasses Research Group
Department of Engineering Materials, University of Sheffield
Sheffield S1 4DU,
United Kingdom

ABSTRACT

The invention of the tank furnace by the Siemens Brothers about 130 years ago was the most important advance yet made in glass melting. The Siemens furnace made continuous production possible, which in turn allowed the progress of mechanization of many forming operations, removed primary combustion of the fuel from the furnace itself and introduced regenerators to recover heat from the waste gases thus making greater thermal efficiency possible. Modern tanks differ from the original only in detail. It has been claimed that earlier furnaces could not exceed 1200°C but this is not likely to be true. This paper considers how some degree of preheat was achieved in wood fired furnaces and why regenerators were already an essential part of the earliest tank furnaces. Other aspects of melting important to any attempt to replace the tank furnace are then considered, especially the homogenizing action of any furnace and control of melt chemistry.

INTRODUCTION

Glass making has developed over several thousand years mainly by experience and intuition. Even today there are many subtle aspects of efficient and economical melting which we do not understand well but increasing concerns about the effects of all industrial processes on the environment as well as efficiency make better understanding very desirable.

Any successful attempt to improve glass melting must do better than the tank furnace, the most important single advance yet made in glass melting practice. A modern specification for making most kinds of glass must consider at least melting, refining, homogenization and control of oxidation: an unsatisfactory result for one of these may easily negate great improvements in some other part of the process. An excellent review of many of the approaches made to faster melting was given by Barton(1) at last year's Madrid Congress. Many attempts to improve glass melting have concentrated only on accelerating melting but this is not sufficient. Two good examples of this are the Glaverbel Brichard(2) flame injection melting furnace and the Owens Illinois RAMAR(3) melter, both of which came near to commercial success but failed because of difficulties with refining, despite much ingenuity being applied to the problems.

The regenerator was an important feature of the original tank furnace and it also today gives glass makers many of their headaches. First some of the reasons why the regenerator was a feature of the original tank are discussed. Secondly some of the other important criteria to be met by any melting technique are considered because the increasing sophistication of glass making will require any successful alternative to the tank furnace to satisfy all of these.

MELTING TEMPERATURES

The minimum temperature at which one can expect to melt any glass is its liquidus temperature and few glasses have liquidus temperatures much below 1000°C, however

experience shows that much higher temperatures are needed to give rapid melting. Figure 1 shows some data of Preston and Turner(4) for batch-free times of a simple soda-lime-silica

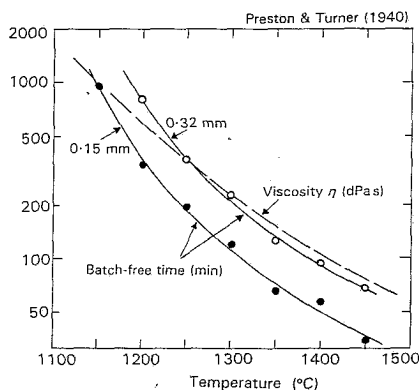


Figure 1: Temperature dependence of batch-free time.

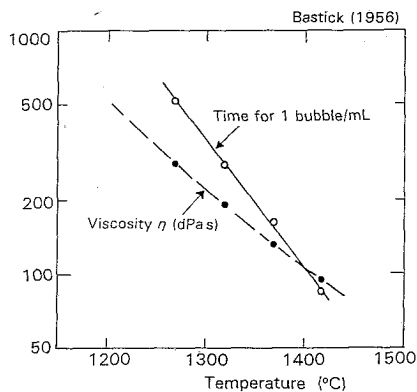


Figure 2: Temperature dependence of time to reach 1 seed/mL.

glass of liquidus temperature 965°C (with two different sand grain sizes) and it is seen that batch-free time varies rather more rapidly with temperature than does viscosity. Many years experience has shown that the greatest overall efficiency is indeed given by using almost the highest feasible temperature. The factors that usually set the practical limit are volatilization, increased attack of furnace refractories or atmospheric pollution. Another reason why this should be so, despite the apparent waste of energy indicated by considering only theoretical heat requirement, which was discussed by Pugh(5), is that rate of refining also increases more rapidly with rise of temperature than the decrease in viscosity, see Figure 2 which shows data by Bastick(6). These facts were surely known to glass makers working before the industrial revolution, despite their lack of ways to make quantitative observations.

It should also be remembered that, when all the wood fuel had to be collected and prepared by the glass makers themselves, it was as important to them as to any modern manufacturer to use their fuel as efficiently possible for each melt. They must have been aware that the maximum *degree of heat* gave the best results. How could they achieve that?

Turner suggested in one of his papers on ancient glass melting that wood fired furnaces could not regularly exceed 1200°C but this is difficult to accept. When one looks at some old glass compositions for containers or flat glass, their compositions are not very different from today's glasses and so low a melting temperature would have given very long melting times. Also some early glasses had liquidus temperatures above 1200°C, confirming that doubt. How could wood fired furnaces achieve the 1350–1400°C which seems more realistic and did the Siemens brothers consciously recognize this need?

The eighteenth century literature on glass melting tells us quite a lot about what glass makers did to achieve good melting temperatures. They clearly realized that the wood needed to be dry; examination of many of the famous Plates from the Diderot and D'Alembert *Encyclopédie* shows that vast quantities of wood were stored above the furnaces to ensure that the fuel was thoroughly dried before used. Glass houses on those days often burned down when stray sparks ignited the wood around the furnace. The net calorific value of wood decreases linearly with increase in moisture content; about 68% water is sufficient to reduce the net calorific value to zero and ordinary air dried wood can, at least in Britain, easily

contain around 23% moisture. Such a value makes the net calorific value only about two thirds of that for dry wood and using low grade heat to dry the wood very worth while.

Next, it was known to the glass makers that the maximum rate of heat release was required. The bark was stripped off branches to ensure more rapid combustion and the size was carefully controlled. Branches which could not be encircled by the thumb and forefinger were considered too big to burn as rapidly as needed and the maximum cross section of sawn planks was about 40x70 mm. Both were used as pieces up to about 1.2 m long.

Very rapid combustion was ensured by the way that the wood was fed into the furnace. Many wood fired furnaces had two fires, one at each end of the furnace chamber, the end wall often being at the end of a relatively narrow passage between the outer walls of the auxiliary furnaces built onto the main furnace chamber. No more than three or four pieces of wood were inserted at one time to lean against the furnace end wall, thus ensuring that it lay more or less at right angles to the incoming air and thus able to burn rapidly. Some of the neglected 18th century writings allow us to make some useful estimates of fuel consumption of the pot furnaces then in use and also tell us how sufficiently high temperatures were achieved.

ENERGY CONSUMPTION OF WOOD FIRED FURNACES

Data obtained from reading the texts of the Diderot(7) *Encyclopédie* and its successor, the *Encyclopédie Méthodique*(8) allow us to estimate the heat input to a wood fired pot furnace. One workman, the *tiseur*, was employed unceasingly in walking around the furnace and every time that he passed a stoke hole he inserted no more than three or four pieces of wood. Let us assume that to mean six pieces of wood 40x70x1200 mm every minute and take the net calorific value of dry wood to be 17 200 kJ/kg. The heat input to the furnace would thus be about 18 800 MJ/h. An only moderately efficient small tank could today be expected to melt about 28 tonnes/day for that heat input. The theoretical air requirement for this quantity of wood is about 1.3 m³s⁻¹ (at 25°C) and the heat needed to raise the combustion products to 1400°C would be around 1.1 MJ/h, which is a very small fraction of the total heat available. If the actual air input is taken to be 2 m³s⁻¹ and it enters the furnace through four apertures of total cross section 1m², the average velocity of entry of air into the furnace through the four apertures would be about 2 m s⁻¹, which is low compared with velocities in

modern furnaces. Ensuring that the wood was all exposed to a draught of air would give as rapid combustion as possible, especially if the air could be preheated. Even a modest preheating could raise the air to a temperature at which wood would ignite and this must have been known, at least intuitively, to the furnace operators.

A description of furnace operation in the Diderot *Encyclopédie* shows how this was done. One Plate shows an end view of the wall which seals the end of the furnace chamber and which has the fire just behind it. This wall has one small aperture for the insertion of wood around 1 m above the floor level. At its base there is a sturdy T-piece which creates a pair of air inlet openings, one at each side, which may be partly obstructed by moveable

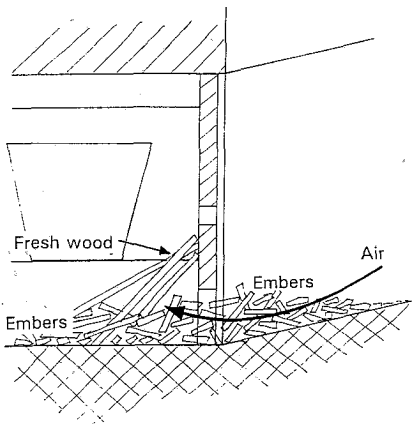


Figure 3: Use of embers as a primitive air preheater in a wood furnace.

tiles acting as dampers to control the air flow. In describing that Plate and the operation of the furnace it is stated that the embers must be regularly raked out from the bottom of the fire itself to maintain a loose bed of still glowing embers outside the furnace but in front of the air inlets (Figure 3) and that the equality of air flow through each side must be carefully balanced. It was also emphasized that premature removal of too much of these embers impaired furnace performance. It is thus clear that a primitive air preheating system was used. It would be interesting to discover what maximum temperature achievable in such a system.

The removal of primary decomposition of the fuel from the melting chamber itself was an important feature of the Siemens furnace and it is suggested that the Siemens brothers recognized that a separate properly engineered heat recovery device to replace the bed of hot embers was necessary to achieve a good melting temperature and this led them to develop the regenerator together with reversal of the furnace to achieve reliable preheating.

FACTORS AFFECTING GLASS QUALITY

MELTING REACTIONS

Silicate glasses are produced by heterogeneous chemical reactions. Even when batch is well mixed some melting segregation is almost inevitable and the demonstrable bad effects of poor batch mixing or segregation between mixer and furnace were demonstrated in a notable paper by Poole(9). Minimizing the segregation that can occur during melting may be very important to the overall efficiency of any melting process.

Looking at the phase diagram for the soda-silica or soda-lime-silica system shows that residual sand grains must be surrounded by an aureole of glass differing in composition from the desired final composition and that this difference is essential to completing dissolution of the sand grains. However, the earliest stages of melting also contribute to the production of inhomogeneity and what happens at this stage can be much influenced by choice of batch materials as well as glass composition. Details of the complex sequence of reactions that may happen can also depend on rate of heating and the degree of completion of the first reaction when further heating makes another reaction begin. Fortunately the literature supplies a telling example of what may happen in the melting of potash-lead oxide-silica glasses, such as English lead crystal. This type of glass is notoriously difficult to make homogeneous and, as there is a region of immiscibility in the system, production of liquid in this region could cause problems in melting.

Figure 4 shows results of two different investigations of the sequence of reactions occurring in potash-red lead-sand batches. Rosenkrands and Simmingsköld(10) took small samples from actual full scale pot melts during the early stages of normal melting and then analysed the composition of the reaction products. One of the lines in the Figure shows their results. Their results are close to what would have happened if the following series of reactions had occurred sequentially:

- 1) All the potash reacted with silica to form K_2SiO_3 ,
- 2) All the lead oxide had reacted with the potassium silicate,
- 3) The remaining silica then dissolved (more slowly) in the melt.

The locus of their actual results is what would be expected if these reactions overlapped somewhat. These results show that compositions of the liquid phase did not go into the immiscibility region and that the main sources of inhomogeneity are, first, the wide range of compositions (hence densities, viscosities and reactivities) of the liquids formed at various stages and, second, the strong tendency of low viscosity liquids to segregate under gravity. The latter is one of the greatest difficulties in making lead crystal.

The Figure also shows results of laboratory studies of another glass by Bezborodov *et al.*(11). These experiments indicate that the first step was formation of a liquid of composition very near to the tetrasilicate ($K_2O.4SiO_2$) rather than the metasilicate but their

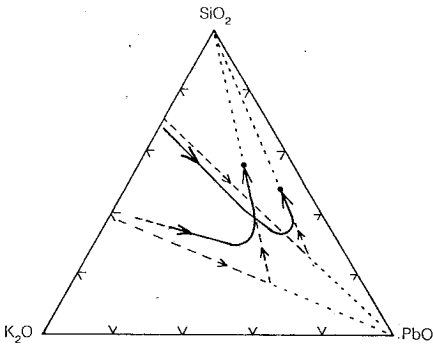


Figure 4: Liquids formed early in melting lead crystal glasses, see text.

results are otherwise similar. There is no reason why the final composition should have caused the different reaction path but examination of their experimental method shows why the behaviour was so different. Bezborodov heated the batch for long periods in a stepwise sequence of rising temperatures, allowing reaction to become very slow before raising the temperature again. It is therefore no surprise to find that much more silica reacted in the "early" stages than with rapid heating and this might have given rather less inhomogeneity than rapid heating.

Proposed improvements to melting which allow the liquid first formed to run away from the rest of the batch may make the problems of melt inhomogeneity much worse.

These early reactions can be much affected by the choice of raw materials. For example, batch-free time tends to be governed largely by the *quartz content of the batch* not the silica content of the glass and faster melting can often be expected from any means of decreasing the quartz content of the batch. Other ways in which the choice of raw materials may affect both batch-free time and the homogeneity of the initial melt should be carefully considered.

MELT OXIDATION

Some of the minor constituents which make up too small a fraction of the total mass of the glass can sometimes have very important effects. One of the most obvious is control of oxidation which can affect colour, especially ferrous:ferric ratio, but also other factors such as the sulphate:sulphide balance. An upset in the iron equilibrium can alter colour and UV or IR absorption to an unacceptable degree and a change in the sulphur equilibrium can affect colour (especially amber) and the tendency to produce blisters or reboil. When other factors are kept more or less constant differences in both melting behaviour and refining can be related to degree of oxidation. Many glass technologists therefore find it very useful to estimate the degree of oxidation of the glass produced by melting any batch by using the oxidation factors developed by Simpson and Myers(12). These are always affected to some extent by melting conditions and cannot be used without some adjustment for each individual furnace but are nevertheless widely used and found helpful. They can often be related to refining and homogeneity as well as to batch-free time. Ignoring effects of proposed changes in melting technique on melt oxidation led to problems with other aspects such as refining, as was seen with both the Brichard and RAMAR melting systems.

HOMOGENIZING

Homogeneity is not often discussed in books about furnace design and operation. It is difficult to find the word *homogeneity* in the index of books earlier than Trier's(13), even though the need for control of flow inside the furnace may be made clear. Yet homogeneity is of overriding importance; no other mass produced materials have such high requirements as glasses. One of the reasons for its neglect must be that homogeneity is a difficult parameter to define accurately. Both the difference in composition (or property) and the size of the inhomogeneities needs to be defined to have a useful index, and this is not easy to do. In very many applications it is usual to fix on a particular *scale of examination*, which should be chosen when something is known of the likely scale of the inhomogeneities themselves, and

then measure the variance of composition or a suitable property. Homogeneity cannot be attained on a nanometre scale in multi-component glasses but may be attempted at a scale between 1 and 100 μm . Such a scale makes it difficult to devise rapid and useful methods of assessing homogeneity and relatively simple techniques which reveal optical distortion within the glass are often used.

PRINCIPLES OF HOMOGENIZATION

Mass transport by diffusion must be the ultimate mechanism of homogenization. The high viscosities of most glass melts mean that flow must be in the laminar regime, which does not favour mixing, and that diffusivities for mass transfer must be low. When diffusive flux, like heat conduction is proportional to the driving force (difference in concentration or temperature) it is inevitable that reduction of concentration differences tends to be roughly exponential with time.

If an inhomogeneity could be represented as a slab of thickness $2b$, with a concentration of solute C_0 , immersed in a large bulk of material with uniform concentration C_∞ , its dimensionless centre concentration, $C^*(0)$, would decay with time according to

$$C^*(0) = (C - C_\infty)/(C_0 - C_\infty) = \text{erf } b/2(Dt)^{1/2} \quad (1)$$

If it were a cylinder the radial diffusion would proceed rather faster according to

$$C^*(0) = 1 - \exp(-b^2/(4Dt)); \quad (2)$$

if it were a sphere the result would be

$$C^*(0) = \text{erf}(b/2(Dt)^{1/2}) - (2/\pi^{1/2})(b/2(Dt)^{1/2}) \exp -b^2/(4Dt). \quad (3)$$

All of these involve the dimensionless time Dt/b^2 , which shows that real time is inversely proportional to diffusivity and directly proportional to square of size. Table 1 shows the predicted times for the maximum concentration to decay to a tenth and a hundredth of its original value for these cases. The geometry has a very significant effect.

A further considerable advantage can be obtained by stretching and folding numerous times to make a laminar structure with alternate layers of the two compositions. If these layers are assumed to be of equal thicknesses and compositions the answer is readily obtained, see Cable(14).

Table 1: Dimensionless times for the change in concentration at the centre of an inhomogeneity of width $2b$

| Type of inhomogeneity | Time (Dt/b^2) to decay to:- | |
|-----------------------|---------------------------------|-------------------|
| | 0.1 ΔC_0 | 0.01 ΔC_0 |
| Isolated:- | | |
| Slab | 31.67 | 3185 |
| Cylinder | 2.37 | 24.87 |
| Sphere | 0.854 | 4.34 |
| Regular array:- | | |
| Alternate layers | 1.031 | 1.97 |

Table 1 shows the times for decay of the central concentrations in isolated layers and in a regular array of flat layers: the advantage of the latter is clear. The faster decay occurs for two reasons. First, the maximum distance over which diffusion must occur is greatly reduced. Second, stretching and folding that layer p times to make one layer of thickness $2b$ into a series of layers each of thickness only $2b/p$ gives a very important decrease in the real time needed.

Examination of these relations make clear that there are three ways in which homogenizing by diffusion can be accelerated: 1) increasing diffusivity by raising the temperature, 2) decreasing the diffusion distances and 3)

decreasing the initial concentration difference which must be reduced. The first of these can only be achieved by raising temperature but that is rarely feasible; the second is the most

attractive and achieved by stirring; the third is often forgotten in general discussions. Real standards of homogeneity depend on actual differences in composition or properties and anything which decreases the initial inhomogeneity is likely to prove well worthwhile. Preventing the development of inhomogeneity is almost certain to be better than trying to cure it afterwards. Alternative methods of melting must recognize this.

THE ROLE OF LAMINAR FLOW

When an inclusion is assumed to have the same viscosity as its surroundings, its deformation is a relatively simple exercise in analysis of flow patterns. The most useful model is steady laminar flow with a constant velocity along a straight flow path but a velocity gradient at right angles, such as will occur in flow along a rectangular open channel. When the inhomogeneities are much thinner than the overall body of fluid and it is reasonable to assume that the local velocity distribution is represented by a straight line although, in many cases, this will be part of a parabola. A rectangular element of length l lying at an angle α_0 to the direction of flow will have its two ends moving at different velocities so that it is stretched out and rotated, see Figure 5.

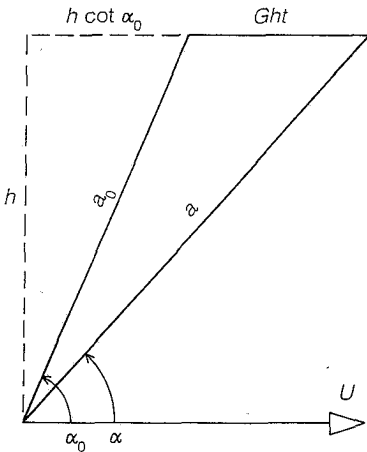


Figure 5: Geometry of deformation by simple shear.

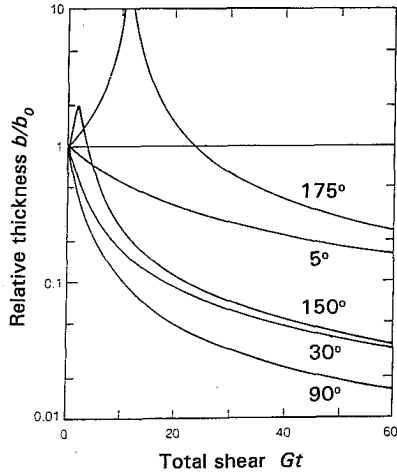


Figure 6: Dependence of attenuation on initial angle α_0 .

This model has been evaluated by several authors including Mohr(15), McKelvey(16) and Cooper(17). The most important facts are that the layers are rotated to become almost parallel to the direction of flow but that the rate of stretching approaches zero as this occurs. For the two dimensional case where the velocity vector U lies along the x axis and $dU/dx = 0$ but $dU/dy = G$ and the liquid is assumed incompressible, this leads to

$$\frac{b}{b_0} = \frac{1}{[1 + Gt \sin 2\alpha_0 + G^2 t^2 \sin^2 \alpha_0]^{1/2}} \quad (4)$$

Note that only the product Gt , the total shear, appears and neither G nor t is itself important. Some of the predictions of this equation are shown in Figure 6. The decrease in thickness with amount of shear is roughly a double exponential of Gt for favorably oriented layers and a factor of ten reduction in thickness is easily achieved but a factor of a hundred is hardly possible. If attenuation by a factor of more than about twenty is required, it is necessary to change the flow pattern and the orientation of the layers relative to the velocity vector.

However much shear is applied, there will always be a narrow range of angles of initial orientation for which matters will be made worse but sufficient shear means that these will occur infrequently (see Figure 6).

Of course, with almost perfect laminar flow, acceleration of the flow will attenuate inhomogeneities in an easily predictable way. The simplest way of achieving this is to make the melt flow through a reduced cross section, such as the throat of a furnace or the orifice of a gob feeder, when all the constituent parts of stream will be reduced in the same proportions as the cross section of the whole flow. However, if the stream expands again, as on exit from the throat, little may have been achieved. Unfortunately this is not likely to assist diffusive mixing very much because of the short residence time in the narrow part of the system. The combined effects of shear and reduction in cross section were discussed by Rhiel (18).

Most inclusions in glass will differ in viscosity from the surrounding matrix and the difference may be large. A rigid inclusion would not deform at all although it would rotate, so intuition rightly suggests that a more viscous inclusion should deform less than one of low viscosity subject to the same stresses. This problem can be elegantly treated by a method devised by Eshelby (19, 20) to deal with elastic inclusions which he kindly demonstrated to the author in 1968. By this method a simple relation can be deduced to describe the difference in deformation of two two-dimensional inclusions, one of the same viscosity as the matrix and the other of different viscosity, when both have been subjected to the same amount of shear. As deformation may be large it is defined in terms of the natural strain s ,

$$s = \int_{a_0}^a \frac{da}{a} = \ln \frac{a}{a_0} \quad (5)$$

The other parameter introduced is the relation between the two viscosities defined by

$$\lambda = (\eta_i - \eta_M) / \eta_M, \quad (6)$$

where the subscripts refer to the inclusion (i) and the matrix (M). The relation between the deformation of the inclusions in the two cases is given by

$$s_a + (\lambda/2) \tanh s_a = s_{aH}; \quad (7)$$

here s_a is the elongation of the longer axis of the cross section of a long cylinder sheared at right angles to its major axis, and s_{aH} is the deformation in the homogeneous ($\lambda=0$) case. For

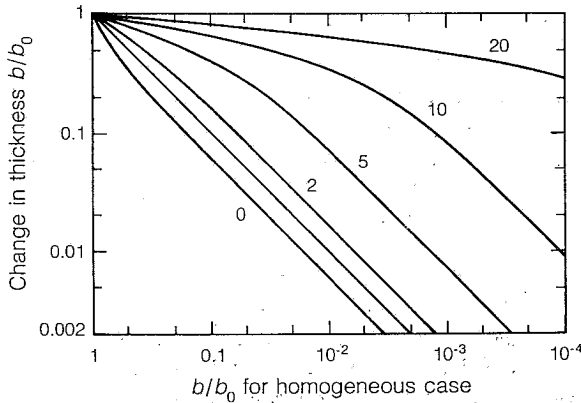


Figure 7: Eshelby's model for the deformation of inclusions of differing viscosities; numbers on curves show viscosity ratios.

the two dimensional case and an incompressible liquid, the minor axis of the inclusion must decrease by the same factor as the major axis increases.

Figure 7 shows how viscosity affects deformation according to this model; it compares the deformations of inclusions of viscosity equal to that of the surrounding matrix with that of inclusions differing in viscosity for the same as yet unspecified amount of shear. Thus a circular inclusion of very low viscosity will stretch by a factor of ten under the shear needed to deform one of equal viscosity by a factor of only about 7; a similar inclusion ten times more viscous than its surroundings will be stretched by a factor of ten only when subject to the shear needed to stretch one of equal viscosity by a factor of about 800: going back to Equation 4 shows the latter amount of shear to be enormous. It is clear that inclusions significantly more viscous than usual cannot be attenuated by any feasible change in furnace operating conditions. It is necessary to find and remove the source of the viscous inclusions to cure the problem; this is something well known to experienced glass makers.

Models of deformation such as these might assist furnace designers. However, it is not always obvious how studies of the predicted flow patterns made by computer analysis can be linked together with estimation of attenuation along various flow paths to provide a good index of homogenizing action. It needs to be remembered that the paths of minimum residence time will often be associated with relatively small rates of shear.

VALIDATION OF COMPUTER PREDICTIONS

It is now much easier to make computations of flow in furnaces than to observe them directly but computations require approximations to be made. There is therefore a need to validate the results. The only relevant experiment that it is easy to make is measurement of residence time by a tracer experiment but even here reasonably close agreement between experiment and prediction does not guarantee detailed similarity of flows. Nor is it clear how residence time distributions are linked to homogenizing action. Achievement of *perfect mixing* as determined by typical experimental or model studies is not a guarantee of outstanding homogenizing action in a furnace. This is a field in which there have been few important publications in recent years.

CONCLUSION

Examination of furnace operation shortly before the invention of the Siemens tank furnace suggests that melting temperatures of 1350–1400°C could be attained by using part burnt embers as a primitive regenerator and that the Siemens brothers probably recognized this and saw that a proper regenerator must be a part of their furnace system. This also led to them to see the need for a reversing direction of firing.

To be readily accepted, improved methods of melting which can replace the tank furnace need to address questions other than merely accelerating conversion of batch into melt. These include the state of oxidation of the melt, refining and homogenizing. The last of these is often the most difficult for the glass maker to satisfy but is rarely discussed in books and articles on furnace design. It is shown that inclusions of higher than usual viscosity represent a very serious challenge to the furnace. Control of the inhomogeneities produced during melting can do much to improve furnace performance.

REFERENCES

1. J.L. Barton, Proc XVI Internat. Glass Congress, Madrid, (1992) Vol.1, 165–184.
2. E. Brichard, J. Soc. Glass Technol. **39** (1955) 162–172.
3. R.S. Richards, see Ref. 1.
4. E. Preston and W.E.S. Turner, J. Soc. Glass Technol. **23** (1940) 124–146.
5. A.C.P. Pugh, 1968 *Glastek. Tidskr.* **23** (1968) 95–104.
6. R.E. Bastick, Proc. *Symposium sur L’Affinage du Verre, Paris 1955* USCIV, Charleroi, (1956) 127–138.
7. D. Diderot and J. D’Alembert, *Encyclopédie ou Dictionnaire Raisonné* (1765) Paris, Plates vol.IV (Glacerie) (1772) *Ibid.* vol.XVII (Verrerie).
8. Anon. *Encyclopédie Méthodique* (1791) Paris: C.J. Panckoucke, vol.VIII.
9. J.P. Poole, Glass Technol. **4** (1963) 143–152.
10. B. Rosenkrands and B. Simmingsköld, Glass Technol. **3** (1962) 46–51.
11. M.A. Bezborodov, A.A. Appen et alia, J. Soc. Glass Technol. **17** (1933) 305–319.
12. W. Simpson and D. Myers, D. Glass Technol. **19** (1978) 82–84.
13. W. Trier, *Glass Furnaces: Design and Construction* (1984) Springer; English translation K.L. Loewenstein, (1987) Society of Glass Technology.
14. M. Cable, In *Materials Science and Technology: A Comprehensive Treatment* (series eds. R.W. Cahn, P. Haasen, E.J. Krämer) (1991) Vol. 9 *Glasses and Amorphous Materials* ed. J. Zarzycki, VCH Verlag, Weinheim, 1–89.
15. W.D. Mohr, in *Processing of Thermoplastic Materials* ed. E.C. Bernhard (1960) Reinhold, New York, Chapter 3.
16. J.M. Mc Kelvey, *Polymer Processing* (1962) John Wiley, New York.
17. A.R. Cooper, Glass Technol. **7** (1966) 2–11; Chem. Engng Sci. **21** (1966) 87–94.
18. F.F. Rhiel, *Glastech. Ber.* **49** (1976) 217–226.
19. J.D. Eshelby, Proc. Roy Soc. London **A241** (1957) 276–296.
20. J.D. Eshelby, Proc. Roy Soc. London **A252** (1957) 561–569.

MODERN GLASS CONDITIONING FROM THROAT TO ORIFICE

Richard Sims

Nikolaus Sorg GmbH & Co KG

Abstract

A review of typical operating conditions of high capacity container production lines clearly indicates the need to increase the cooling capacity and to concentrate this in the working end. The forehearth will be used to achieve the thermal homogeneity, and will need an increase in control zones in order to be able to influence all areas of the glass bath. These changes will lead to more complex installations, and a computer based intelligent control system will be required to obtain optimum results

INTRODUCTION

A wide range of glass compositions are in commercial use, and an equally wide range of forming processes are used to turn the glass into marketable products. The conditions required to melt and process these various glasses also differ, but one factor is common to almost all automatic production lines - the temperature needed to melt the glass is higher than that required for the processing. It is therefore necessary to reduce the glass temperature between the two parts of the manufacturing process.

The cooling process is one part of the complete process which we generally refer to as glass conditioning. A further part of this process, in most cases, is the attainment of an acceptable level of thermal homogeneity for this process.

This situation has always existed on automatic production lines, but technological developments which have taken place in various other parts of the glass manufacturing process have led, in many cases, to significant changes in the conditions under which the glass conditioning has to be carried out.

A number of developments in melting furnace technology are of particular significance in this respect. Over the last 10 years there has been a general increase in the specific melting rate of medium and large furnaces. This has been accompanied by an increased use of electric boosting and bubbling systems which are specifically designed to increase the temperature of the glass in the lower areas of the glass bath in the melter. This had led directly to an increase in the temperature of the glass leaving the melter and entering the conditioning area.

The manufacturers of forming machines have not been idle either, and the last 10 years has seen the introduction of, amongst others, the 12 section IS machine for double gob operation. This machine is capable of processing over 150 tonnes of glass per day. Tandem machines with 16 or more stations have also been installed, capable of handling more than 200 t/24h.

The development of the product itself also plays a significant role. The continuing quest for lighter bottles places increasing demands on both the temperature stability and the thermal homogeneity of the glass supplied to the forming machines.

Putting these points together we are faced with increasing quantities of glass, which are entering the conditioning area at higher temperatures, and which need to have increasing levels of thermal homogeneity at the forming machine.

The extent of this problem can be illustrated by two examples. In the first case the melter is a 110 m² end-fired furnace with a maximum melting capacity of 320 t/24h. Three production lines are attached to the furnace and the glass colour is green. At a melting load of 270 t/24h the glass leaving the riser is typically at a temperature of 1390 °C. Taking the pulls and gob temperatures of the individual lines into account, it is necessary to remove approximately 783000 kcal/h of energy from the glass in the working end and forehearth.

The second example also concerns a large end-fired furnace, this one having a deepened refining area (Deep Refiner). In this case the furnace has a melting area of 100 m², and produces a maximum of 390 t/24h. The temperature of the glass in the riser is typically 1350 °C. At a typical load of 360 t/24h, and once again, considering the heat content of the glass at the riser and at the gobs, a total of 870000 kcal/h must be removed during the glass conditioning. This value can also be expressed as 1,01 MW.

LAYOUT OF MACHINES

Whilst these figures give an idea of the extent of the problem which must be solved, they do not convey the complete story. The layout of the forming machines also becomes an important factor. Although time does not permit an exhaustive review of this subject, both the layout of the cold end and the width of the lehrs have normally to be taken into account. The important point in the context of this paper is the fact that with 3 or 4 production lines, one or two forehearth entries are normally within 3 - 4 meters of the riser. Thus the area of the working end which is available for heat removal is severely limited for these lines.

COOLING

A number of cooling systems are in common use in the industry. Some use cooling air blown into the forehearth, or into a muffle enclosure above the actual forehearth roof, whilst some operate without the use of cooling air. However, almost all of these systems have one thing in common, the fact that they rely on heat transfer from the glass by radiation. This type of heat transfer depends on the transmission of heat from a hot body - the emitter - to a cooler body - the receiver.

Radiative heat transfer is described by the Stefan-Boltzmann law :

$$Q = CA(T_1^4 - T_2^4)$$

| | | | |
|-------|----------------|---|-------------------------|
| where | Q | = | heat quantity |
| | C | = | radiation constant |
| | A | = | radiating area |
| | T ₁ | = | temperature of emitter |
| | T ₂ | = | temperature of receiver |

The fact that the temperatures of emitter and receiver occur to the fourth power clearly shows that the highest levels of heat transfer will be achieved when the largest possible temperature difference between the two temperatures is obtained. In this particular case the glass bath is the emitter, and the temperature of this is given. The temperature of the receiver should therefore be as low as possible. Typical air cooling systems rely on the cooling effect of the air on the refractory superstructure, which then becomes the receiver, being colder than the glass bath. The governing factor then becomes the actual temperature to which the refractory can be reduced. This is limited in practice to temperatures of about 500 °C.

An open radiation cooling, which consists of openings in the refractory superstructure, effectively uses the surroundings as a receiver. These will typically have a temperature below 100 °C, which gives a very large temperature difference compared with the emitter. This type of cooling system thus offers the highest cooling capacity per unit area.

Whatever system is used to remove the heat, the use of radiative heat transfer is advantageous as the heat actually removed from the glass bath does not come entirely from the surface of the glass, but actually from within the body of the glass to a certain extent. However, the main problem encountered with high capacity installations is not that of removing heat from the system, but that of heat transfer within the glass bath itself. The heat can be removed from the upper regions of the glass, but the lower regions must also be cooled. Heat transfer within the glass is also by radiation, but, particularly in the case of coloured glasses, this rapidly becomes the limiting factor in the heat transfer complex.

One practical method of applying cooling to the lower areas of the glass bath is to reduce the depth of the glass at the cooling location. In order to have a significant effect on the cooling of the lower layers it is necessary to reduce the glass bath depth to values in the range 100 - 200 mm. This very shallow glass bath will however exert a very significant effect on the hydrostatic head loss in the system, which can easily lead to glass level problems and a disturbance of the production. Therefore, such shallow glass baths are only applicable over a very limited length, in order to restrict the effect on the glass level.

A study of the glass level loss shows that the shallow glass bath can be compensated by increasing the width of the channel, and for pulls of up to 250 t/24h a glass bath depth of 150 mm is possible.

A further potential problem connected with extremely shallow glass baths at high pulls is the form of the glass current through this area. The reduction in effective cross sectional area leads to a general increase in the flow velocity of the glass through this area. It is important that the flow pattern across the width of the glass bath is as flat as possible in order to minimise the maximum flow velocity and maximise the minimum residence time in the area.

Physical flow modelling of such systems has shown clearly that the location of such an area in a working end with respect to the riser and the forehearth entries, and the geometry of the working end in the area immediately before the reduced glass bath depth, both exert a significant effect on the flow of the glass through the cooling area.

The location of such a system also depends on the space restrictions on each individual installation.

The most advantageous location is directly after the riser, before the glass enters the main working end. This may entail moving the main working end forward in the direction of the machines, which will normally result in shorter forehearth. However, as the use of such a super cooling section in the working end is designed to limit or eliminate the need for active cooling in the forehearth, the shortening of these may be an acceptable solution.

An alternative location would be in the main working end, between the riser and the first forehearth entry. At this location it is more difficult to obtain acceptable flow characteristics, as a result of the 90° corner in the glass flow from the riser into the main part of the working end. However, the physical modelling has also shown clearly that it is possible to design such a system with acceptable flow characteristics.

The amount of heat which can be removed from the glass by means of such a shallow bath cooling system depends on the cooling area which can be used. However, figures of 350000 - 400000 kcal /meter of length are achievable. This equates to between 40 and 60 % of the heat quantity which must be removed in the case of a typical large container plant. For a typical installation a temperature drop of 130 °C can be achieved at a pull of 250 t/24h.

Although heat transfer by radiation from the glass surface is the most commonly used type of cooling, there are two other systems which may be considered. Both of these systems attempt to address the basic problem of the cooling of the lower areas of the glass bath.

BOTTOM COOLING

Bottom cooling of forehearth has been known and applied on a number of occasions in the past. It is possible to obtain a cooling effect by partially or completely removing the insulation underneath the channels and allowing the refractory to radiate heat to the surroundings. Although this method is effective in increasing the heat loss through the bottom, it does not offer any easy method of control of the amount of heat removed. The second method involves the provision of a canal underneath the channel blocks, through which cooling air can be blown. In this case a variation of the cooling effect can be obtained by variation of the air quantity. This type of construction must provide adequate protection against the entry of glass into the canals from leaking channel block joints, but by using suitable detailed design it is normally possible to avoid this problem.

However, irrespective of which system of bottom cooling is used, there remains one major disadvantage. The heat is removed from the glass by conduction from the layer of glass directly in contact with the channel bottom. Therefore, the cooling effect is initially limited to the very bottom layer of glass. Some reheating of this layer will occur as a result of heat transfer within the glass itself, which is equivalent to a cooling effect of the glass above the lowest layer, but as long as the cooling is continued, the lowest layer of glass will remain the coldest. With coloured glasses the reheating takes place very slowly because of the relatively low level of heat transfer within the glass. There is, therefore, a clear limit to the application of such a bottom cooling system. If this limit is exceeded a cold layer of glass will be produced on the bottom of the channel. This may not be registered by the temperature measurement in the forehearth, even if triplex thermocouples are used, as it may lie below the lowest measuring point, but the presence of this cold layer will be visible as a cold streak in the gobs, and may produce backward curvature of the gobs.

In practical terms, bottom cooling may be used to assist the achievement of good thermal homogeneity, being capable of reducing bottom temperatures by 8 - 10 °C on high pull forehearths. The amount of heat which can be safely removed by this method is, however, not significant compared with the total heat quantities which must be removed on high capacity installations.

WATER COOLING

Although widely used in the flat glass industry, immersed water coolers are not often to be found in container operations. Immersed water coolers basically consist of steel pipes, bent in some particular way, which are immersed in the glass, and through which cooling water flows. They may be installed at a fixed location, or they may be arranged to move, in either a linear or rotational sense.

A stationary installation is simpler, but offers a relative limited cooling effect. A layer of cool, viscous glass builds up around the metal, which effectively insulates the metal. This is an advantage in that the metal is protected from damage, but it does limit the heat removal. However, it is possible to use the combination of metallic pipe and cooled glass to influence the glass currents in, for example, a forehearth channel.

A moving cooler can be kept almost free of cold glass, and can therefore produce a much higher cooling effect. This arrangement also has the advantage that it can be used to apply some cooling effect to lower layers of the glass bath. However, once again, the amount of heat which can be removed from the total body of the glass is still relatively small compared with that which is necessary on large capacity container operations.

THERMAL HOMOGENEITY

The thermal homogeneity of glass being presented to a forming machine should ideally be measured as the glass enters the machine - i.e. in the gob in container manufacturing. However, this measurement is not available, at least not in a form which would allow a measurement of the thermal homogeneity. Therefore, this is normally measured at the end of the forehearth channel, before the glass is formed into the gob, but also before it enters the spout bowl.

It is generally agreed that a matrix of 9 temperature measurements, consisting of 3 vertical rows of three measurements each, provides a relatively complete picture of the thermal conditions in the glass. The vertical measurements are generally arranged with the top one about 25 mm below the glass surface, the second one in the centre of the glass bath, and the lower one about 25 mm above the channel bottom.

Although the temperatures themselves show the situation, a mathematical treatment is usually carried out to display the results as a single figure. This value, sometimes incorrectly referred to as the thermal efficiency, is expressed as a percentage. When all temperatures are the same, the formula will give a figure of 100 %. There are several systems for calculating this value, differing only in some details, but one which takes account of the complete picture better than some is defined as follows :

Thermal homogeneity index

$$\text{THI} = (1 - 9\sigma/T_c) \times 100$$

where

$$\sigma = \text{standard deviation of all 9 temperatures}$$

$$T_c = \text{middle temperature of the central triplex thermocouple}$$

Whereas a relatively simple bottle to be produced with the blow-blow process may run well at an index value of 90 %, a lightweight bottle made using the NNPB process will not run smoothly at index values less than 95 %. These are of course generalisations, and the particular conditions on each individual production line and for each bottle must be taken into account. However, the value of this index gives the experienced production man a clear indication of the suitability of the thermal homogeneity for the particular type of production.

Having used the index value to evaluate the homogeneity level, and the actual temperature distribution to determine which areas of the glass bath must be changed to improve the situation, it only remains to make changes to the forehearth operating conditions to achieve the desired effect. However, this may be very difficult or even impossible. Conventional forehearth control normally divides the channel into two or three zones along the length of the forehearth. The first zones (referred to as the cooling zones) will probably be provided with both heating and cooling systems, although the two systems may not have separate control. The final zone will be the so-called equalising zone, with heating only capability.

ADDITIONAL CONTROL ZONES

Obviously, more temperature control zones are necessary in order to be able to apply heating or cooling to specific areas of the glass bath. This does not necessarily mean that the forehearth must be split into more zones along its length, although this can also be advantageous under some circumstances.

Existing zones with heating and cooling facilities can be provided with separate control of the heating and cooling. Whilst the heating is used to maintain the temperature of the glass at the side of the channel, the cooling may be applied to the glass in the centre of the channel. Separate temperature sensors are, of course, required.

A further variation is separate control of the heating of the left and right sides of the channel. This is particularly interesting where the condition of the glass at the forehearth entry leads to significant temperature differences between the glass on the two sides of the channel.

Electrodes installed in the equalising section of the forehearth, and operated in addition to the normal gas heating, can be a very useful tool for the thermal homogeneity. The molybdenum electrodes are normally installed horizontally through the channel side walls, and the electrical circuit is arranged to give a current flow between the electrodes along the channel, rather than across it. This gives the capability to heat the two sides of the channel independently.

The well known problems of blister and molybdenum streaks from the electrodes occur in flint glass. However, heat transfer within flint glass is sufficiently high so that operation without electrodes is possible. The main application of such forehearth boosting systems is in coloured glasses, where the quality problems do not occur.

The increase in the number of control zones in the forehearth, which has been described here, now produces a further problem. The forehearth must be set up to produce the best possible results. Current forehearth control systems are basically very primitive, remaining very much the same as they were more than 20 years ago. Although basically automatic systems, in that temperatures are maintained at a given value, these systems actually require a significant amount of manual intervention, to establish the basic set-up of the forehearth, to optimise operation, and to correct for changes in external operating conditions.

INTELLIGENT CONTROL SYSTEM

Lack of time, and, to some extent, lack of experienced personnel, lead to the conclusion that an increase in control system intelligence is required in order to take advantage of the increased capabilities of the working end and forehearth. This sort of work is ideally suited to computerisation, but in order to provide a significant improvement compared with normal single or coupled loop PID control, such a system must be predictive rather than reactive.

Such a system has now been developed and tested. The programme consists of a large number of mathematical functions which describe the operation of a forehearth. Operating data from the actual forehearth are used to provide constants for these functions, so that the information with which the computer works is specific to the actual forehearth. The system runs on a normal PC, and can work together with any centralised control system or with individual controllers, provided that the system or controllers have full read/write communications capability.

The system in fact covers three areas of forehearth operation :

- prevention of temperature instability resulting from disturbances
- optimisation of forehearth set-up to maximise thermal homogeneity
- speeding up job changes

Temperature instability in forehearth may possibly originate in the forehearth itself, but the most common origin is outside of the forehearth. Disturbances on adjacent lines, especially job changes, are probably the most common source of such disturbances.

Using information from the forehearth entry thermocouple the predictive control allows the control system to think ahead of the disturbance and begin the necessary counter measures before normal reactive control has changed.

Optimisation of forehearth set-up can be made by the computer using the functions which describe the operation and reaction of the forehearth to predict which changes in operation will give the greatest improvement in the thermal homogeneity. These changes are made slowly to avoid disturbing the production, and so that the results can be monitored. Over a period of hours the intelligent control system searches for the optimum forehearth set-up.

When a job change is taking place the main requirement is to achieve stability at the new operating conditions in the shortest possible time. However, the extreme instability of the conditions in the forehearth, especially when the orifice ring is being changed, make it difficult

to define a control strategy for this time period. The intelligent control system uses statistical calculations to determine the beginning of, and to monitor the progress of a job change. The predictive capability of the system is used to decide the best operating conditions at any one time.

Initial operation of the intelligent control system has demonstrated improved operation in all three areas, compared with conventional PID or linked PID control systems.

CONCLUSION

It is the intention of this paper to review the technologies which are required for modern glass conditioning. The first is the shallow bath cooling technology together with an open radiation cooling system, which now offers the possibility to apply a very large cooling effect to the glass as soon as it has entered the working end and, in doing so, to achieve the situation mentioned at the beginning of this paper, of concentrating the main cooling effect in the first part of the conditioning system - in the working end.

The forehearth itself, although no longer required to exert significant cooling effects, must become somewhat more complex so that specific areas of the glass bath can be influenced in order to achieve the necessary level of thermal homogeneity. Finally, in order to take advantage of the extended conditioning capabilities, some form of intelligent control system, utilising predictive functions, is necessary.

OPERATIONAL EXPERIENCES WITH SEVERAL FlexMelter^R FURNACES

Dipl.-Ing. Helmut Pieper, Nikolaus Sorg GmbH & Co. KG, 97816 Lohr/Main, Germany

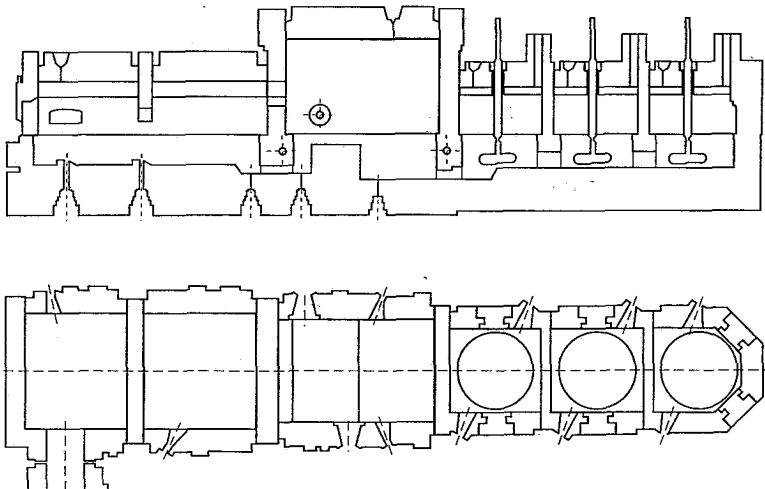
ABSTRACT

The FlexMelter furnace was originally designed to replace pot furnaces. However, a significant number of the many furnaces of this type which have been commissioned are in fact much larger than the size intended for the original concept. In principle the FlexMelter is a narrow, stretched out furnace, in which the three zones for melting, fining and refining are separated from each other in such a way that return flow from one zone to another is not possible. Fining is carried out in a thin layer, in which the maximum glass temperatures are reached. Normally burners are only used in the refining area, whereas the melting zone is electrically heated. However, the waste gases from the refining area are passed through the melting area above the batch, so that optimum energy usage is achieved. The temperature of the waste gases leaving the furnace is low, normally being in the range of 900 to 1000 °C in front of the recuperator. The flexibility of the furnace is not limited to the melting capacity, which can be raised from 0 to 100 % in a very short time. It is also possible to operate the furnace using various combinations of the types of heating. This furnace is much more flexible than conventional furnaces. For example, it is possible to lower the temperature of a FlexMelter for soda-lime glass at any time, and to increase it within a very short period. This means, that the furnace can be operated for one, two or three shift production as required. Furnaces already in operation are extremely versatile and produce excellent glass quality with low energy consumption. The advantages of the FlexMelter furnace concept will lead to the use of this furnace whenever constant high glass quality is required, even when relatively large quantities of glass are to be melted.

1 INTRODUCTION

The original aim of the FlexMelter development was to build a furnace to replace pot furnaces.

Figure 1:
Side and
ground view



However, after the first furnace of this type was commissioned, it became apparent that, in addition to the desired flexibility, the furnace design could well be suitable for melting difficult glasses and for larger tonnages.

The most important feature of the furnace which led to this conclusion is the fact that the residence time of the glass in the refining area is no longer dependent on the temperature, the temperature conditions or the currents, but merely on the throughput. A given temperature, together with a given throughput, leads to a predetermined and reproducible glass quality.

2 THE FURNACE DESIGN

The FlexMelter is a combined electric/fossil fuel heated glass melting furnace. The combined heating offers significant advantages for small furnaces. At the present time the comparative costs of energy mean that even relatively small electric furnaces are much more expensive to run than conventional furnaces. On the other hand, fossil fuel fired furnaces require very large combustion spaces if a reasonable value for the combustion space loading is to be maintained. This means, that these furnaces are very large and have relatively low specific melting rates.

The combination of both forms of energy results in a compact installation with low specific energy consumption, so that the energy costs are below those of both all-electric and pure fossil fired furnaces. In the case of larger units fossil fuels become more economic than electricity as an energy source.

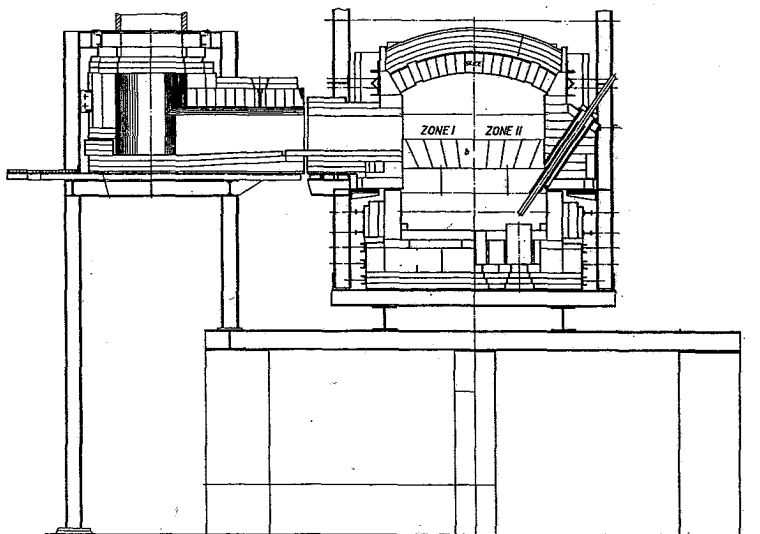
2.1 THE MELTING ZONE

The length/width ratio of the FlexMelter is similar to that of a Unit Melter. However, a dividing wall separates the melting end from the shallow refining zone. The separation between fining and refining occurs by means of a vertical plugflow in an area with horizontal isotherms. The furnace superstructure is divided into a higher part over the refining zone and a lower part over the melting end.

Batch is charged from the back wall across the whole width of the furnace by means of a simple charger. The charger makes a linear movement and can therefore be easily sealed. The batch cover is governed by the amount of electrical energy used. If heating is 30 % electrical the melting area can be completely covered with batch. If the load in the melting end is 2,5 t/m² a third of the area must be kept free of batch when only fossil fuel is used.

The electrodes are installed from the bottom, through the sidewalls or as top electrodes, depending on the type of glass and size of the furnace. In the case of lead crystal glass the furnace can be equipped with tin oxide electrodes. As there is no need to carry out fining in the melting end, the glass bath temperature can be kept relatively low, which increases the lifetime of the electrodes. The melting and refining zones are separated by a water-cooled wall, which has one or more openings in its lower part. The first part of the refining zone is somewhat deeper than the melting end. This is followed by a very shallow area, which is itself followed by another deeper part. The glass then flows on into the working end.

Figure 2:
Installation of
top electrodes



2.2 THE REFINING ZONE

The refining zone is normally gas heated, but electrodes may also be installed at the entrance. The burners are installed in such a way that the glass will have reached its maximum temperature by the end of the shallow area. The location of the superstructure separation between the melting and refining zones depends on the amount of gas heating required in the melting area.

The waste gases from the refining zone pass into the melting area, and over the batch. One or more low arches prevent radiation from the hotter part of the furnace reaching the colder areas. As a result a large part of the energy contained in the waste gases is transferred to the batch, so that the waste gas temperature at the entry to the recuperator lies between 900 °C and 1200 °C, depending on the amount of electrical energy used.

As the waste gas temperatures are low, the recuperator can be a simple design and can be operated in counterflow. The waste gas temperature after the recuperator is in the range between 400 °C to 600 °C, depending on the air pre-heat temperature, which reaches 500 °C. Higher air pre-heat temperatures could certainly be attained by the installation of additional convective recuperators.

2.3 GLASS CURRENTS IN THE FURNACE

Physical model tests were used to investigate the glass currents which develop in the furnace. The dimensions of the furnace which were finally chosen for the first installation give a minimum residence time of between 8 and 12 hours at full load. The ratio of the average and the minimum residence time is 2,8 in the melting end and 1,1 in the refining zone. This

means that almost perfect plug flow is achieved in the refining and fining areas. The critical current path rises to the surface, and runs along to the end of the refining zone. This guarantees optimum gas transfer to the furnace atmosphere.

The reason for the flexibility of this furnace is shown clearly by the glass currents in the model test. There is a clear separation between the glass in the melting area and that in the fining zone, and also between the glass in the fining and refining areas. The glasses at various stages of melting do not mix, even when the temperatures in the furnace are reduced, provided that the temperature differences between the individual zones are more or less maintained. The glass flowing from the melter can be about 100 °C colder than the glass on the surface of the refining zone.

As has already been stated, the critical current path rises to the surface of the glass bath, and so the maximum temperature on the critical current path and the maximum temperature of the glass bath coincide. This means that the glass surface, and therefore the superstructure, can be much colder than in conventional furnaces.

As no batch and only small amounts of foam occur in the refining zone, there is a direct relationship between the crown temperature and the surface temperature of the glass bath. Therefore it is possible to use the crown thermocouple to control the bath temperature. As the glass bath is shallow over the refining zone bank no return current occurs, and so fined and refined glass do not mix. This furnace therefore offers a direct relationship between pull, temperature and glass quality.

No other continuous furnace system has this clear relationship. When the temperature is raised in a conventional furnace the speed of the convection currents increases and more mixing takes place. A temperature rise in such a furnace can therefore reduce the residence time so much that a reduction in quality occurs.

2.4 EMISSION VALUES

As a result of the relatively low amount of gas used per tonne of glass, the amount of waste gas is only about half of that produced by conventional fossil fuel furnaces. All three factors which determine the NO_x concentration in the waste gases, i.e. the amount of excess air, the air pre-heat temperature and the combustion chamber temperature, are particularly favourable in this furnace.

The long flame path, in conjunction with the burners used, allows almost stoichiometric combustion. As a result of the lower waste gas temperatures the air pre-heat temperatures are normally not higher than 500 °C, and usually the maximum temperature in the crown does not exceed 1450 °C. Therefore the NO_2 concentration in the waste gases is very low. Corrected to 8 % O_2 the values measured lie between 400 and 450 mg/Nm^3 in the waste gases. If the mass flow in relation to the quantity of glass is calculated, then the value is extraordinarily low, and even complies with Californian limits.

As a result of the good refining capabilities in the shallow glass bath the refining agents can be reduced to a minimum. It is sufficient to use 600 g sulphate per 100 kg sand as refining agent in the batch. In the case of gas firing this results in a SO_2 concentration of ap-

proximately 300 mg/Nm³ calculated on a basis of 8 % oxygen. These values are far below the current limits set by the TA Luft and will also comply with the anticipated new regulations.

3 OPERATING EXPERIENCE

A total of seven furnaces of this type have already been commissioned. The oldest furnace, which is now 4 ½ years old, melts potash glass for manual production, and still produces high quality glass. Over the past 4 ½ years the average percentage of first grade ware was between 93 and 94 %. Optimisation of the fossil heating made it possible to significantly reduce the amount of electrical energy used compared with the original calculations.

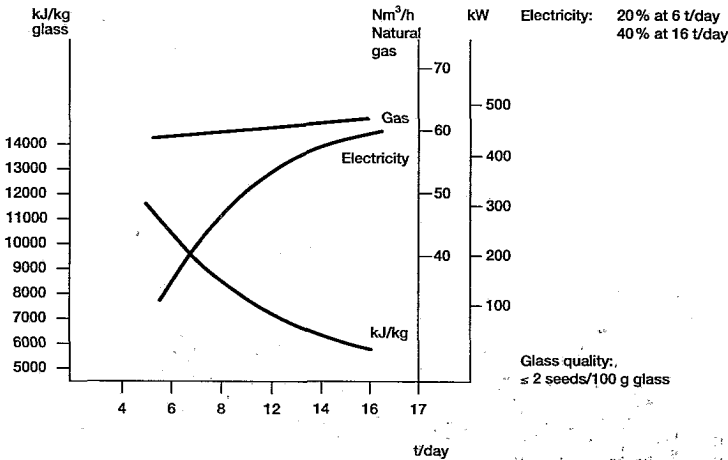


Figure 3: FlexMelter (type 12), Energy consumption - potash glass with 30 % cullet

Another furnace was designed for a completely different type of production. The objective was to melt glass for high voltage insulators, whereby glass faults in the form of inclusions from the batch or from the refractory materials had to be avoided as far as possible.

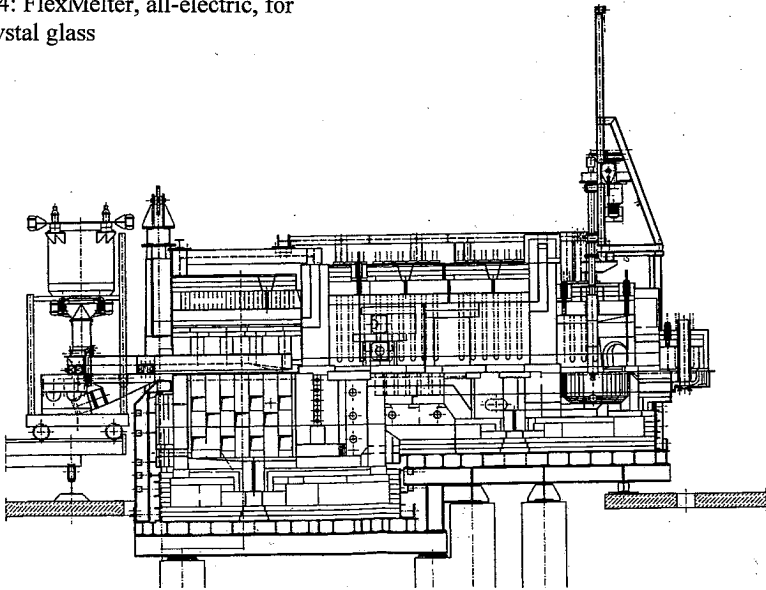
As the minimum residence time of the glass in this furnace is very long, it was assumed that no batch components would be found in the finished-glass, even at low melting temperatures. Furthermore the low bath temperatures automatically lead to very low refractory wear, so that only small numbers of stones from this source were expected. Initially this furnace was designed for a maximum pull of 18 tonnes, but the load was increased shortly to 25 tonnes during operation. In order to limit the refractory wear the furnace was equipped with top electrodes in the melting area. The furnace met all expectations to the full. The glass was found to contain between 3 and 10 stones per tonne, depending on the furnace load. No bubbles or seeds were present.

The furnaces which have been built for soda-lime glass vary in capacity from 7 t/24 h to 50 t/24 h. In all cases the glass quality is excellent, and the seed count is not more than 2 to 3 seeds per 100 g glass.

It has proved possible to greatly simplify operation of the smaller furnaces by providing the basic energy required during a production shutdown period just with the gas burners in the refining zone and completely switching off the electrical energy supply to the furnace. In this way it is possible to achieve the variation in melting rate just with electricity, so that adjustment is limited to the amount of electricity applied, according to the melting rate required. For larger furnaces it is not economic to use just electricity in this way. Therefore the gas quantity and the amount of electrical power are both varied according to the load.

A FlexMelter for lead crystal has now been built. As the customer only received permission to build an all-electric furnace, gas firing had to be omitted. An existing electric furnace was rebuilt, and made shallower, and a FlexMelter refining zone was added. This area, together with the working bays, is also electrically heated, using Kanthal Super heating elements. The furnace is relatively small, with a maximum melting capacity of 7 t/24 h. The melting end works with a cold top, and so it is not possible to reduce the melting rate to zero. At weekends and during the night a certain amount of glass is removed via an overflow.

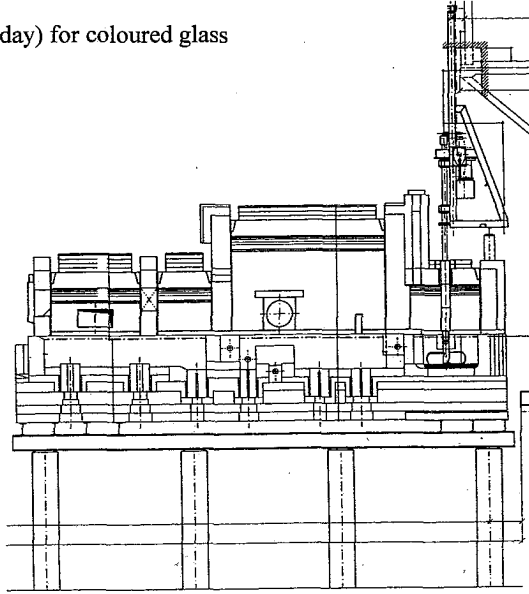
Figure 4: FlexMelter, all-electric, for lead crystal glass



Despite this, the flexibility is still much higher than with a standard all-electric furnace. The temperature in the melting end, and therefore the melting rate, can be greatly reduced without affecting the glass quality. This is possible because refining takes place in the separate refining zone. It is possible to reduce the load to about one third of the maximum, which is not possible with other all-electric furnaces. The electrical energy is introduced into the melting area by tin oxide electrodes. In this case these remain far below the sublimation limit of 1410 °C, as the glass bath temperature in the melt does not normally exceed 1250 °C. The maximum temperature in the refining area superstructure is normally 1380 °C. It has been shown that this temperature is completely sufficient as the same temperature is achieved in the complete glass bath as it flows over the refining bank.

Another small FlexMelter with a maximum capacity of 7 to 8 t/24 h has been built to melt coloured glasses.

Figure 5: FlexMelter (7 t/day) for coloured glass



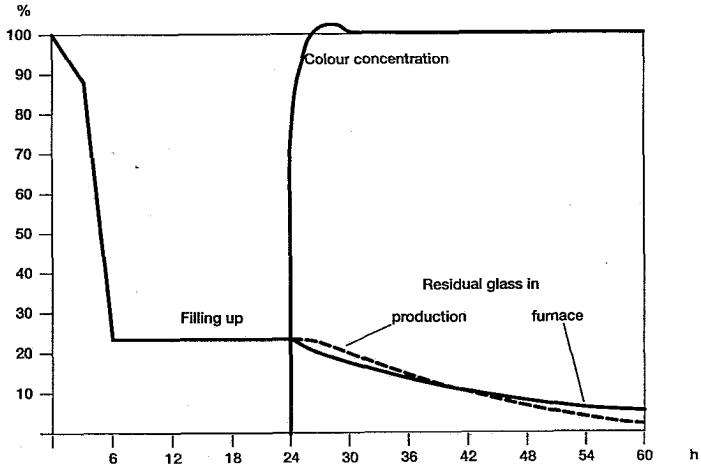
Possible methods of changing the colour in such a furnace have been tested in the laboratory. If the colour change is made on the run, without the short term addition of excess colouring agents, it obviously takes a long time before the correct colour concentration is achieved. Similarly, traces of the original glass will be present in the production for a long period.

The colour change process can be greatly improved by the addition of excess colouring agents for a certain period. If three times the required level of colouring agent is added for three hours the new colour becomes too intense, but reduces to the correct level after about 30 hours. However, the amount of the original glass to be found in the production will still reduce in the same way.

Colour changing on the run is therefore only really suitable for a change of shade within one colour, when the amount of the original glass is of little significance. Another method should be used if the colour is to be changed completely. The initial procedure is the same as described above, i.e. triple amounts of colouring agent are added for three hours. This three hour period comes from the minimum residence time in the melting area.

After three hours no new coloured glass has entered the refining area. The batch charging is stopped, the drain in the refining area is opened and all the glass in the refining area, working end and feeders is drained off. The glass level in the melting tank is reduced to the level of the bank in the refining area, so that the glass left in the melting area amounts to only 23 % of the total glass volume. The colour in the melting area stabilises during the draining period, and reaches the required level as a result of the additional colouring agents added.

Figure 6: FlexMelter (type 6), change with time of colour concentration during colour changing (colour changing with partial draining and overdosing)



As the drained glass has not been mixed with the new glass it can be remelted when the same colour is produced again. When the draining is complete the total available electrical energy can be used, as the electrodes remain completely immersed in the remaining glass bath. It is therefore possible to refill the furnace within 24 hours, and the new colour reaches the correct intensity within 30 hours. The amounts of the original glass remaining in the furnace, and occurring in the production, reduce more quickly than with colour changes on the run, so that only 2 % of the original glass is present in the production after 60 hours. In order to prevent traces of the original glass from causing production problems, it is vital to homogenise the glass before it enters the forehearth. The furnace therefore has a circular distribution tank with a stirrer which prevents colour streaks and so produces an homogeneous colour.

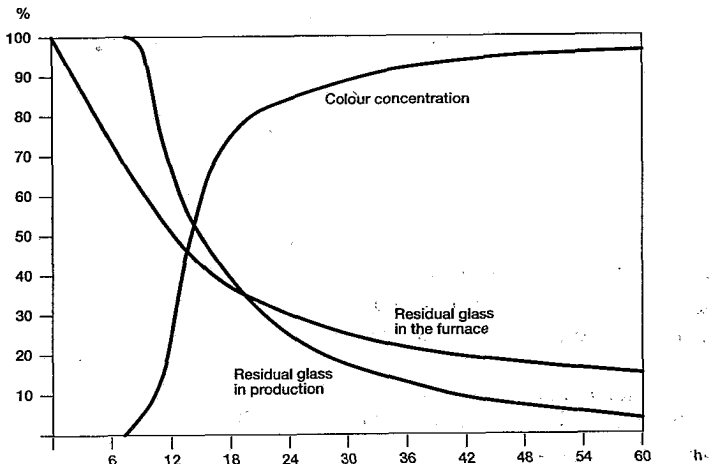


Figure 7: FlexMelter (type 6), change with time of colour concentration during colour changing (colour changing on the run without overdosing of colour)

At present a further furnace for lead crystal glass with 24 % PbO is being designed. In this case the customer has specifically requested that no electricity is to be used. A normal FlexMelter design could therefore be used, with the application of gas instead of electricity in the melting area. This furnace will go into operation at the end of this year.

The excellent glass quality which can be achieved with the FlexMelter, in conjunction with the low energy costs and low emission values, means that the furnace is also an interesting proposition for much higher loads. Experience so far with the FlexMelter clearly indicates that the furnace will be very suitable for borosilicate glasses.

4 SUMMARY

The FlexMelter is a new type of melting furnace, in which the melting, fining and refining areas are separated from one another so that no return currents occur. The furnaces are heated by gas and electricity. Electrodes are used to introduce the electrical energy into the glass bath in the melting area. The refining zone is gas heated. The waste gases are passed through the melting area, which results in a large proportion of the waste gas energy being transferred to the batch.

These innovations have resulted in a very flexible furnace. No glass must be removed during shutdown periods in the third shift or at weekends. Furthermore, this furnace offers a direct relationship between pull, temperature and glass quality, so that the glass quality can be pre-determined. Finally, the advantages of the FlexMelter can be listed as follows:

1. Direct relationship between glass quality, pull and temperature
2. High flexibility with regard to load changes
3. High glass quality
4. Simple operation
5. No glass extraction necessary during standstill periods
6. Fossil fuel and electrical energy are virtually interchangeable
7. Low refractory costs
8. Fast glass type change.

THE DISTRIBUTION OF ELECTRODES AND ITS INFLUENCE ON THE FLOW
OF GLASS

Stanislav Kasa, Antonín Lisý
Institute of Chemical Technology
Department of Glass and Ceramics
Prague, Czech Republic

The glass currents are significantly influenced by the shape and position of electrodes in the melting tank and by the connection of the electrodes to the power supply. The combination of horizontal rod electrodes and plate electrodes as well as the combination of top-electrodes and horizontal rod electrodes, are described in the following contribution. The influences of above mentioned positions of electrodes on the flow of glass have been investigated by means of the method of physical modelling. It has been found that it is necessary to determine the suitable positions of electrodes and the corresponding form of the glass currents for every shape of the melting furnace. It is possible to determine also the optimal technological conditions enabling the minimizing the consumption of energy while maintaining the good quality of melted glass.

The melting of glass is always accompanied by the flow of the melt, and its occurrence in melting furnaces is a necessary condition for the good operation of a glass melting furnace, because it accelerates the processes of the heat and mass transfer. Currents in continuous melting furnaces are caused by the withdrawal of molten glass or are due to the molten glass attaining different temperatures and therefore different densities at various places. These two types of currents are identified as the primary working or "pull" flow and the secondary convection currents.

If the glass is heated from above, the maximum temperature will occur in the middle of the melt surface, with temperature gradients towards the furnace-walls, near which the melt is generally cooler. In zones of maximum temperature, the glass has the lowest densities. The centrally situated warmer and less dense masses are forced upwards. The point of the highest temperature in the middle of the furnace acts as a hot spot with a stream of hot melt flowing from it. A continuous tank furnace

has a maximum temperature in the longitudinal as well as in the transverse direction and the convection currents are formed in both directions. These convection currents combined with the pull of the glass form the total flow in the furnace.

The zone of higher temperatures across the furnace forms a thermal barrier, which divides the furnace into the melting and conditioning zones. These zones play an important role in the melting and in the flow of glass. The presence of the thermal barrier in the furnace is therefore another important condition for the good operation of a glass melting furnace. It is necessary to maintain the thermal barrier on the requisite level related to the pull of the furnace. If we want to increase the pull, it is necessary to reinforce the existing thermal barrier. There exist several means to reinforce the thermal barrier in the furnace. An important method of strengthening the thermal barrier consists in electric boosting.

Similar problems exist also in all-electric glass melting furnaces, because the shape and position of electrodes in the melting tank influence the form and the position of thermal barrier and also the flow pattern of the melt in the furnace. Some information concerning the influence of various locations of vertical, horizontal and inclined rod as well as plate electrodes, on the form of thermal barrier and on the flow pattern of glass melt, may be found in (1,2).

Due to increasing demands placed today on the all-electric melting furnaces, especially from the point of the melting rate and quality of glass, it will be necessary to find some new locations of electrodes in the melting tank. We have to combine and use entirely new distribution of electrodes. For the above mentioned reasons the following locations and combinations of electrodes have been investigated by means of a physical model:

- i) the combination of horizontal rod electrodes and plate electrodes
- ii) the combination of horizontal rod electrodes and top-electrodes

If we wish to feed the electric current into the glass melt by means of electrodes of various shape and location (e.g. the combination of rod and plate electrodes) and to in-

investigate their influence on the flow pattern of glass melt in the melting tank, it is necessary to solve the following problems:

- 1) to find the influence of the power distribution among the individual electrodes on the flow of glass melt
- 2) to find the influence of the mutual positions of electrodes on the flow pattern of glass melt.

I) Horizontal rod electrodes and plate electrodes

1) The investigation the influence of the distribution of the power between the plate electrodes and the horizontal rod electrodes.

The mentioned problem has been solved by four variants. Their experimental arrangement is shown in Table I

Table I

| Variant | Ratio of power inputs [%] between | |
|---------|--------------------------------------|---------|
| | plate el. | rod el. |
| 1 | 100 | 0 |
| 2 | 85 | 15 |
| 3 | 70 | 30 |
| 4 | 50 | 50 |

The glass currents in the neighbourhood of electrodes and their changes caused by the distribution of power between the individual types of electrodes are shown in Figs. 1 - 4. Found values of velocities are shown in Table II.

Conclusion: (Paragraph I.1.) From Figs. 1, 2, 3 and 4 may be seen the influence of the power density distribution and its distribution between the plate and rod electrodes. The position of electrodes in Fig.1 (no power on horizontal rod electrodes) is distinguished by a small cycle of the convection current and by a comparatively powerful thermal barrier. The successive distribution of power into the two layers of electrodes, leads to the increase of the convection cycle and the decrease of the thermal barrier. It seems that in this case a good distribution of power will be at the ratio: 70% in plate electrodes and 30% in rod electrodes. This leads to the increasing of convection

cycle and therefore to the more intensive heat transfer under the batch. The thermal barrier remains sufficiently powerful, too.

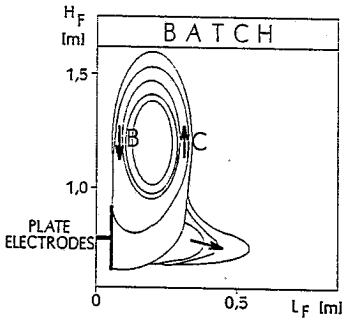


Fig. 1 Stabilized currents in the neighbourhood of electrodes

$P_{\text{plate el.}} = 100\%$
 $P_{\text{rod el.}} = 0\%$

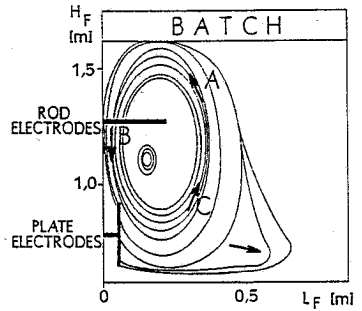


Fig. 2 Stabilized currents in the neighbourhood of electrodes

$P_{\text{plate el.}} = 85\%$
 $P_{\text{rod el.}} = 15\%$

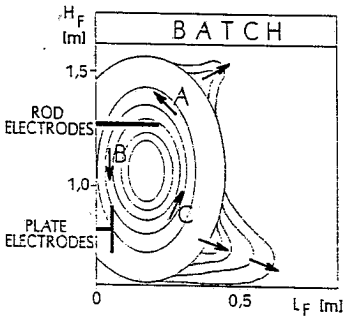


Fig. 3 Stabilized currents in the neighbourhood of electrodes

$P_{\text{plate el.}} = 70\%$
 $P_{\text{rod el.}} = 30\%$

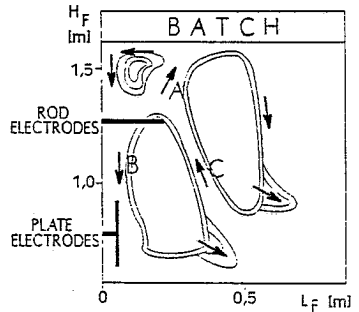


Fig. 4 Stabilized currents in the neighbourhood of electrodes

$P_{\text{plate el.}} = 50\%$
 $P_{\text{rod el.}} = 50\%$

Table II

| C u r r e n t | Ratio of power inputs between the plate and rod electrodes [%] | | | | | | | |
|---------------------------------|---|-------|-------|------|-------|------|-------|-------|
| | 100:0 | | 85:15 | | 70:30 | | 50:50 | |
| | Velocities [cm.min ⁻¹] | | | | | | | |
| | M | F | M | F | M | F | M | F |
| A | | | 0,49 | 1,90 | 1,24 | 4,80 | 1,32 | 5,11 |
| B | 2,72 | 10,53 | 0,99 | 3,83 | 1,62 | 6,27 | 2,72 | 10,53 |
| C | 2,06 | 7,98 | 1,81 | 7,01 | 1,85 | 7,17 | 1,73 | 6,70 |

M - signifies the model, F - signifies the furnace

A - specifies the rising current above the rod electrode

B - specifies the dropping current near the wall

C - specifies the rising current under the rod electrode

2) The reciprocal influence of electrode-position

The reciprocal influence of the positions of plate and rod electrodes on the flow of the glass in their neighbourhood has been investigated by means of three configurations of electrodes described in Table III. The distribution of power among the individual electrodes was in all variants constant ($P_{\text{plate el.}} : P_{\text{rod el.}} = 70\% : 30\%$).

Table III

| Variant | Distance between electrodes [mm] | Distance of plate electrodes from the bottom [mm] |
|---------|--|---|
| 5 | 670 | 200 |
| 6 | 450 | 200 |
| 7 | 280 | 200 |

The flow of the glass melt in the neighbourhood of the electrodes depends on the distance of the plate and rod electrodes. It is shown in Figs. 5 and 6. The experimental arrangement of the position and the distribution of power input among the electrodes in variant 6 is identical to the arrangement in variant 3. It is possible therefore to compare Figs. 5 and 6 with Fig. 3.

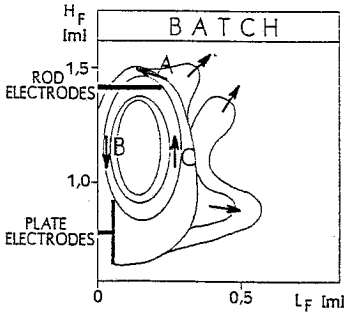


Fig. 5 Stabilized currents
between electrodes
(Variant 5)

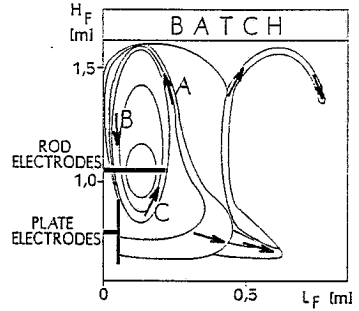


Fig. 6 Stabilized currents
between electrodes
(Variant 7)

The velocities of the glass currents measured on the physical model and recalculated on the furnace for variants 5, 6 and 7 are shown in Table IV.

Table IV

| C u r r e n t | Distance between the electrodes [mm] | | | | | |
|---------------------------------|--|-------|------|------|------|-------|
| | 670 | | 450 | | 280 | |
| | Velocities [$\text{cm}\cdot\text{min}^{-1}$] | | | | | |
| | M | F | M | F | M | F |
| A | 0,54 | 2,09 | 1,24 | 4,80 | 2,15 | 8,32 |
| B | 3,70 | 14,33 | 1,62 | 6,27 | 4,28 | 16,58 |
| C | 1,52 | 5,89 | 1,85 | 7,17 | 1,24 | 4,80 |

M - signifies the model, F - signifies the furnace

A - specifies the rising current above the rod electrode

B - specifies the dropping current near the wall

C - specifies the rising current under the rod electrode

Conclusion: (Paragraph I.2.) Similarly to the previous case, it is necessary to evaluate the measured variants from the point of view of the generation of sufficiently powerful convection flows which evoke an increase of the heat transfer into the

space under the batch. From this point of view the variant 6 seems to be a suitable one. It is identical with the variant 3 - see Fig. 3.

II) Horizontal rod electrodes and top-electrodes

(Variants 8, 9 and 10)

The investigation of the flow of glass melt between the electrodes of the above configuration has been focussed on the dependence on the length of the top-electrodes only. The length of horizontal rod electrodes was identical in all variants (800 mm). The length of top-electrodes was decreased successively from 1200 to 900 and to 600 mm. The flow pattern of glass melt were in all the three variants identical. Above the thermal barrier, the boundary of which is created by the lines connecting the tips of top and horizontal electrodes, the cycles of convection currents occur. The flow of glass melt is shown in one half of the melting tank only, because it is symmetrical on both sides of the furnace. The recalculated values of velocities from model to furnace are shown in Table V.

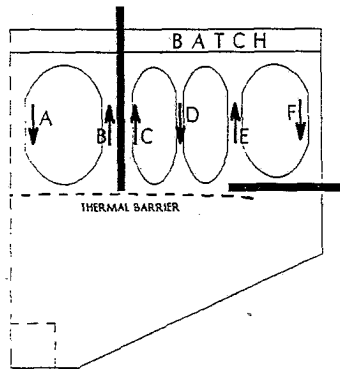


Fig.7 Stabilized currents above the thermal barrier

Conclusion: (Paragraph II) The combination of horizontal and top-electrodes creates a very strong thermal barrier in the melting tank. The tips of the electrodes create this boundary. This means, that by successive shortening of the

Table V

| Variant | Length of the top-electrodes [mm] | Velocities of the currents [cm.min ⁻¹] | | | | | |
|---------|-----------------------------------|--|------|------|------|-------|-------|
| | | A | B | C | D | E | F |
| 8 | 1200 | 2,36 | 6,36 | 5,64 | 3,50 | 12,06 | 10,02 |
| 9 | 900 | 2,47 | 6,51 | 5,95 | 3,71 | 12,10 | 10,10 |
| 10 | 600 | 2,55 | 6,75 | 6,21 | 3,82 | 12,25 | 10,15 |

top-electrodes the thermal barrier is shifted in the direction of the batch. The shortening of the top-electrodes leads to a small increase of the velocities of the flow, but it leads also to an increasing heat transport below the batch. In this case it is necessary to find a compromise between the quantity of the heat transferred below the batch and the size of melting zone, which is determined by the position of the thermal barrier.

Conclusion

Based on the above results, it may be concluded that the position of the electrodes in the melting tank has a great influence on the flow of the glass melt. Similarly, the amount of power which is released by each individual electrode, is of great importance. Considering the large variability of the positioning of electrodes, which is individual for this each furnace, it is necessary to investigate this problem by means of a physical model. This method enables us to estimate the influence of the configuration of electrodes on the flow of glass melt and to find their optimal positions. By means of this method it is possible also to determine the optimal technological conditions for minimizing the consumption of energy while keeping a good quality of melted glass.

References

1. Staněk J. et al., Glass Technology 10 (1969) 43
2. Staněk J., Electric melting of glass, Elsevier Amsterdam 1977

SPECTRAL ELEMENT METHOD FOR THERMOCONVECTION IN A GLASS MELT

N. Vanandruel

Unité de Mécanique Appliquée (CESAME),
Université Catholique de Louvain, Belgium

Abstract

Accurate representation of heat and mass transfer in thermoconvective flows is of great importance in several industrial processes. In particular, this study is motivated by the need to better understand molten glass circulation in glass melting furnaces.

The geometry of furnaces is rather simple: the free surface of the molten glass is horizontal and the refractory walls are parallelepipedic. However, the flow patterns in this geometry are actually 3D as the width of the tank can be restricted at the neck while the height is modified by a step. For these reasons, the solution in the plane of symmetry can no longer be regarded as representative.

For this class of problems, the convective currents are of moderate amplitude, with a typical value of the Reynolds number of $O(1)$, while the Péclet number can be of the order of 300 (given the low conductivity of molten glass). The numerical difficulty is therefore associated with solving the energy equation rather than that of momentum.

While a detailed, steady-state solution is important, the time evolution of the flow structure is also of great interest. Given the intensity of the thermoconvection – the Grashof number is ~ 5000 – no unstationnary solution should be expected. However, a sensitivity study of the variation of the solution under varying operating conditions, e.g. pull rate, thermal boundary conditions . . . , sheds light on the stability and the relative importance of both thermal and viscous effects.

The numerical tool developed to simulate this physical situation is an **unstationnary spectral element** Boussinesq solver. Spatial discretization is realized through the division of the computational domain in a limited (<50) number of spectral elements. On each element, the unknowns are interpolated by a high-order Legendre polynomial. Depending on the value of the Prandtl number of the fluid, a greater number of degrees of freedom can be associated to the thermal problem.

The goal of this presentation is to claim the efficiency of high order methods for the numerical simulation of thermoconvection in the glass melting tank. Comparisons with finite-difference and finite-element solutions demonstrates a lower number of degrees of freedom necessary to obtain specified level of accuracy. A global increase in computing efficiency allows unsteady 3D simulations like time evolution of melting tank during change of glass.

1 Numerical Simulation Models of Glass Melt Thermoconvection

As pointed out in [4], the main problems with 3-D numerical furnace models are not only their need of computational resources –CPU and memory– but also the relative unreliability of input data (conductivity) and the limited possibilities of verification associated with difficult representation of complex solutions.

Efficient high-order methods produce accurate numerical representations within the computational environment of modern computer work station. In this environment, various graphic capacities can handle the results and allow easier interpretation of flow patterns. The problem of unreliable data can be solved by expensive “parameter studies” where successive simulations can be compared, identified with reduced scale models or even with industrial measurements. Another interesting way of using the powerful (but still approximate) numerical tool is in combination with control/identification procedures. In this combined study, exchanges between unsteady numerical simulations and control/identification models can be useful to gain a global understanding of the melt convection and to estimate quality-related parameters such as the temperature profile or the residence time distribution [1].

2 Spectral Methods

The fundamental principle of spectral methods [2] is the decomposition of the unknown fields in a linear combination of a set of basis function

$$u_N(x) := \sum_{n=0}^N a_n \psi_n(x)$$

where u_N is the approximation of the Nth order, the set $\{a_n\}$ is the so-called “spectrum” of this solution with respect to the spectral basis ψ_n .

While, for low-order methods, the basis functions are usually defined such that the $\{a_n\}$ set is actually the set of the values of the function u_N at given points (nodes); for spectral methods this simple relationship does not hold. To evaluate, from the spectrum, the values of the function at given spatial coordinates, an explicit evaluation of the fundamental decomposition is to be used. The computational cost of such an evaluation has been drastically reduced in the case of the Fourier spectral method. For this well-known particular choice of basis functions

$$\psi_n(x) := \cos \pi n \frac{x-a}{L}$$

where $L := b - a$ is the length of the interval $[a, b]$ on which u_N is defined; the relationship between the spectrum and the value of the u_N approximation at the N equally spaced collocation points

$$x_n := a + \frac{(b-a)}{N+1} * n$$

has been optimized and requires only $O(N \log N)$ operations rather than the $O(N^2)$ operations needed by the direct calculation. This evaluation algorithm has been called for this

reason the Fast Fourier Transform (FFT) and historically justifies the interest of spectral methods for scientific computational methods.

There is a strong dependence of the set of basis functions ψ_n on the set of collocation points where the function can be directly evaluated. While Fourier basis functions are associated with equally spaced points, Chebyshev functions produce a set of points with notable refinements near the boundaries. This particularity can be advantageous when greater gradient variations (like boundary layers) are expected at the extremities of the computational domain. A third choice, the Legendre functions, present other interesting properties explained later.

Within this general framework, spectral methods are resolved with the following algorithm: i) the set of partial differential equations is rewritten for the spectrum of the unknown fields; ii) the resulting "spectrum system" is solved; and finally iii) the value of the u_N approximation is evaluated at the collocation points. The industrial applicability of spectral methods is severely restricted by three limitations:

- the computational domain must be "simple", i.e. topologically equivalent to a parallelepipedic box. Several domain decomposition methods have been proposed for the extension of spectral methods to multidomain calculations, but they suffer from difficulties with continuity boundary conditions at the interfaces between subdomains.
- the coefficient of the original spatial equations must be constant to allow direct transformation of the equations from the spatial to the spectral space. The conductivity and viscosity must therefore be constant on the whole computational domain.
- great numerical difficulties appear when solving the spectral set of equations. For this reason different preconditioning strategies have been investigated, leading to linear systems with better numerical conditioning.

Despite this restrictions, spectral methods have shown impressive resolution capacities for different situations such as atmospheric turbulence, crystal growth thermoconvection, and molten tin currents for float glass production.

The most important feature associated with spectral methods is their convergence rate, defined as the error decrease associated with an increase in the number of degrees of freedom (d.o.f.). Low order methods typically present linear or quadratic convergence rates i.e. multiplying the number of d.o.f. by a factor of 2 divides the resulting error by 2 or 4. On the other hand, spectral methods achieve *exponential convergence rates*, i.e. the error decreases like e^{-N} where N is the order of the approximation. Consequently, the computational effort required to attain a given level of accuracy is usually much smaller for spectral methods, subject to the restriction that the physical situation admits the limitations of a constant-coefficient mono-domain problem.

Another useful property of spectral methods is the *à priori* error indication provided by the spectral decomposition. The last terms of the spectrum $\{a_n\}$ must be small and decreasing to ensure that the spectral approximation embodies all the meaningful physical information.

To conclude this extremely rapid overview of spectral methods, it must be mentioned that the usefulness of this class of numerical tools has been increased by the *pseudospectral* algorithm. This algorithm avoids evaluations of the spectrum and manipulates only values of the function at the collocation points. Pseudospectral methods allow Legendre and

Chebyshev functions to be used even though they do not have an immediate fast transform (such as the FFT in the Fourier case).

3 Spectral Element Method

The spectral element method combines the exponential convergence of spectral methods with the geometrical flexibility of finite elements [5]. To achieve this result, the variational form of the problem is solved rather than its spectral transform. If the differential system is

$$L(u) = f$$

then, classically, the variational (or weak form) is obtained by integration of the system with multiplication by a given weight function. The selected weight function is here the basis function ψ_n , leading to the Galerkin formulation

$$\int (L(u_N) - f)\psi_n = \int (L(\sum_{n=0}^N a_n \psi_n(x) - f)\psi_n = 0.$$

The consequences of this numerical artifact is

- to allow decomposition of the domain in subdomains where a spectral discretization is performed. Natural continuity of the solution through interfaces is obtained by the decomposition of the integral on each separated spectral element (through the so called "direct stiffness summation"),
- to express flux boundary condition resulting from the classical integration by parts.

Variational form is also one of the principles of the finite element methods (FEM), but while FEM generally consider a great number of small subdomains (elements) where low order interpolants approximate the unknown fields; spectral element methods (SEM) use high order spectral basis function on a moderate number of subdomains [6].

The function ψ_n used for this spectral element discretization is the set of Legendre functions. Their useful characteristic is their orthogonality

$$\int_{-1}^{+1} \psi_m \psi_n = \delta_{mn}$$

where δ is the Kronecker symbol, leading to a diagonal mass matrix and allowing geometrical deformation of the mesh through classical Jacobian transformation. Combined with this choice of basis function, spectral element methods select the pseudospectral algorithm.

Differences between SEM and h-p type FEM lies in the interpolation order (for a furnace simulation, orders like 15 are usual) and the use of *tensorisation*. Tensorisation is the key for practical efficiency of spectral methods. Suppose we want to know the value of a 3-D basis function at given location (x, y, z) . Instead of the naive calculation

$$\psi_{i,j,k}(x, y, z)$$

we use the tensor form to obtain

$$\psi_{i,j,k}(x, y, z) = \psi_i(x) * \psi_j(y) * \psi_k(z)$$

and reduce the cost of such an estimation from $O(N^6)$ to $O(N^4)$ operations. This reduction is the main reason for the use of iterative solvers combined with spectral element methods. These solvers, requiring limited memory, do not suffer from the "full" matrix structure of the spectral operators which couple a great number of unknowns. Logically, the resolution strategy of non-linear problems will therefore be a time dependent discretization even if the desired solution is a steady state [6].

4 Glass Thermoconvection

According to the particularities of the numerical simulation of glass thermoconvection, specific numerical techniques have been used in conjunction with spectral element methods. These techniques consider the differences both in time and space, between the temperature, velocity, and pressure fields.

From the spatial point of view, it is well known that while steep temperature gradients are encountered near the boundaries, the velocity distribution usually does not produce a boundary layer. The ratio between thermal and velocity boundary layers is measured by the Prandtl number for which a typical glass melt value is in the range of 200 to 300. For this reason, different interpolation degrees have been selected for temperature and velocity fields. For finite elements [8], quadratic temperature and linear velocity interpolations produce accurate results at low CPU cost. In this spectral element method, we select a more adaptative distribution of the number of d.o.f. . In general, the temperature field requires more d.o.f. and a typical distribution is 15 temperature for 10 velocity unknowns. However, in the width direction of the furnaces [7] where moderate values (~ 5) are chosen, equivalent distribution is selected for temperature and velocity.

The pressure field acts, in this incompressible flow problem, as a Lagrangian multiplier to ensure vanishing velocity divergence. The value of the pressure itself is not really pertinent and moreover it does not differ much from the hydrostatic solution

$$p \cong p_o - \rho gh$$

where h is the depth and p_o the atmospheric pressure. Therefore, several methods can be used [3] to ensure incompressibility without explicitly calculating the superfluous pressure field.

Similar differences between velocity, temperature, and pressure are realized for the time discretization. As quantified in [8], the Prandtl number also is a measure of the ratio between velocity and temperature time constants τ_{vel} and τ_{temp} . Selecting the following approximations, which can be verified by numerical experiments,

$$\tau_{vel} \cong \frac{L^2}{\nu} \quad \text{and} \quad \tau_{temp} \cong \frac{L^2}{\kappa}$$

where ν is the kinematic viscosity, κ the thermal diffusivity and L a typical length, the ratio τ_{temp}/τ_{vel} reduces simply to the Prandtl number ν/κ . The velocity time step is therefore smaller than that for the temperature, a good compromise being about 10 velocity time steps for each temperature. The pressure problem is only resolved when the velocity divergence becomes greater than a given tolerance value.

With all these numerical techniques, a required accuracy level can be reached with acceptable CPU costs. Consequently, different unsteady simulations can be realized, including

changes of the operating conditions and mixing. On the other hand, a highly accurate solution – obtained with voluntary “excess” of d.o.f. – is a powerful tool for numerical quality dependent studies like tracking or residence time evaluations [1]. The global approach of the spectral element method, rapidly ensuring grid independance, appears therefore as a good candidate for glass thermoconvection simulations.

5 Acknowledgements

The author acknowledges continuous financial support from the IRSIA (Institut pour l’encouragement de la Recherche Scientifique dans l’Industrie et l’Agriculture) through a research grant. Thanks are also expressed to the GLAVERBEL Centre de Recherche et Développement for valuable collaboration.

References

- [1] R.G. Beerkens, T. van der Heijden, and E. Muijsenberg. Possibilities of glass modeling for the prediction of the quality of melting processes. *Ceram. Eng. Sci. Proc.*, 14(3-4):139–60, 1993.
- [2] C. Canuto, M.Y. Hussaini, A. Quarteroni, and T.A. Zang. *Spectral Methods in Fluid Dynamics*. Springer Verlag, New-York, 1988.
- [3] M. Deville, L. Kleiser, and F. Montigny-Ranou. Pressure and time treatment for Chebyshev spectral solution of a Stokes problem. *Int. J. Num. Meth. Fl.*, 4:1149–63, 1984.
- [4] L. Němec. Analysis and modelling of glass melting. *Bol. Soc. Esp. Ceram. Vid.*, 1(31-C):139–65, 1993. proceedings of the XVI Int. Congress on Glass.
- [5] A.T. Patera. A spectral element method for fluid dynamics: laminar flow in a channel expansion. *J. Comp. Phys.*, 54:468–88, 1984.
- [6] E.M. Rønquist. Spectral element methods for the unsteady Navier-Stokes equations. Lecture series 1991-01, von Karman Institute, Rhode-St-Genèse, Belgium, 1991.
- [7] N. Vanandruel. Spectral element method for thermoconvection in a glass melt. In *proceedings of the 2nd International Seminar on Mathematical Simulation in the Glass Melting*, pages 20–23, Vsetin – Horní Bečva, 1993. Czech Glass Society, Glass Service Ltd.
- [8] N. Vanandruel and M. Deville. Unsteady numerical simulation of circulation and heat transfer in a glass melting tank. In *Fundamentals of Glass Science and Technology*, Venezia, 1993. 2nd International Conference of European Society of Glass Science and Technology. in press.

SIMULATION OF GLASS PROCESSES WITH POLYFLOW, A FINITE ELEMENT PROGRAM

N. Vanandruel

Unité de Mécanique Appliquée (CESAME),
Université Catholique de Louvain, Belgium

Abstract

Polyflow is a general Computational Fluid Dynamics finite element program which simulates the flow of Newtonian and non-Newtonian fluids, with a special emphasis on rheologically complex liquids in industrial processes.

A major objective of Polyflow is Computer Aided Processing: using the computer as a laboratory, the engineer understands, modifies, creates, tests and improves processes in which flow of viscous liquids play a dominant role. The code is used for modeling a variety of processes: extrusion, fiber spinning, laminar mixing, coating, sedimentation, heat transfer, chemical reactions, flow through channels, thermoconvection and many others. Advanced computational methods have been implemented for calculating free surfaces and interfaces which are typical of many processes. Polyflow is also used as a toolbox for developing new applications.

The specificity of the numerical methods (finite element, direct solver), the original physical modeling of glass processes and the ability of solving a wide class of thermal, flow and deformation problems will be the main topics of this presentation.

1 General specifications

Polyflow solves the flow of isothermal and non-isothermal generalized Newtonian and viscoelastic fluids, the flow of viscous fluids through porous media and flows and reactions related to chemical vapor deposition [0][1]. Several types of materials separated by interfaces can co-exist in the flow domain. A typical example of such "multi-domain" calculation is the combined study of melting tank and refractory walls. Rather than imposing a measured – generally inaccurate – value of the heat loss at the furnace boundaries, this technique allows imposition of a room temperature at the external faces of the refractories. The additional computational cost is that of a heat exchange problem in a solid.

All steady-state non-linear problems are calculated with Newton's method; solutions to highly non-linear problems can be reached by means of the versatile "evolution" algorithm implemented in Polyflow. To reach a steady-state simulation of thermoconvection in a glass melting tank, increasing gravity values or decreasing conductivity values are used in this automatic procedure. Starting from an "easy", quasi-linear situation, the calculations automatically advance to solve an increasingly non-linear problem to reach the final values of the required simulation.

On the other hand, time-dependent problems are solved with a fully coupled implicit

method which guarantees stability; the time step is automatically adjusted to satisfy a required accuracy.

Polyflow calculates free surfaces and interfaces in 2-D and 3-D; such calculations are fully implicit and solved with Newton's method. Free surface problems require a remeshing technique of the flow domain. Polyflow contains a library of remeshing techniques of the algebraic and of the elliptic types.

Polyflow contains a wide library of finite elements. Although default selections are available for all flows, the user can easily request other types of interpolation. In particular, sub-refinement is available as well as non-uniform discretization. Solving a high-Péclet and low-Reynolds glass convection problem usually requires much more degrees of freedom for temperature than for velocity. For this reason, higher order shape functions can be chosen for the temperature field whereas ordinary linear shape functions are selected for velocity. This non-uniform discretization technique significantly reduces the computational cost without affecting the global accuracy and will be intensively used for glass convection simulations.

The present paper presents three application domains of Polyflow for glass processes: 1) the TC21 test-case; 2) specific physical modeling of bubbling, boosting and radiative correction and 3) other glass-related processes like fiber spinning or blow molding.

2 TC21

2.1 Benchmarks

The TC21 benchmark consists in the numerical simulation of velocity and temperature fields in a small idealized tank furnace [2]. Given temperature and velocity boundary conditions – temperature profile at the surface, heat loss at the walls, flat batch, horizontal free surface and throat outflow – generate recirculation cells in the glass volume. The numerical simulation of the four different versions of this benchmark was realized by Polyflow without any difficulty as the problem was simply posed in terms of thermoconvective flow. In comparison with other classical numerical methods (finite differences and finite volumes spatial discretization, iterative solver), some major differences have to be pointed out.

As mentioned before, the solver of Polyflow is a *fully coupled direct method*. To reach the final set of physical values characterizing the TC21 benchmarks, 10 steps of increasing non-linearity were necessary and, for each step, ca. 5 iterations of the Newton's scheme were required to reach convergence.

The second particularity lies in the spatial discretization; the high Prandtl number value indicates the predominance of advection in the temperature equation. Therefore, in the library of the available elements, *quadratic temperature and linear velocity* finite elements were selected. The number of degrees freedom for temperature is then increased while the velocity unknowns are represented by lower order interpolation.

Finally, a moderate number of elements was requested for a given level of accuracy – measured by the heat balance –. Typical values of *28*8*6 elements grid* results in a ~5% heat balance. These values are to be compared with the grid points used by uniform low-order methods, typically 35*10*6. The full simulation requires about 20 CPU hours on a Silicon Graphics Personal Iris Workstation.

2.2 Unsteady TC21

While the numerical simulation of the TC21 benchmarks does not require any additional physical modeling, we exploited the Polyflow capacities to simulate two unsteady situations for the TC21 test case [3].

1) The first study is the unsteady simulation of sudden modification of the boundary conditions (10 % increase of the pull, 5°C decrease of the temperature profile at the surface, ...). The time discretization algorithm used in Polyflow allows for the automatic selection of the time step and clearly indicates both temperature and velocity time evolutions. Variations of the conductivity show the influence of this parameter on the thermal time constants while velocity evolutions were apparently unaffected.

2) The second unsteady situation consists in the mixing modeling. When operating an industrial furnace, changes of glass do not occur in the whole domain, but an unsteady mixing is realized. Low diffusion coefficient – leading to high “mixing Péclet” number – were selected and showed the accuracy of numerical resolutions. It should be noted that the concentration is not the result of a tracking calculation but another global variable added to the set of partial differential equations. Residence time calculations realized with Polyflow consist also in the resolution of a new problem defined on the whole thermoconvective domain.

3 Glass Melting Furnace Modeling

Industrial furnaces significantly differ from the idealized benchmark of the TC21. To simulate accurately realistic furnaces, different physical models are presently developed in addition to the basic thermoconvective model flow solver.

3.1 Electrical Heating

The numerical treatment of electrical heating does not present great difficulties. Under classical assumptions the electrical potential field is governed by a Laplace equation. The Polyflow capabilities of simulating the unsteady electrical boosting has been demonstrated [3]. The correction of the Lorentz force is also possible and lead to an accurate description of the molten glass velocity in the vicinity of the electrodes [4].

In most applications the engineer wishes to impose a given current intensity rather than potential difference between electrodes. This problem belongs to the set of commonly called “inverse problems”. A numerical technique is implemented in Polyflow to solve the inverse problem. This method, based on generalized Lagrangian multipliers, avoids classical trial and errors outer iterations on the unknown values and solve the inverse problem at nearly the same cost as that of the direct problem. This inverse method is also useful for electrical heating simulations where connections between electrodes impose equalities of currents and/or potentials.

3.2 Radiative Correction

The importance of internal radiation in the glass melts is well known. The Rosseland approximation appears to be the only practical model that can be used for realistic 3-D

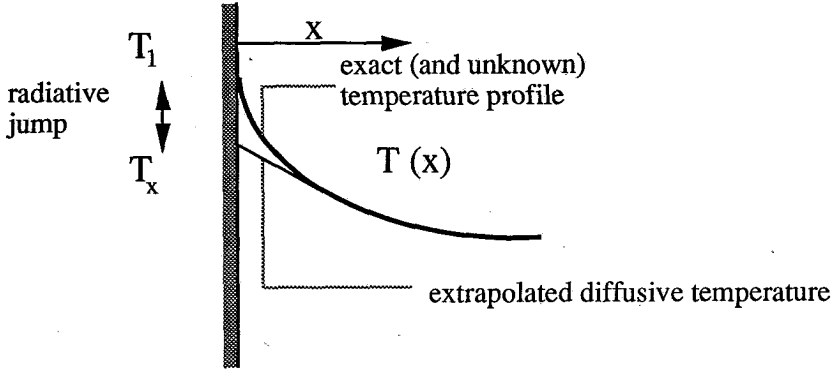


Figure 1: Radiative slip boundary condition

simulations. However, the Rosseland diffusion approximation is unable to take into account the sudden modification of the temperature gradients at the boundary, the so-called “radiation slip” [5]. This temperature difference significantly modifies the amplitude of the thermoconvection in the whole domain. Radiative boundary conditions including the correction to the Rosseland model are proposed in Polyflow, they simulate the radiation slip and provide accurate thermal boundary conditions for the thermoconvective problem. Figure 1 illustrates the principle of the radiative correction: a given temperature T_1 is to be imposed at the wall while the effective numerical boundary condition should rather impose the T_x value such that the correct temperature level is reached in the domain. The relationship between T_1 and T_x involves the values of the wall emissivity and the medium absorptivity and conductivity.

3.3 Bubbling

Air bubblers have become an integral part of glass melting tank design. The numerical simulation of bubbling can follow two different ways: a local description of the bubble trajectory or the global expression of the force exerted by the series of bubble on the convective flow. The Polyflow bubbling simulation consists of an additional force term expressing the global coupling between the bubble stream and the velocity of the molten glass [6]. With that global model, the simulation of bubbling can be realized with a negligible additional CPU cost.

4 Other Glass Processes

To illustrate the open capacities of Polyflow, the numerical simulation of two processes related to the glass industry is finally presented.

4.1 Fiber Spinning

The production of synthetic fibers is a delicate process associated with severe technological requirements. Fiber spinning is characterized by the non-isothermal nature of the flow which, as in the case of polymer melts, is dominated by its extensional behavior. On the basis of the spinneret geometry and the material properties of the fluid, the numerical simulation supplies the geometry of the drawn fiber, the temperature and the stress field together with the relationship between the draw ratio and the axial force exerted on the filament.

Polyflow provides the user with all the necessary ingredients for the successful simulation of fiber spinning: a wide class of viscoelastic models, an accurate calculation of free surfaces including the effect of surface tension, the coupled calculation of heat transfer in the melt and in the die and, finally, special elements for high Péclet number flows. Numerical simulation therefore complements experimentation for a quicker adjustment of the manufacturing process.

4.2 Blow Molding

Blow Molding is a standard process for the mass production of hollow objects. The products may be simple, such as axisymmetric bottles, or have a complex three-dimensional shape, such as gas tanks of large dimension. The numerical simulation of blow molding requires an accurate description of a flowing body with large non-isothermal deformations; the external free surface is constrained by contact with the wall.

An original remeshing technique has been implemented in Polyflow for handling the large deformations of a thin fluid shell, while a robust geometrical algorithm has been developed for detecting contacts between the fluid and the wall of the mold. Since the final thickness is a critical factor for the quality of blown products, tracking of material lines is used for establishing a relationship between the parison thickness and the thickness distribution of the blown product.

Figure 2 shows a combined extrusion-blow molding simulation. Remeshing, moving boundaries, free surfaces, material lines tracking and contact lines are some of the numerical tools used for this industrial simulation.

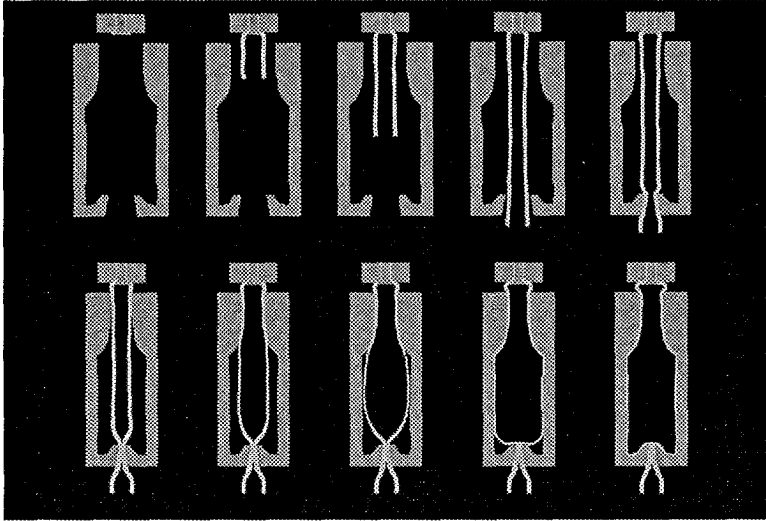


Figure 2: Combined Extrusion-Blow Molding Simulation

5 References

- [0] Polyflow Co.,
Place de l'Université, B-1348 Louvain-la-Neuve, Belgium
- [1] Crochet M.J. , Debbaut B. , Koenings R. and Marchal J.M.,
"Polyflow: a Multi-Purpose Finite-Element Program for Continuous Polymer Flows"
in Computer modelling for extrusion and other continuous processes , K.O. Brien (Ed.)
Hanser, Munich (1992), 25-50.
- [2] Technical Committee 21
"Numerical Simulation of a Glass Melting Furnace" Int. Commission on Glass (1991).
- [3] Vanandruel N. , Deville M.,
"Unsteady Numerical Simulation of Circulation and Heat Transfer in a Glass Melting
Tank" Collected Papers 2d Int. Conf. of the E.S.G. (1993) Venice, in press
- [4] Hofman O. , Philipp G.,
"Importance of the Lorentz force in electrically heated glass melts"
Glastech. Ber. 65 (1992) 142-149
- [5] Siegel R. , Howell J.R.,
Thermal Radiation Heat Transfer, McGraw-Hill, New York (1981)
- [6] Ugan A. , Viskanta R.,
"Effect of Air Bubbling on Circulation and Heat Transfer in a Glass Melting Tank"
J. Am. Ceram. Soc. 69 (1986) 382-91

LABORATORY SIMULATIONS OF BUBBLE DEFECTS IN GLASS

Mustafa ORAN

Research Center, Türkiye Şişe ve Cam Fabrikaları A.Ş.
İstanbul, Turkey

Bubble defect, which is defined as a gaseous inclusion, is one of the most common faults affecting the glass quality. Therefore, the bubble fault diagnosis and elimination are still topics of interest to the glass industry. Various efforts such as experiments on artificial bubble formation including diffusion of gases and bubble modelling are developed to understand and solve the bubble problem, while the gas bubble analysis combined with the deposit, size and position analyses is the most powerful tool for the problem diagnosis.

A project was planned to set up a series of laboratory simulations for surveying the characteristics of bubble defects related to different sources, namely metallic contamination, air entrapment and electrolysis. The bubbles of each source were characterized by observing their time dependent formation and by analyzing their gaseous components. In particular, the changes in bubble compositions, depending on time and temperature, were traced to estimate the location of bubble formation in the glass furnace.

The information obtained from the systematic bubble analysis was well supported by laboratory results, and thus it was possible to make reasonable predictions on the sources of bubble defects.

1. LITERATURE SURVEY

Gaseous inclusions in glass, commonly referred to as bubbles, generate from many sources and frequently cause quality problems in glass manufacturing. Therefore, the diagnosis and elimination of bubble defects are of great interest to the glass industry.

Besides the bubbles from natural sources which cannot be eliminated during refining, newly formed bubbles may come from breakdown sources such as pores in the refractories, electrochemical reaction, thermal reboil, impurities, entrapment of furnace atmosphere by various mechanisms, etc. All bubbles start to interact with the dissolved gases in the melt and this interaction continues until the equilibrium state, "frozen point" of bubble, is reached. The bubble becomes a defect if it reaches its frozen point without elimination. As a consequence of this period, the contents of a bubble has many variations, and the gas analysis of the defect is indexed to the frozen point. Hence, the troubleshooters should need the analysis of the bubbles with sufficient knowledge of the variations in bubble contents as a function of time, temperature and initial composition and size, in order to be able to determine the causes and history of bubbles.

Currently, accurate and reliable methods of bubble analysis are developed with the advanced instrumental technology. Various efforts have been devoted to gain more knowledge about variations in composition of gas bubbles, while the gas bubble analysis combined with the deposit, size and position analyses became the most important tool for problem diagnosis in the production bubble defects. These studies are basically classified in two groups. The first group covers the analytically oriented methods which determine the bubble contents by experimental simulations. The bubbles coming from a different source, are artificially developed and their compositions are investigated by laboratory tests as a function of time and temperature (1-4).

The second group is devoted to the understanding of bubble dynamics by numerical methods which allow the calculation of bubble size and composition. Numerous studies have been concerned with the mathematical analysis of bubble growth and dissolution depending on

the variations in bubble content (5-8). Such models describe how the bubbles might behave in the glass melt, despite uncertainties in the diffusion constants and solubilities of the gases concerned.

2. EXPERIMENTAL

The study presented here is new example of the laboratory simulation, and it was planned to set up a series of experiments for surveying the characteristics of bubble defects due to metallic contamination, air entrapment and electrolysis. Each source was artificially developed either in industrial or laboratory furnaces. The bubbles from each source were characterized by observing their time and temperature dependent formation and by analyzing their gaseous components.

The bubbles produced in the experiments have been analyzed by using a mass spectrometer (Balzers GIA 707), and the total bubble pressure has been calculated with the partial pressures of gases inside the bubble.

2.1. Metallic Contamination

One of the most common sources of bubble causing production losses in most types of glass productions is the metallic contamination due to materials entering the glass with the batch or cullet, such as copper, aluminum, etc. Metallic corrosion occurring between the glass melt and the metal tools such as mixers, bubblers is also another contamination source.

Experimental simulations of metallic contamination were proposed for two different types of glass. In the first simulation, amber container glass cullet was melted in a porcelain crucible. After obtaining the bubble-free melt, metallic particles which represent the impurities inside the cullet, were added to the melt and the formation of bubbles was observed. A set of 8 crucibles was separately kept at two different temperatures (1400°C and 1450°C) for 5, 10, 15 and 20 minutes. The bubbles in each condition were then analyzed, and the gas contents were compared with the bubbles found as defect in glass products.

In the second simulation, float glass cullet was melted in a crucible made out of a refractory block and metallic iron was placed in the bottom, representing the corrosion between the glass melt and metal tools. The bubbles formed in this experiment were kept at 1350°C for 30 minutes.

2.2. Air Entrapment

Another bubble source simulated in this study is the air entrapment where the atmosphere (air in this case) can be accidentally trapped while gathering the gob with the pipe or robotic arm in hand-made glass production.

In the gathering bay of a furnace at ~1150°C, several gobs were gathered by plunging the pipe at different angles to the glass surface in such a way that bubbles were formed by enveloping layers of molten glass.

The behaviour of these bubbles was also examined at the forming stage of hand-made products. The glass plate having the cavities was covered with another plate and they were soaked at 850°C - 1000°C to form bubbles. The gas trapped in the bubbles formed by the above mentioned operations were analyzed and compared with the product blisters.

2.3 Electrolysis

Reboil is considered as one of the most discouraging problems in the glass process since it accidentally occurs after the refining stage of glass. Reboil may be due to several different mechanisms. Oxygen reboil simulated in this study is a specific type of reboil based on the electrochemical reactions in the glass melt. Molten glass is an electrolyte, and the discharge of an electrochemical cell generated between molten glass and adjacent materials (refractories,

metals, atmosphere) allows oxygen anions in the glass structure to lose electrons and form gaseous oxygen molecules which produce bubbles.

The simulation of electrochemical reboil has been developed to identify the exact location of the bubble source occurring in a borosilicate glass melt boosted by electricity. The borosilicate cullet is put in a platinum crucible so that, on heating sufficiently, initial bubbles are removed and well-fined molten glass is obtained for the experiment. A platinum rod is then inserted into the center of crucible. An emf which is between 0-1 volts DC is applied between the rod (anode) and crucible (cathode) (Fig.1).

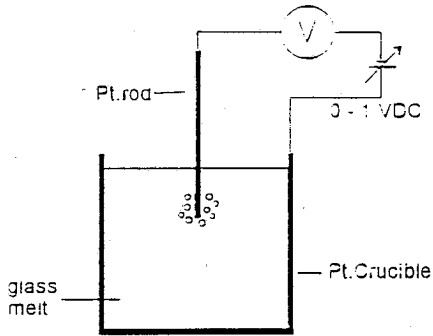


Fig.1. Set-up for electrochemical experiment

This range of potential difference represents the DC voltage occurring in the AC boosting zone and the spout zone where the platinum plunger is used in the furnace. Thus, the experiment is carried out for both these zones having average glass temperatures of 1520°C and 1320°C, respectively, and 1445°C for the transition zone. The durations required for the nucleation of bubbles with respect to the change in emf at three different temperatures were obtained, and the gas analyses of experimental bubbles were compared with the bubbles found in products.

3. RESULTS and DISCUSSION

3.1. Bubbles of Metallic Contamination

The analytical results of bubbles due to metallic impurities are given in Fig. 2.

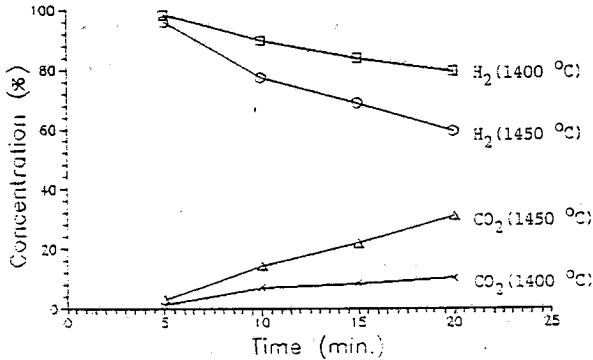


Fig.2. Bubble composition of metallic contamination

The main gas components are H₂ and CO₂ which are of major and minor percentages, respectively. Trace amounts of N₂ and O₂ were also detected. The experiments show that H₂ concentration decreases as the amount of CO₂ increases with the increase of time at constant temperature. But the rate of change in compositions is relatively slower for lower temperatures than that for higher temperatures. This exchange of gases is the result of different diffusion and solubility characteristics of each gas species depending on temperature and partial pressure balance and the glass composition. The evolution of H₂ in this experiment can be speculated to be caused by the reduction of water which is bonded as OH⁻ groups in the glass. This

conclusion is in agreement with Eagan's (9) and Scholze's (10) studies. The results obtained from this set of experiment were interpolated by using inverse distance method, where changes in composition of the bubble have been estimated at 1400-1500 °C for 5-20 minutes (Fig. 3a and 3b).

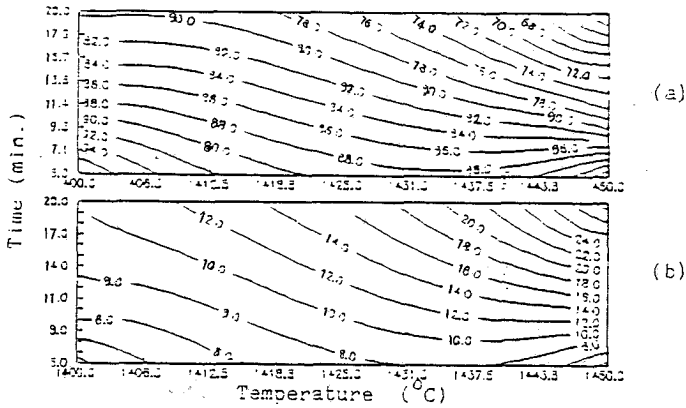


Fig.3. Estimations of a) H_2 distribution. b) CO_2 distribution

This interpolation reveals that the amount of CO_2 , which can help the bubble to rise to the glass surface, quickly increases at higher temperatures if sufficient time is given. Hence, it is concluded that the bubble problem will not exist if the reaction of metallic contaminations starts at the early stages of melting where large amounts of CO_2 are available. However, the defect probability is higher if the reaction occurs at the further stages of the process since the glass is too cool for CO_2 to diffuse into the H_2 bubbles and H_2 in the bubbles to diffuse into the melt. This conclusion is consistent with the H_2 containing bubble defects, found in glass containers.

The analytical results of bubbles formed in the float glass experiment are considerably different from those of first set of experiments. The gas analysis of bubbles shown in Table 1 indicate that the main component of bubble composition is CO_2 . The rest of the volume of bubbles includes N_2 , H_2 , O_2 in decreasing concentrations. This reveals that water reduction is

Table 1. Analytical results of bubbles found in float glass

| Samp. | L(mm) | V(μ l) | P(bar) | CO_2 | N_2 | H_2 | O_2 | Trace |
|-------|-------|-------------|--------|--------|-------|-------|-------|-------|
| Prod. | 0.80 | 0.15 | 0.24 | 62.7 | 30.4 | 4.5 | 2.4 | - |
| Prod. | 0.75 | 0.12 | 0.41 | 58.2 | 27.2 | 3.7 | 7.1 | 3.8 |
| Prod. | 1.56 | 0.32 | 0.64 | 71.3 | 18.8 | 5.2 | 3.9 | 0.8 |
| Exp. | 0.65 | 0.14 | 0.35 | 66.4 | 25.2 | 2.1 | 5.0 | 1.3 |
| Exp. | 0.90 | 0.38 | 0.12 | 85.3 | 14.0 | - | 0.7 | - |
| Exp. | 1.15 | 0.80 | 0.10 | 88.1 | 11.9 | - | - | - |

too difficult and CO_2 release is dominant in this experiment. Nevertheless, similarity between the gas compositions of experimental bubbles and the bubble defects observed in a float production where a metallic part accidentally dropped into the glass melt, indicate the bubble source.

3.2. Air Bubbles

The analyses of experimental bubbles described in 2.2 and some bubbles of the hand-made products are given in Table 2. The table shows that the main gas components for most bubbles are N_2+Ar+O_2 or N_2+Ar , which may be defined as air. Thus it can be estimated that the product bubble defects are probably formed under conditions similar to air entrapment experiment. The bubbles having an N_2/Ar ratio similar to that in air may be defined as air bubbles although O_2 is not present in all. O_2 can be replaced by CO_2 in the glass melt so that

some air trap bubbles may include CO_2 with the main components being $\text{N}_2 + \text{Ar}$. On the other hand, some of the bubbles contain considerable amounts of CO_2 besides N_2 , O_2 and Ar which do not confirm to air composition. However they are defined as the bubbles composed of air+ CO_2 since bubble compositions exhibit $\text{N}_2/\text{Ar}/\text{O}_2$ ratios which, after excluding CO_2 , are similar to that of air.

Table 2. Analytical results of air trap bubbles

| Samp. | L(mm) | V(μ l) | P(bar) | N_2 | O_2 | Ar | CO_2 | Trace |
|-------|-------|-------------|--------|--------------|--------------|-----|---------------|-------|
| Prod. | 5.70 | 6.21 | 0.47 | 73.6 | - | 1.2 | 23.7 | 1.5 |
| Prod. | 3.33 | 19.24 | 0.27 | 89.7 | 8.7 | 0.9 | 0.7 | - |
| Prod. | 1.05 | 0.60 | 0.74 | 65.5 | 16.6 | 0.7 | 17.1 | 0.1 |
| Exp. | 2.85 | 3.11 | 0.52 | 76.1 | 19.1 | 1.2 | 3.6 | - |
| Exp. | 1.71 | 0.36 | 1.27 | 91.6 | 0.8 | 0.7 | 6.9 | - |
| Exp. | 4.30 | 4.06 | 0.79 | 73.8 | 19.7 | 1.1 | 5.4 | - |

The changes in the compositions of air trap bubbles formed in the forming stage where the temperature ranges between 850°C and 1000°C are shown in Fig. 4. Considerable amount of O_2 is observed in all temperatures, the amount of O_2 is lower than that in air as the bubble formation temperature approaches 1000°C . Conversely, the amount of O_2 become equal to that in air if the bubble is formed in lower temperatures, particularly around 850°C . On the other hand, the N_2/Ar ratios are constant and similar to that in air at all temperatures between 850°C and 1000°C . Thus it is possible to detect the location of bubble formation by tracing the amount of O_2 in bubbles.

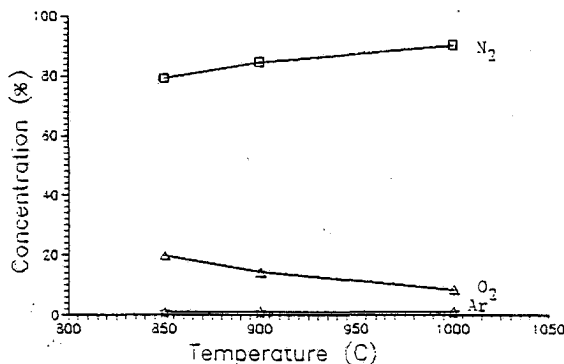


Fig.4. Composition of air trap bubbles

3.3. Electrochemical Bubbles

The size range of bubbles concerned here, formed in different electrochemical cells by applying adjustable emf in different temperatures, is 1-3 mm. The observations of this set of experiments are shown in Fig.5. It has been found that the bubbles are quickly formed at high temperatures by applying even the minimum voltages, ~ 0.2 VDC. The rate of bubble formation diminishes at lower temperatures, so that the time required to form the bubbles at 1320°C with 1 VDC, is about 90 sec. This result reveals that a long enough time and relatively high DC voltages are required to form bubbles in the spout zone. However, in practice, electrochemical reactions are frequently observed in both transition (e.g. forehearth) and spout zones. The gas analyses of experimental bubbles and bubble defects of products given in Table 3 indicate that the major gas component is O_2 . The results indicate that the amount of O_2 is less in the bubbles formed at high temperatures than at low temperatures, because of O_2 diffusion to glass melt. O_2 also helps the refining process, so that the defect risk in the products as a consequence of the electrochemical bubble formation in the melting zone is not as high as in the spout zone. Thus the formation of electrochemical cell to produce

bubble defects gets more critical towards the cooler sections of the furnace.

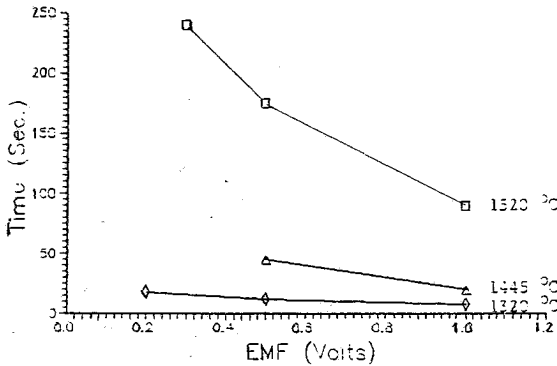


Fig. 5. Formation of electrochemical bubbles

Table 3. Analytical results of electrochemical bubbles

| Samp. | L(mm) | V(μ l) | P(bar) | O ₂ | CO ₂ | N ₂ | Trace |
|-------|-------|-------------|--------|----------------|-----------------|----------------|-------|
| Prod. | 0.94 | 0.43 | 1.46 | 89.6 | 4.1 | 5.1 | 1.2 |
| Prod. | 1.35 | 1.29 | 0.65 | 93.8 | 3.0 | 3.2 | - |
| Prod. | 2.64 | 9.63 | 0.12 | 98.4 | 1.4 | - | 0.2 |
| Exp. | 0.75 | 0.22 | 1.96 | 91.2 | 7.3 | 1.5 | - |
| Exp. | 1.42 | 1.50 | 0.54 | 94.4 | 3.3 | 1.8 | 0.5 |
| Exp. | 1.94 | 3.82 | 0.09 | 97.7 | 2.3 | - | - |

4. CONCLUSION

Three different bubble sources, namely metallic contamination, air entrapment and electrolysis were experimentally simulated in this study. The results revealed that reliable comparisons between the experimental bubbles and the bubbles seen in glass products could give valuable information for problem diagnosis.

5. REFERENCES

1. F. Kramer, SCHOTT Forschungsberichte (1984-1986), 285
2. M. Cable, C.G. Rasul & J. Savage, Glass Technology, 9, (1968), 25
3. F. Kramer, Glästech. Ber., 53 (7), (1980), 177
3. J.H.Cowan, W.M.Buehl & J.R.Hutchings, J. Amer. Cer. Soc. 49, (1966), 559
4. F.G.K. Baucke, Glästech.Ber., 61, (1988), 109
5. D.W.Ready and A.R.Cooper, J. Chem. Engng. Sci., 21, (1966), 917
6. M.C.Weinberg, P.I.K.Onorato & D.R.Uhlmann, J. Amer. Ceram. Soc. 63, (1980), 175
7. F.Kramer, Glästech.Ber., 52, (1979), 43
8. L.Nemec and M.Muhlbauer, J. Non-Cryst. Solids, 38 and 39, (1980), 593-598
9. R.J. Eagan and G.J. Jones, J. Amer. Ceram. Soc., 58, (1975), 300-301
10. H. Scholze, Glass Ind., 47, (1966), 622

MECHANICAL STRENGTH OF ORIGINAL AND CORRODED FLOAT GLASS

Josef Matoušek, Martin Maryška

Institute of Chemical Technology
Department of Glass and Ceramics
166 28 Prague 6, Technická 5
The Czech Republic

Float glass samples were submitted to corrosion static test at 98°C. Water solutions of hydrochloric acid (pH=3.0), sodium hydroxide (pH=12.2) and pure distilled water (pH=5.2) were used as the corrosion medium in the tests.

Bending strength of original and corroded float glass samples was measured using the central symmetric bending method.

The value of bending strength of the original float glass amounted 170.5 ± 26.6 MPa ("tin" side) and 242.6 ± 39.8 MPa ("top" side) respectively. The strength values changed due to corrosion specifically for "bottom" (tin) and "top" sides of the glass samples. The maximum negative departure from the above values was found to be 8% ("top" side corroded in NaOH) while 55% increase in strength was detected as the maximum positive change ("tin" side corroded in HCl).

The results are discussed with respect to the chemical changes of the glass surface layers caused by corrosion.

1. INTRODUCTION

Flat glasses are preferably produced by Float process at present. The glass produced by this process has different chemical composition and in such a way also different properties on the "top" and "tin" side. Also mechanical strength of flat glass differs according to the side exposed to a stress.

Bending strength is usually used to characterize strength of flat glasses. The results of bending strength of float glass published so far mostly indicate higher values for "top" side (1-3). On the other hand Colombin and Jelli (4) found higher strength value in the case of "tin" side. Some of the authors also reported influence of surface damage which causes significant decrease of strength (1-3).

Special attendance was paid to static and dynamic glass fatigue. Recently Chuang and Fuller (5) summarized the results

published so far and created a theory explaining this phenomena.

In practice, flat glass is usually exposed for a long period of time to air corrosion, e.g. to air humidity combined with aggressive acid compounds. Therefore is it of interest to determine if Float glass strength can be influenced by corrosion in water solutions.

2. EXPERIMENTAL

Float glass (thickness of 4 mm) produced by Glavunion Teplice (Czech Republic) was used in experiments. The chemical composition of the glass was 72.5 SiO₂, 1.0 Al₂O₃, 0.07 Fe₂O₃, 8.1 Cao, 3.9 MgO, 13.7 Na₂O, 0.3 K₂O, 0.25 SO₃ (wt.%). Square shaped samples (83x83 mm) were cut and either used directly for strength or submitted to corrosion in aqueous solutions under static conditions at first. Acid solutions (pH=3) was prepared by mixing of 1.05 ml HCl (35 wt.%) with 998.95 ml distilled water, while alkaline solution (pH=12) consisted 3.997 g of NaOH and distilled water (1 litre of the solution). Also pure distilled water (pH=5.3) was used as the corrosion medium in some cases. The square shaped samples were corroded at 96°C for the time 96 hours. The relation between glass sample surface and corrosion medium volume amounted to 1.09 cm⁻¹.

Coaxial ring method was used to determine bending strength of the glass samples. The diameter of the supporting and loading ring was 20 mm and 10 mm respectively. The constant value of stress rate 67 MPa.min⁻¹ was applied in all measurements. The bending strength was measured on the "top" and "tin" side of each sample and calculated using the following relation:

$$\sigma = \frac{3F}{2\pi h^2} \left[(1+\mu) \ln \frac{r_1}{r_0} + (1-\mu) \frac{r_1^2 - r_0^2}{2R^2} \right]$$

where: μ is Poisson's constant, r_1 is the diameter of supporting ring, r_0 is the diameter of loading ring, R is glass sample diameter, h is glass sample thickness, F is loading force.

If square shaped samples are used then $R = 0.605 h$, where h means the length of the square edge (6).

3. RESULTS AND DISCUSION

The bending strength values are summarized in Table I. The parameter s has the meaning of standard deviation defined by the

relation

$$s = \left[\frac{1}{n} \sum_{i=1}^n (x_i - \bar{x})^2 \right]^{1/2} \quad n=20 .$$

TABLE I : Results of bending strength

| Glass | Tin side | | Top side | |
|-----------------------------------|----------------|---------|----------------|---------|
| | σ [MPa] | s [MPa] | σ [MPa] | s [MPa] |
| original (as received) | 170.5 | 26.6 | 242.8 | 39.3 |
| corroded in alkaline solut. | 224.8 | 27.4 | 227.3 | 19.8 |
| corroded in acid solution | 265.5 | 49.7 | 281.3 | 46.7 |
| corroded in distilled water | 203.0 | 36.8 | 220.2 | 38.2 |

Significantly higher value of bending strength of the original glass was found on the top side of the sample.

Corrosion of the tin side leads in all cases to higher values of bending strength. The highest value was found after corrosion in acid solution, while relatively low increase of strength was attained after corrosion in distilled water.

The strength of the top side of the original glass decreases a little after corrosion in alkaline solution and distilled water. The maximum strength value found in this study belongs to the top side corroded in acid solution.

The results in Table I also indicate that bending strength values measured on the tin and top side are close after corrosion in all cases followed. This can be expressed by the factor f

($f = \frac{\sigma_{\text{top}}}{\sigma_{\text{tin}}}$) values of which are summarized in Table II.,

where: 1 is the original glass (as received), 2 is the glass corroded in alkaline solution, 3 is the glass corroded in acid solution and 4 is the glass corroded in distilled water.

Table II.: Relation between bending strength of the top and tin side

| glass | 1 | 2 | 3 | 4 |
|---|-------|-------|-------|-------|
| $f = \frac{\sigma_{\text{top}}}{\sigma_{\text{tin}}}$ | 1.424 | 1.011 | 1.059 | 1.085 |

Factor f goes to 1 especially in the case of relatively strong corrosion (alkaline solution) which can be explained by dissolution of very thin surface layer both on the top and tin side of the glass. This process can in certain extent diminish difference in chemical composition of both sides but mainly effects the smoothness of both glass surfaces which became practically identical.

The main difference in chemical composition of the top and tin side is due to the tin content. It was found that the tin concentration diminishes significantly after corrosion in alkaline solution (Fig.1). As it is seen very thin surface layer (< 5 μm) is depleted by tin. In a smaller extent a depletion was indicated also on the top side of the glass sample (Fig.2).

The results of tin distribution were obtained by step etching of glass sample using very dilute water solution of 0.5% HF and 1% HNO_3 and by following determination of tin content by the AAS method. The chemical analytical approach indicates that corrosion can diminish the difference in chemical composition of tin and top surface. But the difference in tin content on both sides of the glass still remains distinct showing that also surface defects and residual stress in glass surface layer should be considered as the factors responsible for bending strength values of the float glass sample.

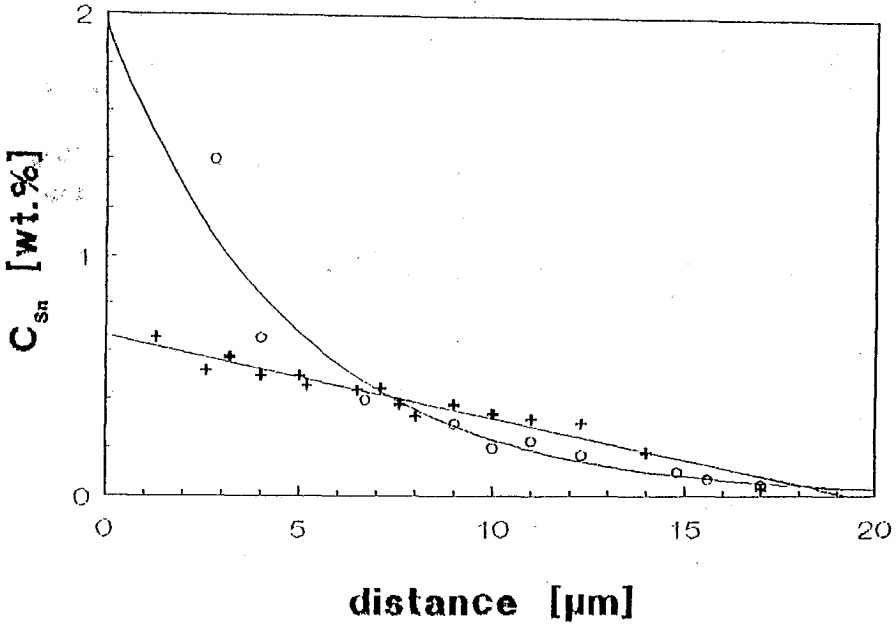


Fig.1: Tin concentration as a function of distance from the surface - tin side. (o...original glass,+...after corrosion in alkaline solution)

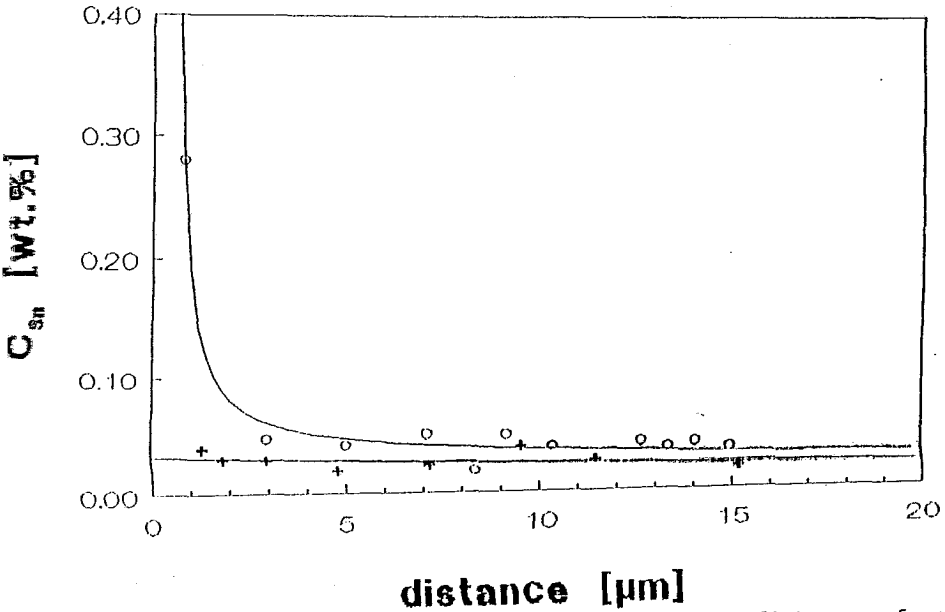


Fig.2: Tin concentration as a function of distance from the surface - top side. (o...original glass, +...after corrosion in alkaline solution)

4. CONCLUSION

Bending strength values of float glass change if the glass is submitted to corrosion.

Corrosion by acid solution significantly increases the bending strength of both sides of the glass compared to the original values.

Alkaline corrosion increases bending strength values of the tin side, while a little decrease was found on the top side.

Distilled water corrosion has similar but not so much pronounced effect on bending strength values as alkaline corrosion.

LITERATURE:

1. Manns P. and Brückner R., *Glastechn. Ber.* 56 (1983) 155
2. Novotný V. and Vích M. and Kubišta P., *Sklář a keramik*
32 (1982) 171
item 32 (1982) 239
3. Novotný V., *Sklář a keramik* 41 (1991) 204
item 41 (1991) 241
item 41 (1992) 41
4. Colombin L. and Jelli A., *Rivista Staz. Sper. Vetro* (1989) 141
5. Chuang T. and Fuller E. R., *J. Amer. Ceram. Soc.* 75 (1992) 540
6. Menčík J.: The strength and fracture of ceramics (in Czech).

SNTL Praha 1990

NEW LEAD-FREE CRYSTAL GLASSES

M. RADA, L. ŠAŠEK, M. MÍKA

Institute of Chemical Technology, Prague, Department of Glass and Ceramics,
Technická 5, 16628 Prague 6, Czech Republic

ABSTRACT

The new lead-free crystal glasses without unhealthy and environmentally harmful lead, arsenic and barium oxides were developed. The refractive index is in the range from 1.520 to 1.545 or higher, the density is about 2500–2700 kg.m⁻³. The melting temperatures are comparable with those of commercial lead crystal glasses, the working temperatures are about 20–100 °C and annealing ranges 80–150 °C higher than the commercial ones. The electrical resistance is similar or lower. The liquidus temperatures are about 830–970 °C. All glasses are within the third class of hydrolytic durability.

INTRODUCTION

It is already three years ago, when Dr. Joseph Graziano at an EPA Symposium on the Bioavailability and Dietary Uptake of Lead had made a presentation, concerning the impact of lead crystal on the dietary uptake of lead, which was published in Lancet.

Since that time leachates of lead have attracted an unusual degree of attention. The leaching of lead from lead crystal glasses can be solved by two different ways :

- i) most usually by strengthening the glass structure, that is by increasing silicon dioxide and reducing alkaline oxides contents,
- ii) or by treatment of the glass surface, which stops the leaching of lead.

Both these ways solve, however, only the problem of the leaching of lead and do not solve the other questions - the problem of atmosphere contamination during melting through the environmentally harmful lead and arsenic oxides,

workers contamination directly in the factory and the problem of grinding sludge.

It is possible to solve these problems by changes of chemical composition, which enable to obtain glasses with properties comparable with those of lead crystal glasses.

Many producers have published the transition to the new lead-free glasses. However, most of them contain barium oxide. In this time barium glasses, because barium as a heavy metal is harmful like lead, are only an interlink to the glasses, which contain neither lead and arsenic nor barium.

Lead and barium oxides increase refractive index and favourably influence the other properties of the glasses of luxurious character.

A similar effect has also zinc oxide, which is in addition "an essential element in human nutrition"; a human organism needs daily 10 to 20 mg of zinc. ZnO stabilizes the glass and has a favourable influence on the chemical durability. To reach a refractive index in the range of 1,52-1,545, it is necessary to join zirconium oxide, which influence on the refractive index is considerable, as well as on the chemical durability.

RESULTS AND DISCUSSION

The glasses developed with zirconium and zinc oxides fulfill the requirement on the refractive index and also favourably affect the other important properties.

These glasses contain in % by weight (1,2) 50-70 SiO₂, 0.1-10 Al₂O₃, 0.5-17 ZrO₂, 10-22 K₂O and/or Na₂O, 2-10 CaO and/or MgO, 0.01-0.025 Fe₂O₃, individually or in a combination 0.1-10 BaO, ZnO, B₂O₃, Li₂O and traces to 1% of Sb₂O₃. Further modifiers are present either individually or in a combination up to 1% of TiO₂ and SnO₂.

These glasses with the content of zirconium dioxide are intended for man-made and machine-made utility glassware with a higher refractive index, they are suitable particularly for glass decorating by cutting and engraving and by other decorative techniques for products of the luxurious character. This glass type is hygienically unharmed concerning the content of detrimental substances in the leaching and its brilliance can compete with the products made of lead crystal glass.

Chemical compositions of commercial lead crystal glasses and new lead-free glasses are given in Table 1 and their main properties are compared in Table 2. Viscosity curves of studied glasses are shown in Fig.1, Fig.2 shows the dependence of electrical resistance on temperature.

Table 1.: Chemical composition of studied glasses

| Component | Lead crystal glass 1 | Lead crystal glass 2 | Lead-free cryst.glass 1 | Lead-free cryst.glass 2 |
|--------------------------------|----------------------|----------------------|-------------------------|-------------------------|
| SiO ₂ | 60.440 | 59.410 | yes | yes |
| ZrO ₂ | - | - | 5.500 | 1.348 |
| PbO | 24.090 | 25.370 | no | no |
| BaO | - | 0.620 | no | no |
| ZnO | 1.490 | - | yes | yes |
| CaO | - | - | yes | yes |
| Na ₂ O | 1.980 | 4.810 | yes | yes |
| K ₂ O | 11.800 | 9.040 | yes | yes |
| B ₂ O ₃ | - | 0.520 | no | yes |
| Al ₂ O ₃ | - | - | yes | no |
| As ₂ O ₃ | 0.200 | 0.180 | no | no |
| Sb ₂ O ₃ | - | 0.050 | yes | yes |

Table 2.: Properties of studied glasses

| Properties | Lead crystal glass 1 | Lead crystal glass 2 | Lead-free cryst.glass 1 | Lead-free cryst.glass 2 |
|--|----------------------|----------------------|-------------------------|-------------------------|
| Index of refraction | 1.5451 | 1.5496 | 1.5509 | 1.5274 |
| Density [g/cm ³] | 2.9368 | 2.9339 | 2.6954 | 2.6087 |
| t _{log n=2} [°C] | 1478 | 1423 | 1425 | 1439 |
| t _{log n=3} [°C] | 1174 | 1128 | 1200 | 1180 |
| t _{log n=4} [°C] | 991 | 951 | 1059 | 1020 |
| t _{log n=7.65} [°C] | 659 | 629 | 788 | 724 |
| t _{log n=13} [°C] | 453 | 430 | 608 | 529 |
| t _{log n=14.5} [°C] | 417 | 395 | 575 | 494 |
| ρ _{el} at t _{log n=2} [Ω.cm] | 6.547 | 5.517 | 3.536 | 6.160 |
| ρ _{el} at 1450°C [Ω.cm] | 7.176 | 5.091 | 3.254 | 5.949 |
| Liquidus temperature [°C] | 740 | 848 | 954 | 873 |
| Hydrolytic resistance ¹ | 0.80 | 0.76 | 0.25 | 0.34 |

¹ Hydrolytic resistance of glass grains at 98°C (ISO 719) - in ml [C = 0.01 mol.l⁻¹] HCl

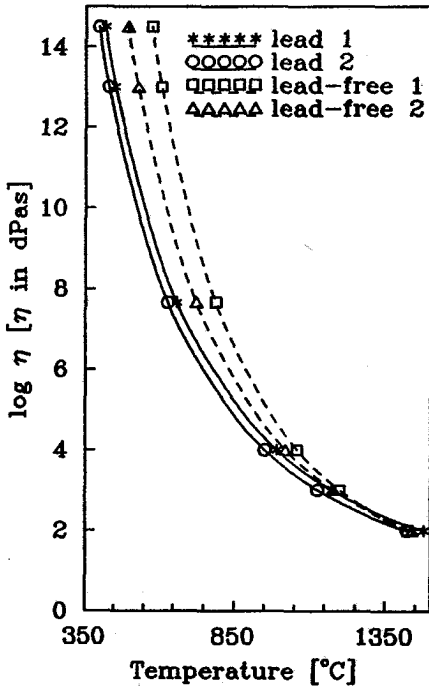


Fig.1 Viscosity curves of studied glasses

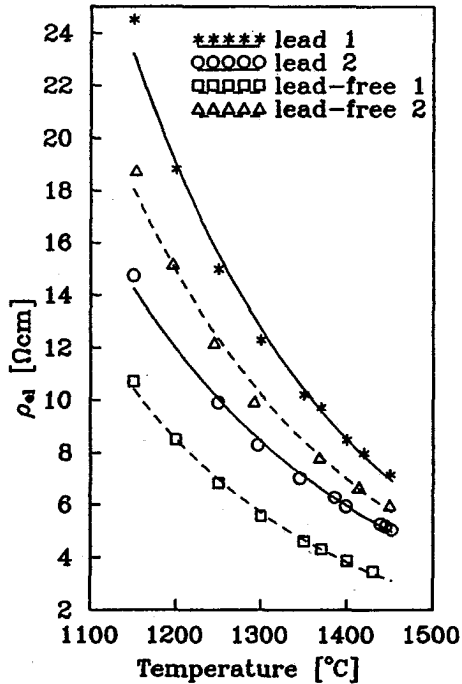


Fig.2 Plots of electrical resistance vs. temperature of studied glasses

CONCLUSIONS

The refractive index of the new lead-free crystal glasses is in the range from 1.520 to 1.545 or higher, their density is about 2500–2700 kg.m⁻³. The melting temperatures are comparable with those of commercial lead crystal glasses, the working temperatures are about 20–100 °C and annealing ranges 80–150 °C higher than the commercial ones. The electrical resistance is similar or lower. The liquidus temperatures are about 830–970 °C. All glasses are within the third class of hydrolytic durability.

REFERENCES

1. European patent application EP 92909183.3, 8.5.1991
2. European patent application EP 91121730.5, 18.12.1991

**SURFACE TREATMENT :
AN ALTERNATIVE TO IMPROVE PROPERTIES OF HOLLOW GLASS**

F HUBERT - SPRL CHIMCOAT - Tarcienne BELGIUM

Since a long time, glass makers have tried to valorize their glass through many processes. Among them, surface treatment has played a continuously growing part.

1. Hot End and Cold End treatments

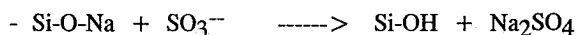
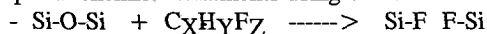
We shall not extend too much on this more classical treatment which is now almost generalized with an aim to increase mechanical resistance of wares.

The Hot End Treatment is classically based on titanium or tin oxide coating; a particular importance should be put on the choice of the reagent to ensure a good quality compact and homogeneous coating.

The Cold End Treatment is carried out through a choice of reagents starting from high grade oleic acid derivatives to high performance polyethylene, with medium range products such as special soaps; an adequate choice between these products allow a tight control of other properties such as hydrophobicity.

2. Increase of chemical stability of glass

Special chemical treatments using one of the following chemical reactions



allow a control of alcalinity of sodalime glass.

Carried out through gas injection to limit the pollution, these treatments are of particular interest to stabilize surface of pharmaceutical containers, surface of finishes to be thermosealed, or to avoid flower development after long time storage.

3. HOT GLOSSING process

Today, an economic way to modify the surface aspect or properties of glass articles is "HOT GLOSSING" which consists in spraying on the articles directly after forming on the machine conveyor, colouring chemical solutions based on metallic compounds, with an overcost of only 15% with regard to flint glass.

Possibilities of the "HOT GLOSSING PROCESS"

Bulk colouring of glass follows (1) table 1.

Spraying metal organic compounds in organic solutions on hot glass to form an oxide coating with a thickness ranging between 500 and 700 Å leads to a wide variety of colours with some correlation to table 1 although different ligand effects have to be considered.

Talbe 1 : Transition metal ions in glasses

| Configuration | Ion | Colour | Configuration | Ion | Colour |
|---------------|------|-------------------------------|---------------|------|--------------|
| d0 | Ti4+ | Colourless | d4 | Cr2+ | Faint blue |
| | V5+ | Faint yellow to colourless | d5 | Mn3+ | Purple |
| | Cr6+ | Faint yellow to colourless | | Mn2+ | Light yellow |
| d1 | Ti3+ | Violet-purple | d6 | Fe3+ | Faint yellow |
| | V4+ | Blue | d7 | Fe2+ | Blue-green |
| | Mn6+ | Colourless | | Co3+ | Faint yellow |
| d2 | V3+ | Yellow-green | d8 | Co2+ | Blue-pink |
| d3 | Cr3+ | Green | d9 | Ni2+ | Brown-purple |
| | | | d10 | Cu2+ | Blue-green |
| | | | | Cu+ | Colourless |

Colours like grey, brown, yellow, blue, pink, green can be obtained; special effects like increasing brightness of glass such as pearly effect on black glass, tinned glass or golden glass can also be obtained by combination of bulk coloured glass and reflective coating with high refractive index.

This method is more used by cosmetic glass producers; the use of this process is also possible on table ware but in this case, a more deep study is necessary to ensure the stability of the coating to alkaline washing such as used for instance in dish-cleaning machines, and to ensure the absence of lixiviation of toxic metals, this last problem being similar to the one of lead lixiviation in cristal glass table ware.

Applications in lighting glasses or pressed glass for building or decoration are also possible.

Our recent developments have also shown that more functional applications of the HOT GLOSSING process are possible using some specific oxides to modify specific radiation transmission outside visible range or some surface properties involving adhesion processes, wettability and so on.

About the process

Spraying is applied on hot articles at a temperature of about 550°C between the forming machine and the annealing lehr with the big advantage to use the internal heat of the articles of the glass itself, thus avoiding the need of a reheating, but with the difficulty to work in open atmosphere.

Electrostatic spraying was first requested because of the low concentration and the low efficiency of the first spraying solutions, the spraying fog being concentrated around the glass bottle (figure 1).

The evolution of the solutions has led to a higher concentration and thus better efficiency. More and more, except for special shape articles, normal pneumatic spraying process can be used allowing lower investment costs.

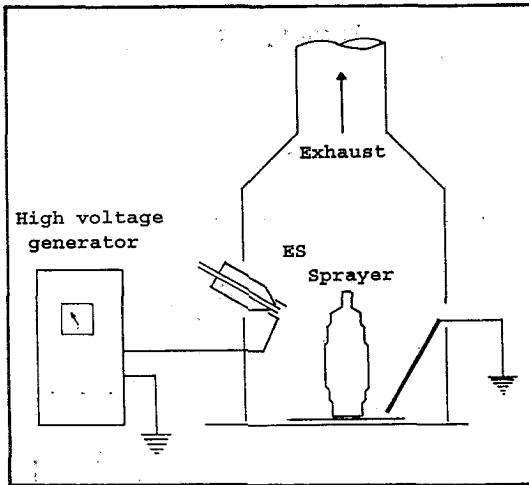


Figure 1 : Schematic view of spraying hood

Chemistry of the process

In the pyrolytic process of flat glass, a solution of organometallic compounds is sprayed in a controlled atmosphere which can be ensured by applying the treatment in a special casing in which the nature of the gas, the exhaust of the fumes, and the temperature can be easily controlled.

Unfortunately when coating hollow glass or pressed glass, the process must be applied in open atmosphere with no or little possibility to control the composition and the temperature of the atmosphere.

Viguié and Spitz (2) have pointed out that the nature of the coating obtained by pyrolytic spray depends on the fate of the spray droplets in terms of the nature and fate of the intermediates that may form (figure 2).

In case A, the liquid droplet reaches the surface and the solvents evaporate to leave a precipitate which reacts on the hot surface.

In case B, solvent evaporation is substantial or complete in the gas phase and aggregates of precipitates reach the surface and react.

In case C, the droplet is completely vaporized and a purely heterogeneous reaction occurs on the surface.

Case A corresponds rather closely to the case using iron chloride aqueous solution : water evaporates only when the droplets come in contact with hot glass and oxidation reaction of the iron chloride takes place as spots corresponding to the impact of the droplets.

Cases B& C, from our experience, are not suitable for use with hollow glass or pressed glass production because, due to the open system, a large amount of the chemical compounds will be lost and the efficiency of the process will be very low.

Moreover, dust of oxides formed in the atmosphere can pollute the articles without cementing in the glass surface.

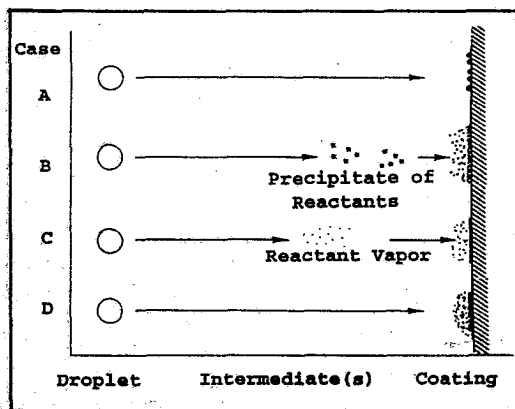


Figure 2 : Fate of the droplets (3)

Considering this theoretical approach, we suggest that the right mechanism leading to uniform bright coating on the glass should be following :

- the reagent solution should arrive on the glass in the liquid form
- the solvent should evaporate on the hot glass surface without leaving any residue on the glass surface except the reagent itself
- the reagent itself should be of such a chemical form that it can vaporize at the temperature of the glass surface allowing a uniform and effective reaction of oxidation around the spot of the droplet (fig. 2 - case D).

The first point implies that the solvent must have a high boiling point and a low vapour pressure.

The second point implies no cracking residue.

The third point implies that the reagent itself has a high vapour pressure at a temperature between the one of the solution and that of the glass and a decomposition temperature which must be as close as possible of the temperature of the glass.

Best metal organic reagents used for this purpose are of the family of metal chelates like beta-diketonates or metal carboxylates ranging from metal acetates to higher organic radicals of the family of naphthenates.

The choice of solvent system will generally be based not only on one solvent but on a mixture of several solvents which will be a compromise between many opposite requirements such as specific solubility, boiling point and safety considerations (toxicology and flammability).

4. Conclusion

Surface treatment of glass appears as an economic alternative to batch changes or to other decorating processes to control properties of containers such as colour, UV transmission, other non visible radiations, chemical properties of the surface or mechanical resistance of the container.

Bibliography

- (1) Treatise on material science and technology/ N.TOMAZAWA, R.DOREMUS - Vol.1 - Chap.1 Interaction with electromagnetic radiation
- (2) J.C.VIGUIE and J.SPITZ : Journal of Electrochem. Soc. 122 (1795) 585
- (3) J.M.BLOCHER Jr : Thin solids films / Vol.77, n°1/2/3 March 6th 1981 - Coating of glass by CVD

**ION-EXCHANGE OF GLASS SURFACE AND SALT MELT:
UNDERSTANDING THE INFLUENCE OF PROCESS-PARAMETERS BETTER
THROUGH COMPUTER MODELLING AND ADEQUATE MEASUREMENTS**

Yurii K. STARTSEV

*Russian Academy of Sciences, Institute of Silicate Chemistry,
ul. Odoevskogo, 24/2, 199 155 St.-Petersburg, Russia*

It is well known that ion-exchange between glass surface and salt melt is widely used not only for strengthening glass articles but for fabricating passive guiding structures for application in integrated optics. The relaxation theory of the glass transition allows us to calculate the influence of thermal treatment on glass properties. This theory was used for explanation of the peculiarities of the property changes of a glass during a modification of its surfaces and after any time-temperature regime heat treatment using only the physical properties of the glass measured in independent experiments. In this paper have been discussed some problems which were connected with property evaluation.

INTRODUCTION

Changes in refractive index resulting from ion exchange in glass are subject of many previous papers (1)-(3). The model proposed in (4)-(6) considers the simultaneous influence of three relaxation processes: structural relaxation in the presence of thermal excitation, structural changes due to the concentration variations of the potassium and sodium ions in the ion exchanged layer and mechanical relaxation. There are many difficulties for finding more precise parameters of the model by experimental or theoretical ways (see some results of calculation, for example, in (7)-(9)). In this paper author tries to show how one can find the parameters to use this model for simulations of the property profiles. Two problems connected with interpretation of experimental results are discussed because they have a general character.

BASIS OF THE MODEL OF COORDINATION RELAXATION

The structure of any liquid, i.e. the characteristics of mutual arrangement of atoms, ions, or molecules in a liquid depends on temperature, pressure and composition. At any temperature, pressure and composition particles forming the liquid tend to get such an arrangement that corresponds to the minimal Gibbs's free energy and therefore to the equilibrium state of the substance. Clearly when speaking about equilibrium at temperatures below the liquidus temperature of the substance one must have in mind metastable states of the substance.

Theoretically some features our approach are more closely based on the analysis of compositional changes and structural relaxation in amorphous materials made by Prabhat K. Gupta in 1985 (10). Phenomenologically a glassy state as a state of supercooled liquid is described by two sets of parameters: the external parameters such as temperature (T), pressure (p), and composition (C) and the internal (or structural) parameters. For given values of external parameters the internal parameters assume their equilibrium values of T , p , and C when the system is in the thermodynamic equilibrium state. The relaxation of these values to the new equilibrium ones is called structural relaxation. The theory of structural relaxation in compositionally homogeneous materials is well established using the idea of internal parameters by Moynihan and Gupta (11) for temperature effects and Mazurin and Leko (12) for pressure.

Various glass properties above, near, and below the temperature of glass transition have a dependence on different parameters that are important for a detailed description of the process under study. It is very important to underline that physical properties of glasses are not only temperature-, pressure-, and composition-dependent, but also time-dependent; i.e. dependent on thermal, pressure, and composition variations during its history.

The theoretical treatment of stress build-up and relaxation due to chemical modification of the glass surface requires an understanding of mechanical and viscoelastic properties as a function of previous thermal history. When speaking of property changes in glasses as a result of the coordination and thermal stimulated structural relaxation we considered the term «property» as any property of the investigated substance including the interdiffusion coefficient. This approach now is widely used on the definition of the temperature and concentration dependencies of this value needs to be revised because the published data where defined these dependencies was not taken into account the thermal history of the sample at all.

As to the most probable mechanism of glass structure reconstruction during and after ion exchange it may be the following. It is well known that in crystals the oxygen coordination number of alkaline ions depends on the size of these ions. Very likely in the alkali containing glasses the number of oxygen atoms in the first coordination sphere also must depend on the size of the corresponding alkaline cation. The reconstruction of glass network after the stuffing a new cation in the glass could be considered as a structural relaxation too. We named (4) this process as a coordination relaxation to differ it from the ordinary structural relaxation, which takes place in the glass transition region. In this way we wanted to stress a most specific peculiarity of this kind of relaxation of glass structure.

In other words the glass structure will change toward the new equilibrium state of coordination number. This process can be described quantitatively as the changing difference between some fictive and actual concentrations. This value will change during coordination relaxation from the value of the concentration change to zero. The difference of mentioned concentrations at every moment characterizes deviation of the microregion structure from its equilibrium in respect to the coordination relaxation.

The offered approach gives the possibility of presenting the changes in glass property with the concentration variation is as follows:

$$C_{fi} = C - \int_0^t \exp\left[-\int_0^{t'} \frac{dt''}{K_c t''}\right] \cdot \frac{dC(t')}{dt'} dt, \quad (1)$$

$$C_f = \sum_i^n g_i C_{fi}, \quad (2)$$

where

$$\sum_i^n g_i = 1, \quad (2a)$$

$$\log \tau_i = [\gamma (C_{fi} - C) - \log K_c] \cdot \frac{C_{fi}}{C} - \log \tau_0 \left[\frac{C_{fi}}{C} - 1 \right], \quad (3)$$

$$C_{fP} = \sum_i^n g_{iP} C_{fi}, \quad (4)$$

where

$$\sum_i^n g_{iP} = 1, \quad (4a)$$

$$P = P_0(C_{fi}) + \int_{C_{fp}}^C \left(\frac{\delta P}{\delta C} \right)_{C_{fp}} dC, \quad (5)$$

where C , C_f , C_{fi} , and C_{fp} - real, fictive, partial, and fictive for the property P concentration respectively; K_c - ratio of the viscosity η to time of the coordination relaxation τ_c in stretched exponent equation; η and $\gamma(C_{fi} - C)$ - viscosity and its concentration dependence respectively; g_i and g_{iP} - partial weight of the relaxation time component; P - some property of the glass (P_0 is the value of P at $t=0$).

The dependencies of properties along the direction normal to the surface of the glass plate are calculated number of steps along this coordinate. Within each step (a layer here) its composition and properties are considered as a constant. It is accepted that the concentration of alkaline ions in the surface glass layer achieves instantly its equilibrium value. Evidently it is very easy to include in the model of any data that show the alkaline concentration difference between the molten salt and the glass surface.

PARAMETERS FOR SIMULATION OF THE PROPERTY CHANGES

The meaning of the parameters used in the model are listed below. Most of parameters are definite physical properties that one can measure directly or calculate from the data of experiments.

LIST OF THE MODEL PARAMETERS

- Elastic modulus / Poisson's ratio;
- stress optical constants ($C_2 - C_1$) to calculate birefringence;
- constants A , B_e , B_i and T_0 in equation:

$$\log \eta = A + \frac{B_e}{T_f - T_0} + B_i \left[\frac{1}{T} - \frac{1}{T_f} \right]$$
- thermal expansion coefficients for the glassy and liquid states;
- ratio of viscosity to composition, structural, and to stress relaxation times in stretched exponent equation;
- τ_0 - preexponential term in the equation for the relaxation times $\tau = \tau_0 \exp[-(\frac{t}{\tau})^\beta]$;
- index β of the stretched exponent for composition, structural, and for stress relaxation;
- relative change in length of K-glass plate resulting from instant full exchange K^+ to Na^+ ;
- relative change in length of Na-glass plate resulting from relaxed full exchange Na^+ to K^+ ;
- relative change in length of Na-glass plate resulting from instant full exchange Na^+ to K^+ ;
- ratio of mole fraction of K^+ ions in the base glass to the sum of Na^+ and K^+ ;
- reference temperature T_r defining equilibrium values of properties;
- interdiffusion coefficient D at T_r for liquid state;
- thermal coefficients of the interdiffusion coefficient for glassy and liquid states.

Really the coordination relaxation changes all properties including the interdiffusion coefficient. It makes considerably more complicated all the dependencies of interest.

Then there is a problem of the realization of the isostructural regime under the iso-concentration conditions. While investigating the structural relaxation the isostructural regime is obtained very easily. It is very difficult to make some experiments where after the concentration variation the value of fictive concentration would be kept constant. At least in most experiments accessible for analysis the composition of ion-exchanged layer that is very thin is not constant during the experiment, because of the non stopping diffusion process.

So to expose the value of parameters of the model is possible as a rule only while complicated experimental dependencies are worked up.

TWO GENERAL PROBLEMS

The first of these problems is the following: are the states of the glasses of the same composition and the same real and structural temperatures absolutely identical if they are produced by two different ways: by melting from raw materials of the given composition substance or by melting of the substance with different composition varied by ion exchange up to given one during the coordination relaxation? In other words, is it possible at the fictive concentration (6) equals the real one in some microregion of glass network completely, to ignore its composition variation history, and use for description of its properties data on homogeneous non-exchanged glass properties?

We think that question is a part of more general problem: is the composition (including all the admixtures and dissolved gases) and the structural temperature of well synthesized glass its exhausting character? Has the metastable liquid the only minimum of the free energy at the given temperature, where the substance's structure does not depend of its history? Are there several minimums and not the only one?

These questions have not only evident theoretical meaning but a great practical significance too. In the science literature now there are many papers on the possible influence on the properties of high-viscous melts with different high temperature history. In this conjunction it is enough to refer to papers by Kordas, Weeks (13) and by Bobkova (14).

The second problem of the general character is the method of defining the value of concentration coefficient of glass properties under the constant structural concentration condition. As it is clear from what was written above, we are interested in corresponding values of density, viscosity, and interdiffusion coefficient. To get reliable results it is necessary to measure these properties of ion-exchanged glasses during the period when the coordination relaxation is diminishing yet small. Such conditions can be chosen without many difficulties for the relaxation of the refraction index, of which the profile can be measured even for a very thin ion exchanged layers. It is well known that scanning along the thickness of the ion exchanged layer is a very difficult task at least at the modern level of the measurement techniques. One can think that it is possible to use a linear dependence of the density and refraction index of the substance that is observed in many varieties of the structural changes of the glasses and even of the crystals. But the peculiarity of this type of structural transformation requires a direct experimental method of measuring this dependence. About viscosity it would be possible to scan the value upon the depth of the thin layer by studying indenter penetration. However it requires working out a high precision measurement technique and very complicated calculations that should consider the thickness viscosity variations and especially of the deformation of more rigid layers lying on the less viscous. It means that this method is not worth using without a primary checking up by more direct experiment.

Ion-exchange of glass surface

All the reasons written above make it absolutely necessary, at least at the first stage of the exploration, to carry out measurements of density and viscosity on the constant composition samples. Their volume must be constant too. In this case two conditions must be provided. First the ion exchange process must last no longer than some working days. Secondly, the experimental conditions must guarantee the negligible degree of the coordination relaxation that takes place during the ion exchange treatment. To fulfill these conditions the sample size has to be small, at least in one of the three directions. For measuring the viscosity the most advisable are the thin fibers. To provide the second condition the most effective method is decreasing of the ion exchange temperature.

CONCLUSION

To sum up, the proposed model of glass property simulation is based on the existence of independent rearranging regions around alkali ion positions in the glass network. This rearranging process we consider as relaxation one and name it as coordination relaxation.

The preparation of this paper was stimulated and my visit in Greece was supported by International Science Foundation under Grant No 0663/1.

REFERENCES

1. T. Findakly, *Optical Engineering* 24 (1985) 244.
2. A. N. Miliou, R. Srivastava, and R. V. Ramaswamy, *Appl. Opt.* 30 (1991) 674.
3. L. B. Glebov, V. G. Dokuchaev, and G. T. Petrovskii, *Fiz. Khim. Stekla*, 14 (1988) 706.
4. O. V. Mazurin, V. P. Kluev, Yu. K. Startsev, *Fiz. Khim. Stekla*, 11 (1985) 706-710.
5. Yu. K. Startsev, *Proc. 14th Int. Congr. on Glass. New-Delhi*. 2 (1986) 363.
6. Yu. Startsev, *Proc. 16th Intern. Congr. on Glass. - Madrid*. 7 (1992) 123.
7. Yu. Startsev, A. Priven, *Proc. Int. Conf. on Science and Technology of New Glasses. Tokyo*. (1991) 169.
8. Yu. Startsev, A. Priven', *Proc. 16th Int. Congr. on Glass. Madrid* 7 (1992) 371.
9. A. Priven', Yu. Startsev, *Gl. Phys. Chem.*, 19 (1993) 43.
10. P. J. Gupta, *J. Non-Cryst. Sol.* 71 (1985) 29.
11. C.T.Moynihan, P.J.Gupta, *J.Non-Cryst. Sol.* 29 (1978) 143.
12. O. V. Mazurin, V. K. Leko, *Proc. 14th Int. Congr. on Glass. New-Delhi*. 2 (1986) 363.
13. G. Kordas, R.A. Weeks, *Proc. 14th Int. Congr. on Glass. New-Delhi*. 1 (1986) 17.
14. N. M. Bobkova, *Fiz. Khim. Stekla*, 13 (1988) 594.

SILICA SANDS OF NORTH EASTERN BULGARIA

D. Mochev, Mineral Processing Engineer

Senior Res. Associate, M.Sc.

Kaolin Plc., 7272 Senovo, Bulgaria

Spread in the North-East of Bulgaria the kaolin deposits are known with their secondary origin. A large paleokarstic complex was formed in limestones rich of carbonates originated from Barremian and Aptain levels. The greater part of North Eastern Bulgdaria lies on carbonate sediments at a depth of some thousands meters. The negative carstic formations originated on the carbonate surface during ancient geological times were filled by transported quartz and feldspar grains. Later on, this material had undergone deep secondary chemocal weathering, forming poorly-cemented and weakly pressed kaolinitic sand rock, covered above by red clays and on its turn by loess.

The clay fraction in the kaolinitic-silica sand deposits contains kaolinite, as well as, small quantities of dickite, nacrite and halloysite. The main part of the non-clay minerals presents quartz sand (98-99 %), also other sand minerals are available - feldspar (orthoclase + microcline up to 3-4 %), as well as small amounts of mica, mainly muscovite.

The investigations show that the "mineral resource" is considered as a part, in which kaolin exceeds as much as 12 %. The contents of useful and harmful components account for: Al_2O_3 - over 29 %; Fe_2O_3 - below 1.6 %; TiO_2 - below 0.35 %. The contents Fe_2O_3 and TiO_2 are of a particular importance for kaolin and silica sand. They have entirely harmful effect because of the fact they colour the products and reduce their refractoriness. Iron and titanium bearing minerals are goethite, hematite, rutile, anatase, brookite, titanite, ilmenite.

The comprehensive study on the raw material has determined the kaolin as fraction under 0.01 mm. and the silica sand in the range of 0.1 - 2.6 mm. This kaolin fraction, named "clayey" fully consists of kaolinite and silica sand fraction is mainly presented by quartz, small amounts of mica (1-3 %) feldspar, accessory minerals.

The mining of kaolin sands is performed in open pits. The raw material is explored by means of a drilling net from (12.5 x 12.5 m) to 6.25 x 6.25 m. at some places. This permits flexible selective output through computing of information obtained from exploration works. The mining is simultaneously carried out on all the benches. The overburden is transported to inner and outer dumps located at a distance of from 500 to 2500 m.

The processing of the kaolin sands is realized by wet gravitational way through a separation between the fine kaolin particles and the coarser sand grains using classification in water medium.

The general flow-sheet comprises raw material desintegration in washing drums, rough classification in sloped spiral classifiers, followed by processing of the kaolin suspension with density of 1.06 g/cm^3 in three stages of hydrocycloning. The enriched kaolin flows into thickeners (18 m dia.) with periphery driving where flocculants for speeding up the settling are used. The material thickened ($1.15 - 1.25 \text{ g/cm}^3$) is fed to chamber filter presses at a pressure of 7-8 atm. On discharging the cake falls down a belt with 30% moisture, which decreases to 12-14 % after drying in belt-dryers.

The exploiting of kaolin sands deposits has started since the early 1920s. Kaolin Plc. With legal offices in Senovo, Russe region presently prospect, investigate and project mining and processing of the raw material. The company has developed a number of kaolin marks for production of porcelain, ceramic tiles, floor tiles, sanitary ceramics, insulators.

Kaolin Plc. is well known for their filler paper grades (both natural white and chemically bleached). Another paper kaolin is the so called "coating clay" - a very competitive, high quality kaolin. Paper kaolins are widely applied as paper fillers, relief printing paper, newsprint, cardboards etc.

Production of chamotte and refractory kaolins are also involved. A 60 m. long rotary kiln is erected for kaolin baking. The chamotte obtained is used in lining and construction of kilns for glass and foundry industry, lining of steel casting buckets etc.

Very fine ground kaolin faces the demands of chemical and rubber industry. This product finds application as a very cheap tyre filler, acid resistant and isolating clothes, plastics, paints, lacquers, lubricants, cables, cosmetics, pesticides, etc.

From the beginning of the flow-sheet, along with kaolin processing silica sands are also produced as a by-product through screening using both wet classification and wet sieving on arch or vibrating sieves.

Meanwhile, very successful trials were effected on production of glass sand with content of Fe_2O_3 (0.02 - 0.008 %) by applying special treatment of mineral acids and organic solvents.

Over the last years new sorts of foundry sands were developed, namely, "cladded sands" - sands treated by resing at high temperature. They are mostly needed in manufacturing of very fine castings.

Kaolin Plc. operates 3 processing plants located nearby the pits.

Part II, Sol-Gel Processing

RHEOLOGY OF SOLS IN THE SOL-GEL PROCESSING

Sumio Sakka and Hiromitsu Kozuka
Institute for Chemical Research, Kyoto University
Uji, Kyoto-Fu, 611, Japan

Rheological properties of sols and their relation with the sol-gel processing are discussed. The change of viscosity of a sol with time gives the information on the progress of sol-to-gel conversion. The viscosity-shear rate relationship gives the knowledge on the structure of the sol and its change with time. It is shown that the spinnable sols exhibit Newtonian or nearly Newtonian flow up to high viscosities where the fibers are drawn, while sols showing shear-thinning or thixotropic behavior are not spinnable.

1. INTRODUCTION

The sol-gel process for preparing materials starts with the sol-to-gel conversion of the solution (1-4). It is well known that the composition of the starting alkoxide solution including the catalyst and water and the reaction conditions affect the rate of hydrolysis, the rate of condensation, the shape of the particles produced in the solution and the state of aggregation of particles, and thus the flow properties of the sols. In this article, the rheological properties, such as the viscosity and the change of viscosity with shear rate, and their implication in the sol-gel processing are discussed.

The rheological property is a macroscopic property and so very important for the processing and forming of the sol (5,6). We can know from the rheological measurement that the condensation and gelation reactions progress in the sol. Also we can have the information on the rate or degree of the reaction. The only rheological measurements, however, do not give us any direct information of the microscopic structure of the sol: the size and shape of the dispersed particles and the aggregation state of particles in the sol. Accordingly, such an information should be provided by other pertinent measurements such as chemical analysis, light scattering and small-angle X-ray scattering.

2. VISCOSITY OF SOLS DURING SOL TO GEL CONVERSION

In this section, some examples of viscosity measurements are shown. The viscosity of the solution gives the information on the rate of hydrolysis-condensation reactions and the time of gelation. Fig. 1 - Fig. 3 show the dependence of viscosity on the reaction time for silicon alkoxide sols.

Fig. 1 shows the time dependence of the viscosity of a $\text{Si}(\text{OC}_2\text{H}_5)_4\text{-H}_2\text{O-C}_2\text{H}_5\text{OH-HCl}$ solution with $[\text{H}_2\text{O}]/[\text{Si}(\text{OC}_2\text{H}_5)_4] = 2$ and $[\text{HCl}]/[\text{Si}(\text{OC}_2\text{H}_5)_4] = 0.01$ for three different temperatures (7). The viscosity increases with time, indicating the progress of hydrolysis-condensation reaction. It is also seen that the increase in viscosity occurs quicker as the temperature rises, reflecting the increase in the rate of the hydrolysis and condensation reactions with temperature.

Fig. 2 compares the time dependences of the viscosity of $\text{Si}(\text{OC}_2\text{H}_5)_4\text{-H}_2\text{O-C}_2\text{H}_5\text{OH-HCl}$ solutions of different water contents (8). The water content is expressed by $r = [\text{H}_2\text{O}]/[\text{Si}(\text{OC}_2\text{H}_5)_4]$ mole ratio. For the solution of $r = 2.0$ the viscosity smoothly increases with time. For $r = 1.0$, however, the viscosity slightly increases until 250 min and then almost no change is seen. This is due to a large shortage of water for hydrolysis of alkoxides. The solution of $r = 1.7$ exhibits an interesting viscosity change; the increasing rate of the viscosity markedly decreases after the viscosity reaches about 1 Pa·sec. The sudden decrease in the rate of viscosity is attributed to the exhaustion of the water for the hydrolysis in the solution. Actually, the viscosity of the solution continues to increase at a lower rate, because the reaction proceeds by the absorption of moisture from air.

Fig. 1 and other data (9) show that the gelation is faster for solutions of higher H_2O and $\text{Si}(\text{OC}_2\text{H}_5)_4$ content, indicating that the hydrolysis proceeds faster when the concentrations of the reactants are larger. The viscosity may roughly represent for the progress of condensation reaction. The hydrolysis reaction must occur, however, for the condensation reaction to take place.

Mizuno et al. (10) and Debsikdar (11) measured the viscosities of $\text{Si}(\text{OCH}_3)_4$ solutions as

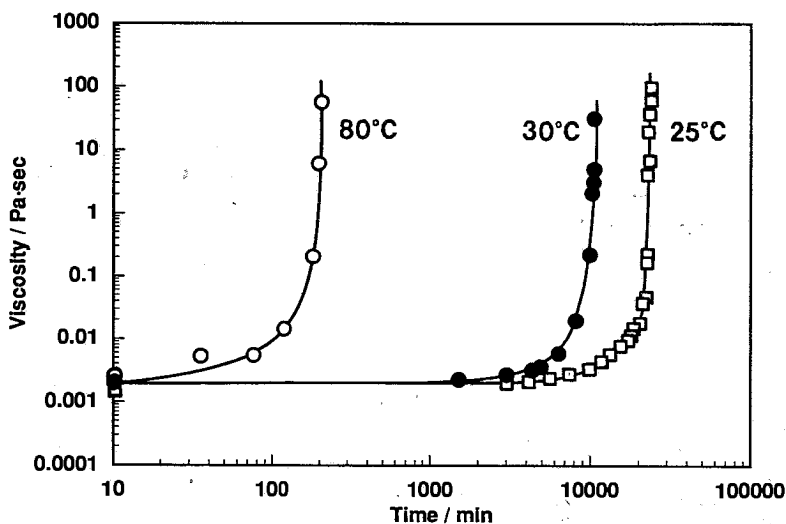


Fig. 1 Variation of the viscosity of a $\text{Si}(\text{OC}_2\text{H}_5)_4\text{-H}_2\text{O-C}_2\text{H}_5\text{OH-HCl}$ solution with $[\text{H}_2\text{O}]/[\text{Si}(\text{OC}_2\text{H}_5)_4] = 2$ and $[\text{HCl}]/[\text{Si}(\text{OC}_2\text{H}_5)_4] = 0.01$ at 25, 30 and 80°C as a function of time (7).

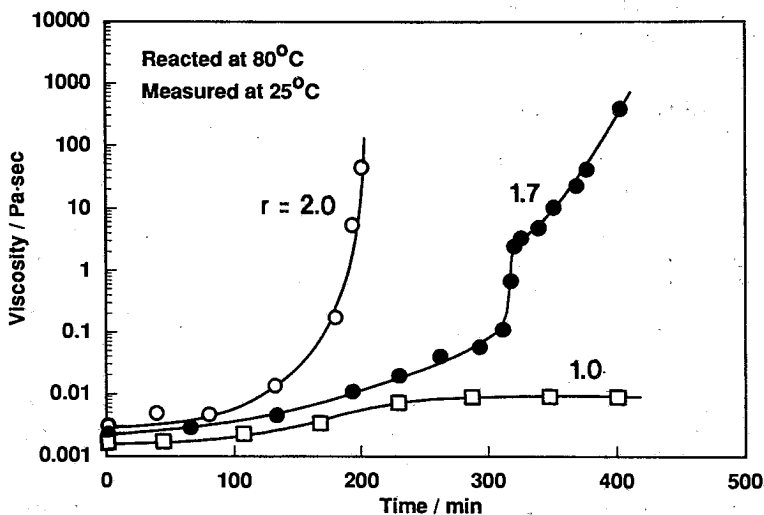


Fig. 2 Variation of the viscosity of $\text{Si}(\text{OC}_2\text{H}_5)_4\text{-H}_2\text{O-C}_2\text{H}_5\text{OH-HCl}$ solutions with varying $[\text{H}_2\text{O}]/[\text{Si}(\text{OC}_2\text{H}_5)_4]$ ratio of 2.0, 1.7 and 1.0 at 80°C as a function of time (8).

a function of time and compared the effects of the components of the starting solution on the overall rate of sol-gel transition. It was shown (10) with acid-catalyzed and neutral solutions that the gelling time decreases and the viscosity at a given reaction time increases with $\text{Si}(\text{OCH}_3)_4$ content. In a neutral condition the viscosity increases with increasing water content. Fig. 3 shows Debsikdar's result (11), indicating that the higher $\text{Si}(\text{OCH}_3)_4$ content promotes the increase in viscosity.

Fig. 4 shows the viscosity-time relationships for $\text{SiO}_2\text{-ZrO}_2$ sols. It is seen that the rate of

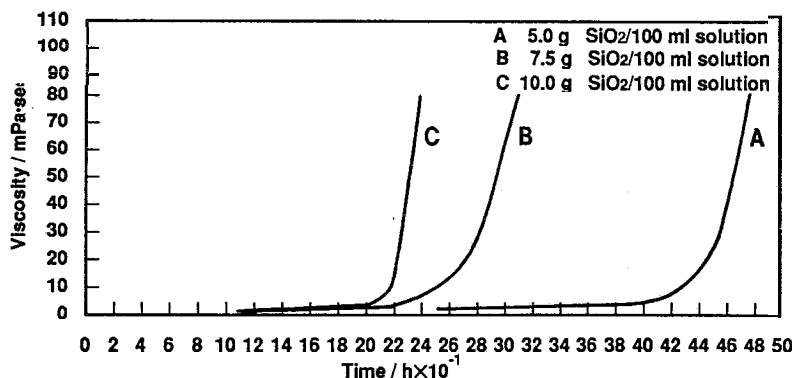


Fig. 3 Effect of solution concentration on viscosity change during sol-gel transition of $\text{Si}(\text{OCH}_3)_4$ for a solution with a $\text{H}_2\text{O}/\text{Si}(\text{OCH}_3)_4$ molar ratio of 2.1 (after Debsikdar (11)).

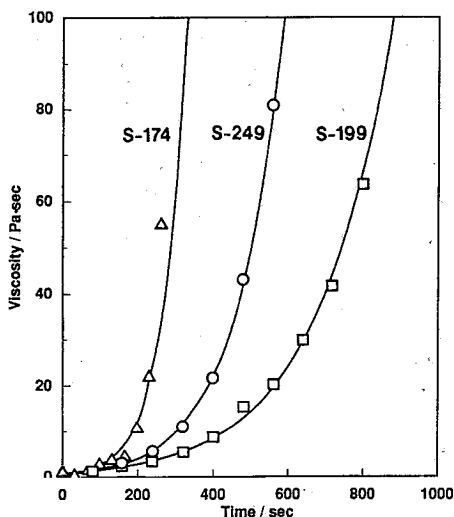


Fig. 4 Variation of the viscosity of $\text{Si}(\text{OC}_2\text{H}_5)_4\text{-Zr}(\text{OC}_3\text{H}_7)_4\text{-Solvent-HCl-Acetylacetone}$ solutions with different solvents at 25°C as a function of time (after Brenna et al. (12)). The solvent is ethanol, dimethylformamide and acetone for S-174, S-199 and S-249, respectively.

increase in viscosity is different for different solvents (12). Fig. 5 shows the viscosity of alumina sols as a function of time (13). Sol A was prepared by peptizing aluminum hydroxide with acetic acid precipitated from aluminum chloride hexahydrate ($\text{AlCl}_3 \cdot 6\text{H}_2\text{O}$) solution by NH_4OH . Sol B was prepared by heating at about 100°C the suspension provided by adding 3.8 mol Al powders to 1 mol $\text{AlCl}_3 \cdot 6\text{H}_2\text{O}$. When the viscosity reaches about 10 Pa-sec, Sol A contains round particles of increased aggregation, and Sol B contains long-shaped particles (13). The higher rate of viscosity increase in Sol A is attributed to the ease of aggregation of particles of Sol A.

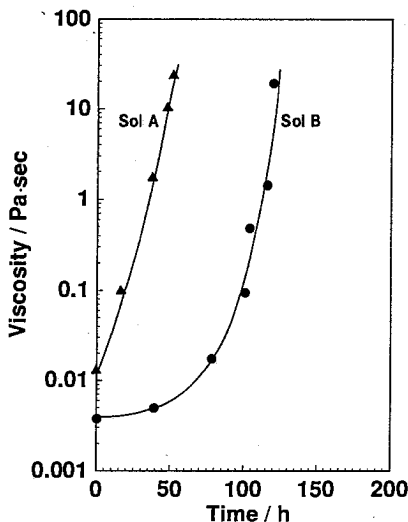


Fig. 5 Variation of the viscosity of alumina sols at 60°C as a function of aging time (13). Viscosity was measured at a shear rate of 2 sec^{-1} .

Fig. 6 shows the time dependence of the viscosity of a $\text{Hf}(\text{OC}_8\text{H}_{17})_4\text{-C}_2\text{H}_5\text{OH-H}_2\text{O-CH}_3\text{COOH}$ sol at 20°C (14). It is seen that the sol viscosity sharply increases at a time near gelation time, where a sharp particle growth, as measured by light scattering, is also seen. This viscosity increase is explained by the particle growth due to condensation of entities resulting from alkoxide hydroxylation.

At the end of this section, our results (7) on the viscosity measurements relating to the shape of particles in the spinnable and non-spinnable silicon alkoxide sols are described. The relation between the reduced viscosity η_{sp}/C and the concentration C , where η_{sp} is the specific viscosity, has been examined. It was found that the spinnable sols follow the relationship for the solution containing linear polymers:

$$\eta_{sp}/C = [\eta] + k[\eta]^2C \quad [1]$$

where $[\eta]$ is the intrinsic viscosity. On the other hand, the non-spinnable sols obeyed the formula which is valid for the solution containing spherical particles:

$$\eta_{sp}/C = K/\rho \quad [2]$$

where K is a constant and ρ is the density of the particles.

Sakka and Kamiya (7) also applied the following formula

$$[\eta] = kM_n^\alpha \quad [3]$$

where k is a constant depending on the kind of polymers, the solvent and the temperature. In

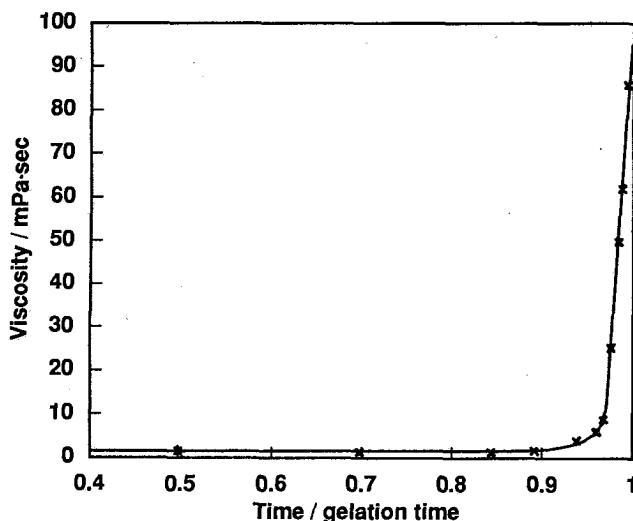


Fig. 6 The change of the viscosity of $\text{Hf}(\text{OC}_2\text{H}_5)_4\text{-C}_2\text{H}_5\text{OH-H}_2\text{O-CH}_3\text{COOH}$ sol at 20°C as a function of time (t/t_g) (after Larbot et al. (14)).

this formula, α is larger than 0.5 for three-dimensional or spherical polymers. For spinnable silicon alkoxide sols, α was larger than 0.5, while for non-spinnable sols α was smaller than 0.5.

3. VISCOSITY-SHEAR RATE RELATIONSHIPS FOR SOLS

The time dependence of the sol viscosity gives us a useful information on the progress of hydrolysis and condensation reactions and growth of sol particles, which eventually leads to gelation of the sol.

Many liquids are not Newtonian, but exhibit Bingham flow, quasi-viscous flow, structural viscosity and other non-Newtonian behaviors. In Newtonian liquids, the viscosity is constant, independent from the shear stress, while in non-Newtonian liquids, the viscosity changes with the shear rate. Accordingly the measurements of the shear rate dependence of the sol viscosity might provide more information than the simple viscosity measurement. Actually, we have found (15) that the spinnable and non-spinnable solution show a different dependence of the viscosity on the shear rate. The results of such measurements on the sols are shown in the followings.

3.1. Results Related to Occurrence of Spinnability

The dependence of the viscosity on the shear rate at various reaction times t for the solutions of the composition $1\text{Si}(\text{OC}_2\text{H}_5)_4\cdot 2\text{H}_2\text{O}\cdot 1\text{C}_2\text{H}_5\text{OH}\cdot 0.01\text{HCl}$ reacted in the open state (OP-1) and closed system (CL-1) is shown in Fig. 7 (16,17). No change in the viscosity with the shear rate is seen up to a highly viscous state ($\eta > 10$ Pa·sec) for OP-1, meaning that OP-1 behaves as a Newtonian liquid until near the gel point. The viscosity of CL-1 decreases with the shear rate after $t = 184$ h and after $t = 188$ h the viscosity value is not recovered on decreasing the shear rate again to the initial state. These indicate that the flow characteristics of solution CL-1 changes from Newtonian to pseudo-plastic and then to thixotropic as the viscosity becomes high. Casson has derived the equation relating the shear stress F to the shear rate D :

$$F^{1/2} = k_0 + k_1 D^{1/2} \quad [4]$$

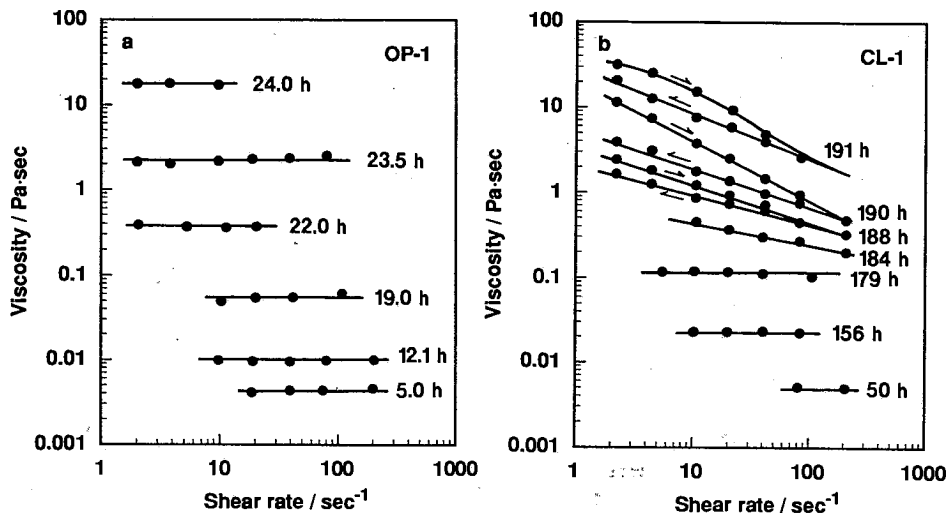


Fig. 7 Viscosity-shear rate relation at various reaction times for the open system solution OP-1 (a) and closed system solution CL-1 (b) of the composition $1\text{Si}(\text{OC}_2\text{H}_5)_2 \cdot 2\text{H}_2\text{O} \cdot 1\text{C}_2\text{H}_5\text{OH} \cdot 0.01\text{HCl}$ (16,17).

| | Cover | Gelling time | Volume loss | Spinnability |
|------|-------|--------------|-------------|--------------|
| OP-1 | No | 1 day | 60% | Yes |
| CL-1 | Yes | 8 days | 0% | No |

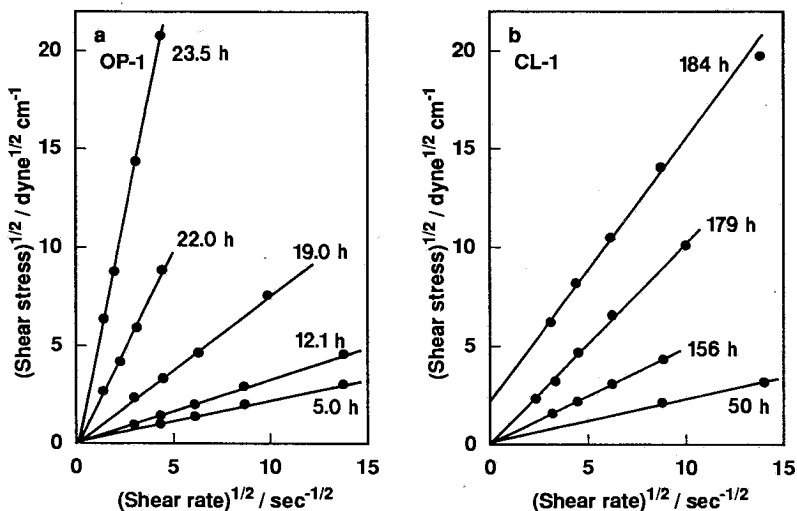


Fig. 8 Casson plots for open system solution OP-1 (a) and closed system solution CL-1 (b) (18).

where k_0 and k_1 are constant values (18). k_0^2 is the yield value of the suspension since k_0^2 is the shear stress F at the shear rate $D = 0$. A plot of $F^{1/2}$ against $D^{1/2}$ should be a straight line with an intercept at $F^{1/2} = k_0$ on the $F^{1/2}$ axis, so one can find from this plot whether the suspension has a yield stress value or not. Naturally, all the Casson plots for OP-1 shown in

Fig. 8a are straight lines, passing through the origin, because the solution is of Newtonian nature. The Casson plot for CL-1 shown in Fig. 8b has an intercept on the vertical axis at $t = 184$ h, indicating that the sol has a yield value.

These observations indicate that when the evaporation of the solvent is allowed during the gelation reaction, the viscosity of the solution increases as a result of the concentration of the solution. Therefore, the solution is characterized by Newtonian flow up to a highly viscous state and shows spinnability. When the evaporation of the solvent is not allowed, the viscosity of the solution increases due to network formation in the solution and characterized by pseudo-plasticity, thixotropy and some elasticity in the viscous state, showing no spinnability at any viscosity (19).

It was found that the sol containing a small amount of CH_3COOH , HCOOH , HNO_3 or $(\text{H}_2\text{SO}_4)_{0.5}$ shows the similar change of flow property, as shown in Fig. 9, when the reaction is

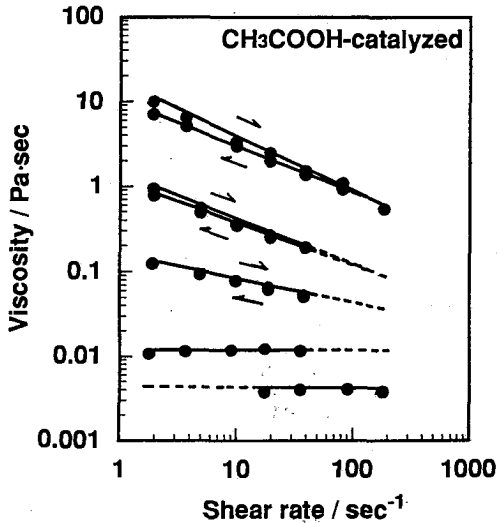


Fig. 9 Viscosity-shear rate relation for the CH_3COOH -containing sol of the molar composition $1\text{Si}(\text{OC}_2\text{H}_5)_4 \cdot 2\text{H}_2\text{O} \cdot 5\text{C}_2\text{H}_5\text{OH} \cdot 0.01\text{CH}_3\text{COOH}$ reacted in the closed system (20).

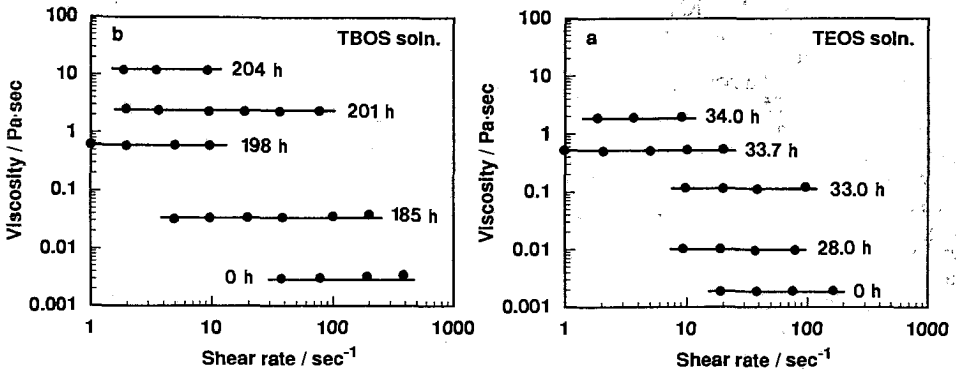


Fig. 10 Viscosity measured at various shear rates in the TEOS solution with $\text{C}_2\text{H}_5\text{OH}/\text{Si}(\text{OC}_2\text{H}_5)_4 = 7$ (a) and TBOS solution with $n\text{-C}_4\text{H}_9\text{OH}/\text{Si}(n\text{-OC}_4\text{H}_9)_4 = 7$ (b) (21).

made in the closed system (20). The flow property of the sol changes from Newtonian to shear-thinning and to thixotropic with time, and no spinnability appears. When the acid-catalyzed alkoxy silane solutions are reacted in the open state, the sols behave as Newtonian liquids (21), as shown in Fig. 10, and show the spinnability whatever the starting alkoxides are.

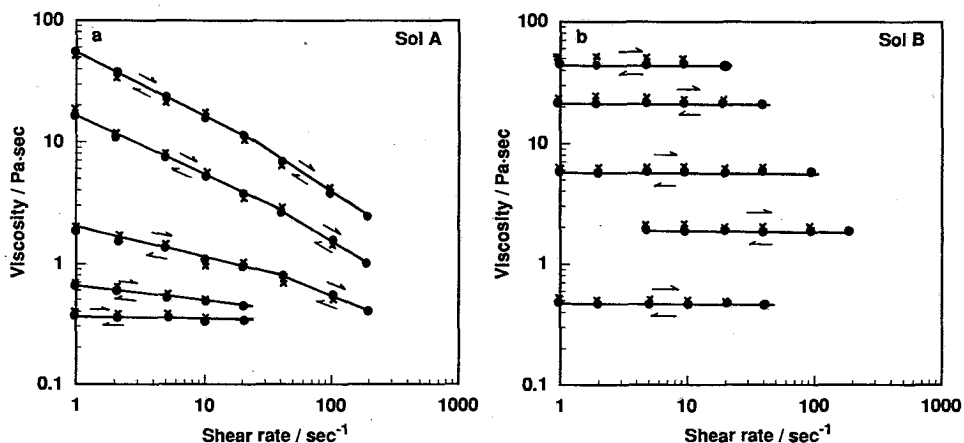


Fig. 11 Plots of viscosity versus shear rate for alumina sols A (a) and B (b) (13). Arrows show the direction of the change of shear rate. The points O and X denote the values obtained when the shear rate is increased and decreased respectively. Sol A and sol B are the same sols cited in Fig. 5.

Fig. 11 shows the viscosity-shear rate relations for alumina sols (13,22). Sol A contains round or granular particles and is not spinnable, while sol B contains ribbon-like particles and is spinnable. It can be seen from Fig. 11 that both sols are Newtonian at viscosities lower than 1 Pa-sec, but at higher viscosities than about 1 Pa-sec, sol A shows a shear thinning behavior. Sol B shows almost Newtonian flow throughout the present viscosity range.

Viscosity-shear rate relations shown in Fig. 12 have been obtained for a TiO₂ sol prepared from the starting solution of the molar composition 1Ti(O-iC₃H₇)₄·2H₂O·1C₂H₅OH·0.53HCl and kept at 40°C in an uncovered beakers. Kamiya et al. (23) could draw fibers from this type of solution to make TiO₂ fibers, indicating that the high viscosity sols are spinnable. Fig. 12 shows that the sols are Newtonian in flow behavior at high apparent viscosities, where they are spinnable.

The viscosity of a solution consisting of acetates of Y, Ba and Cu, from which gel fibers can be drawn (24,25), has been measured as a function of shear rate and is shown in Fig. 13. It is seen that the acetate sols show nearly Newtonian flow behavior, although, strictly, these sols are slightly shear-thinning.

As to the occurrence of spinnability in silica sols, Brinker and Assink (26) showed that the growth of polysilicate species is random and clusters formed do not have necessarily long-shaped forms. They state that the primary criterion for spinnability is high viscosity without premature gelation, and this is achieved by acid-catalyzed conditions employing low values of water to alkoxide ratio. Sacks and Sheu (27) measured rheological properties of silica sol and observed optimum spinnability when the flow behavior was highly shear-thinning, but not thixotropic. This conclusion is different from our experimental results (15) described above.

3.2. Other Results on Rheological Properties of Sols

Song and Chung (28) and González et al. (29) made alumina sols from aluminum alkoxides

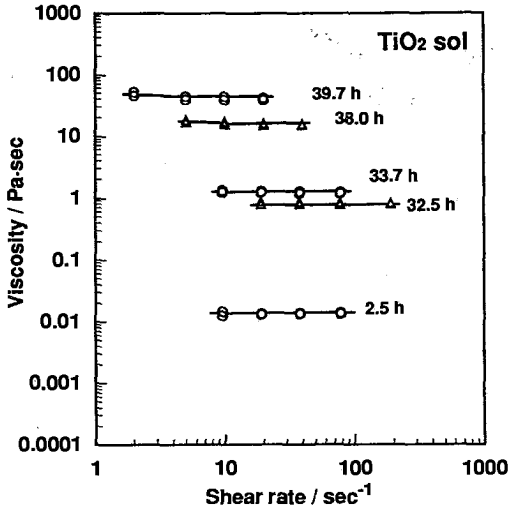


Fig. 12 Viscosity as a function of shear rate at 30°C for a TiO₂ sol (23) prepared from the starting solution of the molar composition, $1\text{Ti}(\text{i-OC}_2\text{H}_5)_4 \cdot 2\text{H}_2\text{O} \cdot 1\text{C}_2\text{H}_5\text{OH} \cdot 0.53\text{HCl}$ by keeping at 40°C in an uncovered beaker (Kozuka and Sakka).

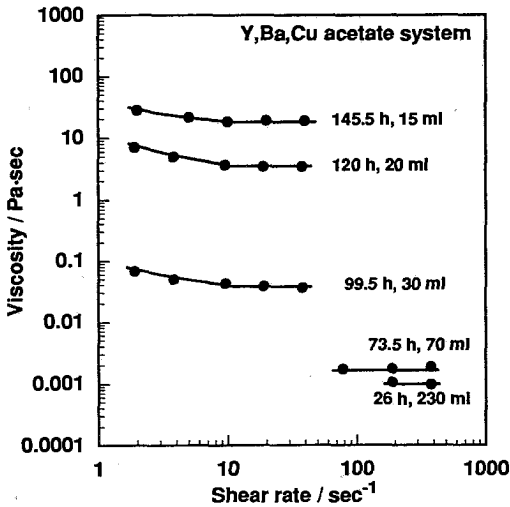


Fig. 13 Viscosity as a function of shear rate of the acetate sol of Y : Ba : Cu = 1 : 2 : 3 in mol. 0.0188 mole of $\text{Y}(\text{CH}_3\text{COO})_3 \cdot 4\text{H}_2\text{O}$, 0.0376 mol of $\text{Ba}(\text{CH}_3\text{COO})_2$ and 0.0564 mol of $\text{Cu}(\text{CH}_3\text{COO})_2$ were dissolved in 300 ml water (Kozuka, Umeda and Sakka). The time of concentrating the solution at 40°C and the volume after concentration are indicated.

$\text{Al}(\text{O-iC}_3\text{H}_7)_3$ and $\text{Al}(\text{O-secC}_4\text{H}_9)_3$. Measuring the viscosity as a function of shear rate and estimating yield values of the sol based on Casson's formula (eq. 4) and modified formula, they discussed the effects of the aging time and temperature, the concentration of the alkoxides, and the concentration of acid or base on the rheological behavior of the sol. Generally, the

sols showed a Newtonian behavior at shorter aging times (at lower viscosities) and shear-thinning and thixotropic behavior at longer aging times (at higher viscosities). The aggregation state of alumina sols was discussed based on the rheological behavior.

The rheological behavior of sols prepared from $Zr(O-nC_3H_7)_4$ was discussed by Wolf and Rüssel (30) using the flow curves (shear stress-shear rate relationship).

Guizard et al. (31) applied the dynamic viscoelastic measurements at small amplitudes using an oscillating rotational viscometer to titania sols and estimated the viscous contribution (loss modulus), G'' , and elastic contribution (storage modulus), G' , in the formula

$$G^* = G' + iG'' \quad (5)$$

$$\tan \delta = G''/G' \quad (6)$$

where G^* is the complex modulus. The measurements were found to provide the information on the structures of the gel and aggregates and the gelation of the sol.

4. CONCLUSIVE REMARKS

Rheological measurements including viscosity and viscosity-shear rate relationship were shown to provide the progress of the reaction in the sol and the structure of the sol. Also, the marked difference in the flow behavior between spinnable and non-spinnable sols was shown; the former are Newtonian or nearly Newtonian at high viscosities, while the latter are non-Newtonian.

References

1. S. Sakka, *Treatise on Materials Science and Technology, Vol. 22, Glass III*, eds. M. Tomozawa and R. Doremus (Academic Press, New York, 1982) p.129.
2. S. Sakka and T. Yoko, *Ceramics International*, **17** (1991) 217.
3. S. Sakka, *Science of Sol-Gel Method* (Agne-Shofu-Sha, Tokyo, 1988) pp.221 (in Japanese).
4. C.J. Brinker and G.W. Scherer, *Sol-Gel Science*, (Academic Press, San Diego, 1990) pp.908.
5. S. Sakka, *J. Non-Cryst. Solids*, **100** (1988) 142.
6. S. Sakka and T. Yoko, *J. Non-Cryst. Solids*, **147&148** (1992) 394.
7. S. Sakka and K. Kamiya, *Emergent Process Methods for High Technology Ceramics, Mater. Sci. Res. Vol. 17*, eds. R.F. Davis, H. Palmour III and R.L. Poter (Plenum, New York, 1984) p.83.
8. S. Sakka, K. Kamiya and T. Kato, *Yogyo-Kyokai-Shi*, **90** (1982) 555.
9. S. Sakka and K. Kamiya, *J. Non-Cryst. Solids*, **48** (1982) 31.
10. T. Mizuno, J. Phallipou and J. Zarzycki, *Glass Technol.*, **26** (1985) 39.
11. J.C. Debsikdar, *Adv. Ceram. Mater.*, **1** (1986) 93.
12. U. Brenna, G. Carturan and G.D. Sorarù, *J. Non-Cryst. Solids*, **137** (1991) 191.
13. T. Maki and S. Sakka, *J. Non-Cryst. Solids*, **100** (1988) 303.
14. A. Larbot, T. Hours, P. Bergez, J. Charpin and L. Cot, *J. Non-Cryst. Solids*, **147&148** (1992) 85.
15. S. Sakka and H. Kozuka, *J. Non-Cryst. Solids*, **100** (1988) 142.
16. H. Kozuka, H. Kuroki and S. Sakka, *J. Non-Cryst. Solids*, **95&96** (1987) 1181.
17. H. Kozuka, H. Kuroki and S. Sakka, *J. Non-Cryst. Solids*, **101** (1988) 120.
18. N. Casson, in *Rheology of Disperse Systems*, ed. C.C. Mill (Pergamon, London, 1959) p.84.
19. H. Kozuka, H. Kuroki and S. Sakka, *J. Non-Cryst. Solids*, **100** (1988) 226.
20. H. Kozuka, H. Kuroki and S. Sakka, *XV International Congr. Glass, Leningrad 1989, Proceedings Vol. 4*, ed. O.V. Mazurin, ("Nauka", Leningrad, 1990) p.98.
21. S. Sakka and H. Kozuka, *Chem. Lett.*, (1987) 1763.
22. T. Maki and S. Sakka, *Bull. Inst. Chem. Res., Kyoto Univ.*, **65** (1987) 242.
23. K. Kamiya, K. Tanimoto and T. Yoko, *J. Mater. Sci. Lett.*, **5** (1986) 468.
24. S. Sakka, H. Kozuka and T. Umeda, *J. Ceram. Soc. Japan*, **96** (1988) 468.
25. T. Umeda, H. Kozuka and S. Sakka, *Adv. Ceram. Mater.*, **3** (1988) 520.
26. C.J. Brinker and R.A. Assink, *J. Non-Cryst. Solids*, **111** (1989) 48.
27. M.D. Sacks and R.-S. Sheu, *J. Non-Cryst. Solids*, **92** (1987) 383.
28. K.-C. Song and I.-J. Chung, *J. Non-Cryst. Solids*, **107** (1989) 193.
29. C. González, J. Gutiérrez, J. Llorens, M.I. Galán and C. Mans, *J. Non-Cryst. Solids*, **147&148** (1992) 690.
30. C. Wolf and C. Rüssel, *J. Mater. Sci.*, **27** (1992) 3749.
31. C. Guizard, J.C. Achddou, A. Larbot and L. Cot, *J. Non-Cryst. Solids*, **147&148** (1992) 681.

**MOLECULAR DESIGN AND PROCESSING EFFECTS ON
SOL-GEL DERIVED THIN FILMS**

Bulent E. Yoldas
PPG Industries, Inc.
Chemicals Group Technical Center
440 College Park Drive
Monroeville, Pennsylvania 15146 U.S.A.

ABSTRACT

Various optical and other coatings may be applied on glass substrates from colloidal suspensions and polymer solutions prepared from metal-organic compounds. These precursor solutions normally contain oxide constituents in chemical association with solvating organic groups and require heat treatment to 300-500°C to obtain glass-like oxide films. The entire coating process is carried out in three sub-steps: (a) solution preparation, (b) solution application and (c) heat treatment. In each of these steps, processing parameters can introduce molecular, structural and morphological variations which in turn affect the properties of the resultant films.

Molecular structures as well as the terminal groups of these structures are established by the condensation parameters during the solution preparation. Application of these solutions under drastically differing shear and drying rates, inherent in the method of application, cause significant divergence in polymer alignment and pore morphology leading to variations in the density and refractive index of the coating. In the heat treatment stage, variations in the heating rate causes changes in the chemical environment at the molecular boundaries, thus affecting chemical bond cleavages. This gives rise to carbon deposition and optical defects. In this presentation, fundamental considerations in the sol-gel coating process and principle effects of processing parameters are reviewed.

INTRODUCTION

The "sol-gel" method of depositing films is finding increasing acceptance in the areas of optics, electro-optics and in the formation of chemical barrier coatings⁽¹⁻⁴⁾. This method allows deposition of films ranging in thickness from less than 100Å to several microns from solutions.

When we look at the "sol-gel" derived glass and ceramic materials, whether they are in bulk or thin film form, three characteristics often stand out: (1) they contain organic and hydroxide groups at temperatures below 500°C; (2) they are initially porous with a range of pore size from tens of angstroms to several hundred angstroms; and (3) their properties are significantly process dependent. We will only be concerned with the last characteristic in this presentation.

The fundamental difference between thermal and sol-gel paths to material formation is the origination point of the structure. In the thermal methods, the inorganic structure is established at fusion temperature in a molten state and proceeds towards room temperature, a condition which is diametrically reversed in the sol-gel method. In the alkoxide based sol-gel processes, hydrolytic condensation reactions create oxide networks of various morphologies framed by hydroxyl and organic groups at or near room temperatures. This crucial difference determines the relative roles thermal and chemical forces play in the establishment of the initial structure. Removal of organic groups in heating the material, e.g. up to 500°C, leaves behind an organic skeleton analogous to the networks of fused silica. Significant variations in stoichiometry and coordination states may occur in this stage leading to photosensitivity. Elimination of these defects requires diffusion dependent heat treatment thus becomes time dependent. In coating systems, additional modifications occur due to coating deposition methods. In the following sections, these process-induced variations are discussed.

PRECURSOR SOLUTION FORMATION

Methods of depositing SiO₂ films from solutions have been known since the early 1940's. Tanner and Lockhart⁽¹⁾ prepared solutions from silicates suitable for deposition of SiO₂ films. It later became evident that esters of silicic acid and alkoxides of silicon were particularly suitable for preparation of SiO₂-depositing solutions.

In most other metal alkoxide systems, however, attempts to deposit oxide films were complicated by the hydrolysis reactions which are quite vigorous in these systems. Given sufficient water, these hydrolysis reactions rapidly lead to condensation of insoluble oxide and hydroxide powders, making the solution unsuitable for optical coating applications. These difficulties were circumvented by Schroeder and others⁽⁵⁻⁶⁾ by using unhydrolyzed or incompletely hydrolyzed metal alkoxide solutions as coating precursors and allowing the air humidity, or surface OH groups present on glass and ceramic surfaces, to hydrolyze the alkoxides. A wide variety of oxides has been deposited by this technique.

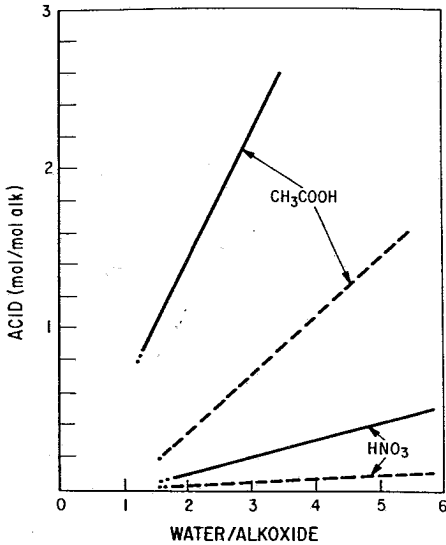


Figure 1. Acid requirement for zirconia solutions at two different solution concentrations when $Zr(OC_3H_7)_4$ is hydrolyzed in 2-propanol. Equivalent ZrO_2 (-) 5%, (---) 2.5%.

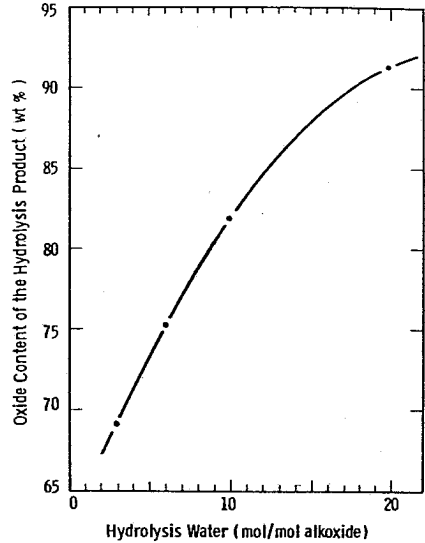


Figure 2. Effect of water/alkoxide ratio on oxide content when $Ti(OC_4H_9)_4$ hydrolyzed in butanol.

More recently, techniques have been developed which allow clear polymerized solutions of almost any oxide to be made⁽⁷⁾. These solutions are prepared by controlled reactions of metal alkoxides with water in a mutual solvent such as alcohols. It often requires presence of an acid and strongly influenced by other condensation parameters as shown in Figure 1. Deposition of oxide films from these solutions does not depend on external supply of H_2O or OH groups to complete the oxide forming reactions. Thus, films can be deposited and baked in any atmosphere, e.g., vacuum.

Condensation reactions that form these solutions are strongly affected by molecular separation of interacting species, their ratios, the reaction medium, the catalyst, the pH, the reaction length and temperature. These parameters alter the chemical and topological make-ups of the condensates in a fundamental way. Significant variations occur in molecular size, molecular topology and nature

of the terminal groups, i.e., OR or OH groups. An important point is that the oxide domains of soluble species must always be terminated by hydroxyl or organic groups.

A hydrolytic polycondensation equation which would take into account the variability of the molecular size as well as the nature and concentration of these terminal groups can be written:



where n is the number of metal ions polymerized in an oxide network, and x and y are the numbers of terminal OH and OR groups framing that network.

The principal variations in single-component condensates fall into three basic categories: molecular size, network topology and nature of the terminal group. The oxide content of the polymer becomes a function of size, n , topology and type of terminal groups. These properties are very sensitive to water/alkoxide ratio. By manipulation of this parameter, one can deposit SiO₂ and TiO₂ films whose oxide content is as low as 70% or as high as 95% by weight as seen in Figure 2.

Hydrolytic condensation of alkoxides with lower alkyl groups generally produce polymers having a higher oxide content. Hydrolysis in lower alcohols gives a higher equivalent oxide content. For example, when Ti(OC₂H₅)₄ is hydrolyzed in ethanol (C₂H₅OH) and dried at 100°C, the oxide content of the gel by weight is ~83 to 84%. This figure drops to about 73% when the hydrolysis is performed in butanol, C₄H₉(OH)^s. Consequently, TiO₂ films deposited from the latter solution have a lower index of refraction and are generally inferior due to their lower density after heat treatment. The index of refraction, varying from 1.4 to 2.4, can be obtained in SiO₂-TiO₂ system.

The nature of the terminal groups, i.e., "OH" or "OR" (which is normally determined by the amount of hydrolysis water), has the most influence on stability of solution as well as on the thermal behavior of the films deposited from these solutions. Titania solutions obtained by <1.6 mole H₂O hydrolysis tend to deposit opaque and discontinuous films; high-water hydrolysis results in unstable viscosity which changes drastically with time leading to gelation of the solution. In the most alkoxide systems, the solution must be given some initial time, e.g., a few hours to a few days, to stabilize. The refractive index of coatings deposited from such solutions may change slightly during this period (e.g., ±0.015) depending on the system. After this initial period, a slight degradation of the index of refraction may occur with long aging in some solutions.

COATING APPLICATION

The precursor solution is applied on substrates by any liquid application methods including dipping, spinning and spraying, depending on the substrate geometry, etc. For optical applications, preferred methods are dipping the substrate into the liquid followed by a controlled rate of pulling the substrate out (or draining the solution), or spinning the solution on substrate.

Basically, there are three ways to control the thickness of the coating by manipulating the solution. They are: equivalent oxide concentrations; degree of hydrolysis; and type of liquid medium. Each of these parameters affects the viscosity of the solution⁽⁸⁾.

It has been found experimentally that an equivalent oxide concentration of 1-5% by weight of the solution gives the best coating properties in both spinning and dipping application techniques as well as producing the most stable solutions. The concentration within this range must be determined in conjunction with the coating technique and other requirements. The type of liquid medium in which the alkoxide is hydrolyzed also has a significant effect. This medium is usually an alcohol containing no water. As expected, higher viscosity alcohols (such as butanols) deposit thicker coatings. However, use of ethyl alcohol or propanol is preferred since it has been observed that butanol-based solutions are less stable with time and are subject to changes in their composition and viscosity.

Different coating methods involve drastically different speeds and shear rates under which the polymer molecules are aligned and deposited on the substrate. Spin coating dries the film in a few seconds in a dynamic condition. Drain coatings, typically at several cm/min., allows for polymer alignment into a denser configuration. Surface roughness of spin coated films is found to be significantly higher than dip or drain coated films. Thus, morphology created by the application of a given polymeric solution is significantly different for the drain process than for the spin process.

Densification of these films, as shown in Figure 3, indicates the fundamental differences between the films deposited by spin coating and dip coating as well as it elucidates the nature of the crazing in these films. When 1 μm thick spin coated film is densified, its thickness is reduced by ~50%, indicating it was initially ~50% porous. The thickness reduction of drain coated films upon densification is approximately half as much as this, indicating that the initial porosity was half as much.

EFFECT OF BAKE TEMPERATURE AND ATMOSPHERE

Reduction of the coating to an organic-free oxide film requires a heat treatment at a temperature of the order of 500°C in most systems. In the TiO_2 system, the temperature requirement may be as low as 350°C. It must also be pointed out that, if a small amount (e.g., a few percent) of organic or hydroxyl components is not objectionable, these heat treatment temperatures can be significantly lowered.

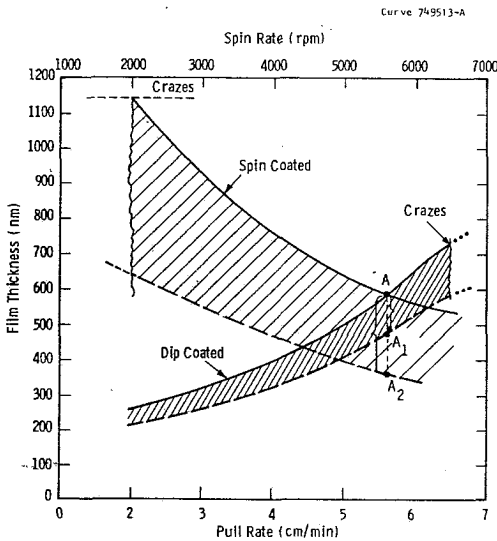


Figure 3. Thickness of SiO_2 films as a function of application rate by spin and dip coating before (solid lines) and after (dashed lines) the densification. Note that after densification, crazing thickness becomes about the same. Also, compare the film shrinkages at point "A" where the as-deposited thickness is the same.

Sintering and densification of sol-gel films are not smooth functions of temperature. There are temperature regimes where there are selective chemical bond cleavages, and certain chemical components are released. Since intermolecular atmosphere within the film is diffusion dependent, the heat rate becomes important, especially as the film gets thicker.

In the thicker films, thermal degradation takes place essentially in the self-generated internal environment. Chemical nature of that environment is determined by the gaseous products of decomposition and modified by diffusive exchange with external atmosphere. This diffusion dependence makes the heating rate an important structural parameter. Thermal degradation of organic groups of silica gel essentially takes place between 250°C and 300°C when in close equilibrium with air, e.g., 1°C/min. heating rate. In the absence of oxygen, e.g., in nitrogen, the bond cleavages shift to the 400-500°C range. A slower heating rate in air shifts the intermolecular chemical environment towards a more oxidizing condition, thus a corresponding shift in the bond cleavages.

The effect of terminal bonds goes beyond the solution state. A consequence of certain chemical reactions during thermal treatment is densification. The driving force for these chemical reactions can be orders of magnitude larger than the driving force, i.e., the surface area reduction, for thermal sintering. Thus, the presence of hydroxyl bonds in the intimate molecular boundaries in these materials leads to chemical activated sintering as seen in Figure 4.

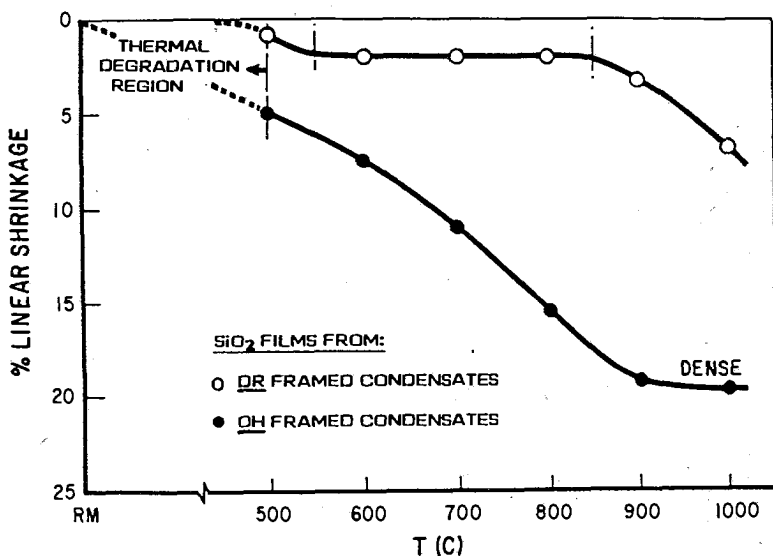
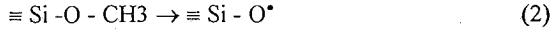


Figure 4. SiO_2 film deposited from OH terminated species show significantly higher densification as indicated by thickness change.

Another interesting effect of terminal bonds occurs in creation of nonstoichiometry and photosensitivity.⁽⁹⁾ The organics can only be removed from the network either by cleavage of carbon-oxygen bond or by cleavage of oxygen-silicon bond. In either case, a defect is created:



In the first case, an electron hole will be localized in a 2p orbital of single-bonded oxygen. In the second case, an electron will be localized in a dangling Sp^3 orbital of three-coordinated silicon in SiO_3 units. These give rise to photosensitivity through electron-photon coupling. This phenomenon may have significant consequences in optical applications, e.g., lasers.

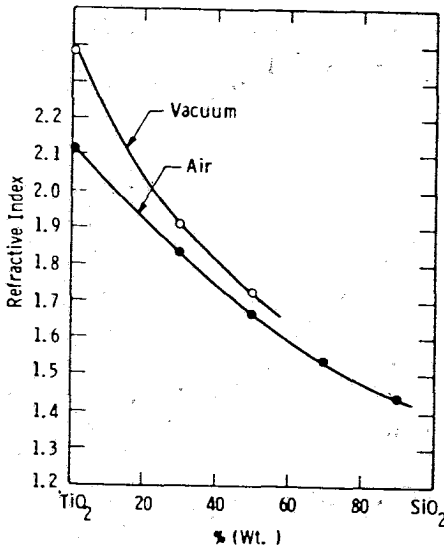


Figure 5. Effect of heat treatment atmosphere on the index of refraction of coating as a function of its composition in the TiO_2 - SiO_2 binary.

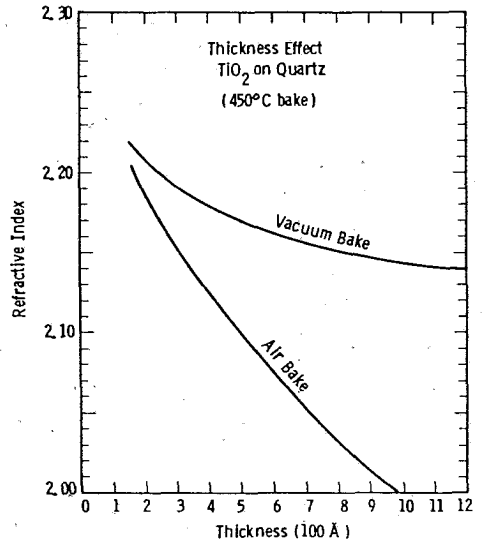


Figure 6. Effect of film thickness on refractive index of TiO_2 films deposited on quartz.

Atmospheric effects are extremely important in certain systems. A 100% TiO₂ film baked in air to 500°C has an index of refraction of ~2.1. The same film gives an index of ~2.4 if the baking is performed in vacuum. Figure 5 shows this effect of heat treatment atmosphere which diminishes as the composition changes from TiO₂ to SiO₂ in TiO₂ - SiO₂ binary. Atmospheric humidity has a significant effect on the densification of silica films. Silica films that are normally densified at around -900-1000°C are found to densify around 450~500°C when heated in humid atmosphere.

THICKNESS EFFECT

Another interesting phenomenon that occurs in sol-gel derived films is dependence of properties to its physical thickness.

Figure 6 brings this aspect of sol-gel deposited films into sharper focus. Here the refractive index indicates that the density of TiO₂ films increases with decreasing thickness. It is even more revealing that the differences between the air bake and vacuum bake films also diminish with decreasing thickness and completely disappears around ~100-150Å. A reasonable interpretation of this is that at around ~100Å thickness, the TiO₂ films become completely dense; a case under which the effect of the bake atmosphere on densification becomes inoperative. The impervious nature of very thin TiO₂ films has also been demonstrated chemically (for example, see Figure 8 in Reference 2).

It is thought that in thinner films, the polymer alignment attained by the spinning or dipping motion is less likely to become disoriented by fast drying and geometrical constraints. This effect of thickness on the index of refraction appears to be operative in all thin films deposited from polymerized solutions. For example, a Ta₂O₅ film similarly deposited and baked at 500°C in air had a refractive index of 1.938 when the film was 475Å thick and 1.917 when the thickness was 675Å. The same effect was found for SiO₂ films.⁽²⁾

SUMMARY

Properties of sol-gel derived oxide coatings are significantly modified in process parameters. Main effects are summarized below:

Precursor Effects: Alkoxides of lower alkyls produce denser films with higher initial oxide

content. The same applies to solvent. Porosity, pore size and surface area are strongly affected by the dispersion medium.

Condensation Effects: Hydrolytic condensation under diluted conditions result in smaller molecular size, finer texture, generally higher porosity. Hydrolysis with higher water/alkoxide ratio gives solutions depositing denser films, with enhanced sinterability.

Method of Deposition Effects: Spin coating gives significantly higher porosity, and surface roughness than dip coated films.

Thickness Effect: There are significant density gradient in the first several hundred angstrom of sol-gel deposited films. The first $\sim 100\text{-}150\text{\AA}$ layer appears to be substantially dense.

Heat Treatment Effects: There are significant atmospheric effects in some oxide systems. There are thermal conditions which lead to selective cleavage of bonds with significant consequences.

REFERENCES

1. C. J. Brinkr, A. J. Hurd, P. R. Schunk, G. C. Frye and C. S. Ashley, *J. Non-Cryst. Solids*, **1992**, 147 and 148, 424.
2. B. E. Yoldas, *Applied Optics*, **1982**, 21, 2960.
3. D. R. Uhlmann, G. Teowee, J. M. Boulton, S. Motakef and S. C. Lee, *J. Non-Cryst. Solids*, **1992**, 147 and 148, 409.
4. B. E. Yoldas and T. W. O'Keefe, *Applied Optics*, **1984**, 23, 3638.
5. H. Schroeder, in *Physicas of Thin Films*, G. Hass and R. E. Thun, Eds. (Academic, New York, 1969), Vol. 5, p. 87.
6. H. Dislich, *Angew. Chem., Int.*, Ed. Eng., **1971**, p. 363.
7. B. E. Yoldas, U.S. Patent 4,346,131, 1982.
8. S. Sakka and K. Kamiya, *J. Non-Cryst. Solids*, **1982**, 48, 31.
9. G. Kordas, *J. Non-Cryst. Solids*, **1992**, 147 and 148, 106.

PREPARATION OF $\text{SiO}_2\text{-TiO}_2\text{-ZrO}_2$ GEL COMPOSITIONS
BY MEANS OF A LIQUID CRYSTAL APPROACH

G. Mezinskis*) and G. H. Frischat

Institut für Nichtmetallische Werkstoffe, Technische Universität Clausthal, 38678 Clausthal-Zellerfeld, Germany

This paper reports first results when the reaction medium is changed from a Si, Ti and Zr alkoxide solution to a liquid crystal medium based on lecithin and ethylene glycol. Both alkoxide and liquid crystal derived $\text{SiO}_2\text{-TiO}_2\text{-ZrO}_2$ compositions were investigated by X-ray fluorescence X-ray diffraction, thermal analysis, and infrared absorption. It is shown that a chemical treatment of the liquid crystal derived compositions leads to a more complete process of heterocondensation and to the formation of a mixed silica-titania network, compared to the alkoxide process. However, the remaining P_2O_5 , supplied by the lecithin, still restricts the application.

Introduction

Since silicon ethoxide (TEOS) and Ti and Zr alkoxides differ significantly in their rates of hydrolysis, various sol-gel routes have been used to prepare binary high melting $\text{SiO}_2\text{-TiO}_2$ (ZrO_2) glasses. Although many attempts were made to influence both hydrolysis and polymerization processes by an appropriate choice of the precursors, homogeneous gels with Si-O-Ti or Si-O-Zr bonds were hardly formed (1 - 4). Heterocondensation processes are not favored in these reactions. Alkoxide sol-gel methods were used also to prepare glasses and coatings in the ternary system $\text{SiO}_2\text{-TiO}_2\text{-ZrO}_2$ (5 - 7), and the kinetics of hydrolysis and condensation steps was studied by nuclear magnetic resonance (NMR) and infrared (IR) spectroscopy techniques (8, 9). It was concluded that even in the liquid phase no evidence of mixed Si-O-Ti and Si-O-Zr bonds could be detected, and only the continuing condensation processes during annealing caused a certain number of Ti and/or Zr atoms to become attracted to $\text{SiO}_4/2$ tetrahedra. However, the number of these bonds diminished further until the final gel glass had been obtained (8).

Recently an investigation on the hydrolysis of TEOS in the surrounding of organized systems attracted the attention with the possibility to perform this hydrolysis process directly to silicic acid within the framework of a liquid crystalline structure (10). This work tries to find out whether different extents of heterocondensation are to be expected if Ti and Zr alkoxides, modified by acetic acid, are added to this silicic acid containing liquid crystal medium.

Experimental

TEOS (Merck AG, Darmstadt, Germany), Ti butoxide (Merck), Zr n-propoxide (Fluka Chemie AG, Neu Ulm, Germany), lecithin, glacial acetic acid, HCl, ethyl alcohol, and ethylene glycol (all from Merck) were used as-received. For comparison gels

*) Permanent address: Department of Silicate Technology, Riga Technical University, Azenes St. 14, Riga, LV-1048, Latvia.

with a target composition (in mol-%) of 70 SiO₂-20 TiO₂-10 ZrO₂ (denoted by sample G) were prepared according to the modified preparation route given in ref. (9). Further, two batches of lyotropic lamellar liquid crystals with TEOS were prepared, see Fig. 1.

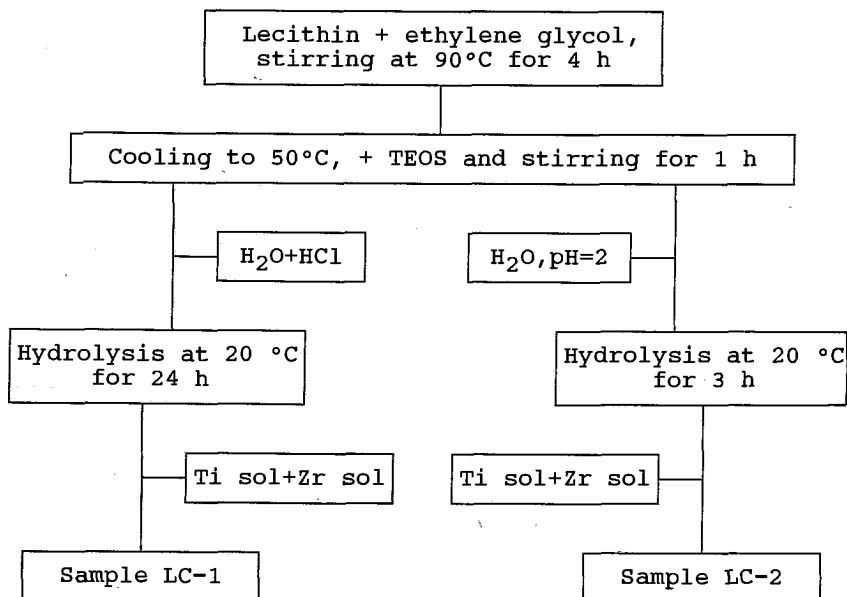


Fig. 1: Preparation of LC sol-gel compositions.

All solutions were prepared to obtain the target composition 70 SiO₂-20 TiO₂-10 ZrO₂. Water for hydrolysis of the alkoxides, acetic acid for the stabilization of the Ti and Zr alkoxides, and ethyl alcohol for the dilution were used in the same molar ratios as listed previously for the SiO₂-TiO₂-ZrO₂ gel glasses (9). Quantities of lecithin (L) and ethylene glycol (EG) used for the liquid crystal preparation were calculated to give volume ratios of TEOS/L = 0.3 and EG/L = 1.1. After preparation all samples (G, LC-1, LC-2) were allowed to gel for one day and were heat treated then for 3 days at 60 °C and 140 °C, respectively. The end products were light-yellow transparent fragments with an average diameter of 2 - 5 mm (G) and monolithic brown samples (LC-1, LC-2). Uncrushed samples G and about 7 - 10 mm thick pieces of compositions LC were used for thermal treatment in an oven at a rate of 0.5 K/min up to 500 °C and 1 K/min to higher temperatures. Heat treatment time was 2 h. Before the heat treatment for 6 h at 1000 °C the samples were finely ground. The chemical analysis of the materials obtained was performed by X-ray fluorescence (PW 1410, Philips, Kassel, Germany), while the phases were determined by X-ray diffraction (PW 1729, Philips). The IR absorption spectra in a wavenumber range from 200 to 4000 cm⁻¹ were recorded using the KBr technique (PU 9712, Philips).

Differential thermal analysis (DTA and TG) was done with a heating rate of 10 K/min (STA 429, Netzsch, Selb, Germany).

Results and discussion

The lecithin is a lipid and contains P in complex groups. Lecithin is insoluble in water, but it can be dissolved in ethanol. A treatment of the LC compositions obtained in distilled water (24 h at 60 °C) was used to enhance a mixed bond formation (reopening of some less stable Ti-O-Ti and Si-O-Si bonds and subsequent transformation into Si-O-Ti bonds (11)). A treatment in ethanol was used to remove at least a part of the P₂O₅-containing fourth component. Table 1 shows the efficiency of this procedure.

Table 1: Chemical analyses of materials synthesized, mol-%. The notations (60) and (140) mean that the water and ethanol treatments were done after heat treatments at 60 °C and 140 °C, respectively.

| Sample | Oxide | SiO ₂ | TiO ₂ | ZrO ₂ | P ₂ O ₅ |
|-----------|-------|------------------|------------------|------------------|-------------------------------|
| G | | 71.9 | 17.8 | 10.3 | 0 |
| LC-1 | | 54.1 | 17.2 | 7.6 | 21.1 |
| LC-1(60) | | 60.6 | 19.7 | 9.6 | 10.1 |
| LC-2 | | 53.2 | 17.5 | 8.8 | 20.6 |
| LC-2(140) | | 55.0 | 18.3 | 9.1 | 17.6 |
| LC-2(60) | | 59.9 | 19.2 | 8.5 | 12.4 |

In composition G crystallization took place above 700 °C, resulting in the precipitation of TiO₂ and ZrO₂ at 800 to 900 °C, and ZrTiO₄, TiO₂, ZrO₂, and α -cristobalite at 1000 °C. The products LC-1 and LC-2 crystallized at 700 °C, and α -cristobalite and SiP₂O₇ were the main crystalline phases. The compositions LC-1(60), LC-2(60), and LC-2(140) also crystallized at T > 700 °C with α -cristobalite, SiP₂O₇, and anatase. In contrast to earlier results (12) no shifts in the positions of α -cristobalite diffraction peaks were observed in this work due to the thermal treatment at lower temperatures.

DTA and TG curves of LC-1 and LC-2 samples dried previously at 140 °C for 3 days displayed an abrupt weight loss accompanied by an exothermic peak at around 300 °C. This effect may be attributed to the decomposition and burning of the alkyl and acetate groups and other organics supplied by lecithin and ethylene glycol. The exothermic peak at about 550 °C is due to the crystallization of SiP₂O₇, while the strong endothermic peak at about 630 °C may be attributed to structural rearrangements leading to nucleation. DTA shown in Fig. 2 and X-ray diffraction data suggest that the removal of lecithin by the chemical treatment leads to the formation of a solid solution of silica and titania at about 700 - 800 °C, followed by the crystallization of SiP₂O₇, α -cristobalite, and anatase, depending on composition.

Fig. 3 and 4 show the IR absorption spectra of G and LC-derived compositions treated at different temperatures. Compared to the spectra of the pure alkoxide-derived products (Fig. 3, see also ref. (9)) important differences in structure may be noted. In the spectra of LC-1(60) the absorption band at 1075 cm^{-1} (curve 4),

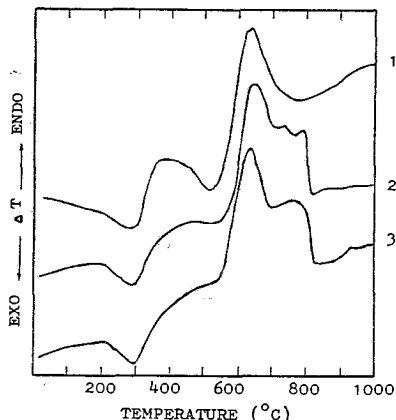


Fig. 2: DTA curves of compositions LC-2(140), curve 1, LC-2(60), curve 2, and LC-1(60), curve 3.

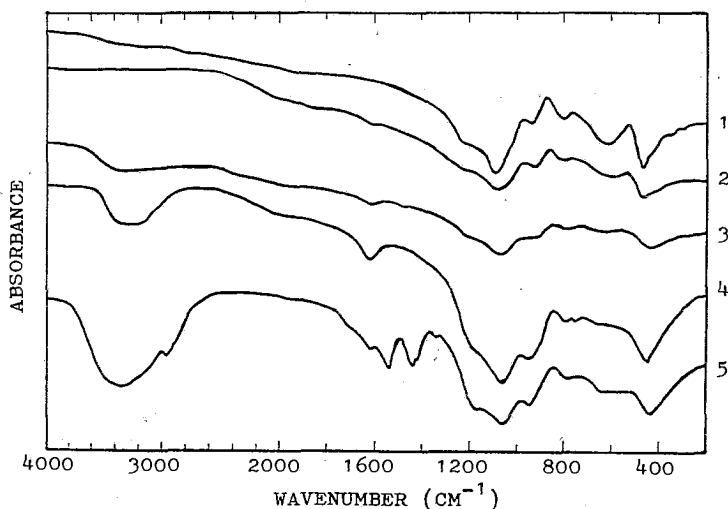


Fig. 3: IR spectra of alkoxide derived composition G, heat treated at $1000\text{ }^{\circ}\text{C}$, curve 1, $900\text{ }^{\circ}\text{C}$, curve 2, $700\text{ }^{\circ}\text{C}$, curve 3, $500\text{ }^{\circ}\text{C}$, curve 4, and $140\text{ }^{\circ}\text{C}$, curve 5.

which can be attributed to the stretching modes of the Si-O-Si bonds, becomes more intense and shifts to higher frequencies (1110 cm^{-1} , curve 1). This indicates that the Si-O-Si bonds are strengthened with increasing heat treatment temperature. The absorption peak at 950 cm^{-1} (curve 3) was found to be a result of the overlapping of the band due to Si-OH bonds and the band

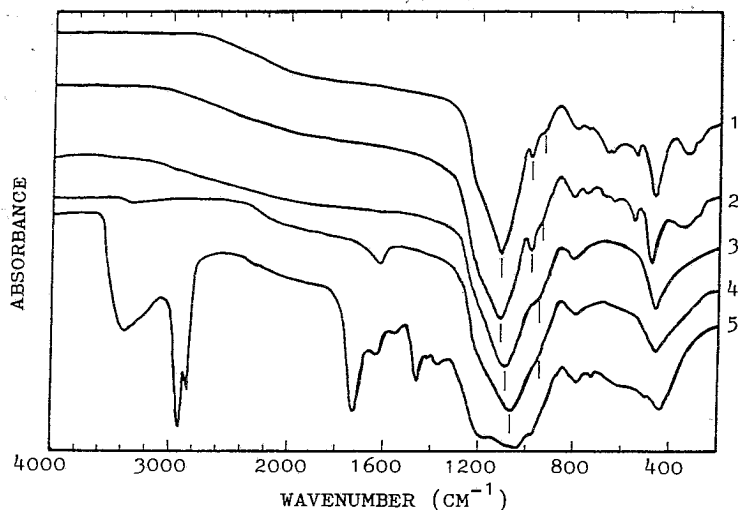


Fig. 4: IR spectra of LC-derived composition LC-1(60), heat treated at 1000 °C, curve 1, 900 °C, curve 2, 700 °C, curve 3, 500 °C, curve 4, and 140 °C, curve 5.

according to Si-O-Ti bonds containing Ti in the 4-fold coordination state (13). The absorption peak at 930 cm^{-1} was attributed to a mixed Si-O-Ti bond (14, 15). With an increase of heat treatment temperature the shoulder observed at 950 cm^{-1} splits into a well defined peak at 975 cm^{-1} and a shoulder at 930 cm^{-1} (curves 1 and 2). The absorption peak at 975 cm^{-1} decreases in intensity with increasing temperature (curves 2 and 1) and similarly as the band at 950 cm^{-1} was attributed to the Si-O-Ti modes of vibration (12). Appearance of the peaks at 975 and 930 cm^{-1} reflect the segregation of the composition into silica and titania rich phases, accompanied by the precipitation of α -cristobalite and anatase. Since the absorption bands at about 650 cm^{-1} and $400 - 300\text{ cm}^{-1}$, which have been attributed to $\text{TiO}_{4/2}$ and $\text{TiO}_{6/2}$ groups (see ref. in (16)), were not observed in the spectra of LC compositions treated below 700 °C , it is reasonable to expect that the 4-fold coordination of Ti^{4+} and the heterocondensation processes are favored at the early stages of synthesis.

The remaining P_2O_5 from the liquid crystal causes serious difficulties. Multicomponent phosphate glasses show strong absorptions at about 1290 , 1100 , 700 , and 500 cm^{-1} , caused by $\text{O-P-O}^-(\text{as-s})$, $\text{P-O-P}(\text{as-s})$, $\text{P-O-P}(\text{s})$, and O-P-O bending vibrations, respectively (17). The formation of octahedrally coordinated Si^{4+} was discussed in sol-gel derived silicophosphate glasses, whose structures depend on the various ways of solution preparation (18).

Conclusions

Hydrolysis and condensation of Si, Ti, and Zr alkoxides have been performed in the framework of a liquid crystal based

on lecithin and ethylene glycol. This synthesis is a promising approach to change the tendency from homo- to heterocondensation of these alkoxides differing in hydrolysis rates. The chemical treatment used not only removed a part of the P_2O_5 , supplied with the lecithin, but lead also to a more complete process of Si-O-Ti bond formation. However, the remaining P_2O_5 still restricts the application.

References

1. B. E. Yoldas, J. Non-Cryst. Solids 38 & 39 (1980) 81.
2. C. I. R. Gonzalez-Oliver, P. F. James and H. Rawson, J. Non-Cryst. Solids 48 (1982) 129.
3. Y. Abe, N. Sugimoto, Y. Nagao and T. Misono. J. Non-Cryst. Solids 108 (1989) 150.
4. K. Yamada, T. Y. Chow, T. Horikata and M. Nagata, J. Non-Cryst. Solids 100 (1988) 316.
5. W. Beier, A. A. Göktas and G. H. Frischat, J. Am. Ceram. Soc. 69 (1986) C 148.
6. W. Beier, A. A. Göktas and G. H. Frischat, J. Non-Cryst. Solids 100 (1988) 531.
7. W. Beier and G. H. Frischat, Mater. Res. Soc. Symp. Proc. 121 (1988) 817.
8. Ch. Wies, K. Meise-Gresch, W. Müller-Warmuth, W. Beier, A. A. Göktas and G. H. Frischat, Phys. Chem. Glasses 31 (1990) 138.
9. U. Wellbrock, W. Beier and G. H. Frischat, J. Non-Cryst. Solids 147 & 148 (1992) 350.
10. S. E. Friberg and Zhuning Ma, J. Non-Cryst. Solids 147 & 148 (1992) 30.
11. M. Schraml-Marth, K. L. Walther, A. Wokaun, B. E. Handy and A. Baiker, J. Non-Cryst. Solids 143 (1992) 93.
12. I. M. Miranda Salvado and J. M. Fernandez Navarro, J. Non-Cryst. Solids 147 & 148 (1992) 256.
13. A. Matsuda, Y. Matsuno, S. Katayama, T. Tsuno, N. Tohge and T. Minami, J. Am. Ceram. Soc. 73 (1990) 2217.
14. Y. Abe, N. Sugimoto, Y. Nagao and T. Misono, J. Non-Cryst. Solids 104 (1988) 164.
15. Q. Chen, G. H. Frischat and J. Cheng, J. Sol-Gel Sci. Technol., in press.
16. G. E. Rindone, Comptes Rendus I, VII Intern. Congress on Glass (1965) 103.
17. G. Fuxi, Optical and Spectroscopic Properties of Glass. Springer, Berlin (1992) 32.
18. G. Mezinskis and U. Sedmalis, Proc. XV Intern. Congress on Glass, Vol. 2a (1989) 371.

ORIGINAL SYNTHESIS OF II-VI SEMICONDUCTOR NANOCRYSTALLITES
EMBEDDED IN A SODIUM BOROSILICATE GLASS

L.Boudes, J.L.Marc, W.Granier, A.Pradel, M.Ribes, J.Allegre* and P.Lefebvre*
LPMS URA 407 CNRS - * GES URA 357 CNRS Université de Montpellier II
34095 MONTPELLIER Cedex 05 (FRANCE)

ABSTRACT

A new route for preparing CdX (X = S, Se, Te, S+Se) nanocrystallites embedded in a sodium borosilicate glass from a gel formed in an aqueous medium was proposed. Chalcogenizing complexing molecules introduced in the solution allowed an "in-situ" crystallite preparation concomitant to gel densification. Prevention of crystallite oxidation and coalescence is thus obtained. Optical characterization indicated that the CdX crystallites present an important quantum confinement effect. Adjustment of crystallite sizes can be obtained by changing the amount of Cd precursor introduced at the beginning of the process.

INTRODUCTION

Non linear optical phenomena are at the origin of ultra fast optical functions such as optical switching, bistability or nonlinear waveguide. Such phenomena are observed in II-VI semiconductors and can be enhanced by quantum confinement effects obtained by structuring the semiconductors into quantum well layers, wires or even boxes. Examples of quantum boxes are semiconductor nanocrystallites in which quantum confinement in the three dimensions of space is observed when the crystal size is of the order of the exciton Bohr radius. These crystallites could be interesting for improving semiconductor lasers or absorbing (emitting) devices at a precise wavelength but a condition needs then to be met i.e., the quality and size of crystallites need to be perfectly controlled. In fact, dispersion in size and/or oxidation of crystallites are generally observed when classical methods for nanocrystallite preparation i.e., colloidal suspensions, inclusion in porous zeolites or in glasses obtained by conventional melting processes are used (1,2). The sol gel process has been proposed as an alternative route for the nanocrystallite preparation (3). In this case, the complete solubility of starting components helps in reducing the dispersion in size of crystallites. However, the materials obtained to date are porous materials with crystallites in an unstable state or xerogels which densification occurs at too high a temperature for avoiding the crystallite growth (3, 4). In this paper, it will be shown that the choice of a new composition for the vitreous matrix i.e., a sodium rich borosilicate glass helped in obtaining the complete and fast densification of gel at much lower temperature. Moreover, the Cd sulphurizing generally obtained by exposing the gel to H₂S gas is now achieved by Cd complexing with sulphurated molecules initially dissolved in an aqueous solution which is then used as the precursor solution. Introduction of selenium or tellurium compounds in this solution made also possible the preparation of CdSe or CdTe crystallites. A similar procedure was recently developed by Minami for preparing CdS with SC(NH₂)₂ (5). The preparation of the gel in an aqueous solution in place of the alcohol solution used by Minami helped us in extending the procedure to several other complexing molecules and in being able to also prepare CdSe and CdTe crystallites in this way.

EXPERIMENTAL

-Glass preparation

The nanocrystallite doped glasses were prepared by the sol gel process in an aqueous solution. The first step of the process consisted in obtaining a solution containing cadmium complexes. Cadmium complexing was achieved by dissolving the cadmium precursor (3CdSO₄, 8H₂O) and the chosen sulphurated molecule in molar ratio 1:1 in distilled water. The quantity of compounds dissolved in water depended upon the required final concentration of crystallites in the glass. This concentration lies between 0.003-mol% to 0.3 mol%. When CdSe (or CdTe) was to be prepared, Se (or Te) was introduced by adding H₂SeO₃ (or H₆TeO₆) at this stage of

the process. The second step of the procedure consisted in dissolving the glass matrix precursors in the solution. Boric acid (H_3BO_3) was first added and the solution was stirred until it became clear. Sodium metasilicate ($Na_2SiO_3 \cdot 9H_2O$) was introduced in the medium to initiate the gelation. Sodium metasilicate and boric acid were added in molar ratio 1:2. Obtention of an homogeneous gel required an aqueous solution with a concentration in solid of 80g/l. The solution was heated to 60-80°C and a stiff gel was obtained after 30 minutes. The gel was maintained at 100°C for 12 hours in order to eliminate solvation water. The monolithic and transparent gel thus obtained was heated up and melted at 750°C. The melt was quenched to room temperature and a yellowish glass with composition $1Na_2O-1B_2O_3-1SiO_2$ containing CdX (X=S, Se, Te) nanocrystallites was obtained.

-Characterization of gel and glass

Thermal degradation of gel and its conversion into glass were studied by DSC and TGA experiments. DSC was performed with a heating rate of 10°C/min on a SETARAM 121 analyzer while TGA was conducted with a heating rate of 5°C/min on a V5.1A DUPONT 2000 equipment. The gel structure at the different stage of treatment was characterized by scanning electron microscopy. Optical absorption spectra were recorded on a JOBIN YVON spectrometer using tungsten light.

RESULTS

Both conversion of gel into glass and thermal degradation of Cd complexes into chalcogenide crystallites occur during the thermal treatment performed further to gel obtention. In order to clearly distinguish between the two processes, they were studied separately.

-Thermal degradation of gel and conversion into glass

Thermal degradation of a gel containing only the precursors of glass matrix was studied by DSC and TGA analysis.

Experimental data are shown in figure 1. TGA curve indicates that the gel loses 18% of its weight between 80 and 500°C. This loss is due to elimination of polycondensation water. According to DSC, the major part of hydroxyl groupments are eliminated at 134°C while the residual part disappears between 300 and 500°C. DSC peaks at 600°C and 730°C are respectively related to the sintering of gel and to the melting of material. Scanning electron micrographs of the gel at 400, 500 and 600°C indicate that the texture changes from one containing mainly open pores of 100µm in diameter at 400°C to that of a sintered material at 600°C. The softening of gel starts occurring below 500°C since the texture observed at this temperature indicates that the pores already started to collapse and to fuse together.

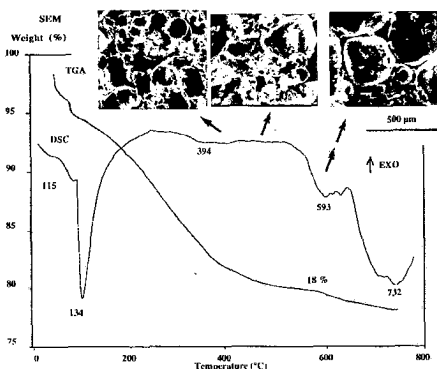


Figure 1: SEM micrograph at 400°C, 500°C, 600°C and thermal analysis spectra of a sodium borosilicate gel

-Preparation of CdX (X=S,Se,Te) nanocrystallites

The first step of preparation of CdS nanocrystallites is the obtention of a Cd complex by reaction of a cadmium precursor with a sulphurated molecule in water. Any sulphurated molecule soluble in water and complexing Cd can be used. The different sulphurated molecules which were used in this work are reported in table 1.

They can be divided into two families depending upon the stability of the Cd complex obtained. Very stable complexes can be prepared when using organic molecules such as 5 sulphosalicylic acid or sodium diethyl dithiocarbamate. A typical complexing reaction is :



Inorganic molecules such as sodium dithionite or ammonium thiocyanate were used to obtain less stable complexes according to the typical reaction:



The thermal degradation of complexes obtained in the absence of any glass matrix precursors in the solution was studied by TGA and Xray diffraction analysis. As an example, TGA graph of degradation of complex obtained with ammonium thiocyanate is shown in figure 2. A major loss of matter is observed at 310°C.

| NAME OF COMPLEXING MOLECULES | CHEMICAL FORMULAE | PK | OXIDATION STEP OF CHALCOGENIDE ELEMENT |
|---------------------------------|--|------|--|
| 5-sulphosalicylic acid | $\text{HOSO}_2\text{C}_6\text{H}_3(\text{CO}_2\text{H})\text{OH}$ | 16.7 | 4 |
| Sodium or ammonium sulphite | Na_2SO_3 or $(\text{NH}_4)_2\text{SO}_3$ | 4.2 | 4 |
| Sodium dithionite | $\text{Na}_2\text{S}_2\text{O}_4$ | - | 3 |
| Sodium or ammonium thiosulphate | $\text{Na}_2\text{S}_2\text{O}_3$ or $(\text{NH}_4)_2\text{S}_2\text{O}_3$ | 3.9 | 2 |
| Ammonium thiocyanate | NH_4SCN | 1.4 | -2 |

Table 1: Sulphurated molecules used for Cd complexing.

This loss of organic matter corresponds to the departure of NH_3 and to the formation of CdS. An Xray diffraction pattern of the product obtained by heating the solution to 310°C and cooling down to room temperature confirms the presence of CdS (figure 2). The CdS formation occurs to higher temperature when more stable complexes are considered. For example, complex derived from reaction with 5 sulphosalicylic acid decomposes at 500°C.

The procedure described above for preparing CdS crystallites can easily be extended to CdSe, $\text{CdS}_x\text{Se}_{(1-x)}$ or CdTe preparation with only few changes. In these cases, an additional reduction of selenium (or tellurium) by sulphur during thermal degradation of Cd sulphurated complex was caused by adding selenous acid (H_2SeO_3) (or telluric acid ($\text{Te}(\text{OH})_6$) to the solution. The Cd sulphurated complex played then only the role of an intermediate complex. Obtention of pure CdSe (or CdTe) crystallites required an addition of acid in molar ratio 1:1 compared to sulphurated molecules. A defect in acid led to the preparation of $\text{CdS}_x\text{Se}_{(1-x)}$ (or $\text{CdS}_x\text{Te}_{(1-x)}$) crystallites. An Xray diffraction study of CdX doped glasses described in the next section showed clearly the complete success of the process in case of selenide crystallites.

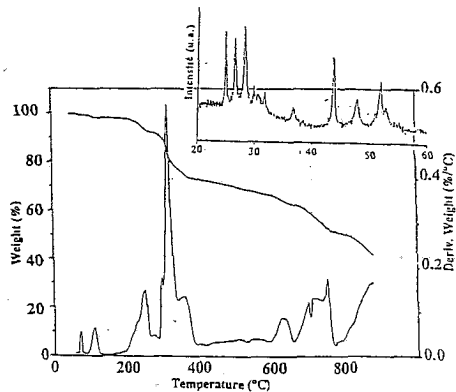


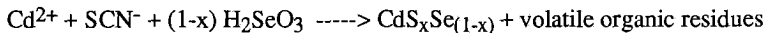
Figure 2 : TGA curves of Cd complex formed from ammonium thiocyanate and X ray diffraction pattern of the powder cooled down from 310°C

Reduction of tellurium remained uncomplete as indicated by the presence of tellurium in diffraction patterns of CdTe doped glasses prepared according to the described procedure. A thermal degradation of gel under H₂ flow was then performed and helped in overcoming the problem.

-Structural characterization of CdX crystallites embedded in glass

Xray diffraction study was performed on CdX doped glasses in order to characterize the obtained crystallites. When the Cd concentration was small, the diffraction patterns were obviously those of an amorphous material, the number and size of crystallites being too small to give well resolved peaks. Peaks started emerging from the background when the Cd concentration was increased (0.03mol%). Diffraction patterns shown in figure 3 are those of materials prepared with no addition of selenous or telluric acid (a) or with addition of selenous (b) or telluric (c) acids in molar ratio 1:1 compared to sulphurated molecule (ammonium thiocyanate in this case). No residual CdS crystallites are observed in the last two spectra indicating a complete reduction of selenium (or tellerium with presence of H₂ flow) by sulphur. The structure of crystallites is of the wurtzite type in case of sulphide and selenide while the blende form is obtained in case of telluride. The flexibility of the process is demonstrated in figure 4.

The diffraction patterns are those of materials obtained while changing progressively the molar ratio of ammonium thiocyanate to selenous acid from 1:0 (top spectrum) to 1:1 (bottom spectrum). The procedure developed in this work allows the obtention of any CdS_xSe_(1-x) solid solution by only adjusting the amount of selenous acid according to:



-Optical characterization of doped glasses

To date, the optical properties of CdS doped glasses alone have been studied. Study of other types of crystallites are currently in progress. Optical absorption spectra for several CdS doped glasses are shown in figure 5. Very different spectra are obtained depending upon the starting Cd concentration. For the largest CdS concentration (0.3 mol%), the spectrum is similar to that of bulk semiconductor with the three sharp absorption bands corresponding to excitons associated with the three valence subbands in hexagonal CdS crystal. While the CdS concentration decreases, the spectra are less and less resolved as a result of simultaneous enlargement and overlapping of different transitions.

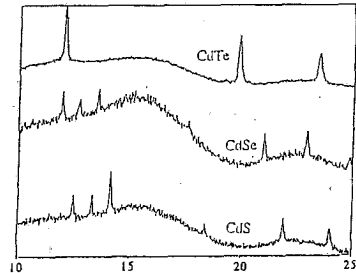


Figure 3: X ray diffraction patterns of crystallite doped sodium borosilicate glass prepared with ammonium thiocyanate (CdS: no addition of acid; CdSe: selenous acid added in molar ratio 1:1, CdTe: telluric acid added in molar ratio 1:1 and H₂ atmosphere)

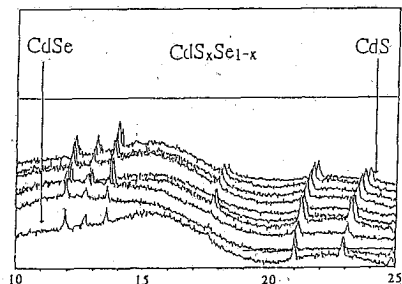


Figure 4: Xray diffraction patterns of crystallite doped sodium borosilicate glass prepared with ammonium thiocyanate and selenous acid in variable molar ratio 1:1 - x, 0 < x < 1

In the same time, the absorption band is shifted to higher energies which is indicative of quantum confinement effect. It is well known that electronic properties of crystallites change when crystallite size changes. In particular, a decrease in crystallite size induces a restricted motion of carriers and thus, a quantification of energy. These results indicate clearly that the size of crystallites depends upon the initial Cd concentration in the solution. The larger this concentration, the larger the crystallites. Theoretical models have been developed to calculate the optical absorption spectrum of crystallites which size and size distribution are known.

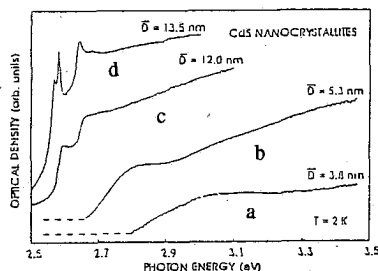


Figure 5: Optical absorption spectra of CdS doped glasses (CdS content: a- 0.003mol%, b-0.01mol%, c- 0.03mol%, d-0.3mol%

These models consist in expressing the absorption coefficient while taking into account the different types of broadening effects such as the finite lifetime of excitons or the statistical distribution of sizes. Comparison of calculated and experimental spectra which was described in detail in ref (7) allowed us to relate the Cd starting concentration with the size and size distributions of the obtained crystallites. The largest Cd concentration (0.3mol%) led to a glass containing crystallites with average size 13.5nm. The crystallite size was decreased to 12nm, then to 5.3nm when the Cd concentration was decreased to 0.03mol% and 0.01mol% respectively to finally reach 3.8nm for the smallest Cd concentration (0.003mol%). In the last case, the size distribution of crystallites was 0.6nm.

DISCUSSION

A sodium borosilicate material was already chosen as the matrix to embed semiconductor crystallites (4). Compared to silica, its main advantage is a lower densification temperature. However the compositions corresponding to about 5mol% in sodium usually chosen still imply, or high temperature of densification (800°C), or long time of densification at lower temperature (several hours). The choice of a sodium rich borosilicate matrix (33mol% Na₂O) helped us in solving the problem. Softening of gel and collapsing of texture occur at 500°C and melting is over below 800°C. Two advantages can be underlined. First, crystallite grains start being enveloped by the viscous matrix and thus protected from both oxidation and coalescence after few minutes from 500°C. Second, a bulk material can easily be obtained at relatively low temperature which ensures complete protection of crystallites as compared to weak protection ensured when porous materials are used.

Compared to the process involving exposure of gel to H₂S gas, the "in situ" process of crystallite preparation used in this work and first explored by Minami (5) has the great advantage of ensuring the complete sulphurizing of cadmium introduced in the solution and a much better homogeneity of crystallite distribution. Moreover, it was shown in this work that many complexing molecules different from thiourea could be used and that the choice was crucial on temperature of complex degradation. It becomes then possible to adjust this temperature from 300°C to 500°C. The main advantage is that concomitant complex degradation and gel densification can be obtained thus avoiding any possible oxidation and coalescence of grains.

The choice of an aqueous medium for gel preparation allowed us to enlarge the "in situ" process to CdSe crystallite preparation. Minami proposed to prepare CdSe crystallite by immersing the gel into selenourea further to preparation (5). Such a method presents equivalent drawbacks to gel exposure to H₂S gas i.e., uncomplete reaction, lack of homogeneity. The main reason of this choice is probably related to the fact that selenourea decomposes for giving selenium in alcoholic medium and this problem prevented him to extend the "in situ" process to CdSe preparation. The "in situ" process in an aqueous medium which we propose here is very

flexible since the preparation of $\text{CdS}_x\text{Se}_{1-x}$ crystallites with perfectly controlled composition can now be obtained. The composition is exactly related to the relative amount of sulphurated molecule and of selenous acid introduced in the solution.

The "in situ" process can also be extended to CdTe preparation. However, the use of reduction atmosphere (H_2) cannot be avoided to obtain a complete reduction of tellurium. The process can then be considered as the alternative in an aqueous medium to the process proposed by Nogami and made in alcoholic medium (3).

Optical characterization indicated that the CdS crystallites present important quantum confinement effect which increases while the starting Cd concentration decreases. Adjustment of crystallite sizes can then be obtained by changing the amount of Cd introduced at the beginning of the process.

CONCLUSION

A new route for preparing CdX (X = S, Se, Te, S+Se) nanocrystallites embedded in a sodium borosilicate glass from a gel formed in an aqueous medium was described. The choice of a sodium rich composition for the glass matrix allowed the obtention of a bulk material at 800°C. Complexing molecules introduced in the solution allowed an "in situ" crystallite preparation concomittant to gel densification. Prevention of crystallite oxidation and coalescence is thus obtained. The process proposed here is very flexible since a perfect control of $\text{CdS}_x\text{Se}_{1-x}$ crystallite composition from pure CdS to pure CdSe can be obtained. Absorption spectra of the CdS doped glasses and theoretical calculations indicated that crystallites with less than 4nm in diameter and 0.6nm in size distribution could be obtained. These parameters can be adjusted by changing the initial Cd concentration.

ACKNOWLEDGEMENTS

The authors wish to thank J.Allegre and P.Levrebre from the "Groupe d'Etudes des Semiconducteurs" (Université de Montpellier II - F) for performing optical measurements.

REFERENCES

1. H. Weller, *Angew. Chem. Int. Ed. Engl.* 32 (1993) 41.
2. L. Steigerwald and L.Brus, *Acc. Chem. Res.* 23 (1990) 183.
3. M.Nogami and K.Nagasaka, *J. Non Cryst. Solids* 147/148 (1992) 331 and references herein.
4. M.Takada, T.Yano, A.Yasumori, M.Yamane and J.D.Mackenzie, *J. Non Cryst. Solids* 147/148 (1992) 631.
5. N.Tohge, M.Asuka and T.Minami, *J. Non Cryst. Solids* 147/148 (1992) 652.
6. T.Gacoin, F.Chaput, J.P.Boilot, M. Mostafasi and M.O.Delcourt, *Eurogel EMRS monographs* eds S.Vilminot, R.Nass and H.Schmidt, Elsevier Science Publishers B.V. vol. 5 (1992) 159.
7. J.Allegre, G.Arnaud, H.Mathieu, P.Lefevbre, W.Granier and L.Boudes, *J.Cryst.Growth* (in press).

PHOTOPHYSICAL PROPERTIES OF DYES INCORPORATED INTO SiO₂ MATRICES BY THE SOL-GEL METHOD

Panagiotis Lianos

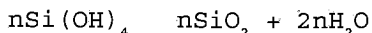
University of Patras, School of Engineering,
Physics Section, 26500 Patras, Greece

Pyrene and pyrene derivatives have been incorporated into a SiO₂ glass made by hydrolysis of tetramethoxysilane and their photophysical properties have been studied by absorption and fluorescence spectrophotometry. SiO₂ glasses have the same effect on the spectra as highly polar solvents. The distribution of dyes in a glass matrix has been studied by time-resolved analysis of electron transfer between ruthenium tris(2,2'-bipyridine) and methylviologen.

INTRODUCTION

Sol-gel produced porous glasses doped with dyes, semiconductors or other physically or chemically active molecules are very promising for a variety of applications, especially, as sensors (1), recyclable catalysts (2), or optical devices (3,4). The great advantages of sol-gel glasses that have attracted such an increasing recent interest are numerous. We enlist a few of them: low temperature processing, allowing non-destructive incorporation of sensitive dyes; they are transparent, thus appropriate for optical applications; they are porous, but at the same time do not allow leaching of the incorporated dopants, so they present a very large reaction area to many reactants; they can be shaped to any desired configuration since their formation starts with a sol; etc.

Metal oxide sol-gel glasses are made by hydrolysis of an alkoxide precursor followed by condensation-polymerization of the ensuing hydroxide, leading to an oxide. In our case, the basic reactions were the following:



The detailed reactions are more complicated (5) but they are usually represented by the above simplified scheme. In the actual preparation (2) we have mixed 2.5 ml of water, acidified with 5μl HCl 37%, with a mixture of 2.5ml tetramethoxysilane (TMOS) and 3 ml CH₃OH, under vigorous stirring for several minutes. The dopants were introduced in water or methanol according to their solubility. The solutions were then poured into plastic cuvettes covered with aluminum foil and left to dry either at room temperature or at 70°C. Higher than room temperatures accelerate gelling of the solutions.

However, drying should always be slow, in order to avoid cracking. Optical measurements were made in the same as above cuvettes.

The presence of optically active dopants in transparent glasses has a double interest. On the one hand, the photophysical properties of the dopants can be studied in the transparent matrix of the glass. On the other hand, the evolution of the glass can be followed by monitoring the photophysical properties of the dopants. In the present work we study the photophysical properties of some dyes which can be useful in optical applications.

PHOTOPHYSICAL PROPERTIES OF PYRENE AND ITS DERIVATIVES ENCAPSULATED IN SiO_2 MATRICES.

Pyrene and its derivatives are aromatic substances which have been extensively used as fluorescent probes of supromolecular assemblies both in biology and physical chemistry. It is then not surprising that sol-gel glasses are also taking a large share (6). Non-substituted pyrene is a symmetric aromatic molecule, therefore, its spectrum contains non-allowed electronic transitions. However, in polar environments, non-allowed transitions are enhanced by dipolar or multipolar interactions leading to extensive modifications, particularly, in its fluorescence spectrum (7). In our case, we have observed an increase of the polarity of the pyrene environment from sol to gel and xerogel (cf. also ref. (6)), by measuring the ratio I_1/I_3 of the first over the third vibronic peak of the pyrene fluorescence spectrum (7). At the same time the fluorescence decay rate of pyrene was 54ns in sol, 154ns in gel and raised to 262ns in xerogel. Pyrene fluorescence decay time is known to vary above 400ns in inert solvents, like cyclohexane. 262ns is approximately a value measured with very low concentrations of pyrene in deoxygenated water solutions. When then pyrene is encapsuled in SiO_2 matrices it is exposed to an equally polar environment. The low decay time of pyrene in sol is due to oxygen quenching. As the solution gels, oxygen quenching is obviously limited. At the same time pyrene is immobilized, therefore several of its non-radiative deexcitation routes are prevented. As a result, the decay time increased from 54 to 262ns during sol-gel-xerogel transition.

The increase of the polarity during transition was also verified by the behavior of the fluorescence spectrum of pyrenecarboxaldehyde and aminopyrene (not shown), by following the characteristic red-shift in their fluorescence maxima (8).

A pyrene derivative which might be very useful for future optical applications is pyrenetetrasulfonate. This molecule has a high fluorescence quantum yield and

high stability when embedded in SiO₂ glasses. Its absorption and fluorescence spectra are shown in fig.1. Its decay time in xerogel was found equal to 12.2ns, i.e. it decays at a much faster rate than pyrene itself. The study of such molecules in glasses is of great interest since they can be used in solar concentrator and laser applications (3).

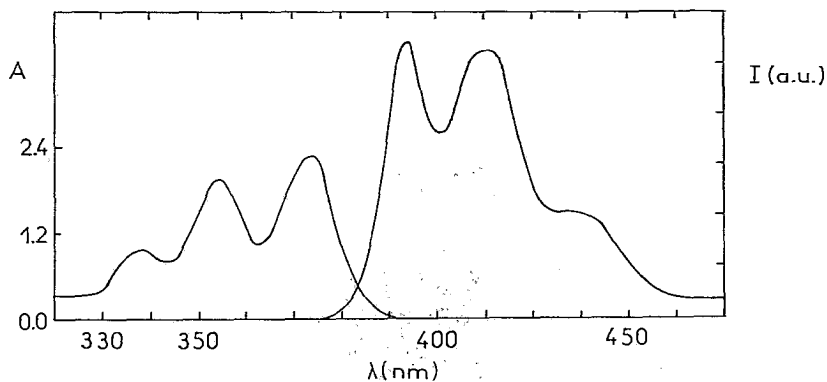


Figure 1. Absorption (A) and fluorescence (I) of pyrenetetrasulfonate in dry SiO₂ glasses. The concentration of the dye in the original sol was 10⁻⁵M.

ELECTRON TRANSFER BETWEEN TRIS(2,2'-BIPYRIDINE) RUTHENIUM [Ru(bpy)₃²⁺] AND METHYLOVILOGEN [MV²⁺] EMBEDDED IN A SiO₂ MATRIX.

Ru(bpy)₃²⁺ and MV²⁺ is a characteristic charge transfer couple which has been employed in numerous studies. We have observed that when embedded in SiO₂ glasses at sufficient concentrations, MV²⁺ quenches Ru(bpy)₃²⁺ luminescence by charge transfer. The excited luminophore acts then as an electron donor (9). Concentrations of MV²⁺ as high as 10⁻²M in the original sol are necessary for substantial charge transfer (10). We have recorded the luminescence decay profiles of Ru(bpy)₃²⁺ both in the absence and in the presence of MV²⁺, in sol, gel and xerogel. When in sol, the decay time of free Ru(bpy)₃²⁺ was 450ns and it progressively decreased in the presence of increasing MV²⁺ concentration. The decay profile was then described by a single exponential form indicating a fast dynamic luminescence quenching, similar to that obtained in a normal solution. When, however, in xerogel, the decay time of free Ru(bpy)₃²⁺ increased up to 650ns while, in the presence of MV²⁺, the decay profile would be no more described by a single exponential. This is expected, since, in xerogel, donor and acceptor are immobilized and quenching is obtained by charge transfer,

which is distance dependent. Indeed, the first order rate for charge transfer is known to depend on distance according to (9,11)

$$K(r) = v \exp(-r/a) \quad (1)$$

where v and a are constants. We have been able to analyze the luminescence decay profiles and calculate the average donor-acceptor distance by using the following model. $\text{Ru}(\text{bpy})_3^{2+}$ concentration was very low (10^{-5}M in the original sol) compared to MV^{2+} concentrations, necessary for substantial transfer. Then the distribution of MV^{2+} in the glass matrix can be described in terms of $\text{Ru}(\text{bpy})_3^{2+}$ molecules, the latter been the center of reference. The sol-gel glasses have a porous percolating structure (cf. fig.2) which favors a non-homogeneous distribution of the majority dopants, i.e. the MV^{2+} molecules.

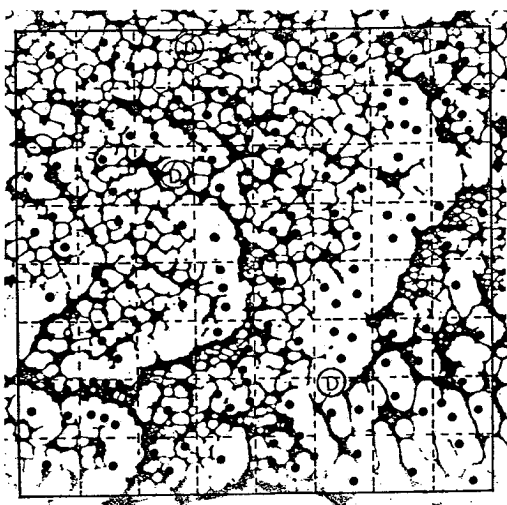


Figure 2. Percolating glass network with distributed acceptors (● ● ●) and donors (circled D's) together with the hypothetical division in compartments.

We may then assume, as in fig.2, that the acceptor population is divided in several clusters distributed in the numerous compartments formed by the glass network. If we assume Poisson statistics for the distribution of acceptors among the different compartments then some of them are empty, some contain 1, some 2, some more acceptors. Some also contain a donor and there is a very low probability that a compartment will contain more than one donor, since the latter is very low concentrated. If

we finally accept an average rate K of charge transfer within each cluster, thus assuming that the probability of transfer is proportional to the number of acceptors in each compartment, then the luminescence decay can be described (10) by the equation:

$$I(t) = I_0 \exp[-k_0 t] \exp[B(\exp(-Kt) - 1)] \quad (2)$$

where $k_0 = 1/\tau_0$ is the decay rate in the absence of acceptors and B is the ratio of the total number A of acceptors over the average number C of clusters, i.e. $B = A/C$. By fitting this model to the decay profile (see also fig.3) the values of the parameters B and K can be calculated.

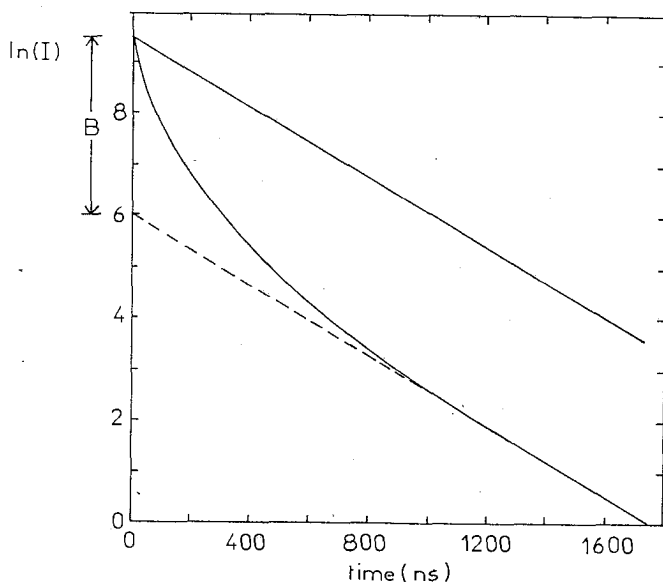


Figure 3. Luminescence decay profile of $\text{Ru}(\text{bpy})_3^{2+}$ in the absence (upper curve) and in the presence (lower curve) of MV^{2+} .

We have actually found $K = 3 \times 10^6 \text{ s}^{-1}$. If we introduce this value in eq.(1) and accept the values of $v = 10^{10} \text{ s}^{-1}$ and $a = 2.2 \text{ \AA}$, given in ref.(9), we get the average donor-acceptor distance in each cluster equal to $r = 18 \text{ \AA}$. This value is a rough measure of the diameter of each domain in the glass network. It is interesting at this point to note that scanning electron micrographs (not shown) reveal a porous glass structure with particle and pore sizes of a few nanometers, i.e. comparable with the above value of average cluster diameter. B was found to

vary proportionally with the MV^{2+} concentration in the original sol. By using the equation $C=A/B$, since A is known and B is calculated, we have obtained the average number of clusters to be equal to about 10^{20} per square centimeter of the glass. In this calculation we have assumed that each dimension in the xerogel is about 1/3 of the corresponding dimension of the original sol.

REFERENCES

1. D.Avnir, S.Braun, O.Lev and M.Ottolenghi, SPIE Proceedings, International Society of Optical Engineering 1758(1992)456.
2. A.Rosenfeld, D.Avnir and J.Blum, J.Chem.Soc.Chem.Comm. (1993)583.
3. R.Reisfeld, J.Non-Crystal.Sol. 121(1990)254.
4. M.Nakamura, H.Nasu and K.Kamiya, J.Non-Crystal.Sol. 135(1991)1.
5. L.L.Hench and J.K.West Chem.Rev. 90(1990)33.
6. K.Matsui and T.Nakazawa, Bull.Chem.Soc.Jpn. 63(1990)11.
7. P.Lianos and S.Georgiou, Photochem.Photobiol. 30(1979)355.
8. P.Lianos, B.Lux and D.Gerard, J.Chim.Phys. 77(1980)907.
9. B.H.Milosavljevic and J.K.Thomas, J.Phys.Chem. 89(1985)1830.
10. S.Modes and P.Lianos, Chem.Phys.Lett. 153(1988)351.
11. D.L.Dexter, J.Chem.Phys. 21(1953)836.

AN ORGANIC-INORGANIC HYBRID GLASS HOSTING PHOTOCHROMIC DYES

L. Hou*, M. Mennig and H. Schmidt

Institut für Neue Materialien, Universitätscampus, Gebäude 43, Im Stadtwald
W-66123 Saarbrücken, Germany

An organic-inorganic (O-I) hybrid glass hosting photochromic spirooxazine dyes has been prepared via the sol-gel method with organically modified silicon alkoxides as starting materials. The utilization of methyltrimethoxysilane (MTMS) and 3-glycidoxypropyltrimethoxysilane (GPTMS) at appropriate mole ratios led to different shapes of the glassy materials. The photochromic response, colour-decay speed, thermal and photochemical stabilities of the dye in the hybrid glass were studied and compared with the dye-in-ethanol (DIE) and dye-in-polymer (DIP) systems. The results reveal that (1) the photochromic response is better than both the DIE and DIP systems; (2) the colour-decay speed is similar to the DIE and much higher than the DIP system, and (3) the thermal stability is better than the DIE and similar to the DIP system, while the photostability is between them. Matrix effect is discussed on the photochromism of the dye in the hybrid glass.

1. INTRODUCTION

In recent years, the importance of organic dyes used for various optical purposes has been increasing significantly. Take photochromic dyes for example, fundamental and applied research work on them have been receiving more and more interests. It is well known that the matrix materials which host photochromic dyes are of great importance to the performance of a photochromic system and that solid matrices possess a number of advantages over liquid matrices, especially in overcoming the aggregation problem of dye molecules and in the improvement of photostability. Since the high temperature-melting of inorganic glasses precludes them from hosting organic dyes, most of the research work on solid matrices for photochromic dyes have been focussed on organic polymer systems (1-3) to date. In a dye-in-polymer (DIP) photochromic system, however, the photochromic response of the dye is deeply depressed so that a high concentration (> 1 wt%) of the dye is necessary to obtain an acceptable photochromic intensity, and the bleaching speed of the activated colour is largely lowered by more than 10 times so that certain applications which require fast bleaching become impossible. Therefore, efforts to seek for better matrix materials for organic photochromic dyes have never ceased. J. A. Blair and co-workers (4) reported the preparation of a new glass for hosting organic compounds by low temperature (< 200 °C) melting of mixed metal carboxylate salts and the dyes. The photochromic dyes, photochrome I and photochrome II, doped in the glass (2 mm thick discs) at a concentration of 0.5 wt% showed photochromic response to sunshine. Other authors have concentrated their efforts on the exploitation of the sol-gel method for the preparation of inorganic oxide glass (5-8) or organic-inorganic hybrid (5, 8) glass matrices hosting photochromic dyes, e.g. spiropyranes (SP) (5-7) and 2,3-diphenylindene oxide (DPIO) (8), because of the many unique and desirable features of the sol-gel process: near-room temperature wet-chemical synthesis, formation of highly homogenous and highly pure porous solids. The composition, structure and properties of the gels can be tailored in response to different material requirements by the chemical design of molecular precursors and the elaborate control of the hydrolysis-condensation process. These

* On leave from Shanghai Institute of Optics and Fine Mechanics, Academia Sinica
201800 Shanghai, China

gels offer encouraging possibilities for the incorporation of a broad variety of organic dyes. We have focussed on a class of photochromic dyes, spiroindolinonaphthoxazine (abbreviated as spirooxazine, SO). They possess good photochromic response to UV irradiation, higher fading speed of the coloured form and higher photostability than the SP dyes, but little work has been published on the incorporation of them into sol-gel derived matrices. In our previous work (9-11) the spectral and photochromic properties of the dyes in aluminosilicate and ORMOCER coatings and gels were reported as compared with those in ethanol solutions. In this paper we describe the preparation of O-I glass rods and discs in various dimensions and coatings of different thickness in the MTMS-GPTMS system by tailoring the viscosity of the sols through optimizing composition and introduction of appropriate additives. We also present experimental results on the photochromic intensity, colour-decay speed, thermal and photochemical stability of the dyes in the O-I glass as compared with DIE and DIP systems.

2. EXPERIMENTAL

2.1 Sol-gel preparation

The preparation procedure of the organic-inorganic glass rod, disc and coating is shown in Fig. 1 using MTMS and GPTMS as starting materials. The final mole ratio of H₂O to silanes (MTMS + GPTMS) is 3.0 and the volume ratio of EtOH to silanes is 0.3. Additives such as NaAc and NaF were introduced 1h before the addition of the SO dye in EtOH solution at a mole ratio of 1×10^{-2} and 5×10^{-4} to the silanes, respectively. All the samples are labelled with MG_mn, where M and G represent MTMS and GPTMS, respectively and m/n denotes the M-to-G mole ratio. For the purpose of comparison SO-PMMA coatings were prepared by spraying on slide glass substrates using the SO-PMMA-EA (ethylacetate) solution. The concentration of PMMA is 15 g / 100 ml EA.

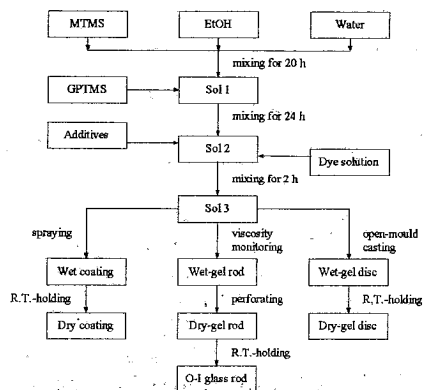


Fig. 1: Preparation procedure of the O-I glass rod, disc and coating

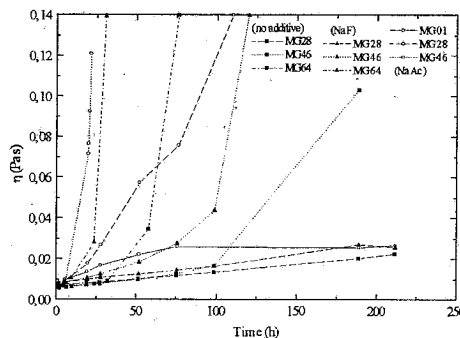


Fig. 2: Viscosity vs. time during the sol-gel transformation with different additives (none, $R_{NaF} = 5 \times 10^{-4}$, $R_{NaAc} = 1 \times 10^{-3}$)

2.2 Measurement of properties

The viscosity at a rotation speed of 500 s^{-1} was taken using the Z₁ measuring system of a computer controlled PHYSICA rotation viscometer to monitor the viscosity evolution during the early stages of the sol-wet-gel transformation. A SUNTEST CPS (Heraeus) apparatus was employed to characterize the photostability of the samples against UV irradiation at the

intensity of 600 W/m^2 . Heat treatment was conducted in a MEMMERT model 100 electric furnace to various temperatures for estimating the thermal stability. The home-made apparatus used for the measurement of photochromism was described in a previous publication (10). The photochromic response expressed in terms of equilibrium absorbance at the steady state under UV irradiation, ΔA_0 , and the fading speed of the activated colour on cessation of UV irradiation expressed in terms of half-life time, $t_{0.5}$, were deduced from the transmission vs. time curves recorded by the apparatus during the colouring-fading process. Due to the temperature dependence of all the photochromism, organic or inorganic, a CONATEX 9010 thermometer was used to measure the real-time temperature at which a photochromism measurement was carried out.

3. RESULTS AND DISCUSSION

3.1 Effect of composition and additive on viscosity evolution

On account of the fact that photochromic dyes doped in pure silica or aluminosilicate gels would either lose their photochromic activity rapidly or change to inverse photochromism (5, 7, 11) even during the sol-wetgel transformation stage, we decided to use organically modified silicon alkoxides, $\text{R}'\text{Si}(\text{OR})_3$, as starting precursors. At first, we tried pure MTMS. It was found that although the doped SO dye exhibits detectable photochromism in the sol-wetgel stage, ΔA_0 would decrease rapidly during the ageing and drying process and vanish as the rigidity of the gels reached a certain level. And what is more, the initial colourless gels changed to yellow or even brown implying that the dye molecules are either passivated or even destroyed due to the high volume shrinkage ($> 80\%$). SO-doped gels were also prepared from GPTMS alone considering that it possesses properties favourable to photochromic dyes, i.e. the long glycidoxypopyl (GP) chain is helpful in creating a more flexible matrix for photochromic dyes and the polymerisation between the epoxy groups would play a certain role in improving the mechanical properties of the gels. However, it was found that the gelling time is too long to allow aquirement of a wetgel within one month although intense photochromic response is maintained.

Using both MTMS and GPTMS as starting precursors, sols having various m/n ratios were prepared via the procedure depicted in Fig.1. The viscosity evolution of the sols of various compositions and with different additives is shown in Fig.2. It can be seen that (1) the viscosity increase with time is significantly accelerated with increasing m/n ratio, (2) this acceleration process is enhanced greatly by the addition of NaAc and moderately by NaF, as is evidenced by the results that the viscosity increase of the MG64, MG82 with NaAc and MG82 with NaF is too fast to monitor, (3) in the case of NaAc-additive only the pure GPTMS sols, while in the case of NaF-additive and no-additive sols with the m/n ratios less than 3:7 would remain ungelled for a pretty long period of time ($\gg 1$ month) if the sols were air-tight. These results suggest that it is possible to tailor the viscosity by changing composition and additives in order to obtain different shapes of the glassy materials. It was in this way that we prepared our O-I glass rods and discs in various dimensions and coatings of different thickness. The utilization of the MG system at appropriate m/n ratios led to moderate gelling time (100–200 h) and volume shrinkage (around 50%) rendering it possible to monitor the variation of the photochromism (ΔA_0 and $t_{0.5}$) of the SO dyes during the sol-wetgel-xerogel transformation as a result of room temperature holding and due to heat treatment or UV irradiation and to make comparisons with the DIE and DIP systems.

3.2 Photochromic response at room temperature

Fig.3 shows ΔA_0 as a function of dye concentration in ethanol, O-I glass coating and PMMA coating, respectively. Note that concentrations are referred to those in SO-EtOH, SO-PMMA-EA solutions and sols for O-I glass coatings. The volume shrinkage factors for the O-I glass coatings and the PMMA coatings are ca. 2.5 and 5.0, respectively. This means comparison between these two systems is reasonable. It is clear that (1) serious aggregation of the dye molecules occurs in the DIE system as the concentration becomes higher than 5×10^{-4} mole/l, (2) although the aggregation problem is overcome to certain extent in the DIP system the photochromic response intensity is at the same time badly depressed, (3) the ΔA_0 of a O-I glass coating is much higher than that of the corresponding PMMA coating and increases monotonically with dye concentration, implying that better photochromic response of the dye is obtained in the O-I glass than in the other two systems.

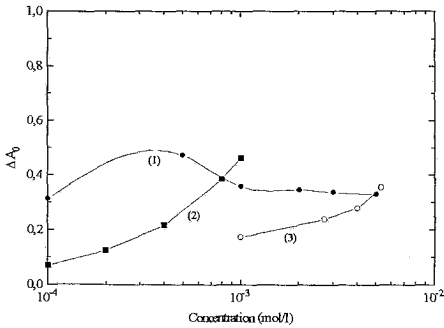


Fig. 3: ΔA_0 ($T=25^\circ\text{C}$) as a function of SO1 concentration in (1) EtOH (10-mm plastic cell), (2) O-I glass coating (0.4 mm thick) and (3) PMMA coating (0.2 mm thick)

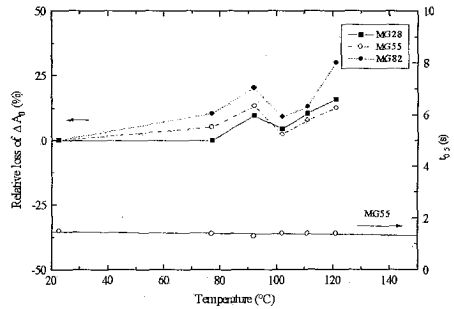


Fig. 4: $t_{0.5}$ and relative loss of ΔA_0 of SO1 (2.5×10^{-3} mol/l)-doped O-I glass coatings (0.2 mm thick) as a function of heat treatment ($T=22.5^\circ\text{C}$)

3.3 Effect of heat treatment on ΔA_0 and $t_{0.5}$

The $t_{0.5}$ and relative loss of ΔA_0 of SO1-doped O-I glass coatings as a function of heat treatment temperature are shown in Fig.4. It follows from the figure that (1) heat treatment has little effect on $t_{0.5}$ up to 120°C , (2) relative loss of ΔA_0 increases with increasing heat treatment temperature and, the greater the content of MTMS, the greater the loss, (3) in the worst case (MG82) the relative loss of ΔA_0 is around 10% before 120°C and amounts to 25% after a heat treatment at 120°C for 6h. Fig. 5 presents the variation of $t_{0.5}$ and ΔA_0 of SO1-PMMA coatings with R.T.-holding and heat treatment. In contrary to the O-I glass coatings, $t_{0.5}$ increases very rapidly with increasing heat treatment temperature; even in the case of R.T.-holding without heat treatment, $t_{0.5}$ increases slowly, too. On the other hand, ΔA_0 shows no significant decrease before 140°C . Heat treatment at 140°C for 6h results in a relative loss of ΔA_0 less than 25%. Comparing Fig. 4 with Fig. 5, it is evident that the thermal stability of $t_{0.5}$ of the SO1-doped O-I glass is much better than the SO1-PMMA system, while the thermal stability of ΔA_0 of the SO1-PMMA system is a little better than the SO1-doped O-I glass.

3.4 Effect of UV irradiation on ΔA_0 and $t_{0.5}$

The relative loss of ΔA_0 as a function of UV exposure (suntest) time on samples described in Table 1 is compared in Fig. 6. It turns out from Fig. 6 and Table 1 that (1) UV irradiation makes no detectable influence on $t_{0.5}$ of all the samples tested, (2) the photostability of the SO-doped O-I glass measured by the relative loss of ΔA_0 is between the DIE and DIP systems, suggesting that further improvement in the photostability is necessary before some applications can be put into effect, (3) with the addition of only a small amount of fluoroalkyltrimethoxysilane (SF) the photostability of the O-I glass can be considerably enhanced, indicating a promising future for the O-I hybrid glass hosting photochromic dyes.

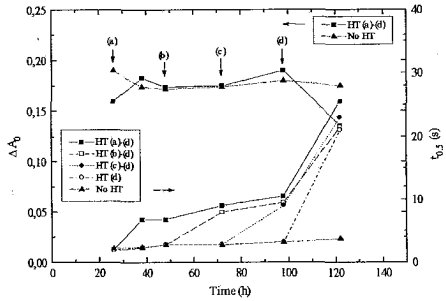


Fig. 5: Variation of ΔA_0 and $t_{0.5}$ ($T=22.5$ °C) of SO_1 (1×10^{-3} mol/l)-PMMA coatings (0.2 mm thick) with R.T.-holding time and heat treatment (HT): (a) 100 °C / 12 h, (b) 110 °C / 6 h, (c) 120 °C / 6 h, (d) 140 °C / 6 h

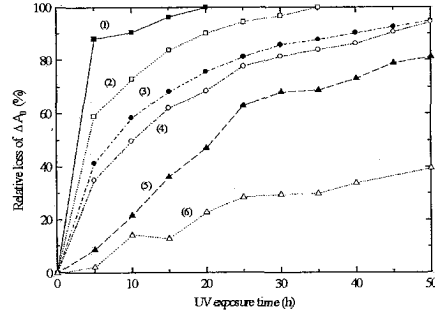


Fig. 6: Relative loss of ΔA_0 ($T=25$ °C) as a function of UV exposure (suntest) time on samples described in Table 1

The different photochromic performance of the SO dyes in the three matrices, ethanol, O-I glass and polymer, is closely related to their structures and thereby the environment surrounding the dye molecules. In ethanol solution, the degree of freedom of the dye molecules is high so that the speed of photochromic transformation is high, but at higher concentrations the probability of aggregation of the dye molecules becomes higher and the photochromic response is passivated. In addition, the poor thermal and photochemical stability of the DIE systems are self-evident. The degree of freedom of the dye molecules in the DIP systems is largely degraded due to the complexity of the structure of polymer with various architectures, e.g. linear flexible chains, graft, H-shaped, ring and star (12), resulting in the deep depression of the photochromic activity of the dyes, reflected by the decrease of ΔA_0 and increase of $t_{0.5}$. However, both the thermal and photochemical stabilities of the dyes in polymer are greatly improved as compared with the DIE systems, although still unsatisfactory. The dye molecules trapped in the pores of the sol-gel derived O-I glasses possess high degree of freedom for photochromic transformation and low degree of freedom to move together for aggregation, so that the photochromic response is better than both the DIE and DIP systems; the colour fading speed is similar to the DIE and much higher than the DIP systems. The porous structure of the O-I glass may favour the thermal stability while make it easier for oxygen to penetrate into the pores and degrade the photostability, behind which the mechanism is still unclear.

Table 1
Measured values of $t_{0.5}$ (s) ($T = 25\text{ }^{\circ}\text{C}$) after various lengths of UV exposure (suntest) time

| Sample No. | Dye (C, mol/l) | Matrix (thickness, mm) | Exposure timelength (h) | | |
|------------|----------------------------|---------------------------|-------------------------|---------|---------|
| | | | 0~10 | 15~25 | 30~50 |
| 1 | SO1 (4×10^{-3}) | EtOH (10) | 1.3 | - | - |
| 2 | SO3 (1×10^{-3}) | O-I GLASS (0.4) | 1.9~2.0 | 1.8~2.0 | - |
| 3* | SO3 (1×10^{-3}) | O-I GLASS (0.4) | 1.9 | 1.7~1.9 | 1.7~1.9 |
| 4** | SO3 (1×10^{-3}) | O-I GLASS (0.4) | 1.9~2.0 | 1.8~1.9 | 1.7~1.9 |
| 5 | SO1 (1×10^{-3}) | PMMA (0.2) | 2.8~3.1 | 2.9~3.0 | 2.8~3.0 |
| 6 | SO1 (5×10^{-3}) | PMMA (0.2) | 2.9~3.0 | 2.7~3.0 | 2.7~3.0 |

* $R_{SF} = 1 \times 10^{-2}$

** $R_{SF} = 5 \times 10^{-2}$

4. CONCLUSIONS

Different shapes and dimensions of organic-inorganic hybrid glasses in MTMS-GPTMS system have been made by the sol-gel process for hosting photochromic dyes. Spirooxazines entrapped in the O-I glass show photochromic response better than both the DIE and DIP systems, colour-decay speed similar to the DIE and much higher than the DIP system, thermal stability similar to the DIP and of course much better than the DIE system. Efforts must be made to improve the photostability of the dye-doped O-I glass photochromic systems before certain applications can be put into practice.

REFERENCES

1. G. H. Brown, *Photochromism - Techniques of chemistry, Vol. III* (Wiley Interscience, London, 1971)
2. H. Dürr, H. Bouas-Laurent, *Photochromism - Molecules and systems* (Elsevier, Amsterdam, 1990)
3. C. B. McArdle, *Applied photochromic polymer systems* (Chapman and Hall, New York, 1992)
4. J. A. Blair, J. A. Duffy and J. L. Wardell, *Phys. Chem. Glasses* **33** (1992) 191
5. D. Levy and D. Avnir, *J. Non-Cryst. Solids* **113** (1989) 137
6. D. Preston, J.-C. Pouxviel, T. Novinson et al., *J. Phys. Chem.* **94** (1990) 4167
7. J. I. Zink and B. Dunn, *J. Mater. Chem.* **1** (1991) 903
8. S. A. Yamanaka, J. I. Zink and B. Dunn, *Proc. SPIE* **1758** (1992) 372
9. L. Hou, M. Mennig and H. Schmidt, Extended Abstract of the Second SAAR-LOR-LUX Meeting, 1992, Saarbrücken
10. L. Hou, M. Mennig and H. Schmidt, *Proc. Eurogel '92* (in press)
11. L. Hou, B. Hoffmann, M. Mennig and H. Schmidt, *J. Sol-gel Sci. Techn.* (in press)
12. E. L. Thomas, *Structure and properties of polymers* (VCH, Weinheim, 1993)

PREPARATION OF COMPOSITE Cu-CuO-SiO₂ COATINGS ON GLASS
STARTING FROM AMINE-CONTAINING SOLUTIONS

N.Maliavski, O.Dushkin, E.Tchekounova
*Dept.General Chemistry, Moscow Civil Engineering University,
Yaroslavskoe sh., 26, 129337 Moscow, Russia*

P.Innocenzi, G.Scarinci and M.Guglielmi
*Dip.Ingegneria Meccanica, Sez. Materiali, Universita di Padova,
via Marzolo, 9, 35131 Padova, Italy*

ABSTRACT

Highly coloured nanocomposite CuO- and SiO₂-containing coatings on glass were prepared by the sol-gel method. Water-ethanolamine solutions of Cu₂(OH)₂CO₃ and SiO₂ were used as the cupric oxide and silica precursors respectively. The samples were treated at temperatures 200-550°C, the thermal evolution of the films was controlled by thermogravimetry, spectrophotometry and X-ray diffraction. The films treated at 200-350°C contain elemental copper whose colloidal aggregates seem to be responsible for the colouration phenomenon in much the same way as in ruby glasses. At higher temperatures all the films present CuO as only crystalline phase. The presence of silica in the films changes substantially their hue, the possible mechanism of such an influence, is discussed.

INTRODUCTION

Copper-containing silicate glasses and glassy films have always been of interest for researchers, mainly due to various colouration effects and the complexity of the colouration mechanism (1,2). A colour of such glasses depends strongly on a redox state of copper ions incorporated in glass structure. The cupric ion, Cu⁺², imparts a blue-green colour to the glass, caused by a broad absorption band near 790 nm. The cuprous ion, Cu⁺¹ as such is optically inactive but can produce ruby colouration of glass after being precipitated in the form of colloidal particles of Cu₂O. The similar effect may be produced by colloidal particles of metallic copper, Cu⁰ (3,4).

During the last decade, copper-containing glasses and coatings were prepared by the sol-gel method using alcohol soluble copper salts as CuO precursors (4,5). On the other hand, it was shown recently that stable aqueous solutions of copper-ethanolamine complex salts may be used for the preparation of CuO-based thin films (6). The corresponding gelling mechanism is connected with a decrease of the complex solubility as water escapes from the film. Two-component CuO -- SiO₂ films prepared in this way, were proposed as darkening coatings on glass with good mechanical resistivity (7).

The objective of this work is to study the thermal evolution of thin films in the system CuO-SiO₂ prepared from ethanolamine-containing aqueous solutions, as well as to explain on this base the variety of intermediate colours forming in the system during the heat treatment.

EXPERIMENTAL

The CuO precursor solution was prepared by mixing cupric basic carbonate $\text{Cu}_2(\text{OH})_2\text{CO}_3$ with an aqueous solution of ethanolamine (EOA) to obtain final concentrations of 7 wt% CuO and 20 wt% EOA. The mixture was stirred for 1 h at 60°C and then filtered resulting in a clear stable solution of the dark blue-violet colour.

SiO_2 precursor solution was prepared as described in (8), by mixing solid silicic acid (79 wt% SiO_2 , REACHIM) with the 30% aqueous solution of EOA at a SiO_2 /EOA molar ratio 0.5. The mixture was stirred for 3 days at room temperature and then centrifugated to separate the solution from a considerable amount of unreacted silicic acid. After additional filtering the resulting clear solution contained 7 wt% SiO_2 and 24.9 wt% EOA.

Two-component solutions were prepared mixing the CuO and SiO_2 precursor solutions at mass ratios from 90:10 to 10:90 with a step of 10%. All the prepared solutions were denoted as $(100-x)\text{Cu}x\text{Si}$ where x is the mass ratio $\text{SiO}_2/(\text{CuO}+\text{SiO}_2)$ in wt%.

Soda-lime glass plates and silicon wafers (for infrared examination) were used as substrates after being cleaned in the sodium silicate solution and rinsed with acetone. Tween-80 (0.01 wt%) was added to all the coating solutions to improve wettability of substrates. The plates were then coated by dipping at withdrawal rates from 1 up to 13 cm/min, dried at 60°C for 15 min and heated up to a final temperature (150-550°C) at a constant heating rate of 20°C/min. Film thicknesses were measured by profilometry on scratches produced on films after drying.

Colour development in the deposited films as a function of heat treatment was studied by UV-VIS spectrophotometry. Glancing angle X-Ray Diffraction (XRD) with an incidence angle of 3°, was carried out to determine the phase composition of the films as well as to evaluate the dimensions of crystalline particles using the Scherrer equation. The form factor value was chosen to be 0.9.

The thermal evolution of coatings was also studied by IR spectroscopy and thermogravimetric analysis (TGA) using a multi-plate platinum sample holder. Thick films of gels (thickness of ca 0.1 mm) were formed on the plates, pretreated at 200°C for 15 min and heated up to 700°C at a constant heating rate of 5°C/min.

RESULTS AND DISCUSSION

Cupric basic carbonate was chosen as a source of CuO because of redox neutrality of the anion and sufficient solubility in the water-EOA systems. Previously S.Zhang *et al.* used it for the wet-chemistry preparation of superconductive fibers (9). It reacts with EOA in aqueous solutions giving very strong amino-complex $[\text{Cu}(\text{EOA})_3]^{+2}$. The instability constant of this complex is sufficiently low ($\text{p}K=10^{-16}$ (10)) to avoid the precipitation of cupric silicates in the presence of polysilicate anions in the two-component solutions.

The freshly deposited coatings, with the exception of 0Cu100Si, show some bluish colouration which is transformed gradually into slightly yellowish during the drying process. The heat treatment of samples of a significant copper content (100Cu0Si - 40Cu70Si) leads to a drastic colour intensification at 150 - 300°C followed by successive colour changes up to 500°C. The scheme of colour transformations proceeded in films with thicknesses 50-100 nm, is shown in Fig. 1.

Whereas a high-temperature brown colour is rather characteristic for CuO-rich films and appears also in the presence of an oxidizing anion (for example, nitrate), the intermediate very intensive green and red colours appear only in the reducing medium and cannot be caused by copper ions in any oxidation state. On the other hand, the intensive colouration effects in silicate glasses (such as ruby glasses) caused by colloidal metal particles dispersed in a silicate matrix, are generally well-known (1,11). Recently such gold-containing glasses were prepared also using the sol-gel technique (12,13).

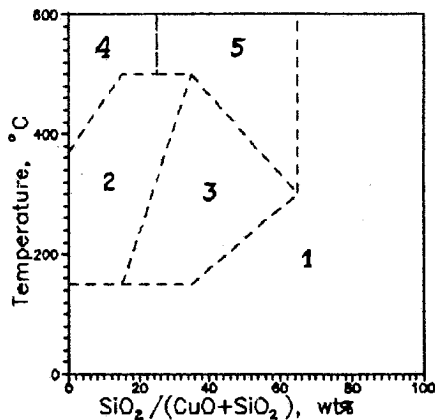
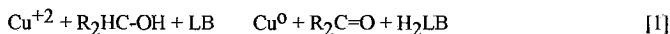


Fig.1. The scheme of film colours (observed in transmission) as a function of a chemical composition and temperature:

1. Slightly coloured
2. Green and greenish-brown
3. Red and reddish-brown
4. Brown with a metallic glitter
5. Brown.

In the studied system, the formation of the colloidal copper particles at temperatures close to the boiling point of EOA, is highly probable. The similar system cupric acetate - triethanolamine was studied by P.Muhl *et al.* and the formation of metallic copper particles of diameters 1-3 nm was observed at heating up to 200°C (14). It is also of note that 1B Group metal colloids are spontaneously formed when alcoholic solutions containing metal cations are exposed to a strong Lewis base (LB), according to the reaction:



whereas in acidic medium such reaction is blocked (13). In the studied system, both alcoholic and amino (strong LB) groups are present in the EOA molecule. Besides copper, ammonium carboxylates, acetaldehyde and formaldehyde may form as reaction products (14) together with resin-like residues that probably act as the silicate glass matrix in ruby glasses.

UV-VIS spectra of intensively coloured green and red films were found to be principally similar to those reported for the gold-coloured gels (12,13) and showed the characteristic plasmon band of the colloidal copper at 560-660 nm. The results obtained for the four films (two green and two red with various thicknesses) are presented in Fig.2.

One can observe that the main difference between the two kinds of films consists of a notable violet shifting of the absorption band for the films having a green colour when observed in transmission. This difference should be connected with different sizes of colloidal aggregates producing colouration effects (11-13).

The XRD results on the crystallisation in the one- and two-component films are presented in Table 1. Only the two crystalline phases were shown, cupric oxide and metallic copper. Cuprous oxide, Cu_2O which also acts as a colouring agent in ruby glasses (1,2), was not detected. The dimensions

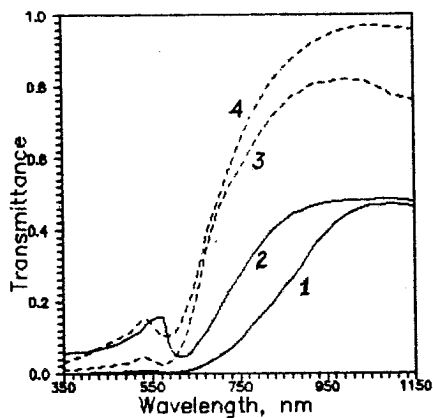


Fig.2. VIS and near IR spectra of one- and two-component films:

1. 100Cu0Si, 90 nm
2. 100Cu0Si, 70 nm
3. 70Cu30Si, 80 nm
4. 70Cu30Si, 55 nm

of the copper crystallites were found to be of the same order of magnitude as in the sol-gel synthesised gold-containing ruby glasses (12,13) and could explain the fact of colouration, for example, according to the resonance coupling approach proposed by M.Quinten *et al.* (15).

Table 1. Crystalline phases found in one- and two-component films

| Sample | Treatment temp., °C | Detected peaks | | Diameter of particles, nm | |
|----------|---------------------|----------------|--------------|---------------------------|-----|
| | | Cu | CuO | Cu | CuO |
| 100Cu0Si | 200 | 43.5 | - | 18 | - |
| | 350 | - | 35.5 38.5 | - | 9.8 |
| | 550 | - | 35.5 38.5 | - | 25 |
| 70Cu30Si | 200 | 43.5 50 | - | 25 | - |
| | 350 | 43.5 | 35.5 38.5 | 16 | 11 |
| | 550 | - | 35.5 38.5 | - | 20 |

On the other hand, the found differences between the sizes of Cu particles in green and red films (100Cu0Si and 70Cu30Si at 200°C) cannot explain the colour diversity. As opposed to the obtained results, the red colouration connected with the violet shifting of the plasmon band, should be produced by the particles of lower diameters as it follows from the Mie theory (11). It is probable, that the colouration mechanism is more complicated and the film colour depends on the variety of structural factors (such as: size distribution, optical properties of the matrix, possible presence of the second dispersed phase etc.) that should be studied in further investigations.

The chemical evolution of the gel films during the heat treatment above 200°C was controlled by thermal analysis and IR spectroscopy. TGA curves for the three colourable compositions are presented in Fig.3.

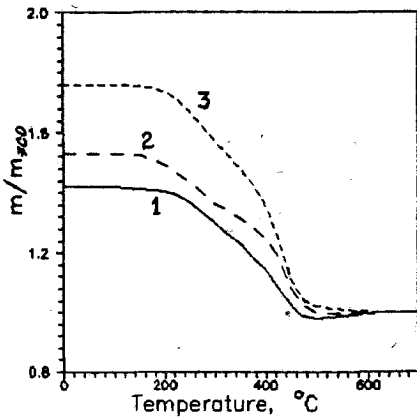


Fig.3. TGA curves of thick films pretreated at 200°C and heated at a rate of 5°/min:

1. 100Cu0Si
2. 90Cu10Si
3. 70Cu30Si.

The transformation of the CuO-based one-component gel to cupric oxide, as resulted from TGA curves and IR spectra could be divided in three stages:

1. 200-400°C. Definitive evaporation of EOA and low-molecular products of its oxidation, accompanied by substantial weakening all the C-H vibration peaks and complete disappearing the C-OH stretching vibration peak (near 1100 cm⁻¹).
2. 400-470°C. Exothermic decomposition of high-molecular resin-like products of EOA oxidation, resulted by almost complete disappearing the diffuse peak at 1600 cm⁻¹ (probably C=C, C=N and C=O stretching bonds).
3. 470-600°C. Oxidation of metallic copper formed previously, accompanied by a mass increase (see Fig.3, curve 1). According to the magnitude of the gravimetric effect it may be suggested that not less than 10% of total Cu atoms passed through the Cu⁰ state. In submicron layers this stage completed at a much lower temperature that explains the absence of Cu XRD peaks at 350°C (see Tab.1).

Two-component gels showed the similar stages of their decomposition however complicated with gradually escaped silanol water. The last factor, for example, masked final stage of copper oxidation on TGA curves (see Fig.3, curves 2 and 3). The IR spectra of these samples showed an additional very intensive peak at 1090 cm^{-1} which was present at all the temperatures studied.

CONCLUSIONS

The stable solutions of CuO and SiO₂ precursors were prepared on the base of aqueous solutions of ethanolamine. One-component, CuO-based and two-component, CuO-SiO₂-based coatings were deposited on glass by dipping. The films containing more than 30 wt% of CuO may be transformed into an intensively coloured state by heating up to temperatures 150-500°C. Whereas the green colour is characterized for the one-component and CuO-rich two-component films, the red and reddish-brown colours developed in the films relatively rich in silica. The colouration processes are caused by the colloid particles of metallic copper which formed under the reducing action of ethanolamine. The colour differences between two types of samples are probably connected with some diversity in structures of nanocomposite films.

REFERENCES

1. S.Bachtik, V.Pospichal. *Zuslehtovani skla*, SNTL, Praha 1964.
2. A.Duran and J.M.Fernandez Navarro, *Glastechn.Ber.* 56K 1983) 1.614.
3. C.R.Bamford, *Phys.Chem.Glasses* 3 (1962) 189.
4. M.Ferreira da Silva and J.M.Fernandez Navarro, *J.Non-Cryst. Solids* 100 (1988) 447.
5. F.Orgas and H.Rawson, *J.Non-Cryst.Solids* 82 (1986) 378.
6. N.Maliavski, E.Tchekounova, O.Dushkin and A.Khripunkov in *EUROGEL'90: Progress in Research and Development of Processes and Products from Sols and Gels*, ed. by S.Vilminot *et al.* North-Holland, Amsterdam, 1992, p.453.
7. N.Maliavski *et al.* *Rus. Patent Appl.*, 92002727/33 (1992).
8. V.Sidorov, A.Khripunkov and N.Maliavski, *Sov.J.Appl.Chem.* 62 (1989) 901.
9. S.Zhang *et al.*, *J.Mater.Res.* 5 (1990) 1806.
10. V.Podchainova and L.Simonova. *Copper*, Nauka, Moscow 1990.
11. W.Eitel. *The Physical Chemistry of the Silicates*, Chic.1954
12. J.M.Fernandez Navarro and M.A.Villegas, *Glastechn.Ber.* 65 (1992) 32.
13. L.Spanhel, M.Mennig and H.Schmidt, *Bol.Soc.Esp.Ceram.Vid.* 31-C (1992) 7, 9.
14. P.Muhl *et al.*, *Metall (GDR)* 44 (1990) 273.
15. M.Quinten *et al.* *Surface Sci.*, 156 (1985) 741.

□

COATING OF GLASS POWDERS BY SOL GEL ROUTE.

M. BOUCHNAFA, B. SOULESTIN, R. GUINEBRETIERE, A. LECOMTE, A. DAUGER

Laboratoire de Matériaux Céramiques et Traitements de Surfaces - UA 320 CNRS -
ENSCI 47 Avenue Albert THOMAS - 87065 - LIMOGES - France.

ABSTRACT.

Coating of low melting temperature glass powders (sodium zinc borosilicate) with a continuous layer of amorphous zirconia precursor was obtained from a modified zirconium n-propoxide sol.

A suspension of processed particles with proper viscosity was used for screen printing onto float glass substrates. After drying, deposits were fired at 630°C for 15 minutes resulting in 30 µm thick glazed layers containing homogeneously dispersed tetragonal zirconia grains in the nanometric size range.

Crystallized phases and microstructure were characterized by X-ray diffractometry and transmission electron microscopy.

I INTRODUCTION.

The performance of advanced ceramics are strongly dependent on factors such as chemical composition, microstructure, texture and morphology. High purity, chemical homogeneity and uniformity of microstructures in very small size ranges are known to be improved by sol gel processing of powders (1). Wet chemical processing can also be utilized to design composite powder particles (2). Several authors have used this way to modify powder properties such as sinterability (3-4) or to elaborate composite materials (5-6). For instance, fine dispersions of tetragonal zirconia second phase in sintered ceramic bodies can be achieved by sol gel coating of alumina (7-8), spinel (7), cordierite (9-10) or mullite (10) primary particles. Mechanical properties are thus enhanced and sintering temperatures of silicate ceramics are lowered (9-10). In the field of glass technology, the melting temperature may be lowered by replacing some raw materials by corresponding metal alkoxide derived precursors (11).

In the present paper, the coating of glass powders with a zirconia precursor is described. The goal was to introduce crystallized particles in a low melting temperature glass enamel without changing its firing temperature. Screen printed deposits on float glass substrates were

fired. The microstructure of glazed layers was characterized by X Ray Diffractometry and Transmission Electron Microscopy and compared to that of products with identical composition, in which zirconia was introduced in the melt.

II EXPERIMENTAL PROCEDURE.

1 Preparation of glass powder.

Reagent grade sodium carbonate, zinc oxide, boric acid and silica were used as starting materials. Appropriate amounts of components were mixed and melted in low corrosion ceramic crucibles for 40 mn at 1300°C in an electric muffle furnace (Fig.1). The molten glass was quenched by pouring the liquid in cold water to obtain friable frits. The glass frits were then ball-milled to obtain a particle size of approximately 5 μm .

2 Zirconia addition.

The introduction of zirconia was achieved by two different routes.

(i) Zirconia addition by melting route.

Zirconium oxide (5wt%) was added to the glass powder. The mixture was then melted and the previously described complete procedure was carried out again.

(ii) Sol gel coating of glass powder with zirconia precursor.

The precursor material for sol gel processing was a solution of zirconium n-propoxide in n-propanol. It was added under mechanical stirring to a mixture of acetylacetonate and n-propanol (Fig.1). According to previous experiments (12), the zirconium concentration was fixed to $[\text{Zr}] = 0.5 \text{ mol/l}$ and the complexing ratio to $[\text{acac}]/[\text{Zr}] = 0.6$.

Glass powder suspension in the clear sol was achieved in relative amounts selected to yield 5 wt% ZrO_2 in final composite powder. After vigorous stirring for one hour, hydrolysis was performed by adding a volume of water selected to give a hydrolysis ratio $[\text{H}_2\text{O}]/[\text{Zr}] = 5$. Gelation was obtained in 3 mn at room

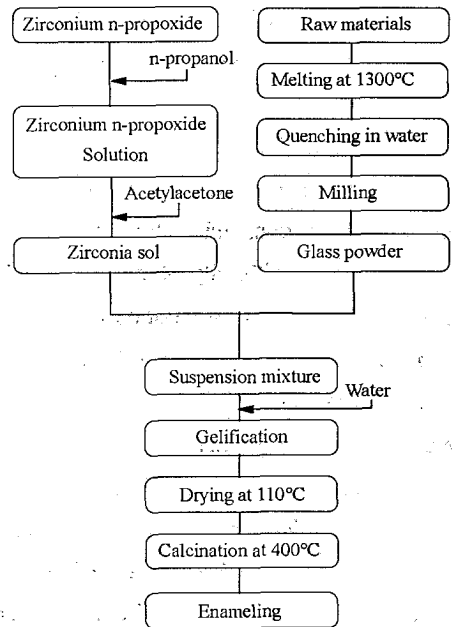


Fig. 1: flow diagram of the coating process of glass powder.

temperature, the gel was dried at 110°C and then coated powders were fired at 400°C for 2 hours.

3 Enameling.

Coated powders were mixed in screen printing oil with appropriate viscosity and concentration. The mixture was applied by screen printing onto commercial soda-lime-silica float glass plates. Approximately 30 μm thick glazed layers were achieved by drying and firing for 15 mn at 630°C, a firing temperature defined by the thermal stability range of the glass substrate.

4 Characterization.

The crystalline phase and microstructure of glass enamels were characterized by X-ray diffraction and transmission electron microscopy. TEM samples were prepared by abrading and ion beam thinning.

III RESULTS.

Figure 2 shows X-ray diffraction results. When zirconia addition is performed by melting route, it doesn't induce noticeable crystallization effect in resulting fired layer (fig.2b). On the other hand, glass enamel obtained from sol-gel coated powders contains small tetragonal zirconia grains (fig.2a).

In the last case, the glass enamel microstructure appears to be uniform and contains homogeneously dispersed crystallized areas such as that of figure 3. Transmission electron micrograph (fig.3a) confirms the very small size of zirconia crystals (about 10 nm). The electron diffraction ring pattern (fig.3b and 3c) is that of the tetragonal metastable form.

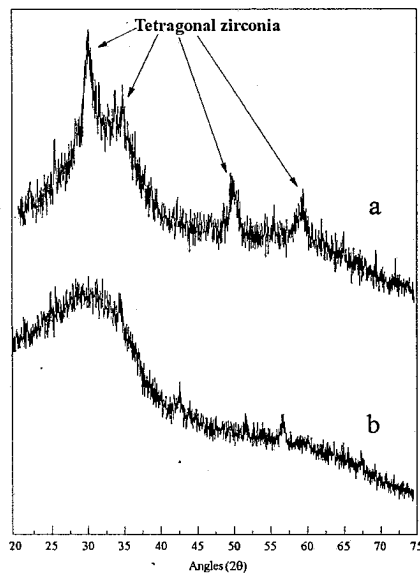
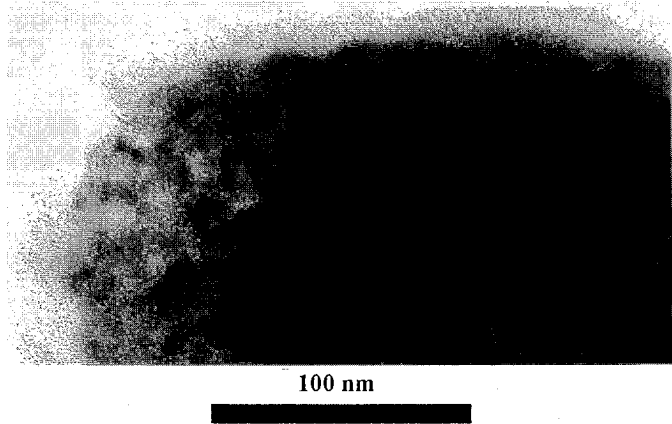


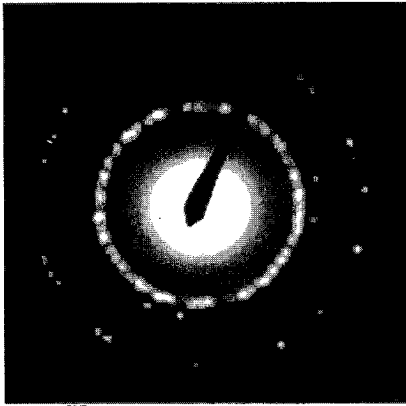
Fig. 2: XRD patterns

(a) enamel obtained with sol gel coated glass powder (5 wt% ZrO_2).

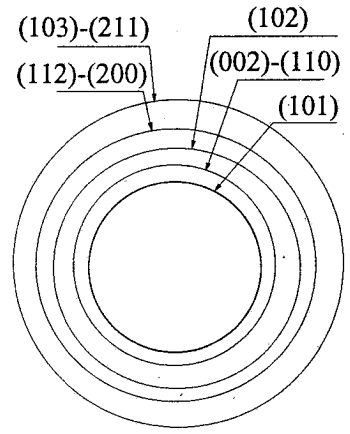
(b) enamel obtained with glass powder containing 5 wt % ZrO_2 added during the melting process.



(a) Bright field micrograph



(b) Diffraction rings of zirconia crystallites



(c) Indexation

Fig. 3: TEM observation of tetragonal zirconia nanoparticles in enamel obtained from sol gel coated glass powder.

IV CONCLUSION.

Adding a limited amount of zirconia to a low melting temperature glass frits, does not change the coating and luster quality of enamel.

For the same glass frits composition and the same thermal treatment, different enamel microstructures can be tailored. Single amorphous phase or finely dispersed zirconia nanocrystals containing glass are obtained depending on whether zirconium oxide added to the melt or by sol gel coating of glass frits particles with zirconia precursor.

Sol gel coating of particles with selected metal oxide precursor opens up new perspectives in the field of physical or chemical properties improvement for low melting temperature glasses.

V REFERENCES.

- (1) L.L.Hench and J.K.West "The sol gel process" *Chem.Rev.* 90(1990)33-72.
- (2) H.Schmidt and G.Ziegler "Analysis and surface chemistry of silicon nitride powder" "Third Euroceramics" Ed. P.Duran and J.F.Fernandez, published by Faenza Editrice Iberica Vol.1 p137-42 (1993).
- (3) T.Y.Tseng, Y.Y.Kuo and Y.L.Lin "Enhanced densification of pure alumina with alumina sol mixing" *J.Mater.Sci.Let.* 8(1989)1274-75.
- (4) P.Cortesi and H.K.Bowen "Continuous coating of alumina particles with alkoxide derived zirconia particles" *Ceramics International* 15(1989)173-77.
- (5) H.Okamara, E.A.Barringer and H.K.Bowen "Preparation and sintering of narrow sized Al_2O_3 - TiO_2 composite powders" *J.Mater.Sci.* 24(1989)1867-80.
- (6) F.A.Selmi and V.R.W.Amarakoon "Sol gel coating of powders for processing electronic ceramics" *J.Am.Ceram.Soc.* 71[11](1988)934-37.
- (7) B.Fegley, P.White and H.K.Bowen "Preparation of zirconia alumina powder by zirconium alkoxide hydrolysis" *J.Am.Ceram.Soc.* 68[2](1985)C60-C62.
- (8) P. Ruin, G. Melin, R. Guinebretiere, A. Lecomte, A. Dager "Coating of Oxide Powders with Alkoxide derived Zirconia" 7th Workshop on Glasses and Ceramics from Gels." July 19-23, 1993 Paris France.
- (9) R.Guinebretière, P.Ruin, A.Lecomte and A.Dager "Sol gel zirconia coating of cordierite powder and characterization of sintered products." "Ceramic Powder Science III", Ed. by The Am. Ceram. Soc., Vol.12 (1990) 929-936.
- (10) R. Guinebretiere, A. Dager, A. Lecomte, B. Soulestin and G. Troilliard "Mullite - Zirconia and Cordierite - Zirconia Composites Produced from Sol Gel Coated Commercial Powders." "Third Euroceramics" Ed. P.Duran and J.F.Fernandez, published by Faenza Editrice Iberica Vol.1 p 851-56 (1993).
- (11) A.Makishima and T.Nagata "Application of the sol gel process to lower the melting temperature of glaze" *J.Non Cryst.Sol.* 100(1988)519-22.
- (12) R.Guinebretière, A.Dager, A.Lecomte and H.Vesteghem "Tetragonal zirconia powders from the zirconium n-propoxide - acetylacetone - isopropanol - water system." *J. Non Cryst. Sol.* 147&148(1992)542-47.

Zircon Containing Ceramic Pigments by Sol - Gel Method

C. C. Trapalis, M.A. Karakassides, K. Golematis, G. Kordas
*Institute of Materials Science, NCSR "Demokritos", Ag.
Paraskevi 153 10, Athens, Greece*

Ceramic pigments of the $\text{Fe}_2\text{O}_3\text{-SiO}_2\text{-ZrO}_2$ and $\text{V}_2\text{O}_5\text{-SiO}_2\text{-ZrO}_2$ systems were prepared. The structural evolution during thermal treatment were observed using X-ray diffraction analysis, infrared and ESR spectroscopy.

Two signals for Fe(III) at $g=4.3$ and $g=2$ were detected, that come from the four-fold and six-fold co-ordinated ions, respectively. The co-ordination of Fe(III) ions was a function of temperature, concentration, and nature of the initial compounds. The Fe(III) $g=2$ signal was present at low temperatures. At higher temperatures, the concentration of the six-fold co-ordinated Fe(III) ions ($g=2$ signal) increased at the expense of the Fe(III) - ($g=4.3$ -signal) in four-fold co-ordination.

1. Introduction

Colour pigments are important in the traditional ceramics industry and are expected to be so for a long time to come. Today they are seen through the prism of new technology and improvements can be related to: rationalisation of production, cost effectiveness, and improved stain intensity, stability and "clearness" of tone. Major advances have been made in the area of zircon stains, in particular for vanadium-turquoise, praseodymium-yellow, and iron pinks [1, 2, 3].

Zircon pigments are usually manufactured by mixing and calcining the components, washing the product and milling it to a pre-determined average particle size. Thus, it is difficult to obtain mixtures with high homogeneity which allows higher reaction grades to be reached at low temperatures [2]. In the recent years, the sol-gel method was used in the preparation of solid solutions, to produce a gel in which the particle size and the degree of homogeneity allow a significant increase in the efficiency of the process at low temperatures [4]. The as-prepared pigments are zircon structure-based solid solutions containing transition metal ions as dopant. There are, however, controversies about the oxidation state of the transition metals, their localisation in the zircon lattice and the role of the mineralises [2, 5].

In this work we report the results of an ESR spectroscopy study of sol-gel derived colour pigments in order to elucidate the colouring mechanism as a function of their composition and thermal treatment temperature.

2. Experimental

Gels with $x(\text{Fe}_2\text{O}_3)\text{-(1-x)(ZrO}_2\text{-SiO}_2)$ where $x=0.01, 0.02, 0.05$ and $(\text{V}_2\text{O}_5)_{0.05} - (\text{SiO}_2) - (\text{ZrO}_2)_{0.9}$ compositions were prepared from tetraethylorthosilicate (TEOS), zirconium iso-propoxide, vanadium (V) oxychloride, iron nitrate and iron-n-butylate, by sol-gel route. Tetraethylorthosilicate were added in absolute ethanol in the molar ratio TEOS:ethanol=1:13. HNO_3 was used as catalyst ($\text{HNO}_3\text{:TEOS}=0.1$). Water

was added in the molar ratio of TEOS:H₂O=1:0.8. Under continuous stirring, the mixture was refluxed at 65°C for 2h before the addition of the transition metal component. Finally, zirconium iso-propoxide was added and the solution was left to gelify at room temperature.

The gels were first dried at 65 °C for a few days and then thermally treated at several temperatures between 300 and 1200 °C for 12h. The heat treated gels were studied using X-ray diffraction and IR spectroscopy. Electron Spin Resonance (ESR) was applied in order to obtain information about the structure and coordination environment of V(IV) and Fe(III) ions during the thermal treatment and lattice formation. ESR spectra were subsequently recorded at room temperature on a Bruker 200-SRC spectrometer operating at 9.42 GHz.

3. Results and Discussion

Transparent gels were prepared from prehydrolyzed TEOS, mixed with the second chromophor-component in ethanol, followed by addition of zirconium(IV)-iso-propoxide. The gels after thermal treatment favour the ZrSiO₄ crystallisation. The X-ray diffraction analysis of vanadium containing gels, thermally treated at 900°C, show that such a thermal treatment is sufficient to complete the crystallisation of monophase V-ZrSiO₄, without using mineralisers.

Figure 1 shows the IR spectrum of a sol-gel vanadium containing pigment, presented together with IR spectrum of commercial pigment of the same composition. It is evident from this comparison that after the thermal treatment a zirconium-silicate network forms in sol-gel derived samples, similar to those obtained by traditional technology. The colour of the V-ZrSiO₄ is green without the introduction of the mineraliser. The colour changes into turquoise for a mineraliser concentration of 3 wt% NaF.

Figure 2 shows the ESR spectra of Fe(III) containing gels, dried at 65°C

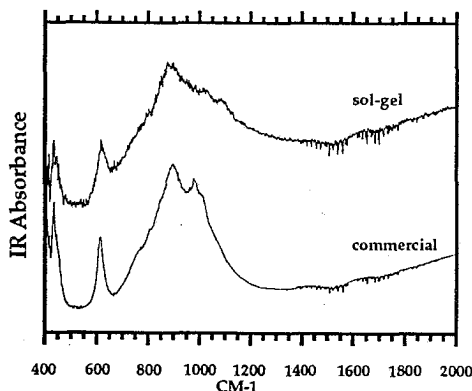


Fig. 1 IR spectra of commercial and sol-gel derived vanadium containing ZrSiO₄, thermally treated at 900°C.

at 500, 900 °C and 1200°C. In these gels the concentration of iron oxide is 0.05 mol%. $\text{Fe}(\text{NO})_3$ was used as a precursor. The spectra of the gels consist of two resonances. The one at 1500 G ($g=4.3$) and the other at 3500 G ($g=2$). Both signals are attributed to the presence of $\text{Fe}(\text{III})$ ions. The commonly accepted interpretation for these signals is that low symmetry rhombic sites of tetrahedral co-ordination give rise to the $g=4.3$ resonance while iron (III) ions in octahedral co-ordination give rise to $g=2$ resonance [6,7,8]. In the gel pigments, the $\text{Fe}(\text{III})$ ions are incorporated mainly into tetrahedral sites ($g=4.3$), although there is a small quantity of iron having octahedral sites ($g=2$). The increase of temperature at 500 °C leaves the structure of iron(III)

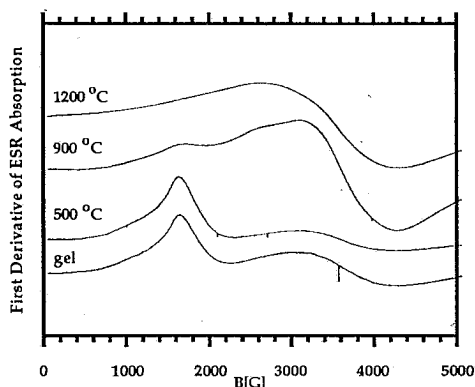


Fig.2 ESR spectra of the gels with 0.05 mol% Fe_2O_3 , after heat treatment.

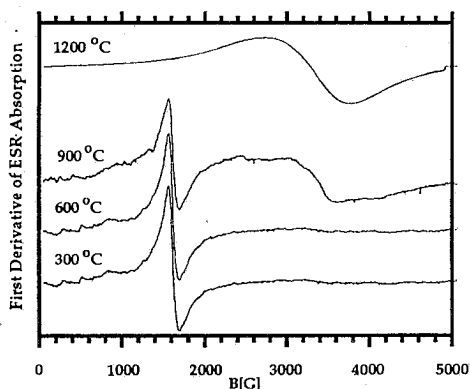


Fig.3 ESR spectra of the gels with 0.02 mol% Fe_2O_3 , introduced with iron butylate, after heat treatment.

unchanged. At 900 °C, two signals are formed at $g=2$ indicating the formation of two inequivalent iron(III) sites. The exact locations of iron will be explained in a later extensive study. The spectra of the same gel, heat treated at 1200°C, is dominated by a signal at $g=2$. This is an indication that iron ions are in six fold co-ordination.

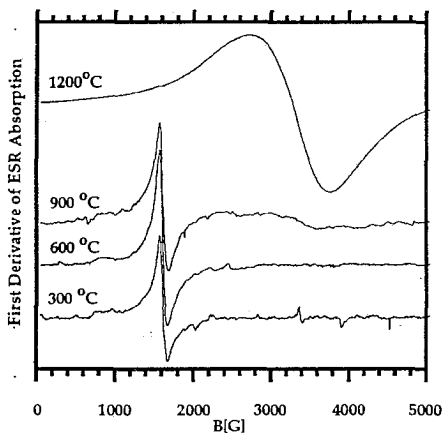


Fig.4 ESR spectra of the gels with 0.01 mol% Fe_2O_3 , introduced with iron butylate, after heat treatment.

At this temperature, single crystalline ZrSiO_4 has been formed in which iron is incorporated in octahedral sites.

Figure 3 shows the ESR spectra of the gels of composition with 0.02 mol% of iron oxide, heat treated at 300, 500, 900 and 1200 °C. In this composition, iron is introduced with iron butylate. It is evident from this figure that gel formation is followed by the appearance of Fe(III) ions predominantly incorporated into tetrahedral sites ($g=4.3$). At 900°C, a signal of significant intensity at $g=2$ is observed. After thermal treatment at 1200°C, a signal at $g=2$ dominates indicating the transition of iron into six fold co-ordination.

In Fig. 4, the ESR spectra of the gels with 0.01 mol% iron are given, recorded after thermal treatment at 300, 500, 900 and 1200°C. In the samples treated up to 500°C, the Fe(III)- $g=4.3$ signal is strong, while the Fe(III)- $g=2$ signal is negligible. Since the $g=2$ resonance is small, we suppose that the concentration of Fe(III)-ions in octahedral sites hardly exists. Heat treatment at higher temperatures is followed by iron transition into octahedral sites ($g=2$), as the spectra at 1200°C shows.

It has been proved that the iron oxides polyhedrons belong to a tetrahedral or octahedral sites after heat treatment. The incorporation of these

ions into these sites depends on both compositions and temperature of the thermal treatment.

4. Conclusions

Zircon-Ceramics pigments containing iron and vanadium oxides, were prepared by sol-gel method. Vanadium containing $ZrSiO_4$ after heat treatment at $900^\circ C$, seem to form a zirconium-silicate network similar to those obtained by traditional technology.

The Fe(III) ions seem to be encapsulated in the particularly formed zircon lattice at low temperatures, following the structure changes of their environment during the thermal treatment. At low temperatures the Fe(III) ions were in four fold co-ordination, whereas at high temperatures they transformed into six-fold co-ordination under strong influence of formed crystalline zircon. Iron alkoxides, compared to iron salts as precursors, favour the four fold co-ordination of Fe(III) ions even at higher temperatures.

REFERENCES

- 1.G. Monros, J. Carda, M.A. Tena, P. Escribano, M. Sales and J. Alarcon, *J. Non-Cryst. Solids* 147&148 (1992) 588.
- 2.R. Carter, *Ceram. Eng. Sci. Proc.*, 8 (1987) 1156.
- 3.R. Oheim, H. Pauls, C. Russel, *J. Mat. Sci. Let.*, 10 (1991) 1171.
- 4.G. Monros, J. Carda, M.A. Tena, P. Escribano, J. Alarcon, *J. Mat. Sci. Let.*, 27 (1992) 351.
- 5.G. Monros, J. Carda, M.A. Tena, P. Escribano, V. Cantavella, *J. Alarcon Mat. Res. Bull.*, 27 (1992) 753.
- 6.D. Loveridge, S. Parke, *Physics Chem. Glasses*, 12(1971) 19.
- 7.G. Kordas, H. J. Oel, *Physics Chem. Glasses*, 25 (1984) 76.
- 8.M. M. Mestdagh, C. Dauby, L. Van Cangh, C. Dupont, *Glass Technology*, 24 (1983) 184.

SOL-GEL PROCESSING AND CRYSTALLIZATION OF ALKALI GERMANATE GLASSES

A. Marotta, M. Catauro, A. Aronne and P. Pernice
Department of Materials and Production Engineering
80125 Naples, Italy

Lithium tetragermanate and sodium tetragermanate gels were synthesised by hydrolytic polycondensation of germanium ethoxide with lithium hydroxide monohydrate and sodium ethoxide respectively, in alcoholic medium. Both lithium tetragermanate gel and sodium tetragermanate gel heated at constant heating rate during a DTA run crystallise, as the oxides glasses of the same composition, in two steps. In lithium tetragermanate gel $\text{Li}_2\text{Ge}_4\text{O}_9$ and GeO_2 microcrystallites are initially formed and then converted at higher temperature into well shaped $\text{Li}_2\text{Ge}_4\text{O}_9$ and $\text{Li}_2\text{Ge}_7\text{O}_{15}$ crystals. In sodium tetragermanate gel metastable $\text{Na}_2\text{Ge}_4\text{O}_9$ crystals are initially formed and then converted into stable $\text{Na}_4\text{Ge}_9\text{O}_{20}$ crystals.

Introduction

The sol-gel method of making inorganic glasses has been intensively studied in recent years[1]. Interest in this process has been stimulated, in part, by the low preparation temperature. The preparation involves hydrolysis and polycondensation of organometallic compounds. A gel forms which is dried to a porous particulate material. Proper thermal treatments are, therefore, required to convert the gel into the glass. Binary alkali silicate gels have been prepared in a variety of ways and with a variety of precursor. No attention has been devoted to binary alkali germanate gels. The ionic size and the ionic charge of Ge^{4+} are very similar to that of Si^{4+} and, therefore, the chemistry of silicates and of the germanate somewhat resemble each other. However, the ionic radius of Ge^{4+} (0.53 Å) is very close to cation/anion radius ratio limit that separates tetrahedral and octahedral co-ordination and, therefore, Ge^{4+} can assume both fourfold and sixfold co-ordination. Investigations on binary alkali germanate gels preparation and their crystallisation behaviour are of interest for elucidating the nature crystallising phases and for research on glass-ceramic materials.

In this work lithium tetragermanate gel and sodium tetragermanate gel were synthesised by hydrolytic polycondensation, and their crystallization behaviour were studied with the aid of X-ray diffraction and differential thermal analysis.

Experimental

Lithium tetragermanate gel and sodium tetragermanate gel were prepared using $\text{Ge}(\text{C}_2\text{H}_5\text{O})_4$ (TEOG) and $\text{LiOH} \cdot \text{H}_2\text{O}$ or $\text{Na}(\text{C}_2\text{H}_5\text{O})_4$ analytical grade reagents as starting materials. Water-free ethanol (EtOH), obtained by distillation with metallic sodium of commercial anhydrous ethanol, was used, since the TEOG is very water-sensitive reagent and to permit control of TEOG/ H_2O molar ratio. Bidistilled water was used for hydrolysis reaction. The

alcoholic solutions were prepared in a dry-box at room temperature. The flow-charts indicating the preparation procedure and the compositions employed are given in fig. 1.

The lithium and sodium content in the gel was verified using atomic absorption analysis.

The nature and temperatures of the various reactions that occur during the heating of the dried gels were determined using simultaneous thermogravimetric (TGA) and differential thermal analysis (DTA). Powdered sample, 20mg of the dried gel was subjected to a TGA/DTA run in N_2 at a heating rate of $10^\circ C/min$ from room temperature to $700^\circ C$. A Stanton-Redcroft analyser STA-780 was used, and powdered Al_2O_3 was used as the reference material.

The amorphous nature of the dried gels and identification of the phases crystallising during the DTA runs were ascertained by X-ray diffraction (XRD) using a Philips diffractometer. Powders of each sample were scanned from $2\theta=5^\circ$ to 60° using $CuK\alpha$ radiation.

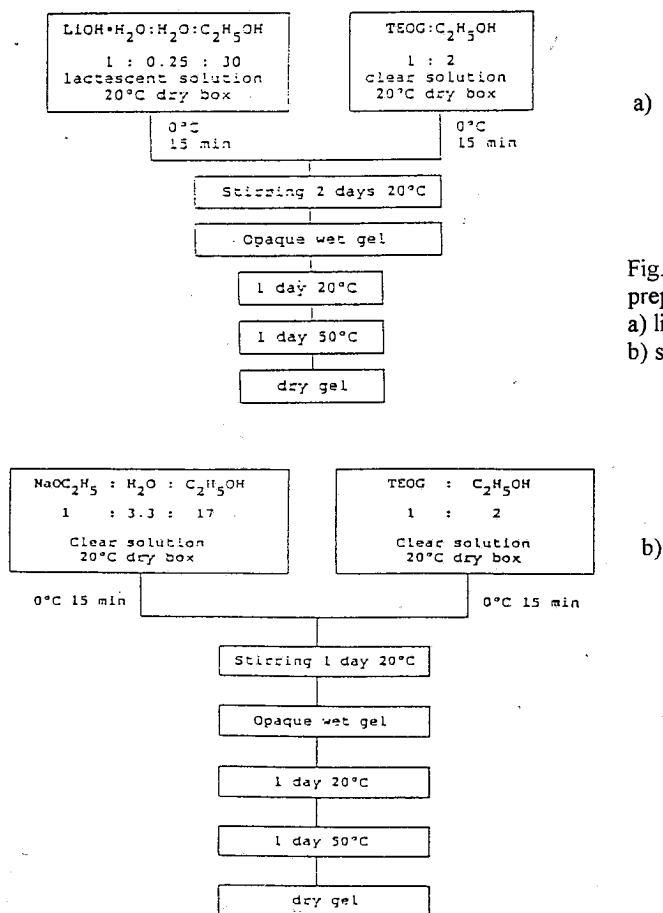


Fig.1 flow-charts of the gel preparation procedure
a) lithium tetragermanate
b) sodium tetragermanate

Results and Discussion

The chemical analysis of the melted gels showed that good composition control was provided by the sol-gel process (table 1). The analyzed and theoretical values are in fairly good agreement. In fig.2 and 3 are showed the TGA/DTA curves of Li-gel and Na-gel respectively.

Tab.1 Chemical analysis of the melted gels.

| Constituent | Alalyzed wt% | Theoretical wt% |
|-------------------|--------------|-----------------|
| Li ₂ O | 6.46 | 6.66 |
| Na ₂ O | 12.90 | 12.74 |

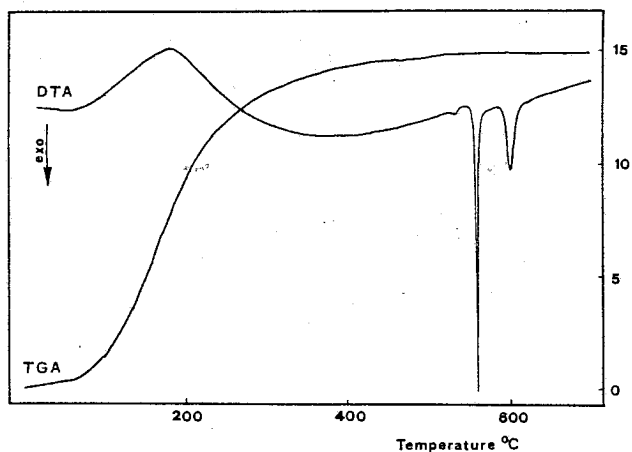


Fig.2 DTA and TGA curves of the dried gel lithium tetragermanate

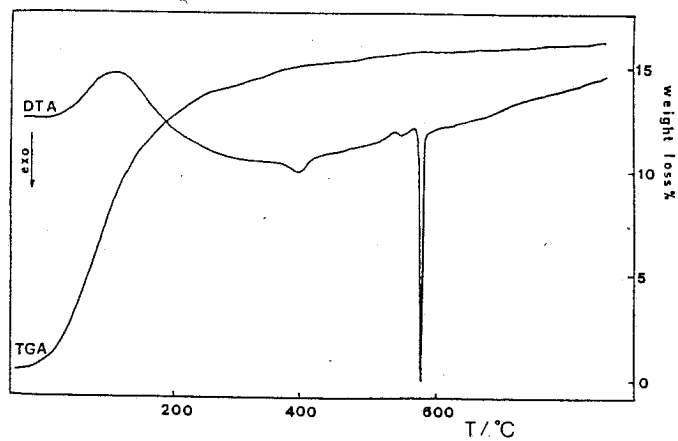


Fig.3 DTA and TGA curves of the dried gel sodium tetragermanate

A large endothermic peak, from room temperature at about 250°C, appears on both the DTA curves, with a maximum at about 150°C, and a simultaneous weight loss occurs in both the TGA curves. The weight loss were 14.9% in Li-gel and 16.0% in Na-gel. These effects were due to evaporation from open pores of the water and alcohol physically trapped in the gel. On the DTA curve of the Na-gel a small exothermic effect occurs at about 400°C that should be related to the pyrolysis of residual organic groups in the gel, which had not reacted by the end of drying step and consequently did not evaporate from the gel before calcing.

The DTA curves of both the gels exhibit a slope change that may be attributed to the glass transition. In this work, the inflection point of the DTA curve was taken as the glass transition temperature ($T_g=532^\circ\text{C}$ in Li-gel and $T_g=546^\circ\text{C}$ in Na-gel).

A high and sharp exothermic peak appears, just above the T_g , on the DTA curve of the Li-gel at the temperature of 565°C. At a higher temperature, 604°C, the DTA curve exhibits a second exo-peak, smaller than the first one. The presence of two exothermic effects on the DTA curve of the studied gel suggests a crystallization process in two steps.

Figure 4 shows diffraction patterns of (a) a dried gel; (b) a dried gel heated in the DTA furnace up to the temperature of the first exo-peak; and (c) a dried gel after a DTA run carried out from room temperature to 700°C. Trace (a) has broad humps characteristic of the amorphous state of the dried gel. The broad reflections on trace (b) of fig.4 were attributed to $\text{Li}_2\text{Ge}_4\text{O}_9$ and GeO_2 microcrystallites. The reflections of trace (c) of the fig 4 correspond to $\text{Li}_2\text{Ge}_4\text{O}_9$ and $\text{Li}_2\text{Ge}_7\text{O}_{15}$ crystals.

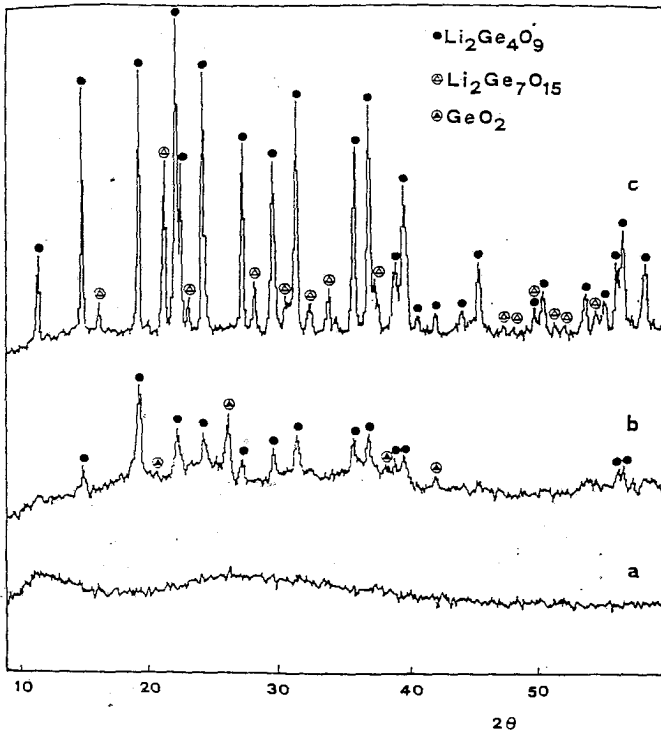


Fig. 4 Powder X-ray diffraction patterns of lithium tetragermanate.

The diffraction pattern of a gel sample heated in the DTA furnace to the temperature of the first exo-peak (see trace (b) in fig.4) shows few broad peaks in an amorphous back-ground. These reflections are attributed to $\text{Li}_2\text{Ge}_4\text{O}_9$ crystals and hexagonal GeO_2 . This result, in spite of the strong thermal effect on DTA curve, suggests the precipitation of a large number of microcrystallites dispersed in a non-crystalline matrix. The diffractogram obtained for a gel sample after the DTA run (trace(c) in fig.4) exhibits a high number of sharp lines that correspond to $\text{Li}_2\text{Ge}_4\text{O}_9$ and $\text{Li}_2\text{Ge}_7\text{O}_{15}$ crystals, while the strongest line of GeO_2 disappears. The crystal structure of $\text{Li}_2\text{Ge}_4\text{O}_9$ contains rings of GeO_4 tetrahedra linked by GeO_6 octahedra forming a three-dimensional network[2]. This structure can be characterized by the formula $\text{Li}_2[\text{Ge}(\text{GeO}_3)_3]$. The oxygen atoms in the network are either bridging atoms between tetrahedrally coordinated Ge atoms or bridging atoms between one tetrahedrally and one octahedrally coordinated Ge atoms. This structure is very similar to that of $\text{Li}_2\text{Ge}_7\text{O}_{15}$ which contains layers of GeO_4 tetrahedra linked by GeO_6 octahedra forming a three-dimensional network and is characterized by the formula $\text{Li}_2[\text{Ge}(\text{Ge}_2\text{O}_5)_3]$ [3]. These results suggest that the non-isothermal crystallization of gel occurs in two steps. First, a high number of microcrystallites of $\text{Li}_2\text{Ge}_4\text{O}_9$ and GeO_2 are formed and then, at higher temperature these are converted into well shaped $\text{Li}_2\text{Ge}_4\text{O}_9$ and $\text{Li}_2\text{Ge}_7\text{O}_{15}$.

This crystallization behaviour is quite similar to that of $\text{Li}_2\text{Ge}_4\text{O}_9$ oxide glass which was found to devitrify in two steps. In the primary transformation, microcrystallites of $\text{Li}_2\text{Ge}_4\text{O}_9$ are crystallized in an amorphous matrix. In the second transformation, well shaped $\text{Li}_2\text{Ge}_4\text{O}_9$ crystals are formed[4]. The formation of GeO_2 (which is not an equilibrium phase), in the first gel transformation, is most likely due to the decomposition or rearrangement of the amorphous gel phase when dehydroxylation occurs on the surface of the gel.[5]

In the case of Na-gel a high and sharp exothermic peak appears, just above the T_g , on the DTA curve of the Na-gel at the temperature of 575°C.

Figure 5 shows the XRD patterns of samples of the treated in different conditions: a) dried gel held 3 h at 450°C; b) dried gel heated in the DSC furnace up to the temperature of the exo-peak (573°C); c) dried gel after a DSC run carried out from room temperature to 700°C.

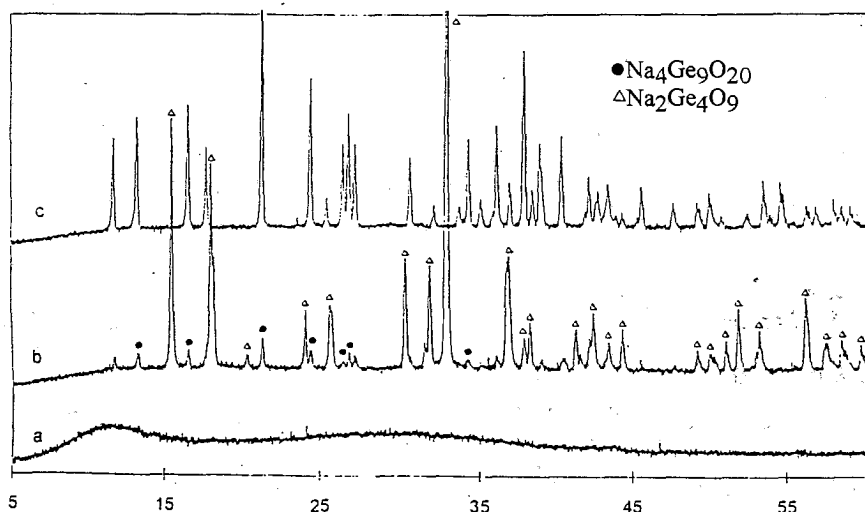


Fig. 5 Powder X-ray diffraction patterns of sodium tetragermanate.

Trace a) has broad humps characteristic of the amorphous state of the gels. The diffractogram b) exhibits several sharp lines. The major crystalline phase was found correspond to $\text{Na}_2\text{Ge}_4\text{O}_9$, a phase which is not reported in the $\text{Na}_2\text{O}-\text{GeO}_2$ phase diagram [6] but which has been obtained [7] by reheating a glass of the same composition. In addition to the peaks due to $\text{Na}_2\text{Ge}_4\text{O}_9$ the strongest reflections of $\text{Na}_4\text{Ge}_9\text{O}_{20}$ were also found in this pattern.

The structure of $\text{Na}_4\text{Ge}_9\text{O}_{20}$ contains isolated GeO_6 octahedra connected by Ge_3O_9 rings consisting of three GeO_4 tetrahedra to form a three dimensional network. $\text{Na}_4\text{Ge}_9\text{O}_{20}$ contains chains of GeO_4 tetrahedra connected by Ge_4O_{16} groups which consist of edge-shared GeO_6 octahedra [8].

The reflections of the diffractogram c) were all assigned to $\text{Na}_4\text{Ge}_9\text{O}_{20}$. No reflections of $\text{Na}_2\text{Ge}_4\text{O}_9$ were found in this pattern. This result suggests a devitrification mechanism in two steps. In the primary transformation metastable $\text{Na}_2\text{Ge}_4\text{O}_9$ crystals are formed, and these are then converted at higher temperatures in thermodynamically stable $\text{Na}_4\text{Ge}_9\text{O}_{20}$ crystals. This crystallisation mechanism is very similar to that of the oxide glass [8].

If more than one crystal is precipitated from gel glass the structure of the metastable phase can be supposed to be more like to the mother glass than the stable one. In the glass the GeO_6 octahedra may be connected with GeO_4 tetrahedra by sharing corner-oxygen and the coalescence of GeO_6 octahedra by sharing edges to Ge_4O_{16} groups may not occur.

From the phase diagram [6] the transformation of $\text{Na}_2\text{Ge}_4\text{O}_9$ into $\text{Na}_4\text{Ge}_9\text{O}_{20}$ requires the precipitation of small amount of another Na_2GeO_3 crystal but no reflections of this phase were found in XRD patterns.

Conclusions

The gels preparation involves hydrolysis and polycondensation of germanium ethoxide with lithium hydroxide monohydrate or sodium ethoxide. The gels thus prepared are an amorphous solid containing water and organic residues that are lost on heating. The necessary temperatures are well below the glass transition temperature of the glass being formed, and therefore, during the heat treatment required for the gel into glass conversion, the gels are kinetically stable to crystallisation.

Both lithium tetragermanate gel and sodium tetragermanate gel heated at constant heating rate during a DTA run crystallise, as the oxides glasses of the same composition, in two steps.

In lithium tetragermanate gel $\text{Li}_2\text{Ge}_4\text{O}_9$ and GeO_2 microcrystallites are initially formed and then converted at higher temperature into well shaped $\text{Li}_2\text{Ge}_4\text{O}_9$ and $\text{Li}_2\text{Ge}_7\text{O}_{15}$ crystals.

In sodium tetragermanate gel metastable $\text{Na}_2\text{Ge}_4\text{O}_9$ crystals are initially formed and then converted into stable $\text{Na}_4\text{Ge}_9\text{O}_{20}$ crystals.

References

1. C.J. Brinker, and G.W. Scherer, Sol-gel Science. 1990. (Accademic Press, Inc., San Diego, CA.)
2. A. Wittman and E. Modern, Monatsh. Chem. 96 (1965) 581.
3. H. Vollenke, A Wittman and H. Nowotny, Monatsh. Chem. 101 (1970) 46.
4. P.Pernice, A. Aronne and A. Marotta, Mater. Chem. Phys (1992) 195.
5. S.P. Mukherjee, J. Non-Cryst. Solids 82 (1986) 293.
6. M.K.Murthy, . and J.Aguaya, J. Am. Ceram. Soc. 1964, 47, 444.
7. A.Wittman, and P.Papamantellos, Mh. Chem., 1960, 92, 855.
8. K.Kamija, T. Yoko, Y.Miki, Y.Itoh, and S.J.Sakka, Non-Cryst. Solids, 1987, 91, 279.

Calcium Hydroxyapatite Formation by Sol - Gel Route

C.C. Trapalis, A. Koufoudakis, I. Dounis, M.A. Karakassides,
and G. Kordas

*National Centre of Scientific Research "Demokritos", Institute of Materials
Science, 153 10, Ag. Paraskevi, Athens, Greece*

Calcium hydroxyapatite powder was prepared by sol-gel method using calcium acetate and $\text{PO}(\text{OR})_3$ $\text{R}=\text{CH}_3$, C_2H_5 radical, as initial compounds, and alcohol (methyl, ethyl, and propyl-alcohol) as solvent. Homogenous solution and gels of the above precursors were prepared using a molar ratio of $\text{Ca/P} = 1.67$. The gels were heat treated using different programs depending upon the reagents. The structural evolution during the calcination was deduced using the data of X-ray diffraction analysis and Infrared spectroscopy. The morphology of hydroxyapatite powder was observed by means of a scanning electron microscope.

1. Introduction

Ceramics, glasses and glass-ceramics containing hydroxyapatite (HA) crystals are promising materials for many medical applications [1]. Hydroxyapatite ($\text{Ca}_5(\text{PO}_4)_3\text{OH}$) is a primary constituent of human hard tissues. The structure of artificially prepared HA is the same as that of the HA of the natural bone. HA because of its good compatibility with the human organism and strong binding to the bone potentially can find different application as, for example, for artificial tooth roots, filler of bone defects, etc [2, 3].

In the last few years there have been many efforts to prepare HA by various ways. Asade et al [4] prepared HA of good sinterability using ammonia-alkaline conditions but found elimination of harmful ammonium nitrate by-products to be difficult. The "pure" method of Akao [5] (by-product only water) which appears difficulties in the control of precipitation conditions, was further developed by Osaka et al [6]. These authors prepared the most thermally stable HA by mixing nearly stoichiometric ratios $\text{Ca/P} = 1.67$ to 1.70. As it concerns the preparation of HA by a sol - gel technique it is not clear whether the technique is suitable because of the volatility and of the low hydrolysis rate of the alkoxy phosphorous compounds [7]. The exception is the water extraction variant of the sol - gel process used by Deptula et al [8]. The aim of this work is a preliminary study of the potential and its feasibility of using the sol-gel technique for HA preparation.

2. Experimental

The experiments were performed in accordance with the following sequence. A 1M solution of $\text{PO}(\text{OR})_3$ was slowly added to a 1.67M calcium

acetate solution (0.5 gr. $\text{Ca}(\text{CH}_3\text{COO})_2/\text{ml}$). The solution was vigorously stirred during the addition in order to prevent any local excess concentrations of phosphorus and local formation of gel of uncontrolled composition. This solution is then cooled to between 5 and 18°C and alcohol is gradually added. The necessary quantity of alcohol for gelation decreases with increasing temperature and in the array Methyl, Ethyl, Propyl alcohol. The gel is then dried 75°C for few days. The received dry product is further thermally treated up to 930°C. Thermal treatment programs were continuous or step by step in order to facilitate the XRD and IR control.

3. Results and discussion

To demonstrate the main results a sequence of XRD and IR spectra were chosen. From the XRD spectra in fig.1 is evident the low degree of crystallisation at 300°C and the presence of organic compounds. After further treatment at 600°C organic compounds are eliminated and HA is clearly

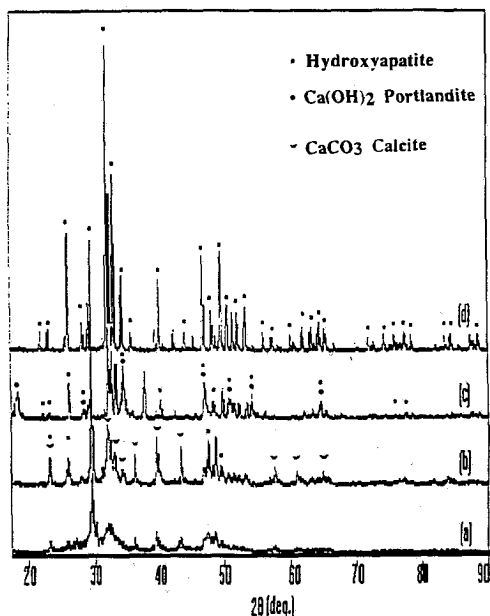


Fig.1. XRD Patterns of calcinated samples: a) 300°C 12h, b) 600°C 162h, c) 800°C 12h, d) 930°C 24h (sample washed with acetic acid and water)

formed. At 800°C HA is dominant, but there is also a small amount of $\text{Ca}(\text{OH})_2$. At higher temperatures $\text{Ca}(\text{OH})_2$ dehydrates to CaO . After treating at 930°C the satisfactory yield of the procedure is evident. Finally after washing the product with acetic acid and water in order to eliminate CaO , a clear HA sample is received fig.1(d). All detectable peaks are assigned to HA. The presence of other phases is undetectable by XRD.

In Fig.2 are presented the infrared spectra of the dry gel and powder samples, heated and stabilised at various temperatures. The spectrum (a) of

the gel 75°C exhibit a variety of sharp lines mainly due to vibrations of solvent molecules and trapped organic groups. Thus the relative sharp line at the 1610 cm^{-1} can be assigned to asymmetric CO stretching vibrations in bidentate acetate group[9]. By thermal treatment of the gel a number of spectral changes take place. First lines related to PO_4 vibrations can be observed at about 1063 cm^{-1} (P-O stretching) and in the 600-550 cm^{-1} frequency region (O-P-O bending) [7, 9]. Second, the bands at 1509, 1425, 880 and 700 cm^{-1} which dominate in spectra (b) and (c) in fig.2 were assigned to carbonate ions. These ions probably came into the system from the oxidation of the acetic anion or the organic solvents. Thus the spectra (b) and (c) show the carbonate asymmetric

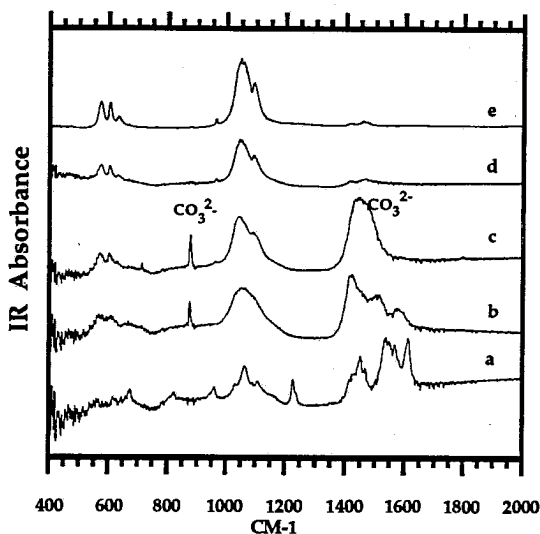


Fig.2. FT-IR spectra of samples thermal treated at: a)75°C 10 days, b)300°C 12h, c)600°C 12h, d)800°C 12h, e)930°C 24h, (sample washed with acetic acid and water).

stretching ν_3 (E') mode (1509, 1425 cm^{-1}) the out of plane deformation ν_2 mode (880 cm^{-1}) and the in plane bend ν_4 (700 cm^{-1})[9]. By increasing the temperature these bands decrease in intensity (spectrum (c) - 600°C) tending to disappear (spectrum (d) - 800°C). It can be concluded that above 800°C the decomposition of residual CO_3^{2-} take place. Spectrum (e) corresponds to sample thermal treated at 930°C after elimination of CaO. The changes between samples treated at 800°C and 930°C recorded by XRD (Fig.1) are not detectable in the given range of IR. The final IR spectra are identical to those of commercially available hydroxyapatite.

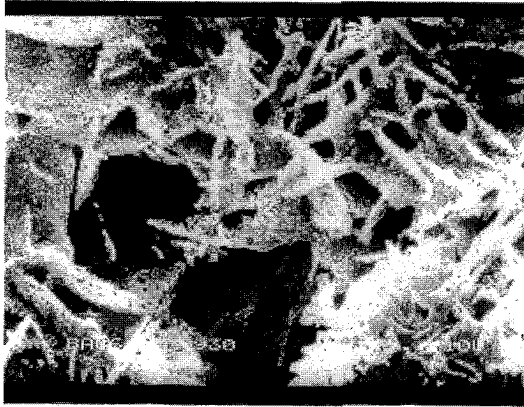


Fig. 3. SEM micrograph of calcium hydroxyapatite powder.

Fig. 3 shows an SEM micrograph of the final powder product after thermal treatment at 930°C for 24 h and washing with acetic acid and water. It exhibits high open porosity formed by evolution of gases during the thermal treatment.

4. Conclusions

The sol-gel method gave satisfactory results and appeared feasible for HA preparation. After final thermal treatment at 930°C samples gave XRD spectra proving a satisfactory yield hydroxyapatite. Beside HA only small amounts of CaO were detectable. To eliminate the calcium oxide from the product it is necessary to wash with acetic acid and water.

REFERENCES

1. R.H. Doremus, *J. Mat. Sci.* 27 (1992) 285.
2. L. L. Hench, *J. Am. Ceram. Soc.*, 74, [7] 1991, 1487.
3. C. Laverinia, J.M. Schoenung, *Ceramic Bulletin*, 70, No.1, (1991) 48.
4. M. Asada, K. Oukami, S. Nakamura and K. Takahashi, *Yogyo Kyokai-Shi (the Ceram. Soc. Japan)* 95 (1987) 703.
5. M. Akao, H. Aoki and K. Kat, *J. Mater. Sci.* 16 (1981) 809.
6. A. Osaka, Y. Miura, K. Takeushi, M. Asada, K. Takahashi, *J. Mat. Sci: Materials in Medicine* 2(1991) 51.
7. T. Brendel, A. Engel, C. Russel, *J. Mat. Sci: Materials in Medicine* (1992) 175.
8. A. Deptula, W. Lada, T. Olczac, A. Borello, C. Alvani, A. di Bartolomeo *J. of Non. Crystalline Solids* 147, 148 (1992) 537.
9. K. Nakamoto, *Infrared Spectra of Inorganic and Coordination Compounds* (Wiley, New York, 1963).

Part III, Glass Structure and Properties

SUB-AMBIENT T_G GLASSES FOR IONIC RUBBERS AND NEW GENERATION SOLID ELECTROLYTES.

Changle Liu, E. Sanchez, and C.A. Angell
Chemistry Department
Arizona State University
Chemistry Department
Tempe, AZ 85287-1604

ABSTRACT

We describe the development of a class of ionic glasses in which the glass transition temperature is deliberately tailored to fall below room temperature, and show that such systems can be converted to solid materials - solid in the sense of having non-zero shear moduli - by incorporation of a small mole fraction of high molecular weight polymer. Such materials constitute a new class of rubber in which the majority components are simple ions, and as such offer a type of "solid" electrolyte which has many advantages over the current "superionic glass" and "salt-in-polymer" electrolytes. Indeed it combines the best features of the two, cationic conduction and rubbery compliances, into a single material.

INTRODUCTION

In this paper we will describe the development of a class of inorganic glasses which are unusual in that they depend for their usefulness on having their glass transition temperatures below ambient temperature. Indeed they are ambient temperature molten salts except for the fact they have dissolved in them a small quantity of a high molecular weight polymer which makes their macroscopic viscosity so high that they no longer flow. Since their microscopic viscosity remains low, they exhibit the characteristics of rubbery materials. As a consequence they make excellent solid electrolytes which are in fact quite closely related to the more successful superionic glass electrolytes in nature but avoid some of their drawbacks. To understand their nature it is necessary to review some of the properties of the rival superionic glass and salt-in-polymer electrolytes.

Ionic Liquids, Mode Decoupling, and Superionic Glasses

It has been known since the early days of molten salt chemistry, that the Walden rule relating equivalent conductivity Λ to viscosity η for electrolyte solutions becomes modified to the form

$$\Lambda = \eta^\alpha \quad (3)$$

in the case of simple molten salts (1). This was originally interpreted as a consequence of differences in Arrhenius activation energies for conductivity and viscous flow processes. In the extended phenomenology of glassforming ionic liquids, the difference appears as a difference in one parameter, B_P , of the Vogel-Fulcher transport equation,

$$P = P_0 \exp \pm B_P / (T - T_0) \quad (4)$$

where P is the transport property in question and T_0 is a constant. This behavior, which was recognized early in the application of the Vogel-Fulcher law to glass forming molten salts, (2) is depicted in Fig. 1 which displays the behavior of both conductivity and fluidity (viscosity)⁻¹ for the typical ionic melt of a superionic glassformer. Recently, (3) the Vogel-Fulcher equation for viscosity η has been found to be more usefully written in the form

$$\eta = \eta_0 \exp \pm D_{\eta} T_0 / (T - T_0), \tag{5}$$

because the parameter D_{η} then expresses the property known as the fragility (3). The fragility, which quantifies the departure from Arrhenius behavior, is believed to be determined in part by the stability of the short and intermediate range structure against temperature-induced degradation, (a reflection of the degeneracy of the configurational microstates of the system), and in part by the energy barriers separating the microstates of the system from one another, (3). The presence of different values of D for different physical properties, implies that the energy barrier component of D certainly plays an important role in the phenomenology. The manner in which the two components of D emerge from the Adam-Gibbs theory of transport processes (4) has been discussed elsewhere (5) and will not be repeated here. The implication of different energy barriers for cooperative rearrangements for different processes was first pointed out by Kawamura and Shimoji (6).

The difference between the D parameters for conductivity and viscosity defines the extent to which the conducting modes are decoupled from the viscous modes in the liquid state. In the simplest case, it determines the conductivity in the glass formed when the temperature is dropped to below the glass transition temperature. At this temperature the anionic network becomes immobile, or "frozen", to provide a matrix in which the cationic diffusion, hence conductivity, can continue. Because the structure no longer changes with further decreases in temperature, however, the Vogel-Fulcher behavior of the conductivity is terminated and instead an Arrhenius law is followed. This phenomenology is summarized in Fig. 1. Note that the pre-exponent of the Arrhenius law is somewhat greater than the extrapolated infinite temperature dc conductivity of the liquid (as indicated by the dashed line in Fig. 1).

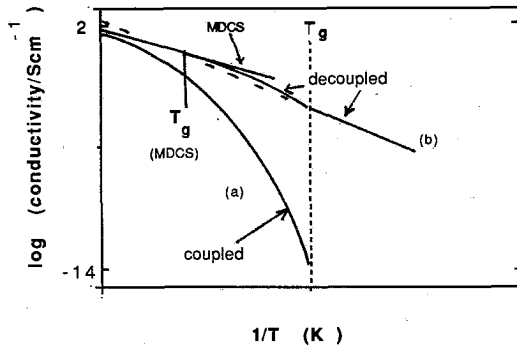


Figure 1. Depiction of the conductivity vs. temperature behavior in Arrhenius form for systems in which the conducting particles are strongly coupled to the viscous modes (curve A) and strongly decoupled from the viscous modes (curve B). The crossover from non-Arrhenius to Arrhenius behavior is associated with the "freezing" of the structure into a single configuration at T_g . Also shown is the behavior of a system which is frozen on a much shorter time scale due to much faster quenching as in the case of molecular dynamics computer-simulated systems. In this case it is clear that the activation energy for conductivity should be even smaller than in the laboratory superionic glass.

The manner in which the freezing of the structure at different temperatures by different cooling schedules can modify the slope of the Arrhenius law for the conducting glass was described in an earlier review paper (7). A particular case of this phenomenology is illustrated by the dashed line in Fig. 1 denoted MDCS to indicate the situation in the Molecular Dynamics Computer Simulation of superionic glasses in which extremely rapid quenches are applied to ionic liquids. Although, as this dashed line indicates, a highly excited state of the liquid is frozen-in in such simulations, there is reason to believe that much of what is revealed by these molecular level "experiments" is indeed pertinent to the understanding of laboratory superionic glasses. Since this provides a useful conceptual background for the later discussion in this paper, we display in Fig. 2 an example of the sort of ionic trajectories which are revealed by simulation.

Fig. 2 shows the projection of all the lithium ion trajectories in a simulated lithium thiosilicate glass executed during a 1500 time-step simulation. Details of this type of simulation are given elsewhere (8) and we mention here only the important points. The trajectory display demonstrates that the microscopic mode of motion which initiates the slower diffusive modes is an anharmonic oscillation of the ion in a quasi-lattice site, or ion trap. The frequency of oscillation, which determines the frequency of infrared photons which are absorbed by the glass, corresponds rather well with the observed far infrared "cation rattling mode" in glass observed by a number of workers (9-12).

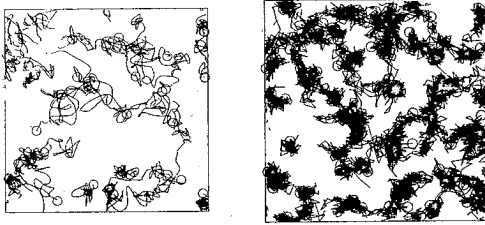


Figure 2. Trajectories of cations in two fast ion conducting glasses $\text{Na}_2\text{O} \cdot 35\text{O}_2$ and $\text{Li}_6\text{Si}_2\text{S}_7$, according to computer simulation studies. The figures show the projections of all mobile cation motions and one face of the periodic box, over the course of runs of 1.5 and 6.0 picoseconds respectively. In each glass the ions tend to move in channels between regions occupied by the silicon-oxygen, and silicon-sulfur polyanions, respectively. Note that the primary motions of the particles are oscillatory in character and that the oscillations are interrupted by occasional drifts between sites of lower energy (shallow traps) as gates in the channels open up by appropriate fluctuations as the anions oscillate. The presence of some deeper traps from which the particles do not escape during the entire length of the simulation, are evident in each case.

The best way of displaying this phenomenology for chosen laboratory examples is to first convert the viscosity and conductivity data to the corresponding relaxation times, τ_{η_s} and τ_{σ} , for the respective processes. These can be measured directly at low temperatures by appropriate electrical and shear modulus relaxation spectroscopies, (13) but for our purposes it is quite sufficient to use the following Maxwell relations involving the conventional viscosity η_{σ} and conductivity σ data

$$\tau_{\eta_s} = \eta_s / G_{\infty} \quad (6)$$

where G_{∞} is the high frequency shear modulus, and

$$\tau_{\sigma} = \rho_0 \epsilon_0 / M_{\infty} = \epsilon_0 / M_{\infty} \sigma_0$$

where ρ_0 is the zero frequency specific resistivity, and M_{∞} is the high frequency ($\gg 1/2\pi\tau$) electrical modulus. This has the advantage of converting the units of the respective processes to the same time units and leads to a description of the decoupling of conductivity from viscosity modes in terms of the ratio of the respective relaxation times. This was originally described by Moynihan et al. (14) for the case of concentrated aqueous solutions and has more recently been used to define the material property $R_{\tau}(T_g)$, which is central to our attempts to clarify the phenomenology of superionic glasses (7, 15-17). An example is shown in Fig. 3. We note from the original publication on these simple halide glasses, (18) that the T_g for the most decoupled case is below room temperature.

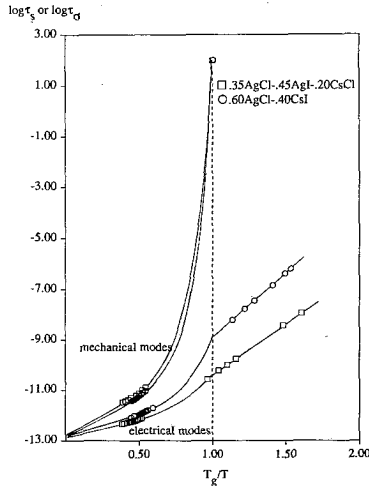


Figure 3. Presentation of results of electrical conductivity and shear viscosity measurements as relaxation times for the respective processes, for the cases of two simple silver halide-alkali halide glasses and their glassforming melts.

By way of contrast with the latter behavior we show in Fig. 4 the variation of conductivity of two lithium iodide-rich compositions in the system LiI - tetra-alkyl ammonium iodide (19) in which the conductivity falls to 10^{-11} S cm^{-1} at the glass transition temperature. In one of these cases T_g falls far below ambient so that the ambient temperature conductivity is quite high despite what is evidently an almost complete coupling of the conducting modes to the viscous modes. The reason for the low decoupling ratio in this case is simply that, in contrast to superionic glass systems like the $\text{Li}_4\text{Si}_2\text{S}_7$ of Fig 2, the Li^+ wins the ionic "tug-o-war", because it has a much higher charge intensity than its large tetra-alkyl ammonium neighbor. Thus where Si^{4+} is the trapped particle in $\text{Li}_4\text{Si}_2\text{S}_7$ and Li^+ is free to roam in the structure, Li^+ is the trapped particle in the mixed salt system (19). Since it rarely escapes from its I-Li-I trap, it can only conduct by moving as part of the same cooperative structural rearrangement which relaxes a shear stress, hence which determines the glass transition. As a superionic system it is therefore a miserable failure notwithstanding its high LiI content.

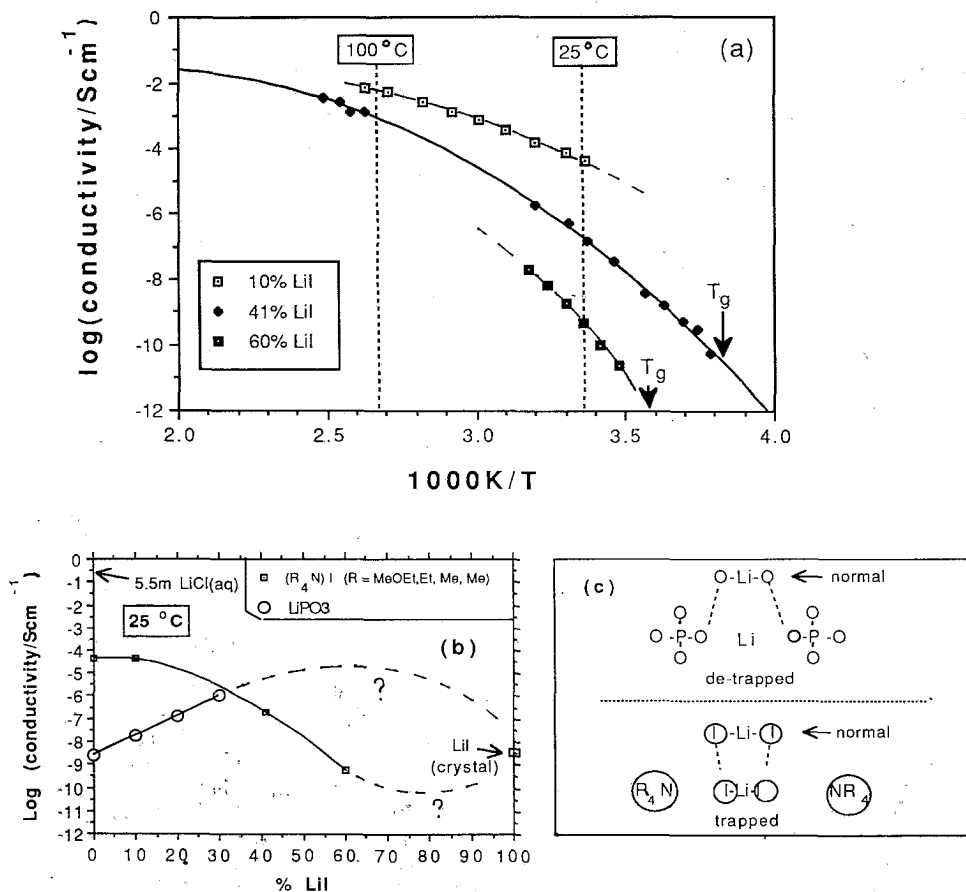


Figure 4 Part (a) Arrhenius plot of the conductivity of two lithium iodide-rich compositions in the system LiI-tetraalkyl ammonium iodide, showing the low values of conductivity at the glass transition temperature in this case. Tetra alkyl cation is [methoxy ethyl ethyl dimethyl (MOE)EM₂N⁺ for good supercooling ability, (see ref. 19).

Part (b) Comparison of ambient temperature conductivities or compositions in the system LiPO₃ + LiI and (MOE)EM₂N⁺-LiI.

Part (c) Explanation of the contrast of behaviors observed in Part (b) in terms of relative electrostatic competitiveness of lithium cation with respect to the second nearest neighbor species (P(V) on the one hand and the large tetra-alkyl ammonium cation on the other. Close approach of iodide anion to the lithium in the latter case results in an effective Li⁺ trap, eliminating decoupled motion as a conductivity mechanism.

The latter behavior is essentially the behavior of lithium salt-in-polymer electrolytes (20) which, however, are highly regarded as solid electrolyte candidate materials (21). The reason that salt-in-polymer electrolytes are well regarded is that the polymer host can provide a non-zero shear modulus above the glass transition, if the polymer is of high molecular weight, due to the chain entanglement phenomenon (22). This bestows rubbery solid properties on the electrolyte. The conductivity in these systems is also of order 10^{-14} S cm^{-1} at T_g , essentially for the same reason as in the case of the LiI salt system - namely, the small cation is thoroughly trapped. In the case of the salt-in-polymer system the trap for the Li^+ is formed by the ether oxygens of the polymer chain which function like the ether oxygens of crown ether type molecules. This trap is even more effective than that due to the loose I^- ions of the previous case. It is this strong coupling of the salt cation to the polymer which is the main problem with this type of "solid" electrolyte since it promotes low cation transport numbers. Low cation transport numbers in turn lead to polarization problems in cells utilizing such electrolytes.

Clearly what is needed is a system which can have both a high degree of decoupling, as in a superionic glass, and a T_g well below room temperature, in which sufficient polymer can be dissolved to give the rubbery modulus as in polymer electrolytes. Below, we describe some systems in which this objective can be achieved (23).

EXPERIMENTAL

Glassforming solutions were prepared by mixing weighed quantities of dried reagent grade materials in stoppered pyrex vials on a hot plate until fusion was complete, and cooling to room temperature. Samples for measurement of glass transition temperatures could be obtained by cooling the vials in liquid nitrogen until they shattered and then removing small quantities for encapsulation in aluminum DSC pans. Usually the glasses were hygroscopic. In low humidity (Arizona winter) conditions, experienced operators could encapsulate samples sufficiently rapidly that T_g data corresponded with those from (more tedious) dry-box loadings. The latter were, however, used in all operations involving AlCl_3 components.

Salt-in-polymer solutions were prepared by direct dissolution of PPO4000 in the melts. To obtain rubbery solutions high molecular weight PPO (MW 106) or PEO (MW 105) was dissolved in solvent (CH_3CN or acetone) and the salt mixture dissolved in the solution. The solvent was then removed by careful heating followed by slow vacuum evaporation. In some cases using high MW PEO we have been successful in obtaining direct dissolution in the molten salt, which is of course the preferable procedure. Success depends critically on complete absence of water.

Electrical conductivity measurements were made using dip-type two terminal cells with twin platinum electrodes which entered the vial through a sealed screw cap. The cell constant was about 0.2. Measurements were made in an automated system (24) in which an HP4192 frequency analyzer scanned frequency on command from a PC on arrival of the temperature of an aluminum block heater at a programmed value. Data were taken over a range of temperature from below the glass transition temperature to $\sim 200^\circ\text{C}$ depending on the thermal stability of the salt and polymer being studied.

RESULTS

Glass transition temperatures for various salts dissolved in lithium acetate, which is itself a strong glassformer, are shown in Fig. 5. This presentation permits estimates of the glass transition temperatures for individual salts which are usually not glassforming by themselves. As can be seen only LiClO_4 and LiClO_3 have T_g 's which are below 0°C . As expected from the close approach to the pure components in Fig. 1, mixtures of these two salts are easily glass-forming

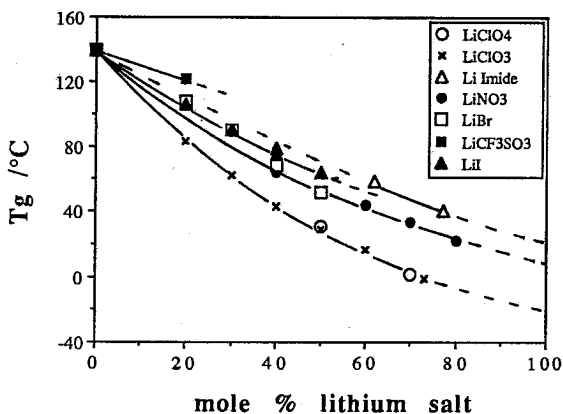


Figure 5 Glass transition temperatures for various binary solutions, based on lithium acetate as the first component. Extrapolations to 100% of the second component permit estimates of the glass transition temperatures for the individual second component salts.

and have T_g values of -10°C almost independent of composition. Of the systems studied by us so far, only melts containing AlCl_3 have lower glass transition temperatures.

A selection of conductivity data are shown in Fig. 6a using the usual Arrhenius representation. It can be seen that conductivities as high as $10^{-2} \text{ S cm}^{-1}$ can be measured at 25°C .

The latter values are obtained in the low T_g AlCl_3 -containing melts which unfortunately are incompatible with polyether polymers. For preparation of polymer-in-salt solutions it was therefore necessary to use LiClO_3 - LiClO_4 binary solutions, LiClO_4 - LiClO_3 - LiNO_3 ternary, or LiClO_4 - LiClO_3 - LiNO_3 - LiBr quaternary mixtures. Data for such solutions are shown in Fig. 6b, where it is noted that the addition of polymer reduces the conductivity of the polymer-free salt melt.

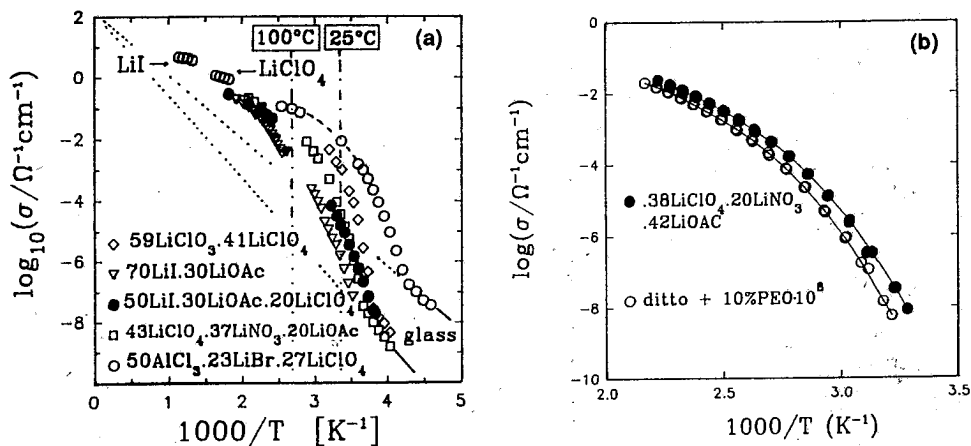


Figure 6 Part (a) Arrhenius plot of the conductivity of various lithium salt mixtures showing the attainment of very high conductivities at ambient temperature in certain cases.

Part (b) Arrhenius plots of LiClO_3 -free lithium salt melts with high resistance to crystallization (but lower conductivity) and its solution with 10 mol % repeat units of high molecular weight (10^8 Daltons).

To see how the high conductivity polymer-in-salt regime is reached from the normal salt-in-polymer regime, new data for the well-studied LiClO_4 -in-PPO4000 system are presented in Fig. 7. The previous highest salt content for which conductivities have been reported was $\text{M}:\text{O} = 1:8$ (25, 26). In this case the initially low conductivity of the pure polymer solvent increases rapidly with increasing salt content, and then passes through a maximum, as is well known from numerous studies, and reviews of studies, in this area (7, 21, 25, 26). It has been normal to terminate investigations of these systems at composition where the conductivity at room temperature has become too low to measure easily. The results in Fig. 7 show that a new regime of increasing conductivity commences at the higher salt concentration where the T_g passes through a maximum. The new regime and its potential for yielding superior rubbery electrolytes is, of course, the focus of this paper.

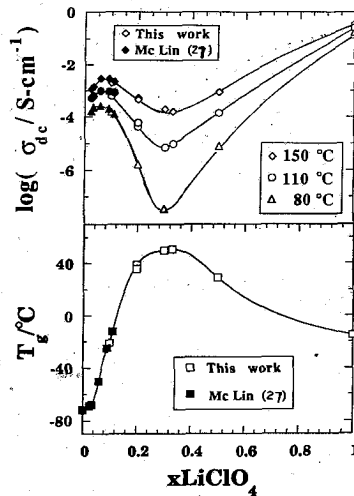


Figure 7 Isothermal conductivities of solutions of lithium perchlorate in PPO4000 showing successive maxima and minima, and the generation of high conductivities in the "polymer-in-salt" domain beyond the conductivity minimum.

DISCUSSION

The new domain commences at the composition where a maximum in the glass transition temperature (which is now far above room temperature) is reached. This composition may be thought of as marking the transition between "salt-in-polymer" and "polymer-in-salt" domains. The salt content at this boundary differs from system to system, and is influenced by both the propensity for formation of ion pairs in the salt and the magnitude of T_g in the pure salt (or salt mixture).

The boundary occurs because the capacity of the salt cations to serve as transient crosslinks between the polymer chains is limited. At the point where additional salt prefers to coordinate with ions rather than with polymer ether ligands, the driving force for increasing glass transition temperatures with increasing salt content is lost. Depending on the properties of the salt itself, the glass transition temperature will then either increase more slowly (for salts with high T_g values,

e.g. lithium acetate, $T_g = 134^\circ\text{C}$) or will decrease (e.g. LiClO_3 , $T_g = -10^\circ\text{C}$). The high conductivities of some of the polymer-in-salt electrolytes are a direct consequence of the decrease of the glass temperature to values well below room temperature in the favorable cases, e.g. LiClO_4 - LiClO_3 based salt mixtures.

It is important to note that T_g values near 0°C would not lead to high ambient temperature conductivities unless the conducting modes were also highly decoupled from the viscous modes. This is seen clearly from the poor ambient temperature conductivity of the strongly coupled 60Li.40TEMAI melt shown in Fig. 4 in which T_g may be far below room temperature. Thus the new electrolytes are also single ion (Li^+) conductors at their T_g and are cation-dominated conductors at temperatures well above T_g , (27). This conclusion has been supported by ion diffusivity and ^7Li spin lattice correlation relaxation time studies reported elsewhere, (28, 29).

Fig. 3 shows how the cation and matrix (anion) relaxation times approach each other as T rises above T_g but suggests that t_+ ($\approx \tau_c/\tau_\sigma$) should remain above 0.9 even at temperatures as high as $2T_g$ ($>200^\circ\text{C}$ for LiClO_4 - LiClO_3 based solutions).

The challenge now is to find chemically and electrochemically stable replacements for the LiClO_3 and LiClO_4 of the present systems which preserve, or preferably lower the present low T_g values, so that truly superior rubbery solid electrolytes suitable for a wide spectrum of electrochemical devices - including traction batteries - can be obtained.

ACKNOWLEDGMENTS

This work has been supported by the DOE under Grant No. DEFG02-89ER4535398 and by an interim "lifesaver" grant from the program of Dr. David Ingersoll of Sandia National Laboratory, for which we are very grateful.

REFERENCES

- (a) S.M. Smedley, *The Interpretation of Ionic Conductivity*, Plenum, N. Y., 1980.
 - (b) G.J. Janz, *Molten Salts Handbook*, Academic Press, New York, N.Y. (1967), pp. 54-58, 287-289.
- C.T. Moynihan, and C.A. Angell, in *Molten Salts*, Mamantov, G., Ed., Marcel Dekker: New York, 1969; p. 315.
- (a) C.A. Angell, *J. Non-Cryst. Sol.*, 131-133 (1991) 13.
 - (b) C. A. Angell in *Relaxations in Complex Systems*, ed. K. Ngai and G.B. Wright, National Technical Information Service, U.S. Department of Commerce, Springfield, VA 22161 (1985), pg. 1.
- G. Adam, and J.H. Gibbs, *J. Chem. Phys.* 43 (1965) 139.
- C. A. Angell, *J. Phys. Chem. Sol.*, 49 (8) (1988) 863.
- (a) J. Kawamura and M. Shimoji, *J. Non-Cryst. Sol.* 88 (1986) 286, 295.
 - (b) J. Kawamura and M. Shimoji, *Mater. Chem. Phys.* 23 (1989) 99.
- C.A. Angell, *Solid State Ionics* 9 & 10 (1983) 3.
- C. A. Angell, L. Boehm, P. A. Cheeseman and S. Tamaddon, *Solid State Ionics* 5 (1981) 659.

9. G. J. Exarhos, P. J. Miller, and W. M. Risen, *J. Chem. Phys.*, **60** (1974) 4145.
10. Changle Liu and C. A. Angell, *J. Chem. Phys.* **93** (1990) 7378.
11. (a) E. I. Kamitsos, M. A. Karakassides, and G. D. Chryssikos, *J. Phys. Chem.* **91**, 1067, 5807 (1987); **93**, 1604 (1989).
(b) E. I. Kamitsos, M. A. Karakassides, and G. D. Chryssikos, *Phys. Chem. Glasses*, **28**, 203 (1987); **30**, 19 (1989).
(c) E. I. Kamitsos, M. A. Karakassides, and G. D. Chryssikos, *Solid State Ionics*, **28-30**, 687 (1988).
12. G.D. Chryssikos and E.I. Kamitsos, *J. Mol. Liq.* **56** (1993) 349.
13. P.B. Macedo, C.T. Moynihan, and R.A. Bose, *Phys. Chem. Glasses* **13** (1972) 171.
14. C. T. Moynihan, N. Balitactac, L. Boone, and T.A. Litovitz, *J. Chem. Phys.* **55** (1971) 3013.
15. C. A. Angell, *Solid State Ionics* **18 & 19** (1986) 72.
16. C.A. Angell, *Mat. Chem. Phys.* **23** (1989) 143.
17. C.A. Angell, *Ann. Rev. Phys. Chem.* **43** (1992) 693.
18. Changle Liu, H. G. K. Sundar and C. A. Angell, *Mat Res. Bull.* **20** (1985) 525.
19. E. I. Cooper and C. A. Angell, *Solid State Ionics*, **9 & 10** (1983) 617.
20. M. B. Armand, Chabagno, J. M. and Duclot, M. J., in *Fast Ion Transport in Solids* Eds. P. Vashista, J.N. Mundy and G. K. Shenoy (Elsevier: North Holland, Amsterdam, 1979).
21. (a) M. Watanabe and N. Ogata, in *Polymer Electrolyte Reviews I*, eds. J.R. MacCallum and C.A. Vincent (Elsevier, London, 1988) Ch. 3; *Br. Polym. J.* **20** (1988) 181.
(b) M. A. Ratner, in *Polymer Electrolytic Reviews I*, Eds. J. R. MacCallum and C. A. Vincent, Elsevier, London, 1987, P. 173.
22. J.D. Ferry, *Viscoelastic Properties of Polymers*, Wiley, NY, 1980.
23. C. A. Angell, C. Liu and E. Sanchez, *Nature* **362** (1993) 137-139.
24. S. W. Martin and C. A. Angell, *J. Non-Cryst. Sol.*, **66** (1984) 429.
25. (a) M. Watanabe, J. Ikeda, and I. Shinohara, *Polymer J.*, **15**, 65, 175 (1983); M. Watanabe, and N. Ogata, *Br. Polym. J.*, **20**, 181 (1988).
26. (b) M. C. McLin and C. A. Angell, *J. Phys. Chem.* **95** (1991) 9464.
27. M. G. McLin and C. A. Angell, *Solid State Ionics*, **53-56** (1992) 1027-1036.
28. Jiang Fan, R.F. Marzke, and C.A. Angell, *Symp. Mat. Res. Soc.*, 1993 (in press).
29. C. A. Angell, J. Fan, R.F. Marzke, and E. Sanchez, *J. Non-Cryst. Sol.*, 1994 (in press).

Ion mobility and structural relaxation in glass

M.D. Ingram,* P. Maass† and A. Bunde†

* Department of Chemistry, University of Aberdeen, Aberdeen, Scotland

† Inst. of Theoretical Physics, Justus-Liebig University, Giessen, Germany.

Abstract

A dynamic structural model is described where ions in glass are mobile and are yet part of the glass structure. The model introduces the concepts of memory, mismatch energy, and fluctuating pathways. Conductivity variations in single and mixed-cation glasses have previously been rationalised on this basis. We examine here some wider implications relative to EXAFS results, internal friction peaks, and the effect which restricted ionic mobility has on the strength/fragility of glass-forming systems.

INTRODUCTION

The general pattern of conductivity/temperature dependence in ionic systems, above and below T_g is well known [1]. One commonly observes linear Arrhenius plots below T_g and curvature in the liquid state where conductivity fits the Vogel-Tamman-Flucher equation, $\sigma = \sigma_0 \exp [-B/(T-T_0)]$. Usually, it is said that conductivity below T_g involves a solid-like mechanism [2,3], where cationic motions occur within a rigid framework. In the melt, on the other hand, ionic motion is a cooperative process, where cations and anions may be equally mobile [4].

The classical theory of ion transport in glass, advanced some years ago by Anderson and Stuart [5], is clearly a solid-state model. Cations move into nearby empty sites, but must first overcome an activation energy, which contains contributions from an elastic strain energy E_s and a coulombic binding energy E_c . This theory assumes that there are plenty of empty sites in glass. The problem is simply how to move the ions from site to site. We argue that it is time to re-examine this postulate in light of the experimental evidence and increasing knowledge of glass structure.

First, we look at information about the coordination of cations in glasses obtained from EXAFS data [6]. Figure 1 shows K^+ and Cs^+ ion environments in K_2SiO_3 , Cs_2SiO_3 and in mixed $KCsSiO_3$ glasses. The K^+ and Cs^+ sites, which emerge clearly in their respective single-cation glasses, can still be recognised in the mixed-cation system. The conclusion is that the alkali cations are not just "dropping into" sites already present in the glass network, but are actively organising the local structure to suit their own *chemical* requirements. It is possible, e.g. ref. [7], that these sites become "frozen in" at T_g , becoming, in effect, a fixture in the glass structure.

We would argue otherwise. Figure 2 contains internal friction peaks obtained by Shelby and Day [8] in $Li_2O.3SiO_2$ and mixed $Li_2O.Na_2O.3SiO_2$ glasses. A dominant feature is the *mixed-alkali peak* which appears in the temperature range between T_g and ambient. Because of the EXAFS result, we can now interpret this peak as involving the interconversion of Li^+ and Na^+ sites, triggered by the movement of these ions into each other's sites. This interconversion involves changing the coordination number as well as the size of the sites.

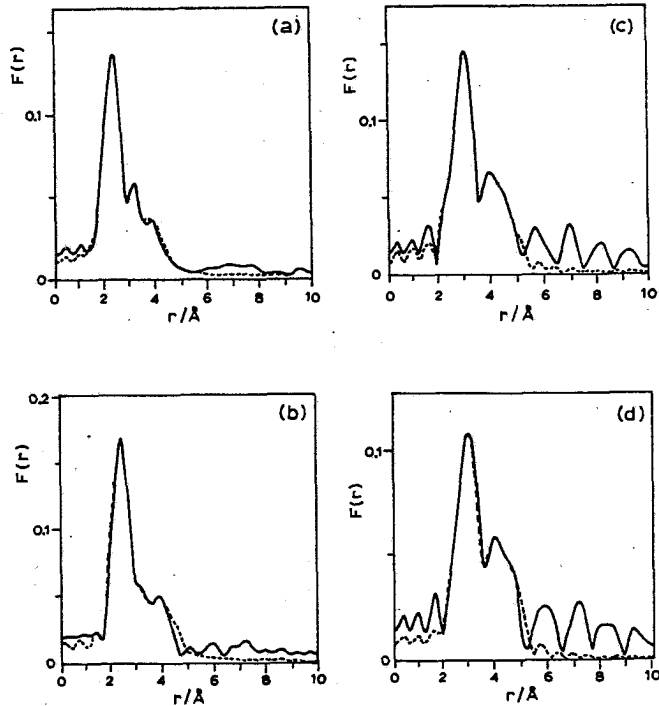


Figure 1 *Fourier transforms of the weighted EXAFS spectra from the K-edge of potassium in (a) $K_2Si_2O_5$, (b) $KCsSi_2O_5$ and the L_{III} edge of caesium in (c) $Cs_2Si_2O_5$ and (d) $KCsSi_2O_5$ (redrawn from reference [6])*

In other words, we are looking at a structural relaxation which, as Isard remarked [9], can lead to some manifestations of a “second glass transition” appearing in mixed-cation glasses. One such manifestation is the *thermometer effect*, where the volume of the thermometer at 0°C changes after heating to 100°C, and cooling again to 0°C.

This “delayed elasticity” is observed in all mixed-cation glasses [10] and has many important technological consequences. Along with other aspects of the mixed-alkali effect it has remained one of the apparently insoluble mysteries of glass science.

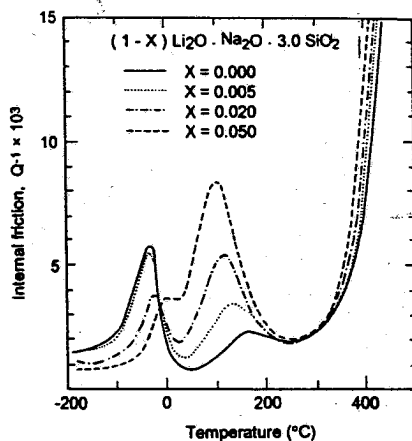


Figure 2 *Internal peaks [8] for single and mixed-cation silicate glasses. Note how even small replacements of Li^+ by Na^+ promote the growth of the mixed-alkali peak, appearing at approx. 100°C . We propose that all such peaks arise from relaxations of the glass structure.*

THE DYNAMIC STRUCTURE MODEL [11,12]

The model is based on three main postulates:

- [i] **Ions in glass migrate by a hopping mechanism.** This does not imply that ions “leap over” energy barriers, but only that they move stepwise from site to site.
- [ii] **Cations determine their own chemical environments.** This is simply the EXAFS result, described above.
- [iii] **Ionic movement below T_g involves structural relaxation.** This follows since even mobile ions are part of the glass structure.

The detailed elaboration of this model by Monte Carlo methods is given elsewhere [11,12]. For simplicity, the cation sites have been placed in the computer calculations on either square or cubic lattices, and some of the sites are left unoccupied. These empty sites can readily receive incoming Li^+ ions, for example, if there is still a *memory* of previous occupancy by Li^+ ions, but this process will be much less easy if the memory is lost, or if it is replaced by a memory of different cation, say Na^+ or K^+ . In either of these two cases a mismatch energy must be overcome, which involves the reorganisation of the local structure to provide the correct environment for the Li^+ ion. This is called a Li site.

What is distinctive about this new model is that it gives rise to *fluctuating* pathways. New pathways in glass are formed by the movement of the ions, but parts of the pathway can also disappear if the ions stop visiting these regions.

Despite (or perhaps because of) the inherent simplicity of the model, it does lead [11,12] to a correct prediction of conductivity variations in single-cation glasses, and to the calculated "crossover" in ionic mobilities which is seen in mixed-cation glasses.

But can the computer calculations now shed any more light on the delayed elasticity (or volumetric) effects which are seen in mixed-cation glasses? In other words, can we add anything more to what has been said above about the thermometer effect? At present we have not attempted a rigorous analysis of this question. Nevertheless it is interesting here to speculate about a topic of such importance to the glass technologist.

Figure 3(a) shows the calculated $A^+\bar{A}$ pathways in a "glass" containing only A^+ ions, and Figure 3(b) the corresponding $A^+\bar{A}$ and $B^+\bar{B}$ pathways in a corresponding system containing equal numbers of A^+ and B^+ ions. The situation regarding conducting pathways has changed dramatically. In the single-cation glass, most cations are on, or close to, an interconnected network of conducting sites. In the mixed-cation glass on the other hand, this network breaks down into small islands of $A^+\bar{A}$ and $B^+\bar{B}$ sites.

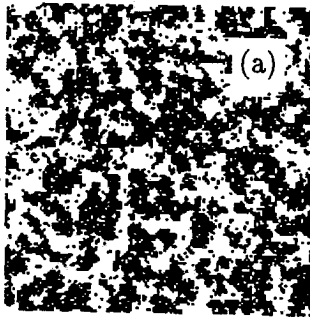


Figure 3(a) *Fluctuating pathways (black squares) generated by Monte Carlo calculation on a square lattice, see ref. [12], for a "glass" where 25% of the sites are occupied by A^+ cations. Note that although this is an instantaneous "snapshot" of the conduction pathway, that many A^+ cations are on or close to an interconnected network of (empty or filled) \bar{A} sites.*

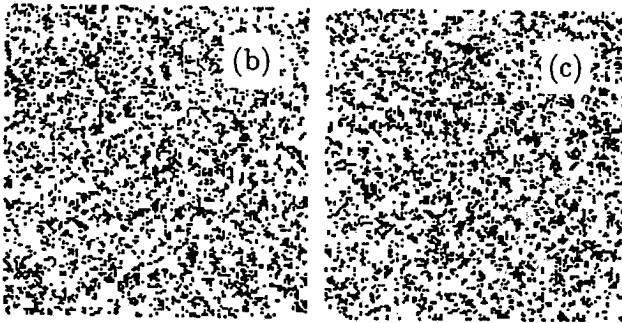


Figure 3(b) and (c) Corresponding conduction pathways (see Figure 3(a)) in a mixed-cation “glass”, where 50% of the A^+ are replaced by B^+ ions. The A^+A^- pathways are shown in (b) and the B^+B^- pathways in (c). Note that neither cation (in this simulation) is able to establish a continuous conduction pathway which does not involve ions moving into “wrong” sites.

Not only has the system lost the property of long-range ionic mobility but, since the ions are effectively stuck in or near to their existing positions, it becomes harder for them to move from “island” to “island”, and for thermal equilibrium to be established. It could be this delay which, in practice, makes the *real* mixed-cation glasses unsuitable for use in thermometers, or in other applications where density or refractive index must not vary once the temperature is fixed.

ION MOBILITY AND GLASS STRUCTURE

In many ways, the dynamic structure model turns on its head the argument which relate ionic conductivity to glass structure. We are now asking not so much how conductivity depends on structure, but rather on how structure depends on ionic mobility.

Elsewhere, Chryssikos *et al.* [13,14] have discussed variations in *fragility* in lithium borate with changing $Li_2O.B_2O_3$ ratios, and with replacement of Li_2O by Na_2O in the mixed-cation $LiBO_2/NaBO_2$ glasses. The fragility *in the melt* was expressed either by the “steepness index”, $d \log \eta/d(T^*/T)$, where T^* is an isoviscous reference temperature close to T_g , or is inferred from values of $\Delta C_p/C_p(\text{liquid})$ at T_g . The fragility is understood by Angell [15] to measure the extent to which structure in the melt is modified by changes in temperature. Conversely, “strength” is an indication of structural persistence.

It is clearly demonstrated that lithium borate melts become more fragile as the Li_2O content is increased, and that they become *less* fragile as Li_2O is partially replaced by Na_2O .

It seems, therefore, that fragility and high cation-mobility go together in these glasses. This result is not surprising in terms of above discussion, where we have argued that ionic movement is itself a catalyst for structural change. There is no contradiction here. The movement of Li^+ ions into Na sites and Na^+ ions into Li sites (discussed above) continues in mixed cation glasses below T_g . The effect is therefore to increase rather than diminish the degree of continuity between molten and glassy states. Volumetric instabilities in the glass are not inconsistent with "strength" in the sense in which the word is used here. In a more general discussion of strength and fragility [13-15], other factors such as the nature of the covalently-bonded networks and also the details of the possible structural changes which occur on cooling will clearly have to be considered. What we are saying here is that the "self-structuring" properties of the mobile cations should not be overlooked.

CONCLUSIONS

We have referred briefly here to a model for ion transport in glass which involves ion-site mismatch energies, memory effects and dynamically determined pathways. The model implies that structural relaxations in glass are strongly coupled to the movements of ions, and that glass structure itself is strongly influenced by ionic mobility. This very simple idea may provide a clearer understanding of the mixed-alkali and thermometer effects, and may also help in the discussion of strength-fragility concepts in glass/melt systems.

The authors are indebted to the British Council and to German Academic Exchange Service for funding an Academic Research Collaboration between our research groups.

References

1. M.D. Ingram, *Phys. Chem. Glasses*, 28, 215 (1987).
2. C.T. Moynihan, N. Balitactac, L. Boone and T.A. Litovitz, *J. Chem. Phys.*, 55, 3013 (1971).
3. C. Angell, *Solid State Ionics* 9-10, 3 (1983); 18-19, 72 (1986).
4. M.D. Ingram and G.G. Lewis, *J. Chem. Soc. Farad. Trans. 1*, 70, 490 (1974).
5. O.L. Anderson and D.A. Stuart, *J. Amer. Ceram. Soc.*, 37, 573 (1954).
6. G.N. Greaves *et al.*, *Inst. Phys. Conf. Ser. No. III*, 411 (1990).
7. G. Tomandl and H.A. Schaeffer, *J. Non-Cryst. Solids*, 73, 19 (1985).
8. J.E. Shelby and D.E. Day, *J. Amer. Ceram. Soc.*, 52, 169 (1969).
9. J.O. Isard, *J. Non-Cryst. Solids*, 1, 235 (1969).
10. A.H. Dietzel, *Glastech. Ber.*, 56, 291 (1983).
11. P. Maass, A. Bunde and M.D. Ingram, *Phys. Rev. Letts.*, 68, 3064 (1992).
12. A. Bunde, M.D. Ingram and P. Maass, *J. Non-Cryst. Solids* (1994, in press).
13. G.D. Chryssikos, J.A. Duffy, J.M. Hutchinson, M.D. Ingram, E.I. Kamitsos and A.J. Pappin, *J. Non-Cryst. Solids* (1994, in press).
14. G.D. Chryssikos, E.I. Kamitsos, J.A. Kapoutsis and A.P. Patsis (published in this Volume).
15. C.A. Angell, *J. Non-Cryst. Solids*, 131, 13 (1991).

IONIC CONDUCTIVITY AND STRUCTURE OF SUPERIONIC GLASSES CONTAINING SILVER AND CUPROUS HALIDES

Tsutomu Minami,^a Masahiro Tatsumisago,^a and Nobuya Machida^b

^aDepartment of Applied Materials Science, Osaka Prefecture University, Sakai, Osaka 593, Japan

^bDepartment of Chemistry, Konan University, Higashinada-ku, Kobe 658, Japan

Three topics in recent progress of superionic glasses containing silver and cuprous halides were reviewed: (1) enhancement on conductivity of superionic glasses containing two kinds of oxoanions, (2) formation of frozen α -AgI in superionic glass matrices at ambient temperature, and (3) relation between glass-forming ability and acidity of the melts for cuprous ion conducting glasses. In the first topic, silver conducting properties and structure of the glasses containing two kinds of oxosalts in the two systems AgI-Ag₂MoO₄-AgPO₃ and AgI-Ag₂MoO₄-Ag₃PO₄ were discussed in order to investigate "the mixed anion effect"; i.e. an enhancement of ion conductivity was observed in glasses containing two kinds of anion species and/or of glass formers. In the second topic, preparation condition and thermal and electrical properties were reported for the rapidly quenched superionic composites of which high-temperature phase α -AgI was frozen in glass matrices at room temperature. In the third topic, the preparation condition of cuprous ion conducting glasses was discussed from the viewpoint of the acidity of the melts containing cuprous ions.

Introduction

Solid electrolytes with high ion conductivities have been extensively investigated for their potential applications to solid-state batteries, electrochromic devices, sensors, and so on (1). The high temperature phase of crystalline silver iodide (α -AgI), which is one of the prototypes of solid electrolytes, has attracted much interest because of its high conductivities of more than 10 Scm⁻¹ comparable to those of the best liquid electrolytes (2). However, α -AgI exhibits a problem to transform at 147°C to the β -phase with a conductivity of only 10⁻⁵ Scm⁻¹. A number of investigations have been done to achieve high ion conductivities at room temperature by use of AgI (3). Vitrification was found to be one of the excellent techniques to achieve high conductivities at room temperature (4); we have developed a number of the so-called "superionic conducting glasses" in the systems based on silver iodide (5, 6). Although these superionic glasses exhibited conductivities as high as 10⁻⁴ ~ 10⁻² Scm⁻¹, further improvement of the conductivities has been desired for their application to most electrochemical devices with high performance.

In the present article, we review three different approaches to the conductivity improvement at room temperature in the glass-based ionic conductors. The first approach is the enhancement of conductivity of superionic glasses containing two kinds of oxoanions. This approach is based on the "mixed anion effect" and/or the "mixed former effect"; i.e. an enhancement of ion conductivity was observed in the glasses containing two kinds of anion species and/or of glass formers (7, 8). The second approach is the formation of frozen α -AgI in superionic glass matrices at ambient temperature by use of twin-roller rapid quenching technique (9-13). This approach is based on the idea that the extremely high quenching rate and the presence of matrix glasses would suppress the α - β transformation of AgI crystal to yield highly conductive crystal-glass composites. The third approach is the development of new cuprous halide-based superionic glasses. This approach is based on the prediction that, since the high ion conductivity of AgI-based glasses is derived from the d¹⁰ electronic

configuration of Ag^+ , which exhibits a soft acid character, cuprous halide-based glasses in which Cu^+ ions have a similar d^{10} configuration and smaller size could become more conductive (14). In this approach, the preparation condition of cuprous ion conducting glasses is discussed from the viewpoint of the acidity of the melts containing cuprous ions, because cuprous ions are easily to disproportionate into Cu^0 and Cu^{2+} ions during melting in the process of glass preparation.

Enhancement on Conductivity of Superionic Glasses Containing Two Kinds of Oxoanions

Recently some papers (15-18) have reported the "mixed anion effect" and/or "mixed former effect"; i.e. a positive deviation from additivity in the ion conductivity is observed in the glasses containing two kinds of anion species and/or of glass formers. This phenomenon shows a striking contrast to the well known "mixed cation effect"; i.e. the conductivity of glasses show the negative deviation from additivity, when two kinds of cation species, which are main carriers for electrical conduction, are mixed. The "mixed anion effect" and/or "mixed former effect" is a subject of interest to see the reason for the phenomenon itself and also to obtain glasses with high ion conductivity, since not all the glasses containing two kinds of anion species and/or glass formers show the enhancement of conductivity. We assume that the enhancement of conductivity closely relates to the structural change of glasses with mixing two kinds of anion species and/or glass formers. Thus we try to prepare silver ion conducting glasses containing two kinds of oxosalts in the system $\text{AgI-Ag}_2\text{MoO}_4\text{-Ag}_3\text{PO}_4$ with the comparison of the system $\text{AgI-Ag}_2\text{MoO}_4\text{-Ag}_3\text{PO}_4$.

The glass-forming regions in the two systems $\text{AgI-Ag}_2\text{MoO}_4\text{-Ag}_3\text{PO}_4$ and $\text{AgI-Ag}_2\text{MoO}_4\text{-AgPO}_3$ are shown in Fig. 1(a) and Fig. 1(b), respectively. In the figures open circles, open triangles and closed circles denote glassy, partially crystalline and crystalline samples, respectively. The glass-forming region of the $\text{AgI-Ag}_2\text{MoO}_4\text{-Ag}_3\text{PO}_4$ system (b) is broader than that of the $\text{AgI-Ag}_2\text{MoO}_4\text{-Ag}_3\text{PO}_4$ system (a), and the glasses without AgI can be obtained in the former system.

Figure 2 shows FT-IR spectra of the $75\text{AgI}\cdot(25-y)\text{Ag}_2\text{MoO}_4\cdot y\text{Ag}_3\text{PO}_4$ glasses over the wavenumber range of $1400\text{-}400\text{ cm}^{-1}$. The composition of these glasses lie on the horizontal line of 75 mol% AgI in the composition triangle (Fig. 1(a)). Three major absorption bands at about 975, 795 and 555 cm^{-1} and two weak absorption bands at about 910

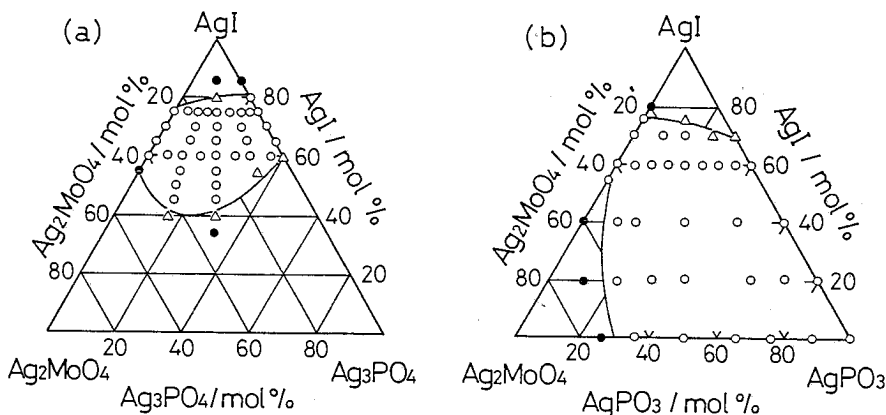


Fig.1. Glass forming regions in the systems $\text{AgI-Ag}_2\text{MoO}_4\text{-Ag}_3\text{PO}_4$ (a) and $\text{AgI-Ag}_2\text{MoO}_4\text{-AgPO}_3$ (b); (o) glassy, (Δ) partially crystalline, (\bullet) crystalline.

and 875 cm^{-1} are observed in each glass. The bands at about 795 and 875 cm^{-1} are weakened and those at about 975 , 910 and 555 cm^{-1} are strengthened with increasing Ag_3PO_4 content. The former bands, 795 and 875 cm^{-1} , are assigned to the ν_3 and ν_1 modes, respectively, of tetrahedral MoO_4^{2-} ions (19). The latter bands, 975 , 910 and 555 cm^{-1} , are assigned to the ν_3 , ν_1 , and ν_4 modes, respectively, of tetrahedral PO_4^{3-} ions (19, 20). There seem to be no other absorption bands in any glasses. These results indicate that those glasses in the system $\text{AgI-Ag}_2\text{MoO}_4\text{-Ag}_3\text{PO}_4$ contain no condensed macroanions and consist of Ag^+ , I^- , and discrete, monomeric ortho-oxoanions MoO_4^{2-} and PO_4^{3-} only, as expected from their compositions, and then suggest that the frame work structure of oxoanions, MoO_4^{2-} and PO_4^{3-} , dose not change with mixing two kinds of oxosalts, Ag_2MoO_4 and Ag_3PO_4 .

Figure 3 shows the FT-IR spectra of the $60\text{AgI}\cdot(40-z)\text{Ag}_2\text{MoO}_4\cdot z\text{Ag}_3\text{PO}_3$ glasses over the wavenumber range of $1400\text{-}400\text{ cm}^{-1}$. The composition of these glasses lie on the horizontal line in Fig. 1(b), i.e. they have a constant AgI content (60 mol%) and various mole ratios of molybdate to phosphate: (a)~(e) are the spectra of $60\text{AgI}\cdot(40-z)\text{Ag}_2\text{MoO}_4\cdot z\text{Ag}_3\text{PO}_3$ glasses, of which the Ag_3PO_3 content increases from (a) to (e). The spectrum (a) is of the $60\text{AgI}\cdot40\text{Ag}_2\text{MoO}_4$ glass, where there are two absorption bands at 795 and 875 cm^{-1} , assigned respectively to the ν_3 and ν_1 modes of monomeric tetrahedral MoO_4^{2-} ions. This result indicates that the active species in the $60\text{AgI}\cdot40\text{Ag}_2\text{MoO}_4$ glass are monomer MoO_4^{2-} ions only, similar to the case of the $75\text{AgI}\cdot25\text{Ag}_2\text{MoO}_4$ glass discussed above.

In the spectrum (e) of the $60\text{AgI}\cdot40\text{Ag}_3\text{PO}_3$ glass, there are six absorption bands at about 1225 , 1050 , 890 , 770 , 510 , and 470 cm^{-1} . The strong absorption bands at 1225 and 1050 cm^{-1} are respectively assigned to the ν_{as} and the ν_s modes of PO_2^- units in meta-phosphate groups, which have chain or ring structure(20). The absorption bands at 890 and 770 cm^{-1} are ascribed to the ν_{as} and ν_s modes of P-O-P stretching, and the bands at 510 and 470 cm^{-1} to O=P-O⁻ units. These results suggest that the phosphate groups in the glass exist as the meta-phosphate anion form of linear chain or ring structure of PO_4 tetrahedra, as expected from the chemical composition.

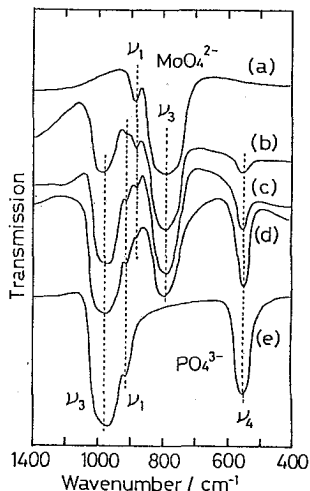


Fig. 2. FT-IR spectra of the glasses $75\text{AgI}\cdot(25-y)\text{Ag}_2\text{MoO}_4\cdot y\text{Ag}_3\text{PO}_4$; (a) $y=0$, (b) $y=6.25$, (c) $y=12.5$, (d) $y=18.75$, (e) $y=25$.

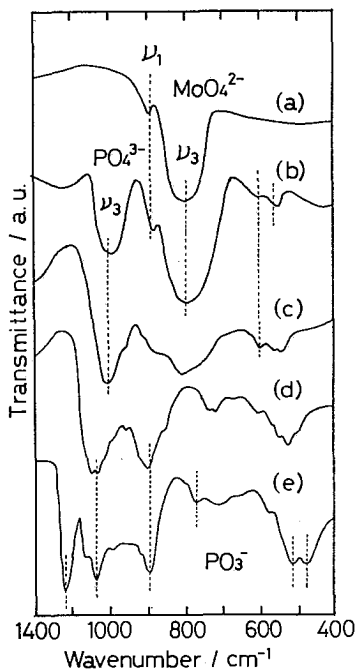


Fig. 3 FT-IR spectra of the glasses $60\text{AgI}\cdot(40-z)\text{Ag}_2\text{MoO}_4\cdot z\text{Ag}_3\text{PO}_3$; (a) $z=0$, (b) $z=10$, (c) $z=20$, (d) $z=30$, (e) $z=40$.

The spectrum (b) is of the $60\text{AgI}\cdot 30\text{Ag}_2\text{MoO}_4\cdot 10\text{AgPO}_3$ glass. In the spectrum, there are three absorption bands at 995, 600, and 550 cm^{-1} , in addition to the two absorption bands at 875 and 795 cm^{-1} ascribed to the ortho-molybdate anions, MoO_4^{2-} . The absorption bands at 995 and 550 cm^{-1} are ascribed to the ν_3 and ν_4 of the monomeric ortho-phosphate ions, PO_4^{3-} , and the absorption band at 600 cm^{-1} is assigned to the ν_{as} mode of Mo-O-Mo bands attributed to the formation of condensed ions of MoO_4 tetrahedra (19).

The absorption bands ascribed to monomeric ortho-phosphate ions, PO_4^{3-} , are weakened and the absorption bands ascribed to condensed units of PO_4 tetrahedra are strengthened with an increase in the AgPO_3 content in the spectra (b) - (d).

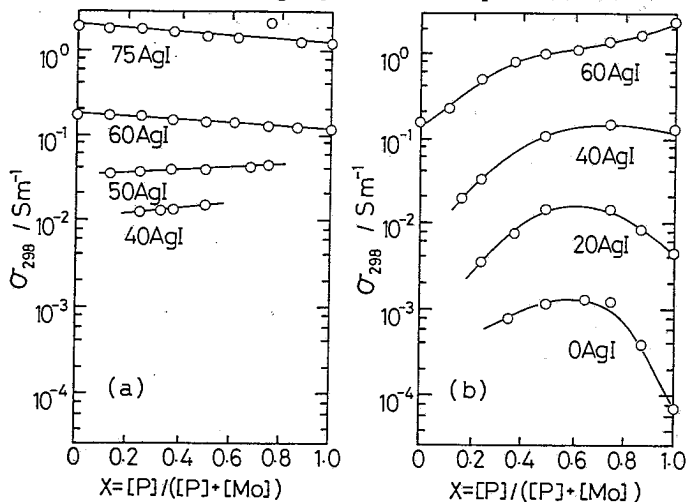


Fig. 4. Conductivities at 298 K, σ_{298} , of the glasses in the two systems AgI- Ag_2MoO_4 - Ag_3PO_4 (a) and AgI- Ag_2MoO_4 - AgPO_3 (b) as a function of the composition parameter x ; $x = [\text{P}] / ([\text{P}] + [\text{Mo}])$.

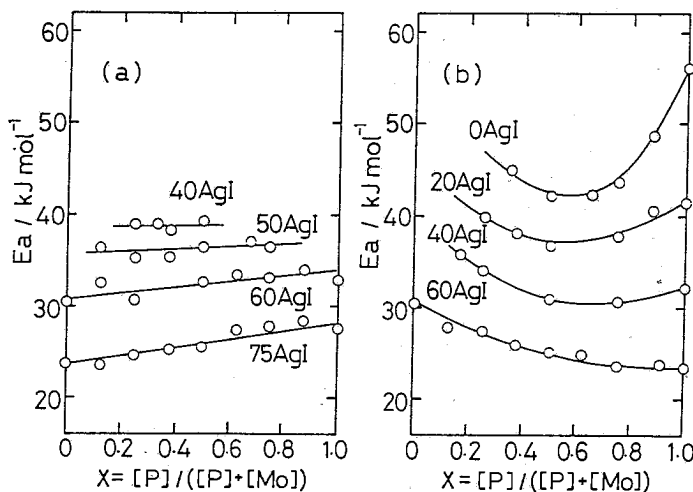


Fig. 5. Activation energies for conduction, E_a , of the glasses in the two systems AgI- Ag_2MoO_4 - Ag_3PO_4 (a) and AgI- Ag_2MoO_4 - AgPO_3 (b) as a function of the composition parameter x ; $x = [\text{P}] / ([\text{P}] + [\text{Mo}])$.

Observation of the absorption bands resulting from such monomeric ortho-phosphate anions, PO₄³⁻, and the condensed units of MoO₄ can be explained by the occurrence of the reaction $2 \text{MoO}_4^{2-} + \text{PO}_3^- \longrightarrow \text{Mo}_2\text{O}_7^{2-} + \text{PO}_4^{3-}$ in the melt. The freezing of the melt through quenching causes the coexistence of these structural units in the glass. This result suggests that the frame work structure of oxoanions is changed by mixing two kinds of oxosalts, Ag₂MoO₄ and AgPO₃.

Figures 4(a) and 4(b) show the composition dependence of ion conductivity at 298 K, σ_{298} , of the glasses in the systems AgI-Ag₂MoO₄-Ag₃PO₄ and AgI-Ag₂MoO₄-AgPO₃, respectively; the abscissa of the figures is a composition parameter x, which denotes the ratio of the number of phosphorus atoms to the total number of phosphorus plus molybdenum atoms included in the glasses; $y = [\text{P}] / ([\text{P}] + [\text{Mo}])$. In the system AgI-Ag₂MoO₄-Ag₃PO₄, the conductivities for four series of glass compositions with a constant AgI content (75, 60, 50 and 40 mol%) are shown in Fig. 4(a). At a given composition parameter x, the conductivity of these glasses increases with an increase in the AgI content. The conductivity of each series of glass composition with 75, 60, 50 and 40 mol% AgI linearly changes with the composition parameter x, and this change of the conductivity with x is governed by additivity. Hence, the enhancement of conductivity is not observed for the glasses in the system AgI-Ag₂MoO₄-Ag₃PO₄, in which the frame work structure of oxoanions, MoO₄²⁻ and PO₄³⁻, does not change with mixing two kinds of oxosalts.

In the system AgI-Ag₂MoO₄-AgPO₃, in which the frame work structure of oxoanions of the glasses is changed by mixing two kinds of oxosalts, the conductivities for four series of glass composition with a constant AgI content (60, 40, 20 and 0 mol%) are shown in Fig. 4(b). The conductivities of each series of glass composition with 60, 40, 20 and 0 mol% AgI show a maximum at around x=0.6. The enhancement of conductivity is observed for these glasses in the system AgI-Ag₂MoO₄-AgPO₃, in contrast to the case of the system AgI-Ag₂MoO₄-Ag₃PO₄. The enhancement of conductivity diminishes with an increase in the AgI content. This behavior probably relates to the fact that the conductivity of the glasses is primary controlled by the AgI content.

The activation energy for ionic conduction, E_a, of the glasses in the systems AgI-Ag₂MoO₄-Ag₃PO₄ and AgI-Ag₂MoO₄-AgPO₃ are plotted in Fig. 5(a) and Fig. 5(b), respectively, as a function of the composition parameter x. In the system AgI-Ag₂MoO₄-Ag₃PO₄ E_a of each series of glass composition with 75, 60, 50 and 40 mol% AgI linearly changes with the composition parameter x. The behavior of E_a with composition is very similar to that of the conductivity as shown in Fig. 4(a).

In the system AgI-Ag₂MoO₄-AgPO₃ (Fig. 5(b)), the minimum in E_a is observed at around x=0.6 in each series of glass composition with 60, 40, 20 and 0 mol% AgI. The position of the minimum in E_a is the same as that of the maximum in σ_{298} of the AgI-Ag₂MoO₄-AgPO₃ glasses. This result suggests that the enhancement of conductivity is dominantly governed by the decrease in E_a with mixing of two kinds of oxosalts.

These results indicate that the mixed anion effect in conductivities is closely related to the structural change of oxoanions, which form frame work structure of the glasses.

Formation of frozen α -AgI in superionic glass matrices at ambient temperature

The superionic conducting phase α -AgI, which is thermodynamically stable only above 147°C, was frozen at room temperature in various kinds of glass matrices in the systems AgI-Ag₂O-M_xO_y (M_xO_y = B₂O₃, P₂O₅, GeO₂, V₂O₅, MoO₃, and WO₃) (9-13).

Figure 6 shows the X-ray diffraction patterns at ambient temperature for the quenched AgI-Ag₂O-B₂O₃ samples with a constant mole ratio Ag₂O/B₂O₃ of 3 (ortho-oxosalt composition) and different AgI content of 78 mol% (a, b) and 82 mol% (c, d, e). Open and closed circles denote the diffraction peaks due to α - and β -AgI, respectively. Since glass formation was observed in the range up to 75 mol% AgI when the metal-plate press quenching was performed, compositions in Fig. 6 are out of the glass-forming range. In the

case of 78 mol% AgI, the diffraction peaks due to β -AgI are observed when the metal-plate press quenching was performed. By using the twin-roller quenching which gives a larger cooling rate, on the other hand, the halo pattern due to glassy state is observed for the same composition. In the case of 82 mol% AgI, the metal-plate press quenching results in the formation of only β -AgI as in the case of 78 mol% AgI. However, when the twin-roller quenching is used, the diffraction peaks due to α -AgI are observed and the peak intensity is increased with an increase in the cooling rate. The estimated cooling rate of these quenchings is shown in the figure.

Figure 7 is a phase diagram for the AgI-Ag₂O-B₂O₃ (Ag₂O/B₂O₃ = 3) system to show which phases are obtained when the cooling rate and the chemical composition are changed (9). Each symbol represents the phases obtained during the melt quenching. From this diagram the α -phase turns out to be only frozen when the AgI content is slightly larger than the glass formation limit. The cooling rate should also be higher than 10⁵ K/s to obtain α -AgI at room temperature.

Figures 8(a) and 8(b) show the typical examples of heating and cooling curves of DSC and the temperature dependence of the conductivities for the samples 78AgI•7.3Ag₂O•14.7MoO₃ and 82AgI•13.5Ag₂O•4.5B₂O₃, respectively. The heating and cooling rates of DSC measurements are 1°C/min. With increasing temperature, the conductivities are increased in the Arrhenius type variation up to around 138–140°C in both samples.

In the case of the heating process of the molybdate sample in Fig. 8(a), an abrupt decrease in conductivity is observed at 138°C and a large increase at 148°C. The large conductivity decrease at 138°C corresponds to an exothermic peak in the heating curve of DSC. This exothermic peak is due to the crystallization of the glass matrices to yield less conductive β -AgI. The large increase in conductivity at 148°C corresponds to an endothermic peak in the heating curve of DSC, which is due to the phase transformation of AgI crystal in the sample from the β - to α -phase. Similar results were obtained for the twin-roller quenched 79AgI•15.8Ag₂O•5.2P₂O₅ and 80AgI•10Ag₂O•10V₂O₅ glasses.

However, in the case of the heating process of the borate sample in Fig. 8(b), there are no drastic changes in conductivity except a small

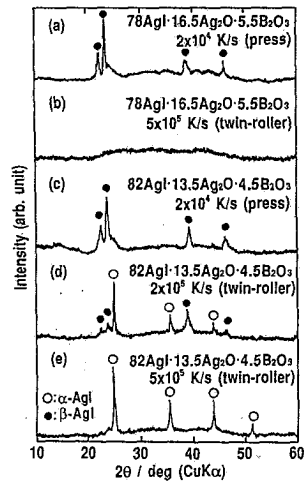


Fig. 6. X-ray diffraction patterns for the melt-quenched samples in the system AgI-Ag₂O-B₂O₃. "Press" and "twin-roller" mean the metal-plate press quenching and the twin-roller quenching, respectively, the estimated cooling rate of which is shown in the figure.

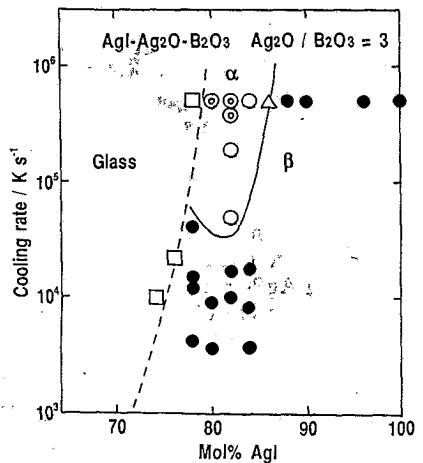


Fig. 7. Crystalline phases observed in the melt-quenching samples with various cooling rates and compositions in the system AgI-Ag₂O-B₂O₃. □; glass, ⊙; α -AgI only, ○; α -AgI > β -AgI, Δ ; β -AgI > α -AgI, ●; β -AgI only.

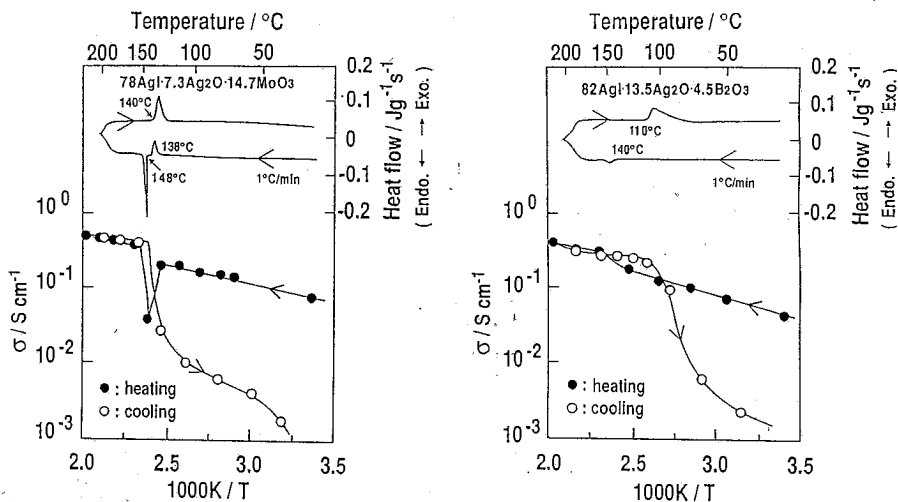


Fig. 8. Heating and cooling curves of DSC and the temperature dependence of conductivities for the twin-roller quenched $78\text{AgI}\cdot 7.3\text{Ag}_2\text{O}\cdot 14.7\text{MoO}_3$ composite (a) and $82\text{AgI}\cdot 13.5\text{Ag}_2\text{O}\cdot 4.5\text{B}_2\text{O}_3$ composite (b).

increase observed near 140°C . Such a small increase in conductivity corresponds to a small endothermic peak at around 147°C in the heating curve of DSC. This endothermic peak is due to the transformation of small amounts of the residual β - to α - phase in the glass matrices. Similar results were obtained for the twin-roller quenched $78\text{AgI}\cdot 11\text{Ag}_2\text{O}\cdot 11\text{GeO}_2$ and $80\text{AgI}\cdot 10\text{Ag}_2\text{O}\cdot 10\text{WO}_3$ glasses. These results indicate that the glass matrices with relatively high T_g like borates, germanates and tungstates are hardly to crystallize at temperature lower than the α - β phase transformation temperature of 147°C , in contrast to the case of the glass matrices with relatively low T_g like molybdates, phosphates and vanadates which are likely to crystallize at temperatures much lower than the α - β transition temperature.

On the other hand, in the case of the cooling process, the conductivity starts to drop at 140 and 110°C in the molybdate and borate samples, respectively, as shown in Figs. 8(a) and 8(b). These large decreases in conductivity also correspond to exothermic peaks in the cooling curves of DSC. These exothermic peaks are due to the transformation of AgI crystals in the glass matrices from the α - to β -phase. These results indicate that even if the cooling rate is small like in the measurements of conductivity and DSC, the presence of glass matrices suppresses the α - β phase transformation of AgI crystals. As shown in Fig. 8(a) and 8(b), the temperature at which the conductivity starts to drop is lower in the case of the composites with B_2O_3 than that in the case of the composites with MoO_3 , indicating that the suppressing effect of the α - β phase transformation in the glasses with B_2O_3 , GeO_2 and WO_3 is stronger than that in the glasses with P_2O_5 , MoO_3 and V_2O_5 . The glasses with B_2O_3 , GeO_2 and WO_3 in which T_g is relatively high, may have higher viscosities at 147°C compared to the glasses with P_2O_5 , MoO_3 and V_2O_5 of low T_g . Such higher viscosities of the glass matrix must suppress strongly the α - β phase transformation of AgI crystals. This suppressing effect of the α - β phase transformation of AgI crystals, which is stronger in the case of highly viscous matrices, may be closely related to the fact that the α - β phase transformation temperature becomes lower under high pressure (21), because the volume of AgI crystals is known to expand largely during the α - β phase transformation (22) and thus the crystals are expected to be compressed by surrounding glass matrices (23-25).

This finding may suggest the possibility of the α - β transformation temperature being lower than room temperature in the composite materials in which α -AgI is frozen at room temperature. It is, thus, of great interest to study low temperature behavior of the composite materials in order to clarify the stabilization mechanism of α -AgI at room temperature in a glass matrix.

Figure 9 shows the temperature dependence of conductivities for the twin-roller quenched $82\text{AgI}\cdot 13.5\text{Ag}_2\text{O}\cdot 4.5\text{B}_2\text{O}_3$ composites in the heating process from 170 to 400 K. The Arrhenius type behavior is observed in the range higher than room temperature, as already shown. The conductivities in this temperature range are as high as 10^{-1} Scm^{-1} and the activation energy E_a is about 15 kJ/mol. At lower temperatures, on the other hand, the temperature dependence is not Arrhenius and the slope is much larger than that at room temperature. The E_a values are increased with decreasing temperature. This behavior is a striking contrast to the fact that the superionic AgI- Ag_2O - B_2O_3 glasses with a smaller amount of AgI exhibit a perfect Arrhenius behavior even at lower temperatures(26).

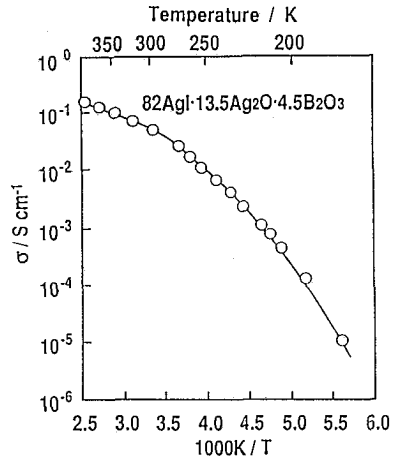


Fig. 9. Temperature dependence of conductivities for the α -AgI-frozen $82\text{AgI}\cdot 13.5\text{Ag}_2\text{O}\cdot 4.5\text{B}_2\text{O}_3$ composite.

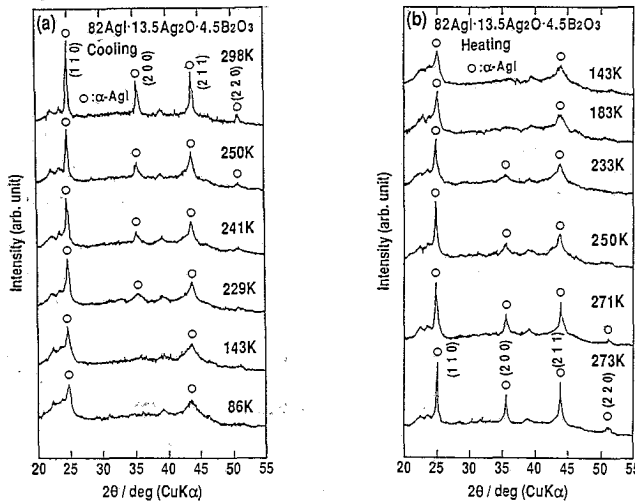


Fig. 10. X-ray diffraction patterns of the α -AgI-frozen $82\text{AgI}\cdot 13.5\text{Ag}_2\text{O}\cdot 4.5\text{B}_2\text{O}_3$ composite. (a): cooling run, (b): heating run.

Figure 10 shows the X-ray diffraction patterns of the rapidly quenched $82\text{AgI}\cdot 13.5\text{Ag}_2\text{O}\cdot 4.5\text{B}_2\text{O}_3$ composite at various temperatures; (a) are for the cooling process from 298 to 86 K and (b) for the heating process from 143 to 298 K. The diffraction peaks due to α -AgI are only observed in the room temperature pattern before cooling, indicating that

the $\alpha\text{-AgI}$ is successfully frozen at room temperature in a glass matrix for this composite. A broadening of the $\alpha\text{-AgI}$ peaks is apparently observed with decreasing temperature down to 86 K. It is noteworthy that the growing of any $\beta\text{-AgI}$ peak does not occur at that time, suggesting that the broadening of the $\alpha\text{-AgI}$ peaks does not mean the $\alpha\text{-}\beta$ transformation being present at the low temperature ranges below room temperature.

The broadened $\alpha\text{-AgI}$ peaks at low temperatures become sharper again with increasing temperature as shown in Fig 10 (b). The profile of the final pattern at 298 K is almost the same as the original one before cooling, indicating that the broadening of the $\alpha\text{-AgI}$ peaks with cooling is a reversible phenomenon.

The broadening of X-ray diffraction peaks is usually caused by an increase in the lattice strain (un-uniform deformation) of the crystal. The lattice strain, η , can be evaluated by the Hall's analysis using more than two diffraction peaks (27).

Figure 11 shows the temperature dependencies of the strain value of η for the $\alpha\text{-AgI}$ crystals frozen in the $82\text{AgI}\cdot 23.5\text{Ag}_2\text{O}\cdot 4.5\text{B}_2\text{O}_3$ composite and of the activation energy, E_a , obtained from the slope in Fig.9; the E_a values at a given temperature were calculated using three data points including two next ones. The η values are almost constant when the temperature is lower than 200K and are steeply decreased at around 260 K, which means that large lattice strain observed in the $\alpha\text{-AgI}$ crystals at low temperatures relaxes at around 260 K. The E_a values, which range from 12 to 36 kJ/mol, are decreased with increasing temperature. The decrease of E_a is not monotonous and the steep E_a change is observed at around 260 K. It is noteworthy that a steep decrease in E_a values is observed at around 260 K where the η values also change steeply.

In our previous paper (23) it was found that a maximum of heat capacity was observed at 260 K from the adiabatic calorimetry for the $82\text{AgI}\cdot 13.5\text{Ag}_2\text{O}\cdot 4.5\text{B}_2\text{O}_3$ composite, as also shown in Fig.11 together with η and E_a . These anomalous behaviors of η , E_a and heat capacity are probably caused by the same reason and associated with the positional ordering of Ag^+ ions in the $\alpha\text{-AgI}$ microcrystals in the composites (23). Therefore, we concluded that this anomalous behavior was attributable to the order-disorder transformation of Ag^+ ions in $\alpha\text{-AgI}$ crystals frozen in the glass matrix (23-25). At temperatures higher than 260 K, Ag^+ ions in AgI crystal are in disordered state as observed in the ordinary $\alpha\text{-AgI}$ crystal with the so-called "averaged structure." The positional ordering of Ag^+ ions of frozen $\alpha\text{-AgI}$ may occur at lower temperatures than 260 K.

Relation between Glass-Forming Ability and Acidity of the Melts for Cuprous Ion Conducting Glasses.

There are many papers concerning the ionic conductivity of glasses; the ion species studied are mainly alkali ions and silver ions. Among those ions, silver is known to show the highest conductivity in spite of the fact that silver ions have a large ionic radius and atomic weight. To explain such a result it has been proposed that the electronic configuration of the

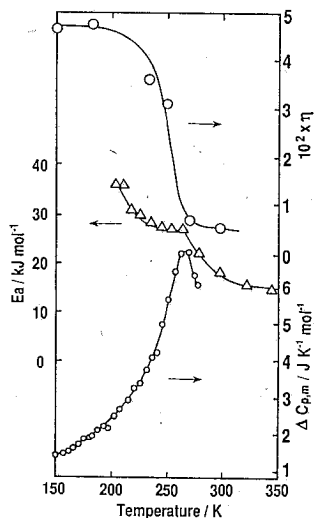


Fig. 11. Temperature dependence of the lattice strain η , and activation energies for conduction, E_a , of the $\alpha\text{-AgI}$ -frozen $82\text{AgI}\cdot 13.5\text{Ag}_2\text{O}\cdot 4.5\text{B}_2\text{O}_3$ composite. The temperature dependence of heat capacities is also shown.

ions, i.e. the d^{10} configuration in the outermost orbital, plays an important role as well as the ionic radius in achieving high ion conductivities (14).

Along the line of the above proposal, we have succeeded in the preparation of Cu^+ ion conducting glasses with high conductivity in the system $\text{CuI-Cu}_2\text{O-MoO}_3$. Cu^+ ions have a similar d^{10} electronic configuration but smaller radius than Ag^+ ions (28). Following this success, some glass-forming systems showing high Cu^+ ion conductivities have been found: for example, the systems $\text{CuI-CuBr-Cu}_2\text{MoO}_4$ (14), CuX ($\text{X} = \text{I, Br, Cl}$)- $\text{Cu}_2\text{MoO}_4\text{-Cu}_3\text{PO}_4$ (29, 30), and CuX ($\text{X} = \text{I, Br, Cl}$)- $\text{Cu}_2\text{MoO}_4\text{-CuPO}_3$ (31-34).

These Cu^+ ion conducting glasses are restricted to the system containing molybdenum oxide and/or phosphorus oxide, and the Cu^+ ion conducting glasses could not be obtained in the systems containing well known glass-forming oxides such as SiO_2 , B_2O_3 , GeO_2 , and so on. The Cu^+ ion conducting glasses are thus only known in very limited glass-forming systems in contrast to the Ag^+ ion conducting glasses which have been obtained in many systems. The reason of this restriction is probably related to the spontaneous disproportionation of Cu^+ to Cu^0 and Cu^{2+} ions during melting in the process of glass preparation. The cuprous ions are known to exist stably in the melts with high acidity. We expect that Cu^+ ions in a melt containing tungsten oxide stably exist, because the melt containing tungsten oxide has high acidity (35). Thus, we try to prepare the glasses in the system $\text{CuI-Cu}_2\text{WO}_4\text{-CuPO}_3$.

Figure 12 shows the glass-forming region in the system $\text{CuI-Cu}_2\text{WO}_4\text{-CuPO}_3$. In the figures open circles, open triangles and closed circles denote glassy, partially crystalline and crystalline samples, respectively. The glasses were obtained over the wide composition range as expected, although the glasses could not be obtained in the pseudobinary system $\text{CuI-Cu}_2\text{WO}_4$.

Figure 13 shows the ESCA spectrum of the $30\text{CuI}\cdot35\text{Cu}_2\text{WO}_4\cdot35\text{CuPO}_3$ glass in order to investigate the valence of copper ions in the glass. This figure also shows the spectra of crystalline CuI , which includes cuprous ions, and of crystalline CuO , which includes cupric ions, for comparison. The spectra of CuI shows two sharp peaks at 952 and 932 eV, which are respectively assigned to the $\text{Cu } 2p_{1/2}$ and $\text{Cu } 2p_{3/2}$. On the other hand, in the spectra of CuO there are four peaks at 962, 954, 944, and 934 eV. The strong peaks at 954 and 934 eV are respectively assigned to the $\text{Cu } 2p_{1/2}$ and $\text{Cu } 2p_{3/2}$ modes, and the peaks at 962 and 944

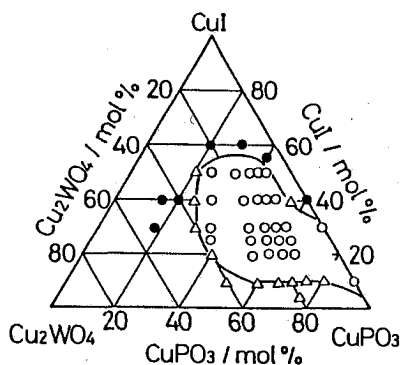


Fig. 12. Glass forming regions in the systems $\text{CuI-Cu}_2\text{WO}_4\text{-CuPO}_3$; (o) glassy, (Δ) partially crystalline, (\bullet) crystalline.

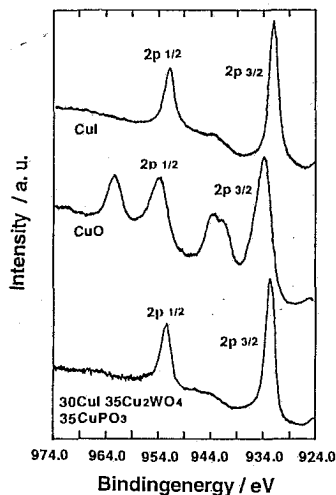


Fig. 13. ESCA spectrum of the $30\text{CuI}\cdot35\text{Cu}_2\text{WO}_4\cdot35\text{CuPO}_3$ glass. The spectra of the crystalline CuI and the crystalline CuO are also shown.

eV are assigned to the satellite peaks of the main Cu 2p_{1/2} and Cu 2p_{3/2} peaks at 954 and 934 eV, respectively. These satellite peaks arise from the lack of symmetry in the electronic configuration of d⁹ of Cu²⁺ ions. In the spectra of the 30CuI•35Cu₂WO₄•35CuPO₃ glass there are only two peaks at 952 and 932 eV and there is no satellite peak. This result suggests that copper ions in the glass exist only as Cu⁺ ions, and thus the disproportionation reaction of Cu⁺ ions to Cu⁰ and Cu²⁺ does not occur during the melting in the process of glass preparation.

Figure 14 shows the composition dependence of conductivities at 298 K of the CuI-Cu₂WO₄-CuPO₃ glasses; the abscissa of the figure is a composition parameter y , which denotes the ratio of the number of phosphorus atoms to the total number of phosphorus plus tungsten atoms included in the glasses; $y = [\text{P}] / ([\text{P}] + [\text{W}])$. These glasses show high ion conductivity in the range of $10^{-2} \sim 10^{-4} \text{ Scm}^{-1}$ at room temperature.

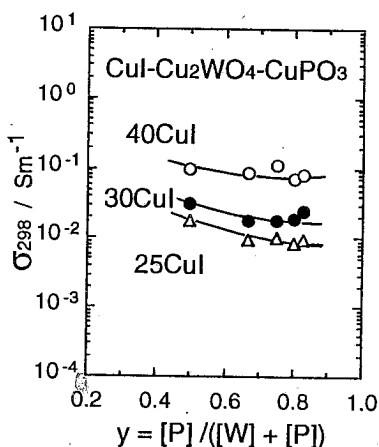


Fig. 14. Conductivities at 298 K, σ_{298} , of the glasses in the systems CuI-Cu₂WO₄-CuPO₃ as a function of the composition parameter y ; $y = [\text{P}] / ([\text{P}] + [\text{W}])$.

Summary

We reviewed three different approaches for the conductivity improvement at room temperature in the glass-based ionic conductors. (1) The "mixed anion effect" and/or "mixed former effect", that is an enhancement of conductivity observed in the glasses containing two kinds of anion species and/or of glass formers, is one of the excellent methods to improve the conductivity of the glasses. The mixed anion effect in conductivity is closely related to the structural change of oxoanions which form network structure of the glasses. (2) Superionic conductor α -AgI, which is stable only above 147°C, was successfully frozen at ambient temperature in AgI-Ag₂O-M_xO_y (M_xO_y = B₂O₃, P₂O₅, GeO₂, V₂O₅, MoO₃, and WO₃) glass matrices by a twin-roller quenching technique. The composite materials in which α -AgI was frozen exhibited extremely high ion conductivity of about $10^{-1} \sim 10^{-2} \text{ Scm}^{-1}$ at room temperature. The matrix glasses with higher glass-transition temperatures had a stronger effect in depressing the α - β transformation of AgI. (3) In the process of preparation of Cu⁺ ion conducting glasses, a problem is posed by the spontaneous disproportionation of Cu⁺ to Cu⁰ and Cu²⁺ during melting. Since the stability of Cu⁺ ions during melting relates to the acidity of the melt, we tried to the glass formation in the system CuI-Cu₂WO₄-CuPO₃, of which the melt was expected to have high acidity. The ESCA spectrum indicated that copper ions in the glasses existed only as Cu⁺ ions, and the CuI-Cu₂WO₄-CuPO₃ glasses showed high ion conductivity in the range of $10^{-2} \sim 10^{-4} \text{ Scm}^{-1}$ at room temperature.

In addition to the above three methods, the twin-roller-rapid quenching is powerful methods to obtain the high conductive glasses which have large amount of carrier ions. Recently, lithium ion conducting glasses in the system Li₂S-SiS₂-Li₃PO₄ were prepared by the twin-roller rapid quenching and the glasses had high ion conductivities more than 10^{-3} Scm^{-1} at room temperature (36). These glasses are promising candidates for the solid-state battery systems, because the glasses have both high ionic conductivities more than 10^{-3} Scm^{-1} at room temperature and high stability against the chemical reaction with lithium metals.

References

1. W. van Gool (ed), *Fast Ion Transport in Solids*, North-Holland (1973).
2. K. Funke, *Prog. Solid State Chem.*, **11** (1976) 345.
3. T. Takahashi, S. Ikeda, and O. Yamamoto, *J. Electrochem. Soc.*, **120** (1973) 647.
4. D. Kunze, *Fast Ion Transport in Solids*, ed by W. van Gool, North-Holland, p.405 (1973).
5. T. Minami, *J. Non-Cryst. Solids*, **73** (1985) 273.
6. T. Minami, *J. Non-Cryst. Solids*, **95/96** (1987) 107.
7. N. Machida, H. Tanaka, T. Shigematsu, N. Nakanishi, and T. Minami, *Chem. Lett.*, (1993) in press.
8. N. Machida, H. Tanaka, T. Shigematsu, N. Nakanishi, and T. Minami, *Solid State Ionics*, submitted for publication.
9. M. Tatsumisago, Y. Shinkuma, and T. Minami, *Nature*, **354** (1991) 217.
10. M. Tatsumisago, Y. Shinkuma, T. Saito, and T. Minami, *Solid State Ionics*, **50** (1992) 273.
11. T. Minami and M. Tatsumisago, *New Materials*, Narosa Publishing House, New Delhi, 1992, p.149.
12. M. Tatsumisago, A. Tanigushi, and T. Minami, *J. Am. Ceram. Soc.*, **76** (1993) 235.
13. T. Saito, M. Tatsumisago, and T. Minami, *Solid State Ionics*, **61** (1993) 285.
14. T. Minami and N. Machida, *Mater. Chem. Phys.*, **23** (1989) 63.
15. M. Tatsumisago, Y. Akamatsu, and T. Minami, *Solid State Ionics*, **31** (1988) 41.
16. M. Tatsumisago, N. Machida, and T. Minami, *J. Ceram. Soc. Jpn.*, **95** (1987) 197.
17. A. Magistris, G. Chiodelli, and M. Duclot, *Solid State Ionics*, **9/10** (1983) 611.
18. B. Carette, M. Ribes, and J. L. Souquet, *Solid State Ionics*, **9/10** (1983) 735.
19. K. Nakamoto, *Infrared and Raman Spectra of Inorganic and Coordination Compounds*, John Wiley & Sons (1986).
20. D. E. C. Corbridge, *Topics in Phosphorus Chemistry*, ed by M. Grayson and E. J. Griffith, Wiley, vol.6, p.235 (1969).
21. B.-E. Mellander, B. Baranowski, and A. Lunden, *Phys. Rev.* **B23** (1981) 3770.
22. A. J. Majumdar and R. Roy, *J. Phys. Chem.*, **63** (1959) 1858.
23. M. Hanaya, M. Nakayama, M. Ogumi, M. Tatsumisago, T. Saito and T. Minami, *Solid State Commun.*, in press.
24. M. Tatsumisago, T. Saito. and T. Minami, *Solid State Ionics*, submitted for publication.
25. M. Tatsumisago, T. Saito and T. Minami, *J. Phys. Chem.*, submitted for publication.
26. A. Magistris, G. Chiodelli, and A. Shiraldi, *Electrochim. Acta*, **24** (1979) 203.
27. H. P. Klug, L.E. Alexander, *X-ray Diffraction Procedures*, 2nd Edition, John Wiley & Sons (1973).
28. N. Machida and T. Minami, *J. Am. Ceram. Soc.*, **71** (1988) 784.
29. N. Machida, Y. Shinkuma, and T. Minami, *J. Ceram. Soc. Jpn.*, **97** (1989) 1104.
30. N. Machida, T. Shigematsu, N. Machida, S. Tsuchida, and T. Minami, *J. Chem. Soc., Faraday Trans.*, **88** (1992) 3059.
31. N. Machida, Y. Shinkuma, and T. Minami, *Solid State Ionics*, **45** (1991) 123.
32. Y. Shinkuma, N. Machida, and T. Minami, *J. Am. Ceram. Soc.*, **74** (1991) 3133.
33. N. Machida, Y. Shinkuma, T. Minami, T. Shigematsu, and N. Nakanishi, *J. Electrochem. Soc.*, **139** (1992) 1380.
34. N. Machida, T. Shigematsu, N. Nakanishi, Y. Shinkuma, and T. Minami, *Solid State Ionics*, **50** (1992) 303.
35. T. Yokokawa and S. Kohsaka, *J. Chem. Eng. Data*, **24** (1979) 1671.
36. M. Tatsumisago, K. Hirai, T. Minami, K. Takada, and S. Kondo, *J. Ceram. Soc. Jpn.*, submitted for publication.

VITREOUS IONIC CONDUCTORS WITH Cu^+

M. MÍKA, L. ŠAŠEK, M. RADA

Institute of Chemical Technology, Department of Glass and Ceramics,
Technická 5, 16628 Prague 6, Czech Republic

ABSTRACT

Cu^+ ion-conducting glasses were prepared in the system $\text{CuI-Cu}_2\text{O-V}_2\text{O}_5\text{-WO}_3\text{-MoO}_3$ using the conventional melt-quenching method. Electrical conductivities were studied. Samples exhibited ionic conductivities at room temperature in the range of $0.55\text{-}0.94\text{ Sm}^{-1}$. Electronic contributions were negligible. X-ray powder diffraction analyses, differential thermal analyses and infrared spectroscopy were performed to get additional information about this ionic conductors.

INTRODUCTION

Fast ion-conducting glasses could be promising materials for applications to various electrochemical devices (i.e. solid state batteries, sensors, memory devices, coulometer cells and resistors). Glasses with high ionic conductivities and very low electronic contributions are suitable for solid electrolytes, which have no problems associated with grain boundaries. Properties of these electrolytes can be easily modified by changing chemical composition (1,2,3). It is known, that many glasses based on AgI exhibit high ionic conductivities at room temperature in the range from 10^{-1} to 10^0 S.m^{-1} (4,5). Cu^+ ion-conducting glasses in the system $\text{CuI-Cu}_2\text{O-MoO}_3$ can also achieve high ionic conductivities, which are greater than those of Ag^+ ion-conducting glasses with the same iodide content in the system $\text{AgI-Ag}_2\text{O-MoO}_3$ (6,7). The present work deals with influence of partial replacement of MoO_3 with V_2O_5 and/or WO_3 on properties of Cu^+ glassy electrolytes.

EXPERIMENTAL METHODS

The Cu^+ ion-conducting glasses were prepared in the system $44\text{CuI}.28\text{Cu}_2\text{O}.x\text{V}_2\text{O}_5.y\text{WO}_3.(28-x-y)\text{MoO}_3$, where x and y varied from 0 to 2. Table 1 gives the chemical compositions of the studied glasses. The raw materials used were CuI , Cu_2O , MoO_3 , V_2O_5 and WO_3 . The components were mixed thoroughly and then melted in silica tubes at 500°C for 1 hour. In order to avoid oxidation of Cu^+ ions and decomposition of CuI a dry argon atmosphere was used (8). The samples were obtained by quenching the melt in a iron mould.

The total electrical conductivities were studied as a function of

temperature (from 50 to 90°C) and frequency (5 Hz–500 kHz). The measured glass discs were shaped of 20 mm in diameter and 1 mm in thickness. Sputtered Pt electrodes were used. The total conductivities were determined by employing the complex impedance analysis (9). Electronic contribution to the total conductivity was determined by means of the Wagner polarization technique by use of the electrochemical cell (-)Cu|glass|Pt(+) [6], where Cu and Pt are reversible and blocking electrodes respectively. X-ray powder diffraction (XRD) analyses at room temperature using CoK_α radiation were performed to detect presence of crystals. Differential thermal analyses (DTA) were carried out at a heating rate of 10 °C/min in nitrogen; a sample weight of 100 mg was used with Al_2O_3 as the reference. The infrared spectra of glassy materials in Nujoll mulls were recorded on a Nicolet 740 FT-IR spectrometer in the range 4000–50 cm^{-1} .

Table 1. Chemical composition of the prepared glasses

| Sample | Chemical composition [mol.%] | | | | |
|--------|------------------------------|-----------------------|----------------|------------------------|---------------|
| | CuI | Cu_2O | MoO_3 | V_2O_5 | WO_3 |
| Mo-1 | 44 | 28 | 28 | 0 | 0 |
| MoV-1 | 44 | 28 | 27 | 1 | 0 |
| MoV-2 | 44 | 28 | 26 | 2 | 0 |
| MoW-1 | 44 | 28 | 27 | 0 | 1 |
| MoW-2 | 44 | 28 | 26 | 0 | 2 |
| MoVW-1 | 44 | 28 | 26 | 1 | 1 |
| MoVW-2 | 44 | 28 | 26.66 | 0.66 | 0.66 |
| MoVW-3 | 44 | 28 | 27.33 | 0.33 | 0.33 |

RESULTS AND DISCUSSION

Prepared materials of the given composition (Table 1) were amorphous, only sample MoW-2 was partially crystalline; a small amount of α -CuI was detected in this sample.

The measured total conductivities fit the equation (1), where σ is the total conductivity, σ_0 is the pre-exponential factor and E_a is the activation energy for conduction. Table 2 presents evaluated constants for equation (1),

$$\sigma T = \sigma_0 \exp\left(-\frac{E_a}{RT}\right) \quad (1)$$

total conductivities at 25°C ($\sigma_{25^\circ\text{C}}$), electron (σ_e) and hole conductivity (σ_h).

Table 2. Electrical properties of the prepared glasses

| Sample | $\sigma_{25^\circ\text{C}}$ [Sm^{-1}] | $\sigma_0 \cdot 10^{-6}$ [Sm^{-1}K] | E_a [kJmol^{-1}] | $\sigma_e \cdot 10^6$ [Sm^{-1}] | $\sigma_h \cdot 10^7$ [Sm^{-1}] | σ_e/σ_h |
|--------|---|--|----------------------------------|---|---|---------------------|
| Mo-1 | 0.94 | 2.71 | 22.75 | 6.7 | 4.5 | 17.8 |
| MoV-1 | 0.65 | 4.00 | 24.60 | 4.4 | 1.8 | 24.4 |
| MoV-2 | 0.62 | 6.18 | 25.80 | 4.8 | 3.7 | 13.0 |
| MoW-1 | 0.55 | 6.02 | 26.05 | - | - | - |
| MoVW-1 | 0.66 | 0.95 | 20.97 | 9.3 | 5.2 | 17.9 |
| MoVW-2 | 0.76 | 8.39 | 25.99 | 8.5 | 4.0 | 21.3 |
| MoVW-3 | 0.88 | 3.28 | 23.36 | 10.8 | 7.0 | 15.4 |

Table 3. Glass transition (t_g), crystallization (t_c) and melting (t_m) temperatures (in °C) of the prepared materials

| Sample | Heating | | | Cooling |
|--------|---------|-----------------|---------|---------|
| | t_g | t_c | t_m | t_c |
| Mo-1 | 93,129 | 134,162,250 | 357,400 | 342,328 |
| MoV-1 | 97,128 | 163,185,280 | 351,420 | 323,297 |
| MoV-2 | 103,134 | 160,279,312,362 | 364,433 | 328,289 |
| MoW-1 | 102,128 | 143,171,269 | 349,450 | 344,329 |
| MoVW-1 | 97,128 | 152,189,263 | 350,431 | 346,315 |
| MoVW-2 | 94,128 | 146,163,185,259 | 343,435 | 340,319 |

The modified molybdenum glasses exhibit the total conductivities at 25°C from 0.55 to 0.94 Sm^{-1} . The total conductivity decreases as the MoO_3 content

decreases. Electronic conductivities were smaller 5 orders of magnitude then

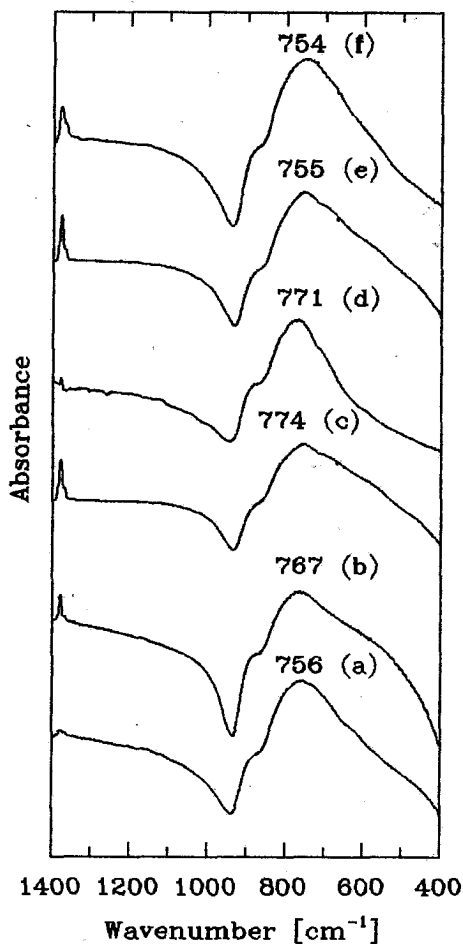


Fig.1 IR spectra of the glasses in Nujoll mulls:
 (a) Mo-1; (b) MoV-1; (c) MoV-2; (d) MoW-1;
 (e) MoVW-1; (f) MoVW-2

the total conductivities and partial replacement of MoO_3 with V_2O_5 and/or WO_3 causes no significant changes. The electronic contribution to the total conductivity is considered to be negligible and the total conductivity is attributed to Cu^+ ion motion. Glass Mo-1 has the highest ionic conductivity. The partial substitution of V_2O_5 and/or WO_3 for MoO_3 caused the decrease in the ionic conductivity. WO_3 affected conductivity more seriously than V_2O_5 .

Figure 1 shows the infrared spectra of glasses in the wavenumber range of $1400\text{--}400\text{ cm}^{-1}$. The replacement of MoO_3 with V_2O_5 or WO_3 caused the shift of

the strong absorption band at 756 cm^{-1} to the higher wavenumber.

Figure 3 shows a typical DTA curve of glass Mo-1. Glass transition (t_g), crystallization (t_c) and melting (t_m) temperatures (in $^{\circ}\text{C}$) of the prepared materials. All the glasses had two endothermic peaks, which are probably associated with t_g of two separate glassy phases. The t_g values are a little higher for the glasses with V_2O_5 or WO_3 . Three or four values of t_c were observed for all the materials studied.

XRD powder patterns at room temperature for glass Mo-1 treated at various temperatures for 1 h in N_2 are shown in Fig.3. Some diffuse peaks are observed at 133°C . $\alpha\text{-CuI}$ and unknown metastable phases were detected at 172°C and $\alpha\text{-CuI}$ and probably two different unknown phases were observed in the material at 268°C .

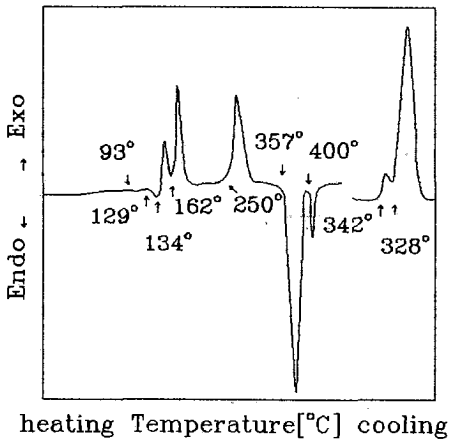


Fig.2 DTA curve for glass Mo-1

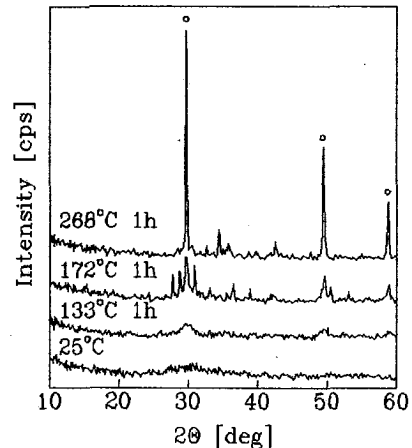


Fig.3 XRD powder patterns at room temperature for glass Mo-1 annealed at various temperatures for 1 h in N_2 (o : $\alpha\text{-CuI}$)

CONCLUSIONS

Fast ion-conducting glasses were prepared in the system $\text{CuI-Cu}_2\text{O-V}_2\text{O}_5\text{-WO}_3\text{-MoO}_3$. The vitreous materials exhibit conductivities at 25°C in the range of $0.55\text{-}0.94\text{ Sm}^{-1}$. Replacement of MoO_3 with V_2O_5 and/or WO_3 results in the decrease of ionic conductivity. Electronic contribution is smaller 5 orders of magnitude than the total conductivity; thus the transport number of Cu^+ ions is practically unity and these glasses are good ionic conductors at 25°C .

REFERENCES

1. R.G.Linford, *Solid State Ionics* 28-30 (1988) 831
2. D.Ravaine, *J.Non-Cryst.Solids* 38&39 (1980) 353
3. M.D.Ingram, *Phys.Chem.Glasses* 28 (1987) 215
4. T.Minami, *J.Non-Cryst.Solids* 73 (1985) 273
5. M.C.R.Shastry and K.J.Rao, *Solid State Ionics* 37 (1989) 17
6. N.Machida and T.Minami, *J.Am.Ceram.Soc.* 71 (1988) 784
7. T.Minami and N.Machida, *Mat.Chem.Phys.* 23 (1989) 63
8. N.Machida, M.Chusho and T.Minami, *J.Non-Cryst.Solids* 101 (1988) 70
9. A.Do, *J.Mater.Sci.* 24 (1989) 749

STRUCTURAL ASPECTS OF THE MIXED ALKALI EFFECT

E.I. Kamitsos, A.P. Patsis, G.D. Chryssikos and J.A. Kapoutsis

Theoretical and Physical Chemistry Institute,
National Hellenic Research Foundation,
48 Vass. Constantinou Ave.,
Athens 116 35, GREECE

Structural aspects of the mixed alkali effect have been investigated in borate glasses by employing infrared reflectance spectroscopy. The nature of sites occupied by alkali metal ions was studied and found to vary systematically with alkali mixing and to lead to new ion-site bonding requirements. These are fulfilled by local structural rearrangements, like the isomerization of boron-oxygen tetrahedra into borate triangles with non-bridging oxygens. Such effects appeared enhanced with increasing the difference between the dissimilar alkalis, or the total alkali content.

1. INTRODUCTION

In the well known mixed alkali effect the presence of a dissimilar alkali metal ion causes a large non-linear decrease in ionic conductivity. Despite the universality of this effect and the large number of theories proposed for its explanation its origin remains highly controversial (1). A number of earlier theories have proposed the presence of dissimilar alkalis in neighbouring sites, i.e. the formation of network-mediated "pairs" of unlike alkalis (2-6). It was further argued that "pairs" of dissimilar alkalis are energetically favoured compared to "pairs" of similar alkalis, with this leading directly to the decrease of ion mobility. Recent theoretical advances on the mixed alkali effect by Bunde, Maass and Ingram have focussed also on the presence of sites suitable for each mobile ion (7,8). Such ion sites were assumed to retain their identity in the mixed alkali glass, and this was shown to lead to mismatch and memory effects and therefore to influence the ion transport process.

As it appears from the above, the detailed knowledge of the kind of sites occupied by metal ions in mixed alkali glasses is an important factor for a better understanding of the mixed alkali effect. Previous studies from this laboratory have demonstrated that infrared spectroscopy can be successfully employed to investigate ion-site interactions in various glass systems (9-14). In this report we present results of an infrared reflectance investigation of mixed alkali glasses (MAG's) in the system: $xM_2O \cdot (1-x)M'_2O \cdot nB_2O_3$ ($M, M' = \text{alkali}$ and $n = 5, 2, 1.2$). Fourier-transform infrared reflectance spectra have been recorded over a broad frequency range and analysed in order to investigate the dependence of the glass structure and the ion-site interactions on the alkali substitution ratio (x), the difference between dissimilar alkalis (M, M') and the total alkali content.

2. EXPERIMENTAL

Glasses were prepared from the stoichiometric amounts of anhydrous B_2O_3 and metal carbonates by conventional melting techniques. Infrared spectra were recorded in the reflectance mode on a Bruker 113v spectrometer. Details of sample preparation and data acquisition and analysis can be found elsewhere (10).

3. RESULTS AND DISCUSSION

3.1 The Structure of the Glass Network.

Typical infrared absorption coefficient spectra are shown in Fig. 1 for MAG's in the

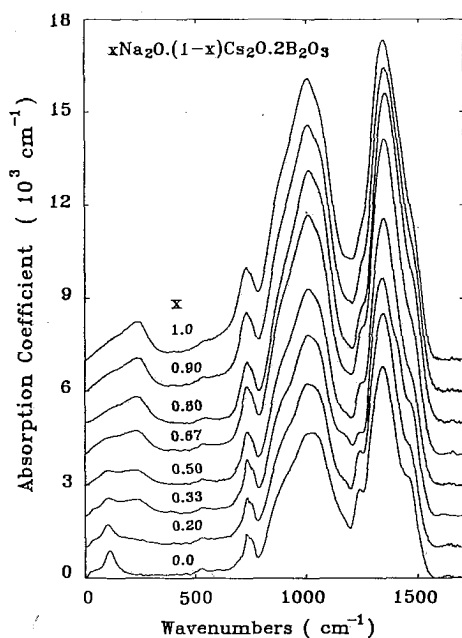


Figure 1. Infrared absorption spectra of mixed alkali glasses $x\text{Na}_2\text{O} \cdot (1-x)\text{Cs}_2\text{O} \cdot 2\text{B}_2\text{O}_3$.

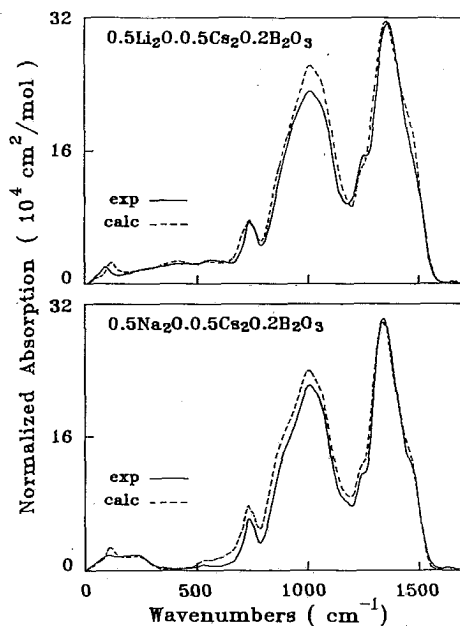


Figure 2. Comparison of experimental and calculated infrared spectra of mixed Li-Cs and Na-Cs diborate glasses at maximum mixing.

system $x\text{Na}_2\text{O} \cdot (1-x)\text{Cs}_2\text{O} \cdot 2\text{B}_2\text{O}_3$. It is obvious that a progressive replacement of one alkali by another results in a systematic variation of the infrared spectrum. It is of interest to investigate whether such spectral variations with x could result from a linear change of the glass structure with alkali substitution. For this purpose we compare in Fig. 2 the experimental infrared spectra of two MAG's, i.e. Li-Cs and Na-Cs of maximum mixing ($x = 0.5$), with those calculated on the basis of a linear average of the spectra of the two end-member glasses ($x = 0, 1$). It is noted that spectral normalization was performed before averaging, by multiplying the absorption coefficient with the glass molar volume, in order to take into account differences in glass density (11, 12). The molar volume of the mixed alkali glass was estimated from the average of the molar volumes of the end-members (1).

Comparison of experimental and calculated spectra in Fig. 2 shows that there is no matching in the various spectral regions. This immediately suggests that, in principle, the structure of a mixed alkali glass can not be described by a linear combination of the structures of the end-member glasses. Of particular interest is the behaviour of the asymmetric absorption band centered at ca 1000 cm^{-1} , which can be attributed to B-O stretching vibration of borate groups containing BO_4^- tetrahedra ($\text{O} = \text{bridging oxygen atom}$) (10-12). Clearly, absorption of the experimental spectrum in this spectral range is less than that predicted on the basis of a linear variation of the glass structure with x .

To quantify this effect we have evaluated the area under the $800\text{--}1100\text{ cm}^{-1}$ absorption band of the experimental spectra and normalized it by multiplying with the corresponding

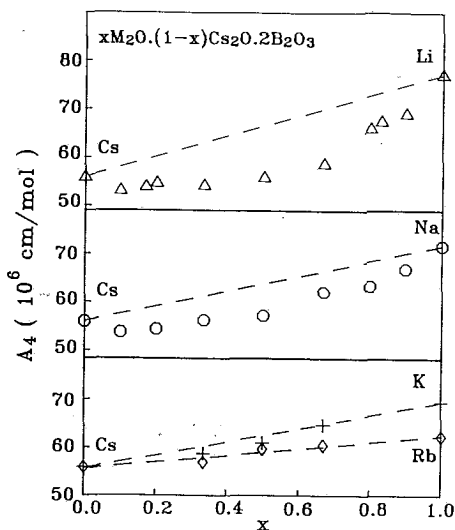


Figure 3. Normalized infrared area of the 800 - 1100 cm^{-1} spectral region of $x\text{M}_2\text{O}\cdot(1-x)\text{Cs}_2\text{O}\cdot 2\text{B}_2\text{O}_3$ glasses.

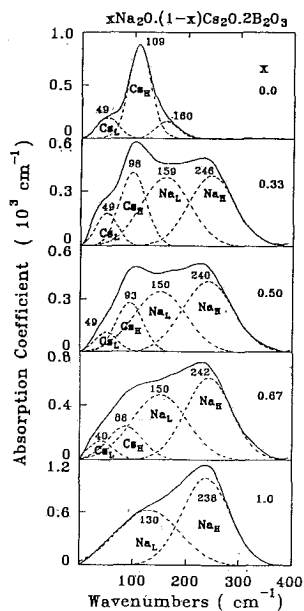


Figure 4. Deconvoluted far-infrared spectra of $x\text{Na}_2\text{O}\cdot(1-x)\text{Cs}_2\text{O}\cdot 2\text{B}_2\text{O}_3$ glasses.

molar volume. The so-obtained normalized areas, A_4 , have been plotted versus x in Fig. 3, for glasses in the mixed alkali systems $x\text{M}_2\text{O}\cdot(1-x)\text{Cs}_2\text{O}\cdot 2\text{B}_2\text{O}_3$ ($\text{M} = \text{Li}, \text{Na}, \text{K}, \text{Rb}$). An interesting non-linear dependence of A_4 on x has been obtained for Li-Cs and Na-Cs systems, demonstrating the non-linear change of the structure of mixed alkali glasses with alkali substitution. This effect tends to be reduced as the difference between the dissimilar alkalis becomes smaller (e.g. the K-Cs and Rb-Cs systems). It was recently shown that the normalized area A_4 scales linearly with the fraction of four-coordinated boron atoms N_4 (11). Therefore, Fig. 3 illustrates a reduction of N_4 from additivity upon alkali mixing, in agreement with the NMR results of Zhong and Bray for mixed alkali diborate glasses with $x = 0.5$ (15). Since for $0 \leq x \leq 1$ the total alkali content remains fixed, the plots in Fig. 3 suggest that the fraction of non-bridging oxygens in BO_2O^- triangles should exhibit a positive departure from linearity with alkali mixing.

3.2 Alkali Sites in Mixed Alkali Glasses

While the vibrations of the glass network are observed mainly in the mid-infrared, the far-infrared parts of the spectra (below $ca 400 \text{ cm}^{-1}$) are dominated by bands attributed to vibrations of alkali cations in their localized network sites (9-13). The Fig. 4 shows the far-infrared parts of spectra in the Na-Cs system. Previous studies on single alkali glasses have shown that their far-infrared profiles can be deconvoluted into two component bands, designated by Na_L , Na_H ($x=1$) and Cs_L , Cs_H ($x=0$) in Fig. 4. Such bands have been attributed to vibrations of alkali ions in two distinct types of ionic site (9-13), which differ mainly in their local optical basicity (14). Note that the band at 160 cm^{-1} of the Cs-glass (see Fig. 4, $x=0$) has been attributed to libration modes of disconnected segments of the borate network, such

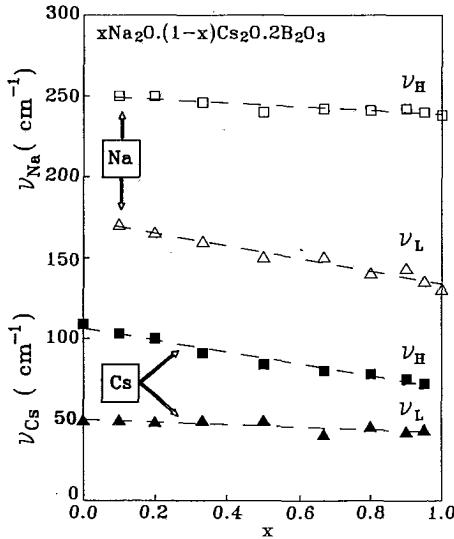


Figure 5. Sodium and caesium cation-motion frequencies in $x\text{Na}_2\text{O} \cdot (1-x)\text{Cs}_2\text{O} \cdot 2\text{B}_2\text{O}_3$ glasses.

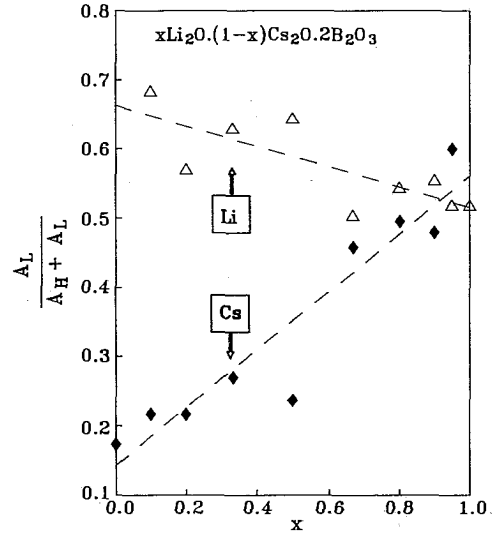


Figure 6. Relative integrated intensity of the low-frequency ion-motion bands ($A_L/A_H + A_L$) for Li^+ and Cs^+ ions in $x\text{Li}_2\text{O} \cdot (1-x)\text{Cs}_2\text{O} \cdot 2\text{B}_2\text{O}_3$ glasses.

as those of metaborate rings (11).

Analysis of the far-infrared spectra of mixed alkali glasses has shown that a meaningful simulation requires the consideration of at least four component bands (9). For the particular case shown in Fig. 4, the two bands at lower frequency (ca 50 and 100 cm^{-1}) can be assigned to vibration of Cs cations in their sites, while the two higher frequency components (ca 150 and 240 cm^{-1}) can be attributed to vibrations of Na cations in their suitable sites. Comparison with the spectra of the $x=0$ and $x=1$ glasses suggests that the two alkalis occupy sites which are not drastically different from their sites in the single alkali glass. Further knowledge about the nature of such sites in MAG's can be gained by examining the composition dependence of the frequencies of the Na⁺- and Cs⁺- motion bands. This is shown in Fig. 5, where ν_{H} and ν_{L} denote high- and low- frequency components, respectively. It is clear that the Cs⁺-motion frequencies, and in particular ν_{H} , decrease upon decreasing the amount of Cs in the glass. This is in contrast with the behaviour of the Na⁺-motion frequencies, particularly that of ν_{L} , which upshift with decreasing the Na content. The results in Fig. 5 are quite interesting since they demonstrate that for a particular alkali the nature of sites and consequently the cation-site interactions are progressively influenced by the presence of a dissimilar cation. Specifically, the alkali - oxygen attractive forces of the high field strength cation (e.g. Na⁺) become stronger, while those of its low field strength partner (e.g. Cs⁺) become weaker upon alkali mixing. This clear influence of one alkali on the other can be effected only by their close proximity in network-mediated "pair" configurations. This results in changes of the individual bonding conditions (manifested by ν_{H} , ν_{L}) through polarization effects (16,17), as compared to their favoured ones assumed in the binary glass. As shown in the previous section, the glass network responds to fulfil the new bonding requirements by suitable rearrangements like the transformation of BO_4^- tetrahedra into their

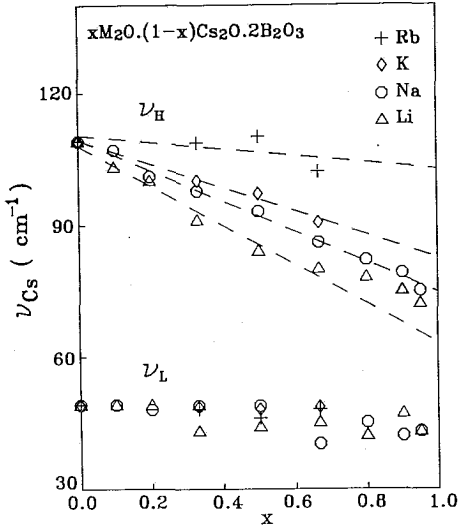


Figure 7. Cs^+ - motion frequencies in $xM_2O \cdot (1-x)Cs_2O \cdot 0.2B_2O_3$ glasses.

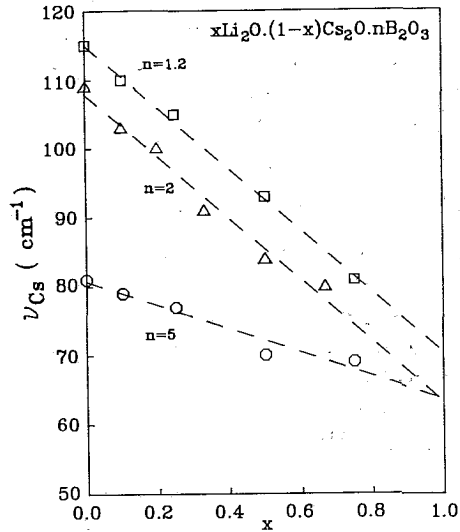


Figure 8. Effect of total alkali content on the ν_H frequency of Cs^+ - motion in $xLi_2O \cdot (1-x)Cs_2O \cdot nB_2O_3$ glasses ($n=5, 2, 1.2$).

isomeric BO_2O^- triangles. Recent EXAFS and molecular dynamics simulation studies of mixed alkali silicate glasses have shown also that the two alkalis affect each other's atomic environment (18, 19).

Besides the observed frequency variations (Fig. 5), a change in the distribution of each alkali ion between its two types of site is also effected upon alkali mixing. As seen in Fig. 4, the two lower-frequency bands (Cs_L , Na_L) gain intensity relative to their higher-frequency counterparts (Cs_H , Na_H), when the two alkalis coexist ($0 < x < 1.0$). The same trend is demonstrated also in Fig. 6 where the relative integrated intensity of the low-frequency component ion-motion bands, $A_L/(A_H + A_L)$, is plotted versus x for glasses in the system $xLi_2O \cdot (1-x)Cs_2O \cdot 0.2B_2O_3$. It is shown that minority cations in mixed-alkali glasses populate preferably the low-frequency sites. We consider this to be an important result, in view of the recent findings in sodium-borate glasses which indicate that the mobile Na^+ ions are those in high-frequency sites (14). Therefore, increase of the population of lower-frequency sites would create discontinuities in the pathways along the higher-frequency sites, with a consequent reduction in ionic conductivity. These structural aspects could be employed as a basis for a better understanding of the mixed alkali effect, as will be discussed in more details elsewhere (20).

3.3. Factors Affecting the Interactions Between Dissimilar Alkalis

The interactions between the dissimilar alkalis were found to depend on their field strength difference. This is demonstrated in Fig. 7 where the variation of the Cs^+ -motion frequencies is utilized as a convenient probe of such interactions. It is shown that the larger the difference between the alkali partners ($M-Cs$) the larger the decrease of the ν_H frequencies of Cs cations, and thus the greater the weakening of the Cs - oxygen interactions. The ν_L frequency shows a much smaller dependence on either M or x .

The effect of the total alkali content on the interactions between alkali cations has been also examined. Preliminary results are presented in Fig. 8 for MAG's in the system $x\text{Li}_2\text{O} \cdot (1-x)\text{Cs}_2\text{O} \cdot n\text{B}_2\text{O}_3$ where $n = 5, 2, 1.2$. Clearly, the higher the total alkali content the more effective the drop of the ν_{H} frequency of Cs^+ with Li^+ substitution. This result suggests that for higher total alkali contents there is a greater probability of finding dissimilar alkalis in neighbouring network sites. A full report on such effects in mixed alkali borate and silicate glasses will be reported elsewhere (20).

4. CONCLUSIONS

Infrared spectroscopy has been applied to investigate structural aspects of the mixed alkali effect, including the network structure which provide the sites for the alkali ions, as well as the alkali - oxygen and alkali-alkali interactions. It was found that the structure of the glass network varies non-linearly with alkali substitution, as this is manifested by the negative departure from linearity exhibited by the fraction of four-coordinated boron atoms. The frequencies of the alkali motion bands in the far-infrared were found to vary with alkali substitution, suggesting the presence of dissimilar alkalis in "pair" configurations and the existence of strong interactions that affect in different ways the alkali ion - oxygen attractive forces. A preferential population of the low-frequency cation sites was also found upon alkali mixing and was proposed as a basis for understanding the reduction in ionic conductivity.

Helpful discussions with Drs. J.A.Duffy, M.D.Ingram and A.Bunde are gratefully acknowledged. This work has been supported by NHRF

REFERENCES

1. M.D.Ingram, *Phys. Chem. Glasses* 28 (1987) 215-234
2. W.A.Weyl and A.C.Marboe, in "The constitution of glasses" Wiley-Interscience, New-York (1964), Vol. 2, Part 1.
3. O.V.Mazurin, in "Structure of glass" Consultants Bureau, New York (1966) Vol. 4
4. J.R.Hendrickson and P.J.Bray, *Phys. Chem. Glasses* 13 (1972) 43-49; 107-115
5. M.D.Ingram, C.T.Moynihan and A.V.Lesicar, *J. Non-Cryst. Solids* 38-39 (1980) 371-376
6. A.H.Dietzel *Phys. Chem. Glasses* 24 (1983) 172-180
7. A.Bunde, P.Maass and M.D.Ingram, *Ber. Bunsenges, Phys. Chem.*, 95 (1991) 977
8. P.Maass, A.Bunde and M.D.Ingram, *Phys. Rev. Letters*, 68 (1992) 3064
9. E.I.Kamitsos, A.P.Patsis and G.D.Chryssikos, *Phys. Chem. Glasses* 32 (1991) 219-221
10. E.I.Kamitsos, A.P.Patsis, M.A.Karakassides and G.D.Chryssikos, *J. Non-Cryst. Solids* 126 (1990) 52-67
11. E.I.Kamitsos, A.P.Patsis and G.D.Chryssikos, *J. Non-Cryst. Solids* 152 (1993) 246-257
12. E.I.Kamitsos, A.P.Patsis and G.D.Chryssikos, in "Physics of Non-Crystalline Solids" eds. L.D.Pye, W.C. La Course and H.J.Stevens (Taylor & Francis 1992) p. 460
13. E.I.Kamitsos, M.A.Karakassides and G.D.Chryssikos, *J. Phys. Chem.* 91 (1987) 5807-5813
14. J.A.Duffy, E.I.Kamitsos, G.D.Chryssikos and A.P.Patsis, *Phys. Chem. Glasses* 34 (1993) 153
15. J. Zhong and P.J. Bray, *J. Non-Cryst. Solids* 111 (1989) 67-69
16. J. Lumsden, *Discussion Faraday Soc.* 32 (1961) 138-146
17. C.T.Moynihan and R.W. Laity, *J. Phys. Chem.* 68 (1964) 3312-3317
18. G.N.Greaves, *Phil. Mag. B* 60 (1989) 795
19. B.Vessal, G.N.Greaves, P.T.Marten, A.V.Chadwick, R.Mole and S.Houde-Walters, *Nature* 359 (1992) 504
20. E.I.Kamitsos, A.P.Patsis, G.D.Chryssikos, and J.A.Duffy, in submission

THERMAL TRANSPORT BY LOCALIZED AND EXTENDED PHONONS IN GLASS

G. S. Dixon, T. Doyle, P. A. Watson, W. P. Allen,
B. D. Gault, S. Shi, P. G. Dixon, R. Snider, and E. T. Knobbe
Department of Physics, Oklahoma State University, Stillwater, OK 74078.

Measurements of the thermal diffusivities of glasses from 90 to 500 K are presented. In each of the systems which were studied, the thermal diffusivity becomes proportional to temperature in the high temperature limit of this range. In most of these glasses, the thermal diffusivity at low temperatures is a decreasing function of temperature so that the diffusivity passes through a minimum in the temperature range of these experiments. The linear temperature regime is characteristic of transport via thermally activated hopping of localized phonons, while the low temperature behavior is suggestive of conventional extended state phonons as the carriers. The data have been analyzed with a two-carrier model for the transport. The "boson peak" from Raman scattering has been used as a measure of the phonon mobility edge. By studying families of chemically substituted glasses it has been possible to follow the dependence of the phonon relaxation times on the frequency of the mobility edge. Excellent agreement with the ω^4 dependence characteristic of the three-phonon process studied by Jagannathan, et al. is obtained for both the localized phonons and the extended phonons.

Introduction

Glasses lack the translational symmetry that leads to plane wave eigenvectors for the phonons in crystalline solids, except in the long wavelength limit where the glass may be regarded as an elastic continuum and Brillouin scattering reveals sharp peaks corresponding to modes of well defined wave vector and polarization. The onset of a continuous Raman spectrum at frequencies typically as low as a few 10^3 of cm^{-1} , shows that a large fraction of the phonons in glasses are poorly described as plane waves. At temperatures well above the plateau in the thermal conductivity, these Raman-active modes are a significant fraction of the thermal phonon population and may be significant heat carriers.

Consensus on the nature of the phonons that are the important heat carriers at high temperatures has not yet been reached. The most successful models hypothesize that some or all of the Raman-active phonons are weakly localized by the disordered structure of the glass. The thermal transport process is one in which the localized phonons diffuse among neighboring localization sites by a random walk or hopping process. Cahill and Pohl (1) have used a random walk model in which the localized phonons have strong, temperature-independent damping and diffuse among energetically equivalent sites. Their model predicts that the thermal transport coefficients will become independent of temperature in the high temperature limit. Orbach and coworkers (2) have developed a model for fractal glasses in which the localized phonons (fractons) execute thermally-activated hopping (TAH) among inequivalent sites. We shall refer to this as the TAH model. Although this model has been controversial because of its assumption of a fractal mesoscale structure for the glass to

facilitate computation, we have argued elsewhere (3) that the minimum conditions for TAH (low frequency extended phonons separated from higher frequency localized modes by a mobility edge) will also exist in non-fractal glasses. The TAH model predicts that the thermal transport coefficients will be proportional to T at high temperatures.

Experimental

In this paper the thermal diffusivities, α , of several silicate glasses, belonging to two families that are related by chemical substitution of a network modifier, are studied between 90 and 500 K using a transient technique described previously (3). These glasses were $15M_2O \cdot 5ZnO \cdot 5BaO \cdot 5Eu_2O_3 \cdot 70SiO_2$, where M is Li, Na, K, Rb, or Cs, and $15Na_2O \cdot 15MO \cdot 5Eu_2O_3 \cdot 65SiO_2$, where M is Mg, Ca, Sr, Ba, or Zn. Results are also reported for NdP_5O_{14} glass, fused silica, and a silica xerogel of density 1.7 g/cm^3 .

Raman spectra of the glasses were obtained in 90° scattering at room temperature using the macrochamber of a Jobin-Yvon U-1000 spectrometer with excitation by an Ar-ion laser.

Results and Discussion

The results in Figs. 1, 5 and 7 clearly show a high temperature region where $\alpha \propto T$ indicating a significant contribution due to TAH in the complex glasses. At low temperatures the thermal diffusivities tend to be decreasing functions of temperature as would be expected if the transport were due to a gas of extended phonons. Both regimes can be modeled by introducing an effective "hopping velocity" $v_h = R/\tau_{loc}$ for the localized modes with R being the mean hopping distance and τ_{loc} their mean lifetime. The usual kinetic expression for the thermal diffusivity of a phonon gas then becomes

$$\alpha = \frac{1}{3} \frac{C_{ext}}{C} v_s^2 \tau_{ext} + \frac{1}{3} \frac{C_{loc}}{C} \frac{R^2}{\tau_{loc}} \quad (1)$$

The first term is the contribution of the extended states, moving with the sound velocity v_s and having mean lifetime τ_{ext} , and the second is the contribution due to the localized states.

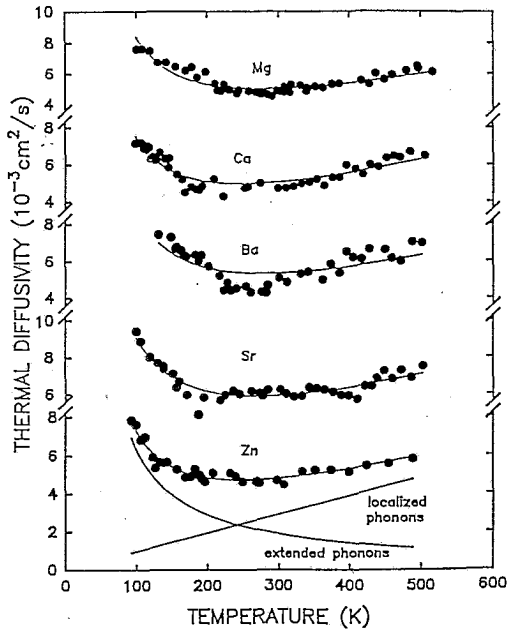


Fig. 1. Thermal diffusivities of several silicate glasses with compositions $15Na_2O \cdot 15MO \cdot 5Eu_2O_3 \cdot 65SiO_2$, where M is Mg, Ca, Sr, Ba, or Zn.

C is the heat capacity per unit volume. At high temperatures C_{loc} dominates the heat capacity, and the proportionality of the TAH to T arises from the inverse dependence on τ_{loc} . This relaxation time is due to the three phonon anharmonic process illustrated in Fig. 2. Its rate is controlled by the thermal population of facilitator phonons.

Because of the mesoscale inhomogeneities in the density and elastic properties, plane-wave states of large wave vector q will undergo strong scattering in a glass. The system is no longer able to support plane wave normal modes when the mean free path Λ becomes short enough that the Ioffe-Regel criterion, $q\Lambda > 1$, fails. Numerical studies by Bell and Dean (4,5) indicate that this breakdown signals phonon localization. The loss of wave vector conservation is also responsible for the low frequency Raman activity of glasses. Thus, it is attractive to associate the onset of Raman activity with phonon localization. The Raman edge should represent a critical length scale ξ_c at which $q\xi_c \sim 1$, so that v_s/ξ_c is the mobility edge ω_c .

Fig. 3 shows the low frequency portion of the Raman spectrum of the same glasses whose thermal diffusivities are displayed in Fig. 1. For similar glasses such as these, it is reasonable to expect that ξ_c will scale as the "formula unit" radius $r_f = (3M_o/4\pi\rho)^{1/3}$ of the smallest sphere that can contain the mean chemical composition (molecular weight M_o) at the bulk density ρ of the glass. This scaling relation is displayed in Fig. 4 for 11 different silicate glasses with compositions of 65 -70% SiO_2 . The expectation of a linear relation is well satisfied. It is also notable that this relation extrapolates to zero near the density corresponding to cristobalite, to which the silica network would devitrify. This linear relation gives confidence that the shift in the Raman edge represents a changing length scale as the network modifiers are changed.

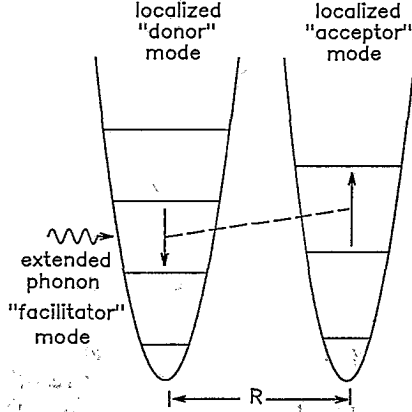


Fig. 2. The TAH process. A donor phonon is de-excited, creating a phonon of slightly different frequency on a neighboring acceptor. This is facilitated by an extended phonon to conserve energy.

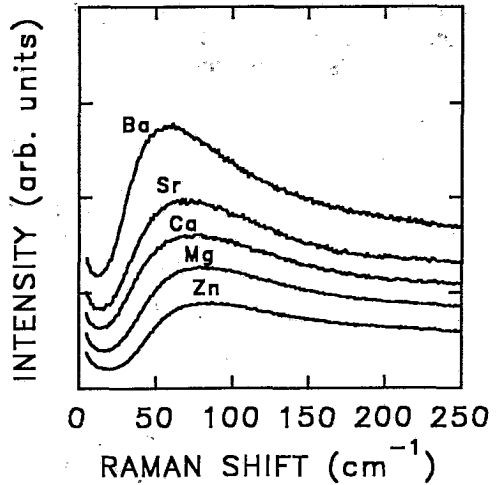


Fig. 3. Low frequency Raman spectra of the $15Na_2O.15MO.5Eu_2O_3.65SiO_2$ glasses.

Fig. 5 displays α for the $15M_2O \cdot 5ZnO \cdot 5BaO \cdot Eu_2O_3 \cdot 70SiO_2$ glass family. These results differ from those for the 65% SiO_2 family in that the regime of proportionality to T persists to lower temperatures, indicating stronger aharmonicicity.

Because our measurements on all ten of these glasses are in a regime where $kT > \hbar\omega_c$, the thermal population of facilitator modes will be proportional to $\hbar\omega_c/kT$ and the functional form of α will be

$$\alpha = (C_{ext}/C)AT^{-1} + (C_{loc}/C)BT, \quad (2)$$

assuming that the anharmonic process shown in Fig. 2 is the dominant resistive process for the extended phonons. The curves shown in Figs. 1 and 5 are least squares fits to this form. These can be seen to agree well with the measurements. The heat capacities have been estimated using the sound velocities in a Debye approximation for C_{ext} and a multiterm Einstein approximation with frequencies obtained from the Raman spectrum for C_{loc} . Details of this procedure have been described elsewhere (3).

Jagannathan, et al. (2) have studied the frequency dependence of the process in Fig. 2 in the fracton approximation. Their results, taking $\xi_c = v_s/\omega_c$ and averaging over the thermal phonon population give

$$\tau^{-1} = GC_3^2 \omega_c^4 T / (\rho^3 v_s^3), \quad (3)$$

where G is a geometrical factor depending on the structure of the glass, C_3 is the average anharmonic coupling constant, and ω_c is the mobility edge. The extended and localized phonon each follow this form with different G 's. Since all the structural information is contained in G , this form can

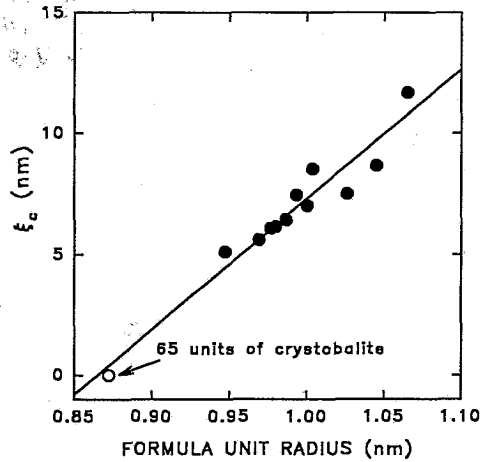


Fig. 4. Scaling of the characteristic length for the Raman edge with the "formula unit" radius. Both parameters are defined in the text.

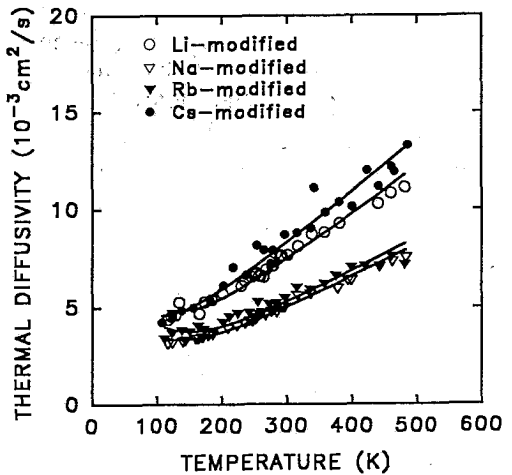


Fig. 5. Thermal diffusivities of the $15M_2O \cdot 5ZnO \cdot 5BaO \cdot 5Eu_2O_3 \cdot 70SiO_2$ glasses. The K-modified glass, not shown, is similar to the Na- and Rb-modified glasses.

be expected to apply to non-fractal glasses, as well as fractal ones. As shown in Fig. 6 excellent agreement with the predicted ω_c^4 dependence is obtained when the Raman edge is identified with the mobility edge for these glasses.

In Fig. 7 thermal diffusivities are presented for $\text{NdP}_5\text{O}_{14}$ glass, fused silica, and two silica xerogels. These are also well represented by contributions from extended and localized phonons. Note that α for $\text{NdP}_5\text{O}_{14}$ glass decreases much more rapidly below room temperature than either of the silicate families discussed above. The Raman edge for this glass is at 170 cm^{-1} , so that $\hbar\omega_c > k_B T$. Thus, the low temperature approximation for the phonon occupation number gives $\tau_{\text{ext}} \propto \exp(\hbar\omega_c/k_B T)$ rather than the proportionality to T^{-1} given by the high temperature approximation used in eq.[2]. Again, use of the Raman edge as the mobility edge gives excellent agreement with experiment.

Fused silica exhibits only a slight increase in α between 300 and 500 K, but a more significant one when data (6) to 1100 K are included. This indicates that fused silica is less anharmonic than the more complex glasses we have studied, so that it is more difficult to facilitate the TAH. This view is supported by the behavior of the extended phonons. The low temperature behavior can be described in the two carrier model with a τ_{ext} that does not explicitly depend on T , as would be the case if static scattering centers, rather than phonon-phonon processes limited the transport, also indicating a low anharmonicity.

The silica xerogel is similar to that in which Boukenter, et al. (7) used Raman spectroscopy to show that the phonon density of states was well described by the model of Alexander and Orbach (8) for a fractal

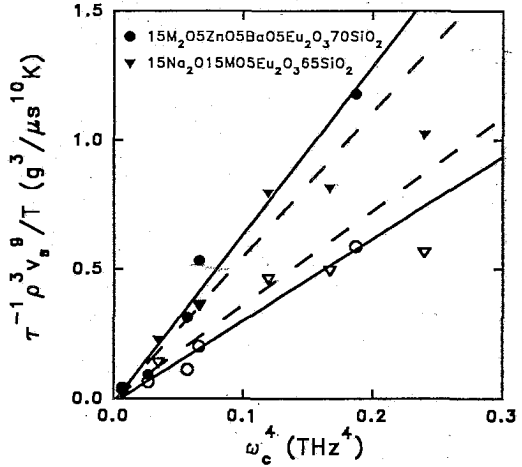


Fig. 6. Dependence of the phonon relaxation rates on the mobility edge. Note the agreement with the predicted ω_c^4 dependence. Open symbols are localized phonons; filled symbols, extended phonons.

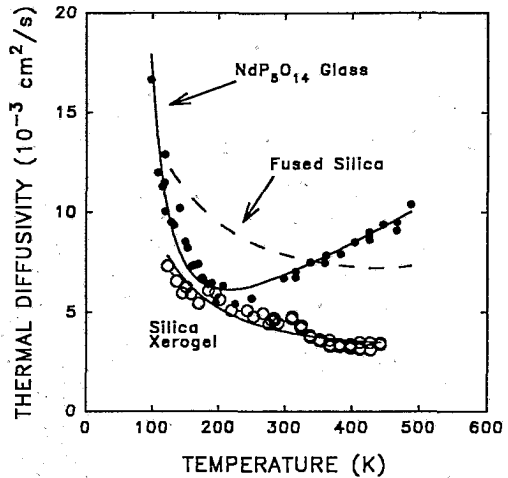


Fig. 7. Thermal diffusivities of $\text{NdP}_5\text{O}_{14}$ glass, fused silica and a silica xerogel.

fractal

system. Our Raman measurements also show such a density of states for this glass. The thermal diffusivities for this silica xerogel are preliminary, but to a first approximation the transport in this glass follows the same behavior as fused silica. This may indicate that heat transfer is by extended and localized phonons within the skeleton of the silica network and that the localized modes associated with the fractal structure of this network, and responsible for the low frequency Raman intensity in this glass, are not important heat carriers at the temperatures studied here.

Summary

It has been shown that a two carrier model of localized and extended phonons accounts well for the thermal diffusivities of a variety of glasses. When the phonon mobility edge is varied by chemical substitution of network modifiers within families of similar glasses, the predicted frequency dependence of the phonon relaxation rates due to anharmonic interaction between localized and extended phonons (2) is obtained if the mobility edge is identified with the low frequency Raman edge in these glasses. In all cases the relaxation times are long enough that $\omega\tau > 1$ so that both the localized and extended phonons are well-defined excitations throughout the temperature range of these experiments. The Ioffe-Regel criterion is also satisfied for the extended phonons.

Acknowledgements

It is a pleasure to thank Prof. R. C. Powell for providing many of the samples studied here. Thanks are also due to Profs. J. J. Martin and J. P. Wicksted for numerous discussions. The support of the National Science Foundation is gratefully acknowledged.

References

1. D. G. Cahill and R. O. Pohl, *Solid State Commun.* **70** (1989) 927.
2. S. Alexander, C. Laermans, R. Orbach, and H. M. Rosenberg, *Phys. Rev. B* **28** (1983) 4865; S. Alexander, O. Entin-Wohlman and R. Orbach, *Phys. Rev. B* **34** (1986) 2726; A. Jagannathan, O. Entin-Wohlman, and R. Orbach, *Phys. Rev. B* **39** (1989) 13465.
3. G. S. Dixon, B. Gault, S. Shi, P. A. Watson, and J. P. Wicksted, *Phys. Rev. B* (in press).
4. R. J. Bell, *Rep. Prog. Phys.* **35** (1972) 1315.
5. P. Dean, *Rev. Mod. Phys.* **44** (1972) 127.
6. H. Kanamori, N. Fujii, and H. Mizutani, *J. Geophys. Res.* **73** (1968) 595.
7. A. Boukenter, B. Champagnon, E. Duval, J. Dumas, J. F. Quinson, and J. Serughetti, *Phys. Rev. Lett.* **57** (1986) 2391.
8. S. Alexander and R. Orbach, *J. Phys. (Paris)* **43** (1982) L625.

DYNAMIC PROPERTIES OF ZINC HALIDE GLASSES AND MELTS

S.N. Yannopoulos and E.A. Pavlatou

Institute of Chemical Engineering and High Temperature
Chemical Processes

and

Department of Chemical Engineering, University of Patras.
P.O. Box 1414, GR 26500 Patras, GREECE

ABSTRACT

Photon correlation and Brillouin spectroscopy have been applied in the glass forming systems ZnCl_2 , ZnBr_2 and the 50% ZnCl_2 - ZnBr_2 mixture, in order to study the dynamics of local density fluctuations below T_g and far above T_m . The density correlation function of pure ZnCl_2 near T_g is well represented by the non-exponential form $\exp(-t/\tau)^\beta$ with $\beta=0.706\pm 0.012$ insensitive to temperature. The high value of β parameter categorizes ZnCl_2 in the class of relative "strong" glasses with an Arrhenius temperature dependence of relaxation time τ near T_g ($T_g+80^\circ\text{C}$). The hypersonic properties of pure components and the 50% mixture were also studied in the GHz region where a single relaxation process was revealed ($\beta=1$). The limiting sound velocities v_0 and v_∞ were calculated, showing up a linear decrease with temperature. The longitudinal relaxation time τ_l was found to follow an Arrhenius type relation.

INTRODUCTION

Although a large number of structural studies for ZnX_2 ($\text{X}=\text{Cl}, \text{Br}$) in the glassy and liquid states exists in literature (1), concerning their structural properties, very few dynamical studies have been performed. The high value of the shear viscosity of these salts near the melting point, implies that molecular readjustment is comparatively slow and the structural relaxation is responsible for ultrasonic and hypersonic dispersion (2-6). The longitudinal ultrasonic absorption (2,3) and longitudinal relaxation measurements (4-6) of pure ZnCl_2 at high temperatures (300-600°C) have revealed that a single relaxation time process is proper to characterize structural relaxation in this temperature range. The longitudinal relaxation time in the melt has an Arrhenius type temperature relation (4, 5) but there is a sharp deviation of sound velocity near T_g (25-110 °C) (5).

In recent years, photon correlation spectroscopy (PCS) has been mainly applied on amorphous polymers in order to investigate density, concentration and optical anisotropy fluctuations near and above T_g . Only few PCS studies in inorganic glasses (oxide (7) and ionic (8) glasses) have been appeared in literature. Maisano et al (9,10) performed PCS measurements on vitreous ZnCl_2 and suggested the presence of a correlation function that decays with a single relaxation time. These dynamics appeared to be incompatible with the actual glass transition behavior of pure ZnCl_2 melt with $T_g=102^\circ\text{C}$ (11). The relaxation characteristics of this glassformer is of particular interest since this network inorganic salt displays intermediate behavior between "strong" and "fragile" glasses (11).

The purpose of the present work is to investigate the structural relaxation time of ZnX_2 ($\text{X}=\text{Cl}, \text{Br}$) glasses near and above T_g over a broad temperature range, using PCS and Brillouin spectroscopy.

EXPERIMENTAL

A. Samples preparation

The reagent grade chemicals ZnCl_2 and ZnBr_2 were purchased from Merck (purity >98%) and Cerac/Pure Inc. (purity 99.5%) respectively. The starting materials were further

purified by bubbling gaseous HCl or HBr at 450-500 °C and then filtering under pure nitrogen atmosphere. In order to obtain ultrapure sample, this procedure has been applied twice to most of the samples used in this work. The anhydrous chemicals were handled in a nitrogen filled glove box with a water content less than 1 ppm. Mixtures were prepared by combining appropriate amounts of the desired zinc halides and transferred into clean, dry and degassed fused silica tubes (10 mm O.D., 8mm I.D. and 5-6 m length). All the optical cells were evacuated carefully and sealed.

The purified samples were heated at 600°C for several hours (minimum 7 hr) and the melts were quenched in water, forming the glasses. All the glasses were transparent, clear and enough dust free to be used for spectral measurements. The high chemical and physical purity of the salts, allowed us to obtain measurements down to ~ 40°C below the corresponding melting points and ~ 80 °C above their glass transition temperature (T_g). It was found that the crystallization temperature ranges of the ZnCl₂, 50% ZnCl₂- 50% ZnBr₂ and ZnBr₂ are respectively : 180-280, 150-380 and 170-270 °C. Thus, no spectral measurements could be obtained in these ranges.

B. Photon correlation spectroscopy (PCS)

The time correlation functions, $G(t)$, of the light scattered intensity for ZnCl₂ were mainly measured at a scattering angle of $\theta = 90^\circ$ at temperatures between 25-420 °C. Furthermore, two additional angles (45° and 90°) were used to examine the influence of q on $G(t)$. The excitation light source was an Ar⁺ laser (Spectra Physics 2020-4W) operating at $\lambda = 488$ nm with a stabilized power of 200 mW. Both vertical (V) and horizontal (H) polarized scattered light were measured using a Glan-Thomson polarizer.

The function $G(t)$ covering nine decades in time (10^{-7} -10s), was measured with a multiple digital correlator (ALV-5000/FAST) with 280 channels. The zinc chloride samples used in this study seem to be optically homogeneous, displaying a low value of the Landau-Plazcek intensity ratio (6-8 at 25 °C) in the Rayleigh-Brillouin spectra. Hence, the desired normalized density correlation function $g(t)$ is related to the measured $G(t)$, under the assumption of homodyne conditions, by the equation :

$$G(t) = A [1 + b |g(t)|^2] \quad [1]$$

where A is the baseline determined at long delay times and the amplitude b is considered as a fitting parameter.

The PCS measurements have been obtained at three different temperature regions : 25-100 °C below T_g , 120-180 °C in the supercooled region, and 280-420 °C in the liquid state. A home-made, water cooled optical furnace, with temperature gradient $\pm 1^\circ\text{C}$ near the window openings, was used for performing spectra at high temperatures. Thermal equilibration at each measurement was found to be crucial for reproducible results, but no measurable effect on $G(t)$ functions was found to be present related with the variation of thermal history of the sample.

C. Brillouin Spectroscopy (BS)

The light source for the Brillouin experiment was a Spectra Physics 2040-20 W Ar-ion laser operating at 488nm at about 0.2 W. Single mode was achieved by using an intracavity etalon. Scattered light was analysed by a single pass piezoelectrically scanned Fabry-Perot interferometer (Burleigh RC110). The mirrors were 5cm in diameter, $\lambda/200$ flat and had a reflectivity of about 0.98. The analysed light after passing a 200 μm pinhole behind Fabry-Perot was imaged on the cathode of a photomultiplier (EMI) cooled to -20°C, having a low dark current. Spectra were taken at one sweep with a typical scan of about 10³s. The piezoelectric elements were driven by a ramp generator (Burleigh RC23). Finally spectra were recorded by an acquisition interface board (ASYST) and transferred to computer for data handling.

RESULTS AND DISCUSSION

A. Photon correlation measurements of pure ZnCl₂.

The measured composite net correlation functions at various temperatures for ZnCl₂ at scattering angle $\theta = 90^\circ$ for VV configuration are shown in Fig.1. Near the glass transition temperature $T_g=102^\circ\text{C}$ the autocorrelation function is composed by at least two processes, where the first "main" process is sensitive to temperature evolution and the second "slow" process cannot be fully detected even at very long sample-time measurements ($\sim 30,000\text{s}$). The time correlation functions $G(t)$ near and above T_g of the "main" process are well represented by the KWW decay function according to :

$$[G(t)/A-1]^{1/2} = b \exp(-t/\tau)^\beta \quad [2]$$

with b, τ and β adjustable fitting parameters.

The value of β is a measure of the width of the distribution of relaxation times implied by the non-exponential character of the relaxation function. The results of the KWW analysis τ and β for different samples of ZnCl₂ as a function of temperature in the region near to $T_g \rightarrow T_g+80^\circ\text{C}$, are shown in Fig.2. The distribution parameter β is equal to 0.706 ± 0.012 virtually independent of temperature (Fig. 2b). In turn, the relaxation time τ experiences a temperature effect which is represented by an Arrhenius type relation as denoted in the Fig.2a. The Arrhenius fit yields an apparent activation energy $E_a=63 \text{ Kcal mol}^{-1}$. The relaxation parameters τ and β seems also to be insensitive to the sample cooling rate variation and generally to the thermal history of the examined samples. Moreover, the relaxation time of this "main" process is not affected by q variations (see insert of Fig.1), as expected for local density fluctuations when examined with light scattering (12).

The second "slow" process is characterized by large relaxation times in the whole range of $100\text{-}180^\circ\text{C}$ and cannot be detected within the long time limit of the correlator. It is noteworthy that the "slow" process is also present in all the obtained VH correlation functions and appears to be slightly affected by q variation (see insert Fig.1). Attempts of quantitative interpretation of this process spectra were doubtful, due to lack of a definite baseline, but indicate that the $G(t)$ function could not be represented by the empirical KWW equation. Taking into consideration the peculiar structure of ZnCl₂, which is a 3D network consisted of tetrahedral groups combined in various ways (1), the formation

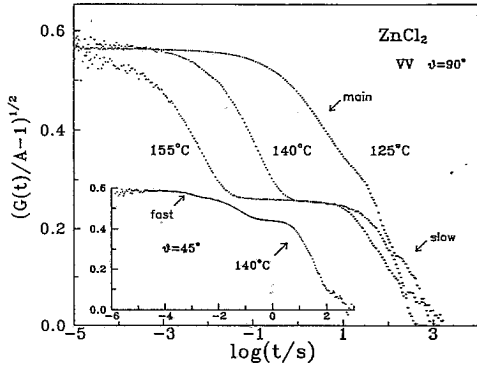


Figure 1: Temperature dependence of measured correlation functions of ZnCl₂ for scattering angle $\theta=90^\circ$ and VV configuration. The insert shows the experimental function $G(t)$ for $\theta=45^\circ$ at 140°C .

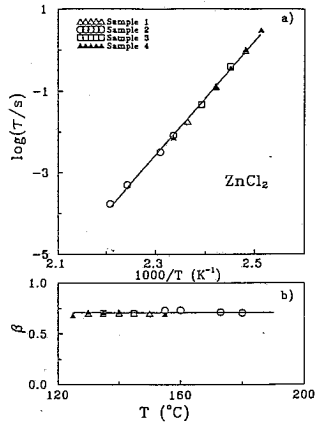


Figure 2: Temperature dependence of (a) the relaxation time τ and (b) the distribution parameter β obtained from the single KWW analysis of the density correlation function.

of superstructural units i.e. clusters is possible. Thus, the "slow" process could be tentatively attributed to reorientational motions of large "aggregates" or clusters. Furthermore, careful measurements of the correlation functions in the time range 10^{-7} - 10^{-4} at 125-150 °C, revealed the existence of a third "fast" process, which is shown better in the insert of Fig.1. Preliminary results of the inverse Laplace transform analysis of the $G(t)$ (8), have shown that the retardation times followed an Arrhenius type dependence with temperature, quite similar to the corresponding of "main" process.

Maisano et al (9) performed PCS measurements on vitreous $ZnCl_2$ at 98-180°C and observed a correlation function that decays with a single relaxation time ($\beta=1$) and measured mean relaxation times in the magnitude of few seconds. They have used a home-made correlator with a restricted time range (10-100s) and probably the obtained correlograms for which the measured baseline is not reached-monitored only a part of the "slow" process which is shown in Fig.1. Moreover, our PCS data at 260-430°C revealed no measurable correlation functions in the time region of 10^{-7} - 10^{-2} s and contradict the findings of Magazu et al (10).

From Brillouin measurements described in the following section, a single relaxation time process ($\beta=1$) appears to be proper for the characterization of the structural relaxation in the temperature range of 400-600°C. Figure 3 depicts a T_g^* -scaled modified Arrhenius plot for τ measured by PCS, US (2,3) and BS (4-6) techniques. The temperature T_g^* is defined as the value T where $\tau=100$ s. To visualize and compare different glass formers, the second curve corresponds to the measured values of τ from several techniques for the $3KNO_3 \cdot 2Ca(NO_3)_2$ ionic mixture (8). This glass exhibits one of the largest deviations from the Arrhenius law, broad structural relaxation functions in the vicinity of T_g ($\beta=0.47$) and is considered as a typical "fragile" material. An opposite behavior is demonstrated for $ZnCl_2$ and could be classified as a relatively "strong" glass former showing a strong resistance against structural degradation when heated through the supercooled regime. As it has been recently pointed out for a lot of examples of different glassformers (11), it seems that there is a correlation between fragility and nonexponentiality for linear response data.

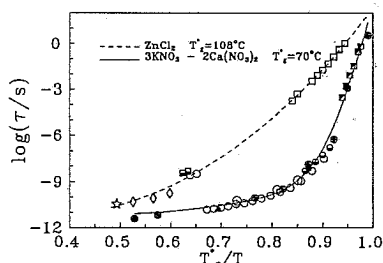


Figure 3: Modified Arrhenius plot of structural relaxation time τ for $ZnCl_2$ measured by PCS \square (this work), US \bullet (Ref.2.) \circ (Ref.3) and BS \diamond (Ref.5) \star (this work). The solid line represents the corresponding values of τ for $3KNO_3 \cdot 2Ca(NO_3)_2$ obtained by several complementary techniques (Ref.8).

B. Brillouin measurements of pure $ZnCl_2$, $ZnBr_2$ and 50% $ZnCl_2$ - $ZnBr_2$ mixture

Brillouin spectra of $ZnCl_2$, $ZnBr_2$ and of the 50% $ZnCl_2$ - $ZnBr_2$ mixture in the glass and molten state were recorded in a wide temperature range, i.e., 20-800°C, at 90° scattering angle. Figure 4 shows the Brillouin spectra of glassy and molten $ZnCl_2$ - $ZnBr_2$ mixture covering the whole temperature range indicating the onset of a dispersion region at about 500°C. The drastic changes in Brillouin shift and broadening have been also observed for the pure components.

The spectra were deconvoluted, using Lorentzian lines, in order to attain more accurate values for the shift and broadening. The hypersonic velocity v was determined from the relation: $v = f_B \lambda_0 / 2n \sin(\theta/2)$ where f_B is the frequency shift, λ_0 is the incident light wavelength, n is the refractive index of the material, and θ the scattering angle. The refractive index used for the mixture was estimated as a linear combination of the refractive indexes of pure melts.

Refractive index values for $ZnCl_2$ were taken by Iwadate et al.(13) and the values for $ZnBr_2$ were calculated by using the Clausius-Mossotti equation expressed in terms of the molar refractivity, R_m

$$n^2 = \frac{V_m + 2R_m}{V_m - R_m} \quad [3]$$

where $V_m = M_m/\rho$ is the molar volume. The density ρ values for $ZnBr_2$ are given in ref.(14).

The basic idea employed was that molar refractivities can be analysed into contributions from the individual ions. ($R_m = R_m^+ + 2 R_m^-$). The R_m values were calculated at different temperatures from the ion refractivities R_m^\pm which are related to the measured values of the electronic polarizabilities α^\pm (15) by the equation $R_m^\pm = \frac{4\pi N_A}{3} \alpha^\pm$ (N_A : Avogadro's number).

The damping of longitudinal sound waves is described by the sound absorption coefficient a which is related to the Brillouin linewidth $\Delta\omega_B$, $a = \pi \Delta\omega_B / \nu$. Accurate values of $\Delta\omega_B$ were obtained by subtracting the half width of central elastic line from the Brillouin linewidths.

In the case of the pure components, there was a temperature region, at the absorption maximum, in which the determination of the absorption coefficient, could not be determined. In that region the damping of the acoustic phonons was too large, $\lambda \approx 1$, and the lineshape was quasi-Lorentzian in accordance with the theory which predicts Lorentzian lines only if $\lambda \ll 1$. In Figure 5 sound velocity and absorption coefficient are plotted as a function of temperature. The two limited velocities ν_0 and ν_∞ for low and high frequency respectively are indicated as dashed lines. The temperature dependence of these velocities in ms^{-1} are given below for $ZnCl_2$ and the $ZnCl_2$ - $ZnBr_2$ mixture.

$$\begin{aligned} ZnCl_2: \quad \nu_0 &= 992 - 0.32 t \text{ (}^\circ C\text{)} \\ \nu_\infty &= 2230 - 0.94 t \text{ (}^\circ C\text{)} \\ ZnCl_2-ZnBr_2: \quad \nu_0 &= 756 - 0.29 t \text{ (}^\circ C\text{)} \\ \nu_\infty &= 1645 - 0.83 t \text{ (}^\circ C\text{)} \end{aligned}$$

Similar relations for $ZnBr_2$ were difficult to calculate due to spectral-noise especially at temperatures below 460 $^\circ C$. For this sample only the maximum of the absorption could be roughly estimated, resulting to a tentative calculation of the longitudinal relaxation time $\tau_l \approx 44.6$ ps.

Longitudinal density fluctuations decay with a characteristic relaxation time, τ_l , which can be estimated from the maximum of the absorption coefficient curve. The τ_l values for the three sample are:

| Sample | τ_l (ps) |
|---------------------|---------------|
| $ZnCl_2$ | 36.3 |
| $ZnBr_2$ | 44.6 |
| $ZnCl_2$ - $ZnBr_2$ | 49.4 |

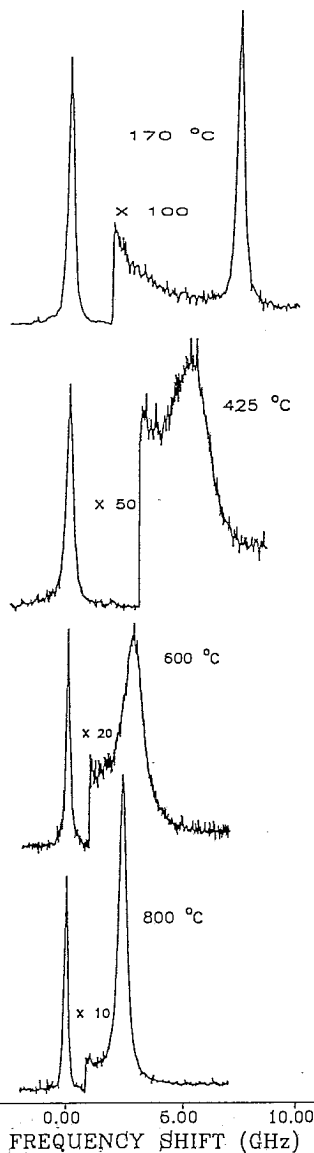


Figure 4: Brillouin spectra of glassy and molten 50% $ZnCl_2$ - $ZnBr_2$ mixture at scattering angle 90° , at various temperatures.

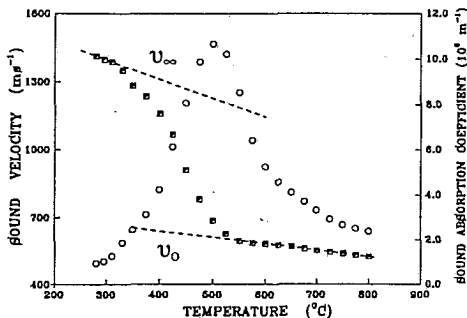


Figure 5: Graph of velocity and sound absorption coefficient for the 50% ZnCl_2 - ZnBr_2 mixture vs temperature. The dashed lines show the limiting velocities U_0 and U_∞ .

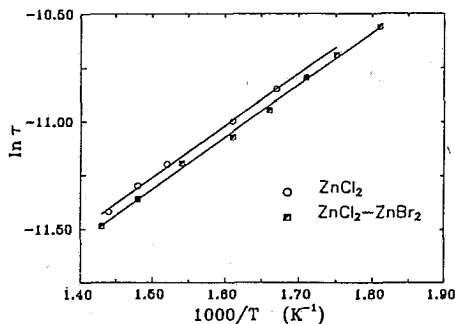


Figure 6: Plot of the longitudinal relaxation time of ZnCl_2 and the 50% ZnCl_2 - ZnBr_2 mixture.

It appears from these values that the mixture conserves sound propagation longer than the pure components.

In accordance with the single relaxation time theory (2) an expression for the longitudinal relaxation time can be obtained

$$\tau = \frac{1}{2a} \frac{v^2 - v_0^2}{v^3} \quad [4]$$

Figure 3 shows that $\ln \tau$ varies linearly with $1/T$. Linear fitting gave the following activation energies:

$$E_a = 41.7 \text{ KJ mol}^{-1} \quad \text{for } \text{ZnCl}_2$$

and

$$E_a = 39.6 \text{ KJ mol}^{-1} \quad \text{for } \text{ZnCl}_2\text{-ZnBr}_2$$

It seems that within experimental errors, the activation energies for the pure component and the mixture are similar. Furthermore, the calculated longitudinal relaxation times seems to depend strongly on temperature, indicating considerable structure variations in the melts.

CONCLUSIONS

Photon correlation and Brillouin spectroscopy measurements of the glass forming systems ZnCl_2 , ZnBr_2 and 50% ZnCl_2 - ZnBr_2 in the vitreous and liquid states have shown that: (a) The autocorrelation functions $G(t)$ of pure ZnCl_2 indicate the existence of two at least processes occurring at temperatures near T_g . The first "main" process is attributed to density fluctuations and is very well represented by the KWW equation with $\beta=0.706 \pm 0.012$, which is insensitive to temperature and sample cooling rate variations. The relaxation time τ is independent from q variation and exhibits an Arrhenius type temperature behavior in the region $T_g \rightarrow T_g + 80$ °C. ZnCl_2 can be classified as a relative "strong" glass, with small deviations from exponential response and nearly Arrhenius type structural relaxation time through $T_g \rightarrow T_m + 200$ °C. The second "slow" process is tentatively attributed to reorientational motions of large "aggregates" or clusters formed in the 3D-network structure.

(b) The dynamic behavior of density fluctuations in the 10^{-9} - 10^{-11} s time domain, was studied by Brillouin spectroscopy for ZnCl_2 , ZnBr_2 and 50% ZnCl_2 - ZnBr_2 . Increasing temperature, the velocities at limiting low and high frequency, were found to decrease with roughly the same slopes. The longitudinal relaxation times indicate that structure changes occur with increasing temperature in the melt.

ACKNOWLEDGEMENTS

The authors are indebted to Profs. G. Fytas and G.N. Papatheodorou for helpful discussions during the course of the present investigation and for valuable comments on the manuscript.

REFERENCES

1. E. A. Pavlatou in this Proceedings (and ref. therein)
2. G.J. Gruber and T. A. Litovitz, *J. Chem. Phys.* 40 (1964) 13
3. H. Zhu, Y. Sato, T. Yamura and T. Ejima in "Proceedings of 7th International Symposium on Molten salts" (1990) 152
4. H. E. G. Knappe, *J. Chem. Phys.* 80 (1984) 4788
5. M. Soltwisch, J. Sukmanowski and Q. Quitmann, *J. Chem. Phys.* 86 (1986) 3207
6. H. M. Zhu, Y. Sato, T. Yamamura and K. Sugimoto in "Proceedings of 8th International Symposium on Molten salts" (1992) 41
7. C. Lai, P.B. Macedo and C. Montrose, *J. Amer. Ceram. Soc.* 58 (1975) 120
8. E. A. Pavlatou, A. K. Rizos, G. N. Papatheodorou and G. Fytas, *J. Chem. Phys.* 94 (1991) 224
9. G. Maisano, D. Majolino, F. Mallamace, M. L. Cacciola and C. Vasi, *Solid St. Commun.* 57 (1986) 509
10. S. Magazu, G. Maisano, F. Mallamace, P. Migliardo, F. Alliota and C. Vasi, *Phil. Mag. B* 56 (1987) 155
11. R. Böhmer, K. L. Ngai, C. A. Angell and D. J. Plazek, *J. Chem. Phys.* 99 (1993) 4201
12. G. Fytas, G. Floudas and K. L. Ngai, *Macromolecules* 23 (1990) 1104
13. Y. Iwadate, K. Kawamura, K. Murakami, K. Igarashi and J. Mochinaga, *J. Chem. Phys.* 77 (1982) 6177
14. G.J. Janz in "Molten salts Handbook", Academic Press Inc. N. Y. (1967)
15. Y. Iwadate, J. Mochinaga and K. Kawamura, *J. Phys. Chem.*, 85 (1981) 3708

STRUCTURAL PROPERTIES OF ZnCl₂-ZnBr₂ GLASSES AND MELTS

E.A. Pavlatou

Institute of Chemical Engineering and High Temperature
Chemical Processes

and

Department of Chemical Engineering, University of Patras.
P.O. Box 1414, GR 26500 Patras, GREECE

ABSTRACT

Raman spectra of ZnCl₂, ZnBr₂ and their mixtures were measured in the glassy and liquid state, at various temperatures and compositions. The overall behavior of the spectra indicates the presence of different bonding states in the "network" structure, where halogen atom sharing of the ZnX₄ (X=Cl,Br) tetrahedral groups occurs. Furthermore, at elevated temperatures the "network" structure breaks up, creating in the melt non bridging halogen atoms which are bound to a three-fold coordinated Zn atom. The spectra of the binary ZnCl₂-ZnBr₂ system show that the mixtures are formed by a random closest packing of halogen atoms. The observed similarities between depolarized reduced Raman spectra and the total density of vibrational states in the glassy and liquid state are presented and discussed.

INTRODUCTION

Among pure liquid inorganic halides, ZnCl₂ and ZnBr₂ are unusual for their high viscosities (1) near their melting points, and for their consequent abilities to supercool and vitrify in macroscopic quantities. The unusual physical properties of zinc halides indicate peculiar structural properties, which have been extensively investigated by a variety of spectroscopic techniques (2). X-ray scattering (3-5), EXAFS (6) and neutron diffraction (7-8) spectroscopy have been applied for studying pure ZnCl₂ (3, 5-8) and ZnBr₂ (4, 6, 8) in both vitreous and liquid states. All these diffraction studies confirmed a common structural model for glassy and liquid ZnX₂ (X=Cl,Br), where the Zn²⁺ ions occupy tetrahedrally coordinated "sites" in a closely packed ion structure with strong intermediate ordering. This tetrahedrally coordinated "network" structure was further supported by Raman (9-14), IR (10) and inelastic neutron scattering measurements (11, 15) of disordered (vitreous and liquid) ZnCl₂. Zinc bromide and ZnCl₂-ZnBr₂ mixtures are less studied except for a few Raman works in glassy state (16, 17). In general, the peculiar features of the reported spectra were attributed to the existence either of polynuclear in Zn aggregates (9, 12) or of bridging and non bridging states of halide ions (10, 12, 14, 16-17).

Dynamical studies of ZnCl₂ at temperatures below T_g to above T_m (18-20), have pointed out that the glass could possess a higher level of structural organization, responsible for the composite measured time correlation functions of scattered light (20). From the point of view of transport and relaxation properties (21), ZnCl₂ displays intermediate behavior between strong (oxide) and fragile (K-Ca-NO₃) glasses, implying resistance of the short and medium range order to thermal degradation.

The purpose of the present work is to investigate by Raman spectroscopy the structural properties of the ZnCl₂-ZnBr₂ system in both vitreous and liquid state. Systematic temperature and composition dependence measurements are reported and the data are interpreted in terms of different bridge-bonding states of the anions participating in the "network" like structure.

EXPERIMENTAL

High-purity anhydrous ZnCl₂ and ZnBr₂ were prepared from the corresponding Merck (purity >98%) and Cerac/Pure Inc. (purity 99.5%) reagents by bubbling gaseous HCl or HBr

at 450-500 °C and then filtering them under nitrogen atmosphere. The anhydrous chemicals were handled in sealed fused silica containers or in a nitrogen filled glove-box (<1 ppm H₂O), where all chemical transfers took place.

The Raman (optical) cells were made of fused silica tubes of constant diameter (4mm o.d., 3mm i.d.) and 30-40 mm length. Preweighed amounts (total weight ~200 mg) of the clean chemicals were transferred into the dry, flamed and degassed cells and after sealed under vacuum. All optical cells were heated at 550 °C for several hours (~7 hr) and the melts were quenched in water at room temperature. The obtained glasses were clear, transparent and did not fluoresce when the Ar⁺ lines were used to excite the spectra.

The Raman spectroscopic system, the optical furnace and the techniques for measuring relative intensities from samples in different cells, were the same as those described in detail elsewhere (22). A personal computer was interfaced with the spectrometer for storage of the spectra and for direct calculation of the reduced Raman intensity and depolarization ratios.

RESULTS AND DISCUSSION

The measured first-order Stokes Raman intensity $I(\omega)$ at frequency ω is related to the reduced Raman intensity $R(\omega)$ according to the following equation (23,24)

$$R(\omega) = I(\omega) \omega (\omega_0 - \omega)^{-4} [n(\omega) + 1]^{-1} \quad [1]$$

where ω_0 is the excitation laser frequency and $[n(\omega) + 1] = \left[\exp \frac{h\omega}{KT} - 1 \right]^{-1} + 1$, the Boltzmann thermal population factor. The reduction procedure [1] could be applied equally for the I_{VV} and I_{HV} spectra, in order to separate the anisotropic R_{aniso} and R_{iso} components of the reduced Raman intensity according to the relations :

$$\begin{aligned} R_{\text{iso}}(\omega) &= R_{VV}(\omega) - \frac{4}{3} R_{HV}(\omega) \\ R_{\text{aniso}}(\omega) &= R_{HV}(\omega) \end{aligned} \quad [2]$$

Totally symmetric vibrations are distinguished from overlapping depolarized modes by using and comparing R_{iso} and R_{aniso} spectra.

An advantage for using this correction is that it suppresses the Rayleigh line - especially at elevated temperatures - and "Boson" peaks of amorphous samples, emphasizing in that way the low frequency features ($\omega < 100 \text{ cm}^{-1}$) of the spectra. The effect of the thermal population factor is also important for quantitative measurements of the relative intensities of species in equilibrium, with Raman bands in the intermediate frequency region ($\omega < 500 \text{ cm}^{-1}$) (22).

Shuker and Gammon (23) and later Galeener and Pen (24) derived general expressions in the harmonic approximation, in which the first-order reduced Raman spectrum $R(\omega)$ is directly comparable to the infrared absorption coefficient $a(\omega)$ and the reduced inelastic scattering cross section $G(q, \omega)$. The $R(\omega)$ spectrum is directly related to the vibrational density of states g_b (VDOS) through the coupling coefficients C_b :

$$R(\omega) \sim \sum_b C_b(\omega_0, \omega) g_b \quad [3]$$

where b represents a "band" of states.

The coefficients C_b could not be determined experimentally but a substitute procedure is to compare the optical spectrum $R(\omega)$ with the effective vibrational density of states (VDOS) $G(q, \omega)$, which can be determined from inelastic neutron scattering data:

$$G(q, \omega) = A(q, \omega) g(\omega) \quad [4]$$

Figure 1 illustrates a comparison of the anisotropic reduced Raman (R_{aniso}) spectra with the neutron effective (VDOS) (15) for pure ZnCl₂ in the glassy and molten states. In general, a considerable similarity between the two curves is revealed - remarkable in the case of vitreous

Structural properties of ZnCl₂-ZnBr₂ glasses and melts

ZnCl₂ - but the vibrational sub-bands are not resolved in the VDOS spectra as well as in the R_{aniso} spectra. The R_{aniso} spectra are characterized by two intense bands at 110 and 275 cm⁻¹ and four weaker at 80, 232, 315 and 375 cm⁻¹. The VDOS spectra of both glass and liquid, are dominated by two broad features centered at the same frequency of the corresponding most intense peaks of R_{aniso} spectra. In a recent neutron study (15) these features were ascribed to the F₂ modes of ZnCl₄²⁻. It is noteworthy, that the neutron bands have widths >50 cm⁻¹, which are much larger than the corresponding widths in the optical spectra. Thus, the additional optical features of R_{aniso} spectra could be possibly associated with separate peaks in the VDOS spectra, which are not observed due to inadequate resolution of neutron data (~40-50 cm⁻¹). The different shape and intensity ratio of the peaks observed in R_{aniso} spectra in comparison with the G(ω) spectra may actually reflect the frequency dependence of the coupling coefficient C_b(ω) much more than that of the subband density of states especially in the low frequency region up to ~150 cm⁻¹ (Fig.1b). The observed similarities of R_{aniso}(ω) and neutron spectra of vitreous and liquid ZnCl₂ indicates that the reduced Raman spectra could be represented as a linear combination of the subband density of states, and provide a convenient way for extracting the vibrational density of states from Raman data.

Most of the Raman spectra obtained in the present work are at elevated temperatures, and it is necessary for quantitative comparisons of the intensities to use the R(ω) representation of the spectra. Figure 2 shows the reduced R(ω) of pure ZnCl₂ for the VV configuration at various temperatures from 25 °C up to 700 °C. Details of the low frequency spectrum of the glass at 135 °C, are given in the insert of Fig.2. A multicomponent fit of a set of symmetric Lorentzian-Gaussian curves were applied to most of the obtained spectra. The comparison of the R_{aniso} and R_{iso} spectra indicates two highly polarized bands at 232 and 275 cm⁻¹ and two less polarized at 315 and 375 cm⁻¹. In the low frequency region, two depolarized bands are seen, and a third one - deconvoluted in the isotropic spectra - at 128 cm⁻¹ is polarized. Minor variations of the raw relative intensities I(ω) were detected with increasing temperature. However, the overall R(ω) intensity decreases drastically with evolution of temperature and the band intensities at 275 and 375 cm⁻¹ increase relatively to the 230 cm⁻¹. The intensity of 315 cm⁻¹ seems not to be affected by temperature, within the accuracy of deconvoluted measurements.

The behavior of ZnBr₂ spectra was similar to ZnCl₂ spectra and the R(ω) intensity changes were more drastic with increasing temperature (Figure 3). The R(ω) spectra of pure ZnBr₂ are characterized by four highly polarized bands at 150, 173, 215 and 285 cm⁻¹. As in the case of ZnCl₂, three bands are located at lower frequencies, two depolarized at 63 and 81 cm⁻¹ and a polarized at 96 cm⁻¹ (see insert Fig.3). The intensity of 150 cm⁻¹

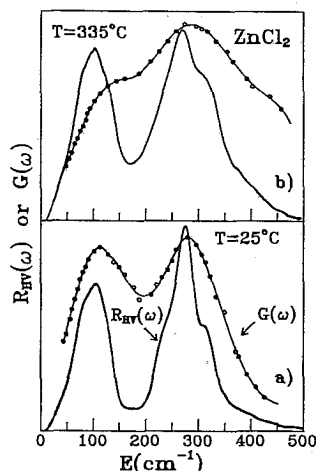


Figure 1: Comparison of the reduced Raman (R_{HV}) spectra with the effective VDOS of vitreous and liquid ZnCl₂. The circles correspond to the VDOS obtained from INS data of Ref. 15.

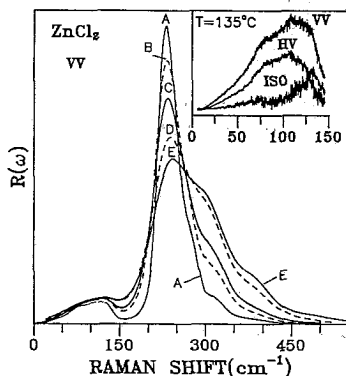


Figure 2: Temperature dependence of the reduced Raman spectra of ZnCl₂ at A:25, B:295, C:400, D:600 and E:700°C. The insert shows the low frequency R(ω) spectra at 135°C for different polarizations.

decreases rapidly with increase of temperature, while an opposite behavior is demonstrated for the intensities of 173 and 285 cm^{-1} . The 215 cm^{-1} band seems to display the same intensity profile as the 315 cm^{-1} ZnCl_2 -band with variation of temperature.

The overall temperature dependence of the thermal population free $R(\omega)$ spectra for ZnX_2 ($X=\text{Cl}, \text{Br}$) liquids (Fig.2,3), revealed discreet changes in the relative intensities of the observed bands. This dynamic behavior of the intensity profiles indicates that, structural changes occurred with increasing temperature, which affect the vibrational frequencies of the ZnX_4 tetrahedra participating in the "network" like structure. Diffraction studies of crystalline ZnCl_2 (3) and ZnBr_2 (4) have confirmed a vertex tetrahedral sharing structure of single bridged halogen X atoms. However, neutron study of liquid ZnCl_2 (7) showed that the Zn-Zn coordination number is 4.7, pointing out that on the average there are more than four ZnCl_4 tetrahedra around each ZnCl_4 group.

Considering the space topology of the tetrahedra and the 4.7 Zn-Zn coordination number, it is possible in the ZnCl_2 network to have one Cl atom sharing the vertices with more than two ZnCl_4 groups and/or two Cl atoms bound in a common edge of two tetrahedra (edge sharing). Figure 4 presents schematically three such structures, one having single vertex having (SV), the other with double vertex sharing (DV) and the third with edge sharing (E). The similarity of the structure of crystalline- ZnBr_2 to the corresponding of ZnCl_2 , supports also the presence of such different type connections between the ZnBr_4 units as shown in Fig.4. These "structures" i.e. SV, DV or E create non-equivalent halogen atoms of the ZnX_4 groups and consequently different Zn-X stretching vibrational frequencies are expected.

This structural model is supported by the temperature dependence of the Raman $R(\omega)$ spectra (Fig.2,3). The 232 and 150 cm^{-1} bands of ZnCl_2 and ZnBr_2 respectively, could be assigned to a Zn-X stretching mode, which is weakened by single bridging of more than two ZnCl_4 at a common X atom (e.g. structure DV). Increasing temperature tends to reduce the number of ZnCl_4 bound to a common X atom, which in turn strengthens the Zn-X bond moving the vibrational mode to higher frequencies (i.e. the 275 and 173 cm^{-1} of ZnCl_2 and ZnBr_2). Thus, an equilibrium between "species" of SV with DV type gives an account for the reversible temperature changes of the relative $R(\omega)$ intensities. In this context, the 375(ZnCl_2) and 285(ZnBr_2) cm^{-1} bands could be attributed to Zn-X vibrations of non bridged X atoms (structure TB). Recent thermal neutron data (8) of liquid ZnCl_2 indicate a decrease (~7%) of the coordination number of Zn-Cl at elevated temperatures, implying the formation of ZnCl_3 units having a Zn-Cl terminal bond.

The composition dependence of the $R(\omega)$ spectra for the binary ZnCl_2 - ZnBr_2 glasses at room temperature is shown in Figure 5. In the high frequency region (above 100 cm^{-1}), the spectra of mixtures show new bands that shift with composition variation, while the main bands of the pure components either shift or lose their intensity. A possible assignment (17) of these "new" bands is to the presence of mixed halide tetrahedral groups of $\text{ZnCl}_x\text{Br}_{4-x}$ ($x=0-4$) type, which participate as basic units in the "network" structure. Thermodynamic properties

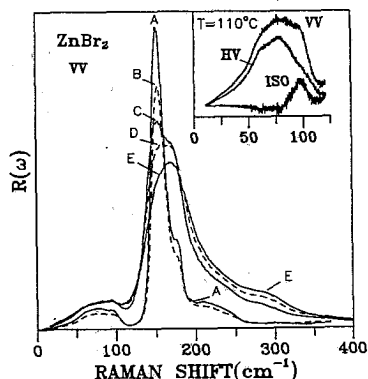


Figure 3: Temperature dependence of the reduced Raman spectra of ZnBr_2 at A:25, B:110, C:450, D:550 and E:660°C. The insert shows the low frequency $R(\omega)$ spectra at 110°C for different polarizations.

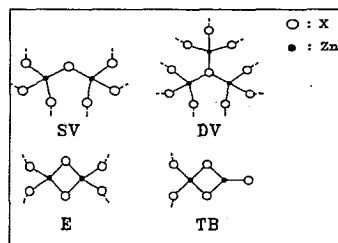


Figure 4: Structural models for bonding of the ZnX_4 groups in glass/liquid ZnX_2 ($X=\text{Cl}, \text{Br}$) SV: single vertex, DV: double vertex, E: edge sharing, TB: terminal bond, indicates the presence of non-bridging X atoms.

of liquid ZnCl₂-ZnBr₂ system (25) implied that the mixtures could be described in terms of a random closest packing of Cl and Br atoms which offers tetrahedral sites for the formation of ZnCl_xBr_{4-x} groups. In such an arrangement, it's rather unlikely to find clusters of the same halogen atoms giving spectral features close to those of the pure components. The formation of such kind of clusters is excluded in the R(ω) spectra, where for the 75% ZnCl₂ mixture the 150 cm⁻¹ ZnBr₂ band is completely absent.

The temperature dependent spectral measurements for the mixtures as glasses or liquids, have shown that the SV and TB configurations are favored at higher temperatures, consequently forming increasing amounts of mixed ZnCl_xBr_{4-x} units and terminal bonds Zn-X participating in the network. At temperatures above 450 °C, the presence of the bands due to TB structures are more pronounced. Furthermore the addition of small amounts of ZnCl₂ in the ZnBr₂ network seems to favored the SV structure.

The low frequency R(ω) spectra of the mixtures ZnCl₂-ZnBr₂ resembles the corresponding of pure components (Fig.2,3). The spectral properties of these bands seems to be unaffected by the local thermostructural changes occurring in the "network". The systematics followed in the obtained spectra, indicate a "collective" character of the vibrational modes in this low energy region.

CONCLUSIONS

Raman spectroscopic measurements of the ZnCl₂-ZnBr₂ system in the glassy and liquid states have shown that:

1. The temperature dependence of reduced Raman spectra, R(ω), of pure ZnX₂(X=Cl,Br) liquids revealed discreet changes in the relative intensities of the observed bands. The data are interpreted to indicate the presence of different bonding states in the network structure, where halogen atom sharing of the ZnX₄ tetrahedral groups occurs. Additionally, at higher temperatures the network breaks up creating ZnX₃ units having non-bridged halogen atoms.
2. For ZnCl₂, there are similarities between R_{aniso}(ω) and the neutron VDOS in the vitreous and liquid state.
3. The ZnCl₂-ZnBr₂ mixtures are formed by a random closest packing of chlorine and bromide atoms which offers tetrahedral sites for the formation of ZnCl_xBr_{4-x} groups. The formation of clusters having locally large numbers of the same halogen atoms X is excluded.

ACKNOWLEDGEMENTS

The author is indebted to Prof. G.N. Papatheodorou for helpful guidance during the course of this work.

REFERENCES

1. a) M. V. Susic and S. V. Mentus, J. Chem. Phys. 62 (1975) 744
b) F. Ma and M. Zhang, J. Non-Cryst. Solids 113 (1989) 106
2. J. Wong and C. A. Angell in "Glass Structure by Spectroscopy", Marcel Dekker, N.Y. (1986)
3. H. L. Yakel and J. Brynestad, Inorg. Chem. 17 (1978) 3294
4. C. Chieh and M. White, Z. Kristallogr. 166 (1984) 189
5. R. Triolo and A. H. Narten, J. Chem. Phys. 74 (1981) 703
6. K. Kadono, H. Kageyama, N. Kamijo and H. Tanaka, J. Non-Cryst. Solids 123 (1990) 291
7. S. Biggin and J. E. Enderby, J. Phy. C 14 (1981) 3129

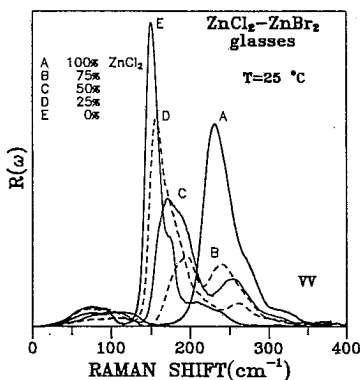


Figure 5: Composition dependence of the reduced Raman spectra of ZnCl₂-ZnBr₂ glassy mixtures at 25 °C.

8. D. A. Allen, R. A. Howe and N. D. Wood, *J. Chem. Phys.* 94 (1991) 5071
9. R. B. Ellis, *J. Electrochem. Soc.* 113 (1966) 485
10. C. A. Angell and J. Wong, *J. Chem. Phys.* 53 (1970) 2053
11. F. L. Galeener, J. C. Mikkelsen, A. C. Wright, R. N. Sinclair, J. A. E. Desa and J. Wong, *J. Non-Cryst. Solids* 42 (1980) 23
12. F. Aliotta, G. Maisano, P. Migliardo, C. Vasi, F. Wanderligh, G. P. Smith and R. Triolo, *J. Chem. Phys.* 75 (1981) 613
13. M. L. Cacciola, S. Magazu, P. Migliardo, F. Aliotta and C. Vasi, *Solid State Commun.* 57 (1986) 513
14. M. Itoh, K. Sakai and T. Nakamura, *Inorg. Chem.* 21 (1982) 3552
15. D. L. Price, M. Saboungi, S. Susman, K. J. Volin and A. C. Wright, *J. Phys.: Condens. Matter* 3 (1991) 9835
16. R. M. Almeida, *J. Non-Cryst. Solids* 95&96 (1987) 279
17. K. Kinugawa, K. Kadono and H. Tanaka, *J. Non-Cryst. Solids* 110 (1989) 265
18. a) H.E.G. Knappe, *J. Chem. Phys.* 80 (1984) 4788
b) M. Soltwisch, J. Sukmanowski and D. Quitmann, *J. Chem. Phys.* 80 (1987) 3207
19. G. Maisano, D. Majolino, F. Mallamace, P. Migliardo, F. Aliotta and C. Vasi, *Phil. Mag. B* 56 (1987) 155
20. a) G. Fytas, G. N. Papatheodorou and E. A. Pavlatou to be submitted
b) S. N. Yannopoulos and E. A. Pavlatou see paper in these Proceedings
21. C. A. Angell, *J. Non-Cryst. Solids* 102 (1988) 205
22. S. Boghosian and G. N. Papatheodorou, *J. Phys. Chem.* 93 (1989) 415
23. R. Shuker and R. W. Gammon, *Phys. Rev. Lett.* 25 (1970) 222
24. F. L. Galeener and P. N. Sen, *Phys. Rev. B* 17 (1978) 1928
25. G. N. Papatheodorou and O. J. Kleppa, *Z. anorg. Chem.* 401 (1973) 132

Fragility and decoupling in glass: A chemical perspective

G. D. Chryssikos, E. I. Kamitsos, J. A. Kapoutsis and A. P. Patsis

Theoretical and Physical Chemistry Institute, National Hellenic Research Foundation, 48, Vas.
Constantinou Ave., 11635 Athens, Greece

Abstract

Glass forming liquids often experience chemical alterations upon cooling. The identification of the nature and extent of these alterations as a function of composition is possible by spectroscopic and devitrification experiments. This paper provides several examples where the chemistry of vitrification can be related to trends in properties such as the strength/fragility and the decoupling of the conductive motions from the structural relaxations.

INTRODUCTION

The formation of glass is associated with the capture of high temperature structures in a metastable solid configuration. Hence, the knowledge of the channels available for the chemical relaxation of a system upon quenching is of special interest. The gamut of liquids that vitrify upon fast cooling (quenching) is enormous and the chemical understanding of vitrification requires a broad structural perspective based on the hierarchy of local, intermediate and long-range structural correlations.

The real time mapping of the chemical relaxations accompanying the quenching of a melt is rarely available. More easily accessible is the temperature dependence of 'physical' properties such as the heat capacity (C_p), and the shear viscosity (η). Angell has employed the variation of these properties in the glass transition range to cast a broad classification of glassforming substances (1). According to this classification, 'strong' liquids approach the glass transition range with Arrhenius viscosity-temperature dependence and exhibit small changes in C_p on going from the liquid to the glassy state. On the other hand, 'fragile' systems exhibit sublinear $\log \eta$ vs $1/T$ dependence and larger ΔC_p values. Another index particularly valuable for the classification of ionically conducting glasses involves the extent of the decoupling between structural and conductivity relaxation modes in the glass transition range (2).

The scope of this paper is the identification of the compositional dependence of strength/fragility and decoupling in selected glass families and the advancement of a chemical reasoning for their understanding. The study focusses on binary and ternary alkali borates because these systems have broad glass forming ranges and significant chemical richness (3).

ON THE GLASS STRUCTURE

Figure 1, adapted from Liu and Angell (4), shows the spectral response of a typical sodium borate glass from d.c. up to the beginning of the infrared, and for temperatures up to T_g . In a logarithmic frequency scale, each spectrum is dominated by a dc plateau and a dielectric dispersion region, both due to relatively long range ionic motions. Over these frequency ranges, the effect of the chemical microstructure on the dispersion of the glass is averaged out, at least to some extent. It is of no surprise then that time-temperature superpositions work out well (5) and lead to the establishment of 'universalities' (6). As the frequency increases, the spectral response is due to

increasingly localized motions. As a result, the particular chemical characteristics of a glass become increasingly more important. For instance, in the higher frequency end of the spectra in Fig. 1a, the far-infrared response involves the localised vibrations of the alkali cations in their equilibrium sites (7, 8), and constitutes the limit of d.c. conductivity at infinitely high temperatures (4). At higher frequencies (not included in Fig. 1), the mid-infrared spectrum is governed by the composition-specific local vibrations of the glass network units (8).

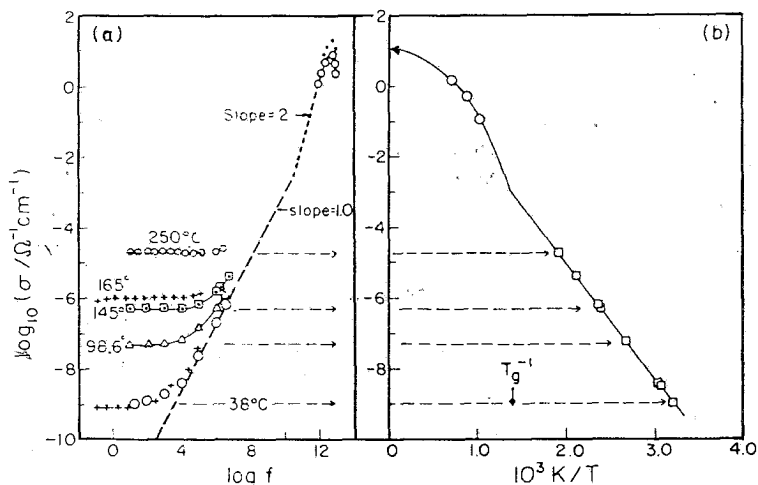


Figure 1. (a) Conductivity spectra of $0.35\text{Na}_2\text{O} \cdot 0.65\text{B}_2\text{O}_3$ glass and (b) Temperature dependence of d.c. conductivity (from ref. 4).

The temperature range of interest here is from above the liquidus to below the glass transition and includes the passage through the crystallization zone. This temperature range is often marked by the pronounced non-Arrhenian dependence of the structural (1) and conductivity (9) relaxation times (see also Fig. 1b). A complete spectroscopic investigation of the type of Fig. 1a, emphasizing the temperature dependence of the far- and mid-infrared response of typical glass forming systems, would be critical in evaluating whether the extent of non-linearity is related to identifiable structural changes occurring at T_g . To perform such investigations by varying systematically the composition is a Herculean task. Nevertheless, for widely studied glasses such as the alkali borates, some information on the temperature and composition dependence of the structure is available.

It is now known that the structure of B_2O_3 changes upon increasing temperature: the six-membered boroxol rings which are abundant in the glassy solid are progressively destroyed above T_g (10). In this particular case the structural changes involve mostly the extent to which the borate polyhedra (triangles) combine below T_g to form ring structures with well-defined intermediate range order. Binary glasses containing moderate fractions of alkali oxide modifiers M_2O are known to contain a fraction of borate tetrahedra, N_4 , which depends on the M_2O mole

fraction x and exhibits a maximum at *ca.* $x=0.3$ (3). Interestingly, for lithium and sodium compositions in the $0 < x < 0.25$ range, N_4 is found temperature dependent and decreasing above T_g . The charged borate unit favoured at high temperatures is the metaborate triangle with two bridging and one non-bridging oxygen atoms (11). A similar conclusion was reached by the detailed vibrational and devitrification study of lithium metaborate glass, $0.50 \text{ Li}_2\text{O} \cdot 0.50 \text{ B}_2\text{O}_3$ (12). The structural scenario which resulted from the latter studies is depicted schematically in Figure 2. In terms of local structure it involves the abrupt transformation of metaborate triangles to isomeric tetrahedra upon cooling through the glass transition range. Moreover, it implies that glass formation is associated with the formation of rigid pseudophases preserving the structural sequence of tetrahedra-containing LiBO_2 polymorphs.

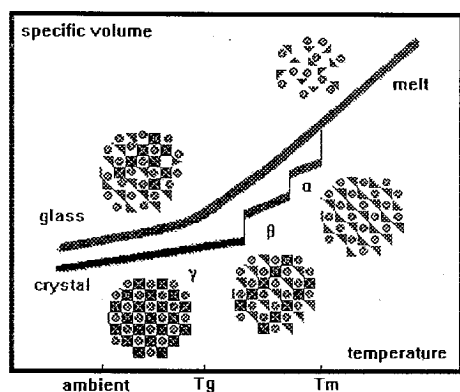


Figure 2. A typical specific volume vs. temperature plot for the crystallization and vitrification of a metaborate melt, based on data for the lithium system. The structural changes associated with either process are shown schematically. Squares and triangles represent BO_4 and BO_3 units, circles depict lithium cations. The melt to crystal transition involves two polymorphic transformations. Upon fast quenching these occur partially and only with considerable undercooling. Their onset corresponds to the glass transition.

Structural changes in both local and intermediate ranges of the type described above can have an impact on the viscoelastic and enthalpic aspects of glass transition. In the case of ionic conducting glasses such as the alkali borates, it is expected that the same chemical changes can have an effect on the magnitude and temperature dependence of ionic mobility. These latter aspects will be discussed in the following sections.

LITHIUM BORATE GLASSES

Understanding the strength/fragility trends in melts of variable composition requires the knowledge of the reactions available for the chemical relaxation of the melts upon quenching (13). In the particular case of lithium borates, $x \text{ Li}_2\text{O} \cdot (1-x) \text{ B}_2\text{O}_3$, with x increasing from 0 towards the metaborate stoichiometry ($x=0.50$), the increasing capability of the melt to undergo upon cooling chemical transformations of local- (e.g. isomerizations, disproportionations), intermediate- (e.g. ring formation), and long-range (e.g. polymorphic transformations, and formation of pseudophases), would imply that fragility increases with x (14). The trend has been verified recently on the basis of new Differential Scanning Calorimetry measurements (14) and viscosity data (15).

In search for the manifestation of the fragility trend in the cationic transport of lithium borates, melt and glass conductivity data are compiled from the literature (16) and plotted in Figure 3 versus inverse temperature normalized by T_g (17), as suggested by Angell (2, 9). For $(T_g/T) < 1$, the data have been fitted to the Vogel-Fulcher-Tamman equation, $\sigma = \sigma_0 \exp[-DT/(T-T_0)]$ where T_0 and D are constants. The composition dependence D^{-1} which is a fragility indicator, is shown in Figure 4b. The observed monotonic increase of fragility indicated by the conductivity data is in accordance with the trends deduced from viscosity and thermochemical data (14), which are shown in Figures 4c and 4d respectively.

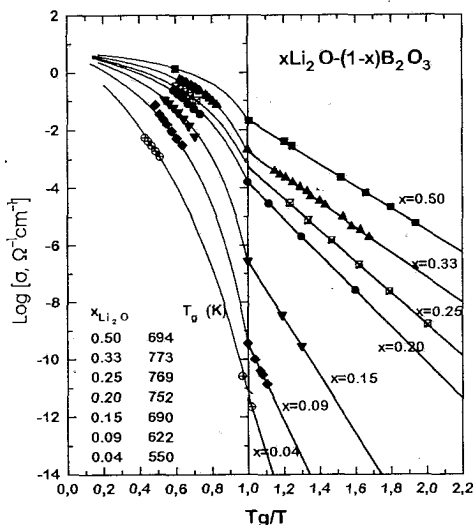


Figure 3. Conductivity of lithium borate glasses and melts containing 4-50 mol% Li_2O , temperature-normalized at T_g . Conductivity data and T_g values are from refs. 16 and 17, respectively. The points at $T_g/T=1$ are extrapolated from low temperature data. High temperature VTF, and sub- T_g Arrhenius fits are shown. For details see text.

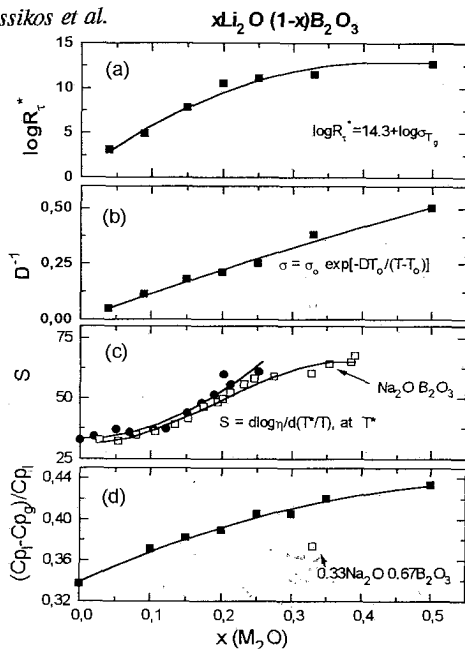


Figure 4. Composition dependence of (a) the decoupling index at T_g , (b) the fragility index D^{-1} obtained by the VTF fitting of the high temperature conductivity data, (c) the viscoelastic fragility index S , taken from ref. 14, and (d), the normalized change of C_p at T_g , also from ref. 14. Filled symbols are for lithium borate glasses, open squares for their sodium analogs. Lines are guiding the eye.

In addition to the fragility trend, the conductivity data of Figure 3 allow for the estimate of the decoupling index at T_g , $\log R_{T_g}^* = 14.3 + \log \sigma_{T_g}$. (2). Increasing x from $x=0.04$ to 0.50 results in the monotonic increase of the decoupling index by some ten orders of magnitude (Figure 4a). In broad structural terms, this increase of the decoupling index would imply that the average B-O network interactions strengthen with increasing x in comparison to those between lithium and oxygen (c.f. Angell's presentation in these proceedings). One way to confirm this trend involves optical basicity and far-infrared spectroscopic measurements which yield the dependence of oxygen and cationic charges in alkali borate glasses as a function of composition (18).

MIXED ALKALI GLASSES

It is not the purpose of this publication to address fully the phenomenological aspects and suggested explanations of the mixed-alkali effect (19). However, it is now recognized that the non-additive variations of several glass properties upon alkali mixing has a structural counterpart. The synergy of the two alkalis produces network arrangements alien to the single alkali end-member compositions. In mixed alkali borates the structural mixed alkali effect is pronounced and manifested by a minimum in the fraction of four-coordinated boron atoms, N_4 (20, 21, see also Kamitsos et al., these proceedings). Following the reasoning developed above for single alkali borates, decreasing N_4 while keeping the modifier content fixed, would imply that the extent of the

chemical alterations associated with quenching and the glass transition is reduced. Additional evidence for the composition dependence of what can be called the 'structural smoothness' of the glass transition comes from the devitrification experiments on mixed lithium-sodium metaphosphate glasses (21). These experiments have been interpreted to indicate that alkali mixing not only reduces N_4 , but also results in a less pronounced pathway morphology. All the above suggest that an important manifestation of the mixed alkali effect is the reduced fragility of the intermediate compositions.

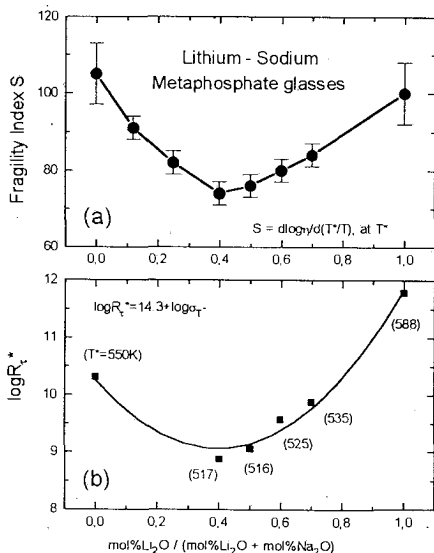


Figure 5.

(a) Dependence of the viscoelastic fragility index S on the alkali mixing ratio of lithium-sodium metaphosphate glasses, based on the viscosity data in ref. 22.

(b) Composition dependence of the decoupling index at T^* in the same glass family. The index is calculated by extrapolating glass conductivity data from ref. 23 to T^* . Values of T^* , the temperature at which $\eta = 10^{13}$ Poise, are taken from ref. 22 and shown in parentheses. Lines are guiding the eye.

To check the generality of this suggestion we present in Figure 5a the dependence of the fragility index S on the alkali mixing ratio in lithium sodium metaphosphate glasses, for which appropriate viscosity and conductivity data are available. The index is calculated on the basis of shear viscosity data (22) as in Figure 4c. A minimum in fragility is clearly observed at roughly maximum mixing. Fortunately, glass ionic conductivity data for the same system are available (23) in the literature and allow the calculation of the decoupling index at T^* (Figure 5b). The variation of $\log R_T^*$ with alkali mixing is also shown to be a non-linear function of alkali mixing, exhibiting a minimum at roughly maximum mixing.

CONCLUSIONS

The structural investigation of glass forming oxides as a function of temperature and composition can be correlated with the observed trends in their thermochemical, viscoelastic and ionic transport properties. The understanding of the structural origin of compositional trends in the strength/fragility or decoupling indexes is of great theoretical and practical value.

The authors are indebted to Dr. J. A. Duffy (Univ. of Aberdeen) for helpful discussions.

References

- 1 C. A. Angell, *J. Non-Cryst. Solids*, 131-133, 13 (1991)
- 2 C. A. Angell, *Annu. Rev. Phys. Chem.*, 43, 693 (1992), and references therein.
- 3 E. I. Kamitsos and G. D. Chryssikos, *J. Molec. Spectr.*, 247, 1 (1991), and refs therein
- 4 C. Liu and C. A. Angell, *J. Chem. Phys.*, 93, 7378 (1990)
- 5 V. Provenzano, L. P. Boesch, V. Voltera, C. T. Moynihan and P. B. Macedo, *J. Am. Ceram. Soc.*, 55, 492 (1972)
- 6 R. W. Rendell and K. L. Ngai, in *Relaxation in Complex Systems*, (K. L. Ngai and G.B. Wright, Eds.) Government Printing Office, Washington DC, 1985, p.309
- 7 E. I. Kamitsos, M. A. Karakassides and G. D. Chryssikos, *J. Phys. Chem.*, 91, 5807 (1987)
- 8 G. D. Chryssikos and E. I. Kamitsos, *J. Molec. Liq.*, 56, 349 (1993)
- 9 C. A. Angell, *Chem. Rev.*, 90, 523 (1990)
- 10 G. E. Walrafen, S. R. Samanta and P. N. Krishanan, *J. Chem. Phys.*, 72, 113 (1980), and, A. K. Hassan, L. M. Torell and L. Borjesson, *J. de Physique IV*, C2-265 (1993)
- 11 V. G. Chekhovskii and A. P. Sizonenko, *Fiz. Khim. Stekla*, 14, 194 (1988)
- 12 G. D. Chryssikos, E. I. Kamitsos, A. P. Patsis, M. S. Bitsis and M. A. Karakassides, *J. Non-Cryst. Solids*, 126, 42 (1990); G. D. Chryssikos, E. I. Kamitsos, M. S. Bitsis and A. P. Patsis, *ibid*, 131-133, 1068 (1991)
- 13 C. A. Angell, C. A. Scamehorn, D. J. List and J. Kieffer, *Proc. XV Int. Congress on Glass, Leningrad 1989*, Vol. 1a, p.204
- 14 G. D. Chryssikos, J. A. Duffy, J. M. Hutchinson, M. D. Ingram, E. I. Kamitsos and A. P. Pappin, *J. Non-Cryst. Solids*, (1994), *in press*
- 15 S. V. Nemilov, *Neorg. Mat.*, 2, 349 (1966), and, N. E. Volkova and S. V. Nemilov, *Fiz. Khim. Stekla*, 16, 207 (1990)
- 16 O. V. Mazurin, M. V. Streltsina and T. P. Shvaiko-Shvaikovskaya, *Handbook of Glass Data, Part B*, Elsevier 1985, pp. 162-186; D. P. Button, L. S. Mason, H. L. Tuller and D. R. Uhlmann, *Solid State Ionics*, 9&10, 585 (1983)
- 17 M. Affatigato, S. Feller, E. J. Khaw, D. Feil, B. Teoh and O. Mathews, *Phys. Chem. Glasses*, 31, 19 (1990)
- 18 J. A. Duffy, G. D. Chryssikos and E. I. Kamitsos, *Phys. Chem. Glasses*, 1994, *in press*
- 19 M. D. Ingram, *Phys. Chem. Glasses*, 28, 215 (1987), and references therein
- 20 E. I. Kamitsos, A. P. Patsis and G. D. Chryssikos, in 'The Physics of Non-Crystalline Solids', (L. D. Pye, W. C. La Course and H. J. Stevens, Editors), Taylor and Francis, London 1992, pp. 460-465, and references therein.
- 21 G. D. Chryssikos, J. A. Kapoutsis, E. I. Kamitsos, A. P. Patsis and A. J. Pappin, *J. Non-Cryst. Solids*, 167, 92 (1994)
- 22 R. Wäsche and R. Brückner, *Phys. Chem. Glasses*, 27, 87 (1986), I. A. Avramov, G. P. Roskova and T. P. Shvaiko-Shvaikovsaya, *Izv. Khim. Bolg. Akad. Nauk*, 9, 333 (1976), I. Gutzow, M. V. Streltsina and E. Popov, *Bulg. Acad. Sci., Commun. Dep. Chem.* 1, 19, 1968, and H. Kawazoe, M. Hasegawa and T. Kanazawa, *J. Ceram. Soc. Jpn.*, 80, 251 (1972)
- 23 H. M. J. M. Van Ass and J. M. Stevels, *J. Non-Cryst. Solids*, 15, 215 (1974); and N. V. Gurjev, K. K. Evstropiev, G. T. Petrovskii and G. V. Savinova, *Fiz. Khim. Stekla*, 9, 125 (1983)

VIBRATIONAL SPECTRA OF SILICATE GLASSES MODELLED ON THE BASIS OF SiO₄ - RING STRUCTURES

B.D.Mihailova, N.S.Zotov⁺, M.S.Marinov
and L.L.Konstantinov

*Institute of Applied Mineralogy, Bulgarian Academy of Sciences,
Rakovski str. 92, Sofia - 1000, Bulgaria*

⁺*Present address: Institute of Crystallography,
Theresienstr. 41, 8000 Munchen 2, Germany*

Abstract

The infrared absorption spectrum of vitreous silica is calculated using the quasi-cluster method for determining the eigenfrequencies and atom vector displacements of rings composed of silicon-oxygen tetrahedra. The results show that the observed infrared spectrum of v-SiO₂ can be successfully explained by the existence in the glass of puckered 4- and 6-membered rings as well as of a small amount of 3-membered planar rings.

1. Introduction

The interpretation of experimental Raman and infrared (IR) spectra of silicate glasses through calculated normal modes of systems composed of tetrahedra provides valuable information on the structure of such materials. According to numerous investigations (1,2) vitreous silica can be considered as a random network consisting of different kinds of rings of SiO₄ tetrahedra. Every ring built of regular SiO₄ tetrahedra is usually specified by three parameters: (i) the number of tetrahedra in the ring, n (the ring order), (ii) the degree of puckering, η , given by the tilt angle of the tetrahedra along their bridging oxygen edges, and (iii) the sign of η for the individual tetrahedra and their mutual orientation in the ring, a parameter referred to hereafter as ring topology, σ .

The purpose of this work is to model the experimental infrared absorption spectrum of fused silica through an appropriate combination of calculated spectra for a relatively small number of various SiO₄-ring structures.

2. Modelling

The vibrational spectra of various rings were modelled using a computer program (3) based on known theoretical methods for calculating eigenfrequencies (4) and intensities of polarized and isotropic Raman-active (5,6) as well as IR-active (4) modes of vibration of the ring under study. The spectral lines were broadened by Lorentz functions of a half-width, $\Gamma(\omega)$, inversely proportional to the frequency (7).

The random network of rings in the glass is modelled by imposing non-periodic boundary conditions on the elements of the dynamical matrix (8). Then, the experimental spectrum, $I(\omega)$, was fitted by a linear combination of intensities, I_t , calculated for different types of rings with appropriate weight coefficients, q_t :

$$I_{tot}(\omega) = \sum_t q_t I_t(\omega), \quad (1)$$

where t denotes the type of the ring structure involved. Therefore, in the framework of our approach the values of the coefficients q_t can serve as a measure of the partial concentration of the rings of a particular type, t , present in the silicate glass being modelled.

The values of the parameters used in the calculations throughout this study are as follows:

- the length of all the Si-O bonds 1.62 Å,
- the angle O-Si-O 109.47°
- the silicon- to -bridging oxygen bond stretching force constant 450 N/m,
- the silicon- to -non-bridging oxygen bond stretching force constant 560 N/m,
- the O-Si-O bond bending force constant 40 N/m,
- the Si-O-Si bond bending force constant 6.5 N/m.

In the case under study the Si-O-Si bond angle is a variable as it depends on the ring order, degree of puckering and topology.

3. Results and Discussion

A detailed and systematic investigation of the influence of the ring order, degree of puckering and topology of isolated rings on their polarized and isotropic Raman as well as IR spectra has been already performed (9).

In this paper 3-, 4-, 5-, 6-, and 7-membered planar and puckered rings with different values of η and different topology have been considered. On this basis one can conclude that:

- (i) the ring order affects only the mode localization, thus changing the spectral line position and intensity,
- (ii) the degree of puckering determines the value of the Si-O-Si angle and sensitively affects the Raman and IR peaks in the mid-frequency range, and
- (iii) the ring topology determines the total number of Raman- and IR-active modes and affects mainly those localized in bridging oxygen atoms leading to mode frequency splitting.

It is worth noting that by linear combinations of spectra calculated for isolated rings one cannot reproduce the experimental Raman (4) and IR spectra (Fig.1, curve a) of vitreous silica. This fact is most probably due to the strong effect of the amorphous matrix being ignored in this case. In the present paper this effect is taken into account with the result a much more satisfactory agreement with experimental data. As an illustration Fig.1. shows the experimental spectrum (curve a) together with the best model spectrum (curve b) obtained with the weight coefficients given in Table.1. The spectra used in the modelling are given in Fig.2.

As seen, the contribution of the spectra of puckered 4- and 6- membered rings of topology 1100 and 111000, respectively, to the model spectrum is dominant, while that of the 3-membered planar rings is only minor. The sharp features in the HH-Raman spectrum of ν -SiO₂ ascribed by Galeener to small-order planar rings (10) originate from modes not active in IR absorption due to symmetry restrictions (11). This means that one can consider the silicate glass under study as built mainly of 4- and 6-membered puckered rings.

The results could be improved if a third silicon- to -linked oxygen stretching force constant were introduced (linked are the oxygen atoms binding the ring with the surrounding). Such an approach means that in addition to both different kinds of oxygen atoms, namely the non-bridging ones belonging to a tetrahedron and those connecting two tetrahedra, a third type of oxygen atom is present in the silicate glass. The curve c in Fig.1 represents the spectrum calculated with a silicon- to -linked oxygen bond stretching force constant equal to 360 N/m, all other parameters and weight coefficients being the same as previously. It is evident that the introduction of this third force constant considerably improves the agreement with experiment.

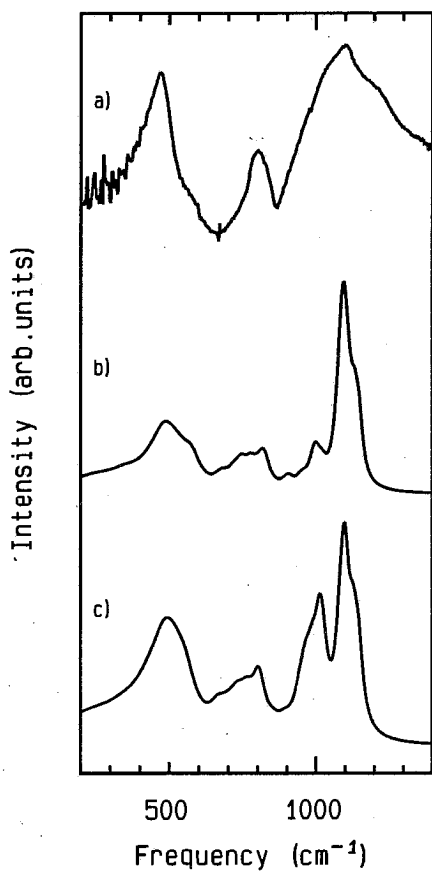


Fig.1. IR spectra of fused silica :

- a) Experimental spectrum measured by a Perkin-Elmer 1430 Ratio Recording IR Spectrometer with a slit width of 3 cm^{-1} .
- b) The spectrum calculated according to equation(1) with the spectra shown in Fig.2.
- c) The spectrum calculated using silicon-to-linked oxygen stretching force constant equal to 360 N/m

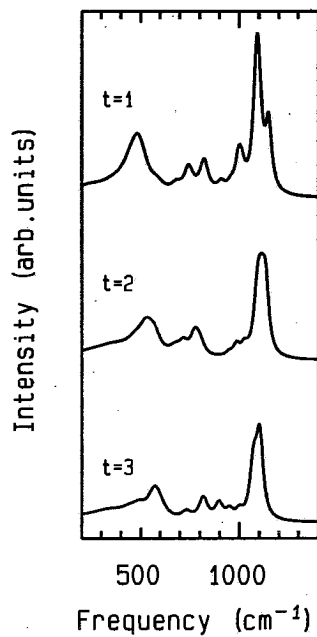


Fig.2. Calculated IR spectra of the rings related to the spectrum b) in Fig.1.

Table 1. The ring parameters and the weight coefficients of ring structures best representing the experimental spectrum. Zeros and unities label, respectively, negative and positive η for the corresponding tetrahedron.

| t | 1 | 2 | 3 |
|------------|--------|------|-----|
| n_t | 6 | 4 | 3 |
| σ_t | 111000 | 1100 | 111 |
| η_t | 47° | 30° | 0° |
| q_t | 45% | 40% | 15% |

4. Conclusions

By fitting the IR spectrum of fused silica with a sum of spectra of different rings calculated under random boundary conditions one can model the structure of amorphous silica as a random network of rings among which those of topology 1100 and 111000 as well as 3-membered planar rings are dominant. This assumption is in a good agreement with published results (10,12) on the structural properties of silicate glasses based on minimization of the structure energy with respect to various ring parameters.

Acknowledgements:

The financial support of this work by the Ministry of Science and Education under contract number SR F-213 and by the Copolym Co Ltd is gratefully appreciated. We wish to thank Mr. J. Nikolov for his help in computer programming.

4. References

1. A. C. Wright, J.A. Erwin Desa, *Phys.Chem. Glasses* 19 (1978) 140
2. R. A. Murray, W. Y. Ching, *Phys. Rev B* 39 (1989) 1320
3. M. S. Marinov, B. D. Mihailova, J. B. Nikolov, N. S. Zotov and L. L. Konstantinov, *Proc. 7-th Int. School Cond. Matter Phys.: Electronic and optoelectronic materials for the 21st century*, eds. J. M. Marshal, N. Kirov and A. Vavrek (World Scientific, Singapore-New Jersey-London-Hong Kong 1993) 601
4. T. Furukawa, K. E. Fox and W. B. White, *J. Chem. Phys.* 75 (1981) 3226
5. R. J. Bell, *Meth. Comp. Phys.* 15 (1976) 215
6. E. R. Lippincott and J. M. Stutmant, *J. Phys. Chem.* 68 (1964) 2926
7. S. Brawer, *Phys. Rev. B* 11 (1975) 3173
8. B. D. Mihailova, N. S. Zotov, M. S. Marinov and L. L. Konstantinov, to be published
9. B. D. Mihailova, N. S. Zotov, M. S. Marinov, J. B. Nikolov and L.L. Konstantinov, *J.Non-Cryst.Solids* (in press)
10. F. L. Galeener, *Solid Stat. Commun.*44 (1982) 1037
11. N. Zotov, B. Mihailova, M. Marinov and L. Konstantinov, *Physika A* 201 (1993) 402
12. B. C. Chakoumakous, R. J. Hill and G. V. Gibbs, *Am. Mineralogy* 66 (1981) 1237

CALCULATION OF RAMAN SPECTRA OF GLASSES

M.S.Marinov, N.S.Zotov⁺, B.D.Mihailova and L.L.Konstantinov

Institute of Applied Mineralogy, Bulgarian Academy of Sciences,

Rakovski str. 92, Sofia - 1000, Bulgaria

⁺*Present address: Institute of Crystallography,*

Theresienstr. 41, 8000 Munchen 2, Germany

Abstract

A theoretical approach for studying structural disorder in glasses on the basis of the corresponding crystal model is presented. Relationships for calculating Raman spectra are obtained in the lowest self-consistent Born approximation (SBA) and averaged *t*-matrix approximation (ATM). The Si_2O_7 dimer is considered as a model structural unit of $\text{M}_2\text{O} \cdot \text{SiO}_2$ glasses (*M* denotes an alkaline metal) containing infinite silicate chains.

1. Introduction

The main experimental method for studying the short and intermediate range order in disordered materials is the vibrational spectroscopy. The modelling of the vibrational spectra to fit experimental data is usually rather complicated due to the absence of three-dimensional periodicity. The problem simplifies considerably when additional assumptions are introduced such as central force interactions between nearest neighbours only (1), Bethe lattice boundary conditions (2-4) or light scattering by individual bonds (5,6). A very useful method for calculating Raman and IR spectra of amorphous materials provides the relationship with the vibrational density of states (VDOS) (7-9). Raman and IR spectra could be calculated as well using their being related to the Green's function of the system (4,7,10).

The modelling of Raman and IR spectra should reproduce the frequency, intensity and width of the spectral lines, but the majority of the reported results have been concerned only with calculation of the line position and intensity. The manner in which the widths of the vibrational spectral lines of glasses are affected by the structural disorder has not been yet studied systematically.

A theoretical approach for treating the influence of the structural disorder in glasses on the Raman spectra and VDOS using a self-consistent approximation for the self-energy of minimum-sized structural units has been recently developed (11).

The present communication advances this approach to study the dependence of the Raman line positions and widths in a model glass on the degree of disorder. The approximations proposed give results in good agreement with experiment.

2. Theory.

As Raman scattering in disordered materials is known to be sensitive to the short and intermediate range order, one of the most effective methods for studying the lattice dynamics of such materials would be to consider them as built of specific structural units best representing on this scale the atomic configurations (12, 13). As a first approximation in calculating the vibrational properties of the material one can use an averaged structural unit. For example, silicate glasses have been successfully studied by such approximations (14,15,16).

The intensity of the Raman spectrum can be presented in the following form (11)

$$I_a(\omega) \propto (2\omega)^{-1}(\omega + Y)^4 Y^{-1} n(\omega) \sum_p C_a(\omega_p) D_p(\omega), \quad (1)$$

where a is the scattered light polarization index, Y is the laser frequency, $n(\omega)$ is the averaged number of phonons with vibrational frequency ω , the summation being carried out over all modes p of the averaged structural unit. In eq(1) $C_a(\omega_p)$ is a coupling constant related with the polarizability tensor invariants, and $D_p(\omega)$ is the partial contribution of the p -th vibrational mode to VDOS defined through

$$D_p(\omega) = (2\omega/\pi) \text{Im} \mathcal{G}_p(\omega), \quad (2)$$

where \mathcal{G}_p is the averaged Green's function of the glass which is related to the averaged scattering matrix of the p -th mode, t_p , through the equation

$$\mathcal{G}_p(\omega) = g_p(\omega) + g_p(\omega) t_p(\omega) g_p(\omega). \quad (3)$$

In eq(3) g_p is the Green's function of the averaged structural unit and

$$t_p(\omega) \approx \sum_k \langle V_{pk} V_{kp} \rangle \mathcal{G}_k(\omega), \quad (4)$$

where V_{pk} is the matrix element of the perturbation to the dynamical matrix of the averaged structural unit and $\langle \dots \rangle$ denotes averaging over all possible configurations of atoms in the structural unit.

The averaged Green's function of the glass is estimated in the self-consistent Born approximation (SBA) and the averaged t-matrix approximation (ATM) (11).

In the calculations throughout this work the following approximation for $\langle V_{pk}V_{kp} \rangle$ is used :

$$\langle V_{pk}V_{kp} \rangle = \epsilon^2 \left(\sum_{(\alpha\beta)} U_{\alpha}^p U_{\beta}^k \right)^2, \quad (5)$$

where $(\alpha\beta)$ denotes the summation over the nearest-neighbour atoms α, β in the averaged structural unit and U_{β}^k is the β -th component of the eigenvector of the mode k of the unit. In eq(5) $\epsilon^{0.5}[cm^{-1}]$ is the random disorder parameter, describing the effect of the disorder in the structural unit on its dynamical matrix.

The eigenfrequencies and eigenvectors of the averaged structural unit can be found using standard normal mode calculations.

3. Numerical results.

We calculated the position, width and intensity of the lines in HH Raman spectrum of $Na_2O.SiO_2$ glass using as averaged structural unit the Si_2O_7 dimer which is the smallest structural unit suitable for describing the Si-O-Si bridging angle and the dihedral angle disorder in silicate glasses. This unit is shown inserted in Fig.1. The values used for the force constants (f. c.), the interatomic distances and the angles in Si_2O_7 are as follows (14):

| | |
|------------------------------|-------------------------|
| Si-O bond stretching f. c. | 5×10^5 dyn/cm, |
| O-Si-O bond bending f. c. | 5×10^4 dyn/cm, |
| Si-O-Si bond bending f. c. | 5×10^3 dyn/cm, |
| Si-O nonbridging bond length | 1.592 Å, |
| Si-O bridging bond length | 1.639 Å, |
| O-Si-O bond angle | 109.47° , |
| Si-O-Si bond angle | 135° , |

the plane formed by Si[6], O[5] and Si[1] being a mirror symmetry plane. The obtained eigenfrequencies, $\omega_N[cm^{-1}]$, and the integral Raman intensity, I [arb. units], of the different modes and their type in Si_2O_7 are listed in the Table.

As seen in Fig.1, the calculated HH Raman spectra in both SBA and ATM approximations for the Green's function of the glass are in good agreement with the experimental spectrum. One can further improve the agreement between the positions of the peaks in the experimental and theoretical spectra by adjusting the values of the force constants, but this aspect is out of the scope of the present work.

| N_0 | ω_N | I | type of atomic vibrations |
|-------|------------|------|--|
| 1 | 1055 | 1.37 | asymm. stretching of bridging O atoms |
| 2 | 1014 | 0.50 | asymm. stretching of nonbridging O atoms |
| 3 | 1011 | 0.26 | |
| 4 | 1007 | 1.66 | |
| 5 | 1005 | 1.18 | |
| 6 | 891 | 1.40 | symm. stretching of bridging O + stretching of nonbridging O atoms |
| 7 | 762 | 0.00 | |
| 8 | 639 | 2.97 | |
| 9 | 491 | 0.21 | mixed vibrations of bridging and nonbridging O atoms |
| 10 | 484 | 0.21 | |
| 11 | 456 | 0.17 | |
| 12 | 415 | 0.68 | |
| 13 | 414 | 0.70 | |

The disorder parameter $\epsilon^{0.5}$ was specified in such a way that the width of the peak at 639 cm^{-1} be close to 56 cm^{-1} , a value corresponding approximately to that observed in Raman spectra of $\text{Na}_2\text{O} \cdot \text{SiO}_2$. This peak is chosen because it is well separated in the spectrum and the effect of the other modes on its position and width is quite weak.

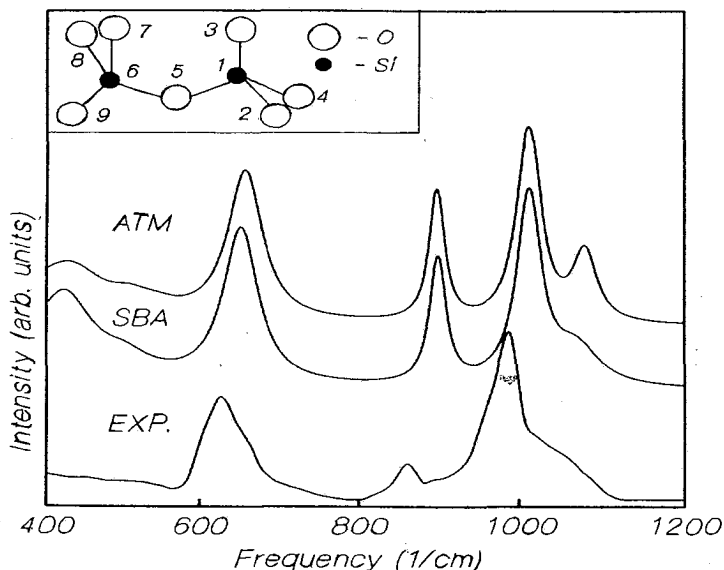


Fig.1. HH Raman spectra of $\text{Na}_2\text{O} \cdot \text{SiO}_2$: experimental (15) and calculated in SBA and ATM approximations.

For the glass under study the mode frequency shifts away from the corresponding eigenfrequencies of Si_2O_7 as well as the linewidths depend on the value of the disorder parameter. These dependencies are shown in Fig.2 and Fig.3 for the Green's function of the glass in SBA.

The following features are evident from these figures:

- (i) The line width increases on increasing the disorder.
- (ii) The line width generally increases on decreasing the frequency in good agreement with the results of McKeown et al (17) for silica-rich sodium aluminosilicate glasses.
- (iii) As a whole, the spectrum broadenes as a result of the high-frequency modes being shifted in frequency upwards, while the low-frequency ones downwards, some mid-frequency modes remaining approximately unshifted. These results are in accordance with the calculations performed by Mattis (18) for the eigenfrequencies in the Debye approximation.
- (iv) The broadening of the spectrum increases on increasing the disorder.
- (v) The disorder affects in a different way the line positions and widths of different types of vibrational modes (see the Table).

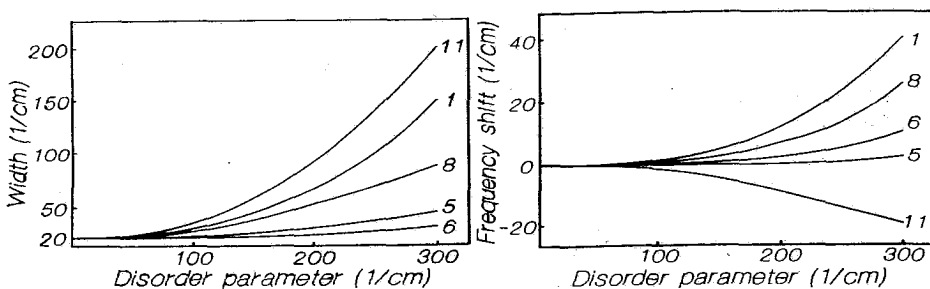


Fig.2. Line width of some modes as numbered in the Table vs. the disorder parameter $\epsilon^{0.5}$.

Fig.3. Frequency shift of some modes as numbered in the Table vs. the disorder parameter $\epsilon^{0.5}$.

4. Conclusions.

The effect of random disorder in the nearest-neighbour-interaction matrix elements on the line positions and widths of the Raman spectra of a model glass is analyzed in the self-consistent Born approximation for the Green's function. It is shown that the disorder leads to broadening of the vibrational spectrum. A narrowing of the spectral lines with increasing the frequency is predicted in the framework of this approach.

The width of the individual lines depends, however, on the type of the atom vibrations involved. The line widths and frequency shifts increase on increasing the disorder.

This theoretical approach, being much simpler than the other methods discussed in the literature, gives results in a good agreement with experimental data reported for alcalioxide-silicate glasses.

Acknowledgements: The financial support of this work by the Ministry of Science and Education under the contract number SR F 213 and by the Copolym Co Ltd is gratefully appreciated. We wish to thank Mr. J.B. Nikolov for his help in computer programming.

References

1. P. N. Sen, M. F. Thorpe, *Phys. Rev. B* 15 (1977) 4030
2. M. F. Thorpe, D. Weaire, *Phys. Rev. B* 4 (1971) 3518
3. R. B. Laughlin, J. D. Joannopoulos, *Phys. Rev. B* 16 (1977) 2942
4. R. A. Barrio, F. L. Galeener, E. Martinez, *Phys. Rev. B* 31 (1985) 7779
5. R. J. Bell, *Methods. in Comput. Phys.* 15 (1976) 258
6. R. A. Murray, W. Y. Ching, *Phys. Rev. B* 39 (1989) 1320
7. F. L. Galeener, P. N. Sen, *Phys. Rev. B* 17 (1978) 1928
8. R. Shuker, R. W. Gammon, *Phys. Rev. Lett.* 25 (1970) 222
9. V. Mazzacurati, M. Montagna, O. Pilla, G. Viliani, G. Ruocco, G. Signorelli, *Phys. Rev. B* 45 (1992) 2126
10. R. M. Martin, F. L. Galeener, *Phys. Rev. B* 23 (1981) 3071
11. M. Marinov, N. Zotov, B. Mihailova, J. Nikolov and L. Konstantinov, submitted to *J. Phys.: Cond. Matter*
12. J. H. Ziman, *Models of disorder* (Cambridge: Cambridge University Press, 1979)
13. A. Wright, *Adv. Struct. Develop. Diff. Methods* 5 (1974) 1
14. T. Furukawa, K. Fox, B. White, *J. Chem. Phys.* 75 (1981) 3226
15. S. Brawer, *Phys. Rev. B* 11 (1975) 3173
16. E. Dowty, *Phys. Chem. Minerals* 14 (1987) 67
17. D. A. McKeown, F. L. Galeener and G. E. Brown, *J. Non-Cryst. Sol.* 68 (1984) 361
18. D. C. Mattis, *Phys. Lett. A* 117 (1986) 297

MEDIUM RANGE ORDER IN SILICATE GLASSES

Kaj H. Karlsson and Kaj Fröberg
Department of Chemical Engineering
Åbo Akademi
20500 Åbo, Finland

Medium range order in glass is discussed by comparing a structural model for polyanions in alkali silicate melts with experimentally determined Si-O-Si angles in glass. Problems arise in determining the relative contribution of different Si-O-Si angles to the diffraction pattern. Below 50 mole per cent soda, the structural model predicts two principal anions. One between 20 and 28 mole per cent soda, which depolymerises around 30 per cent. The Si-O-Si angles calculated for these two anions agree, when appropriately weighted, with results from X-ray diffraction.

Introduction

Medium range order in silicate glass has been discussed since Zachariasen's days, but got its first real support by a set of experiments performed by Bockris and his coworkers^{1,2}. However, evidence exists that similar structural units can be expected in melts and glasses. It is partly supported by infrared measurements, but the so far strongest indication is the interesting high temperature NMR results obtained by Stebbins and his coworkers³. Their investigation shows that in the acidic range (20 ... 30 % alkali oxide) we may extrapolate information from glass to melt and vice versa. Again in the alkaline range, the melt structures resemble crystals. This is an important finding, because experimental tools for studying melt structures are still quite few. In this paper a neutralization-depolymerization model as derived from high-temperature voltammetry is compared to X-ray diffraction measurements on one acidic and one alkaline soda-silica glass.

The polyanion model

Raman studies on glasses suggest four-rings of silica tetrahedra in the acidic range, which at increasing alkali decrease in number, while three-rings increase. The two are equal in number at disilicate composition⁴. By further alkali additions the four-rings continue to decrease and reach almost zero at metasilicate composition. Unless long chains of three-rings are assumed, which are quite improbable at melt temperatures, the stoichiometric constraints require also six-rings in the acidic range (eight-rings can be considered, but are less familiar in silicate structures in general). A model has been presented, which contains the simplest possible structures that can be built from these units⁵. Combining two three-rings gives three four-rings and the structure shown in figure 1a. This corresponds to the disilicate ion $\text{Si}_6\text{O}_{15}^{6-}$. More acidic compositions require introduction of six-rings. By combining four disilicate units, this condition can be met in two ways, either by letting only three-rings face the interstice, figure 1b, or by letting only four-rings face the interstice, figure 1c. The former corresponds to the ion $\text{Si}_{24}\text{O}_{54}^{12-}$, the latter to $\text{Si}_{24}\text{O}_{52}^{8-}$. The corresponding alkali content is 20.0 and 14.3 mole per cent, respectively. When adding alkali, oxide bridges open and neutralization

proceeds until around 28 mol per cent, after which further the alkali additions causes depolymerization. This is repeated around 30 mol per cent, when the disilicate ion $\text{Si}_6\text{O}_{15}^{6-}$ is formed.

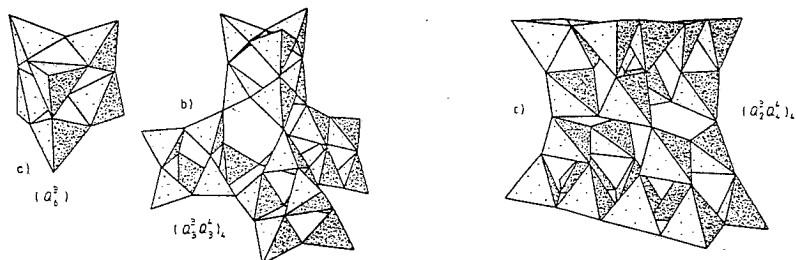


Figure 1: Structural units with (a) three- and four-rings, (b) three-, four- and six-rings, the three-rings facing the interstice, (c) three-, four- and six-rings, the four-rings facing the interstice.

Some of the experimental evidence for this type of polyanions has been discussed^{5,6,7}. From voltammetry in melts it was concluded that the ion $\text{Si}_{24}\text{O}_{54}^{12-}$ represents sodium silicates and $\text{Si}_{24}\text{O}_{52}^{8-}$ potassium silicates³. Alkali additions neutralize the ion, i.e. oxygen bridges are opened until depolymerization occurs. If six-rings are broken, the model predicts that neutralization occurs at 22.5, 25.0 and 27.5 mole per cent sodium oxide. In potash glasses neutralization should also occur at 17.2 mole per cent. After 27.5 per cent all six-rings are broken and depolymerization must occur. This happens at 29 and 33.3 mol per cent alkali oxide.

This model is also in conformance with Bockris' and his coworkers density measurements². At temperatures above 1200°C the density increases up to 20 mol per cent Na_2O , i.e. as long as the network is continuous. From 20 per cent onwards the density decreases due to increasing distance between discrete anions.

The model has also been tested by implication tests. At alumina additions to a 22 mol per cent soda containing silicate melt, the voltammetric current decreases and reaches zero at 1.5 mole per cent Al_2O_3 , the durability increases up to 1.5 mole per cent, while the additions have hardly any effect on viscosity⁶. The explanation to these effects is that the aluminate ion forms a bridge between two non-bridging oxides within the anion. The possibility to form such chelates is thus a requirement of any polyanion model.

Si-O-Si angles in polyanions

The model should, however, also stand a comparison with results from X-ray diffraction. Recently Murray and his coworkers⁸ have measured the Si-O-Si angle in sodium silicate glasses and found for a glass with 22.2 mol per cent Na_2O the value $143.0^\circ \pm 14.3$ and for one with 33.3 mole per cent $151.6^\circ \pm 17.4$.

In figure 2 the Si-O-Si angles in figure 1a and 1b are defined. In order to express their interrelation, we introduce an auxiliary variable, the *tilt angle* α , defined as the

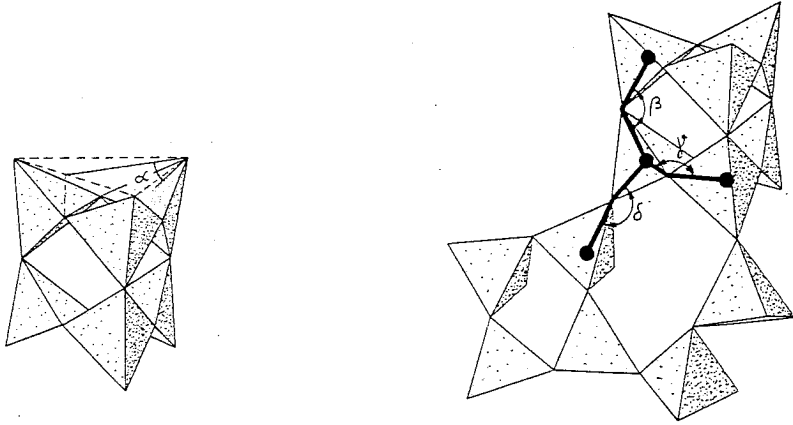


Figure 2: The tilt angle α and the angles β , γ and δ used to denote Si-O-Si angles in figure 1a and 1b.

angle between a plane going through three tetrahedron corners of a three-ring and the bottom face of any tetrahedron in this ring. Then an angle β may be defined as the Si-O-Si angle between two three-rings, i.e. in a four-ring. In terms of α this is

$$\beta = 180 - 2\alpha \tag{1}$$

An angle γ is defined as the Si-O-Si angle between two tetrahedra in the same three-ring. In terms of α this is

$$\gamma = \arccos \left(\frac{\sin^2 \alpha + 2\sqrt{2}(1 + \cos \alpha)(\sin \alpha) - 4 \cos \alpha + 2}{6} \right) \tag{2}$$

Finally, an Si-O-Si angle δ is defined as the angle alternating with γ in a six-ring. In terms of α this is

$$\delta = 109.4 + 2\alpha \tag{3}$$

Assuming that the oxide ions can be represented by rigid spheres, the extremes of any angle is determined by the fact that, when $\beta = 109.4^\circ$ or $\beta = 180^\circ$, opposite oxide ions in a four-ring touch each other. This gives the condition

$$0^\circ \leq \alpha \leq 35.3^\circ \tag{4}$$

The problem is then to find the weighted average, w_a , between β and γ in $\text{Si}_6\text{O}_{15}^{6-}$ and between β , γ and δ in $\text{Si}_{24}\text{O}_{54}^{12-}$, which corresponds to Murray's and his coworkers X-ray results. Two possibilities are

- multiplicity weighting, i.e. the average angle w_a is proportional to the number of angles of each type

$$w_a = \frac{\beta + 2\gamma}{3} \tag{5a}$$

and

$$w_a = \frac{2\beta + 4\gamma + \delta}{7} \quad (5b)$$

respectively, and

- derivative weighting, i.e. the average angle w_a is proportional the steepness at which the Si-O-Si angle changes with α

$$w_a = \frac{\frac{\Delta\beta}{\Delta\alpha}\beta + \frac{\Delta\gamma}{\Delta\alpha}\gamma}{\frac{\Delta\beta}{\Delta\alpha} + \frac{\Delta\gamma}{\Delta\alpha}} = \frac{\Delta\beta \cdot \beta + \Delta\gamma \cdot \gamma}{\Delta\beta + \Delta\gamma} \quad (6a)$$

and

$$w_a = \frac{\frac{\Delta\beta}{\Delta\alpha}\beta + \frac{\Delta\gamma}{\Delta\alpha}\gamma + \frac{\Delta\delta}{\Delta\alpha}\delta}{\frac{\Delta\beta}{\Delta\alpha} + \frac{\Delta\gamma}{\Delta\alpha} + \frac{\Delta\delta}{\Delta\alpha}} = \frac{\Delta\beta \cdot \beta + \Delta\gamma \cdot \gamma + \Delta\delta \cdot \delta}{\Delta\beta + \Delta\gamma + \Delta\delta} \quad (6b)$$

Testing by X-ray diffraction

In table 1 a calculation is shown using the derivative weighting. The results are compared to Murray's and his coworkers data. For a soda-silica glass with 22.2 mol per cent Na_2O , equation (6b) and a tilt $\alpha = 15^\circ$ gives a weighted average that is close to the measured angle of 143° . The corresponding angle $\gamma = 128^\circ$ and $\delta = 157^\circ$, which fit nicely with mean \pm standard deviation. The angle β falls between these extremes. Using equation (5b) gives an inferior fit.

For the disilicate ion, equation (6a) and a tilt $\alpha = 6^\circ$ gives a weighted average that is close to the measured angle 151.6° . The corresponding angle $\beta = 168^\circ$ fits with the mean+standard deviation. On the other hand, $\gamma = 115.2^\circ$ is lower than mean-standard deviation. However, no other tested model gave any closer fit.

Table 1: Characteristics of the relaxed $(\text{Na}_2\text{O})_x(\text{SiO}_2)_{1-x}$ models. X-ray data from Murray & al.⁸ and calculated values from eqs. (1)–(3) and (6).

| x | Mean Si-O-Si angle ⁸ | STD Si-O-Si angle ⁸ | Mean +/- STD | α | w_a | β | γ | δ |
|-------|---------------------------------------|--------------------------------------|-----------------|----------|-------|---------|----------|----------|
| 0.222 | 143.0 | 14.3 | 157.3/128.7 | 24 | 143.1 | 132.0 | 128.0 | 157.4 |
| 0.333 | 151.6 | 17.4 | 169.0/134.0 | 6 | 151.6 | 168.0 | 115.2 | |

Although the model still needs further testing, it is interesting to note that for vitreous silica Zarzycki⁹ and later Mozzi and Warren¹⁰ found that a spread existed in the value of the Si-O-Si angle, but that 144° is most probable. Gladden¹¹ reports, also for vitreous silica, angles between 147 and 150° , although he concluded that there are about twice as many five-rings as six-rings. On the other hand, in vitreous silica he reported three-rings to be almost absent and mainly existing as 'defects'. Besides

Murray's and his coworkers paper, very little information is available on binary and ternary silicate glasses.

Conclusions

The proposed neutralization-depolymerization scheme for sodium silicate melts seems to imply the existence of medium range order also in glasses. The scheme has been tested with high-temperature voltammetry, with viscosity measurements on melts and with density and durability determinations in glass. Checking its validity against X-ray diffraction requires appropriate weighting of the three different Si-O-Si angles predicted by the scheme. However, a derivative weighting of the angles gives results at two different compositions that fall within the limits of standard deviation in X-ray determinations.

References

1. J.O'M. Bockris, J.D. Mackenzie and J.A. Kitchener, Viscous flow in silica and binary liquid silicates. *Trans. Faraday Soc.* 51 (1955) 1734-1748.
2. J.O'M. Bockris, J.W. Tomlinson and J.L. White, Structure of liquid silicates - Partial molar volumes and expansivities. *Trans. Faraday Soc.* 52 (1956) 299-310.
3. J.F. Stebbins, J.B. Murdoch, E. Schneider, I.S.E. Carmichael and A. Pines, A high-temperature high-resolution NMR study of ^{23}Na , ^{27}Al and ^{29}Si in molten silicates. *Nature* (London) 314 (1985) 250-252.
4. F.L. Galeneer, Phonones in glasses. In: M.F. Thorpe (Ed.): *Excitations in Disordered Systems*, Plenum Press, New York 1982, p. 359-369.
5. K.H. Karlsson, and M. Perander, Some experimental evidence for medium-range order in molten silicates. In: P.H. Gaskell, J.M. Parker, E.A. Davis (Eds.): *The Structure of Non-Crystalline Materials 1982*, Taylor & Francis, London & New York 1983, p. 92-107.
6. K. Fröberg, and K.H. Karlsson, Stabilisation of the glass structure by trivalent cations, *Diffusion and Defect Data* 53-54 (1987) 299-304.
7. K.H. Karlsson, K. Fröberg, and B. Skrifvars, Chemical approach to medium range order in glass. *Glastech. Ber.* 63 (1990) 37-47.
8. R.A. Murray, L.W. Song and W.Y. Ching, Structural models for $(\text{Na}_2\text{O})_x(\text{SiO}_2)_{1-x}$ glasses with periodic boundaries, *J. Non-Cryst. Solids* 94 (1987) 133-143.
9. J. Zarzycki, *Glasses and the Vitreous State*. Cambridge Univ. Press, Cambridge 1991.
10. R.L. Mozzi and B.E. Warren, Structure of vitreous silica. *J. Appl. Crystallgr.* 2 (1969) 164-172.
11. L.F. Gladden, Medium-range order in v-SiO₂. *J. Non-Cryst. Solids* 119 (1990) 318-330.

GLASS FORMATION AND STRUCTURE OF NON-OXIDE GLASSES

Fuxi GAN

Shanghai Institute of Optics and Fine Mechanics, Academia Sinica
P.O. Box 800-211, Shanghai 201800, P.R. China

In this paper the characteristics of glass formation and structure of non-oxide glasses have been summarized and some basic points have been discussed. There are as follows:

- 1) The nature of chemical bond is the determinative factor for the formation and structure of glass.
- 2) Glass formation ability can be calculated on the basis of chemical bond parameters.
- 3) Inorganic glass systems can be classified according to their characteristics of short range order.
- 4) Structural models of non-oxide glasses have been proposed.

1. Introduction

A great number of non-oxide glass forming systems have been emerged in recent years. The structure and glass formation of these non-oxide glasses look different from those of ordinary oxide glasses. We will try to generally discuss the glass formation and structure of non-oxide glasses in comparison with oxide glasses and summarize the results into several basic points.

2. Chemical bond nature is the determinative factor of formation and structure of non-oxide glasses

As we have pointed out previously the nature of chemical bond is a determinative factor for formation and structure of glass^[1]. The existence of a hybrid in the metallic, ionic and covalent bonds is a prerequisite to glass formation. Ionic and metallic bond materials, such as CsF crystal and Cs metal respectively, exhibit high coordination numbers and non-directional bonds, and are difficult to vitrify. Pure covalent bond molecules, such as F₂, combine each other by Van der Waals forces, which are also non-directional. Therefore, pure covalent bond materials are also difficult to form glasses. When ionic and metallic bonds mix with covalent bonds, the chemical bond exhibits direction and saturation through strong polarization. It is then favorable to form low coordinations between nearest atoms and the glass formation is easy to take place. As an example, Table 1 shows the relationship between the tendency of glass formation and the nature of chemical bond of arsenic and zinc compounds. The intermediate compounds, such as As₂S₃ and As₂Se₃, ZnCl₂ and ZnBr₂, have a mixed chemical bond nature and reach high glass formation ability.

Table 1 Tendency of glass formation, electronegativity and chemical bond character of As and Zn atoms with VI and VII group elements

| System | Compound | Electronegativity | Tendency of glass formation | Character of chemical bond |
|-----------|---------------------------------|-------------------|-----------------------------|----------------------------|
| Oxide | As ₂ O ₃ | O | 3.5 | Covalent |
| Sulfide | As ₂ S ₃ | S | 2.5 | |
| Selenide | As ₂ Se ₃ | Se | 2.4 | Metallic |
| Telluride | As ₂ Te ₃ | Te | 2.1 | |
| Fluoride | ZnF ₂ | F | 4.0 | Ionic |
| Chloride | ZnCl ₂ | Cl | 3.0 | |
| bromide | ZnBr ₂ | Br | 2.8 | Covalent |
| Iodide | ZnI | I | 2.5 | |

According to chemical bond characteristics the inorganic glass materials can be classified into three groups:

1) Metalloid + non-metallic elements. The metalloid elements are located at IIIA, IVA and VA groups of the periodic table, and the non-metallic elements are located at VIA and VIIA groups.

2) Metalloid + metallic elements. The metallic elements are mainly transition metals and noble elements.

3) Metallic A + metallic B elements. The metallic A elements are located at IIA, IIB, IIIB, IVB groups of the periodic table, and the metallic B elements are noble and rare-earth elements.

The chemical bonds in all inorganic materials mentioned above involve *sp*, *spd* and *spdf* hybrid bonds, respectively.

The non-oxide glasses, including halide and chalcogenide glasses, belong to the first group.

3. Glass formation ability in terms of chemical bond parameters

We propose two chemical bond parameters to characterize the glass formation ability of binary, ternary and multi-component systems [2]. ΔX is the difference of electronegativity and Z/r_c is the ratio of number of valence electron to covalent radius (in Å). Fig. 1 shows the chemical bond parameter diagram, which demonstrates the glass formation ability of different compounds. Cs, CsF, F₂ represent the pure metallic, ionic and covalent materials, which are located at the vertex of the triangle diagram. Within the solid line the cooling rate for glass formation is less than 10⁻¹ °C /s, and within the dot line the cooling rate is up to 10³ °C /s. The cooling rate was determined empirically.

For multi-component non-oxide glass systems the average values $\frac{1}{n} \sum_n \Delta X_{ij}$ and $\frac{1}{n} \sum_n \frac{Z}{r_c}$ can be taken. It can be seen from Fig. 1 that the critical cooling rate for the formation of most non-oxide glasses are between 10-10³ °C /s. Some glass forming

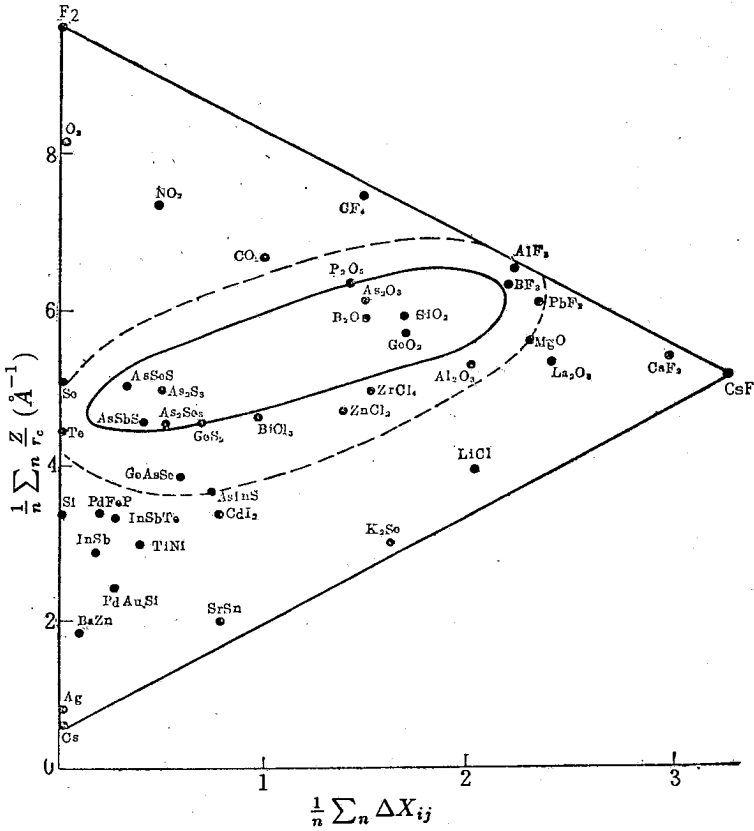


Fig. 1. Relationship between chemical bond parameters and glass formation.

fluorides and chalcogenides are rather stable, such as BeF_2 , As_2Se_3 , GeS_2 etc., the cooling rate is less than $10\text{ }^\circ\text{C}/\text{s}$.

Liang Zhenhua discussed the chalcogenide glass forming tendency in terms of the chemical bond approach [3]. The ionicity R_σ^{AB} and metallicity R_π^{AB} of an A-B bond are defined as follows [4]:

$$R_\sigma^{AB} = (r_s^A + r_p^A) - (r_s^B + r_p^B) \tag{1}$$

$$R_\pi^{AB} = (r_s^A - r_p^A) + (r_s^B - r_p^B) \tag{2}$$

Here the r_s and r_p represent the orbitally dependent ionic radii of s -orbital and p -orbital respectively [4]. The glass forming tendency of IIIA and IVA elements in the As-Se glass system (the ratio $\text{As}/\text{Se}=0.5\sim 0.7$) and the R_σ^{AB} and R_π^{AB} values of IIIA and IVA elements with Se atoms are shown in Table 2. It can be seen that higher content of most of IIIA and IV group elements in the As-Se glass systems corresponds to lower ionicity and metallicity.

Table 2 Content of IIIA and IVA groups element in As-Se glass system and the character of chemical bond of selenides

| Element | B | Al | Ga | In | Tl | Si | Ge | Sn | Pb |
|-------------------|------|-------|-------|-------|-------|-------|-------|-------|-------|
| Content (at%) | 40 | 3 | 18 | 3 | 50 | 50 | 52 | 10 | 30 |
| Bond | B-Se | Al-Se | Ga-Se | In-Se | Tl-Se | Si-Se | Ge-Se | Sn-Se | Pb-Se |
| R_σ (a.u.) | 0.25 | 0.49 | 0.35 | 0.58 | 0.50 | 0.20 | 0.27 | 0.48 | 0.48 |
| R_π (a.u.) | 0.31 | 0.49 | 0.55 | 0.58 | 0.64 | 0.23 | 0.45 | 0.48 | 0.54 |

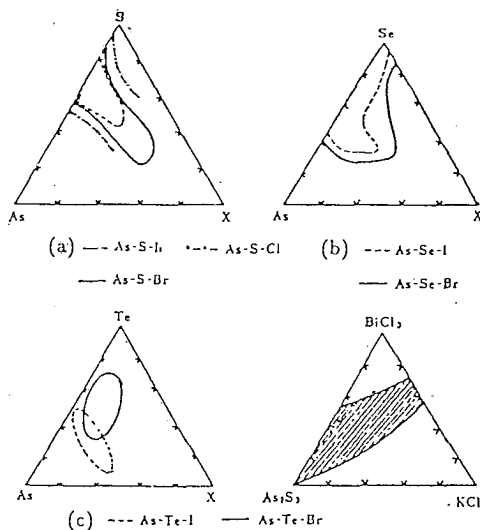


Fig. 2: Glass forming regions of As-S-X (a), As-Se-X (b), As-Te-X (c) and As_2S_3 - $BiCl_3$ -KCl systems.

In mixed anion glasses we found that the glass forming range can be enlarged with anions of similar electronegativity [5]. According to the electronegativity values of VI and VII group elements shown in Table 1, fluoride is easy to form mixed anion glasses with oxide and it is well known that the fluoro-phosphate and fluoro-borate glasses are rather stable. Also, chloride with sulfide, bromide with selenide, and iodide with telluride always possess large glass forming regions than with others. This is obviously due to the similarity of chemical bonds. Fig. 2 shows the glass forming region of As atoms with VI and VII group elements, while sulfide (As_2S_3) can continuously form glasses with chlorides ($BiCl_3+KCl$).

4. Characteristics of short range order of glassy state and chemical bond

The short range order involved in the arrangement of the nearest neighboring atoms can be expressed by three structural parameters: the bond length between the central atom and the nearest neighboring atom, the bond angle and the coordination

number [6]. These three structural parameters for non-oxide glasses are also different from those of the crystalline state, cf. Table 3. Comparing the element and the compound glasses with the crystalline state, it can be seen clearly that the short range structural similarity depends upon the properties of the chemical bond. These can be classified by three categories: the first class involves ionic-covalent bond compounds very stable for forming glass, such as BeF_2 , GeSe_2 , etc. Their tetrahedral $[\text{BeF}_4]$, $[\text{GeSe}_4]$ structures are in agreement with those of the crystalline states (i.e. agreement in bond length, bond angle and coordination number). The second class contains elements with covalent bonds as major constituents, such as Si, Ge, Se, As and III-V compound, As_2S_3 compounds etc. In comparison with the crystalline state, the coordination numbers and the bond lengths are the same, whereas the bond angles have greater difference. This indicates that in the glassy state, the tetrahedra are similar but not exactly the same as those in crystals (or distorted tetrahedra). The third class contains compounds more ionic in the nature, such as AlF_3 , ZrF_4 , ZnCl_2 etc. For cations the bond angle is different with in crystalline ones, but for anions three parameters (bond angle, bond length and coordination number) are different. In three glass classes the connected angles between polyhedra are not monotonous in glassy state. They have a certain variation range, e.g. the angular variation of Be-F-Be is around 140° , which provides freedom for the vertex angle rotation and reflects the topological disorder of three dimensional structure in the glassy state. All information of short range order of glassy materials shown above is closely connected with chemical bond nature.

Table 3 Short range structural parameters of element and compound non-oxide glasses

| Types | I | | | | II | | | | | III | | | | | |
|---------------------|----------------|---|-----------------|----|----|----|----|-------------------------|---|----------------|----------------|----|-----------------|----|----|
| Composition | BeF_2 | | GeSe_2 | | Si | As | Se | As_2S_3 | | AlF_3 | ZrF_4 | | ZnCl_2 | | |
| Central atom | Be | F | Ge | Se | Si | As | Se | As | S | Al | F | Zr | F | Zn | Cl |
| Bond angle | o | o | o | • | • | • | • | • | • | • | • | • | • | • | • |
| Bond length | o | o | o | o | o | o | o | o | o | o | • | o | • | o | • |
| Coordination number | o | o | o | o | o | o | o | o | o | o | • | o | • | o | • |

(o) denotes single value and (•) denotes a range of values

5. The structural model of non-oxide glasses

It is very difficult to present various kinds of glasses with a single structural model due to the fact that each has its own different characteristics. But we believe that the random polyhedra packing model can be summarized as a structural model for non-oxide glasses.

Consequently one can be based on the existence of a polyhedron $[AB_n]$ composed of two atoms (or ions) A, B of unequal radii. This is the most fundamental condition for the short range order in glass as we discussed above, and the most fundamental unit in glass as well. The polyhedron may be a triangle, tetrahedron, octahedron or a polyhedron with even higher coordination number. The polyhedra can be bonded at the vertex angles, sides or faces, and be packed disorderly in space to form the spatial arrangement according to the minimum energy principle. Other atoms (or ions) with even greater radii (C), which are located at the vacancies of the disorder polyhedra, forming an arrangement of even higher coordination number together with atoms (or ions) B.

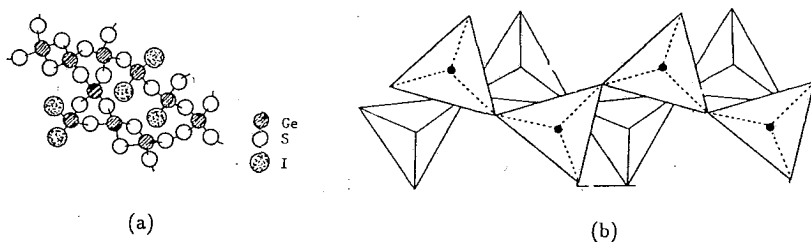


Fig. 3. Structural model of Ge-S-I glass.

(a) atomic arrangement; (b) polyhedra packing

In traditional oxide glasses, such as silicate, borate, phosphate glasses, B^{3+} , Si^{4+} and P^{5+} cations with O^{2-} anions form triangles $[BO_3]$ and tetrahedra $[BO_4]$, $[SiO_4]$, $[PO_4]$, these triangles and tetrahedra are connected at the vertex points and form three dimensional structural networks. Some ions with greater radii, such as alkali and alkaline earth ions, R^+ , R^{2+} are located at the vacancies of the structural network. This is the random network model, which can be regarded as a special case of random packing of polyhedra model. The BeF_2 , $ZnCl_2$ and AlF_3 -based halide glasses are included in this category. Be^{2+} and Zn^{2+} form tetrahedra $[BeF_4]$ and $[ZnCl_2]$, and Al^{3+} forms tetrahedra $[AlF_4]$ or octahedra $[AlF_6]$. The As- and Ge based chalcogenide glasses can also be regarded as belonging to this category. Fig. 3 shows the structural model of a halo-chalcogenide (Ge-S-I) glass. The tetrahedra $[GeS_4]$ and $[GeS_3I]$ connect each other by vertex to form rings and chains. The structural model of alumino-fluoride (RO- AlF_3) glasses is illustrated in Fig. 4, where the octahedra $[AlF_6]$ and tetrahedra $[AlF_4]$ are connected by vertex too.

In fluoride glasses with cations of greater ionic radii, such as zirconium fluoride and thorium fluoride-based glasses, the cations and the anions form polyhedra with even higher coordination numbers, such as $[ZrF_8]$, $[ThF_8]$ etc. These polyhedra are connected to each other at the vertex as well as at the sides, which form three dimensional random packing. Figure 5 shows the structural model for BaF_2 - ZrF_4 .

To increase the stability of the random packing of polyhedra the close packing

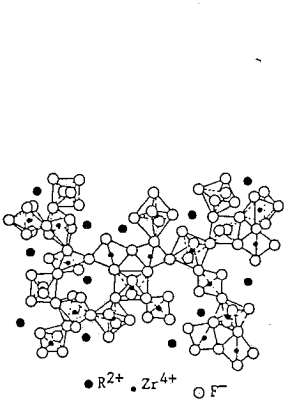
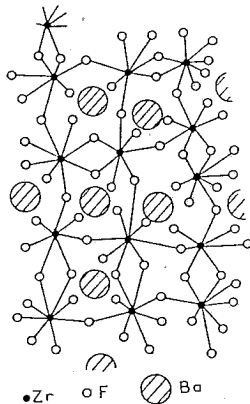
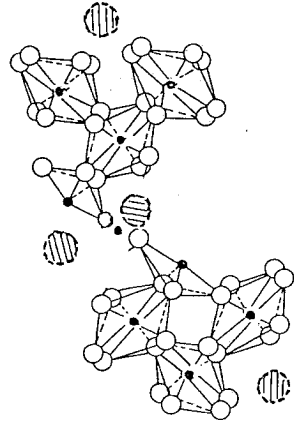


Fig. 4. Structural model of polyhedra packing of RF_2-AlF_3 glass



(a)



(b)

Fig. 5. Structural model of BaF_2-ZrF_4 glass (a) atomic arrangement; (b) polyhedra packing

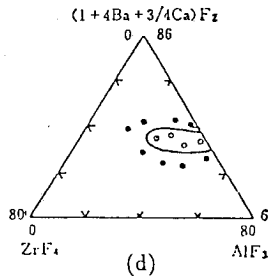
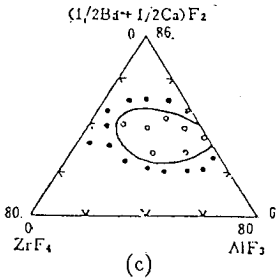
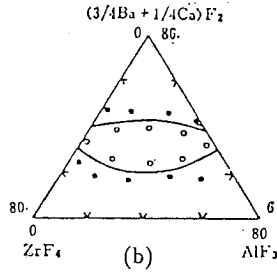
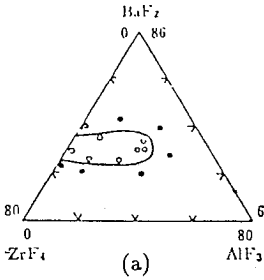


Fig. 6. Glass forming regions of $ZrF_4-AlF_3-RF_2$ systems

of polyhedra should be avoided to make more space available at the vertex of polyhedra. In this case the atoms (or ions) with greater radii are outside the polyhedra and play an important role. Taking the ZrF_4+AlF_3 -based fluoride glasses as an example [7], the alkaline earth ion with larger ionic radius, such as Ba^{2+} , makes the "non-bridging" fluorine at the vertex of $[ZrF_8]$ polyhedra and increases the space freedom of connected polyhedra. Therefore, $ZrF_4(ThF_4)$ -based fluoride glasses always

contain a large amount of BaF_2 , and $\text{ThCl}_4(\text{BiCl}_3)$ -based glasses can be doped by a lot of KCl and NaCl . It is worth pointing out that for stabilizing the fluoride glass structure, the electric field strengths of cation A forming the polyhedron and cation C at the vacancy between polyhedra should be matched, because the cations C are located around the negatively charged fluorine polyhedra for charge compensation. The ratio of the electric field strengths of cations A and C, $(Z_A/r_A^2)/(Z_B/r_B^2)$ is about 5-6. The optimal electric field strength ratio can decrease the structural stress. Therefore, it is easy to form glass, when ZrF_4 combines with BaF_2 and AlF_3 with CaF_2 . As shown in Fig. 6, when CaF_2 replaces the BaF_2 , the glass forming regions are gradually moved from the ZrF_4 rich area to the AlF_3 rich area. Therefore, the content of fluoride with high field cation should be matched with the content of fluoride with low field cation. The ratio is about 3:2, it means that 20% "non-bridging" fluorines are existed.

6. Conclusion

On the basis of chemical bond characteristics we can predict the glass formation ability and classify the non-oxide glasses by short range structure. In addition we can propose the random polyhedra packing model to unify the different structural models for inorganic glass systems.

References

1. Fuxi Gan, Chinese Science Bull., No.2(1963)18.
2. Fuxi Gan, Chinese Cer. Soc. Bull., No.3(1984)1.
3. Zhenhua Liang, J. Non-Cryst. Solids, 127(1991)298.
4. J. R. Chelikowsky and J. C. Philips, Phys. Rev. B17(1978)2453.
5. Fuxi Gan, J. Non-Cryst. Solids, 140(1992)184.
6. R. P. Messmer and J. Wong, J. Non-Cryst. Solids, 45(1981)1.
7. Yuan Cao and Fuxi Gan, J. Chinese Cer. Soc., 16(1988)50.

VELOCITY OF ULTRASOUND AND ELASTIC PROPERTIES OF LITHIUM BORATE GLASSES

M. Kodama, K. Yamakawa and T. Matsushita

Department of Industrial Chemistry, Kumamoto Institute of Technology, Ikeda, Kumamoto 860, Japan

A series of lithium borate glasses $x_2\text{Li}_2\text{O}\cdot(1-x_2)\text{B}_2\text{O}_3$, where x_2 is the mole fraction of Li_2O , is prepared for the composition range $0 \leq x_2 \leq 0.28$ and the glass transition temperature, the density and the two velocities of longitudinal and transverse ultrasonic waves are determined as a function of the composition. Ordinary elastic constants such as longitudinal modulus, shear modulus, bulk modulus and Young's modulus are calculated from the density and the two ultrasonic velocities; it is found that these elastic constants increase monotonously with increasing x_2 . In order to elucidate the relationship between the elasticity and the structure of lithium borate glasses, it is assumed that lithium borate glasses are composed of the three structural units defined as BO_3 , $\text{Li}^+\text{B}\text{O}_2\text{O}^-$ and $\text{Li}^+\text{B}\text{O}_4^-$, where O represents a bridging oxygen and O^- a nonbridging oxygen, and these structural units have their respective elastic constants. The elastic constants of the three structural units are defined on the basis of a thermodynamic equation of a deformed body. The elastic property of lithium borate glasses is analysed in terms of the elastic constants of the structural units to conclude that the elastic property as a function of the composition can be explained by the reaction $2\text{B}\text{O}_3 + \text{Li}_2\text{O} \rightarrow 2\text{Li}^+\text{B}\text{O}_4^-$.

Introduction

Spectroscopic studies on alkali metal borate glasses have revealed that the structure of alkali metal borate glasses is dependent not only upon the content of the alkali metal ion but also upon the difference in the alkali metal ion (1). Thus, we cannot discuss the structure and properties of alkali metal borate glasses in the same way without taking note of the difference in the alkali metal ion. Since ultrasonic velocity is sensitive to such differences in structure of glass, it would be of great interest to study the velocity of sound in each binary system of the alkali metal borate glasses. The present authors have measured the velocity of sound in each binary system of sodium, potassium, rubidium and caesium borate glasses (2-5); it was found especially that the ultrasonic velocity in two binary systems of sodium and potassium borate glasses shows a single maximum while the ultrasonic velocity in two binary systems of rubidium and caesium borate glasses exhibits a maximum, a minimum and another maximum in succession. Thus, it is evident that the difference in the alkali metal ion causes differences in the structure and properties of alkali metal borate glasses. In order to complete a series of experiments on the ultrasonic velocity in alkali metal borate glasses, this paper reports the results of the velocity of sound in and elastic properties of lithium borate glasses.

Experimental

Glass preparation

We denote the composition of lithium borate glasses by the formula $x_2\text{Li}_2\text{O}\cdot(1-x_2)\text{B}_2\text{O}_3$, where x_2 denotes the mole fraction of Li_2O . Ota and Soga (6) studied the glass-forming region of lithium borate glasses as a function of the cooling rate of their melts to show that the glass-forming region extended from $0 \leq x_2 \leq 0.12$ to $0 \leq x_2 \leq 0.70$ as the cooling rate was increased from 1.2×10^{-3} K/s to 1.0×10^5 K/s. However, sizable specimens of lithium borate glasses can be made only in the composition range $0 \leq x_2 < 0.30$ by pouring their melts into a mould (7). A series of lithium borate glasses was prepared at regular intervals of 0.02 mole fraction

through the composition range $0 \leq x_2 \leq 0.28$; an attempt was made to prepare the sizable glass specimens with the compositions of $x_2 = 0.30, 0.32, 0.34$ and 0.36 but all of their respective melts crystallized quickly after casting. All the glasses were prepared with high homogeneity and without strains or bubbles in order that they might transmit ultrasound satisfactorily.

Analytical reagent grade $\text{LiOH} \cdot \text{H}_2\text{O}$ (higher than 99.0% purity, the main residue is lithium carbonate) and H_3BO_3 (higher than 99.7% purity) were used as the starting materials. With the aim of preparing glasses with high homogeneity, the starting materials were initially made to react in an aqueous solution. Amounts of the starting materials calculated to yield 25 to 28 g in the melts were dissolved in a beaker made of poly(tetrafluoroethylene) by adding distilled water. Then the solution was transferred to a dry box and after the complete evaporation of the water a chemically reacted powder was obtained.

The powder was fused in a 20 cm³ platinum crucible at temperatures from 1050 to 1300°C for about 4 h by heating with an SiC resistance electric furnace; these temperatures were decreased as x_2 increased. The liquid was occasionally stirred with a platinum-rhodium wire to make it more homogeneous. The liquid was then poured into a cylindrical graphite mould 15 mm in diameter and 30 mm deep which had been preheated at 300°C in an electric muffle furnace. Subsequently, the cast glass in the mould was held at 300°C for 1 h, then cooled at a rate of 1 K/min to room temperature while passing dry nitrogen through the muffle furnace. The residual liquid was poured onto an aluminium plate and later used for chemical analysis and for differential thermal analysis (DTA). Several cast glasses in which small bubbles were included were not used in the present experiment. The glass of each composition was stored in a hermetic vial.

Chemical analysis

Boric acid combines with mannitol to form a mannitol-borate complex (8). This complex compound is a moderately strong monobasic acid and therefore can be titrated with a strong base solution. By a potentiometric titration described in a previous paper (5), the actual compositions of all of the prepared lithium borate glasses were determined: in brief, by use of a sodium hydroxide solution as the titrant, the amount of the lithium ion was titrated by means of back titration and subsequently the amount of the boron was titrated by means of the mannitol method, where the two equivalence points were determined from their respective inflection points of the potentiometric titration curve. The accuracy and the precision in the determination of Li_2O and B_2O_3 were within 3×10^{-4} mole fraction and within 1.0×10^{-4} mole fraction, respectively.

Glass transition temperature and annealing

The glass transition temperature of lithium borate glasses as a function of x_2 was determined by differential thermal analysis; the apparatus used was described in a previous paper (5). We define the onset temperature, the peak temperature and the end temperature of glass transition in the manner described in a previous paper (5) and denote these temperatures by T_g , T_p and T_e , respectively; T_g is often referred to as the glass transition temperature. In the present differential thermal analysis, the cooling rate over the whole transition range was 15 ± 5 K/min and the heating rate was varied from 10 to 40 K/min. By fitting a least-squares parabola to each set of T_g , T_p and T_e as a function of heating rate, these characteristic temperatures where the heating rate was extrapolated to zero were calculated, from which the glass transition range of lithium borate glasses was determined as a function of x_2 .

In order to stabilize the physical properties of a glass, it is necessary that the glass should be carefully annealed by cooling slowly from above the temperature range of glass transition. Every cast glass was annealed in a high purity nitrogen gas atmosphere according to the following annealing schedule: (1) the temperature was raised from room temperature to T_e at a constant rate of 1 K/min, (2) the temperature was kept constant at T_e for 2 h, and (3) the temperature was lowered from T_e to room temperature at a constant rate of 1 K/min. Every annealed glass was transparent and showed no opalescence.

Density

The density of each annealed glass was measured at 298 K by means of the hydrostatic weighing method described in a previous paper (5): in brief, a silicon single crystal was used as a density standard (9) for calibrating the density of the immersion liquid (carbon tetrachloride) so that the density of each glass was measured within an accuracy of $1.0 \times 10^{-3} \text{ g/cm}^3$.

Ultrasonic velocity

In order to measure the ultrasonic velocity, each annealed glass was at first ground with a coarse SiC abrasive and then polished with a fine alumina abrasive and machine oil on a flat glass plate to give a pair of end faces that were flat and parallel. The dimensions of the polished glasses were 15 mm in diameter and normally 17 mm in length; the length was measured with a micrometer reading to 1 μm . Inspection with a strain viewer showed that all specimens were transparent and almost free from strain.

The ultrasonic travel time was measured at a frequency of 10 MHz and at a temperature of 298 K by means of the pulse-echo overlap method (10). The apparatus used was constructed in the present authors' laboratory and the circuit was described in a previous paper (11). X-cut and Y-cut quartz transducers resonating at a fundamental frequency of 10 MHz were used for the longitudinal wave and for the transverse wave, respectively. For both types of the transducers, a pair of electrodes was deposited onto a 10-mm-diameter quartz disc by evaporating first chromium and then gold in such a way that the active area was an 8-mm-diameter circle and two electrode terminals were placed on one side of the disc. The transducer was bonded to the specimen on one of the two parallel faces with phenyl benzoate (12) and used for both generation and detection of ultrasound. The specimen with the transducer attached was set in a hermetic specimen holder and controlled at 25°C by placing the holder in a water bath.

McSkimin (13) proposed a criterion for determining the correct cyclic overlap between echoes in order that the ultrasonic travel time could be measured with high accuracy. Once two echoes are properly overlapped according to the McSkimin criterion, it is possible to measure the ultrasonic travel time within an error of 0.02% for round trips greater than 5 μs (13). The McSkimin criterion was extended in a previous paper (14) for application to ordinary glass specimens and this was used in the present measurements.

Results and Discussion

Figure 1 shows three characteristic temperatures, T_g , T_p and T_c , of glass transition for lithium borate glasses as a function of x_2 ; we see that each of these characteristic temperatures shows a tendency to have a maximum at $x_2 \approx 0.28$. Figure 2 shows the density, ρ , of lithium borate glasses plotted against x_2 ; we see that the density increases with increasing x_2 in such a way that the slope is almost constant up to $x_2 \approx 0.20$ and then decreases gradually with further increasing x_2 . Figure 3 shows both the longitudinal velocity, V_l , and the transverse velocity, V_t , of lithium borate glasses plotted against x_2 ; we see that each velocity increases with increasing x_2 in such a way that the slope decreases gradually with increasing x_2 .

From ρ , V_l and V_t , ordinary elastic constants such as longitudinal modulus L , shear modulus G , bulk modulus K , and Young's modulus E , can be calculated according to the formulas

$$L = \rho V_l^2, \quad (1)$$

$$G = \rho V_t^2, \quad (2)$$

$$K = L - (4/3)G, \quad (3)$$

$$E = G(3L - 4G)/(L - G). \quad (4)$$

Figure 4 shows L , G , K and E as a function of x_2 ; we see that each of these elastic constants increases with increasing x_2 in such a way that the slope increases gradually with increasing x_2 .

The relationship between the elasticity and the structure of lithium borate glasses is analysed in the following in terms of the three structural units defined as $B\emptyset_3$, $Li^+B\emptyset_2O^-$ and $Li^+B\emptyset_4^-$, where \emptyset represents a bridging oxygen and O^- a nonbridging oxygen, on the assumption that these structural units exhibit their inherent elastic properties and hence have their respective elastic constants. The elastic constants of the structural units in alkali metal borate glasses have been defined in previous papers (3-5) on the basis of a thermodynamic equation of a deformed body so that only the final result will be given in the following.

For the sake of simplicity, we shall write the three structural units as $B\emptyset_3 \equiv a$, $Li^+B\emptyset_2O^- \equiv b$ and $Li^+B\emptyset_4^- \equiv c$. Let M_{Li_2O} and $M_{B_2O_3}$ be the molar masses of the component Li_2O and the component B_2O_3 , respectively. Then the molar mass, M_s , of the structural units is defined as

$$M_s = \frac{1}{2(1-x_2)} \{x_2 M_{Li_2O} + (1-x_2) M_{B_2O_3}\}. \quad (5)$$

Let E_a , E_b and E_c be the elastic constants of the structural units a , b and c , respectively. Then the required equation is written as

$$M_s V^2 = \left(1 - \frac{x_2}{1-x_2}\right) E_a + \left(\frac{x_2}{1-x_2} - N_4\right) E_b + N_4 E_c, \quad (6)$$

where V is the velocity of sound and N_4 is the fraction of boron atoms in tetrahedral coordination.

A NMR study on lithium borate glasses by Jellison, Feller and Bray (15) showed that $N_4 = x_2/(1-x_2)$ for $0 \leq x_2 < 0.28$ and $N_4 < x_2/(1-x_2)$ for $x_2 > 0.28$. We can therefore assume that the relation of $N_4 = x_2/(1-x_2)$ holds in the composition range $0 \leq x_2 < 0.28$ and thus in the range $0 \leq x_2/(1-x_2) < 0.39$. Substitution of $N_4 = x_2/(1-x_2)$ into Equation (6) gives

$$M_s V^2 = \left(1 - \frac{x_2}{1-x_2}\right) E_a + \frac{x_2}{1-x_2} E_c, \quad (7)$$

so that a plot of $M_s V^2$ against $x_2/(1-x_2)$ should be a single straight line in the composition range $0 \leq x_2/(1-x_2) < 0.39$.

Figure 5 shows a plot of the longitudinal elastic constant, $M_s V_l^2$, against $x_2/(1-x_2)$ and the least-squares line through the data points. Figure 6 shows a plot of the shear elastic constant, $M_s V_t^2$, against $x_2/(1-x_2)$ and the least-squares line through the data points. We see that both plots can be represented by a straight line, indicating that the relation of $N_4 = x_2/(1-x_2)$ holds. Thus, the structural unit a is converted only into the structural unit c in the composition range $0 \leq x_2 < 0.28$ by the reaction



Such a simple reaction occurs only in lithium borate glasses; in the case of potassium, rubidium and caesium borate glasses (3-5), the structural unit b forms above the composition of $x_2 \approx 0.07$.

The values of E_a and E_c calculated from Equation (7) are as follows: for the longitudinal wave, $E_a = 0.415$ MJ/mol and $E_c = 3.96$ MJ/mol; for the transverse wave, $E_a = 0.125$ MJ/mol and $E_c = 1.25$ MJ/mol. The value of E_c is ten times as great as the value of E_a for each of the longitudinal and transverse waves. This difference indicates that the structural unit c increases the rigidity of the glass, which can be attributed to the fact that the structural unit c forms a three dimensional covalent bond in the glass network.

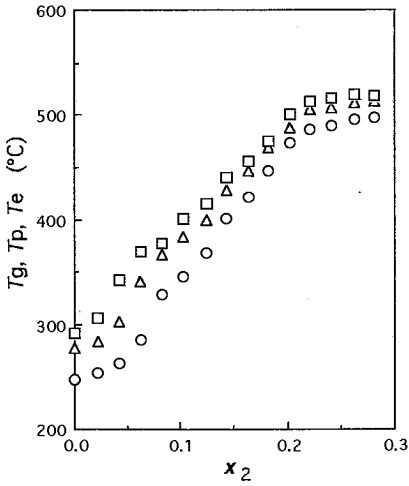


Figure 1. The plot of T_g (○), T_p (△) and T_e (□) against x_2 .

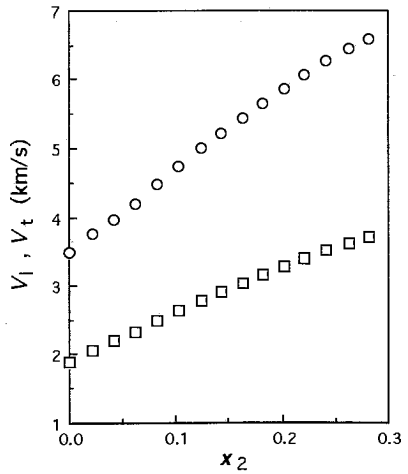


Figure 3. The plot of V_1 (○) and V_t (□) against x_2 .

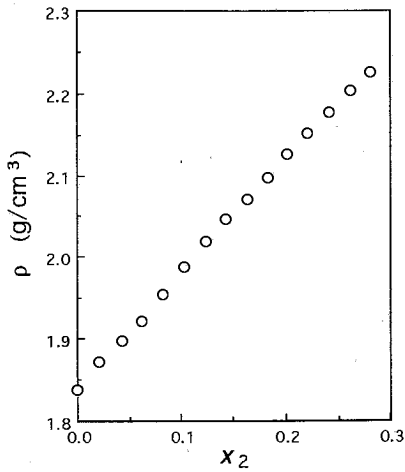


Figure 2. The plot of ρ against x_2 .

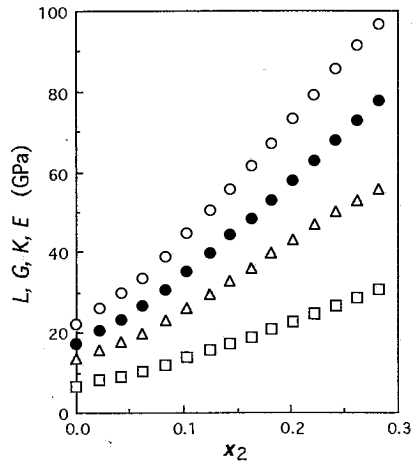


Figure 4. The plot of L (○), G (□), K (△) and E (●) against x_2 .

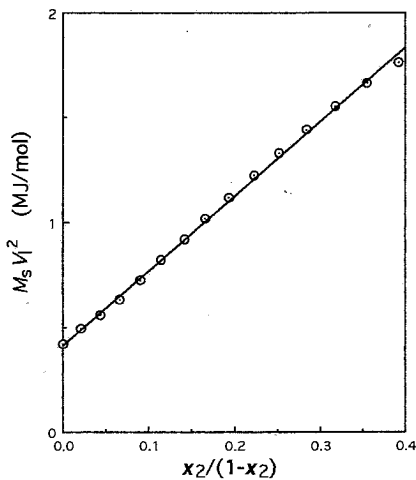


Figure 5. The plot of $M_s V_i^2$ against $x_2/(1-x_2)$.

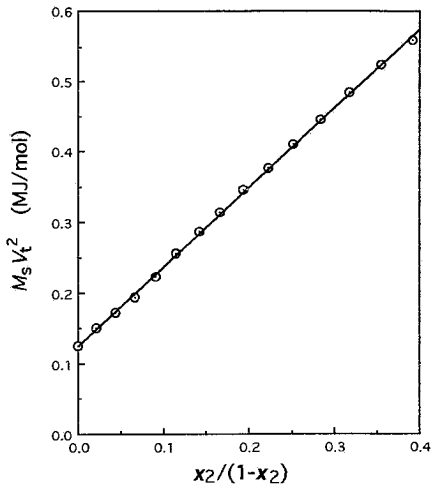


Figure 6. The plot of $M_s V_i^2$ against $x_2/(1-x_2)$.

References

1. E. I. Kamitsos and G. D. Chryssikos, *J. Molec. Struct.* 247 (1991) 1.
2. M. Kodama, *J. Mater. Sci.* 26 (1991) 4048.
3. M. Kodama, *J. Non-Cryst. Solids* 127 (1991) 65.
4. M. Kodama, *J. Am. Ceram. Soc.* 74 (1991) 2603.
5. M. Kodama, T. Hirashima and T. Matsushita, *Phys. Chem. Glasses* 34 (1993) 129.
6. R. Ota and N. Soga, *J. Ceram. Soc. Japan* 91 (1983) 265.
7. S. A. Feller, W. J. Dell and P. J. Bray, *J. Non-Cryst. Solids* 51 (1982) 21.
8. J. J. Kankare, *Analyt. Chem.* 45 (1973) 2050.
9. H. A. Bowman, R. M. Schoonover and C. L. Carroll, *Metrologia* 10 (1974) 117.
10. E. P. Papadakis, in: *Physical Acoustics*, Vol. 12, eds. W. P. Mason and R. N. Thurston (Academic Press, New York, 1976) p. 277.
11. M. Kodama and S. Hayashi, *Bull. Kumamoto Inst. Technol.* 3 (1978) 121.
12. M. Kodama, *Jpn. J. Appl. Phys.* 21 (1982) 1247.
13. H. J. McSkimin, *J. Acoust. Soc. Am.* 33 (1961) 12.
14. M. Kodama, *Phys. Chem. Glasses* 26 (1985) 105.
15. G. E. Jellison, S. A. Feller and P. J. Bray, *Phys. Chem. Glasses* 19 (1978) 52.

PHYSICAL PROPERTIES AND SPECTROSCOPY OF RUBIDIUM AND CAESIUM BORATE GLASSES WITH EXCEPTIONALLY HIGH ALKALI CONTENT

S. FELLER, S. NIJHAWAN, M. ROYLE, J. MACKENZIE, J. TAYLOR, M. SHARMA

Physics Department, C oe College, Cedar Rapids, IA 52402, USA

E.I. KAMITSOS, G.D. CHRYSOSIKOS, A.P. PATSIS

National Hellenic Research Foundation, Athens 116-35, Greece

P.J. BRAY, P.E. STALLWORTH

Department of Physics, Brown University, Providence, RI 02912, USA

The glass formation range in rubidium and caesium borates is greatly enlarged through the use of the alkali oxide instead of the more common alkali carbonate in the batch. Density and glass transition temperature (T_g) measurements were performed on both families of glasses and comparisons to results obtained previously from lithium, sodium, and potassium borate glasses are drawn. ^{11}B NMR data were obtained and compared with Raman spectra in order to model the short-range order found in these glasses. The structures present in these glasses differ considerably from those found in the lighter alkali borate glasses. A discussion of possible structural models is also given.

I Introduction

It has been observed recently that rubidium and caesium borate glasses of very high alkali content can be readily formed from oxide starting materials (1,2,3). This is in contrast to the polycrystalline materials obtained, when the more conventional carbonate starting materials are used. It is the purpose of this paper to report densities and glass transition temperatures along with Raman and NMR measurements for these glasses.

II Experimental Procedure

The glasses were prepared from appropriate quantities of alkali oxide and boron oxide. Composition was controlled using the parameter R , which is defined as the molar ratio of alkali oxide to boron oxide. Batches, 5 to 10 g in mass, were prepared in either platinum, zirconia, or vitreous carbon crucibles. The samples were heated to between 900 and 1000 $^\circ\text{C}$ for approximately 15 minutes using an electric muffle furnace. A weight check to verify sample composition was performed after 10 minutes of heating. The resulting melts were formed into glasses via plate quenching or by pouring the melt into a brass mold. Due to the highly hygroscopic nature of these glasses, appropriate measures were taken to ensure that the samples remained dry (3).

The weight check showed a consistent loss of approximately 10-15% of the starting alkali oxide. The observation that small

quantities of rubidium are lost was previously made during Raman spectroscopy (4) and density studies (5). The R values assigned to these samples were adjusted to account for this loss. R_{batch} values reflect the composition of the batch and have not been adjusted for the alkali losses. Samples with $R > 1.5$ prepared for density measurements were prepared in zirconia or vitreous carbon crucibles only due to the much greater interaction of the samples with platinum crucibles in this range. While samples for T_g determination were prepared in both platinum and vitreous carbon crucibles, it was determined that the difference in results from samples of the same composition prepared in the two types of crucibles was within the experimental error. Raman and NMR samples were prepared in platinum crucibles.

The T_g s were measured using a Perkin-Elmer Model II Differential Scanning Calorimeter (DSC), scanning from 325 to 770 K at a rate of 40 K/min. The sample and reference chambers of the DSC were kept under dry nitrogen. The transition temperature (onset) was determined through the thermal analysis software of Laboratory Microsystems, Troy, NY. Each data point is the average of the individual sample runs made from one batch, with a conservative estimate of the absolute experimental error being ± 5 K.

The densities of these glasses were measured on a Quantachrome model MPY-2

micropycnometer. Mass was measured in a nitrogen atmosphere using a Sartorius model A210P digital balance sensitive to 0.0001 g. A conservative estimate of experimental error in density is $\pm 0.03 \text{ g/cm}^3$. The densities of low Rb and Cs content borate glasses agreed well with published data (6), after the weight loss of the alkali oxide was accounted for.

Raman measurements were made on a Ramanor HC 2S Jobin-Yvon spectrometer using the 514.5 nm line of a Spectra Physics 165 Argon ion laser and a vacuum cell to avoid hydrolysis and CO_2 uptake. The power level of the laser was approximately 200 mw. A 90° scattering geometry was employed and data were collected at 4 cm^{-1} resolution. Several spectra were acquired at each composition.

Non-adiabatic superfast passage (NASP) techniques were used to acquire the ^{11}B NMR spectra. All measurements were done at 15.70 MHz using a Varian Associates Model V2100B electromagnet, a Varian cross-coil probe, Mid-continent Instruments Model 5005 RF unit, Princeton Applied Research Model HR-8 lock-in amplifier, Matec 110 oscillator, and a Kepco bipolar operational power amplifier (modulation amplifier) and a Nicolet Model 1170 signal averager. All measurements were performed at room temperature. In order to determine the quadrupolar parameters for each spectrum the integrated spectra were computer simulated using a program developed by Taylor and Bray (7).

III Experimental Results and Discussion

The densities of the rubidium and caesium borate glasses are shown in Figure 1 along with the densities of the lighter alkalis previously reported by the Coe College group (8, 9, 10).

A useful method for introducing the alkali dependence of the density is to convert the data to the volume per mole B_2O_3 , V_{mol} , determined by (4, 11)

$$V_{\text{mol}} = \frac{(R \cdot mw(M_2O) + mw(B_2O_3))}{\rho} \quad (1)$$

where M is the alkali and mw represents molecular weight.

Figure 2 shows V_{mol} versus R for each

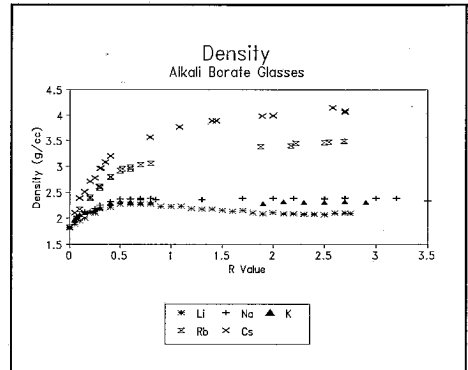


Figure 1:
Densities of alkali borate glasses

of the alkali borate glass families. At low R values, the trends are complicated by the formation of four-coordinated borons (f_2 units) from three coordinated borons (f_1 units), and the consequent contraction of the glass network (12,13). The most explicit evidence of this can be found in the lithium borates, where V_{mol} actually decreases until $R \approx 0.5$.

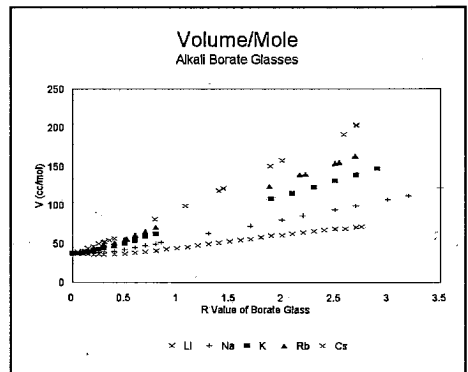


Figure 2:
Volume per mole B_2O_3 in alkali borate glasses

In the other alkali borates the slope of V_{mol} versus R is not as steep in the region $0 \leq R \leq$

0.5 as it is in the region $0.5 \leq R$.

In the region $0.5 \leq R$, V_{mol} is a linear function of R . This is the result of the dominant formation of nonbridging oxygens (NBOs), a trend consonant with much spectroscopic evidence (13, 14, 15). The slope of this region is dependent on the alkali incorporated with the glass.

A unit change in R in this region results in each boron gaining an alkali ion and half of an oxygen ion. The added volume per boron (ΔV_B) can be expressed as:

$$\Delta V_B = \frac{1}{2} V_{\text{Oxygen}} + V_{\text{Alkali}} \quad (2)$$

where V_{Oxygen} and V_{Alkali} are the volumes of the oxygen and alkali ions, respectively. Table 1 lists the ionic radii (adjusted for coordination number) (16, 17, 18, 19, 20), and the resulting volumes for each ion using Equation (2). Table 1 also lists ΔV_B calculated for each of the alkali families using Equation (2).

Table 1
Differential filled space ratios
of alkali borate glasses.

| Ion | Radius (Å) | ΔV_B (Å ³) Calculated | ΔV_B (Å ³) Experimental | Differential Filled Space Ratio |
|-----|------------|--|--|---------------------------------|
| Li | 0.78 | 5.52 | 13.5 | 0.41 |
| Na | 1.20 | 10.8 | 21.7 | 0.50 |
| K | 1.65 | 22.4 | 33.7 | 0.66 |
| Rb | 1.77 | 26.8* | 40.9 | 0.66 |
| Cs | 1.95 | 34.6 | 52.6 | 0.66 |
| O | 1.19 | | | |

ΔV_B was also derived from the slopes of the V_{mol} versus R graph (see Table 1). It is evident that in all cases the calculated ΔV_B is smaller than this experimentally derived ΔV_B . It is proposed that this is because the calculated ΔV_B does not include the empty space that is associated with each borate unit in the actual glass. The ratio of the two sets of ΔV_B , $(\Delta V_B)_{\text{Calculated}} / (\Delta V_B)_{\text{Experimental}}$, defined as the differential filled space ratio, is also listed in Table 1. It is noted that this ratio increases to a uniform value of 0.66 for the alkali with radii much greater than that of

oxygen, i.e. K, Rb, and Cs. This ratio is close to the maximum value for the filling of space by hard spheres (0.74). This is indicative of the fact that, for glasses incorporating these larger alkalis, in the region $0.5 \leq R$, it is the alkali ions which dominate the filling of space, while the borate units fill voids and charge-compensate the alkali ions. When the smaller alkalis (Li and Na, which have radii less than that of oxygen) are considered, it is evident that the filling of space is controlled by the boron-oxygen network and not the alkali ions. This results in the reduction in the efficiency of filling space to 0.50 (Na) and 0.41 (Li).

The T_g s of the rubidium and caesium borates, along with those of the lighter alkalis previously reported by the Coe College group (21), are shown as a function of R in Figure 3. It is noted that the data extend over a wide range of alkali concentrations from boron oxide out past the orthoborate composition ($R = 0$ to $R = 4$).

The transition temperature rises rapidly initially with increasing R , reaching a

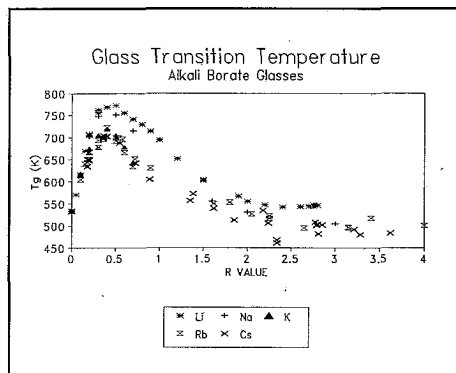


Figure 3:
Glass transition temperatures of alkali borate glasses

maximum at $R \approx 0.4$. As R increases beyond $R \approx 0.4$, there is a wide region of R for which the decrease in T_g is a nearly linear function of R . In the manner of the analyses of Shelby (22), Button *et al.* (23), Martin *et al.* (24), and Affatigato *et al.* (21), it is noted that there is

a strong correlation between the T_g and the fraction of f_2 units present (25). There is a slight discrepancy in the location of the maxima of T_g and f_2 , which occurs at $R \approx 0.5$ for the f_2 units (13), as opposed to $R \approx 0.4$ for the T_g s. It is noted that the T_g s correlate better with the average number of bridging boron-oxygen bonds per boron (15). At high R values the T_g levels off, presumably due to the absence of f_2 units. It is noted that for small R the T_g s of Rb and Cs borate glasses are considerably lower than those of the Li and Na borate glasses; at higher R the T_g s of Na, Rb, and Cs borate glasses become comparable while those of Li borate glasses remain higher.

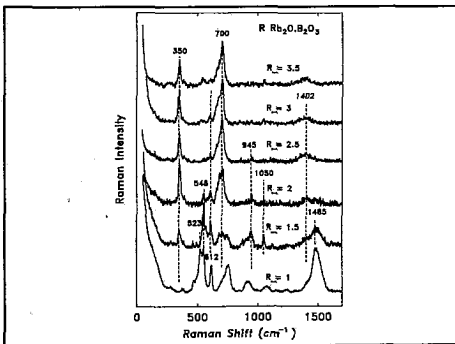


Figure 4(a):
Raman spectra of rubidium borate glasses.
Note that R is R_{Batch} in all cases.

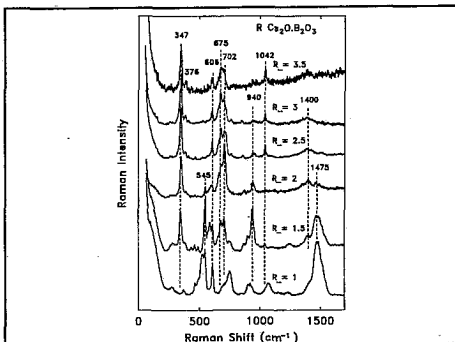


Figure 4(b):
Raman spectra of caesium borate glasses.
Note that R is R_{Batch} in all cases.

Figures 4 (a) and (b) present the Raman spectra from the rubidium and caesium borate glasses with $R_{\text{Batch}} \geq 1$, respectively. The similarity between the two sets of data are striking and suggestive of a common physical origin for these spectra.

The Raman spectra for the $R_{\text{Batch}} = 1$ glasses indicate the presence of ring type metaborate units, f_3 , (~ 610 cm^{-1} , 1400 - 1600 cm^{-1}) and tetrahedral borate groups (~ 545 cm^{-1} , 910 cm^{-1}), as well as other units in small amounts (26). The actual positions of these peaks vary a negligible amount between the Rb and Cs cases, with the responses from the Cs glasses being a few cm^{-1} lower. By $R_{\text{Batch}} = 1.5$ new responses near 675 - 700 cm^{-1} , 377 cm^{-1} , and 345 cm^{-1} can be seen. These new frequencies have been hypothesized to result from the formation of a new type of borate arrangement at the orthoborate composition (the orthoborate composition with two NBOs (26)). As the alkali concentration increases to near the orthoborate composition ($R_{\text{Batch}} = 3.5$) the spectra for both alkali systems simplifies to just the responses near 345 cm^{-1} , 376 cm^{-1} , 612 cm^{-1} , and 675 cm^{-1} through 700 cm^{-1} . In addition, the f_3 responses appear as weak features in the spectrum (the weak response near 1050 cm^{-1} is due to some small amount of CO_2 present in the glasses). It is specifically noted that the responses due to the more usual trigonal pyroborate and orthoborate units (f_4 at ~ 805 and 1180 cm^{-1} and f_5 near 860 cm^{-1}) (15, 26) are extremely weak or missing. It is expected that the new tetrahedral orthoborate unit would increase the glass density since, with two bridging oxygens associated with it, it would be more able to form a percolating network, and the tetrahedral nature of the units makes them intrinsically more dense than trigonal units. While it is possible to use this model in the interpretation of the density data, it must be noted that no definitive evidence is provided by the latter for the existence of such a unit.

Figures 5 (a) and (b) present the ^{11}B NMR spectra from the rubidium and caesium borate glasses. Superimposed on these data are the computer simulations of the spectra. Like the Raman spectra shown in Figures 4 (a) and (b), the ^{11}B NMR spectra show a remarkable degree of consistency between the rubidium borate results and those from

caesium borates. In addition, the spectra are fairly static at high values of R.

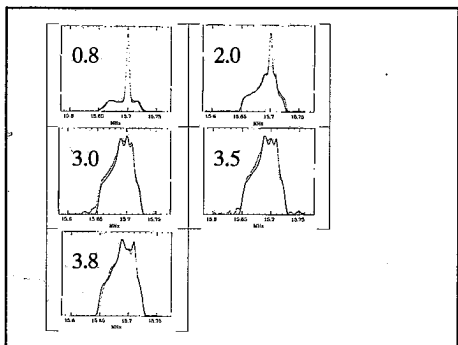


Figure 5(a):

^{11}B NASP NMR spectra of Rb borate glasses. R_{Batch} values are shown with the spectra.

The spectra from rubidium borate glasses depicted in Figure 5 (a) were deconvoluted into three distinct types of responses (the results for caesium are very similar). These three responses, described in terms of the quadrupole coupling constant and asymmetry parameter, have been previously assigned (27) to symmetric trigonal borons (f_1 and f_5), asymmetric trigonal borons (f_3 and f_4), and tetrahedral borons with all bridging oxygens (f_2). Table 2 lists the fractions of borons in each of these structures.

Table 2

Fractions of the borate units found in high rubidium content borates from ^{11}B NASP NMR

| R_{Batch} | f_1 and f_5 | f_3 and f_4 | f_2 |
|--------------------|-----------------|-----------------|-------|
| 0.8 | 0.37 | 0.19 | 0.44 |
| 2.0 | 0.01 | 0.86 | 0.14 |
| 3.0 | 0.01 | 0.99 | 0.00 |
| 3.5 | 0.02 | 0.96 | 0.02 |
| 3.8 | 0.04 | 0.95 | 0.01 |

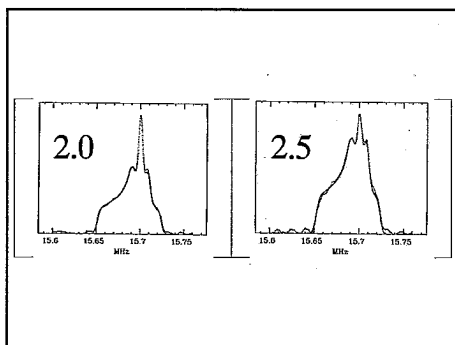


Figure 5(b):

^{11}B NASP NMR spectra of Cs borate glasses.

R_{Batch} values are shown with the spectra.

At very high alkali concentrations ($R_{\text{Batch}} > 2$) the results obtained show a very large fraction of asymmetric trigonal borate units present in the glass. On the basis of composition these would presumably be in the form of f_4 groups, although the presence of f_3 units can not be ruled out. These results, taken on their own, imply that the glass is undermodified even after taking the loss of alkali in the fusion of the glass into account.

Both Raman and NMR measurements confirm that in the Rb and Cs borate glasses with $R \geq 3$, the presence of trigonal orthoborate units is negligible. Thus, the structure of these glasses differs greatly from that of the analogous Li and Na borates. Both structural techniques indicate that at these high modification levels the structure is dominated by asymmetric borate units (of C_{2v} symmetry), with two non-bridging oxygens per boron. A series of further experiments including NMR, X-ray, crystallization, thermal measurements, and neutron diffraction, are expected to clarify the nature of this unit.

IV. Acknowledgements

This work was supported by the NSF under grants DMR 90-03151 and DMR 93-01247 (Coe College) and DMR 89-20532 (Brown University). The National Hellenic Research Foundation is thanked for hosting S. Feller in the fall of 1990. Coe College is thanked for providing housing for summer research students, and Brown University for hosting S. Nijhawan in the summer of 1992.

References

1. E. I. Kamitsos, G. Chryssikos, A. Patsis, S. A. Feller, K. Farooqui, *Unpublished data*.
2. S. A. Feller, K. Farooqui, P. Pandikuthira, S. Nijhawan, K. Budhwani, Paper 47-G-91F presented at the Electronics, Glass, and Optical Materials Meeting of the American Ceramic Society, Arlington, VA, October, 1991.
3. M. Royle, M. Sharma, S. Feller, J. MacKenzie, S. Nijhawan, *Phys. Chem. Glasses* 34 (4)(1993) 149
4. S. Koritala, K. Farooqui, M. Affatigato, S. Feller, S. Kambeyanda, S. Ghosh, E. I. Kamitsos, G. D. Chryssikos, A. P. Patsis, *J. Non-Cryst. Solids*, 134 (1991) 277.
5. E.J. Khaw, Independent study paper, Coe College, 1989
6. O.V. Mazurin, M.V. Streltsina, T.P. Shvaiko-Shvaikovskaya, Handbook of Glass Data, Part B: Single Component and Binary Non-Silicate Oxide Glasses. Elsevier, Amsterdam, 1985.
7. P.C. Taylor and P.J. Bray, *J. Mag. Res.* 2 (1970) 305
8. M. Shibata, C. Sanchez, H. Patel, S. Feller, J. Stark, G. Sumcad and J. Kasper, *J. Non-Cryst Solids* 85 (1986) 29
9. A. Karki, S. Feller, H.P. Lim, J. Stark, C. Sanchez and M. Shibata, *J. Non-Cryst. Solids* 92 (1987) 11
10. H.P. Lim, A. Karki, S. Feller, J. Kasper and G. Sumcad, *J. Non-Cryst. Solids* 91 (1987) 324
11. K. Takahashi, O. Osaka, R. Furuma, *J. Non-Cryst. Solids*, 55 (1983) 15
12. P.J. Bray, J.G. O'Keefe, *Phys. Chem. Glasses*, 4(2)(1963) 37
13. J. Zhong, P.J. Bray, *J. Non-Cryst. Solids*, 111 (1989) 67
14. E. I. Kamitsos, M. Karakassides, G.D. Chryssikos, *Phys. Chem. Glasses*, 28(5) (1987) 203
15. G.D. Chryssikos, E.I. Kamitsos, M.A. Karakassides, *Phys. Chem. Glasses*, 31(3) (1990) 109 and 30 (6) (1989) 229.
16. J.E. Huheey, Inorganic chemistry. 1978. Harper, New York
17. F.A. Cotton, G. Wilkinson, Advanced inorganic chemistry. 1988. Wiley & Sons, New York.
18. R. L. Mozzi and B. E. Warren, *J. Appl. Crystallogr.* 3 (1970) 251.
19. R.D. Shannon, Acta Crystallogr. A, 32 (1976) 751
20. W.H. Zachariasen, Acta Crystallogr. 17(6) (1963) 749
21. M. Affatigato, S. Feller, E.J. Khaw, D. Feil, B. Teoh, O. Mathews, *Phys. Chem. Glasses* 31 (1) (1990) 19
22. J.E. Shelby, *J. Am. Ceram. Soc.* 66 (1982) 225
23. D.P. Button, R. Tandon, C. King, M.H. Velez, H.L. Tuller, D.R. Uhlmann, *J. Non-Cryst. Solids* 49 (1982) 129
24. S.W. Martin, C.A. Angell, *J. Non-Cryst. Solids* 66 (1984) 429
25. B.C.L. Chong, S.H. Choo, S. Feller, B. Teoh, O. Mathews, E.J. Khaw, D. Feil, K.H. Chong, M. Affatigato, D. Bain, K. Hazen, K. Farooqui, *J. Non-Cryst. Solids* 109 (1989) 105
26. G. D. Chryssikos, E. I. Kamitsos, A. P. Patsis, M. A. Karakassides, *Matr. Sci. Eng. B7* (1990) 1.
27. Y. H. Yun and P. J. Bray, *J. Non-Cryst. Solids* 27 (1978) 363.

PHYSICAL PROPERTIES OF ALKALI BOROSILICATE GLASSES RELATED TO ATOMIC ARRANGEMENTS

S. FELLER, R. BOEKENHAUER, H. ZHANG, D. BAIN, D. FEIL, C. PARAMESWAR, K. BUDHWANI, S. GHOSH, S. NIJHAWAN, J. MACKENZIE

Physics Department, Coe College, Cedar Rapids, IA 52402, USA

The densities and glass transition temperatures of a large number of glasses in the lithium, sodium, and potassium borosilicate systems are reported. Comparisons are made between the trends known from the binary borates and silicates and those derived from these measurements of the borosilicates. Models are presented which link atomic arrangement (based upon spectroscopy) and these physical properties.

I. Introduction

The alkali borosilicates represent a technologically important family of glasses with well researched structures (1, 2, 3, 4, 5) and properties (6, 7, 8). Consequent qualitative relationships between property and structure have been found for these glasses, but quantitative relations between the structure and properties are difficult to obtain due to the complexity of the structural information and the fact that the models for atomic arrangement are often reported as functions of ratios of the constituents, R (molar ratio of alkali oxide to boron oxide) and K (molar ratio of silica to boron oxide), whereas most of the available physical property data is expressed in terms of weight or molar percentage families. This makes it difficult to make comparisons between structural models and experimental data.

It is the purpose of this paper to report density and glass transition temperature (T_g) measurements as functions of R for fixed K families in the lithium, sodium, and potassium borosilicate systems, and to compare this information with structural models based on spectroscopic studies of these glasses. These measurements were taken on samples of very widely varying alkali concentrations going beyond, in many cases, regions where data have been previously reported. This work is intended to be complementary to and make use of

data already reported from binary borate and silicate systems (9, 10, 11, 12, 13, 14, 15, 16).

II. Experimental Procedures

A large number of glasses were prepared in the lithium, sodium, and potassium borosilicate systems for the fixed K families of 0, 0.5, 1, 1.5, 2, 3, 4, and 6 with R varying from 0 through 10. Appropriate amounts of alkali carbonate, boric acid, and silica or alkali oxide, boron oxide, and silica were placed in platinum crucibles, mixed, and heated at temperatures ranging from 1000 to 1600 °C in Thermolyne electric furnaces. The samples were heated for periods of 15 to 30 minutes, with weight loss measurements taken to verify sample composition and to detect possible carbon dioxide retention (17).

Samples were cooled by one of the following techniques: roller-quenching (cooling rate of 10^5 K/s), plate-quenching (cooling rate of 10^3 to 10^4 K/s), or by slow-cooling within the crucible (cooling rate less than 10^2 K/s). Only very small changes were found in density (< 0.01 g/cm³) or T_g (< 5 K) due to cooling rate effects. Since a great many of these samples exhibit hygroscopicity, care was taken to prepare samples and measure their properties in controlled atmospheres of dry air or dry nitrogen.

Density was measured using a

modified sink-float technique with a combination of acetone and diiodomethane as the Archimedes' fluids. This technique was especially suitable for roller-quenched glass flakes of just a few milligrams in mass. Density was also measured with a micropycnometer (Quantachrome model MPY-2) using dry helium as the Archimedes' fluid. The estimated absolute error in density for either technique is a conservative $\pm 0.02 \text{ g/cm}^3$.

The glass transition temperature was determined using a Perkin-Elmer DSC-II employing software furnished by Laboratory Microsystems (Troy, NY). The heating rate was 40 K/min and the onset definition for T_g was used. Two or three samples at each composition were run and the absolute error in the reported T_g is approximately $\pm 5 \text{ K}$.

Samples were prepared from oxide starting materials in order to check if the physical properties were sensitive to starting materials and the effect of CO_2 retention. In these families of glasses both density and T_g were unaffected within experimental limitations.

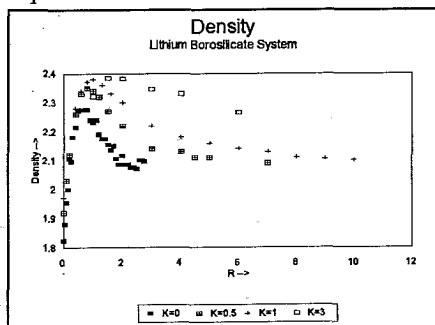


Figure 1

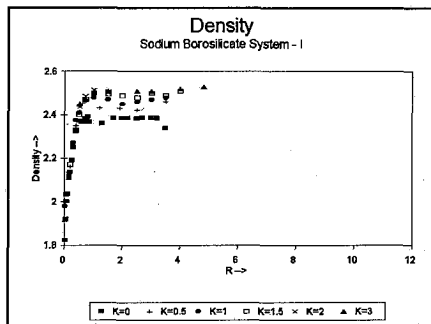


Figure 2

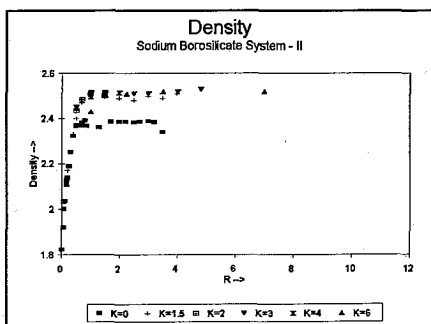


Figure 3

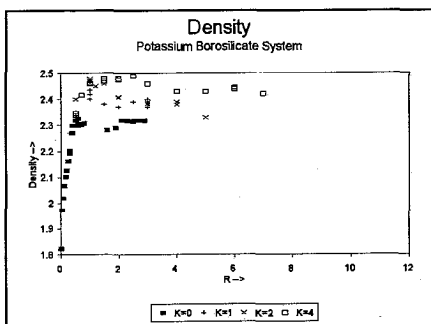


Figure 4

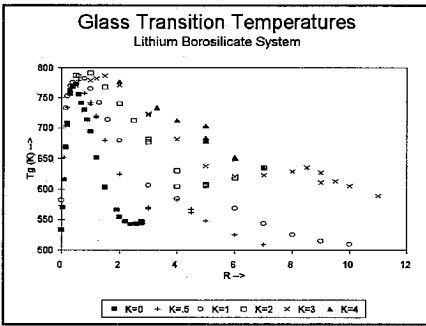


Figure 5

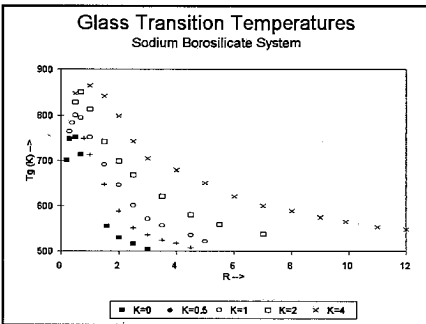


Figure 6

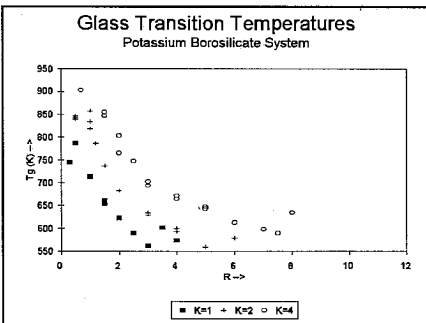


Figure 7

III. Results and Discussion

Figures 1 through 7 present the density and T_g data for the lithium,

sodium, and potassium borosilicate families. One of the most predominant trends in density is that the addition of silica generally increases the density of these glasses, on occasion beyond that of either the alkali borates or alkali silicates. It is hypothesized that this is due to structural changes occurring in the alkali borosilicates(18). In particular, it has been observed that borosilicate glasses with higher densities than the corresponding borate or silicate glasses also have a higher fraction of four-coordinated borons (f_2) than the binary systems. It is possible to formulate a quantitative model for these densities, based on several key assumptions. First, fractions of the borate structural units (and by extension the silicate units) are based on the Dell structural model(4). Second, it is hypothesized that the only short-range structural arrangements present in these alkali borosilicates are those already known to exist in the binary borates and silicates. Finally, volumes of the borate and silicate units are the same as those derived from the alkali borate and silicate density data (this implies that the same amount of empty space per unit is present in the borosilicate case as in the binary cases).

The density can then be expressed as:

$$\rho_{Glass} = \frac{Mass_{Borate} + Mass_{Silicate}}{Vol_{Borate} + Vol_{Silicate}}$$

where $Mass_{Borate}$ and Vol_{Borate} , and $Mass_{Silicate}$ and $Vol_{Silicate}$ are the masses and volumes of the borate and silicate parts of the glass, respectively. These masses and volumes can be found by multiplying the fractional abundance of each structural unit present in the glass by the corresponding volume or mass for that unit.

The Dell model defines the abundance of four structural borate units; f_1 (trigonal borate group with all bridging oxygens), f_2 (tetrahedral borate group with all bridging oxygens), f_3 (trigonal borate

group with one non-bridging oxygen per boron), and f_4 (trigonal borate group with two non-bridging oxygens per boron). The rather complicated abundances of these borate units(4,19,20) are functions of R and K and are summarized in Figure 8 for the representative $K = 3$ family.

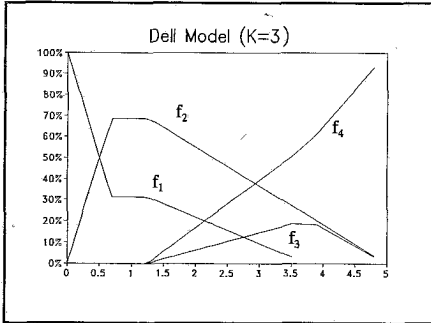


Figure 8

The silicate network in these alkali borosilicates has been studied using ^{29}Si MAS NMR(21,22,23,24) and found to have the same atomic arrangements as the binary alkali silicates. These structures are denoted by Q_i where Q is a silicon tetrahedron bonded to four oxygens and i is the number of bridging oxygens, ranging from 0 to 4. The fractions of these units were found by allocating alkali according to the Dell model and assuming a simple lever rule model for the Q_i units; a result consonant with the ^{29}Si MAS NMR data.

The volumes of the structural groups, determined from the binary densities and use of the Dell model when $K = 0$ (the borate case), and a simple lever rule in the silicate case and through use of a non-linear least squares analysis, are given in Table 1.

Table 1
Volumes of structural units (\AA^3)

| | Li | Na | K |
|-------|------|------|-------|
| f_1 | 31.1 | 30.1 | 30.1 |
| f_2 | 29.5 | 39.6 | 52.9 |
| f_3 | 40.3 | 51.4 | 65.6 |
| f_4 | 51.0 | 67.2 | 93.2 |
| Q_4 | 45.3 | 45.3 | 45.3 |
| Q_3 | 52.9 | 60.2 | 71.3 |
| Q_2 | 64.0 | 78.9 | 103.3 |

The resulting model densities are compared with several representative examples of experimental data as shown in Figures 9 through 14. It can be seen that the fit is reasonable.

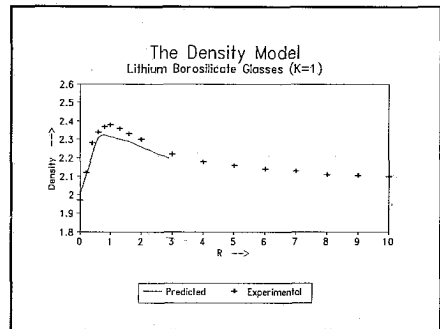


Figure 9

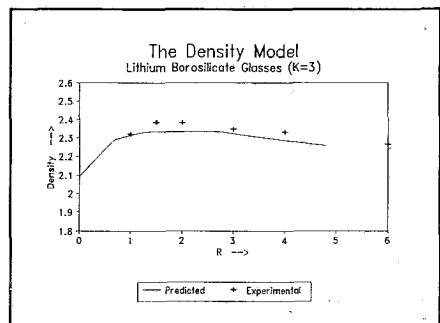


Figure 10

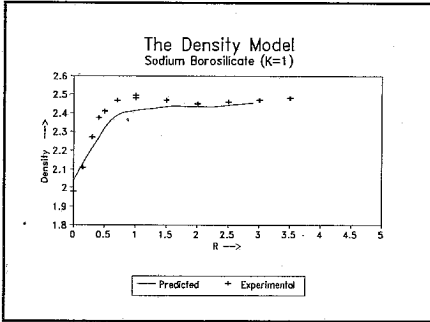


Figure 11

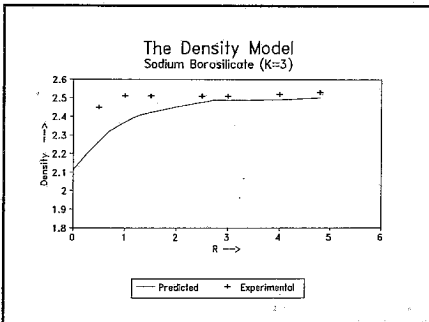


Figure 12

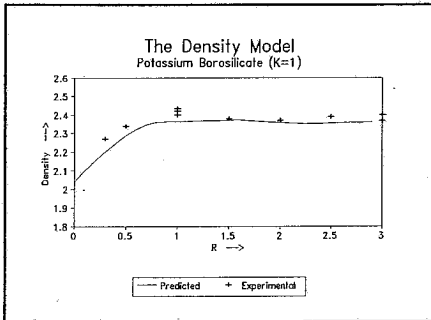


Figure 13

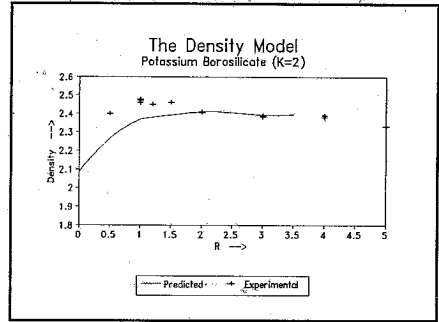


Figure 14

The glass transition temperatures are described in a more qualitative manner. In each alkali system studied the T_g initially increases with R until the range $R = 0.5$ to 1 , with the higher values associated with the higher values for K . Additional alkali results in a decrease in the T_g until the T_g 's either level out (sodium case) or enters a smaller but clearly present second maximum (lithium and potassium systems). In each family the initial rise in the T_g 's is attributed to either f_2 unit abundance(25) or with the numbers of bridging oxygens per boron(26). The decline after the first maximum is attributed to the formation of significant numbers of non-bridging oxygens. In the lithium case the slope of this decline can be modelled in terms of a simple proportional sharing of the alkali between the borate and silicate networks (furthermore, the peak T_g is nearly constant in these glasses at approximately 785 K).

Table 2
Post-first maxima slopes of
 T_g versus R for the Li-B-Si system.

| K | Experimental Slope ($^{\circ}\text{C}/\text{R}$) | Binary (K=0) slope modified by proportional sharing of the alkali ($^{\circ}\text{C}/\text{R}$) |
|-----|--|---|
| 0 | -173 | -173 |
| 0.5 | -113 | -115 |
| 1 | -80 | -87 |
| 2 | -57 | -58 |
| 3 | -43 | -43 |
| 4 | -31 | -35 |

Table 2 compares the experimental slopes of these declining T_g s in the lithium case with the slope of the binary lithium borates modified by proportional sharing. The agreement is excellent, however, this simple model is not very useful in describing either the sodium or potassium cases. Both of these families exhibit very similar T_g dependencies. In these glasses the maximum T_g is a strong function of K, rising several hundred $^{\circ}\text{C}$ as K increases from 0 to 4. This causes a reversal from the binary case where the lithium glasses have the largest maximum T_g , followed by sodium and potassium, respectively. Furthermore, the slopes of the declines are much more rapid than in the lithium glasses with these slopes not being predictable by a simple proportional sharing model. This would be consistent with a strong interaction between the borate and silicate networks as proposed by Dell *et al.*(4) in the formation of reedmergnerite units, $(\text{BSi}_4\text{O}_{10})^{-1}$.

In the lithium case the peak of the second maxima occurs at the orthoborate-orthosilicate composition ($R = 3 + 2K$). Above this composition significant CO_2

retention occurs, as evidenced by a decrease in the weight loss and on the basis of chemical analysis (17). Thus the ternary glass becomes a quaternary one containing CO_2 . In both the sodium and potassium systems significant retention of carbon dioxide occurs at lower R values than $3 + 2K$.

IV. Acknowledgements

This work is supported by the NSF under grants numbered DMR 90-03151 and DMR 93-01247. The National Hellenic Research Foundation (Athens, Greece) is thanked for hosting S. Feller in the fall of 1990. Coe College is thanked for providing summer tuition waivers and housing for students working on this project.

References

1. J.C. Brethous, A. Levasseur, G. Villeneuve, P. Echegut, and P. Hagenmuller, *J. Solid State Chem.* 39 (1981) 199-208.
2. X.W.Wu, F. Tian, X.Q. Zhang, L.Z. Pan, S.L. Wu, *Collected Papers, XIV Intl. Congress on Glass* (1986) Vol. 1 32-40.
3. J. Zhong, X. Wu, M.L. Liu, and P.J. Bray, *J. Non-Cryst. Solids*, 107 (1988) 81-87.
4. W.J. Dell, P.J. Bray, *J. Non-Cryst. Solids*, 58(1983) 1-16.
5. S.W. Martin, S. Feller, D. Bain, K. Budhwani, *J. Am. Ceram. Soc.*, 75 (5) (1992) 1117-1122.
6. A host of data is summarized in O.V. Mazurin, M.V. Streltsina, and T.P. Shvaiko-Shvaikovskaya, *Handbook of Glass Data: Part C*, (Elsevier:Amsterdam) 1987.
7. H. Zhang, R. Boekenhauer, S. Feller, D. Bain, S. Kambeyanda, K. Budhwani, P. Pandikuthira, F. Alangir, A.M. Peters, S. Messer, and K. Loh, submitted to *J. Non-Cryst. Solids*.
8. V.V. Akimov, *Fizika i Khimiya Stekla* 17(4) (1991) 640.
9. M. Shibata, C. Sanchez, H. Patel, S. Feller, J. Stark, G. Sumcad, and J. Kasper, *J. Non-Cryst.*

- Solids, 85 (1986) 29.
10. A. Karki, S. Feller, H.P. Lim, J. Stark, C. Sanchez, and M. Shibata, *J. Non Cryst. Solids*, 92 (1987) 11.
11. H.P. Lim, A. Karki, S. Feller, J. Kasper, and G. Sumcad, *J. Non-Cryst. Solids* 91 (1987) 324.
12. B.C.L. Chong, S.H. Choo, S. Feller, B. Teoh, O. Mathews, E.J. Khaw, D. Feil, K.H. Chong, M. Affatigato, D. Bain, K. Hazen, and K. Farooqui, *J. Non-Cryst. Solids*, 109 (1989) 105-111.
13. M. Royle, M. Sharma, S. Feller, J. MacKenzie, S. Nijhawan, *Phys. Chem. Glasses*, 34(4) (1993).
14. A.M. Peters, F.M. Alamgir, S.W. Messer, S.A. Feller, K.L. Loh, submitted to *Phys. Chem. Glasses* (1993)
15. M. Affatigato, S. Feller, E.J. Khaw, D. Feil, B. Teoh, and O. Mathews, *Phys. Chem. Glasses* 31(1) (1990) 19-24.
16. S. Koritala, K. Farooqui, M. Affatigato, S. Feller, S. Kambeyanda, S. Ghosh, E.I. Kamitsos, G.D. Chryssikos, and A.P. Patsis, *J. Non-Cryst. Solids*, 134 (1991) 277-286.
17. H. Zhang, S. Koritala, K. Farooqui, R. Boekenhauer, D. Bain, S. Kambeyanda, and S. Feller, *Phys. Chem. Glasses* 32(5) (1991) 185-188.
18. J. Zhong, X. Wu, M.L. Liu, and P.J. Bray, *J. Non-Cryst. Solids*, 107 (1988) 81
19. D. Feil, Honor's Paper, Coe College (1989)
20. K. Budhwani, Honor's Paper, Coe College (1993)
21. S.W. Martin, D. Bain, K. Budhwani, S. Feller, *J. Am. Ceram. Society* 75(5) 1992 1117
22. S.W. Martin, A. Bhatnagar, C. Parameswar, S. Feller, submitted to *J. Am. Ceram. Soc.*
23. S.W. Martin, J.W. MacKenzie, A. Bhatnagar, S. Bhowmik, S. Feller, M.L. Royle, submitted to *J. Am. Ceram. Soc.*
24. J.W. MacKenzie, A. Bhatnagar, D. Bain, S. Bhowmik, C. Parameswar, K. Budhwani, S.A. Feller, M.L. Royle, submitted to *J. Non-Cryst. Solids*
25. J.E. Shelby, *J. Am. ceram. Soc.* 66 (1982) 225
26. G.D. Chryssikos, E.I. Kamitsos, M.A. Karakassides, *Phys. Chem. Glasses* 31(3) (1990) 109 and 30(6) (1989) 229

ANALYSIS OF X-RAY DIFFRACTION PATTERNS OF CRISTALLIZED AND AMORPHOUS Fe BORATE GLASSES

MARIA DO ROSARIO P. CORREIA, SUSHIL KUMAR MENDIRATTA

DEPARTAMENTO DE FÍSICA, UNIVERSIDADE DE AVEIRO, 3000 AVEIRO, PORTUGAL

ABSTRACT: The aim of this work is to analyse the change in the structure of the amorphous phase in the devitrified glasses in the systems $x\text{Fe}_2\text{O}_3$, PbO $2\text{B}_2\text{O}_3$, with the increasing amount of cristallinity. We have used the technique which permits the separation of scattering pattern due to amorphous phase, we have described before [8], and we confirm the reliability of the procedure by comparing the results obtained at two different X-ray wavelengths (1 Å at synchrotron and 1.5 Å of Cu $K\alpha$, in the normal x-ray diffractometer). Further we show that some features of the reduced radial distribution function, $G(r)$, obtained by deconvoluting the scattering patterns can be associated with the relative content of Fe ions amorphous phase.

Introduction

The determination of the structure of multicomponents glasses from the x-ray (or neutron) diffraction data is a difficult problem if one wants to know the structure beyond the immediate coordination. Even in simple glasses like B_2O_3 there are differing opinions [1] as to the unambiguous determination of the fraction and the ring number of the boroxyl rings; these rings are formed out of basic coordination unit BO_3 triangles. Some authors [2] doubt that it is possible to infer even the existence of boroxyl rings solely from the radial distribution function calculated from the diffraction data. However, it is the multicomponent glasses and glass-ceramics obtained by adding modifying metal oxides (in oxide glasses) to the base glass that yield materials with industrially useful properties. Therefore, some effort to assess the information obtained by inverting the diffraction data of multicomponent glasses may be considered worthwhile.

We have studied the transition metal (Fe, Ni, Cr) oxide and rare earth oxide (Gd, Eu, Nd) mixed in the lead borate (LB) glass in the varying concentrations to investigate the coordination and the state of aggregation of these modifier ions by analysing their magnetic and electrical properties [3,4,5]. The direct structural evidence, however, is lacking. Therefore, we present here a preliminary report of our efforts in this direction. We have calculated the reduced radial distribution function of the Fe glasses (as example) and Fe glass-ceramics in which Hematite ($\alpha\text{-Fe}_2\text{O}_3$) has been identified as the crystalline phase. We compare various $G(r)$ curves and draw some conclusions regarding the effect of crystalline phase.

Experimental:

All the glasses were prepared by normal air melting, quenching and subsequent annealing processes; the details can be found in the references of our previous work. X-ray diffraction data were taken at the SERC synchrotron source at Daresbury using 1 Å wavelength of the incident beam. For the sake of comparison we also

analysed the data diffraction for the same sample taken with the $\text{CuK}\alpha$ (1.5\AA) radiation in a commercial diffractometer (Rigaku-Denki).

The following glasses were studied:

(LB) $\equiv \text{PbO } 2\text{B}_2\text{O}_3$; $0.4\text{Fe}_2\text{O}_3$ (LB); $0.5\text{Fe}_2\text{O}_3$ (LB); $0.6\text{Fe}_2\text{O}_3$ (LB)

The concentration of the modifier ion in the composition is in mole fraction units. 0.5Fe and 0.6Fe glasses contain Hematite and we separated the contribution of the crystalline part from the total scattering using the method described before [6]. As an example we show (Fig.1) the diffraction pattern (corrected for the primary beam intensity) of 0.4Fe glass obtained at the Daresbury facility, and the obtained at Department of Ceramics at University of Aveiro (DCVUA). Compton scattering correction was made on the Daresbury data using the published scattering data of atoms [9]. There was no necessity of any correction on DCVUA data, because the system has a monochromator on the scattering beam.

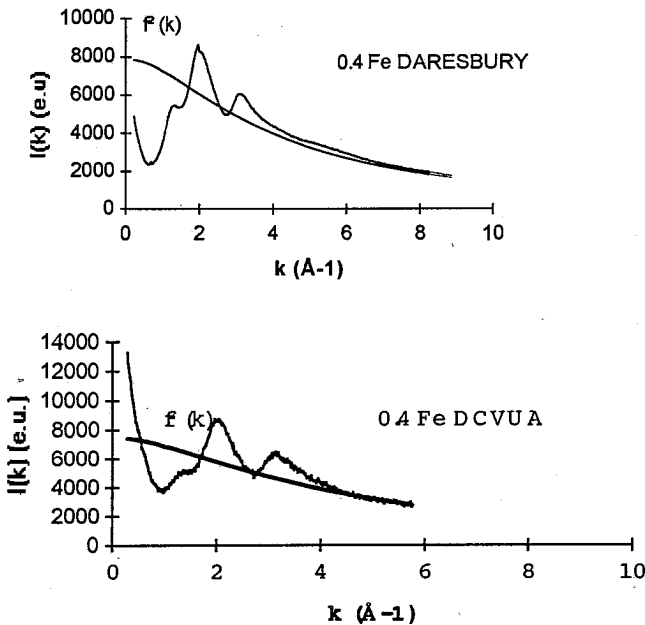


(Fig 1)

From the amorphous part of each sample we obtained the reduced radial distribution function defined as [7],

$$G(r) = \frac{2}{\pi} \int_0^{k_{\max}} F(k) \sin kr \, dk = \frac{2}{\pi} \int_0^{\infty} F(k) M(k) \sin kr \, dk$$

where

$$F(k) = k \left[\frac{I_m / N - \langle f^2 \rangle}{\langle f \rangle^2} \right], \quad \langle f^2 \rangle = \sum_{i=1}^n x_i f_i^2, \quad \langle f \rangle = \sum_{i=1}^n x_i f_i$$

$$M(k) = \frac{k_{\max}}{\pi k} \sin \left(\frac{\pi k}{k_{\max}} \right)$$

$M(k)$ is the damping factor to eliminate the spurious peaks in RDF due to finite value of k_{\max} .

The f-factors were obtained from International Tables of X-ray Crystallography [10]

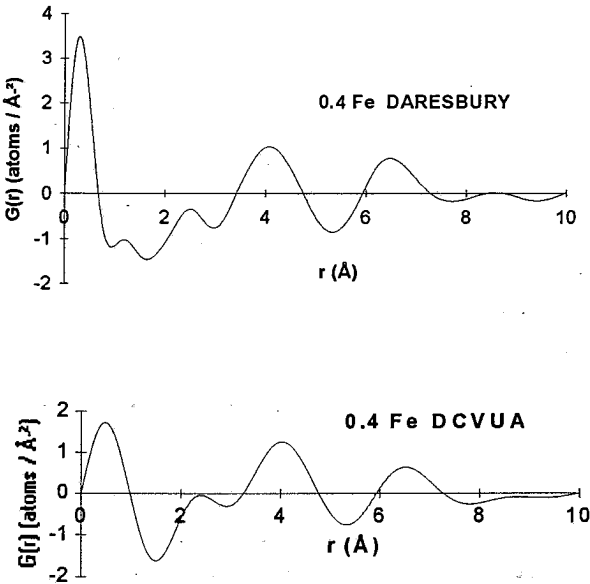


(fig 2)

We show in Fig 2, the $G(r)$ for two data of the Fig 1, despite the differences in the relative intensities, it is seen easily that the peak positions are the same for both the data. The peak position for all the data is collectively shown in Tables I and II. We see that peak positions, and specially the changes in a given peak with composition, is the same in both the data.

Table I: Peak position for data taken at Daresbury

| PbO 2B ₂ O ₃ r (Å) | 0.4 Fe ₂ O ₃ (LB) r (Å) | 0.5 Fe ₂ O ₃ (LB) r (Å) | 0.6 Fe ₂ O ₃ (LB) r (Å) |
|---|--|--|--|
| 0.31 | 0.30 | 0.29 | 0.29 |
| 1.22 | 1.18 | 1.19 | 1.13 |
| 2.57 | 2.50 | 2.55 | 2.53 |
| 4.24 | 4.07 | 4.07 | 4.07 |

Table II: Peak position for data taken at DCVUA

| PbO 2B ₂ O ₃ r (Å) | 0.4 Fe ₂ O ₃ (LB) r (Å) | 0.5 Fe ₂ O ₃ (LB) r (Å) | 0.6 Fe ₂ O ₃ (LB) r (Å) |
|---|--|--|--|
| 0.56 | 0.30 | 0.29 | 0.29 |
| ----- | ----- | ----- | ----- |
| 2.55 | 2.40 | 2.55 | 2.55 |
| 4.28 | 4.03 | 3.99 | 3.99 |

Discussion:

A consistent interpretation of the results can be proposed if we make a reasonable assumption that the strongest and dominant peaks are those involving ions with large scattering power (or large electron density). Thus, for example the first most important peak in the RDF of the base glass PbO 2B₂O₃ would be from the pair Pb-O. And the amorphous medium containing Fe ions, the Fe-O peak should be the most prominent, followed by Fe-O-Fe. The latter proposition is based upon the observation that the magnetic properties [3,4,5] indicate that at such high concentration of Fe ions, almost all the Fe ions are connected to each other through a oxygen atom. The Pb-O-Fe connections when exist are fewer in number and only on the boundary of the Fe rich regions.

We identify 2.55 peak with Pb-O pair, 4.24 peak with Pb-O-Pb group and 4.07 with Fe-O-Fe group. Regarding the peak due to Fe-O pair, we note that it should be quite near 2.50 because the *d* spacing corresponding to the highest relative intensity peak in the crystalline pattern of the devitrified glasses (0.5 Fe and 0.6 Fe) is precisely at 2.50 Å. Following this line of argument, Fe-O-Fe peak should remain unchanged in

the Fe containing glasses, because the amorphous parts containing Fe are rich in Fe and contain very few Pb atoms. This amounts to saying that in glasses with such high concentration of Fe ion (Fe to Pb ratio varies from 0.8 to 1.2) there is a phase separation in Fe and Pb rich regions and the crystallization of Hematite occurs from within such Fe rich regions.

According to this picture the Pb-O-Pb (4.24 Å) groups are deep within the Pb rich regions and maintain their approximate structure.

Since Pb-O and Fe-O pairs are almost at the same distance and Pb-O contribution is larger due to larger scattering power of Pb, we can think that Fe-O contribution in $\text{PbO } 2\text{B}_2\text{O}_3 \cdot 0.4 \text{Fe}_2\text{O}_3$ glass is in modifying (on the average) the Pb-O peak. It should be observed that as crystallization takes place Fe ions in the amorphous part are reduced so much so that, in 0.6 Fe sample we should not expect Fe ions to influence Pb-O distances.

Conclusions:

The RDF analysis of the amorphous part in series of $\text{PbO } 2\text{B}_2\text{O}_3 \cdot x \text{Fe}_2\text{O}_3$ is consistent with the structural model suggested by magnetic properties measurements: the glasses contain regions rich in Fe and others where it is absent. The crystallization takes place within the Fe rich regions precipitating, mainly, Hematite.

Acknowledgements: We are grateful to Dr. Graham Bushnell-Wye at Daresbury for help in the experiments as well as for useful comment on Compton scattering corrections, we also thank José Carlos Azevedo for help in data analysis.

References

1. P.A.V. Johnson *et al*, *Journal of Noncrystalline Solids*, **50**, 281, (311)
2. F.M. Dunlweary and A.R. Cooper, "The structure of Noncrystalline Solids", Ed. P.J. Gaskell, Taylor and Francis, London
3. S.K. Mendiratta, XVI International Glass Congress, Madrid, 1992
4. S.K. Mendiratta *et al*, *J. of Noncrystalline Solids*, **134**, 100, (1991)
5. S.K. Mendiratta *et al*, *J. of Materials Science Letters*, **9**, 301, (1990)
6. S.K. Mendiratta *et al*, VII Congresso Nacional de Física, 1992, Vila Real, Portugal
7. S.R. Elliot, "Physics of Amorphous Materials", Longmans, London
8. HASYLAB, Annual Report, 1991
9. Hubbel, J.H *et al*, " Atomic Form Factors, Incoherent Scattering Functions, and Photon Scattering Cross Section", *J. Phys. Chem.ref. data*, Vol 4, No.3,(1975), pp.471-838
10. International Tables for x-ray Crystallography, vol IV, International Union of Crystallography, Kynochpress, 1974

INFLUENCE OF ALKALINE EARTH ON DYNAMIC RESPONSE IN
SILICATE GLASSES BY
IR REFLECTIVITY AND BRILLOUIN SCATTERING

Yann Vaills, Yves Luspain, Georges Hauret, Tiana Parot-Rajaona

Centre de Recherches sur la Physique des Hautes Températures
Centre National de la Recherche Scientifique,
45071 Orléans, France

We present infrared reflectivity results and elastic constants measurements obtained by Brillouin scattering in sodium magnesium silica and sodium calcium silica glasses. Values and variations of elastic constants with cationic Mg^{2+} and Ca^{2+} percentage are discussed in terms of middle range order. Both infrared spectra and their analysis in terms of dielectric response show very similar behaviours for calcium and magnesium in soda-silicate glasses.

INTRODUCTION

In alkaline silicate glasses calcium and magnesium are well known to be modifiers, and on another hand, several works, as those of Gaskell [1] and Farnan [2], have shown that they could, nevertheless, generate order in such glasses. Moreover, magnesium may have a different behaviour than that of calcium in alumino-silicate glasses for example [3]. So it was interesting to compare silicate glasses containing calcium and magnesium in a multispectroscopic analysis.

GLASS PREPARATION AND COMPOSITION

Glasses were prepared from mixtures of reagent-grade $CaCO_3$ or $Mg(OH)_2$, Na_2SO_4 and SiO_2 ; the batches were melted under an ambient atmosphere in a covered electrically heated Pt-Rh crucible at 1600°C for two to three hours; optically homogeneous and bubble-free slabs were cast on a cold stainless steel plate, annealed for three hours at T_g and cooled down to room temperature. There was no sign of phase separation in any of the studied glasses.

Measurements have been performed in four series of silicate glasses with the cationic percentage of silicon kept constant for each series : $0.67SiO_2-xMO-0.5(0.33-x)Na_2O$ (M=Ca, Mg) labelled respectively SCN67 and SMN67, and $0.55SiO_2-xMO-0.5(0.45-x)Na_2O$ (M=Ca, Mg) labelled respectively SCN55 and SMN55. The silicon percentage have been chosen to be compatible with the existence of the corresponding binary glass ($x = 0$).

BRILLOUIN SCATTERING RESULTS

The Brillouin spectrometer is a pressure-scanned triple-pass-plane Fabry-Perot interferometer (effective finesse 70, resolving power 760000) which is frequency-controlled by a Michelson interferometer in tandem. The light source is a single frequency Ar-ion laser emitting at $\lambda_0 = 514.5$ nm. Right angle scattering configuration has been used. In this geometry, the shifts of frequency with respect to the laser line are related to the velocities of acoustic waves by:

$$\text{longitudinal waves} \quad v_L = n \cdot V_L \sqrt{2} / \lambda_0$$

$$\text{transverse waves} \quad v_T = n \cdot V_T \sqrt{2} / \lambda_0$$

n is the refractive index at wavelength λ_0 , V_L and V_T are the acoustic wave velocities which are related to the elastic constants C_{11} and C_{44} by : $V_L = (C_{11}/\rho)^{1/2}$ and $V_T = (C_{44}/\rho)^{1/2}$, ρ is the density. The refractive indices have been measured at λ_0 . The densities of the samples have been measured by the buoyancy method. These values are reported in table 1, where an overall accuracy of 0.5% is estimated.

| SCN67 | | | SCN55 | | |
|---------------|--------|-------|---------------|--------|-------|
| $10^2 \times$ | ρ | n | $10^2 \times$ | ρ | n |
| 0 | 2.500 | 1.506 | 0 | 2.480 | 1.505 |
| 3 | 2.515 | 1.510 | 4 | 2.510 | 1.516 |
| 7 | 2.545 | 1.519 | 9 | 2.570 | 1.529 |
| 14 | 2.550 | 1.530 | 15 | 2.610 | 1.544 |
| 18.5 | 2.580 | 1.539 | 23 | 2.680 | 1.566 |
| 21 | 2.595 | 1.544 | 27 | 2.710 | 1.576 |
| | | | 33 | 2.760 | 1.592 |

| SMN55 | | | SMN67 | | |
|---------------|--------|--------|---------------|--------|--------|
| $10^2 \times$ | ρ | n | $10^2 \times$ | ρ | n |
| 0 | 2.466 | 1.5060 | 0 | 2.392 | 1.4930 |
| 4.5 | 2.470 | 1.5080 | 4 | 2.395 | 1.4950 |
| 9.5 | 2.479 | 1.5115 | 7.5 | 2.398 | 1.4970 |
| 13.5 | 2.488 | 1.5155 | 12 | 2.402 | 1.5000 |
| 17.5 | 2.502 | 1.5210 | 15.3 | 2.410 | 1.5040 |
| 24.5 | 2.535 | 1.5320 | 20 | 2.432 | 1.5100 |
| 31 | 2.574 | 1.5420 | | | |

Table 1. Densities ρ in $g.cm^{-3}$ and refractive indices n at λ_0 of the four series of studied glasses SCN67, SMN67, SCN55 and SMN55.

The elastic constants of all our glasses are reported on figures 1 and

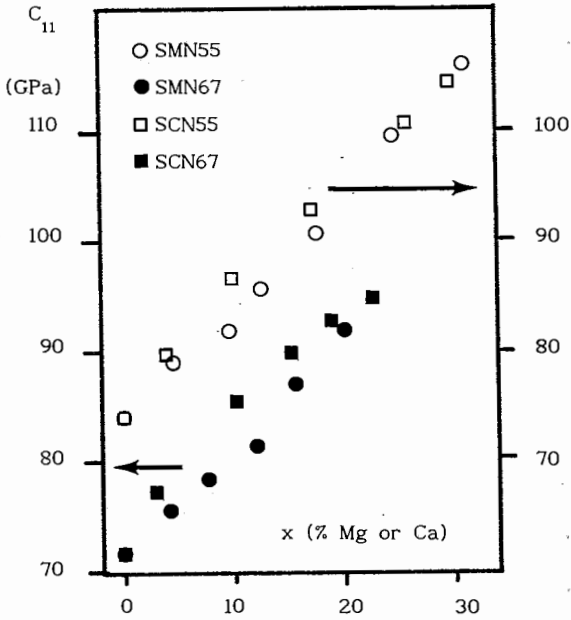
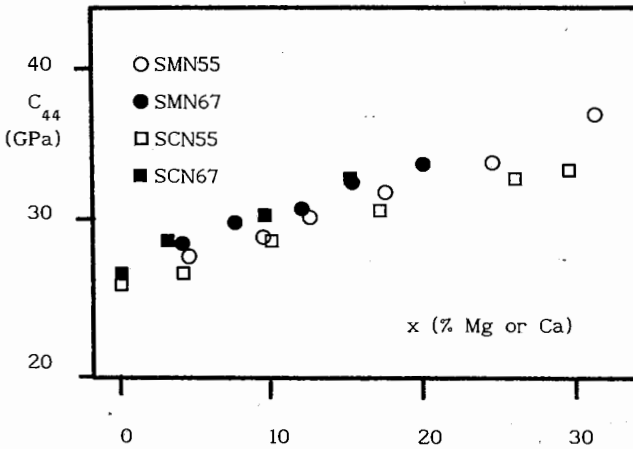


figure 1

Elastic constants measured by Brillouin scattering

figure 2



2. We can note that : starting from the binary glasses $\text{SiO}_2\text{-Na}_2\text{O}$ ($x=0$), the elastic constants are growing up with the divalent cation content. This evolution is rather similar for both calcium and magnesium glasses. In the binary glasses the compressive constant C_{11} is lower than in pure silica ($C_{11} = 80$ GPa, [4]). The introduction of more than around 10% of divalent cation gives glasses in which C_{11} is greater than in pure silica. This result is paradoxical if we compare it with the well known modifier role played by calcium and magnesium in alkaline-silicate glasses. In a recent paper [4] we have shown that our results are consistent with the Gaskell supposition of high ordered CaO_6 octahedra in $(\text{CaO})_{48}(\text{SiO}_2)_{49}(\text{Al}_2\text{O}_3)_3$ glass [1], and with the Farnan hypothesis of a high degree of ordering of network-modifying cations Mg and K around non-bridging oxygens in $(\text{SiO}_2)_{80}(\text{MgO})_{10}(\text{K}_2\text{O})_{10}$ glass [2].

INFRARED REFLECTIVITY

All spectra were recorded with a Bruker IFS 113 Fourier transform infrared spectrometer, in the wavenumber range 20 to 4000 cm^{-1} . The responses of TO and LO modes were deduced from the spectra by fit of a dielectric function model of the form (1) to reflectivity data as detailed in ref. [5].

$$\frac{\epsilon(\omega)}{\epsilon_\infty} = \prod_j \frac{\Omega_{j\text{LO}}^2 - \omega^2 + i\gamma_{j\text{LO}}\omega}{\Omega_{j\text{TO}}^2 - \omega^2 + i\gamma_{j\text{TO}}\omega} \quad (1)$$

We emphasize here two particular interesting points concerning Ca and Mg :

a) Calcium vibrates at 245 cm^{-1} and magnesium at 340 cm^{-1} . The ratio of frequencies is 1.39, which is close from square root of ratio of masses of these two cations : 1.28. This means that the force constants of both oscillators, which reflect the short-range chemical bonding, are very similar.

b) the observed triplet at high frequency (900-1200 cm^{-1}) has the same behaviour for both Ca and Mg. We note, particularly, that the middle-band frequency depends only on content of divalent ion (see figure 3).

The Coulombian field is related to the trace of the dynamical matrix that measures the splitting of polar vibrational modes into TO and LO components in the form

$$\sum_j (\Omega_{j\text{LO}}^2 - \Omega_{j\text{TO}}^2) = \frac{1}{\epsilon_v V} \sum_k \frac{(Ze)_k^2}{m_k} \quad (2)$$

The summation in the right hand side of this last equation is over all ions which occupy the elementary volume V . $(Ze)_k$ represents the average effective charge carried by ion of type k , m_k its mass, and ϵ_v is the dielectric constant of vacuum. Using the TO and LO frequencies that we have determined, combined with the electric neutrality of the sample, we are left with only two equations. The number of atoms is four in our

case. One reasonable approximation is to consider for sodium the formal valence +1. The effective charge has been found to be 2.28 and 2.42 for Z_{Si} , depending on the silicon content 55% and 67%. We found $Z_{Ca}=1.8$ and $Z_{Mg}=1.4$.

A complete discussion of our infrared reflectivity results is presented in [6].

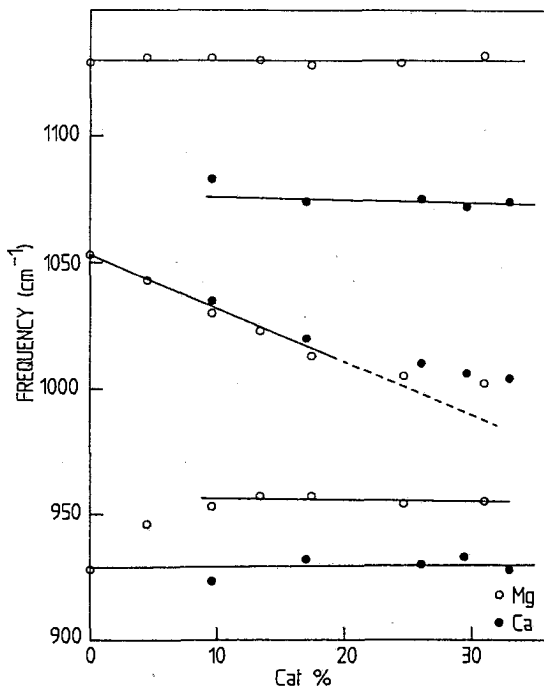


figure 3

Evolution of the band frequencies in the high frequency triplet (the line drawn are only guides for the eye)

COMPARISON OF RESULTS AND CONCLUSION

The effective charges found in this study for Ca and Mg correspond to a degree of ionicity of 0.9 for calcium and 0.7 for magnesium. This result can explain why Mg might have a different behaviour than that of calcium for some compositions, as it is the case in aluminium-silicate glasses. Nevertheless, in our study, we observe very similar behaviors for sodium-silicate glasses containing magnesium or calcium.

REFERENCES

1. P.H.Gaskell, M.C.Eckersley, A.C.Barnes and P.Chieux. *Nature* 350 (1991) 675.
2. I.Farnan, P.J.Grandinetti, J.H.Baltisberger, J.F.Stebbins, U.Werner, M.A.Eastman and A.Pines. *Nature* 358 (1992) 31.
3. C.J.Merzbacher and W.B.White. *J Non-Cryst. Solids* 130 (1991) 18.
4. Y.Vaills, Y.Luspin, G.Hauret and B.Coté *Sol.Stat.Comm.* 87,12 (1993) 1097
5. F.Gervais, A.Blin, D.Massiot, J.P.Coutures, M.H.Chopinnet and F.Naudin *J. Non-Cryst. Solids* 89 (1987) 384
6. G.Hauret, Y.Vaills, Y.Luspin, F.Gervais and B.Coté *J. Non-Cryst. Solids* in press (1994).

RAMAN AND FAR-INFRARED STUDY OF ALUMINUM AND BORON SUBSTITUTED SODIUM TRISILICATE GLASS

E. I. Kamitsos and J. A. Kapoutsis

Theoretical and Physical Chemistry Institute,
National Hellenic Research Foundation,
48 Vas. Constantinou Ave.,
116 35 Athens, Greece

H. Jain and C. H. Hsieh

Department of Materials Science and Engineering,
Lehigh University, Bethlehem, PA 18015, USA

The structure of glasses in the system $\text{Na}_2\text{O}\cdot x\text{R}_2\text{O}_3\cdot(3-2x)\text{SiO}_2$ ($\text{R}=\text{Al}, \text{B}$) has been studied by employing Raman spectroscopy. The purpose of this work is to elucidate the role of aluminum and boron substitution on glass structure and properties while keeping the $\text{Na}/(\text{Si}+\text{R})$ ratio fixed. Aluminum was found to enter the silicate network and occupy Q^3 sites, causing the equilibrium $2\text{Q}^3 \rightleftharpoons \text{Q}^4 + \text{Q}^2$ to shift to the left. The role of boron was found to be opposite, since it induces the destruction of Q^3 species in favour of the highly charged Q^1 and Q^2 species and the fully polymerized Q^4 silicate units.

INTRODUCTION

The influence of boron and aluminum substitution for silicon on the properties of silicate glasses is well known (1, 2). Of particular interest is the behaviour of ionic conductivity, which increases when Al_2O_3 substitutes for SiO_2 , but decreases when B_2O_3 is added to the silicate glass (3-5). Aluminum and boron have, therefore, the opposite effect on ionic conductivity, regardless of the fact that both trivalent ions are thought to behave as network formers in silicate glasses (3-6).

To elucidate the origin of such different effects of Al and B we have undertaken a Raman study of sodium-aluminosilicate (SAS) and sodium-borosilicate (SBS) glasses of the general formula $\text{Na}_2\text{O}\cdot x\text{R}_2\text{O}_3\cdot(3-2x)\text{SiO}_2$ ($\text{R}=\text{Al}, \text{B}$). This compositional variation was chosen to maintain a constant network modifier (Na) to network former ($\text{Si}+\text{R}$) ratio, while SiO_2 is gradually replaced by Al_2O_3 or B_2O_3 . The far-infrared spectra were also measured to investigate the interactions between sodium ions and their sites in the glass, which are relevant to ion conduction properties. Results of this investigation are reported in this work.

EXPERIMENTAL

SAS ($x=0, 0.2, 0.4, 0.6$) and SBS ($x=0, 0.2, 0.4, 0.6, 0.8, 1.0$) glasses were prepared by melting stoichiometric mixtures of reagent grade Na_2CO_3 , H_3BO_3 , Al_2O_3 and SiO_2 and subsequent quenching into a stainless steel mold. Melting temperatures in the range 1100-1640°C were required, depending on composition. Details on glass preparation can be found elsewhere (6). SAS glasses with $x=0.8$ and 1.0 could not be prepared with sufficient homogeneity due to the high viscosity of the melt.

Raman spectra were recorded on a Ramanor HG 2S Jobin-Yvon spectrometer coupled to a PC for data acquisition and analysis. Excitation was provided by the 488.0 nm line of a Spectra Physics 165 argon ion laser (500 mW at 90° geometry). To reveal clearly the low-frequency Raman scattering ($<200 \text{ cm}^{-1}$) the temperature-reduced Raman intensity, I_{red} , was calculated by

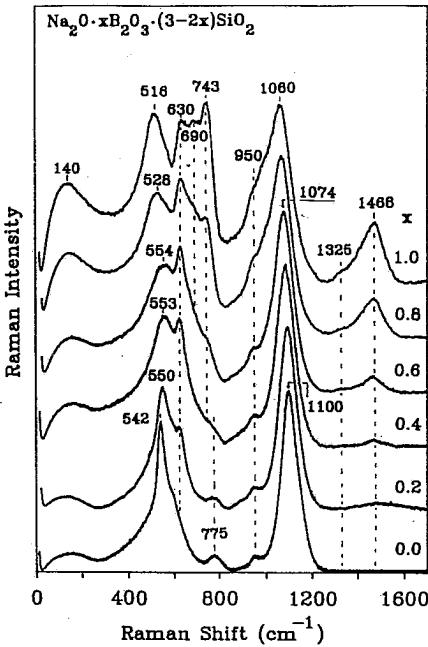


Fig. 1. Raman spectra of SBS glasses

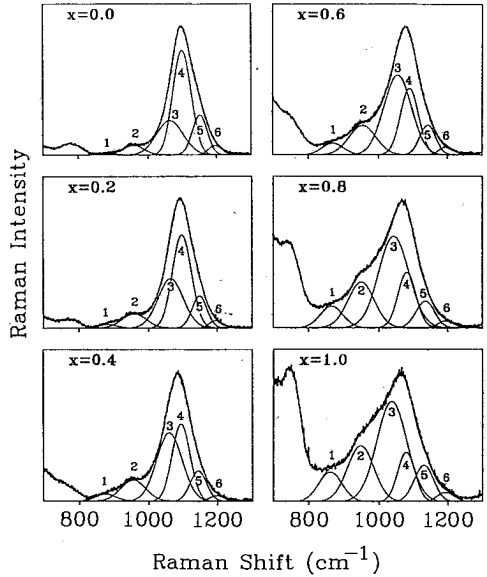


Fig. 2. Deconvolution of the 800-1200 cm⁻¹ profiles of the Raman spectra of SBS glasses.

$$I_{red} = I(\nu) / (1 + n(\nu)) \tag{1}$$

where $I(\nu)$ is the measured Raman intensity and $n(\nu)$ is the Bose-Einstein distribution factor,

$$n(\nu) = [\exp(hc\nu/k_B T) - 1]^{-1} \tag{2}$$

where ν is the Raman shift (cm⁻¹), c is the speed of light, T is the temperature and k_B and h are the Boltzmann and Planck constants, respectively.

Infrared spectra were measured in the reflectance mode (11° off-normal) on a Fourier-transform spectrometer (Bruker I13v). The reflectance data were analysed by the Kramers-Kronig transformation method to obtain the absorption coefficient spectra reported in this work.

RESULTS AND DISCUSSION

The Structure of Sodium-Borosilicate Glasses

The Raman spectra of SBS glasses are shown in Fig. 1. Replacement of Si by B induces systematic spectral variations, which imply corresponding structural changes. In the low frequency range new bands develop at 630, 690 and 743 cm⁻¹ as x increases. Bands in the region 400-700 cm⁻¹ have been attributed to a delocalized vibration of Si-O-Si bridges; this mode having a mixed stretching-bending character (7-9). The frequency of this mode increases

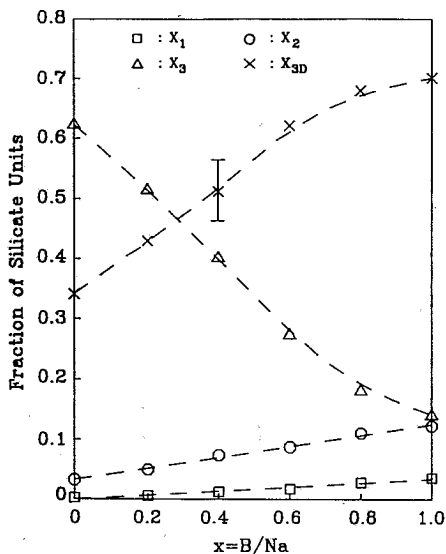


Fig. 3. Effect of boron substitution for silicon on the relative abundance of silicate tetrahedra in SBS glasses.

range (10).

Of particular interest is the effect of boron substitution on the 800-1250 cm^{-1} envelope, which appears to broaden and downshift upon increasing the boron content. Bands in this frequency range of the Raman spectra of modified silicate glasses originate from the overlapping contribution of Si-O stretching vibrations of the various coexisting Q^i silicate tetrahedra (7-9, 11-14). Thus, the spectra of Fig. 1 suggest that the relative abundance of silicate units is a function of boron content. The quantification of this effect requires the deconvolution of the 800-1250 cm^{-1} envelopes, where scattering arises from Q^i silicate units.

Deconvolution of the Raman profiles was done according to standard techniques (15) and the results are shown in Fig. 2. It was found that six bands were adequate to achieve a reasonable agreement between experimental and simulated spectra. These bands can be assigned to Q^i tetrahedra as follows: band 1 (885-862 cm^{-1}) to Q^1 , band 2 (960-948 cm^{-1}) to Q^2 and band 4 (1100-1080 cm^{-1}) to Q^3 (11). Bands 5 (1152-1135 cm^{-1}) and 6 (1197-1194 cm^{-1}) are attributed to Q^4 species, i.e. to fully polymerized silicate tetrahedra (11). Band 3 (1065-1040 cm^{-1}) originates from scattering of silicate species containing bridging oxygen atoms, like Q^4 (11) and Q^3 , Q^2 , Q^1 (14).

The relative intensities of the deconvoluted bands can be subsequently employed to estimate the abundance of silicate tetrahedra. Following Mysen et al (14) the mole fraction X_i of species Q^i ($i = 1, 2, 3$) with $4-i$ non-bridging oxygens is given by:

$$X_i = A_i \alpha_i \quad (3)$$

where A_i is the relative Raman intensity and α_i is the normalized Raman cross section of species Q^i . The values $\alpha_1 = 0.33$, $\alpha_2 = 0.5$ and $\alpha_3 = 1.0$ were used for species Q^1 , Q^2 and Q^3 ,

as the degree of silicate network depolymerization increases, i.e. upon decreasing the number of bridging oxygen atoms per silicon tetrahedron Q^i ($i =$ number of bridging oxygen atoms). Based on the results of previous Raman studies of silicate glasses we assign the band at 630 cm^{-1} to Si-O-Si bridges between Q^2 species and the one at 690 cm^{-1} to Si-O-Si bridges between Q^1 species. Thus, it appears that the presence of boron favours the formation of Q^2 and Q^1 silicate tetrahedra.

Borate centers are present mainly in the form of BO_4^- tetrahedra ($\emptyset =$ bridging oxygen atom), as well as BO_2O^- triangles. Evidence for BO_4^- tetrahedra is provided by the band at 743 cm^{-1} which develops at high B/Si ratios. Bands at similar frequencies in the spectra of alkali borate glasses have been attributed to six-membered borate rings containing BO_4^- tetrahedra (10). The asymmetric envelope developing in the region 1300-1600 cm^{-1} is indicative of the formation of BO_2O^- borate triangles, since the localized stretching vibration of their B-O bonds is active in this frequency

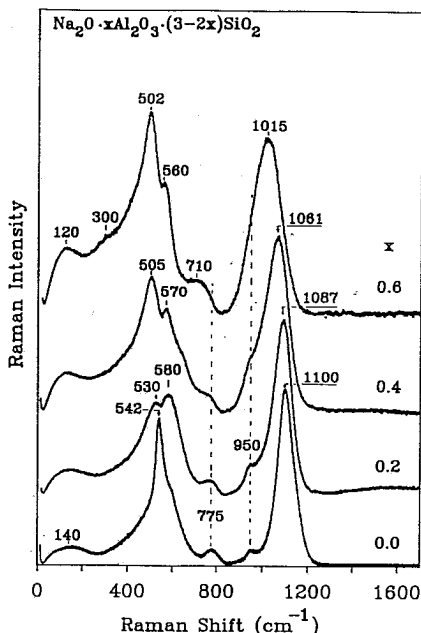


Fig. 4. Raman spectra of SAS glasses.

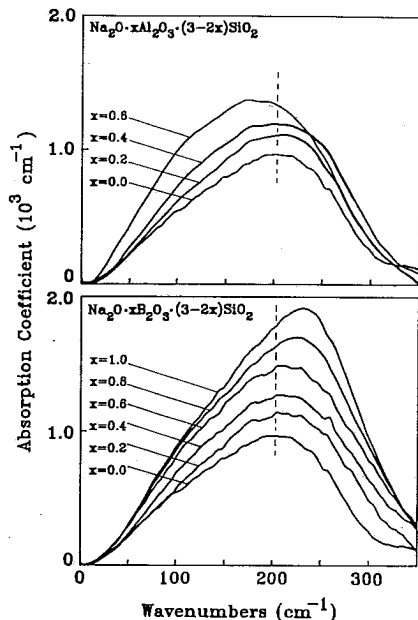


Fig. 5. Comparison of the effects of boron and aluminum substitution for silicon on the Na^+ -motion bands active in the far-infrared

respectively (14). The mole fraction of Q^4 units is determined from the difference:

$$X_{3D} = 1 - \sum_{i=1}^3 X_i \quad (4)$$

The calculated mole fractions of silicate units are shown in Fig. 3 as a function of boron content. It is noted that the results for the sodium trisilicate glass ($x=0$) agree quite well with those of previous Raman studies (14, 16), as well as those of ^{29}Si NMR measurements (17).

It is quite clear from Fig. 3 that the decrease of the relative abundance of Q^3 species with increasing boron content is accompanied by the increased abundance of Q^2 , Q^1 and Q^4 species. It is recalled at this point that additional evidence for the creation of Q^2 and Q^1 species is provided by the development of the lower frequency bands at 630 and 690 cm^{-1} respectively.

The Structure of Sodium-Aluminosilicate Glasses

The Raman spectra of SAS glasses are shown in Fig. 4. As in the case of SBS glasses, the high-frequency envelope between 800 and 1200 cm^{-1} broadens and downshifts with increasing Al content. However, the behaviour of this envelope alone is not very informative for a possible change in the relative abundance of silicate tetrahedra with Al substitution. This is because of the strong coupling of Si-O and Al-O vibrations (18) in mixed aluminosilicate arrangements, $\text{Si}(\text{OAl})_n$ ($n=1-4$), in addition to the coexisting Q^i silicate tetrahedra. Nevertheless, inspection of the lower frequency region shows the absence of bands

characteristic of Q^2 (630 cm^{-1}) and Q^1 (690 cm^{-1}) species.

The presence of mixed Si-O-Al bridges is supported by the band developing at ca 500 cm^{-1} , while the feature at 560 cm^{-1} is characteristic of Al-O-Al bridges, where Al is tetrahedrally coordinated (19). The aluminum-oxygen stretching vibration of AlO_4^- tetrahedra is responsible for the band at ca 710 cm^{-1} (20).

It appears from the above that the effect of Al is different from that of B, since neither Q^2 nor Q^1 species are created. Instead, the presence of Si-O-Al bridges suggest that AlO_4^- tetrahedra enter the silicate network and occupy Q^3 sites, i.e. sites of the same formal charge. This is in agreement with the results of XPS (6), molecular dynamics (21) and EXAFS (22) studies.

When Q^3 species are replaced by AlO_4^- tetrahedra the equilibrium,



is shifted to the left. This process implies that the negative charge becomes more uniformly distributed on the silicate network, when compared to $Na_2O \cdot 3SiO_2$ glasses.

Interactions Between Sodium Ions and Their Sites in SAS and SBS glasses

The change in the relative abundance of silicate tetrahedra in the presence of boron affects the distribution of the negative charge on the silicate network. This charge appears to be progressively accumulated on the highly charged Q^2 and Q^1 species upon increasing B content. On the contrary, aluminum was found to favour the homogeneous distribution of negative charge on the glass network. Such changes are expected to affect the charge density of the sites hosting Na^+ ions and thus to influence the Na^+ -site interactions. Infrared spectroscopy can be used to probe such effects. This is because the frequency of the Na^+ -motion bands, which are active in the infrared, is proportional to an effective charge $q^* = (q_{Na}q_A)^{1/2}$, where q_{Na} , q_A are the effective charges of sodium ion and network site, respectively (15). While a detailed infrared study will be reported elsewhere (23), Fig. 5 shows the far-infrared regions of the spectra of SBS and SAS glasses. It is observed that the Na^+ -motion band shifts to higher frequencies upon B substitution, suggesting a progressive strengthening of the Na^+ -site interactions. This trend is opposite to that exhibited by SAS glasses, where the far-infrared envelope shifts eventually to lower frequencies upon increasing Al contents.

A key result of the XPS study of the same glasses (6) was that Na^+ ions are more ionized in SAS than in SBS glasses of the same R/Si ratio (i.e. $q_{Na}(SAS) > q_{Na}(SBS)$). This result combined with the far-infrared behaviour of these glasses suggests that the average charge density of sites hosting Na^+ ions is smaller in SAS than SBS glasses. In terms of the Anderson and Stuart model for ionic conduction (24), the present results would imply a smaller electrostatic energy term for the ion motion activation energy in SAS glasses. In addition, excess volume arguments have suggested that the strain energy term is also smaller in SAS glasses (5). Both terms combined suggest an overall activation energy for ionic conduction smaller in SAS than SBS glasses, as it was found experimentally in previous studies (3-5).

CONCLUSIONS

The study of the Raman and infrared spectra of $Na_2OR_2O_3(3-2x)SiO_2$ ($R = Al, B$) glasses has revealed a number of differences between Al and B substitution for Si. It was found that in the presence of B the silicate network disproportionates to highly charged Q^2 and Q^1 species and to fully polymerized Q^4 tetrahedra at the expense of Q^3 units. Substitution of Si by Al causes the opposite effect, since the equilibrium $2Q^3 \rightleftharpoons Q^2 + Q^4$ shifts to the left and induces a structural homogenization. Such structural rearrangements affect the distribution

of the negative charge on the glass network and therefore the interactions between Na⁺ ions and their sites. These effects are discussed in relation to ion conduction properties exhibited by these glasses.

Support for this work was provided by NSF, NHRF and the Humbolt Foundation

REFERENCES

1. D. E. Day and G. E. Rindone, *J. Am. Ceram. Soc.* 45 (1962) 489 ; 45 (1962) 496
2. J. O. Isard, *J. Soc. Glass Technol.* 43 (1959) 113
3. K. Otto, *Phys. Chem. Glasses* 7 (1966) 29
4. H. Wakabayashi, *Phys. Chem. Glasses* 30 (1989) 51
5. H. Jain and C. H. Hsieh, in: *Physics of Non-Crystalline Solids*, eds. L. D. Pye, W. C. LaCourse and H. J. Stevens (Taylor & Francis, London 1992) p. 447.
6. C. H. Hsieh, H. Jain, A. C. Miller and E. I. Kamitsos, *J. Non-Cryst. Solids*, in press
7. S. A. Brawer and W. B. White, *J. Chem. Phys.* 63 (1975) 2421
8. T. Furukawa, K. E. Fox and W. B. White, *J. Chem. Phys.* 75 (1981) 3226
9. T. Furukawa and W. B. White, *J. Non-Cryst. Solids* 38-39 (1980) 87
10. E. I. Kamitsos, M. A. Karakassides and G. D. Chryssikos, *Phys. Chem. Glasses* 28 (1987) 203; 30 (1989) 19
11. P. McMillan, *Am. Mineral.* 69 (1984) 622
12. N. Umetsuki, N. Iwamoto, T. Tatsumisago and T. Minami, *J. Non-Cryst. Solids* 106 (1988) 77
13. F. Domine and B. Piriou, *Am. Mineral.* 71 (1986) 38
14. B. O. Mysen, D. Virgo and F. A. Seifert, *Am. Mineral.* 70 (1985) 88
15. E. I. Kamitsos, A. P. Patsis and G. D. Chryssikos, *J. Non-Cryst. Solids* 126 (1990) 52; 152 (1993) 246
16. B. O. Mysen, *Am. Mineral.* 75 (1990) 120
17. H. Maekawa, T. Maekawa, K. Kawamura and T. Yokokawa, *J. Non-Cryst. Solids* 127 (1991) 53
18. F. Gervais, C. Lagrange, A. Blin, M. Aliari, G. Hauret, J. P. Coutures and M. Leroux, *J. Non-Cryst. Solids* 119 (1990) 79
19. P. McMillan, B. Piriou and A. Navrotsky, *Geochim. Cosmochim. Acta* 46 (1982) 2021
20. P. McMillan and B. Piriou, *J. Non-Cryst. Solids* 53 (1982) 279; 55 (1983) 221
21. D. M. Zirl and S. H. Garofalini, *J. Am. Ceram. Soc.* 73 (1990) 2848
22. D. A. McKeon, G. A. Waychunas and G. E. Brown, *J. Non-Cryst. Solids* 74 (1985) 349
23. E. I. Kamitsos, J. A. Kapoutsis, H. Jain and C. H. Hsieh, *J. Non-Cryst. Solids*, in press
24. O. L. Anderson and D. A. Stuart, *J. Am. Ceram. Soc.* 37 (1954) 573

ALKALI SITES IN SILICATE GLASSES

J. A. Kapoutsis, E. I. Kamitsos, G. D. Chryssikos, Y. D. Yiannopoulos
and A. P. Patsis

*Theoretical and Physical Chemistry Institute
National Hellenic Research Foundation
48 Vass. Constantinou Ave. Athens 116 35, Greece*

M. Prassas
*Corning Europe, 7 Bis Avenue de Valvins
F-77210 Avon, France*

The nature of sites occupied by metal ions in glass can be investigated by infrared spectroscopy. This work presents the results of an infrared reflectance study of alkali silicate glasses of the type $x\text{Na}_2\text{O} \cdot (1-x)\text{SiO}_2$ ($0.1 \leq x \leq 0.45$) and $\text{M}_2\text{O} \cdot 2\text{SiO}_2$ ($\text{M}=\text{alkali}$). The analysis of the far infrared absorption profiles showed the existence of two bands with frequencies scaling approximately with the inverse square root of cation mass. It was therefore concluded that silicate glasses, similarly to borates, are characterized by two distinct site distributions for the alkali cations. The frequencies of the two cation motion bands were found to increase with sodium oxide content. This was attributed to the increasing charge density of the cation-hosting sites, as a result of the formation of highly charged silicate species.

INTRODUCTION

Addition of a modifier oxide to a glass former causes progressive changes of the glass structure. It has been suggested that the need of the modifier cations to create their own suitable coordination is one of the driving forces that determine the nature of structures assumed by the glass network (1). The establishment of characteristic environments/sites of the metal ions in glass has been revealed by various techniques, including far infrared measurements (2,3), EXAFS studies (4) and neutron scattering experiments (5). The elucidation of the nature of sites occupied by metal ions in glass is an important factor for understanding properties such as the ionic conductivity (6-8), the glass basicity (9) and the operation of color centers or lasers (10,11).

Recent infrared studies of alkali borate glasses have shown that alkali cations are present in two major distributions of anionic site environments (12,13). These two types of sites differ mainly in their electron density, i.e. they exhibit different local basicities (9,14). It is of interest to note also that mobile cations were found to occupy mainly the higher basicity sites (9).

While far infrared spectra of alkali silicate glasses have been reported by a number of authors (15-21), no systematic investigation of the cation-site interactions in such systems has been undertaken so far. This work reports on the findings of an infrared reflectance investigation of alkali silicate glasses of the type $x\text{Na}_2\text{O} \cdot (1-x)\text{SiO}_2$ ($0.1 \leq x \leq 0.45$) and $\text{M}_2\text{O} \cdot 2\text{SiO}_2$ ($\text{M}=\text{alkali}$). The main purpose of this work is to investigate the alkali sites in silicate glasses and, therefore, to explore the possibility that our previous findings regarding borate glasses have some generality beyond these glass systems. In this context, we have studied the effect of alkali content and type on the alkali-site interactions, as well as the structure of the glass network which provides the sites for alkali ions.

EXPERIMENTAL

The glasses investigated were prepared from stoichiometric mixtures of alkali carbonates and SiO_2 . Melting was performed in platinum crucibles in the temperature range 1000-1400 °C depending on composition. After approximately two hours, the melt was cast into preheated at 300 °C steel molds to form discs of 2 cm in diameter and 3 mm in thickness. All samples prepared were clear and transparent. Those used for infrared

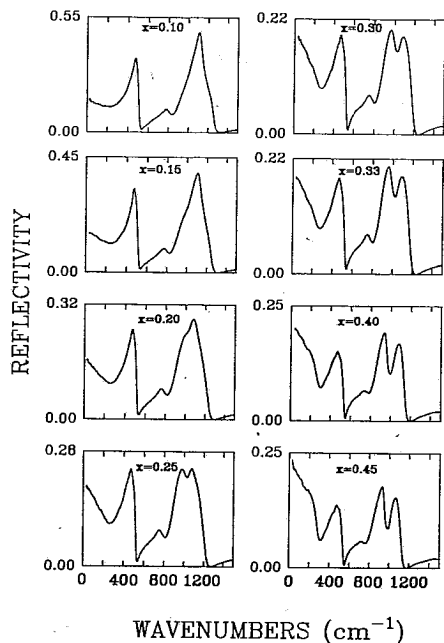


Fig.1. Infrared reflectance spectra of sodium-silicate glasses $x\text{Na}_2\text{O} \cdot (1-x)\text{SiO}_2$

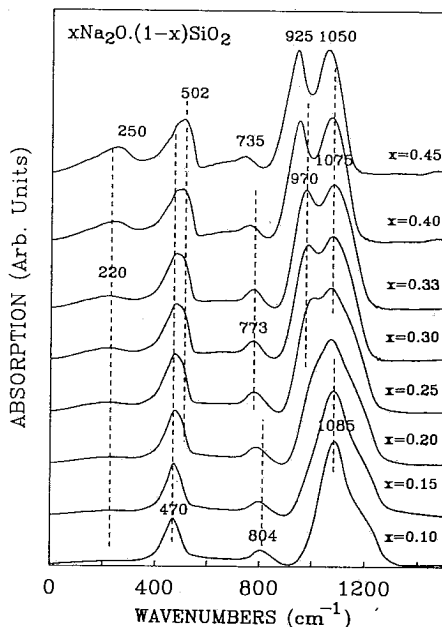


Fig.2. Absorption coefficient spectra of sodium-silicate glasses $x\text{Na}_2\text{O} \cdot (1-x)\text{SiO}_2$

measurements were ground flat and polished on one side. To minimize surface hydrolysis, the samples were kept in desiccators and repolished a number of times prior to spectral acquisition and until reproducible reflectivity data were obtained.

Infrared spectra were measured on a Fourier-transform vacuum spectrometer (Bruker 113v). An 11° off-normal specular reflectance attachment, with a high reflectivity aluminum mirror as reference, were utilized for reflectivity measurements. A combination of sources, detectors and beam splitters was employed to achieve continuous spectral coverage in the range $30\text{--}4000\text{ cm}^{-1}$. Each spectrum is the average of 200 scans at 2 cm^{-1} resolution. The reflectance spectra were transformed by the Kramers-Kronig method to obtain the optical and dielectric properties required for the calculation of absorption coefficient spectra (14).

RESULTS

The infrared reflectance spectra of sodium-silicate glasses are shown in Figure 1 for sodium contents spanning the range $0.1 \leq x \leq 0.45$. For the $x=0.1$ glass composition a spectrum quite similar to that of vitreous SiO_2 (22) has been obtained, except for its small reduction in reflectivity. Increase of the Na_2O content causes further reduction in reflectivity and drastic changes of the spectral profiles. In particular, the peak at 1100 cm^{-1} develops a shoulder at $ca\ 980\text{ cm}^{-1}$ ($x \leq 0.2$) and this becomes eventually the main reflectivity peak (950 cm^{-1}) for high values of x . A similar behavior was observed in earlier mid infrared absorption (23,24) and reflectance (25, 26) studies of sodium-silicate glasses.

Increasing x causes also the progressive increase of the far infrared reflectivity, which dominates the spectrum of glasses with high sodium content. While there are no well defined maxima in the far infrared reflectivity spectra, the absorption coefficient spectra (Figure 2) illustrate clearly the development of a far infrared feature at $ca\ 220\text{ cm}^{-1}$. The intensity and frequency of this band increase with Na_2O content. Similar far infrared

features are exhibited by the spectra of all alkali silicate glasses, as shown in Figure 3 for the disilicate composition ($x=0.33$ and $M=Li, Na, K, Cs$). The frequency and bandwidth of the far infrared peak increase upon decreasing the alkali size, while for $M=Li$ this feature is not resolved due to its considerable overlapping with the band at $ca 500\text{ cm}^{-1}$.

DISCUSSION

The Structure of the Silicate Network

Information about the structure of the silicate network and its dependence on the sodium content can be obtained from the mid infrared spectra ($400\text{--}1400\text{ cm}^{-1}$). Three spectral regions ($400\text{--}550\text{ cm}^{-1}$, $700\text{--}850\text{ cm}^{-1}$ and $850\text{--}1300\text{ cm}^{-1}$) can be seen in the spectra depicted in Figure 2. The low frequency envelope ($400\text{--}550\text{ cm}^{-1}$) can be attributed to the rocking motion of Si-O-Si bridges, while the bending mode of the same bridges is responsible for absorption in the $700\text{--}850\text{ cm}^{-1}$ region (27). The high frequency envelope ($850\text{--}1300\text{ cm}^{-1}$) originates from the asymmetric stretching vibrations of Si-O-Si bridges (27) and Si-O dangling bonds of Q^n silicate tetrahedra (n is the number of bridging oxygens per silicon tetrahedron) (23, 28).

Based on the results of previous Raman (29-31) and infrared (23,28) studies of modified silicate glasses, we assign the bands at $ca 1085, 1075$ and 935 cm^{-1} to Q^4, Q^3 and Q^2 sites, respectively. Therefore, the evolution of the high frequency envelope with sodium oxide content (Figure 2) shows a progressive depolymerization of the silicate network by increasing the number of non-bridging oxygens per silicon site.

The behavior of the $400\text{--}550\text{ cm}^{-1}$ envelope is also consistent with this structural evolution. The frequency of the rocking motion of Si-O-Si linkages increases upon increasing network depolymerisation. This is in accord with the composition dependence of the Raman active vibration of Si-O-Si bridges (a mixed stretching-bending mode) which appears in the same frequency range (29).

The mid infrared and Raman results regarding the structure of the glass network in sodium-silicate glasses are fully compatible with the findings of ^{29}Si NMR (32,33) and XPS (34) studies on similar glass compositions.

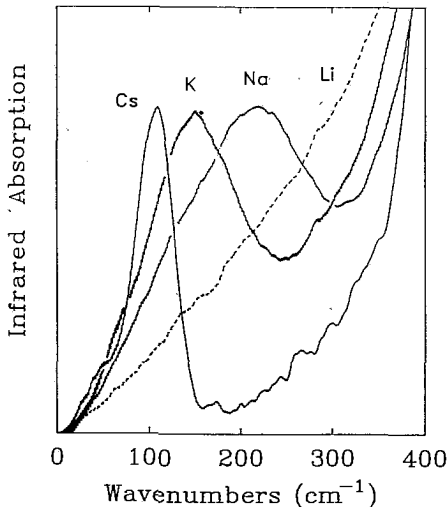


Fig.3. Far infrared spectra of alkali-disilicate glasses $0.33M_2O.0.67SiO_2$.

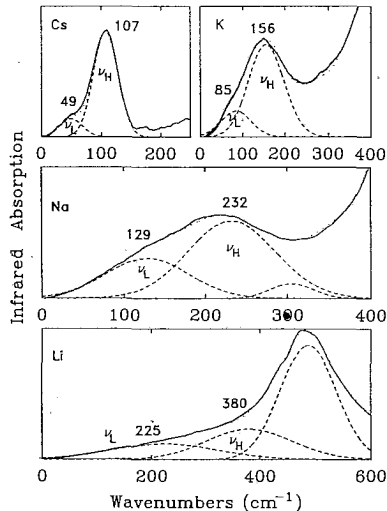


Fig.4. Deconvolution of the far infrared spectra of $0.33M_2O.0.67SiO_2$ glasses. The simulated spectra are shown by dotted lines.

The Localized Vibrations of Alkali Metal Ions

Intense bands in the far infrared spectra of ionic glasses have been assigned to vibrations of metal ions in their localized sites in the glass (15). As shown in Figures 2 and 3, the far infrared profiles of the alkali silicate glasses are asymmetric, thus suggesting the existence of more than one band. To investigate the origin of such asymmetries we have deconvoluted the far infrared profiles, using techniques applied previously to borate glasses (12-14) and employing the minimum number of bands to achieve a reasonable fit of the experimental spectra. For the case of Li, Na and K glasses it was necessary to consider also the silicate band at $ca\ 500\text{ cm}^{-1}$ because of its overlapping with the alkali motion band.

The results of the deconvolution are shown in Figure 4. It is clear that the far infrared asymmetry can be well accounted for by the presence of two Gaussian type components with frequencies designated by ν_H and ν_L . The weak band resolved at 305 cm^{-1} for the Na glass could originate from a silicate deformation mode (see below). Figure 5 shows that the far infrared frequencies ν_H and ν_L scale with the inverse square root of the mass of the alkali ion. It is therefore reasonable to attribute both bands to vibrations of alkali ions in their network sites. This result is similar to that obtained for alkali borate glasses (12-14) and suggests that the observed asymmetries of the far infrared profiles present a universal structural characteristic of glasses modified by ionic oxides.

The origin of such a universal characteristic cannot be traced to the details of the network structure, since the latter depends strongly on the nature of the glass forming

oxide, as well as on the modifier oxide content. It was argued elsewhere that the two far infrared component bands indicate the presence of two different distributions of anionic site environments, which may signal the presence of structural inhomogeneities (12-14). It is of interest to note that computer simulation studies have given evidence for the existence of inhomogeneities in alkali silicate glasses (35-37), which are manifested by an inhomogeneous distribution of alkali ions in alkali-rich and silica-rich pseudophases. Because of differences in site charge density, alkali ion motions in the former pseudophase would occur at higher frequencies (ν_H) than those in the silica-rich pseudophase (ν_L).

The effect of sodium content on the ion motion bands is shown in Figure 6 where deconvoluted far infrared spectra of representative compositions are presented. Besides the two Na motion bands with frequencies ν_H and ν_L , a third component is resolved for $x < 0.40$ with relative intensity decreasing upon increasing sodium content (see also Fig. 4, M=Na).

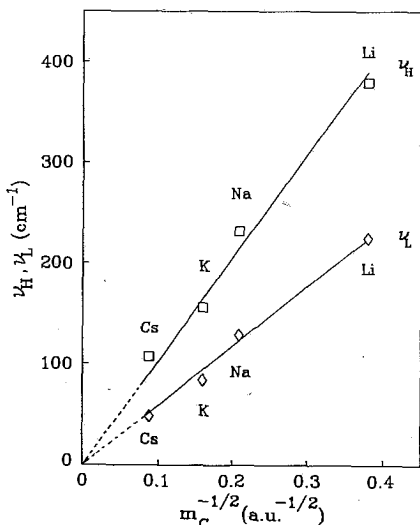


Fig. 5. Cation-motion frequencies versus $m_C^{-1/2}$ in $0.33M_2O \cdot 0.67SiO_2$ glasses, where m_C is the cation mass. High- (ν_H) and low-frequency (ν_L) band maxima were obtained by deconvoluting the far infrared spectra (see Figure 4).

This $ca\ 305\text{ cm}^{-1}$ feature was not resolved in the $x=0.45$ glass spectrum of Figure 6 because it is probably overmasked by the enhanced 254 cm^{-1} component. We attribute the $ca\ 305\text{ cm}^{-1}$ band to a silicate network deformation mode (38).

Despite the large variation of the silicate network structure with Na_2O content (Figure 2) the far infrared envelope could be always simulated by two Na ion motion bands.

These findings strengthen the argument that the presence of two major distributions of ionic site environments is beyond the details of the glass network structure. Of course, the change of the latter with Na_2O content affects the sites hosting Na ions. This is demonstrated in Figures 6 and 7 where the increase of the Na motion frequencies upon increasing x is evident. This result is in agreement with earlier studies on borate (12) and silicate (19) glasses and can be attributed to the progressive increase of the corresponding site charge density resulting from the depolymerization of the silicate network.

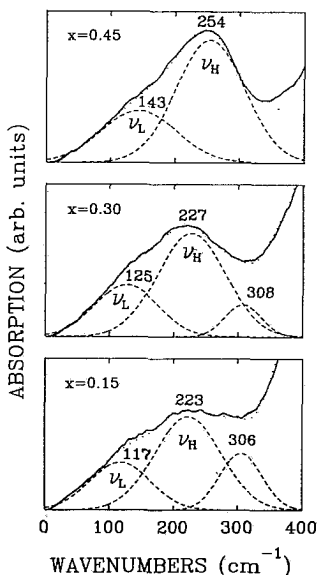


Fig.6. Deconvolution of the far infrared spectra of $x\text{Na}_2\text{O} \cdot (1-x)\text{SiO}_2$ glasses. The simulated spectra are shown by dotted lines.

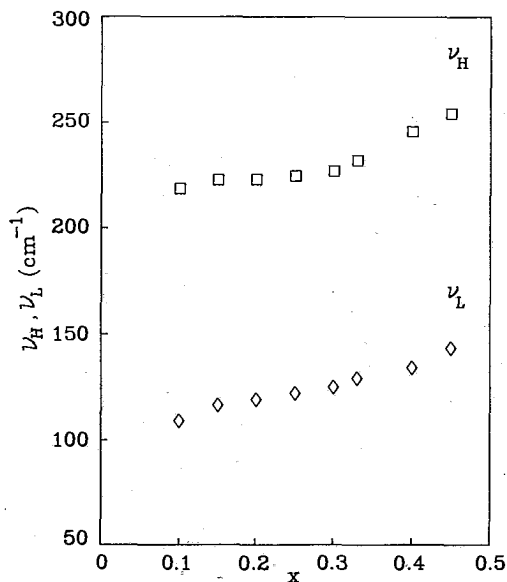


Fig.7. Composition dependence of the sodium ion motion frequencies in $x\text{Na}_2\text{O} \cdot (1-x)\text{SiO}_2$ glasses.

The presence of sites with different charge density would subsequently imply differences in their local optical basicity (9). This aspect of the work is in progress and will be reported elsewhere.

CONCLUSIONS

It has been shown that the far infrared spectra of alkali silicate glasses can be simulated by two bands assigned to vibrations of alkali ions in two distributions of anionic environments. The nature of the environments surrounding the metal ions was found to depend on the alkali content. In particular, the anionic charge of the ion-hosting sites increases with alkali content as a result of network depolymerization. The asymmetries of the far infrared profiles which give rise to the two ion motion bands appear to present a universal behavior of modified oxide glasses. The origin of this can be traced to structural inhomogeneities inherent to such glasses.

Helpful discussions with Dr. J. A. Duffy (University of Aberdeen) are gratefully acknowledged. This work has been supported by NHRF and the British Council (ATH/609/3/30).

REFERENCES

1. A. H. Dietzel, *Phys. Chem. Glasses*, 24 (1983) 172
2. G. B. Rouse, P. J. Miller and W. M. Risen, *J. Non-Cryst. Solids*, 28 (1978) 193
3. E. I. Kamitsos, A. P. Patsis and G. D. Chryssikos, *Phys. Chem. Glasses*, 32 (1991) 219
4. G. N. Greaves, *J. Non-Cryst. Solids*, 71 (1985) 203 and *Phil. Mag. B60* (1989) 793
5. P. H. Gaskell, M. C. Barnes and P. Chieux, *Nature*, 350 (1991) 675
6. G. N. Greaves, S. J. Gurman, C. R. A. Catlow, A. V. Chadwick, S. Houde-Walter, C. M. B. Henderson and B. R. Dobson, *Phil. Mag.* 64 (1991) 1059
7. A. Bunde, P. Maass and M. D. Ingram, *Ber. Bunsenges. Phys. Chem.* 95 (1991) 977
8. P. Maass, A. Bunde and M. D. Ingram, *Phys. Rev. Lett.* 68 (1992) 3064
9. J. A. Duffy, E. I. Kamitsos, G. D. Chryssikos and A. P. Patsis, *Phys. Chem. Glasses*, 34 (1993) 153
10. S. Todoroki, S. Tanaka, K. Hirao and N. Soga, *J. Non-Cryst Solids*, 136 (1991) 213 and 122 (1990) 59
11. M. J. Weber, *J. Non-Cryst. Solids*, 123 (1990) 208
12. E. I. Kamitsos, M. A. Karakassides and G. D. Chryssikos, *J. Phys. Chem.* 91 (1987) 5807
13. E. I. Kamitsos, G. D. Chryssikos, A. P. Patsis and M. A. Karakassides, *J. Non-Cryst. Solids*, 131-133 (1991) 1092
14. E. I. Kamitsos, A. P. Patsis and G. D. Chryssikos, *J. Non-Cryst. Solids*, 152 (1993) 246
15. G. Exarhos and W. M. Risen, *Solid State Commun.* 11 (1972) 755
16. E. I. Kamitsos and W. M. Risen, *J. Non-Cryst. Solids*, 65 (1984) 333
17. G. D. Minser and W. B. White, in *Spectroscopic Investigations of Glass Structure*, US Department of Energy Annual Report no. DOE/ER/450077-1 (1984)
18. N. Soga and K. Hirao, In *Structure and Bonding in Non-Crystalline Solids*, eds. G.E. Walrafen and A. V. Revesz, Plenum, New York (1986) p. 119
19. C.I. Merzbacher and W. B. White, *Am. Miner.* 73 (1988) 1089
20. F. Gervais, C. Lagrange, A. Blin, M. Aliari, G. Hauret, J. P. Coutoures and M. Leroux, *J. Non-Cryst. Solids*, 119 (1990) 79
21. A. Burns, H. P. Brack and W. M. Risen, *J. Non-Cryst. Solids*, 131-133 (1991) 994
22. F. L. Galeener, A. J. Leadbetter and M. W. Stringfellow, *Phys. Rev. B27* (1983) 1052
23. D. Crozier and R. W. Douglas, *Phys. Chem. Glasses*, 6 (1965) 240
24. J. R. Ferraro and M. H. Manghnani, *J. Appl. Phys.* 43 (1972) 4595
25. S. I. Simon and H. O. Mc Mahon, *J. Am. Ceram. Soc.* 36 (1953) 160
26. D. M. Sanders, W. B. Person and L. L. Hench, *Appl. Spectr.* 28 (1974) 247
27. G. Lucovsky, C. K. Wong and W. B. Pollard, *J. Non-Cryst. Solids*, 59&60 (1983) 839
28. C.I. Merzbacher and W. B. White, *J. Non-Cryst. Solids*, 130 (1991) 18
29. T. Furukawa, K. E. Fox and W. B. White, *J. Chem. Phys.* 75 (1981) 3226
30. P. Mc Millan, *Am. Miner.* 69 (1984) 622
31. B. O. Mysen, *Am. Miner.* 75 (1990) 120
32. R. Dupree, D. Holland and D. S. Williams, *J. Non-Cryst. Solids*, 81 (1986) 185
33. H. Maekawa, T. Maekawa, K. Kawamura and T. Yokokawa, *J. Non-Cryst. Solids*, 127 (1991) 53
34. D. Spenger, H. Bach, W. Meisel and P. Gutlich, in *Physics of Non-Crystalline Solids*, eds. L. D. Pye, W. C. LaCourse and H. J. Stevens, Taylor & Francis, London (1992) p.42
35. C. A. Angell, *Solid State Ionics*, 9&10 (1983) 3 and 18&19 (1986) 72
36. C. H. Huang and A. N. Cormack, *J. Chem. Phys.* 93 (1990) 8180 and 95 (1991) 3634
37. B. Vessal, G. N. Greaves, P. T. Marten, A. V. Chadwick, R. Mole and S. Houde-Walters, *Nature*, 356 (1992) 504
38. M. Handke and W. Mozgawa, *Vibrational Spectrosc.* 5 (1993) 75

³¹P AND ²⁷Al NMR SPECTROSCOPY OF GLASSES: DETERMINATION OF THE STRUCTURE, OF REACTIONS IN THE BATCHES AND OF CRYSTALLISATION PHENOMENA

C. Jäger¹⁾, D. Ehr²⁾, G. Kunath³⁾

¹⁾ Max-Planck-Institut für Polymerforschung, Postfach 3148, D-55021 Mainz, Germany

²⁾ Friedrich-Schiller-Universität Jena, Chemische Fakultät, Otto-Schott-Institut, D-07743 Jena, Germany

³⁾ Friedrich-Schiller-Universität Jena, Physikalisch-Astronisch-Technikwissenschaftliche Fakultät, D-07743 Jena, Germany

Abstract: Nuclear Magnetic Resonance is a powerful tool for probing the structure on an atomic scale in amorphous and polycrystalline solids. ³¹P NMR and ²⁷Al NMR have been used to study both the structure of glasses but also of either recrystallized glasses and ceramics. Furthermore, NMR has been exploited to study high temperature solid state reactions in the batches of multicomponent glasses. This enables a detailed study of the main reactions and allows the melting procedure to be optimized. Additionally, crystallisation phenomena can also be investigated in detail as a function of the heat treatment conditions. Several examples are discussed. The recent progress in ²⁷Al NMR spectroscopy (Satellite Transition Spectroscopy (SATRAS)) is demonstrated in detail. It allows for the first time the correct quantification of the ²⁷Al NMR spectra in disordered materials such as glasses.

1) INTRODUCTION:

Among the variety of physical methods to investigate the microstructure of amorphous solids and in particular of glasses, NMR is beginning to play an increasingly role. There are several reasons for that.

First of all NMR is a selective method. This is due to the fact that each NMR accessible nucleus has a different resonance frequency. Hence, interpretation of the spectra is much easier compared with other methods, since it is clear what nucleus is resonating.

Secondly, NMR is a local method. The interactions responsible for the NMR spectra, such as dipole-dipole interaction, anisotropic chemical shifts and quadrupole interaction are extremely sensitive to changes in the first and second coordination shell only. This is because of their spatial dependence (e.g. r^{-3} for the dipole interaction, with r being the distance between the nuclei). It is this fact that makes NMR so valuable for studying amorphous materials since no three-dimensional translational symmetry of any unit cell is required in order to obtain the spectra. Compared with perfect crystalline materials the NMR lines are broadened only by about a factor of ten due to distributions of bonding angles and distances in glasses. This allows the quantification of the spectra even if both crystalline and amorphous phases are present simultaneously as e.g. in ceramics or in partially crystallized glasses.

Finally, NMR provides quantitative results, because the areas of the various lines in the spectra are proportional to the number of resonating spins.

In the lecture various examples are shown how NMR can provide useful and sometimes

unique information on the glass structure (coordination number, relative amount of the structural units), reactions in the batches of multicomponent glasses and their crystallisation behaviour.

2) APPLICATION OF ^{31}P AND ^{27}Al NMR

2.1) ^{31}P NMR

In order to obtain high resolution NMR in solids special techniques have to be used. Magic angle sample spinning (MAS, 1) is extremely powerful for $I=1/2$ nuclei. It has been exploited by many groups to narrow the NMR spectra. Concerning ^{29}Si and ^{31}P the degree of condensation of the anions (Q^n nomenclature: n - number of bridging oxygen atoms to surrounding like PO_4 or SiO_4 units, respectively) can easily be determined (e.g. 2-4). This also includes the identification of the cations and the possibility of obtaining quantitative results.

We have extensively studied the high temperature melting reactions of fluoroaluminate glasses with low content of phosphates. These are multicomponent systems with one or two different polyphosphates and up to six different fluorides. It turned out, that despite the fact of only about 10 mole-% polyphosphate present in the batches, detailed information is obtainable by ^{31}P NMR. The inserted polyphosphate is decomposed by the excess of AlF_3 . The temperature/time dependence has been studied allowing conclusions for optimizing the melting procedure. Finally a model of the melting process has been established (5).

In the same way, the crystallisation behaviour of this type of glasses has been studied. As mentioned earlier phosphate containing crystal phases can be detected unambiguously. It has been shown the the crystallisation of AlPO_4 has to be prevented in order to stabilize the glasses. A new crystal phase has been found in the stabilized glasses after extremely long heat treatment. It is called FADP (fluoroaluminodiphosphate) and consists of $(\text{P}_2\text{O}_7)^{4-}$ anions which are directly bound by oxygen into branched fluoroaluminate chains. The basic advantage of NMR for those investigations is its selectivity, since only about 10 mole-% of phosphate is present in the glasses.

2.2) ^{27}Al SATELLITE TRANSITION SPECTROSCOPY

In the last part the recent progress in ^{27}Al NMR spectroscopy is shown concerning structural investigations of disordered solids. The major problem with NMR of quadrupolar nuclei (^{27}Al possesses a nuclear spin $I=5/2$) is that the NMR lineshape is governed by the quadrupole interaction. This results in considerable line broadening by second order quadrupole effects. Under these circumstances even MAS does not average out those second order broadening (e.g. 6,7).

Recently it has been shown that these severe limitations of MAS NMR of quadrupolar nuclei can be overcome by exploiting the so-called "Satellite Transitions". Using again the simple MAS experiment the spectral resolution is improved by a factor three. This effect has been mentioned first by Samoson (7), but has been exploited only recently (8-12). The details of this experimental approach is described in (12).

In the lecture various examples will be presented in order to show that now for the first time reliable quantitative information can be obtained on the coordination of aluminium in amorphous solids. Also, by observing the satellite transitions rather than the central transition used so far, all relevant interaction parameters are obtained with just a single experiment.

Furthermore, ²⁷Al signals of crystalline phases can be discriminated from those of amorphous parts by this NMR method.

3) CONCLUSIONS

NMR is a powerful tool for probing the microstructure of disordered solids. Its role for those structural investigations will definitely improve in the near future. Especially the recent progress of NMR of quadrupolar nuclei will result in many more applications in materials research. This is particularly important for commercial applications, because NMR can in principle be used for testing the manufacturing of various materials, such as glasses, ceramics, alumina and others.

REFERENCES:

1. E.R. Andrew, A. Bradbury, R.G. Eades, *Nature* 182 (1958) 1659
2. G. Engelhard, D. Michel, *High resolution solid state NMR of silicates and zeolites* Wiley Chichester 1987
- 3) C. Jäger, D. Ehrt, U. Haubenreißer,
Investigations of Solid State Reactions of Binary Polyphosphate - Fluoride Systems
by Means of Thermal Analysis, X-Ray Diffraction and NMR Spectroscopy
I. System Ba(PO₂)₃ + BaF₂
Zschr. f. Physikal. Chemie: Neue Folge 159, 75 (1988)

II. Systems M(PO₃)₂ + MF₂, M= Sr, Ca
Zschr. f. Physikal. Chemie: Neue Folge 159, 89 (1988)

III. System Mg(PO₂)₃ + MgF₂
Zschr. f. Physikal. Chemie: Neue Folge 159, 103 (1988)

IV. Systems M(PO₃)₃ + MF₃, M= Al, La
Zschr. f. Physikal. Chemie: Neue Folge 162, 97 (1989)

V. Systems Sr(PO₃)₂ + 4 AlF₃ ; 5 CaF₂ ; MgF₂
Zschr. f. Physikal. Chemie: Neue Folge 162, 109 (1989)

VI. Reactions of Mg(PO₃)₂, Ba(PO₃)₂ and La(PO₃)₃ with Excess of AlF₃
Zschr. f. Physikal. Chemie: Neue Folge 165, 55 (1989)
- 4) P. Lusso, B. Schnabel, C. Jäger, U. Sternberg, D. Stachel, D.O. Smith,
³¹P NMR Investigation of Binary Alkaline Earth Phosphate Glasses of Ultraphosphate
Composition
J. Non-Cryst. Solids 143, 265 (1992)
- 5) D. Ehrt, C. Jäger, W. Vogel
3. International Otto-Schott-Colloquium Jena, 1986

- in: *Wiss. Zschr. FSU Jena, Naturw. Reihe*, 36 (1987) 867
- 6) H.J. Behrens, B. Schnabel *Physica B*114 (1982) 185
 - 7) A. Samoson, A. Kundla, E. Lippmaa, *J. Magn. Reson.* 49 (1982) 350
 - 8) C. Jäger
How to Get More From ^{27}Al MAS NMR by High-Speed Satellite Transition Spectroscopy, *J. Magn. Reson.* 99, 353 (1992)
 - 9) C. Jäger, W. Müller-Warmuth, C. Mundus, L. van Wüllen,
 ^{27}Al MAS NMR Spectroscopy of Glasses: New Facilities by Application of "SATRAS", *J. Non-Cryst. Solids* 149, 209 (1992)
 - 10) G. Kunath, P. Losso, H. Schneider, S. Steuernagel, C. Jäger
 ^{27}Al Satellite Transition Spectroscopy of Polycrystalline Aluminium Borate $9\text{Al}_2\text{O}_3 \cdot \text{B}_2\text{O}_3$
Solid State Nucl. Magn. Reson. 1, 261 (1992)
 - 11) C. Jäger, G. Kunath, P. Losso, G. Scheler
Determination of Distributions of the Quadrupole Interaction in Amorphous Solids by ^{27}Al Satellite Transition Spectroscopy
Solid State Nucl. Magn. Reson. 2, 73 (1993)
 - 12) C. Jäger
Satellite Transition Spectroscopy of Quadrupolar Nuclei
in press: Springer Verlag (1993) *NMR: Basic Principles and Progress* Vol. 32:

CROSS CHECKING OF VIBRATIONAL AND NMR INFORMATION IN GLASSES.

T. PAROT-RAJAONA, B. COTE*, C. BESSADA, D. MASSIOT, F. GERVAIS

Centre de Recherche sur la Physique des Hautes Temperatures, CNRS, 45071 Orléans, France

*Saint-Gobain Recherche, 39 quai Lefranc, BP 135, 93303 Aubervilliers Cedex, France

Lithium aluminosilicate glasses of the join $\text{LiAlO}_2\text{-SiO}_2$ and $\text{Li}_2\text{Si}_2\text{O}_5\text{-Al}_2\text{O}_3$ (with $\text{Al}_2\text{O}_3 \leq 25$ mol.%) have been investigated by infrared reflectivity and silicon-29 nuclear magnetic resonance spectroscopy. For comparison, Ca glasses with high Al and high Ca content and some Na glasses are also investigated. By fitting the infrared spectra with a dielectric function model, silicon and oxygen effective charge are deduced. Values of the silicon effective charge are compared to the ^{29}Si chemical shift. Results show linear correlations : the slopes of the line depend on all elements which contribute to the Coulombic field. Thus, it appears that chemical shift is sensitive to several contributions and not just the Coulombic field.

INTRODUCTION

Infrared spectroscopy appears as an useful tool to investigate the chemical bonding in glasses (1,2). On the other hand, ^{29}Si chemical shift is affected by the silicon environment (3). It appears therefore instructive to compare results obtained by infrared reflectivity and nuclear magnetic resonance (NMR) spectroscopy (4,5). Earlier studies have shown that weakening of the force constants shown by infrared spectroscopy agrees well with structural change, viz. substitution of Si by Al within the network former, probed by ^{29}Si NMR. In this paper, we focus our investigation on the density of charge around the silicon. Chemical composition of studied glasses are reported in figure 1.

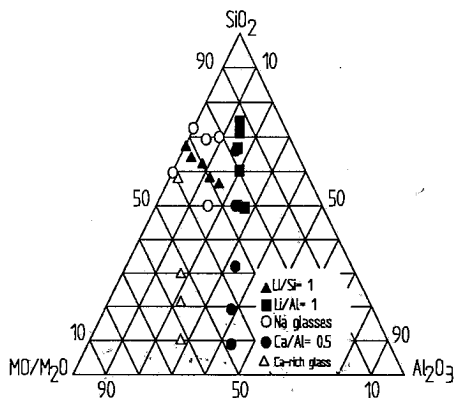


Figure 1. Composition of the glasses investigated in this study.

INFRARED REFLECTIVITY

Infrared reflection spectra have been recorded with a Fourier spectrometer Bruker IFS 113 in the wavenumber range 20 to 4,000 cm^{-1} . Glass is a dielectric medium which can be described satisfactorily with the phenomenology inherited from the studies of crystals. Use of dielectric function model

$$\frac{\epsilon(\omega)}{\epsilon_\infty} = \prod_j \frac{\Omega_{j\text{LO}}^2 - \omega^2 + i\gamma_{j\text{LO}}\omega}{\Omega_{j\text{TO}}^2 - \omega^2 + i\gamma_{j\text{TO}}\omega} \quad [1]$$

to fit infrared spectra of glasses has been successful (6). Adjustable parameters are transverse (TO) and longitudinal (LO) optical frequency (Ω) and damping term γ . One advantage of the fitting procedure is to get accurate frequency value, a result which is not straightforward when the spectrum contains broad bands. Infrared spectrum results of the interaction between infrared light and the dipole moment induced by the relative motion of cations and anions. It is thus possible to deduce the effective charge carried by each ion. In glasses, even with the structural disorder, the Coulombic field is uniform enough to orient the local dipoles in a particular direction (7). This phenomenon produces TO-LO frequency splitting, which is related to the Coulombic field via

$$\sum_j (\Omega_{j\text{LO}}^2 - \Omega_{j\text{TO}}^2) = \frac{1}{\epsilon_v V} \sum_k \frac{(Ze)_k^2}{m_k} \quad [2]$$

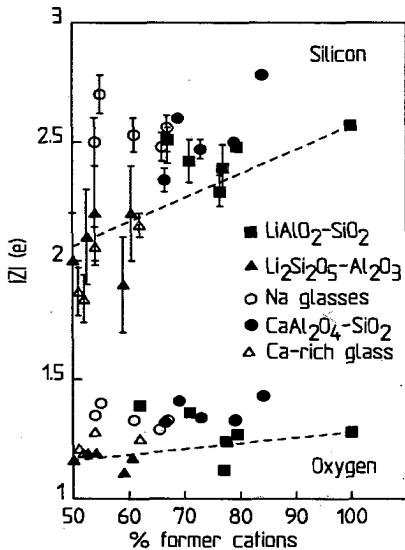


Figure 2. Evolution of silicon (top) and oxygen (bottom) effective ionic charge with the content of glass former cations.

Here ϵ_v is the dielectric constant of vacuum, and the summation of the right side of the equation is over all atoms of effective charge $(Ze)_k$ and individual mass m_k , contained in the elementary volume V . The effective charge is directly related to the concept of ionicity. When all TO and LO mode frequencies are available, the equation [2] combined with the electrical neutrality of the sample give rise to two equations with as many unknown effective charge as the number of atomic constituents in the glass under consideration. Then, the alkali effective charge is allowed to vary from 0.7 and 1 and the Ca effective charge from 1.7 to 1.9. Since both Al-O and Si-O bonds are involved in the glass former network, we assumed that they have the same value of ionicity, i.e. $\frac{Z_{\text{Al}}}{3} = \frac{Z_{\text{Si}}}{4}$.

Silicon and oxygen effective charge are then deduced straightforwardly. The silicon sites is not taken under consideration, so that average silicon charge is actually

determined. This approximation holds also for oxygen. Results are shown in figure 2. A significant decrease of oxygen effective charge is observed for glasses with high Li content. In the same way, in glasses with high modifier content (Li or Ca), the Si effective charge is weaker than that of silica, whereas little change is noted for other glass compositions. There are two possibilities to explain such an observation : whether Si-O bond becomes more hybridised in depolymerized glasses, or Li and Ca are less ionic than we have supposed.

NMR EXPERIMENTS

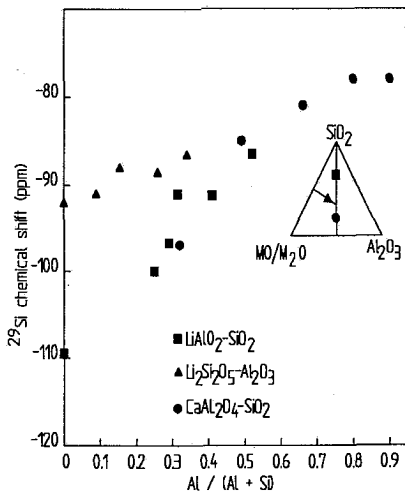


Figure 3. Evolution of ^{29}Si chemical shift with Al content.

by Al shifts the peak maxima toward less negative chemical shift as it is shown in figure 3. In other words, the silicon atoms become less shielded when the number of neighboring aluminum atoms increases. In the series $\text{Li}_2\text{Si}_2\text{O}_5\text{-Al}_2\text{O}_3$, the variation of chemical shift is smaller than in fully polymerized glasses. It appears that in the first series, chemical shift results from balance of two opposite tendencies : one is the deshielding due to aluminum neighbors, the other is shielding involved by polymerization of the network.

COMPARISON OF INFRARED AND NMR DATA

The silicon chemical shift is a charge dependent parameter (8). It is thus tempting to compare the electric field shift probed by silicon-29 NMR and the silicon effective charge deduced by infrared spectroscopy. Results are shown in figure 4. Correlations exist between ^{29}Si chemical shift and the dynamic charge. In the case of calcium glasses, the straight line is shifted to the right (with respect to Li glasses) due to high Al content. On the other hand, glasses with high modifier content lies in the left side of the figure and do not follow the general trend. This departure illustrates that the chemical shielding is not just the effect of the Coulombic field. Structural parameters, as bond angle, bond length, and of course hybridisation effect must be taken into account.

Investigations were carried out with a Bruker MSL 300 spectrometer operating at 59.62 Mhz for ^{29}Si nuclei in a magnetic field of 7.4 T. All experiments were performed using a standard 7 mm MAS probe from Bruker, with a sample powder spinning at 2.5 and 4 kHz. All spectra were referenced to the ^{29}Si response in tetramethylsilane (TMS). The experimental error of the measured chemical shifts have been estimated of ± 2 ppm.

^{29}Si chemical shift is sensitive to the surrounding of silicon and appears primarily affected by the nature of the silicon next-nearest-neighbor (3). In aluminosilicate glasses, the broad NMR band do not allow discrimination between Q_m^n units (Q_m^n represents a Si tetrahedron with n ($0 \leq n \leq 4$) bridging oxygen atoms and m ($0 \leq m \leq n$) aluminum as next nearest neighbour). However, the substitution of Si

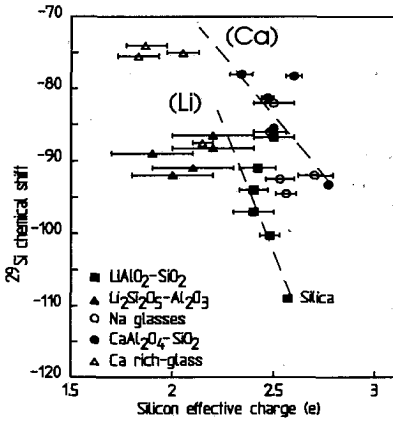


Figure 4. Correlations between silicon effective charge and chemical shielding.

CONCLUSION

Lithium aluminosilicate glasses of the join $\text{LiAlO}_2\text{-SiO}_2$ and $\text{Li}_2\text{Si}_2\text{O}_5\text{-Al}_2\text{O}_3$ (with $\text{Al}_2\text{O}_3 \leq 25$ mol.%) have been investigated by infrared reflectivity and silicon-29 nuclear magnetic resonance spectroscopy. The effective ionic charge deduced by infrared measurements is compared to the silicon-29 chemical shift. Results show good correlations except for glasses with high modifier cation content or high Al content. Thus, the electric Coulombic field is not sufficient to report the chemical shielding probed by NMR spectroscopy.

REFERENCES

1. F. Gervais, C. Lagrange, A. Blin, M. Aliari, G. Hauret, J.P. Coutures and M. Leroux, *J. Non-Cryst. Solids* 119 (1990) 79.
2. T. Parot-Rajaona, B. Coté, Y. Vaills and F. Gervais, *J. Phys., Coll. C2, suppl. JP III n° 10, 2* (1992) 227
3. R.J. Kirkpatrick, in *Spectroscopic Methods in Mineralogy and Geology*, Rev. Min., Vol.18, Ed. F.C. Hawthorne (1988) 341.
4. C.I. Merzbacher, K.J. McGrath and P.L. Higby, *J. Non-Cryst. Solids* 136 (1991) 249.
5. T. Parot-Rajaona, B. Coté, C. Bessada, D. Massiot and F. Gervais, *submitted to J. of Non-Cryst. Solids*.
6. F. Gervais, A. Blin, D. Massiot, J.P. Coutures, M.H. Chopinet and F. Naudin, *J. Non-Cryst. Solids* 89 (1987) 384.
7. M.C. Payne and J.C. Inkson, *J. Non-Cryst. Solids* 68 (1984) 351.
8. G. Engelhardt and D. Michel, in "High Resolution Solid State NMR of Silicates and Zeolites", Ed. J. Wiley & sons (1987) Ch.IV.

DISSOLUTION STUDIES OF PHOSPHATE GLASSES AND RELATIONSHIPS TO STRUCTURE

James E. Dickinson, Corning, Incorporated, Corning, NY 14831 USA

Raman spectra collected from a series of alkali zinc phosphate glasses reveal a consistent pattern of cation dependent depolymerization of phosphate groups. Substitution of alkali cations for zinc at constant phosphorus produces pyrophosphate groups at the expense of ortho- and longer chain length phosphate species. The dissolution rate of pyrophosphate glasses goes through a minimum at pH 8-8.5 and decreases with increasing temperature in acidic solutions. These results can be rationalized by models relating the partial charge on oxygens to the ability to undergo exchange reactions with protons in solution.

INTRODUCTION

Recently it has been shown that phosphate glasses with low glass transformation temperatures can be extruded and injection molded with high temperature thermoplastics to produce glass-polymer microcomposites(1). Critical to the performance of these composites is their stability in aqueous solution which is, primarily, a function of the durability of the glass. The research described below was carried out to investigate phosphate glass structure in general and, specifically, to address the nature of the relationship between the structure of phosphate glasses and their durability.

EXPERIMENTAL

Melts for structural and dissolution studies were made by mixing together appropriate amounts of reagent grades oxides, carbonates, and NH_4HPO_4 in 500-1000 gram batches. Melting temperatures ranged from 1000-1200°C for 4-6 hours in silica crucibles, depending on the composition. Melts were quenched by pouring onto a steel slab.

Raman scattering measurements were made using the 514.5 nm line of an Ar⁺ laser with a 90° scattering geometry. The scattered light was resolved with a Spex 1403 double monochromator with slit widths of 4 cm⁻¹. Glass samples were pieces approximately 1 cm³ broken from the poured glass patty.

Glass durability was evaluated using the pH stat titration technique. In this technique the change in pH of a solution containing glass powder is monitored and acid or base added to keep the pH constant. The dissolution rate is calculated from the amount of acid or base consumed over the timeframe of the experiment.

RESULTS

Glass Structure

Raman spectra for glasses along the binary join ZnO-P₂O₅ are shown in Fig. 1. These compositions range from ultraphosphate to slightly more Zn rich than a pyrophosphate (molar ZnO/P₂O₅=0.33).

The predominant structural effect of increasing ZnO is to produce increasingly depolymerized phosphate groups. Composition A has molar $\text{MO}/\text{P}_2\text{O}_5 > 1$ and, therefore, is expected to have branching groups present. This is clearly illustrated in Fig. 1 by the presence of the band at 1324 cm⁻¹, indicative of the P=O stretching vibration.

The presence of phosphate groups with 2 non-bridging oxygens (i.e. chain like groups) is indicated by the intense band at 1204 cm⁻¹, due to the symmetric stretch of the non-bridging oxygens and by the strong band at ~700 cm⁻¹, due to symmetric stretching of the bridging oxygens. Interestingly, less polymerized species such as orthophosphate (970 cm⁻¹) and pyrophosphate (2) (1040 cm⁻¹) are also present, although at low concentrations.

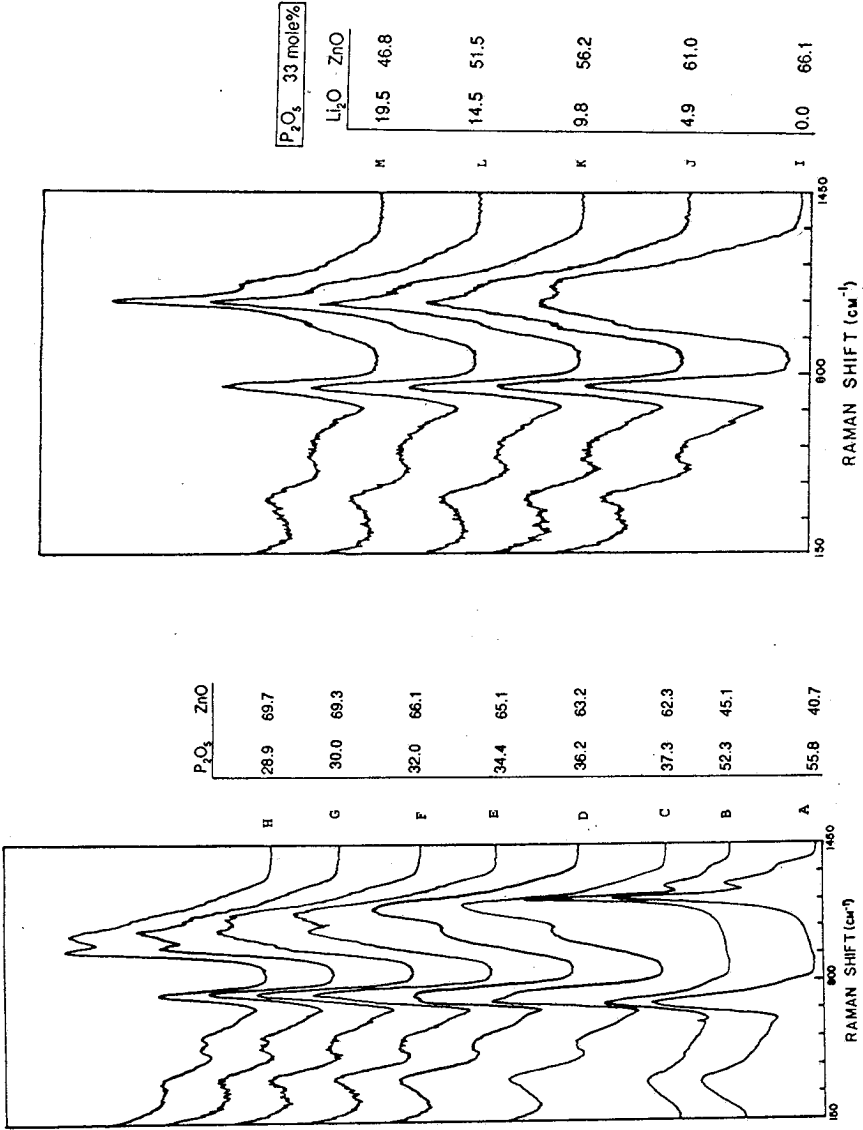


Figure 1. Raman spectra of ZnO-P₂O₅ glasses

Figure 2. Raman spectra of Li₂O-ZnO-P₂O₅ glasses

Dissolution studies of phosphate glasses

The band at 1266 cm^{-1} is not due to a separate phosphate species, but is the asymmetric stretch of bridging POP bonds.

As expected, the addition of ZnO (B-H) causes disruption of the cross-linked groups as well as further depolymerizing the chain species. The result of the depolymerization is to increase the concentration of ortho- and pyrophosphate groups, as shown by the steady and consistent increase in intensity of the bands at 970 cm^{-1} and 1040 cm^{-1} and 760 cm^{-1} .

Intermediate chain length species (e.g. 3-12 PO_4 tetrahedra) are important constituents of compositions between C and H. This is suggested by the observation that there is a gradual downshift in frequency of the band maximum from B (1204 cm^{-1}) to D (1174 cm^{-1}) to H (1106 cm^{-1}). The frequencies of the PO_2 symmetric stretching vibration of intermediate length chain naturally lie between those of the two "end-member" species, pyrophosphate (at 1040 cm^{-1}) and metaphosphate (at 1204 cm^{-1}). This behavior is similar to that calculated for silicates (3) and indicates that progressively smaller phosphate chains are being created. Another observation consistent with the presence of intermediate length chains is that the width of the 1204 cm^{-1} band increases from B to C. This implies that at each composition a distribution of chain lengths exists, the width of the band being directly related to the "broadness" of the chain length distribution. One might, for example, visualize the band at 1152 cm^{-1} in D as being composed of several bands lying between ~ 1100 cm^{-1} and 1204 cm^{-1} with natural linewidths similar to that of the 1204 cm^{-1} band, but which overlap to the extent that they are individually unresolvable, their sum producing the broad band centered at 1174 cm^{-1} . The shift of band frequency from 1204 to 1106 cm^{-1} , then, is a result of the changing relative intensities of the component bands. In any case, as judged by the relative intensity changes in this spectral region, there is a systematic decrease in the concentration of intermediate chain length species relative to ortho- and pyrophosphate species.

Finally, it should be noted that relatively small changes in composition can produce large changes in glass structure. For example, comparison of F and E shows that an ~ 2.0 mole% change in P_2O_5 results in an observable change in glass structure. These changes occur rapidly over a narrow range of compositions and may result in rapid changes in T_g and glass durability.

As shown in Fig. 2, the most pronounced changes resulting from the substitution of Li_2O for ZnO are observed in the spectral region above 800 cm^{-1} . In particular, the bands at ~ 970 cm^{-1} and 1120 cm^{-1} show a dramatic decrease in intensity relative to the band at 1050 cm^{-1} . The substitution of Li_2O for ZnO, therefore, shifts the phosphate species equilibria



to the left, producing pyrophosphate groups at the expense of ortho- and intermediate length chain species.

Glass Durability

The variation of the dissolution rates of a mixed alkali pyrophosphate glass with pH in .01M KCl solution is shown in Fig. 3. For this glass the dissolution rate goes through a minimum at pH=8. Illustrated in Fig. 4 is the effect of temperature on the dissolution rate. Increasing temperature results in a decrease in the dissolution rate for pH<9, but increases the rate in solutions with pH>9. In addition, the pH of minimum dissolution rate shifts slightly to lower pH with increasing temperature.

DISCUSSION

As demonstrated above, the addition of ZnO to P_2O_5 results in progressive depolymerization of the phosphate network. In ultraphosphate compositions, both long chain and branching groups exist, along with small amounts of ortho- and pyrophosphate groups. With further addition of ZnO, branching and long chain species are broken down to produce shorter chain species and increasing amounts of ortho- and pyrophosphate species.

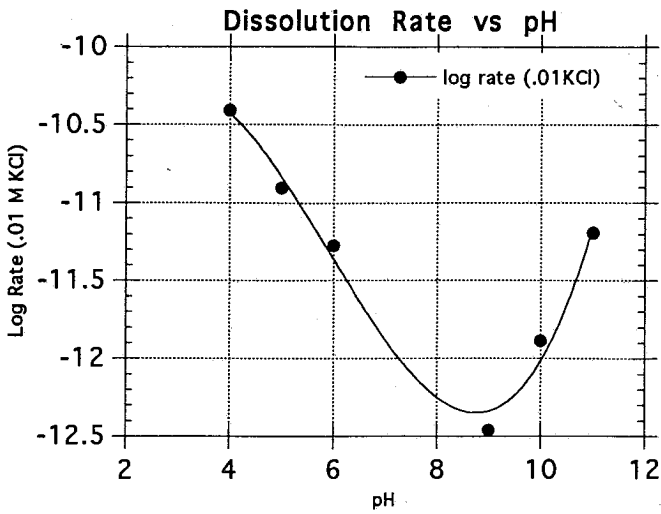


Figure 3. Dissolution rate vs. pH for a mixed alkali pyrophosphate glass.

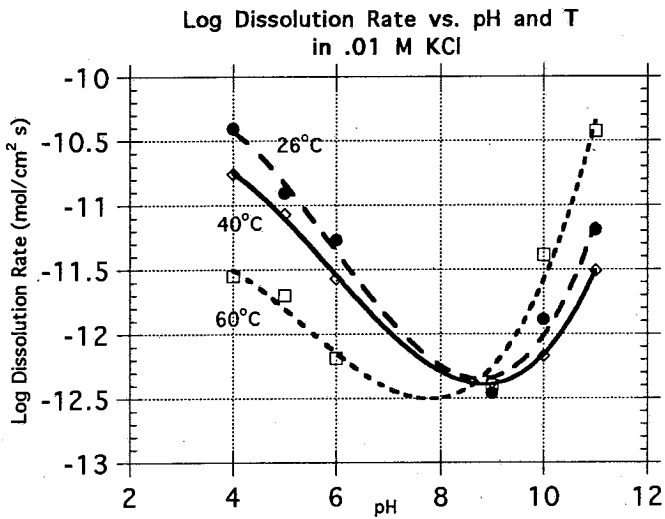


Figure 4. Effect of temperature on dissolution rate

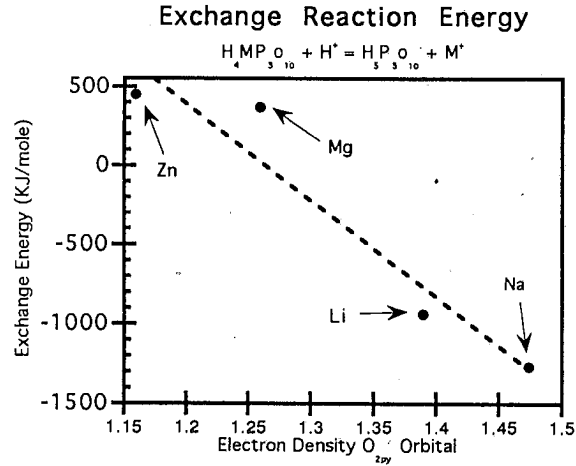


Figure 5. Energy for proton exchange

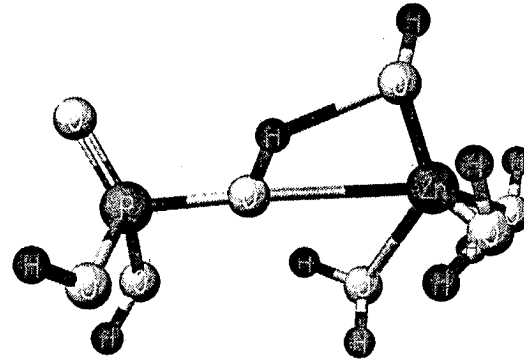
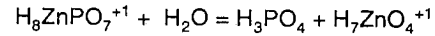
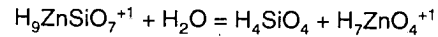


Figure 6. Model of hydrolysis of ZnOP bond.

Table 1. Calculated Thermodynamic Data for Hydrolysis



| T(K) | G(kcal/mole) | $G_{\text{act}}^{\text{Zn}}$ | $G_{\text{act}}^{\text{P}}$ | K_f^{Zn} | K_f^{P} | K_{eq} |
|------|--------------|------------------------------|-----------------------------|--------------------|--------------------|--------------------|
| 300 | -3.75 | 14.05 | 11.41 | 3.66×10^2 | 3.05×10^4 | 5.36×10^2 |
| 360 | -4.24 | 15.65 | 14.41 | 2.38×10^3 | 1.34×10^4 | 3.74×10^2 |
| 400 | -3.81 | 18.17 | 16.80 | 9.90×10^2 | 5.54×10^3 | 1.20×10^2 |



| | | | | | | |
|-----|------|--|--|--|--|-----------------------|
| 300 | 9.73 | | | | | 8.20×10^{-6} |
| 360 | 9.43 | | | | | 1.88×10^{-6} |
| 400 | 9.75 | | | | | 4.72×10^{-6} |

As alkali is substituted for ZnO further changes occur related to the production of pyrophosphate groups at the expense of ortho- and longer chain species. The production of shorter chain species results in increased durability as shown by tabulations of stability constants for aqueous phosphate species (4). For the same cation the order is meta- < tetra- < tri- < pyro- < orthophosphate. Additionally, for the same bulk composition (e.g. pyrophosphate) the stability constants vary systematically with cation type, being greater (implying increased durability) for cations with high field strengths.

The correlation of durability with field strength can be related to the partial charge on the oxygen involved in bonding (5). As a result, it is expected that the ease of protonation of a particular site will depend on the distribution of electron density in the POM bond. Fig. 5 shows the results of ab initio quantum mechanical calculations (STO-3G basis) relating the energy of the exchange reaction of protons with modifying cations to the partial charge on oxygen. Consistent with the variations in aqueous stability constants, low exchange energies (less durable glasses) are associated with high oxygen partial charges. In these cases, the oxygens in the POM bonds are easy to protonate.

Perhaps the most interesting result to come from this study is the observation that the dissolution rate decreases with increasing temperature. A model of this process involving hydrolysis of ZnOP bonds is shown in Fig. 6. This figure shows one possible activated complex formed in the hydrolysis reaction calculated using semi-empirical theory. The thermodynamic properties calculated for the reaction are given in Table 1. As illustrated the activation energies for both possible activated complexes (i.e. H₂O coordinating to Zn or P) increase with increasing T as they should, and the calculated equilibrium constant decreases with increasing T, again consistent with experiment. For comparison, similar calculations for hydrolysis of ZnOSi bonds show that dissolution should increase with increasing T (K_{eq} increases), consistent with observation (6).

CONCLUSIONS

The results of this study show that the addition of modifying cations to P₂O₅ reveals a consistent pattern of cation dependent depolymerization. The substitution of Li for Zn at constant molar P₂O₅ shifts the phosphate species distribution to produce pyrophosphate species at the expense of ortho- and longer chain species. The presence of pyrophosphate species results in increased glass durability as does the presence of cations with high field strengths. Calculations show that high field strength cations reduce the partial charge on oxygen, thus reducing the possibility of protonation reactions.

Glass durability studies on a pyrophosphate composition show that durability is a maximum at pH 8-8.5 and increases with increasing temperature in acidic solutions. This unexpected temperature effect can be explained using quantum mechanical calculations on small clusters modeling hydrolysis of the ZnOP bond.

REFERENCES

1. C.J. Quinn, G.H. Beall and J.E. Dickinson, Proceedings of the XVI International Congress on Glass 4 (1992) 79.
2. M. Tatsumisago, Y. Kowada and T. Minami, Phys. Chem. Glasses 29 (1988) 63.
3. J.E. Dickinson, Mineral Assoc. Canada 12 (1986) 154.
4. K.B. Yatsimirskii and V.P. Vasil'ev, Instability Constants of Complex Compounds Consultants Bureau Enterprises, New York.
5. K. Tanaka and K. Tamaru, Bull. Chem. Soc. Japan 37 (1964) 1862.
6. R. Srycha, Colloids and Surfaces 5 (1982) 147.

GLASS FORMATION AND STRUCTURAL MODELS OF TELLURITE GLASSES

Y. Dimitriev

Higher Institute of Chemical Technology, Sofia-1756, Bulgaria

This work is a summary of the results obtained by a group from Department of Silicate Technology in Sofia concerning tellurite glasses. The structure of these materials was investigated by X-ray diffraction and IR-spectroscopy. The main structural units were determined as $[\text{TeO}_4]$ groups. With the introduction of other components transition from $[\text{TeO}_4]$ to $[\text{TeO}_3]$ groups was established. The presence of a free electron pair influences the low vitrification ability of pure TeO_2 . The glass formation and liquid phase separation regions were determined in three component systems. Different microheterogeneous structures were analyzed using electron microscopy. New manycomponent semiconducting and optical glasses were obtained and their properties were analyzed on the basis of structural peculiarities and the phase diagrams.

INTRODUCTION

The place which the tellurite glasses occupied between the other oxide glasses is determined from short history of their obtaining. Stanworth (1952) (1) started with the investigation of glasses in the system TeO_2 - MoO_3 , TeO_2 - BaO and TeO_2 - V_2O_5 . Later data for glass formation ranges of large number of three component tellurite systems were obtained by Imaoka et al. (1962-1976) (2). The first manycomponent tellurite glasses suitable for industrial production were synthesized by Yahkind and Ovcharenko (1968, 1972) (3). The possibility for obtaining mixed tellurite-halid and tellurite-sulfate glasses were carefully discussed by Vogel et al. (1973) (4). Our own experiments in this field began in 1968 year with vitrification of pure TeO_2 and V_2O_5 with the aid of splat quenching technique (5). After that in our laboratory have been studied glass formation, electric conductivity, chemical resistance and density in different three component tellurite systems (6-8). Essential part of the research performed was connected with the obtaining of structural information for these amorphous materials. The performance of this research program was developed in a several directions:

Determination of the main building units (short range order) which participate in the formation of the network of tellurite glasses.

Construction of the topological models of the networks on the basis of X-ray diffraction and IR-spectra data.

Dependence of the structure of the glasses on composition and relationship with corresponding equilibrium phase diagrams.

Relation between the properties (electrical and optical) and the structure of the glasses.

EXPERIMENTAL

All the glasses were synthesized by melting in silica or in golden palladium crucibles with the application of different cooling rates poring over cooper plate and fast quenching by twin rollers. For the determination of the short range order element and the kind of the structural units were used X-ray diffraction, IR-spectroscopy, TEM, SEM and microprobe analysis (9).

RESULTS AND DISCUSSION

X-ray diffraction. From the X-ray data are obtained radial distribution functions and the main interatomic distances are presented in Table 1. They are assigned respectively to $\text{Te-O}(r_1)$, $\text{O-O}(r_2)$ and $\text{Te-Te}(r_3)$. The main structural units in vitreous TeO_2 are $[\text{TeO}_4]$ -groups. The kind of the polyhedra and the distances between atoms in the network-former are influenced significantly by the type and by the amount of the other components (9-12).

Table 1

| Composition | X-ray source | $r_1, \text{Å}$ | $r_2, \text{Å}$ | $r_3, \text{Å}$ | Structural Units |
|---|------------------|-----------------|-----------------|-----------------|--|
| 80TeO ₂ · 20B ₂ O ₃ | CuK _α | 1,991 | - | 4,12 | TeO ₄ |
| 60TeO ₂ · 40SeO ₂ | CuK _α | 2,00 | - | 4,05 | TeO ₄ + SeO ₃ |
| 25TeO ₂ · 75SeO ₂ | CuK _α | 1,95 | - | 4,12 | TeO ₃ + SeO ₃ |
| 70TeO ₂ · 30GeO ₂ | MoK _α | 1,92 | 2,82 | 3,57 | TeO ₄ + GeO ₄ + GeO ₆ |
| 50TeO ₂ · 50GeO ₂ | MoK _α | 1,87 | 2,83 | 3,42 | TeO ₄ + TeO ₃ + GeO ₄ + GeO ₆ |
| 67TeO ₂ · 33V ₂ O ₅ | MoK _α | 1,82 | 2,79 | 3,62 | TeO ₃ + VO ₅ |
| 50TeO ₂ · 50VO ₂ | CuK _α | 2,00 | - | 3,40 | TeO ₃ + VO ₅ |
| TeO ₂ , 800° C | MoK _α | 1,95 | - | 3,60 | TeO ₄ |
| TeO ₂ , 1200° C | MoK _α | 1,98 | 2,83 | 3,72 | TeO ₄ |
| 80TeO ₂ · 20WO ₃ | MoK _α | 2,00 | 2,73 | 3,82 | TeO ₄ + WO ₄ |
| 60TeO ₂ · 40WO ₃ | MoK _α | 1,95 | - | 3,78 | TeO ₄ + WO ₄ + WO ₆ |
| 67TeO ₂ · 33MoO ₃ | CuK _α | 1,96 | - | 3,80 | TeO ₄ + MoO ₅ |
| 45TeO ₂ · 55MoO ₃ | CuK _α | 2,05 | 2,77 | 3,90 | TeO ₃ + MoO ₅ |
| 80TeO ₂ · 20Nb ₂ O ₅ | MoK _α | 2,00 | 2,81 | 3,85 | TeO ₄ + NbO ₆ |
| 80TeO ₂ · 20BaO | MoK _α | 1,97 | 2,83 | 3,89 | TeO ₄ + BaO ₈ |
| 60TeO ₂ · 40BaO | MoK _α | 2,02 | - | 3,95 | TeO ₄ + BaO ₈ |

IR-spectra. The bands in the IR-spectrum of crystalline TeO_2 are assigned according to C_{2v} point symmetry in the following manner:

$$V_{\text{TeOeq}}^s = 780 \text{ cm}^{-1}; V_{\text{TeOeq}}^{\text{as}} = 714 \text{ cm}^{-1}; V_{\text{TeOax}}^{\text{as}} = 765 \text{ cm}^{-1}; V_{\text{TeOax}}^s = 635 \text{ cm}^{-1}.$$

In the pure TeO_2 -glass the V^s band at 635 cm^{-1} increases markedly instead of $V_{\text{ax}}^{\text{as}} = 675 \text{ cm}^{-1}$ and becomes a determining one. The rise of the V_{ax}^s intensity is the result of a decrease in the symmetry of the polyhedra in the glass network.

The comparison of the IR-spectra indicates that tellurite glasses may divide into several groups:

i) glasses which are characterized by an intensive maximum at $640\text{-}635 \text{ cm}^{-1}$ and a shoulder at about $670\text{-}660 \text{ cm}^{-1}$ possess deformed $|\text{TeO}_4|$ groups.

ii) the second group is characterized by the presence of an intensive maximum at $670\text{-}665 \text{ cm}^{-1}$ and shoulder at $635\text{-}620 \text{ cm}^{-1}$. The main structural unit is again $|\text{TeO}_4|$ group which however is more symmetrical (typical examples are TiTe_3O_8 and ZrTe_3O_8).

iii) the spectra of the third group of glasses are characterized by an intensive band at $680\text{-}675 \text{ cm}^{-1}$. These glasses are build up by $|\text{TeO}_3|$ groups with C_{3v} symmetry (13-16).

Glassformation and liquid phase separation. The introduction of B_2O_3 and GeO_2 in tellurite glasses stimulates the occurrence of liquid phase separation and the formation of a microheterogeneous structure in the glasses as a result of metastable immiscibility. The reason for this behavior is the formation of a new different structural units (Bo_3 , Bo_4 , TeO_4 , TeO_3 , GeO_6 , GeO_4) which are compatible in the network only in a narrow concentration region. The regions of the glass-formation are determined in the $\text{TeO}_2\text{-B}_2\text{O}_3\text{-M}_n\text{O}_m$ systems (Table 2). The introduction of some modifiers as third components narrows the area of the phase separation and stimulates the formation of homogeneous one -phase glass while certain transient ions (Nb^{5+} , W^{6+}) enhance the immiscibility. Different microheterogeneous structures were analyzed using TEM, SEM, MPA (17-20). MoO_3 and SeO_2 stimulate the formation of homogeneous glasses in which network participate $|\text{MoO}_5|$, $|\text{Mo}_2\text{O}_8|$, $|\text{MoO}_6|$ and $|\text{SeO}_3|$ units. It is found that with the increasing of the SeO_2 content the transformation of the network appears from layers to chains and ring-formations. This is a result of the good compatibility of the structural units of the networkformers which participate simultaneously in the structure (21-25). In accordance with the model developed the free electron pair in $|\text{TeO}_4|$ -polyhedra is playing an active role in trend for vitrification of tellurite compositions. The repulsive forces in this zone hindered the free random displacement of the polyhedra in the space during the cooling of the melt. As a result it is difficult to vitrify the pure TeO_2 . The vitrification of complex tellurite compositions may be facilitated by one of the following manners:

i) by an introduction of new structural units compatible with the $|\text{TeO}_4|$ -groups from another components which take part in the composition.

ii) by partly transformation of $|\text{TeO}_4|$ into $|\text{TeO}_3|$ groups.

iii) by creating of non-bridging bonds in the network introducing modifiers.

Phase diagrams. Phase diagrams of the tellurite systems Cu-Te-O , $\text{CuO-TeO}_2\text{-V}_2\text{O}_5$, $\text{Ag}_2\text{O-TeO}_2\text{-V}_2\text{O}_5$, $\text{B}_2\text{O}_3\text{-TeO}_2\text{-V}_2\text{O}_5$ and others are build up (Table 3). A correlation between the structure of the glasses and the kind of the phase diagrams is found. The addition of GeO_2 , B_2O_3 and V_2O_5 in three component systems does not stimulates the formations of new complex compounds. That is why one and the same structure is preserved in more wide composition regions (26-27).

Electrical and optical properties. It is obtained semiconductive tellurite glass with the

Table 2

| Glassformation and Structure of Glasses in Tellurite Systems | Structural Units |
|---|--|
| TeO ₂ TeO ₂ - V ₂ O ₅ TeO ₂ - VO ₂ TeO ₂ - Ag ₂ O TeO ₂ - V ₂ O ₅ - M ₂ O (M=Ag, Li, Na, K, Pb, Cs) TeO ₂ - CuO TeO ₂ - Cu ₂ O - CuO TeO ₂ - V ₂ O ₅ - CuO | TeO ₄ , TeO ₃ VO ₅ , VO ₄ , VO ₆ |
| TeO ₂ - GeO ₂ TeO ₂ - GeO ₂ - M _n O _m (M = V, B) | TeO ₄ , TeO ₃ GeO ₄ , GeO ₆ |
| TeO ₂ - B ₂ O ₃ TeO ₄ TeO ₂ - B ₂ O ₃ - M _n O _m (M=Ag,Cu,Mg,Ca,Sr,Ba, Cd,Zn,Al,In,Sc,La,Ga,Ce,Ti, Nb,Co,Ni,Cr,Fe,Mo,W) | BO ₃ , B ₃ O ₆ BO ₄ , |
| TeO ₂ - B ₂ O ₃ - PbO - Bi ₂ O ₃ TeO ₂ - B ₂ O ₃ - MnO - Fe ₂ O ₃ | |
| TeO ₂ - MoO ₃ TeO ₂ - MoO ₃ - M _n O _m (M = Ce, V) TeO ₂ - WO ₃ TeO ₂ - SeO ₂ V ₂ O ₅ - SeO ₂ TeO ₂ - SeO ₂ - M _n O _m (M=B,Ge,V,Nb,La,Bi,Mo) TeO ₂ - SeO ₂ - V ₂ O ₅ - MoO ₃ | TeO ₄ , TeO ₃ Mo ₂ O ₈ MoO ₆ WO ₄ , WO ₆ TeO ₄ , TeO ₃ SeO ₃ VO ₅ |

Table 3

Tellurite Phase Diagrams

$\text{TeO}_2 - \text{Ag}_2\text{O}$
 $\text{TeO}_2 - \text{CuO}$
 $\text{TeO}_2 - \text{B}_2\text{O}_3$
 $\text{TeO}_2 - \text{GeO}_2$
 $\text{TeO}_2 - \text{SeO}_2$
 $\text{Te} - \text{Cu} - \text{O}$
 $\text{TeO}_2 - \text{SiO}_2$
 $\text{V}_2\text{O}_5 - \text{CuO}$
 $\text{V}_2\text{O}_5 - \text{SeO}_2$
 $2\text{TeO}_2 \cdot \text{V}_2\text{O}_5 - \text{Na}_2\text{O} \cdot \text{V}_2\text{O}_5 \cdot 2\text{TeO}_2$
 $2\text{TeO}_2 \cdot \text{V}_2\text{O}_5 - \text{Ag}_2\text{O} \cdot \text{V}_2\text{O}_5 \cdot 2\text{TeO}_2$
 $\text{TeO}_2 - \text{Ag}_2\text{O} \cdot \text{V}_2\text{O}_5 \cdot 2\text{TeO}_2$
 $\text{Ag}_2\text{O} \cdot \text{TeO}_2 - \text{Ag}_2\text{O} \cdot \text{V}_2\text{O}_5 \cdot 2\text{TeO}_2$
 $\text{Ag}_2\text{O} \cdot \text{V}_2\text{O}_5 \cdot 2\text{TeO}_2 - \text{Ag}_2\text{O} \cdot \text{V}_2\text{O}_5$
 $2\text{TeO}_2 \cdot \text{CuO} - 2\text{TeO}_2 \cdot \text{V}_2\text{O}_5$
 $\text{TeO}_2 \cdot \text{CuO} - 2\text{TeO}_2 \cdot \text{V}_2\text{O}_5$
 $2\text{TeO}_2 \cdot \text{V}_2\text{O}_5 - \text{CuO}$
 $2\text{TeO}_2 \cdot \text{V}_2\text{O}_5 - \text{B}_2\text{O}_3$
 $\text{CuO} - \text{TeO}_2 - \text{V}_2\text{O}_5$
 $\text{Ag}_2\text{O} - \text{TeO}_2 - \text{V}_2\text{O}_5$
 $\text{TeO}_2 - \text{V}_2\text{O}_5 - \text{B}_2\text{O}_3$
 $\text{TeO}_2 - \text{GeO}_2 - \text{B}_2\text{O}_5$

New Tellurite phases

$\text{Ag}_2\text{O} \cdot \text{TeO}_2$
 $\text{SeO}_2 \cdot \text{TeO}_2$
 $\text{Na}_2\text{O} \cdot 3\text{V}_2\text{O}_5 \cdot 6\text{TeO}_2$
 $\text{Ag}_2\text{O} \cdot 3\text{V}_2\text{O}_5 \cdot 6\text{TeO}_2$

participation of V_2O_5 . Glasses of TeO_2 - V_2O_5 - CuO system merit particular interest. Electric memory and threshold switching devices are obtained from these glasses. A nucleation theory was suggested to explain the switching phenomena. The higher conductivity of the tellurite glasses in comparison to the other oxide amorphous semiconductors can be explained by the peculiar inclusion of $[TeO_3]$ groups in the vanadate network without a destruction of the bridging V-O-V bonds (28-32).

CONCLUSION

The results obtained show that it is possible to be synthesized stable low melting glasses in multicomponent tellurite systems if the participation of different modifiers and network formers. It is established that the tellurium changes its coordination against the oxygen (TeO_4 - TeO_3) with the variation of the composition. By this manner it is possible to be formed different networks and to modify the properties of the glasses in more wide limits.

ACKNOWLEDGEMENTS

The author would like to thank to Dr. Y. Ivanova, Dr. V. Dimitrov, Dr. E. Gattef, Dr. E. Kashchieva, Dr. L. Lakov, Dr. H. Petkov and Dr. M. Arnaudov for their experimental support and helpful discussion of many years joint research collaboration. The preparation of this work and the possibility to be submitted has been achieved by the financial support by Ministry of Education and Science contract No. 208, 1993.

REFERENCES

1. J. E. Stanworth, *J.Soc. Glass.Tech.*, 34(1952)171.
2. M. Imaoka and T. Yamazaki, *Rep.Inst.Ind.Sci.Univ.,Tokyo*, 26(1)(1976)1.
3. A.K.Yahkind, H.Ovcharenko and G. Petrovskii, *Pat.USSR 358280(1972)*.
4. W. Vogel, P. Eckart and H. Burger, *Pat. DDR 97188(1988)*.
5. Y. Dimitriev, M.Marinov and A.Stoianov, *Compt.Rend.Acad.Bulg.Sci.*, 21(1968)661.
6. Y. Dimitriev, M.Marinov and Y.Ivanova, *Compt.Rend.Acad.Bulg.Sci.*, 22(1969)1047.
7. Y. Dimitriev, M. Marinov and Y.Ivanova, *Compt.Rend.Acad.Bulg.Sci.*, 24(1971)319,897,1069.
8. Y.Dimitriev, M.Marinov, Y.Ivanova and L.Lakov, *Compt.Rend.Acad.Bulg.Sci.*, 25(1972)1533.
9. V. Dimitrov, Thesis (1978), HICHT, Sofia.
10. Y. Dimitriev, V. Dimitrov, E. Gattef, E. Kashchieva and H.Petkov, *J.Non-Cryst.Solids*, 95/96(1978)937.
11. Y.Dimitriev and V. Dimitrov, *Mat.Res.Bull.*, 13(1978)25.
12. H. Petkov, Thesis (1988) HICHT, Sofia.
13. M.Arnaudov, V. Dimitrov, Y.Dimitriev and L.Markova, *Mat.Res.Bull.*, 17(1982)1121.
14. Y. Dimitriev, V. Dimitrov, M.Arnaudov, *J.Mat.Sci.*, 18(1983)1353.
15. Y. Dimitriev, M.Arnaudov, V.Dimitrov and H.Petkov, *ISCMP Proc.Disordered Systems and new Materials*, (eds. M.Borisov,N.Kirov,A.Vavrek, World Sci. Singapore, 1989),p. 530.
16. M. Dimitrova-Pankova, Y.Dimitriev, M.Arnaudov and V.Dimitrov, *Phys.Chem.Glasses*, 30(1989)260.
17. E.Kashchieva, Thesis (1984)Sofia.
18. Y. Dimitriev, E.Kashchieva and E.Gurov, *Mat.Res.Bull.*, 11(1976)1379.
19. Y. Dimitriev, E. Kashchieva, *J.Mat.Sci.*, 10(1975)1419.
20. Y. Dimitriev, E.Kashchieva and M.Koleva, *J.Mat.Sci.*, 16(1981)3045.
21. L.Lakov, Thesis(1988)HICHT, Sofia.
22. L.Lakov, Y.Dimitriev, *Phys.ChemGlasses*, 22(1981)76.
23. L.Lakov, Y.Dimitriev, Y.Ivanova and V.Dimitrov, *J.Mat.SciLett.*, 84(1986)124.
24. Y.Dimitriev, V.Dimitrov, L.Lakov, *Phys.Chem.Glasses*, 29(1988)45.
25. Y. Dimitriev, JcJ Bart, Y.Ivanova, V.Dimitrov, *Z.anirg.allq.Chem.*, 562(1988)175.
26. Y.Ivanova, Thesis(1974)HICHT, Sofia.
27. Y.Ivanova, Y.Dimitriev, *Mat.Chem.Phys.*, 12(1985)397.
28. E.Gattef, Thesis (1984), Sofia University.
29. E. Gattef, Y.Dimitriev, *Int.J.Electr.*, 62(1987)757.
30. E.Gattef, Y.Dimitriev, *Phil.Mag.B43(1981)333*.
31. Y.Dimitriev, E.Gattef, A.Eneva, *Int.J.Electr.*, 50(1981)385.
32. E.Gattef, Y.Dimitriev, *Proc.Int.Conf.Amourph.Semicond.*, Pardubice, 1978, p. 585

STRUCTURE OF VANADATE GLASSES

Vesselin Dimitrov

Higher Institute of Chemical Technology
Sofia 1756, Bulgaria

It is established on the basis of IR-spectral data of binary vanadate glasses from the $Me_xO_y-V_2O_5$ systems (Me = Mg, Ca, Sr, Ba, Pb, Co, Ni, Cu, Mn, Zn, and Cd) that the frequency of the V-O vibrations decreases with increase in Me_xO_y content in the case of transitions toward meta-, pyro-, and orthovanadate glass structure. This is related to the change in the coordination number of vanadium from 5 to 4. Structural models of the glasses are suggested on the basis of VO_5 , V_2O_6 , V_2O_7 , and VO_4 units.

INTRODUCTION

Vanadate glasses form a relatively new class of vitreous materials belonging to the amorphous oxide semiconductors and possessing electronic conductivity. Since electron transport depends on the structure it is of interest to study the short range order of these glasses. The present investigation is one of a sequence of papers presented by us, on the structure of vanadate glasses, using IR-spectroscopy (1-6). The purpose of the present work is an IR-spectral study on the structure of a great number of binary vanadate glasses with different Me_xO_y/V_2O_5 ratio (Me = Mg, Ca, Sr, Ba, Pb, Co, Ni, Cu, Mn, Zn, and Cd).

EXPERIMENTAL

The glasses were obtained by melting chemically pure oxides or metal carbonates and V_2O_5 in porcelain and quartz crucibles in the 800-1200°C temperature range. Vitrification was achieved by rapid cooling of the melt using a roller technique. The IR-spectra of the glasses and crystal products were recorded on a two-beam UR-10 spectrophotometer (Karl Zeiss, Jena) in the 1200 - 400 cm^{-1} range. The samples for these measurements were prepared as suspensions in liquid paraffin. The precision of the absorption maxima is $\pm 1,5 cm^{-1}$ for the crystalline samples and $\pm 3 cm^{-1}$ for the glasses. The individual crystalline and vitreous phases were identified using a X-ray DRON-IN diffractometer (CuK_{α} - radiation, Ni-filter).

RESULTS AND DISCUSSION

The IR-spectra of pure crystalline and vitreous V_2O_5 are presented in Fig. 1. Figs. 2, 3 show the IR-spectra of metavanadate glasses and crystalline phases $Me(VO_3)_2$ and MeV_2O_6 . Fig. 4 give the IR-spectra of the pyrovanadate glasses and crystals $Me_2V_2O_7$. The IR-spectra of $Pb_3(VO_4)_2$ glass and corresponding crystal are presented in Fig. 5.

The comparison of the glass spectra with the spectra of crystal products is carried out in accordance with the concept of independent vibrations in glasses, discussed in detail in the works by Tarte (7, 8) and Condrate (9). It is assumed that vibrations of the characteristic groups of atoms in the network are independent of the vibrations of the other groups. Such an empirical treatment can provide significant information on the arrangement of atoms in glasses. The approach used requires preliminary analysis

of the structures and spectral data on the crystalline phases formed in the systems.

IR-spectra of vanadates in crystalline and vitreous state have characteristic bands in the 1020-750 cm^{-1} range. The IR-spectrum of pure crystalline V_2O_5 (Fig. 1) is characterized by an intense band at 1020 cm^{-1} , referred to the vibration of the isolated $\text{V}=\text{O}$ vanadyl groups in the VO_5 trigonal bipyramids, a wide absorption band at 830-820 cm^{-1} related to vibrations of the V-O-V chains in the lattice and bands about 600 cm^{-1} which correspond mainly to the bending vibrations (10-12). It is found that the IR-spectrum of the vitreous V_2O_5 is similar to that of the crystal (1). As obviously seen in Fig. 1 the band at 1020 cm^{-1} is preserved. This signifies that the isolated $\text{V}=\text{O}$ bonds are preserved in the vitreous structure. This is an indication that VO_5 groups similar to those in the crystal take part in the glass network.

In the case of transitions toward meta-, pyro-, and orthovanadates, the frequency of the V-O vibrations decreases and this is related to the decrease in the coordination number of vanadium.

Crystalline metavanadates show two types of chain structure depending on the coordination number of the V^{5+} -ion. When VO_4 groups are presented, the metavanadate chains are built up by corner linking these groups, as in alkaline metavanadates and $\text{Ba}(\text{VO}_3)_2$ (13, 14). Moreover, two of the V-O bonds are shorter and non-bridging ones, forming VO_2 groups. The main unit for such structures is $(\text{VO}_3)_n^n$. The normal coordinative analysis of the VO_3 -ion in alkaline crystal metavanadates has been carried out by Botto et al. (15). There are symmetrical stretching vibrations of the VO_2 groups ($\nu^s_{\text{VO}_2} = 960\text{-}910 \text{ cm}^{-1}$) and antisymmetrical stretching vibrations of the same groups ($\nu^{\text{as}}_{\text{VO}_2} = 900\text{-}840 \text{ cm}^{-1}$). Similar spectra possess crystalline $\text{Ca}(\text{VO}_3)_2$ and $\text{Ba}(\text{VO}_3)_2$ (16, 17).

The high-frequency band in the spectra of the alkaline-earth metavanadate glasses (Fig. 2) is present in the 935-920 cm^{-1} range. The similarity in the spectra of the different glasses with that of crystalline $\text{Ca}(\text{VO}_3)_2$ and $\text{Ba}(\text{VO}_3)_2$ (16, 17), give an indication for similarities of the short range order. Therefore, the bands in the 935-920 cm^{-1} range in the IR-spectra of alkaline-earth metavanadate glasses could be assigned to the stretching vibrations of VO_2 groups in the VO_4 tetrahedra.

The other type of metavanadate structure is typical of the MeV_2O_6 compounds ($\text{Me} = \text{Cu}, \text{Co}, \text{Zn}$) (18-20), which consist of VO_5 groups as coordination polyhedra of vanadium. The polyhedra are bonded in a chain by means of common edges, but in such way that here also two of the V-O bonds are shorter and non-bridging ones, forming VO_2 groups. The basic unit of these structures is $(\text{V}_2\text{O}_6)_n^{2n}$. The non-planar complexes of this type possess 8 IR-active vibrations according to Nakamoto (21), four of which are stretching vibrations of the VO_2 groups and four are V_2O_2 bridge vibrations.

It is seen from the spectra presented in Fig. 3 that the spectra of Co and Cu metavanadate glasses in general lines repeat the spectra of the corresponding crystals, which is an indication for a similarity in the structure. This means that the structure of these glasses could be interpreted mainly on the basis of VO_5 groups with two terminal V-O bonds.

The spectra of Ni, Zn, and Cd metavanadate glasses demonstrate an exception from the series (Fig. 3). Together with the bands in the 960-955 cm^{-1} range, a high-frequency band is observed at 1010-1005 cm^{-1} , which is absent in the spectra of the crystals. Therefore,

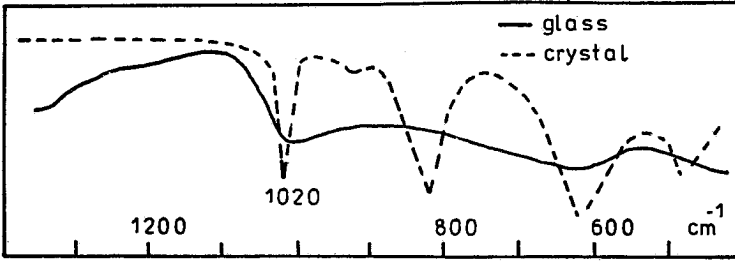
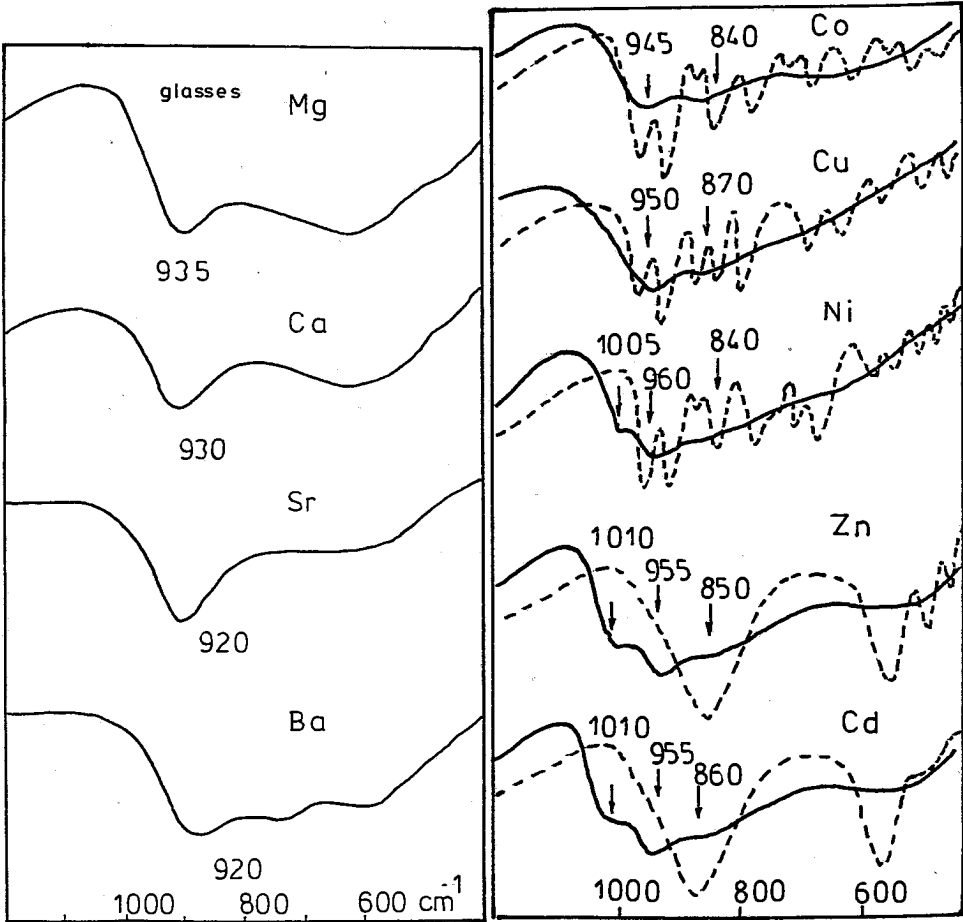


Fig. 1. IR-spectra of V_2O_5 ,



Figs. 2,3. IR-spectra of metavanadate phases

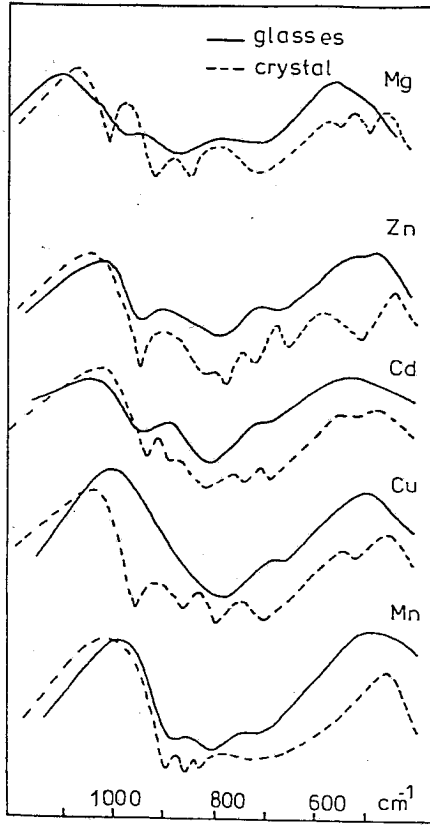


Fig. 4. IR-spectra of pyrovanadate phases

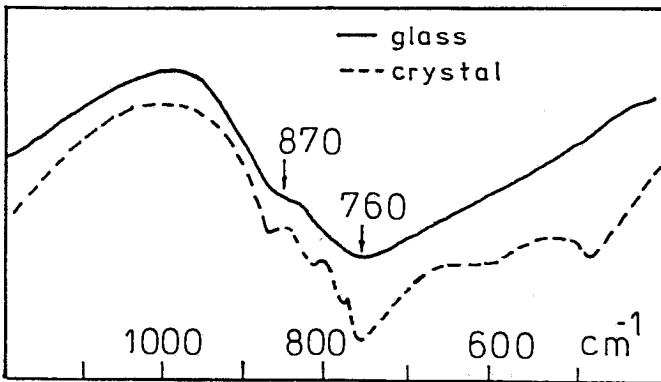


Fig. 5. IR-spectra of $Pb_3(VO_4)_2$

besides the fragments of the chain structure (bands at 960-955 cm^{-1}), structural units similar to V_2O_5 , with a shorter non-bridging bond (band at 1010-1005 cm^{-1}), are present.

Simultaneously a high-frequency band in the spectra of crystalline ZnV_2O_6 and CdV_2O_6 lies at 860 cm^{-1} . This fact may be explained with the localization of the Zn and Cd-ions in the area of the VO_2 groups. This creates favourable conditions for the realization of bonds of the Zn(Cd)-O-V type where the isolated nature of the VO_2 groups decreases. Thus the band at 860 cm^{-1} of the crystal spectra may be assigned to the vibrations of this type of bonds.

Crystal pyrovanadates show two type of structures also according to the kind of V-O-V bridge in the isolated V_2O_7 ($\text{O}_3\text{V-O-VO}_3$) pyro-groups. The main coordination polyhedra of vanadium are VO_4 tetrahedra. Mg, Ca, Sr, Zn and Co pyrovanadates belong to type of dichromate structure (22) with the V-O-V angle being smaller than 180°. Cd, Cu and Mn pyrovanadates belong to type of tortvaitite structure (23) and V-O-V angle in pyro-groups is 180°. The normal coordinate analysis of V_2O_7 -ion in a great number crystalline pyrovanadates has been carried out by Baran et al. (24). The symmetrical and antisymmetrical stretching vibrations of the terminal VO_3 groups are found in the ($\nu^s_{\text{VO}_3} = 980\text{-}880 \text{ cm}^{-1}$) and ($\nu^{\text{as}}_{\text{VO}_3} = 920\text{-}850 \text{ cm}^{-1}$) ranges. In addition to them, there are also two stretching vibrations of the V-O-V bridge in the case of pyrovanadates with dichromate structure ($\nu^{\text{as}}_{\text{VOV}} = 770\text{-}650 \text{ cm}^{-1}$, $\nu^s_{\text{VOV}} = 590\text{-}530 \text{ cm}^{-1}$).

It is seen from Fig. 4 that a good correspondence exist between the IR-spectra of crystalline and vitreous pyrovanadates. The band in the 950-880 cm^{-1} range in the spectra of glasses is close in value to the vibration $\nu^s_{\text{VO}_3}$ in the crystals. The band in the 850-760 cm^{-1} range falls in the range of the antisymmetrical stretching vibrations of the terminal VO_3 groups ($\nu^{\text{as}}_{\text{VO}_3}$). The band in the 700-650 cm^{-1} range can be interpreted as $\nu^{\text{as}}_{\text{VOV}}$ of the V-O-V bridges between two adjacent VO_4 tetrahedra in the V_2O_7 units. One is impressed by the fact that in the spectra of the pyrovanadate glasses no band is observed which could be related to the symmetrical vibration of the V-O-V bridge. According to (25) this means a change of the V-O-V bridge angle to 180° in the glass structure.

As a final member of the vanadate glasses investigated here, the lead orthovanadate glass $\text{Pb}_3(\text{VO}_4)_2$ is examined. The characteristic absorption band (Fig. 5) is located at 760 cm^{-1} , with a shoulder at 870 cm^{-1} . The spectrum of the corresponding crystalline phase is better resolved, but is similar. On the basis of the results in (26, 27) for the spectral and structural data for crystalline orthovanadates, the band at 760 cm^{-1} in the spectrum of the glass should be assigned to the threefold stretching vibration (ν^d_{VO}). The shoulder at 870 cm^{-1} may be assigned to the symmetrical stretching vibration (ν^s_{VO}) of the V-O bonds of the VO_4 tetrahedra.

CONCLUSION

The experimentally observed bands in the spectra of different vanadate glasses have been assigned and structural conclusions have been made for the short range order. It is established that the basic structural units participating in the formation of the glass forming networks are VO_5 , V_2O_6 , V_2O_7 and VO_4 groups possessing isolated non-bridging V-O bonds.

This research work was supported by the Bulgarian Foundation of Science,

Contract X-208, 1993.

REFERENCES

1. Y. Dimitriev, M. Arnaudov and V. Dimitrov, *Mh. Chem.* 107 (1976) 1335.
2. Y. Dimitriev, V. Dimitrov, M. Arnaudov and D. Topalov, *J. Non-Cryst. Solids* 57 (1983) 147.
3. V. Dimitrov and Y. Dimitriev, *Ann. Ecole Super. Chimie Techn.* 29 (1983) 376.
4. V. Dimitrov and Y. Dimitriev, *Proc. Colloq. Spectr. Int. XXIV, Garmisch-Partenkirchen 1* (1985) 160.
5. V. Dimitrov and Y. Dimitriev, *J. Non-Cryst. Solids* 122 (1990) 133.
6. V. Dimitrov and Y. Dimitriev, *Proc. Int. Conf. on Science and Technology of New Glasses, Tokyo, (1991)*, p.305.
7. P. Tarte, *Spectrochim. Acta* 18 (1962) 467.
8. P. Tarte in *Physics of Non-Cryst. Solids* (Elsevier Science Publ., Amsterdam, 1964) p. 101.
9. R. A. Condrate in *Introduction to Glass Science* (Plenum Press, New York, 1972) p. 101.
10. C. C. Barraclough, J. Lewis and R. S. Nyholm, *J. Chem. Soc. A* (1959) 3552.
11. T. R. Gilson, O. Bizri and N. Cheethom, *J. Chem. Soc. Dalton Trans. Inorg. Chem.* 3A (1973) 291.
12. L. Abello, E. Husson, Y. Repelin and G. Lucazeau, *Spectrochim. Acta* 39A (1983) 641.
13. H. Evans, *Z. Kristallogr.* 114 (1960) 257.
14. S. Launay and J. Thoret, *C. R. Acad. Sc. D* 27 (1973) 541.
15. I. Botto, E. Baran and P. Aymonino, *Mh. Chem.* 107 (1976) 1127.
16. L. Frederckson and D. Hausen, *Anal. Chem.* 35 (1963) 818.
17. J. Duppuis, *Therm. Acta* 24 (1968) 252.
18. J. Angenault and A. Rimski, *C. R. Acad. Sc. C*, 267 (1968) 227.
19. D. Lavand and J. Gally, *Bull. Soc. fr. Min. Cryst.* 95 (1972) 134.
20. B. Tonnies and H. Buschbaum, *Z. anorg. allg. Chem.* 508 (1984) 77.
21. K. Nakamoto, *Infrared and Raman Spectra of Inorganic and Coordination Compounds* (John Wiley Sons, New York, 1978).
22. R. Gopal and C. Calvo, *Canad. J. Chem.* 51 (1973) 1004.
23. P. Au and C. Calvo, *Canad. J. Chem.* 45 (1967) 2297.
24. E. Baran, J. Pedregosa and P. Aymonino, *Mh. Chem.* 106 (1975) 1085.
25. E. Baran and P. Aymonino, *Z. anorg. allg. Chem.* 365 (1969) 211.
26. E. Baran, I. Botto, J. Rames and P. Aymonino, *Mh. Chem.* 109 (1978) 1139.
27. E. Baran, *Mh. Chem.* 106 (1975) 1.

INDUCED CRYSTALLIZATION OF GLASSES

I. Gutzow, A. Dobрева

Institute of Physical Chemistry, Bulgarian Academy of Sciences, Sofia 1113, Bulgaria

The possibilities and limitations of different methods of induced crystallization of glasses - introduction of active crystallization cores, of surfactants and surface induced crystallization - are analyzed from the standpoint of the classical theory of nucleation. Particular attention is given to the problem of determination of the activity of solid substrates by using an approach in which both the energetics of adhesion and structural mismatching are taken into account. Experimental results on the nucleating activity of metal nucleants in model glass forming systems are considered.

A comparative study is made on the advantages and restrictions of different methods of induced crystallization and possible technical applications are discussed.

INTRODUCTION

The classical theory of phase formation indicates that there are three ways to catalyze nucleation in an undercooled melt (1,2):

i/ to decrease the viscosity of the melt

ii/ to introduce active substrates

iii/ to lower the interfacial energy at the crystal/melt boundary.

The first method, decreasing the viscosity of the melt, has found a wide application in the technology of organic polymers. Crystallization from solution can be considered as a limiting case of this method.

The second method, introduction of active substrates, acquired significance in the production of glass ceramic materials (3,4). The main advantage of heterogeneous nucleation is that with sufficiently active substrates, the number of crystallites formed is directly determined by the number of the insoluble crystallization cores. Further, a wide spectrum of nucleating agents can be used in the heterogeneous catalysis in order to guarantee the most efficient nucleation in different liquids.

Polymer systems, both organic and inorganic, because of their relatively low melting temperatures, known crystallization parameters and easy possibilities for quenching may serve as convenient experimental models in investigating the nucleating activity of insoluble foreign additives (5,6).

This paper deals with the problem of the nucleating efficiency of active cores and considers the factors on which it depends on from a generalized thermodynamic standpoint. Experimental data for the activity of noble metal particles in the induced crystallization of organic and inorganic glass formers are also given.

NUCLEATING ACTIVITY OF SUBSTRATES

The studies of the nucleating activity of substrates have been based so far on the principle of crystallographic matching and mismatching (7). However, experiments during the past two decades have shown that this approach (including Dankov's rule) can not serve as a background for a specific interpretation of catalytic efficiency of substrates in inorganic glass forming systems and in polymers. Besides the crystallographic misfit, the forces of interaction between the substrate and the overgrowing crystal should also be accounted for, as done in the present analysis.

In the framework of the capillary version of the classical theory of nucleation, the steady state rate, I , of homogeneous formation of three dimensional nuclei can be defined as

$$I = \text{const}_1 \left(\frac{N_o}{\eta} \right) \exp \left(- \frac{A_k}{kT} \right) \quad /1/$$

Here η is the bulk viscosity of the undercooled melt at temperature T , A_k is the thermodynamic work of formation of three dimensional nuclei, k is Boltzmann's constant and N_o is the concentration of ambient phase molecules.

When active substrates are added in the system, the thermodynamic work A_k^* for heterogeneous nucleation is lowered by a factor Φ , i.e.

$$A_k^* = A_k \Phi \quad /2/$$

The factor Φ which accounts for the nucleating activity of foreign substrates can vary from $\Phi = 1$ (inactive substrates) to $\Phi = 0$ (very active crystallization cores). If $\Phi < 0$, two dimensional nucleation should be expected.

Accepting Kaischew's model of a cubic crystal on a flat substrate (8), the nucleating activity, Φ , can be defined in a very general way as

$$\Phi = 1 - \frac{\beta}{2\sigma_{cf}} \quad /3/$$

Here β is the adhesion energy between the newly formed phase and the substrate and σ_{cf} is the specific surface energy at the crystal/ambient phase interface. The adhesion energy, β , can be expressed through the values of the specific surface energy at the crystal/melt interface (σ_{cf}), at the substrate/melt boundary (σ_{sf}), at the crystal/substrate interface (σ^*) and through the total energy E_d of misfit dislocations as follows

$$\beta = \sigma_{cf} + \sigma_{sf} - \sigma^* - E_d \quad /4/$$

Following van der Merwe (9), E_d can be determined by the expression

$$E_d \approx \frac{K_{in} d_i}{4\pi^2} f(s, c) \quad /5/$$

where d_i denotes a reference lattice parameter, K_{in} is the shear modulus at the substrate/crystal interface and $f(s, c)$ is a complicated function of the natural misfit existing between the substrate and the deposit crystal. At small misfits $f(s, c) \approx 0$ and for misfits larger than 10%, $f(s, c) \approx 1$.

The quantities appearing in eq./4/ can be easily expressed through the forces of cohesion in the substrate ψ_{ss} , in the crystal ψ_{cc} and in the melt ψ_{ff} (σ) as

$$\sigma^* \approx \frac{1}{2d_i^2} \left[(\psi_{ss})^{1/2} - (\psi_{cc})^{1/2} \right]^2 \quad /6a/$$

$$\sigma_{sf} \approx \frac{1}{2d_i^2} \left[(\psi_{ss})^{1/2} - (\psi_{ff})^{1/2} \right]^2 \quad /6b/$$

$$\sigma_{cf} \approx \frac{1}{2d_i^2} \left[(\psi_{cc})^{1/2} - (\psi_{ff})^{1/2} \right]^2 \quad /6c/$$

$$E_d \approx \text{const} \left(\psi_{ss} + \left(\frac{z_c}{z_s} \right) \psi_{cc} \right) f(s, c) \quad /6d/$$

Here z_c and z_s denote the coordination number of the crystal and of the substrate, respectively.

Introducing eqs./4,6/ into eq./3/ we obtain

$$\Phi = C_1 - \left(\frac{1}{\varepsilon_2}\right)^{1/2} \left(\frac{\psi_{ss}}{\psi_{cc}}\right)^{1/2} (1 - C_2) \quad /7/$$

Here C_1 and ε_2 are constants dependent only on the cohesive forces of the nucleated system (the undercooled melt and the respective overgrowing crystal). For crystals melting without molecular reconstruction ε_2 is about 1.10^{-1} . The term C_2 is proportional to the misfit existing between the lattices of the deposit crystal and the substrate i.e.

$$C_2 = const v_1 f(s, c) = const \left[\left(\frac{\psi_{ss}}{\psi_{cc}}\right)^{1/2} + \left(\frac{z_c}{z_s}\right)^{1/2} \left(\frac{\psi_{cc}}{\psi_{ss}}\right)^{1/2} \right] f(s, c) \quad /8/$$

Accounting for the proportionality of the cohesive forces with the heat of sublimation, λ_{ki} , with the heat of melting λ_{mi} , and the temperature of melting T_{mi} , eq./7/ can be easily transformed into

$$\Phi = C_1 - \left(\frac{1}{\varepsilon_2}\right)^{1/2} \left(\frac{z_c \lambda_{ks}}{z_s \lambda_{kc}}\right)^{1/2} (1 - C_2) \quad /7a/$$

$$\Phi = C_1 - \left(\frac{1}{\varepsilon_2}\right)^{1/2} \left(\frac{z_c \lambda_{ms}}{z_s \lambda_{mc}}\right)^{1/2} (1 - C_2) \quad /7b/$$

$$\Phi = C_1 - \left(\frac{1}{\varepsilon_2}\right)^{1/2} \left(\frac{z_c T_{ms}}{z_s T_{mc}}\right)^{1/2} (1 - C_2) \quad /7c/$$

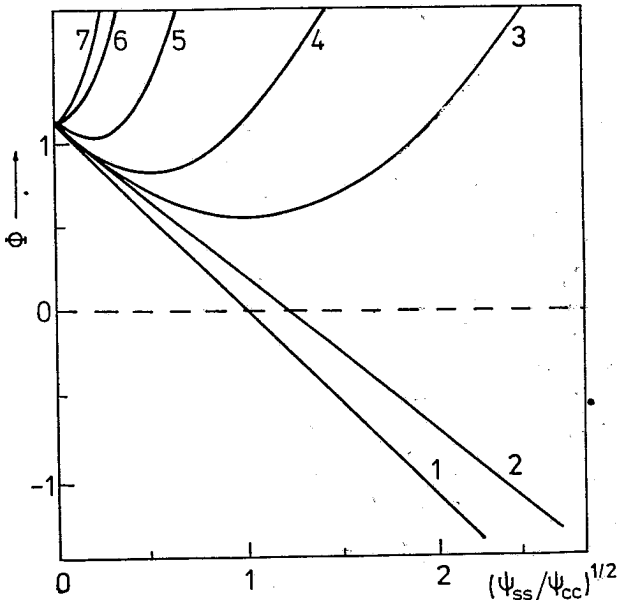


Figure 1: Dependence of the substrate activity Φ on the ratio $(\psi_{ss}/\psi_{cc})^{1/2}$ for the induced crystallization in undercooled melts for different values of the ratio $q = C_2/v_1$: 1 - $q = 0.01$; 2 - $q = 0.1$; 3 - $q = 0.5$; 4 - $q = 1$; 5 - $q = 3$; 6 - $q = 10$; 7 - $q = 15$.

Thus, eqs./7/ allow direct comparison with experimental data. When $C_2 \ll 1$ i.e. at negligible misfit effects, eqs./7/ are reduced to

$$\Phi = C_1 - \left(\frac{1}{\varepsilon_2} \right)^{1/2} \left(\frac{\psi_{ss}}{\psi_{cc}} \right)^{1/2} \quad /9/$$

$$\Phi = C_1 - \left(\frac{1}{\varepsilon_2} \right)^{1/2} \left(\frac{z_c \lambda_{ks}}{z_s \lambda_{kc}} \right)^{1/2} \quad /9a/$$

$$\Phi = C_1 - \left(\frac{1}{\varepsilon_2} \right)^{1/2} \left(\frac{z_c \lambda_{ms}}{z_s \lambda_{mc}} \right)^{1/2} \quad /9b/$$

$$\Phi = C_1 - \left(\frac{1}{\varepsilon_2} \right)^{1/2} \left(\frac{z_c T_{ms}}{z_s T_{mc}} \right)^{1/2} \quad /9c/$$

and a decreasing Φ vs. $(\psi_{ss})^{1/2}$ dependence (respectively Φ vs. $(\lambda_{ks})^{1/2}$, Φ vs. $(\lambda_{ms})^{1/2}$ or Φ vs. $(T_{ms})^{1/2}$) should be expected having a slope proportional to the cohesive forces in the overgrowing crystal (see fig.1).

In the case when $C_2 \gg 1$ i.e. at dominant misfit effects, eqs./7/ predict a more complicated Φ vs. $(\psi_{ss})^{1/2}$ dependence as seen from fig.1. For narrow λ_{ks} intervals at relatively high λ_{ks} values an increasing Φ vs. $(\lambda_{ks})^{1/2}$ course also can be expected.

EXPERIMENTAL EVIDENCE

Experimental data on the nucleating activity of noble metal particles in the induced crystallization of sodium metaphosphate (NaPO_3), sodium tetraborate ($\text{Na}_2\text{B}_4\text{O}_7$), polyethylene terephthalate (PET) and polyvinyl chloride (PVC) will be considered in the framework of the formalism developed in the previous section.

The crystallization of sodium metaphosphate melts catalyzed by Ag, Au, Cu, Rh, Pd, Pt and Ir was studied by Gutzow et al (11). NaPO_3 melts are constructed of anionic polymer chains. Upon crystallization, orthorhombic $\alpha\text{-Na}_3\text{P}_3\text{O}_9$ crystals are formed as a result of a process of anionic reconstruction. Figure 2a shows the dependence of the activity Φ of the noble metals on their heats of sublimation. It is seen from the figure that the substrates can be arranged in the following sequence of increasing nucleating activity: $\text{Au} < \text{Ag} \approx \text{Rh} < \text{Cu} < \text{Pd} < \text{Pt} < \text{Ir}$ (or $\Phi_{\text{Ir}} < \Phi_{\text{Pt}} < \Phi_{\text{Pd}} < \Phi_{\text{Cu}} < \Phi_{\text{Rh}} \approx \Phi_{\text{Ag}} < \Phi_{\text{Au}}$).

Considering eq./9a/, the slope of the Φ vs. $(\lambda_{ks})^{1/2}$ dependence is determined by the heat of sublimation of sodium metaphosphate. Thus, the λ_{ks} for NaPO_3 is about 100kJ/mol which is a reasonable value.

In ref.(12) it was found that the metal crystals employed in the case of NaPO_3 can also induce crystallization in polyethylene terephthalate. The dependence of the value of Φ on the heats of sublimation of the substrates is presented on fig. 2b. In comparing fig. 2a and fig. 2b it is seen that the values of Φ in NaPO_3 are considerably lower than those in PET. Moreover, the Φ vs. $(\lambda_{ks})^{1/2}$ course in NaPO_3 is a decreasing one according to eq./9a/ with zero misfit while in PET this function is an increasing one. In terms of eq./7/ this trend is an indication for considerable misfit effects in PET/noble metal systems.

Figure 2c shows the nucleating activity of Au, Pd, Pt, Ru in the induced crystallization of polyvinyl chloride films obtained from cyclohexanone solutions (13). It is seen from the figure that the substrate with the highest melting temperature as in the case of NaPO_3 , is the

most active ($Au < Pd < Pt < Ru$ or $\Phi_{Ru} < \Phi_{Pt} < \Phi_{Pd} < \Phi_{Au}$). The slope of the $\Phi (\lambda_{ks})^{1/2}$ dependence gives a value of λ_{ks} equal to 500 kJ/mol (see eq. /9a/).

Semiquantitative results on the nucleation ability of metal cores in sodium tetraborate are presented in fig. 2d (14). A decreasing $\Phi (\lambda_{ks})^{1/2}$ dependence is again observed.

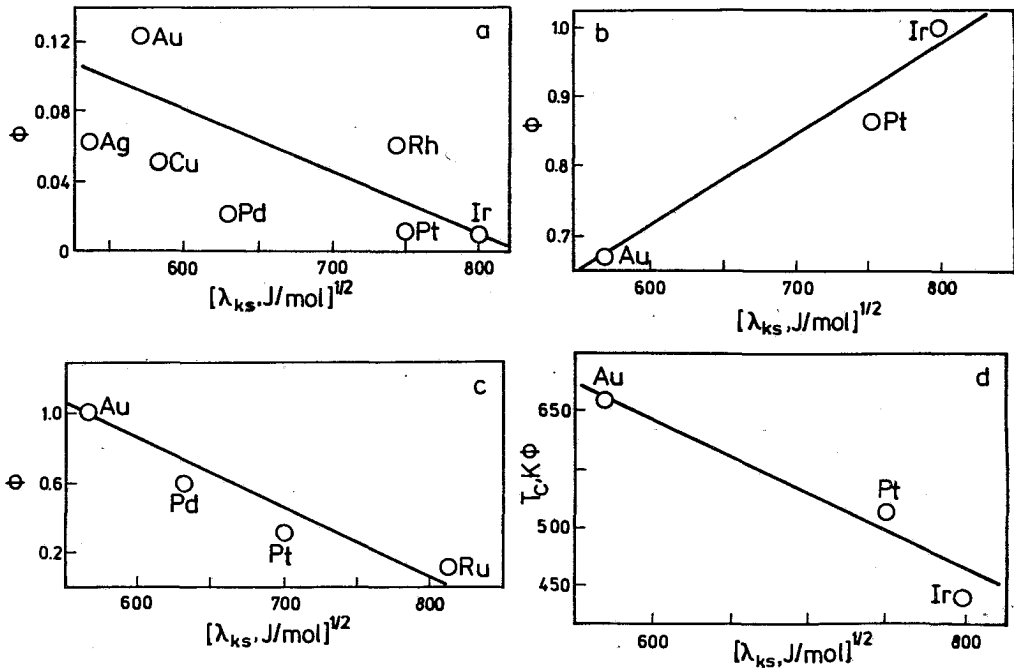


Figure 2: Activity Φ of noble metal nucleants as a function of their heat of sublimation: a - NaPO₃; b - PET; c - PVC; d - Na₂B₄O₇.

CONCLUSIONS

The analysis of the existing experimental data on the catalyzed nucleation of glass forming melts shows that it is possible to correlate the nucleating activity of a given substrate with its heat of sublimation (or with its temperature of melting). From fig. 2 it is seen that two courses of Φ vs. $(\lambda_{ks})^{1/2}$ (respectively Φ vs. $(\lambda_{ms})^{1/2}$ or Φ vs. $(T_{ms})^{1/2}$) functions are observed - a decreasing one corresponding to the absence of misfit effects and an increasing one corresponding to the case where misfit contribution to the adhesion energy can not be neglected.

Following the present analysis a simple two point method of predicting the activity of a given substrate can be suggested. According to this method only two Φ vs. T_{ms} determinations (for two different isotypical substrates) are sufficient to predict nucleants with maximum or minimum adhesion energy or activity.

REFERENCES

1. M. Volmer, *Kinetik der Phasenbildung* (Steinkopf, Dresden and Leipzig, 1939).
2. J. P. Hirth and G. M. Pound, *Condensation and Evaporation* (Pergamon Press, London, 1963).
3. M. Vogel, *Struktur und Kristallisation der Glasser* (Deutscher Verlag für Grundstoffindustrie, Leipzig, 1966).
4. I. Gutzow and I. Penkov, *Wiss. Z. Friedrich-Schiller Univ., Jena, Naturwiss.*, R 36 (1987) 907.
5. F. Rybnikar, *J. Appl. Polym. Sci.* 13 (1969) 827.
6. F. Binsbergen, *J. Appl. Polym. Sci., Polym. Phys.* 11 (1973) 117.
7. I. Gutzow, *Contemp. Phys.* 21 (1980) 121.
8. R. Kaischew, *Bull. Bulg. Acad. Sci. (Phys.)* 1 (1951) 100.
9. J. van der Merwe, in "*Treatise on Materials Science and Technology*", Ed. H. Hermann (Acad. Press, London 1973) chap. 1.
10. A. Dobрева, I. Gutzow, *J. Non Cryst. Solids* 162 (1993) 1.
11. I. Gutzow, S. Toschew, M. Marinov, E. Popov, *Kristall u. Technik* 3 (1968) 37.
12. I. Gutzow, V. Dochev, E. Pancheva and K. Dimov, *J. Polym. Sci., Polym. Phys.* 16 (1978) 1155.
13. A. Dobрева, T. Gantcheva, I. Gutzow, *Cryst. Res. Technol.* 27 (1992) 743.
14. I. Gutzow, S. Toschew, in "*Advances in Nucleation and Crystallization of Glasses*" Eds. L. Hench and S. Freiman (American Ceramic Society, Columbus, 1971) p. 116.

NON STEADY STATE EFFECTS IN THE KINETICS OF CRYSTALLIZATION OF GLASS FORMING MELTS

A. Dobreva, I. Gutzow

Institute of Physical Chemistry, Bulgarian Academy of Sciences, Sofia 1113, Bulgaria

It is shown that the induction period τ_{ind} for the onset of crystallization in a glass forming melt is constituted of two additive terms - the non steady state time lag $\tau_{\#}$ and the time at which detectable crystallization τ_1 is reached. A detailed analysis shows that the ratio $\tau_{\#}/\tau_1$ depends exponentially on the undercooling ΔT . Thus, it follows that in the vicinity of the temperature of vitrification T_g always $\tau_{\#} \gg \tau_1$ (i.e. non steady state time lags are dominant) while at small undercoolings near the melting temperature T_m the induction period is determined by the time at which just detectable amount of crystallites is formed. It is estimated that the two terms change their relative significance at $T/T_m \approx 0.85 - 0.9$. Experimental data on the kinetics of overall crystallization in a typical organic polymer - polyethylene terephthalate, are analyzed and the importance of non steady state effects is demonstrated.

INTRODUCTION

As shown first by Zeldovich (1), the nucleation process by its very physical nature is of a non steady state character. The most common approach for demonstrating the non steady state effects in the kinetics of nucleation of glass forming melts is to analyze the time dependence of the number of grown nuclei (2-5). This scheme, however, can be applied only for glass formers which form well defined crystal entities and exhibit relatively low nucleation rate in the temperature interval under investigation. In the present contribution we develop an alternative approach for demonstrating the significance of non steady state effects in the kinetics of nucleation which overcomes the shortcomings of the classical one. Our method is based on the analysis of the induction times in the kinetics of overall crystallization. We use a formalism advanced by Gutzow and Kashchiev (6) for the rate of overall crystallization at constant undercooling under non steady state conditions. Our method allows, also to point out the temperature region in which the non steady state effects are dominant.

The theoretical analysis, developed here, is corroborated by an experimental evidence for a typical organic polymer - polyethylene terephthalate.

THEORETICAL BACKGROUND

The kinetics of overall crystallization process is described by the well known Kolmogorov- Avrami equation (7)

$$\alpha(t) = 1 - \exp(-Kt^n) \quad (1)$$

where $\alpha(t)$ is the degree of transformation at time t , K is the overall crystallization rate coefficient and n is the Kolmogorov- Avrami exponent. At constant temperature T , the overall crystallization rate coefficient K is determined by the nucleation rate, I , and by the growth rate, G , as;

$$K = \omega I G^{n-1} \quad (2)$$

where ω is a geometric shape factor.

The overall crystallization process can be also characterized by the time τ_{α} for reaching the degree of crystallization α

$$\tau_{\alpha} = \left[\frac{-\ln(1-\alpha)}{K} \right]^{1/n} \quad /3/$$

Equation /1/ has been derived for systems with steady state nucleation rate.

The influence of the non steady state nucleation on the course of the overall crystallization process is considered by Gutzow and Kashchiev (6) (see also (8)). The main object of their analysis is that instead of the steady state nucleation rate, I , they have used a time dependent value of the nucleation rate. The final result of the treatment, performed in ref.(6), can be approximated by the equation

$$\alpha(t) \approx \begin{cases} 0 & 0 \leq t \leq b\tau_{\#} \\ 1 - \exp[-K(t - b\tau_{\#})^n] & b\tau_{\#} < t < \infty \end{cases} \quad /4/$$

Here $\tau_{\#}$ is the non steady state time lag and b is a numerical coefficient, close to unity. It is seen from eq./4/ that the kinetics of overall crystallization under non steady state conditions can be described to a first approximation by an S-shaped $\alpha(t)$ curve but it is shifted along the time axis by a factor $b\tau_{\#}$, in comparison with the $\alpha(t)$ curve for stationary conditions.

In considering the experimental investigations of the overall crystallization process a shift in the $\alpha(t)$ curve and an existence of induction periods τ_{ind} are often observed. In analyzing the induction periods two factors have to be accounted for - the physics of the process i.e. the theoretical course of the $\alpha(t)$ curve as well as the method of measurement which determines the detectable limit. It should be pointed out that the induction period, measured by a certain experimental method will depend on the critical degree of crystallization α_c which is determined by the detectable limit of the method used (see fig. 1).

A similar analysis of the induction periods for the case of industrial crystallization from solution is performed by Kashchiev (9).

It can be considered that the induction period for the onset of overall crystallization τ_{ind} is consisted of three additive terms:

i/ In reaching the desired temperature of the experiment i.e. the respective supersaturation the new phase will begin to form. The method of measurement will register the existence of a new phase at time $t = \tau_1$ when the critical degree of crystallization α_c is attained. In this case

$$\tau_{ind} = \tau_1 \quad /5/$$

In the differential scanning calorimetry and dilatometry the accuracy of determination of the $\alpha(t)$ curves is about 1-2%. Taking into account the S-shaped form of the $\alpha(t)$ curves, the existence of a detectable limit will lead to a considerable shift of the curves along the time axis.

ii/ If we assume that the induction period is not only due to the time τ_1 but also includes non steady state time lags $\tau_{\#}$ (see eq./4/), the expression for τ_{ind} becomes

$$\tau_{ind} = \tau_1 + \tau_{\#} \quad /6/$$

iii/ Finally the time τ_0 necessary to reach the desired temperature should be also accounted for. Then eq./6/ is transformed into

$$\tau_{ind} = \tau_1 + \tau_{\#} + \tau_0 \quad /7/$$

In determining the optimal experimental conditions the inequality $\tau_0 \ll \tau_1 + \tau_{\#}$ should be fulfilled. The circumstance that in a limited temperature interval τ_0 has no temperature dependence, can be used for distinguishing the values of τ_0 and $\tau_1 + \tau_{\#}$.

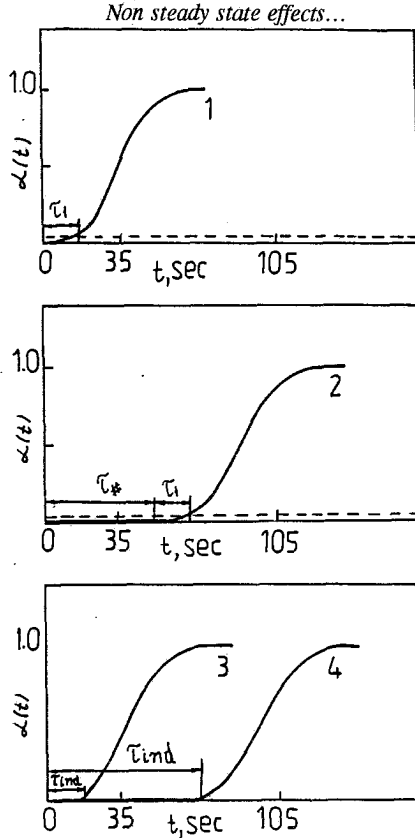


Figure 1: Curve 1 - theoretical $\alpha(t)$ curve according to the classical Kolmogorov-Avrami equation (eq. /1/). Curve 2 - the same theoretical $\alpha(t)$ curve but with $b\tau_{\#} = 50$ sec. If the detectable limit is 2%, τ_1 is 18 sec. for both curves. Curve 3 and 4 - $\alpha(t)$ curves 1 and 2 as they should be detected with an experimental method with detectable limit 2%. Curve 3 with $b\tau_{\#} = 0$ and $\tau_{ind} = 18$ sec. Curve 4 with $b\tau_{\#} = 50$ sec and $\tau_{ind} = 68$ sec.

Taking into account the above considerations, the Kolmogorov-Avrami equation can be extended in the form

$$\alpha(t) = \begin{cases} 0 & 0 \leq t \leq \tau_{ind} \\ 1 - \exp[-K(t - \tau_{ind})^n] & \tau_{ind} < t < \infty \end{cases} \quad /8/$$

At $\tau_{ind} = 0$, eq. /8/ transforms into eq. /1/.

In deriving the approximate solution of the non steady state overall crystallization problem (eq. /4/), which follows from the exact expression developed years ago by Gutzow and Kashchiev (6) (see also ref. (8)), the classical assumption due to Kolmogorov and Avrami is made i.e. that the deterministic growth of sufficiently large overcritical clusters is constant in time. In more recent developments of the theory, Shi and Seinfeld (10) and Shneidman and Weinberg (11) have introduced size dependent growth kinetics. In this case additional contributions are to be included into the induction times which in the present simplified version are accounted in a more elementary form by the time τ_1 . It can be shown, as done in our

recent paper (12) that these further developments do not alter at least qualitatively the results of the present analysis.

If $\tau_{ind} \neq 0$, the next step of the analysis is to consider the temperature dependence of τ_{ind} . Let's restrict the treatment only for the conditions for which $\tau_0 \ll \tau_1 + \tau_{\#}$. In this case eq./7/ can be rewritten in the form

$$\tau_{ind} = \tau_{\#} \left(1 + \frac{\tau_1}{\tau_{\#}} \right) \quad /9/$$

Taking into account that for $\alpha \ll 1$, $-\ln(1 - \alpha) \approx \alpha$, eq. /3/ becomes

$$\tau_1 = \left(\frac{\alpha}{K} \right)^{1/n} \quad /10/$$

It can be easily shown (13) that in the vicinity of the melting temperature T_m , the temperature dependence of K is totally determined by the temperature dependence of the steady state nucleation rate i.e. that τ_1 is proportional to $1/I$. Thus τ_1 can be defined as a time for the appearance of the first nucleus.

The temperature dependence of the non steady state time lag $\tau_{\#}$ is given by the expression

$$\tau_{\#} = \frac{const}{\Delta\mu^2} \eta \quad /11/$$

Here η is the bulk viscosity of the system and $\Delta\mu$ is the undercooling.

Thus, it turns out that the induction period will be determined by the ratio $\tau_{\#} / \tau_1$.

Taking into account that $\tau_1 \approx 1/I$ we can write

$$I\tau_{\#} = \frac{\tau_{\#}}{\tau_1} = const_1 \exp\left(-\frac{A_k}{kT}\right) \quad /12/$$

where

$$A_k = \frac{16}{3} \pi \frac{\sigma^3 V_m^2}{\Delta\mu^2} \quad /13/$$

is the work of three dimensional nucleation. In the above equation σ is the specific surface energy at the melt/crystal interface, k is the Boltzmann constant and V_m is the molar volume of the system. Equation /12/ has the advantage that it does not depend on any kinetic quantities. From the expression for A_k (eq. /13/) it follows that in the vicinity of the melting temperature $A_k \rightarrow \infty$ and thus $\tau_1 \gg \tau_{\#}$. At temperatures near the glass transition $A_k \approx const$ and $\exp(-A_k/kT) \ll const_1$ and thus $\tau_1 \ll \tau_{\#}$. By introducing reasonable values of the quantities appearing in eq. /12/ it follows that $\tau_1 \approx \tau_{\#}$ at $T/T_m \approx 0.85-0.9$.

EXPERIMENTAL EVIDENCE

The experimental data for the overall crystallization and flow behavior of polyethylene terephthalate (PET) are used in order to check the applicability of the approach developed in the previous section.

The polyethylene terephthalate, used, is an industrial grade with an average molecular weight 18 400. The density of the amorphous sample is 1.35 g/cm³. The glass transition temperature T_g and the melting temperature T_m , determined by DSC, are 342K and 542K, respectively.

The rheological measurements are performed by using HAAKE rotational viscometer. It is found that the temperature dependence of the viscosity η reads

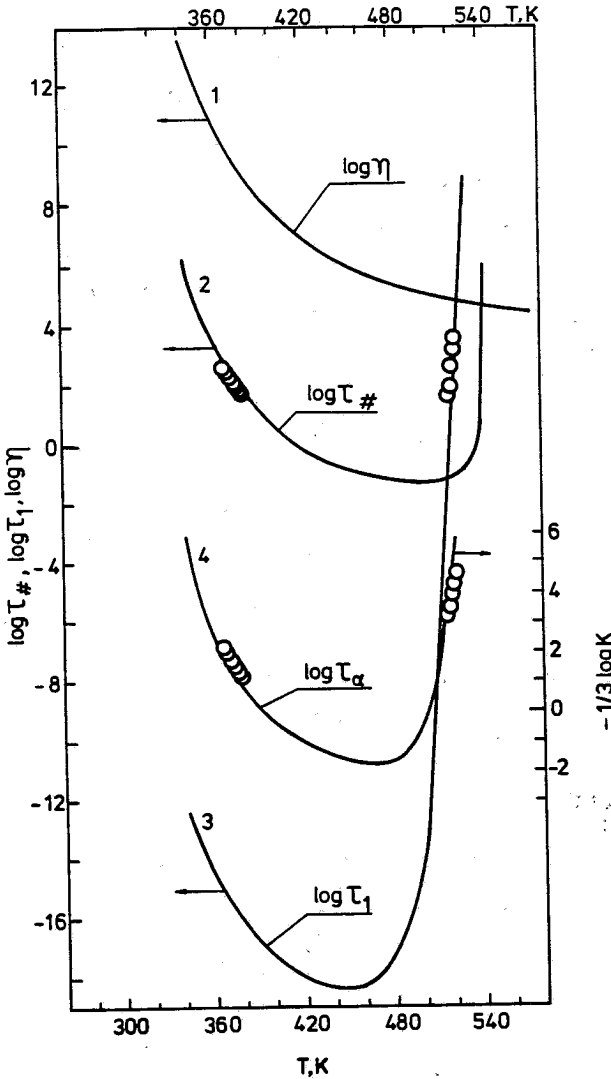


Figure 2: Temperature dependence of the viscosity according to eq. /14/ (curve 1). Temperature dependence of the non steady state time lag according to eq. /11/ (curve 2). Temperature dependence of the rate of nucleation $\tau_1 \approx 1/I$ (curve 3). Temperature dependence of the time τ_α for reaching degree of transformation α according to eq./3/. The points at each curve are the experimental data for PET.

$$\log \eta = -1.4 + \frac{850}{T - 271} \quad /14/$$

Details on the experimental procedure and the analysis of the experimental results can be found in ref. (14).

The kinetics of overall crystallization of PET is studied by using a METTLER differential scanning calorimeter. The $\alpha(t)$ curves are analyzed by using a computer program in order to determine the values of n , K and τ_{ind} .

Figure 2 shows the temperature course of the basic parameters of the crystallization process of PET. The viscosity curve (curve 1) is constructed according to eq. /14/. The temperature dependence of the non steady state time lag $\tau_{\#}$ is plotted according to eq. /11/ while the temperature dependence of τ_1 and τ_{α} (curves 3 and 4) follows eq. /10/ and eq. /3/, respectively. Figure 2 shows also our experimental data for the induction periods and the overall crystallization rate coefficients, determined by the analysis of the $\alpha(t)$ curves. It is seen that the values of τ_{ind} for samples crystallized at large undercoolings i.e. at $T \rightarrow T_g$ are situated on the curve describing the temperature dependence of the nucleation rate.

From fig. 2 it is seen that for PET crystallization $\tau_{\#} > \tau_1$ at $T/T_m < 0.9$. The exponential character of the dependence of τ_1 on A_k determines the steep rise of τ_1 at $T \rightarrow T_m$ and at these conditions $\tau_1 \gg \tau_{\#}$. On the other hand the high temperature coefficient of the viscosity at $T \rightarrow T_g$ determines the inequality $\tau_{\#} \gg \tau_1$.

CONCLUSIONS

The analysis performed in the present study shows:

i/ The kinetics of overall crystallization and especially the analysis of the temperature dependence of the induction periods can be used in order to demonstrate the non steady state character of the nucleation process.

ii/ At $T \rightarrow T_m$ the induction periods are determined by the time of the appearance of the first nucleus while at $T \rightarrow T_g$ the induction period is governed in fact by the non steady state time lag.

REFERENCES

1. J. Zeldovich, *Acta Physicochim. USSR* 18 (1943) 253.
2. I. Gutzow, S. Toschew, M. Marinov and E. Popov, *Kristall u. Technik* 3 (1968) 37.
3. I. Gutzow and S. Toschew, *Kristall u. Technik* 3 (1968) 485.
4. A. Kalinina, B. M. Fokin and B. A. Filipovich, *Fiz. Khim. Stekla* 3 (1977) 122.
5. P. F. James, *Phys. Chem. Glasses* 15 (1974) 95.
6. I. Gutzow and D. Kashchiev, in: "Advances in Nucleation and Crystallization in Glasses" Eds. L. L. Hench and S. W. Freiman, *Am. Ceram. Soc.* 1972, p. 116.
7. M. Avrami, *J. Chem. Phys.* 7 (1939) 1103.
8. I. Gutzow, D. Kashchiev and I. Avramov *J. Non Cryst. Solids* 74 (1985) 477.
9. D. Kashchiev, in: "Industrial Crystallization'87" Eds. J. Nyvlt and S. Zasec, Elsevier 1989, 3.
10. G. Shi and J. H. Seinfeld, *J. Mater. Res.* 6 (1991) 2091, 2097.
11. V. A. Shneidman and M. C. Weinberg, *J. Non Cryst. Solids* 160 (1993) 89.
12. I. Gutzow, A. Dobрева, submitted for publication.
13. A. Dobрева and I. Gutzow, *Cryst. Res. Technol.* 26 (1991) 863.
14. A. Dobрева, *Polymer*, submitted for publication.

CRYSTALLIZATION KINETICS OF A $\text{Li}_2\text{O}\cdot 2\text{SiO}_2$ MELT
BASED ON A LIQUID MODEL

R.Ota, N.Mishima, T.Wakasugi and J.Fukunaga
Kyoto Institute of Technology, Kyoto 606, Japan

A liquid model was proposed whereby crystal embryos may exist in melts at temperatures even above the melting temperature or liquidus temperature. Crystallization behavior of a $\text{Li}_2\text{O}\cdot 2\text{SiO}_2$ melt was studied. Isothermal heat-treatment (600°C for 20-60min) of the $\text{Li}_2\text{O}\cdot 2\text{SiO}_2$ melt showed that different number of crystals emerged in the glass depending upon the thermal history, i.e. melting temperature and time. The number density of precipitated crystals decreased with increasing temperature of melting. This is consistent with the proposed model, which claims that a melt contains smaller number of embryos as the temperature of melting increases. The possibility of phase separation was carefully discussed and another possibility of structural change was inferred.

1. Introduction

A slag melt can be quenched to a glass. The vitrification point, defined as a lowest temperature from which melt can be quenched as glass, decreased with increasing quenching rate(1). The amount of precipitated crystals in the glass quenched from different temperature decreased with increasing temperature(1). To explain these phenomena a liquid model was proposed by Ota et al(1). The liquid model includes an assumption that liquids contain crystal embryos at even above the melting point or

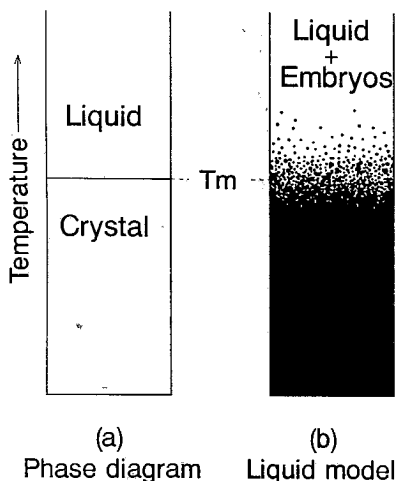


Fig.1 Phase diagram(a)congruently melting compound having a melting point(T_m) and a liquid model(b)

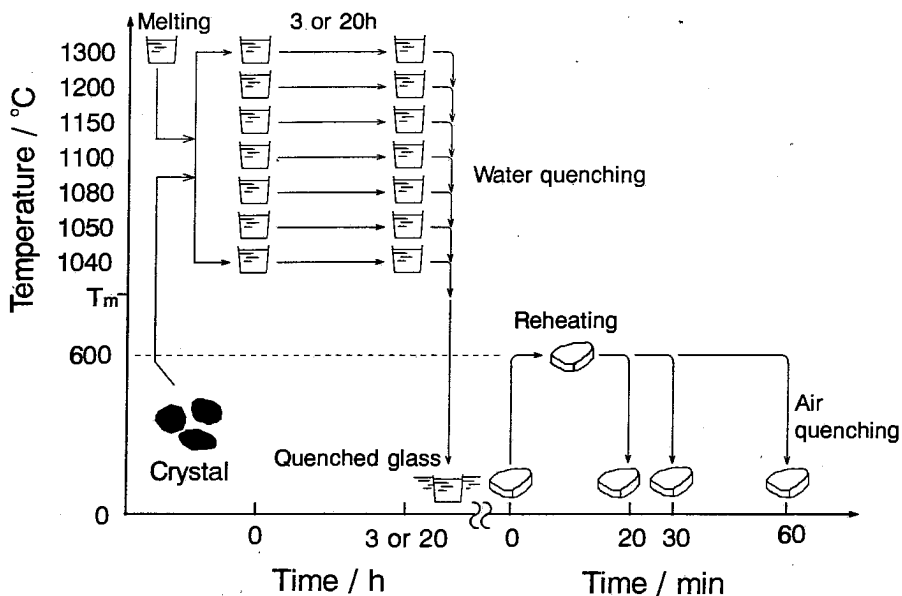


Fig.2 Temperature schedule for the melting and heat-treatment of the glass

liquidus temperature. The number density of the embryos may decrease as the temperature increases. The liquid model is schematically shown in Fig.1. Figure 1(a) indicates the phase diagram of a system having a melting point T_m . Figure 1(b) shows the liquid structure after the model. At the melting point solid phase is coexistent with liquid phase. With increasing temperature crystal embryos decrease in number and volume. In the present study a model experiment was carried out in order to show the validity of the liquid model. A $\text{Li}_2\text{O}\cdot 2\text{SiO}_2$ composition was chosen because this compound melts congruently at $T_m=1033^\circ\text{C}$ and is situated away from the liquid-liquid immiscibility region observable in the $\text{Li}_2\text{O}-\text{SiO}_2$ glass(3). The $\text{Li}_2\text{O}\cdot 2\text{SiO}_2$ glass has been known to exhibit a homogeneous nucleation(2). Optical microscopy and SEM observation were used to detect the crystal embryos frozen in the glass matrix.

2. Experimental

The experimental scheme is shown in Fig.2. The molten glass was maintained at given temperatures in the range $1040-1300^\circ\text{C}$ for 3-20h. The glass melts were then quenched in water at a certain cooling rate. The resulted glasses were inspected of possible nucleation which must have originated from the pre-existing embryos. If nucleation was not detected in the quenched glasses additional heat-treatment was conducted on the glasses to enhance the crystal growth. By this method we may be able to estimate the number density of the embryos present in the melt from the observation of the number density of the grown crystal as a function of melting temperature. Starting

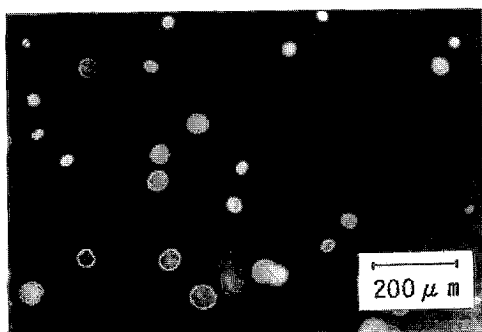
materials for the melts in the present experiments were reagent grade lithium carbonate and silica powder. Batches were melted using a platinum crucible at 1300°C for 2h. The melts were transferred to ovens of fixed temperatures. They were kept there for 3h or 20h. Then the melts were quenched in water, resulting in glasses. Even small crystals were not visible by either optical microscopy or SEM observation in such an as-quenched glasses. To enhance the crystal growth of the presumably frozen-in embryos in the glass, the glass specimens were heat-treated at 600°C for different period of time in the range 20-60 min. The surface of the specimen was removed and the interior of the glass was inspected with the optical microscopy. The number of the crystals were counted in the microscopic view (Fig.3), and the number density N of crystals/ mm^3 was calculated. The maximum size of the grown crystal was also measured by the microscope as a function of melting temperature.

3. Results and discussion

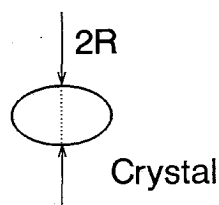
3.1 Number density of crystals after heat-treatment

The number density of precipitated crystals in the heat-treated glass (600°C , 30-60min) is shown in Fig.4 as a function of melting temperature. The melting duration is 3h. The number density decreases from 8-10/ mm^3 at melting temperature of 1040°C to 1/ mm^3 at 1200°C or higher with 30min heat-treatment. This result agrees with what the liquid model claims. However, unexpected phenomenon occurred on further heating at 600°C , for example, for 60min. Nucleation takes place at higher rate in higher temperature (1200 - 1300°C) than in those of lower temperature (1040 - 1200°C) as shown in Fig.4.

Figure 5 indicates the number density of crystals in glasses quenched from the melts maintained for 20h and submitted to a heat-treatment at 600°C for 20 or 30min. It is seen that the number density of crystals increases at higher rate in 20h-melting glass than in 3h-melting glass (Fig.4) when compared at the same temperature.



(a)



(b)

Fig.3 Microscopic view of a heat-treated glass (600°C , 30min) with a scale of $200\mu\text{m}$ (a). $\text{Li}_2\text{O}\cdot 2\text{SiO}_2$ crystals are seen with the short axis radius R (b).

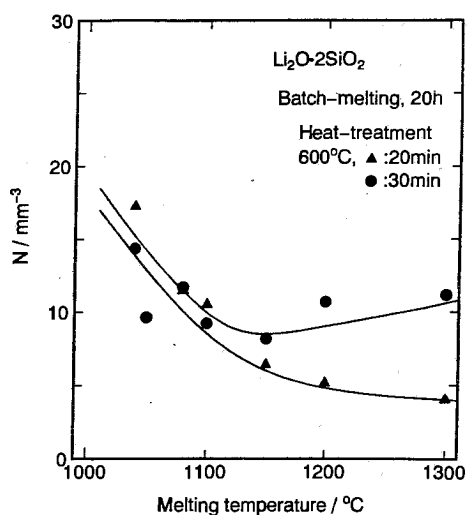
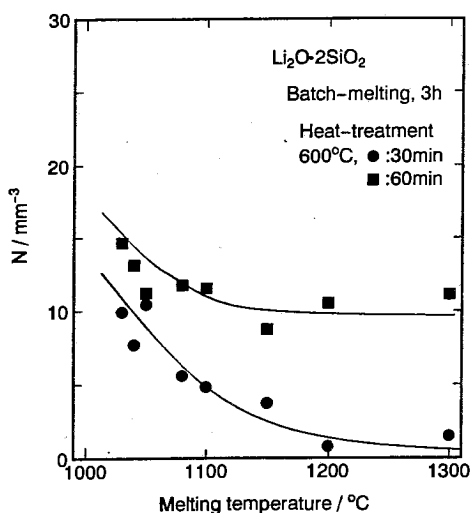


Fig.4 Variation of number density of crystal particles in the Li₂O·2SiO₂ glass prepared from batch-melting for 3h.

Fig.5 Variation of number density of crystal particles in the Li₂O·2SiO₂ glass prepared from batch-melting for 20h.

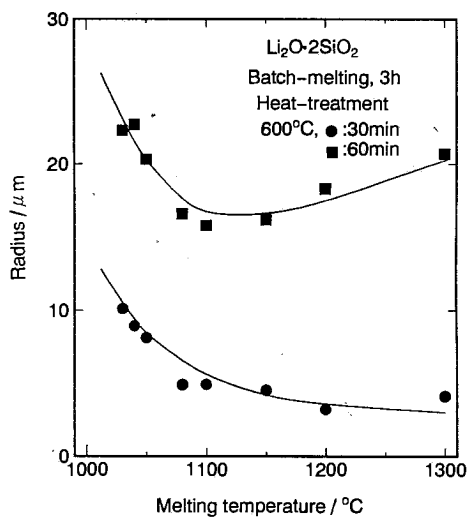
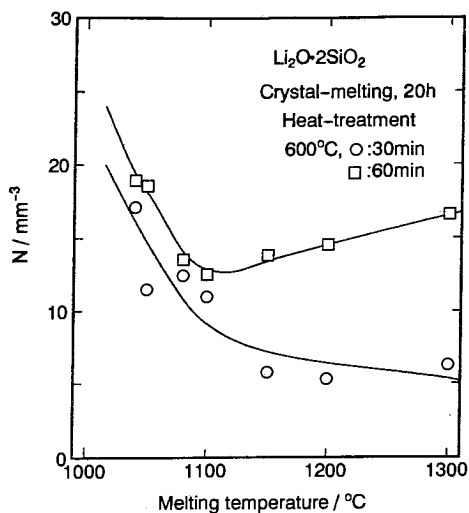


Fig.6 Variation of number density of crystal particles in the Li₂O·2SiO₂ glass prepared from crystal-melting for 20h.

Fig.7 Variation of radius of crystal particles in the Li₂O·2SiO₂ glass prepared from batch-melting for 3h.

A study was made if there are some differences in the number density in the glasses depending on the scheme of glass preparation; batch-melting or crystal-melting. Specimens of $\text{Li}_2\text{O}\cdot 2\text{SiO}_2$ crystal were prepared from a glass of the same composition by heating at temperature 150°C above the T_g for about 5h. The result (Fig.6) indicates that after a 30min heat-treatment nucleation rate is somewhat suppressed at higher temperature range ($1200\text{-}1300^\circ\text{C}$) in crystal-melting glass compared with that in batch-melting glass (Fig.5).

3.2 Growth rate of precipitated crystals

The size of the precipitated crystalline particle of $\text{Li}_2\text{O}\cdot 2\text{SiO}_2$ was measured by the optical microscopy (Fig.3). Because there is a size distribution in the precipitated crystals, only the largest crystal visible in the scope was traced with heating time up to 60min at 600°C . The diameter of the short-axis was measured. The particle radius decreased with melting temperature as illustrated in Figs.7 and 8. Fig.7 indicates that the radius in 3h batch-melting glass increases with heating time (30-60min) but the growth rate becomes larger at higher temperature range over 1100°C . However, as Fig.8 shows, the particle radius in 20h batch-melting glass becomes 50% smaller compared with that in 3h batch-melting glass for the same heating time 30min.

The fact that the particle radius is larger at lower temperature range than at higher temperature range can be understood as the crystal growth must have started from the existing embryos of larger radius. This result agrees with what the liquid model would suggest.

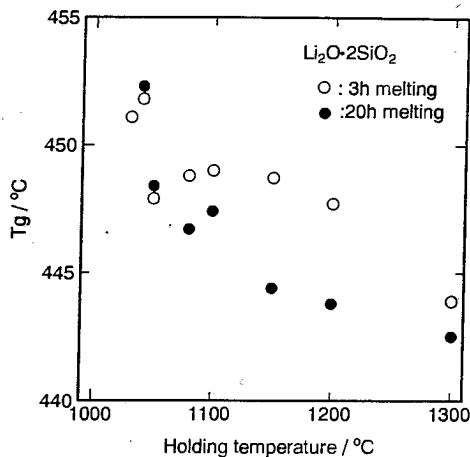
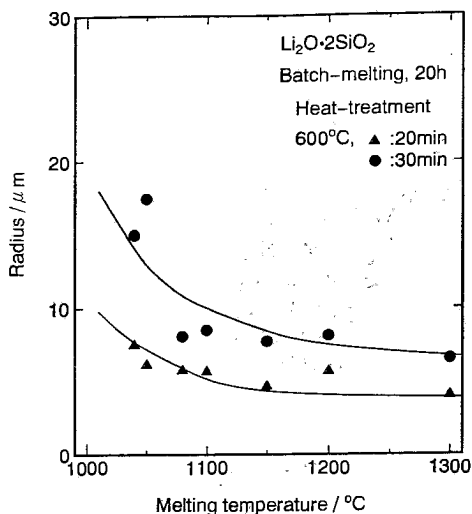


Fig.8 Variation of radius of crystal particles in the $\text{Li}_2\text{O}\cdot 2\text{SiO}_2$ glass prepared from batch-melting for 20h.

Fig.9 Glass transition temperature of the $\text{Li}_2\text{O}\cdot 2\text{SiO}_2$ glass melted at different temperatures.

3.3 Liquid structure and crystallization

As pointed out before (Figs.4, 5, 6), nucleation rate becomes larger at high melting temperature range. There are two possibilities (a) and (b) for this phenomenon. Possibility (a) includes the occurrence of phase separation at 600°C due to the alkali evaporation from the glass surface during heating. The miscibility gap in the $\text{Li}_2\text{O}-\text{SiO}_2$ system lies at composition range of Li_2O content less than 30.4mol%(3). Chemical analysis of the quenched glasses showed that the analyzed chemical composition was almost constant in a range $\text{Li}_2\text{O}=34.4\pm 1.9\text{mol}\%$ despite the heating period of time up to 20h. No evidence of phase separation was seen by optical microscope or SEM observation in the transparent glass specimens. Possibility (b) includes a structural or chemical change in glass. Since glass structure is affected by the thermal history in the molten state, it is possible that a glass of high temperature melting assumes a high fictive temperature(4). To confirm this idea glass transition temperature T_g was determined from the DTA method on quenched glasses having different thermal history; i.e. different temperature for 3h and 20h(Fig.9). High fictive temperature corresponds to a low T_g . Fig.9 indicates high temperature melting glass assumes a low T_g , implying a low viscosity. The above mentioned phenomenon can not be explained in the viscosity term alone, however, because at 600°C the frozen-in glass structure may relax in a very short time less than 1 second as estimated from the viscosity and shear modulus of the glass. Some kind of structural changes which may accompany a local compositional change must be figured out then. The precise model of the structural change is not clear at the moment. It might include a micro-scale disproportionation reaction where nominal glass constituent $\text{Li}_2\text{O}\cdot 2\text{SiO}_2$ decomposes into several structure units such as alkali rich unit ($\text{Li}_2\text{O}\cdot\text{SiO}_2$) and silica rich one ($\text{Li}_2\text{O}\cdot 3\text{SiO}_2$), and so on as the temperature of melting increases.

4. Conclusion

A liquid model has been proposed based on a hypothesis "small crystal embryos may exist in liquids at temperatures even above the melting point or liquidus temperature. The number density of the embryos should decrease as the temperature increases". To confirm the validity of this liquid model, melts of $\text{Li}_2\text{O}\cdot 2\text{SiO}_2$ composition were quenched from various temperatures and the resulted glasses were examined of their crystallization behavior after additional heat-treatment. The number density of the crystal particles decreased with increasing melting temperature in accordance with the prediction of the liquid model.

References

1. R.Ota, J.Fukunaga and N.Yoshida, *J.Soc.Mater.Sci.Japan (Zairyo)*, **38**(1989)8.
2. K.Matusita and M.Tashiro, *J.Non-Cryst.Solids*, **11**(1973)471.
3. M.Tomozawa, *Phys.Chem.Glasses*, **13**(1972)161.
4. R.Lillie, *J.Am.Ceram.Soc.*, **16**(1933)619.

PHASE TRANSITIONS IN MIXED-NETWORK GLASSES
CRYSTALLOCHEMICAL AND STRUCTURAL ASPECTS

L. Stoch

University of Mining and Metallurgy, 30-059 Cracow, Poland

Abstract. The regularities governing the multistage crystallization of polycomponent glasses are considered.

A mixed, diffusion-less (anion network) and diffusional (cations) mechanism for the formation of the first intermediate, metastable phase near the T_g temperature has been proposed.

INTRODUCTION

The term mixed-network glasses is used here as referring to glasses with network made of two or more different components (in the sense used for the component in the phase rule) or one component in the form of various coordination polyhedra (triangles, tetrahedra etc.) [1].

The transition of mixed-network glasses from the vitreous state, to the crystalline equilibrium state is complicated. It involves the formation of metastable intermediate phases as a result of the step-by-step reconstitution of the structure of glass and later on, equilibrium crystalline phases. Multistage crystallization is a typical to many mixed-network glasses.

The metastable phase formation in solid systems has been pointed out by Oswald at the end of the 19th century, and is known as the " rule of steps ". This paper attempts to explain the causes of the metastable phase formation during the heat treatment of the glasses. It summarizes the experimental data obtained earlier [2] and [3].

MULTISTAGE PHASE TRANSITIONS IN GLASSES

Depending on the composition of glass, the first crystallization products are usually compounds of simple composition, made of components not participating to the network. Crystallization of nucleators like fluorite CaF_2 , spinel $\text{MgO Al}_2\text{O}_3$ or $\text{Al}_2\text{Ti}_2\text{O}_7$ and

TiO₂ in glasses rich in aluminum and magnesium and containing admixtures of TiO₂ are typical examples. The crystallization of these compounds usually initiates the spontaneous bulk crystallization of more complex substances. Some of them are of the solid solution type.

Such a substance is the solid solution with the structure of quartz ($\text{Li}_{2-2(x+y)}\text{Mg}_x\text{Zn}_y\text{O} \cdot \text{Al}_2\text{O}_3 \cdot z\text{SiO}_2$). At higher temperatures the ordering of the structure of these solutions connected with the segregation and redistribution of the chemical components, leads to the gradual formation of crystal phases which are increasingly closer to the stable thermodynamic phases proper for a glass of a given chemical composition.

In SiO₂ - Al₂O₃ - Li₂O glasses the first crystallization product is a quartz solid solution. With passing time and/or increasing temperature, this is transformed into a spodumene-like solid solution and next into spodumene Li₂O·Al₂O₃·4SiO₂. In cordierite glasses the first crystallization product is quartz solid solution yielding, by way of successive structural rearrangement sapphirine and finely cordierite 2MgO·2Al₂O₃·5SiO₂.

In SiO₂ - Al₂O₃ - CaO - Na₂O glasses the crystallization of wollastonite Na_xAl_x(CaMg)_{1-2x}(O,F)SiO₂ instead of CaO·SiO₂ takes place [4].

The crystallization of vitreous basalt has also a multistage course. The crystallization products of basalt glass, heated for 2 hours at different temperatures are shown in the Table 1.

Additional examples of multistage crystallization of glasses can be found in the recent scientific literature, [5] and [6]. According to [5] xLi₂O·(1-x)GeO₂ glasses crystallize into forming microcrystallites of Li₂Ge₄O₉ the structure of which contains GeO₄ tetrahedra linked by GeO₆ octahedra. This compound does not appear in the phase diagram of Li₂O - GeO₂. At higher temperatures it is transformed into Li₂Ge₇O₁₅ which is the stable compound and has a more complex layer structure.

Similar multistage phase transitions take place in amorphized crystal solids and gels [7].

MECHANISM OF MULTI-STAGE PHASE TRANSITIONS

The phenomenon of the multistage phase transitions is the result of the limited mobility of the various structural components. Only those chemical components which at given

temperature have the possibility of displacement, can participate in the formation of the new phases inside the parent solid structure. The diffusion coefficient of these structural components increases with temperature but depends on their chemical nature as well. Hence, at various temperatures different chemical components can become capable of forming new compounds, and substances differing in their chemical composition can be successively formed.

Up to the transformation temperature (T_g) the glass behaves like a brittle body of rigid structure. A little above this temperature it has viscoelastic properties. At this range of temperatures, the possibility for structural rearrangement is limited and the only phases which are formed easily, are those with chemical composition and structure close to the parent glass structure.

The formation of certain structures similar to the parent glass structure can be possible through small rearrangements in the anion network, similar to those which occur during the so-called displacive or distortional polymorphic transitions (according to Buerger's classification [8]) or martensitic transitions. This mechanism is termed: diffusionless.

The formation of the intermediate phases in the multicomponent mixed-network glasses involves more complex mechanisms. The network changes in a diffusionless manner, but the mobile cations (modifiers or others) become displaced at considerable distances in a diffusional mode: diffusionless/diffusive mechanism.

The disorder - order transformations in pyroxenes and feldspars could be described in such a way.

The crystal phases formed according to the diffusionless mechanism have coherent diffused grain boundaries, which are distinguished with difficulty. With time or increasing temperature, the grain boundaries become more distinct, but they

are retaining their irregular shape.

When the temperature increases the glass shows ability for viscous deformations. This indicates the increasing mobility of the primary structure elements and decreasing of their dimension. Accordingly the proportion of the long distance diffusive displacements may increase, and this can cause a change in the phase transition mechanism. Crystallization can now occur by the diffusional mechanism. Diffusion enables the exchange of the components between the phases formed earlier as well as between them and the amorphous matrix. This permits the decomposition of the metastable phases and the crystallization of those which are thermodynamically stable. Later on, crystallization by the formation of free nuclei and crystal growth according to the crystallization of liquids theory is possible. These crystals are usually distinguished by their geometric idiomorphic habit.

When examining molten and vitrified basalt it has been observed that a structural change takes place above T_g , which causes a step-wise reduction of the volume (Fig.1). This takes place before the exothermic DTA peak of crystallization. This peak is not accompanied by a subsequent change in volume [2], [3].

The above observation has let the author to assume that the rearrangement of the atoms in the glass structure, mentioned above, and the formation of domains with chemical composition and structure close to those of the crystallization products take place. This structure rebuilding process is accompanied by an irreversible endothermic effect, which distinguishes it from the small irreversible effect of the glassy state transformation at T_g .

Recently Gutzov and Dobrova [9], on the basis of thermodynamic consideration founded on Gibbs and Prigogine's relations proved the possible existence of a stage of structural ordering, preceding glass crystallization.

The considered mechanism of crystallization and recrystallization by way of internal rearrangement allows to obviate the energy barrier of the formation of new interface, of different surface tension and other properties when the solid nucleus is formed in the liquid medium.

As the consequence the phase transitions in glass may start at relatively low temperature, close to T_g .

Table 1. Phase transitions in basalt glass

| | |
|---|---|
| diffusional redistribution of weakly bond, mobile, non-network cations | basalt glass 700° C (Fe,Ti) ₃ O ₄ titanomagnetite |
| diffusionless (anion network) and diffusional (cations) transformation | 740 - 890° C (Ca, Mg, Fe ²⁺)[SiO ₃] pyroxene I |
| anions and cations diffusive redistribution and reconstitution of structure | 930 - 1050° C (Ca, Mg)[SiO ₃]+(Mg, Fe ²⁺) ₂ [SiO ₄] pyroxene II olivine |
| | 1200 - 1250° C Ca[Al ₂ Si ₂ O ₈] anorthite |

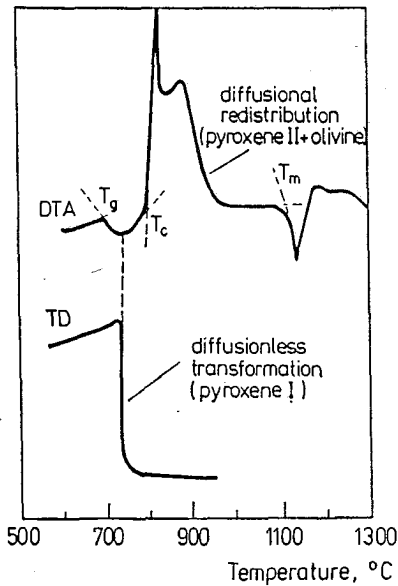


Fig.1 Dilatometric (TD) and DTA curves of basalt glass

Glass composition (weight %):
 43.76SiO₂, 17.30Al₂O₃, 2.20Fe₂O₃
 7.80FeO, 2.31TiO₂, 11.03CaO,
 10.26MgO, 3.45Na₂O, 1.53K₂O

FINAL REMARKS

According to Prigogine's theory the free energy, ($-\Delta G$) is a measure of the chemical affinity and driving force of the chemical process [10]. At the beginning of internal structure rearrangement processes, close to T_g , the reagents are strongly bound in the parent structure and the force of chemical affinity is not sufficient to overcome the diffusion barriers. At that time only small diffusionless cooperative rearrangements of glass network polyhedra and short distance displacements of modifiers are possible. When the temperature is higher the operation of this force allows to make mobile the components of the weakest structural bonds (modifiers and other non-network components). At that stage these components participate mainly in the formation of a new phase by a diffusion governed process.

With increasing temperature the freedom of the displacement of the structural elements increases and the chemical affinity of reagents become sufficiently strong to be the only factor determining the reaction product. Hence, thermodynamically stable phases of appropriate composition and ordered structure are formed. This explains the multistage course of the phase transitions in glasses.

REFERENCES

1. L. Stoch, High Temp. Materials and Processes, 10 (1992) 245.
2. L. Stoch, J. Thermal Anal., 32 (1987) 1655.
3. L. Stoch and P. Wyszomirski, Raw Materials and Technology of Petruurgy. Mineralogical Transactions No 45, Polish Academy of Sci., Cracow, 1976.
4. Z. Strnad, Glass - Ceramic Materials, Elsevier, Amsterdam, 1989.
5. A. Marotta, P. Pernice, A. Arone and M. Catauro, J. Thermal Anal. 40 (1993) 181.
6. A. Habeck, and R. Bruckner, 2d Int. Conf. European Society of Glass Sci. and Tech., Abstracts, Venice 1993.
7. L. Stoch and I. Waclawska, J. Thermal Anal. (in press).
8. A. B. Thompson and E. H. Perkins, Lambda transitions in minerals, in Thermodynamics in Minerals and Melts (R. C. Newton, A. Navrotsky and B. J. Wood), Springer Verlag, Berlin 1977.
9. I. Gutzow and A. Dobрева, 2d Int. Conf. European Glass Sci. and Tech., Abstracts, Venice 1993.
10. I. Prigogine and R. Defay, Chem. Thermodyn., Longman, London 1954

MULTISTAGE CRYSTALLIZATION OF AMORPHIZED SOLIDS AND GLASS
- A COMPARATIVE STUDY

I. Waclawska, L. Stoch

University of Mining and Metallurgy, 30-059 Cracow, Poland

ABSTRACT

The phase transitions of the amorphous solids obtained by thermal decomposition of hydrated borates and melt-quenched glasses of the same composition were studied. The amorphous borates have properties of the vitreous solids but their structure contains preserved elements of the primary crystal structure. This micro-heterogeneity enhances the crystallization rate and changes the order of appearance of the crystalline products.

INTRODUCTION

Products of heat treatment of some crystalline solids are amorphous and they can retain this state in a wide range of temperature. Inorganic polymers such as silicates, borates and phosphates amorphize relatively easy at relatively low temperatures.

Thermal amorphization of crystalline solids can be obtained by: 1. thermal dissociation of compounds (dehydration of some hydrous silicates, phosphates etc.), 2. destruction or distortion of the crystal structure of a solid under prolonged heat treatment (quartz) [1].

As amorphized solids are considered here substances in which internal structure order is distorted or destroyed to a degree excluding appearance of X-ray diffraction lines characteristic for them.

During heating of some amorphous solids strains of their internal structure can be relaxed giving rise to reversible effect similar to the glass transition T_g .

The glass transition effect indicates the vitreous nature of these solids. On the other hand XRD and IR study indicate that the structure of amorphized solids contains preserved elements of the precursor structure. The amorphous products of thermal dissociation are microporous. This distinct micro- and macro-heterogeneity distinguishes them from a real glass and can influence their crystallization process.

The subject of this paper is the comparison of the crystallization behaviour of amorphous solids and melt-quenched glasses of the same chemical composition. Anhydrous borates are taken as model substances in this study.

EXPERIMENTAL

Several coarse-crystalline borate minerals from the collection of Mineralogical Museum at Wroclaw University has been examined. They were: colemanite - $\text{Ca}_2\text{B}_6\text{O}_8(\text{OH})_6 \cdot 2\text{H}_2\text{O}$, borax - $\text{Na}_2\text{B}_4\text{O}_5(\text{OH})_4 \cdot 8\text{H}_2\text{O}$, pandermite - $\text{Ca}_2\text{B}_5\text{O}_8(\text{OH})_3 \cdot 2\text{H}_2\text{O}$, kaliborite - $\text{HKMg}_2\text{B}_{12}\text{O}_{16}(\text{OH})_{10} \cdot 4\text{H}_2\text{O}$, ulexite - $\text{NaCaB}_5\text{O}_6(\text{OH})_6 \cdot 5\text{H}_2\text{O}$.

Conventional TG, DTG and DTA analysis were performed at a heating rate of 2,5 deg/minute. In order to examine the structural changes during heating the samples were heated at the same rate in TA apparatus up to the characteristic temperatures, quenched and next subjected to X-ray diffraction and IR spectroscopic examinations.

RESULTS and DISCUSSION

The stability of the amorphous state and the course of crystallization depend on the chemical composition of the borates. Few examples are discussed below.

The thermal decomposition of colemanite $\text{Ca}_2\text{B}_6\text{O}_8(\text{OH})_6 \cdot 2\text{H}_2\text{O}$ proceeds in two stages at 369°C and 386°C . This process is accompanied by the gradual destruction of the primary structure of the borate. At 400°C sample is X-ray amorphous. A small endothermic DTA peak appears at 650°C resembling the glass transition effect (T_g). At 741°C amorphous substance recrystallizes and crystalline $2\text{CaO} \cdot 3\text{B}_2\text{O}_3$ is formed. It melts at 950°C (Table 1) [2].

Dehydration and dehydroxylation of pandermite $\text{Ca}_2\text{B}_5\text{O}_8(\text{OH})_3 \cdot 2\text{H}_2\text{O}$ results in the formation of an X-ray amorphous substance (580°C). At 650°C a small endothermic peak of transformation appears. At 745°C the crystallization of $\text{CaO} \cdot \text{B}_2\text{O}_3$ starts followed by $\text{CaO} \cdot 2\text{B}_2\text{O}_3$ formation according to the stoichiometry of composition of the amorphous substance (Table 1) [3].

Table 1. Stages of the internal reconstitution of the amorphous Ca-borates

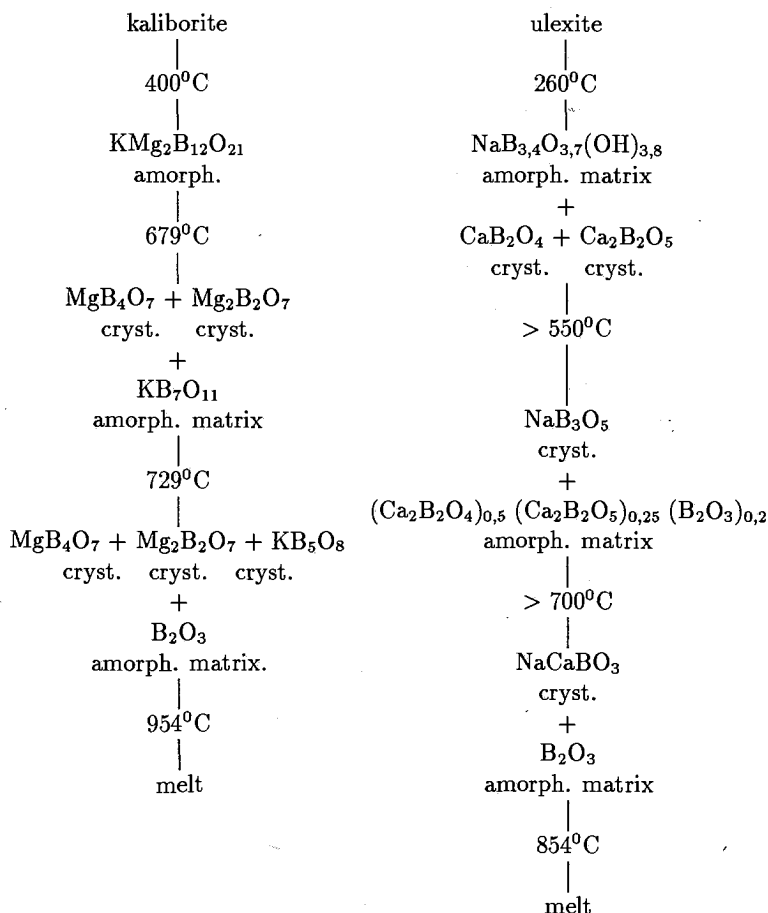
| colemanite | pandermite |
|---|---|
| 400°C | 580°C |
| $\text{Ca}_2\text{B}_6\text{O}_{11}$ amorph. | $\text{Ca}_4\text{B}_{10}\text{O}_{19}$ amorph. |
| 741°C | 745°C |
| $\text{Ca}_2\text{B}_6\text{O}_{11}$ cryst. | CaB_2O_4 + CaB_4O_7 cryst. amorph. matrix |
| 950°C | 800°C |
| melt | CaB_2O_4 + CaB_4O_7 cryst. cryst. |
| | 1100°C |
| | melt |

The thermal decomposition of kaliborite $\text{HKMg}_2\text{B}_{12}\text{O}_{16}(\text{OH})_{10} \cdot 4\text{H}_2\text{O}$ proceeds in two steps (258°C and 272°C). Water molecules and OH groups are gradually released up to 400°C . Thermal amorphization of anhydrous kaliborite proceeds in a step by step mode as all the OH groups are released. As a result of the dehydration process the borate chains of kaliborite structure become destroyed. During the further heating at 640°C the endothermic effect of transformation appears. Above 679°C the multistage crystallization of amorphous substance takes place (Table 2) [4].

The solid product of the ulexite $\text{NaCaB}_5\text{O}_6(\text{OH})_6 \cdot 5\text{H}_2\text{O}$ dehydration is the amorphous

matrix containing OH^- groups in which calcium borates crystallize at once. Above 550°C the OH^- groups are gradually removed and new compounds crystallize (Table 2) [5].

Table 2. Stages of the internal reconstitution of the amorphous K, Mg, Na and Ca-borates



The processes considered above indicate that during the heating of the amorphous decomposition products their internal structure progressively changes. Internal reconstitution of crystal lattice caused by amorphization leads to the formation of domains, having chemical composition and structure close to structural units of the precursor structure. Formation of first crystal phase inside the amorphous matrix, may be realized by rearrangement and ordering of these domains.

In amorphous solids having a complex chemical composition, with increasing temperature a redistribution of chemical elements takes place and new phases are formed. Segregation and redistribution of chemical elements occur according to their chemical af-

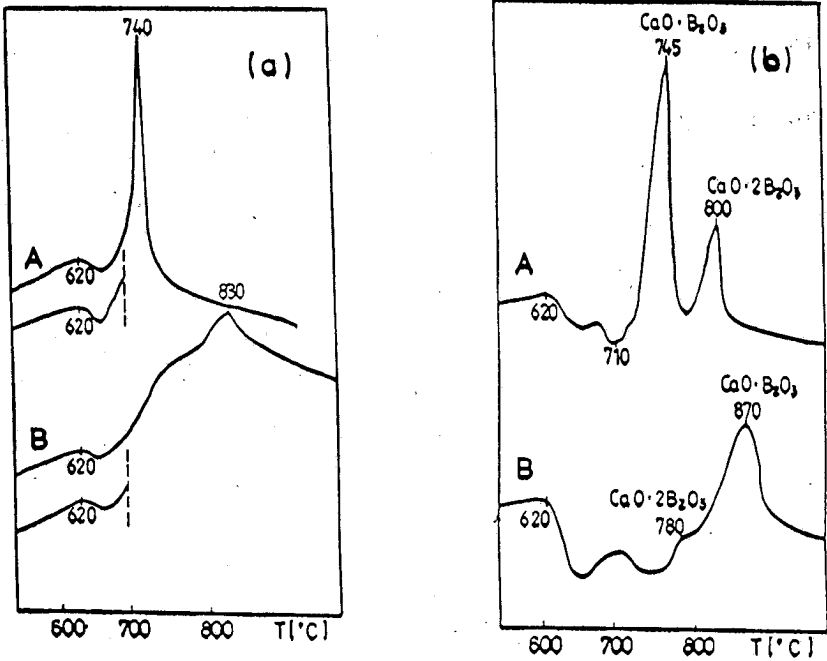


Fig.1. DTA curves of amorphous borates (A) and glasses of borate composition (B)
 (a) amorphous colemanite and 2CaO·3B₂O₃ glass
 (b) amorphous pandermite and 4CaO·5B₂O₃ glass

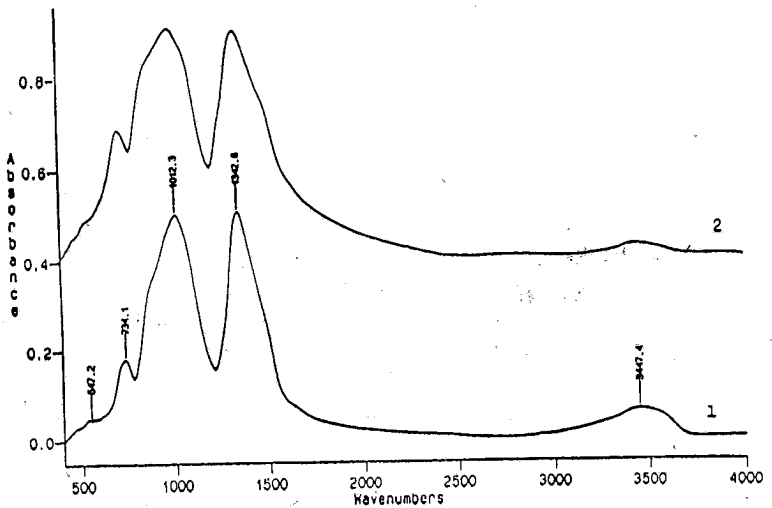


Fig.2. IR spectra of: (1) amorphous colemanite, (2) 2CaO·3B₂O₃ glass

finity principles. Usually recrystallization of this solid is a multistage process. Thermal reactions of Ca, Na and K borates are the illustration of regularities mentioned above (Tab.1,2).

The amorphous product of the thermal decomposition of colemanite has exactly the chemical composition of the compound $2\text{CaO}\cdot 3\text{B}_2\text{O}_3$ which crystallizes at 740°C (Table 1). This crystallization is the process of the internal structure rearrangement, occurring much below the melting temperature of the compound (950°C). Glass with the composition $2\text{CaO}\cdot 3\text{B}_2\text{O}_3$ crystallizes in the same manner, but the temperature of crystallization is little higher (Fig.1a).

The chemical composition of anhydrous pandermite in the two component $\text{CaO} - \text{B}_2\text{O}_3$ phase diagram, lies in the area of coexistence of $\text{CaO}\cdot\text{B}_2\text{O}_3$ and $\text{CaO}\cdot 2\text{B}_2\text{O}_3$ compounds. Both of them are formed during crystallization of amorphous anhydrite pandermite, however they are not created simultaneously (Table 1). The state of equilibrium of solid is attained gradually and compound $\text{CaO}\cdot\text{B}_2\text{O}_3$ crystallizes first. The appearance of crystallization products of a glass of the pandermite composition obtained by melting of the mixture of oxides, is reverse and the temperatures of the proper DTA peaks are higher (Fig.1b).

According to the principle of structural similarity [6] the first crystallization products of the amorphous phases are compounds with composition and structure close to the chemical composition and structure of some micro regions (domains) inside the precursor structure. The crystals of $\text{CaO}\cdot\text{B}_2\text{O}_3$, are formed inside an anhydrous matrix with a composition close to the compound $\text{CaO}\cdot 2\text{B}_2\text{O}_3$ at 800°C . The higher crystallization temperature of $\text{CaO}\cdot 2\text{B}_2\text{O}_3$ may be accounted for by the difficulty in the formation of the more complex boron-oxygen anions, which requires greater displacements of the pieces of the matrix structure on longer distances. Both processes take place below the solidus temperature (823°C).

From this data it is obvious that internal synthesis of new compounds in amorphous decomposition products and their crystallization start with the formation of compounds having structures and chemical compositions close to elements or domains of the primary structure (crystallization of Ca and Mg borates). It may occur by small displacement of pieces of the polymeric anion and diffusional displacements of the cations to small distances - translative diffusionless rebuilding stage. At higher temperatures when the diffusion becomes intensive, the redistribution of the chemical components, the decomposition of the previously formed metastable phases and the formation of the equilibrium crystal phases take place. At this stage of recrystallization chemical elements bind together according their affinity. The formation of Na-borates and NaOH in the amorphous matrix of some borates is an example.

These results indicate that the crystallization of these amorphous compounds is a multistage process of the micromechanism similar to the mixed network glasses crystallization [7].

CONCLUSIONS

1. The products of the thermal decomposition of hydrated borates are amorphous and maintain this form over relatively wide temperature ranges. Their amorphization ability and the thermal stability of the amorphous decomposition products

depend on their chemical composition and structure. These amorphous borates have properties of vitreous solid, but their structure contains preserved elements of parent structure and they are porous. These micro- and macro-heterogeneities distinguish them from normal glass.

2. The similar character of the IR spectra of amorphous borates heated to temperature close to T_g and glasses of the same compositions obtained by melting oxide mixtures (Fig.2), indicates that the two substances have networks of the similar short range order. These substances differ in the middle range order of their structure.
3. Internal synthesis of new compounds in amorphous decomposition products and their crystallization start with the formation of compounds having structure and chemical composition similar to the elements or domains of the primary structure. The synthesis may occur by small displacements of pieces of the polymeric anion and diffusional displacements of the cations to small distances (translative, diffusionless rebuilding stage). At higher temperatures when the diffusion becomes intensive, the redistribution of the chemical components, the decomposition of the previously formed metastable phases and the formation of the equilibrium crystal phases take place.
4. Glasses of the borate-like composition obtained by melting oxides mixtures crystallize more slowly and at a higher temperature. Differences in the glass and amorphized borates crystallization can be explained as a consequence of the different degree of similarity between the structure of a crystallizing compound and that of the parent substance.
5. Thermal amorphization is a convenient low temperature procedure for the formation of vitreous substances. The amorphized solids can be utilized to process glass-ceramics of different phase composition and structure, when proper parent material and heat treatment procedures are chosen.

REFERENCES

1. L. Stoch, M. Łączka, I. Waclawska, *Mineralogia Polonica* 16 (1985) 43
2. I. Waclawska, L. Stoch, J. Paulik, F. Paulik, *Thermochim. Acta* 126 (1988) 307
3. L. Stoch, I. Waclawska, *Thermochim. Acta* 215 (1993) 255
4. L. Stoch, I. Waclawska, *Thermochim. Acta* 215 (1993) 265
5. L. Stoch, I. Waclawska, *J. Therm. Anal.* 36 (1990) 2045
6. L. Stoch, *Thermochim. Acta* 148 (1989) 149
7. L. Stoch, *High Temperature Materials and Processes* 10, 4 (1992) 246

CRYSTALLIZATION OF CORDIERITE-TYPE GLASS NUCLEATED BY Ag

M. RAPPENSBERGER & I. SZABÓ

University of Veszprém, Department of Silicate Chemistry and Technology
H-8200 Veszprém, Egyetem str.10., Hungary

ABSTRACT

The glass forming ability and the crystallization characteristics of $\text{Na}_2\text{O}-\text{MgO}-\text{Al}_2\text{O}_3-\text{SiO}_2$ system, nucleated by Ag were studied. The nucleation and crystallization sequences were investigated by DTA, XRD, SEM and EDS. Nepheline, cordierite and forsterite crystalline phases were detected by XRD in the heat treated glass samples.

The crystallization of the bulk samples characterized by surface nucleation, however at certain Ag concentrations and heat treatment temperature both bulk and surface crystallization were observed.

INTRODUCTION

Besides the common glass-ceramic articles of the everyday life e.g. tableware and cooking plates, the importance of high technology glass-ceramic products made by sintering and crystallization of fine grained glass powder like printed circuit boards or fibre reinforced glass-ceramic composites have significantly increased nowadays.

The crystallization of $\text{Na}_2\text{O}-\text{MgO}-\text{Al}_2\text{O}_3-\text{SiO}_2$ glasses can yield the formation of crystalline phases having high melting point e.g. forsterite, cordierite and nepheline, therefore production of glass-ceramic material having good high temperature properties can be achieved.

In the $\text{MgO}-\text{Al}_2\text{O}_3-\text{SiO}_2$ (MAS) system the most important crystalline phases are cordierite ($2\text{MgO}\cdot 2\text{Al}_2\text{O}_3\cdot 5\text{SiO}_2$), sapphirine ($4\text{MgO}\cdot 5\text{Al}_2\text{O}_3\cdot 2\text{SiO}_2$), enstatite ($\text{MgO}\cdot \text{SiO}_2$), forsterite ($2\text{MgO}\cdot \text{SiO}_2$), spinel ($\text{MgO}\cdot \text{Al}_2\text{O}_3$) and mullite ($3\text{Al}_2\text{O}_3\cdot 2\text{SiO}_2$). In the Na_2O containing MAS system other important phases can also be formed e.g. albite ($\text{Na}_2\text{O}\cdot \text{Al}_2\text{O}_3\cdot 6\text{SiO}_2$) and nepheline ($\text{Na}_2\text{O}\cdot \text{Al}_2\text{O}_3\cdot 4\text{SiO}_2$) (1-2; 5). Forsterite has a melting point of 1850°C , spinel of 2135°C , nepheline of 1540°C and the melting point of cordierite which has many favourable mechanical properties is 1465°C (1-3).

The purpose of the present work was to produce glass-ceramic material containing cordierite, forsterite and nepheline phases, to study the sequences of crystallization and to investigate the microstructure of the crystalline product. In this study Ag nucleating agent was added to the $\text{Na}_2\text{O}-\text{MgO}-\text{Al}_2\text{O}_3-\text{SiO}_2$ base glass in different concentrations in order to provide volume crystallization.

Differential Thermal Analysis (DTA), X-Ray Powder Diffraction (XRD), Scanning Electron Microscopy (SEM) and Energy Dispersive X-Ray Microanalysis (EDS) methods were used for study the crystallization process and for identification of crystalline phases.

The linear thermal expansion of parent glasses and their crystalline glass-ceramic derivatives were determined by dilatometric measurement.

EXPERIMENTAL

Glass samples were prepared in 100g batches using Analar grade Al_2O_3 and reagent grade MgO , Na_2CO_3 and quartz. The Ag nucleating agent was used in the form of Analar grade Ag_2O . Table I. shows the composition of glasses prepared.

The thoroughly mixed batches were melted in Pt/Rh crucibles at 1500°C for 3 hours. The molten glass was quenched in distilled water and the glass frit was dried at 105°C . In order to provide good homogeneity of the glasses, the batches were remelted at 1500°C for 2 hours, then the temperature was raised to 1550°C for another hour. Part of the molten glass was cast into graphite-coated steel mould to form a glass rod and the rest of the melt was water-quenched. The glass rod was annealed at 600°C and subsequently cut up into 5 mm thick plates.

Fine glass powder (particle size $< 1\mu\text{m}$) and $1 \times 1 \times 0.5\text{cm}$ glass plates were used for the heat treatments. The surface of the glass plates were cleaned prior to the heat treatments by ultrasonic bath using ethyl-alcohol medium. According to the results of our previous experiments with MAS glasses, this pre-treatment has no effect on the crystallization sequence (4). Both types of samples were crystallized by single step heat treatment in the $800\text{--}1100^\circ\text{C}$ temperature range on an Al_2O_3 ceramic substrate.

RESULTS AND DISCUSSION

1. Differential Thermal Analysis

The nucleation and crystallization temperatures and the melting point of the glasses were determined by DTA experiments. The non-isotherm method was used for the measurements with 3, 5, 10, 15 and $20^\circ\text{C}/\text{min}$ heating rates. The exothermic peaks of crystallization were shifted towards higher temperatures with increasing heating rate. This phenomena was used for the calculation of the activation energy of crystallization. The calculations were based on the modified KISSINGER-equation (Equation 1.) developed by MATSUDA and SAKKA (6-7).

Two exothermic peaks were observed on the DTA-traces (Fig. 1.). According to the results of XRD measurements the first peak belongs to the crystallization of nepheline, whereas the second peak belongs to the simultaneous crystallization of indialite (hexagonal modification of cordierite) and forsterite. At higher heating rates the second exothermic peak has shrunk to form a small shoulder which caused difficulties in the accurate determination of the peak maxima, and this is partly responsible for the scattering of the activation energy values determined for the second exothermic peak.

The modified KISSINGER-equation:

$$\ln \left[\frac{\alpha^n}{T_0^2} \right] = - \frac{mE}{RT_0} + \text{const.} \quad (1.)$$

where α : the heating rate

n : the AVRAMI exponent

m : the numerical factor depending on the crystallization mechanism

E : the activation energy for crystal growth

T_0 : the temperature at the maximum of the crystallization peak

Since the particle size of glass powder used for the DTA measurements were $<1\mu\text{m}$ surface crystallization mechanism can be assumed, therefore $n=m=1$. The KISSINGER-type plots used for the calculation are shown on Fig. 2. and the values of the calculated activation energy can be seen in Table II.

The values of activation energy for the first peak (E_1) were between 300–305 kJ/mol and were not dependent on the concentration of the nucleating agent. The activation energy values determined for the second peak showed broad scattering which was mainly caused by the co-crystallization of indialite and forsterite.

2.X-Ray Powder Diffraction

Three main crystalline phases were identified by XRD in the crystallized samples: nepheline, indialite and forsterite. In the glasses crystallized at 800°C the first crystalline phase that appeared was the low temperature modification of carnegieite (whose chemical composition is identical with that of nepheline) and weaker reflections of nepheline were also identified. The heat treatment at 850°C resulted in nepheline as the main crystalline phase and minor phases of indialite and forsterite were also detected. In the samples crystallized at and above 850°C carnegieite was not detectable.

The intensity of nepheline reflections were the strongest in the whole temperature region above 850°C. The intensity of forsterite peaks slightly increased until 900 °C and at higher temperatures remained on a nearly constant, low value. The indialite reflections showed the largest changeability in the examined temperature range. The intensity of indialite peaks varied between the values of nepheline and that of forsterite.

The development of crystalline phases as a result of the increasing heat treatment temperature is shown on Fig. 3.

3.Scanning Electron Microscopy

SEM was used for morphological and microstructural examinations of the surface and the interior of crystallized bulk glass samples. The chemical composition of the crystals were determined by EDS. For morphological investigations the samples were etched by 1:1 mixture of 2wt% HF and 10wt% HNO₃ acid solutions for 5 seconds, whereas unetched samples were used for EDS analysis.

The first crystals were detected on the surface of bulk samples after 850°C heat treatment. Crystals of hexagonal nepheline, radial-shaped indialite and lens-shaped forsterite were identified (Fig. 4.). The size of nepheline crystals decreased with increasing

concentration of nucleating agent and the radial-shaped crystals of indialite became dominant (Fig. 5.).

At constant nucleating agent concentration the increase of the heat treatment temperature promoted the crystallization of nepheline and indialite and resulted in finer grained microstructure (Fig. 6–7.). The EDS analyses of the crystals grown on the surface are shown on Fig. 8.

The morphological examination of the cross-section of bulk glasses confirmed that the crystallization started with formation of thin crystalline layer growing from the surface towards the interior. 1000°C heat treatment of the samples containing 0.100mol% Ag₂O nucleating agent resulted in expanding dendritic grains originating from the thin surface nucleated crystalline layer. Nepheline formed the main branches of dendrites whereas the fine microstructural areas at the sides of the dendrites consist of indialite and nepheline. At the edges of the dendrites, fibrous structured forsterite crystals were observed with small spinel crystals attached to them (as determined by EDS analysis). In the samples containing 0.150mol% nucleating agent after the 1000°C heat treatment the dendritic grains occupied the whole volume of the sample.

After the 1000°C heat treatment, randomly oriented fibrous crystals of forsterite filled the interior of the samples, and the areas between the forsterite crystals were occupied by nepheline and indialite crystals as well as a residual glassy phase. The increasing nucleating agent concentration reduced the amount of the residual glassy phase and led to the formation of spherulitic aggregates of the fibrous forsterite crystals.

The samples containing 0.150mol% nucleating agent after this heat treatment resulted in a fully crystalline glass-ceramic material. The interior of the sample was dominated by fibrous forsterite crystals which were mainly randomly oriented, however in some areas spherulitic orientations were also observed. The areas between the fibrous crystals were completely filled up by nepheline and indialite crystals having a fine microstructure.

4. Dilatometry

The value of linear thermal expansion of the parent glasses as determined by dilatometry, were between $3.3\text{--}3.5 \times 10^{-6}$ 1/K (in the temperature range of 400–600°C) and were independent of the concentration of nucleating agent. In the case of glass-ceramic products crystallized at 1100°C for 5 hours the value of thermal expansion varied between $3.8\text{--}4.3 \times 10^{-6}$ 1/K (in the temperature range of 400–600°C). The crystalline samples have not shown softening up to 1000°C, the maximum temperature of the experiment.

CONCLUSIONS

Both surface and bulk crystallization were observed in Na₂O–MgO–Al₂O₃–SiO₂ glasses containing Ag nucleating agent, when crystallized in the temperature range of 800–1100°C.

Nepheline, indialite, forsterite and carnegieite were identified in the crystallized glass powders. The SEM–EDS examinations of bulk glasses showed surface formation of indialite and nepheline, whereas in the interior the formation of forsterite and nepheline were dominant.

On the basis of the results of non-isotherm DTA experiments the activation energy of crystallization calculated by the modified KISSINGER-equation was 300–305 kJ/mol in the case of nepheline. The values of activation energy calculated for the second crystallization peak showed larger scattering due to the coincidence of the crystallization exotherms of indialite and forsterite.

Controlled crystallization resulted in a glass-ceramic product which has medium range linear thermal expansion and contains high melting point crystals of nepheline, indialite and used for high temperature applications.

REFERENCES

- (1) P.W.McMILLAN: Glass Ceramics, 2nd Ed., Academic Press, London (1979)
- (2) W. HINZ: Silikate, 2. Ausgabe, VEB Verlag für Bauwesen, Berlin (1971)
- (3) J. HLAVAC: The Technology of Glass and Glass-Ceramics, Elsevier, Oxford (1983)
- (4) I. SZABÓ, W. PANNHORST, M. RAPPENBERGER: Investigation on the effect of surface crystallization of the MgO-Al₂O₃-SiO₂ glass, Proc. of the XVI. International Congress on Glass, Madrid, in: Boletín de la Sociedad de Cerámica y Vidrio, Vol.5., Glass-ceramics, (1992) pp.119–124.
- (5) A.I. BEREZHNOI: Glass Ceramics and Photo-Sitalls, Plenum Press, London (1970)
- (6) K. MATSUTA, S. SAKKA, Y. MATSUI: Determination of activation energy for crystal growth by Differential Thermal Analysis, J. Mater. Sci., 10(1975) pp.961–966.
- (7) K. MATSUTA, S. SAKKA: Kinetic study on crystallization of glass by Differential Thermal Analysis—criterion on application of Kissinger plot, J. Non-Cryst. Solids 38–39 (1980) pp.741–746.

Table I. The compositions of Na₂O-MgO-Al₂O₃-SiO₂ glasses prepared.

| NUCLEATING AGENT c, mol% | COMPONENTS OF GLASS c, wt% | | | |
|-----------------------------|-------------------------------|--------------------------------|------------------|-------------------|
| | MgO | Al ₂ O ₃ | SiO ₂ | Na ₂ O |
| 0.000 | 12.06 | 30.51 | 44.95 | 12.48 |
| 0.050 | 12.04 | 30.45 | 44.87 | 12.46 |
| 0.075 | 12.03 | 30.43 | 44.82 | 12.45 |
| 0.100 | 12.02 | 30.39 | 44.78 | 12.44 |
| 0.150 | 11.98 | 30.40 | 44.64 | 12.42 |

Table II. Activation energies of crystal growth calculated by the modified KISSINGER-equation (E₁ belongs to the first peak; E₂ belongs to the second peak).

| NUCLEATING AGENT c, mol% | ACTIVATION ENERGY E, kJ/mol | |
|-----------------------------|--------------------------------|----------------|
| | E ₁ | E ₂ |
| 0.000 | 305 | 355 |
| 0.050 | 299 | 261 |
| 0.075 | 302 | 375 |
| 0.100 | 301 | 368 |
| 0.150 | 312 | 883 |

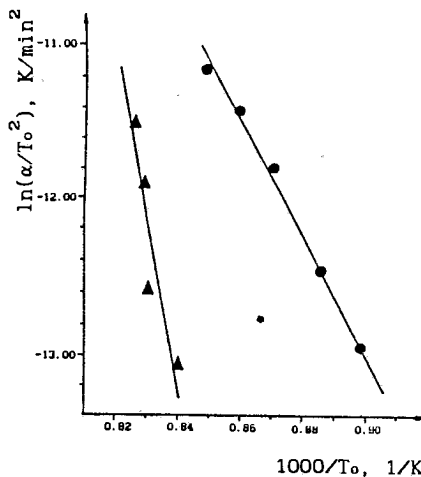


Fig. 2. KISSINGER-type plots of obtained from DTA curves of Na₂O-MgO-Al₂O₃-SiO₂ glass containing 0.150 mol% Ag₂O nucleating agent (●: first peak; ▲: second peak).

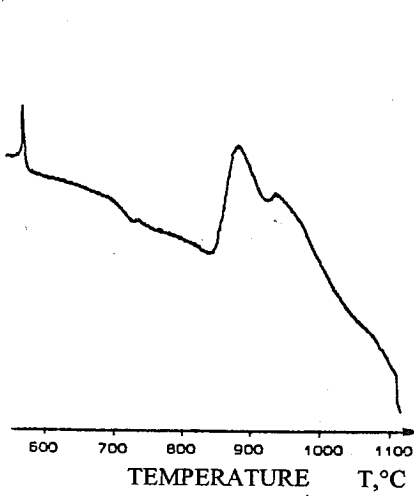


Fig. 1. DTA trace of Na₂O-MgO-Al₂O₃-SiO₂ glass containing 0.150 mol% Ag₂O nucleating agent (10°C/min heating rate).

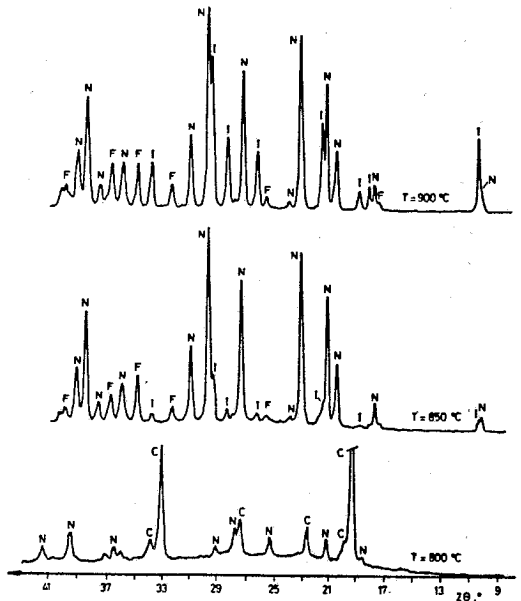


Fig. 3. XRD traces of Na₂O-MgO-Al₂O₃-SiO₂ glasses crystallized at different temperatures (C: carnegieit; N: nepheline; I: indialite; F: forsterite).

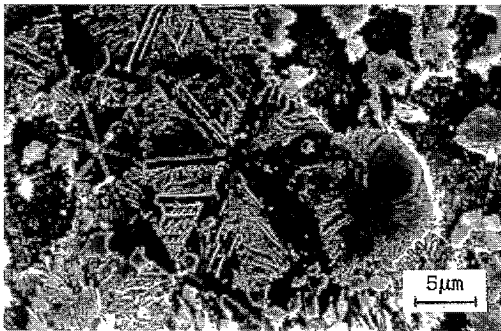


Fig. 4. Surface of the bulk glass after 850°C/3 h heat-treatment.

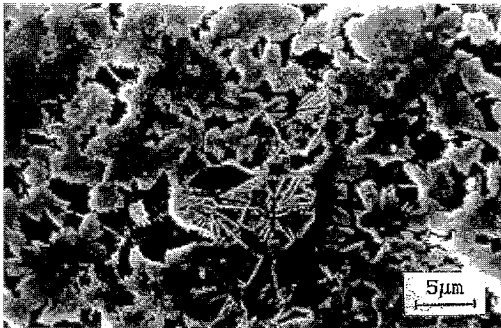


Fig. 5. Nepheline crystals developed on the surface after heat treatment 850°C/3 h. The glass was nucleated by 0.150 mol% Ag₂O.

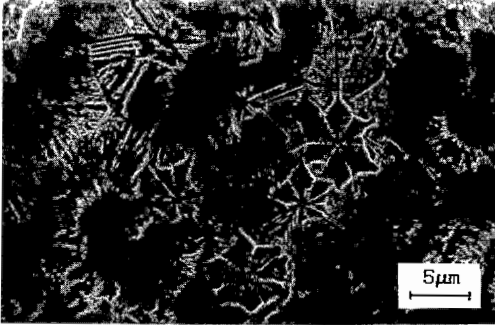


Fig. 6. Effect of the heat treatment (900°C/3 h) on crystallization of bulk glass nucleated by 0.150 mol% Ag₂O.

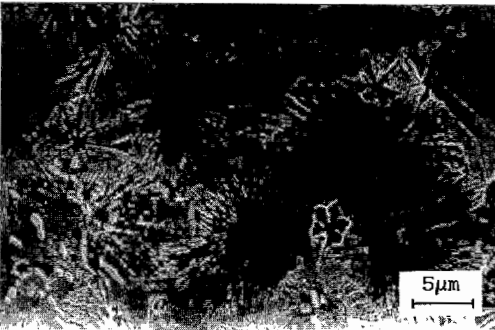


Fig. 7. Effect of the heat treatment (950°C/3 h) on crystallization of bulk glass nucleated by 0.150 mol% Ag₂O.

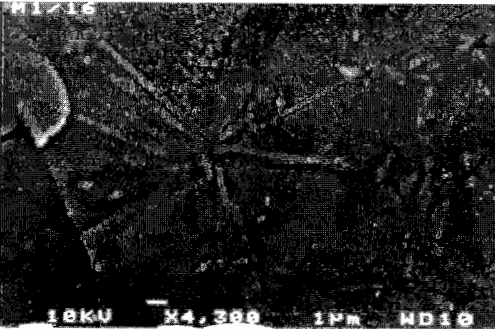
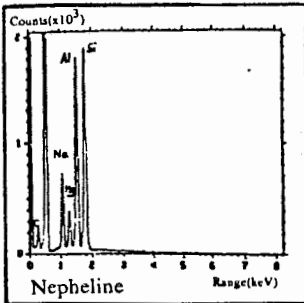
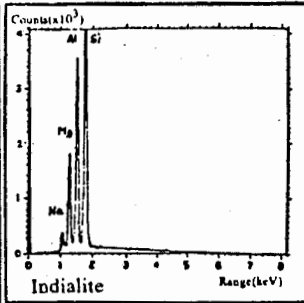


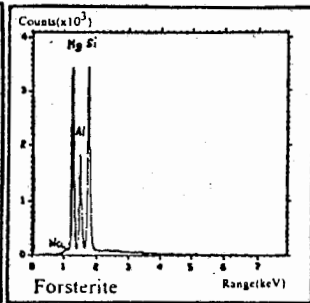
Fig. 8. Results of the EDS analysis. The glass was nucleated by 0.075 mol% Ag₂O and heat treated at 1000°C/3 h.



Analysis by thin-film window



Analysis by Be window



Analysis by Be window

A MICROWAVE STUDY OF CHARGED DEFECTS IN GLASSES

I. Ciccarello, M. Guccione and M. Li Vigni

Istituto di Fisica dell'Università, via Archirafi 36, 90123 Palermo, Italy

Abstract

It is shown that charged defects in glasses give rise to cyclotron resonance under the combined effect of an electric and a magnetic microwave fields and a dc magnetic field. The effect is ascribed to the motion of paired electrons between charged defects. It has been investigated by studying signals radiated by the glasses by way of the induced electric polarisation oscillating at the second-harmonic frequency of the driving field. Experiments performed in samples of different nature lead to the conclusion that concentration of charged defects is low in pure amorphous silica. A higher concentration is present in non-stoichiometric α - SiO_2 . The concentration of defects in pure SiO_2 can be much increased by straining it in inert atmosphere. Charged defects have been also found in borate glasses containing Al_2O_3 and Na_2O or Li_2O .

1. Introduction

It is well known that a glass material is not an entirely disordered structure, it shows short range order determined by the minimization of the energy locally. Randomness appears in the second-neighbor distance. An ideal glass is the one in which each atom satisfies its normal valence requirements by forming the appropriate number of bonds to its neighbors. At a finite temperature the glass is unstable against the formation of defects, where defect is any deviation from the ideal configuration. In particular, charged defects are believed to be present in glasses at a high concentration since they require a small energy of formation [1-3]. They originate as a consequence of the breaking of chemical bonds. When a chemical bond breaks in the glass network two neutral centres D^0 are produced; they have unpaired spins and are paramagnetic. However, the concentration of D^0 centres in glasses should be low since most glasses are diamagnetic.

Street and Mott [2] made the assumption that D^0 centres can lower their energy by forming charged D^- and D^+ centres, according to the reaction $2\text{D}^0 \rightarrow \text{D}^+ + \text{D}^-$. These defects form the so-called valence-alternation-pairs. The positive correlation energy to form a D^- centre, with two paired electrons, is thought to be more than counterbalanced by the energy gained in the distortion of the network. Charged centres in amorphous materials have either two antiparallel, or zero, electrons. The interaction between the electrons of a D^- defect is believed to be quite strong, so that paired electrons can transfer at once from D^- to D^+ , converting D^+ into D^- and viceversa, either by tunneling through, or hopping over, the potential barrier.

We have observed an effect of second-harmonic (SH) generation in dielectric glasses

when they are exposed to a dc magnetic field H^0 and intense microwave magnetic H^ω and electric E^ω fields /4/. The effect is explained as due to the motion of paired electrons induced by the fields and gives an indirect evidence of charged defects in amorphous materials. The mechanism which we propose is the following: the intense electric field induces the two electrons of a D^- centre to move to a nearby D^+ ; the motion does not occur along a straight line since H^0 forces the electrons to a circular trajectory which is modulated because of the presence of H^ω . Therefore, since a dipolar field is associated to the motion of the electrons an electric polarization with harmonic components is induced in the glasses.

We report a study of the signals radiated by the component of the polarization vector oscillating at the second-harmonic frequency of the driving fields. SH signals were observed in non-stoichiometric and in strained amorphous SiO_2 . Pure pristine a- SiO_2 showed very weak, or undetectable, SH signals. SH signals were also observed in borate glasses.

2. Experimental

The sample, dimensions $4 \times 4 \times 4 \text{ mm}^3$, is located inside a bimodal cavity oscillating at the angular frequencies ω and 2ω . The fundamental mode of the cavity is fed by an intense pulsed power from a triode oscillator, which gives a peak power up to 1000 W, lasting 1.0 μsec with a pulse repetition rate of 200 pps. A low-pass filter at the input of the cavity reduces any harmonic content of the oscillator by more than 60 dB. The SH signal generated by the sample in the cavity is filtered and detected by a superheterodyne receiver.

The field geometry in the region of the cavity where the sample is located is shown in Fig.1. E^ω and H^ω are the electric and magnetic microwave fields, respectively, due to the excitation of the ω -mode by the intense input power. $E^{2\omega}$ is the electric field due to the excitation of the 2ω -mode by the component of the polarization vector induced in the sample oscillating at the SH frequency. The angle θ can be varied over the full range 0° - 360° . All fields are coplanar. Measurements were performed at the fundamental frequency $\omega/2\pi = 2.9 \text{ GHz}$, at 4.2 K. The most intense SH signals were detected when the samples were located in a region of the cavity where the microwave fields E^ω and H^ω are both significant.

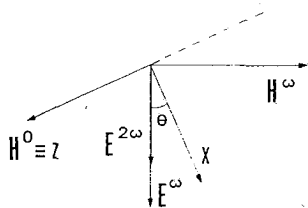


Fig.1 Field geometry in the region of the cavity where the samples are located.

3. Sample preparation and results

Several hypotheses have been put forward on the nature of charged defects in pure a- SiO_2 and no general agreement is found in the literature about their concentration. According to Greaves /5/ D^+ defects (also indicated as T_3^+) consist of three-fold coordinated silicon and D^- of one-fold coordinated oxygen. Lucovsky /6/ believes that D^+ and D^- centres are formed by over- and undercoordinated oxygen. Mott /7/ suggested that charged pairs in a- SiO_2 consist of T_3^+ and O_2^- , the O_2^- originating from oxygen dissolved in the bulk.

Since no SH signals have been observed in pure pristine a- SiO_2 , independently of its

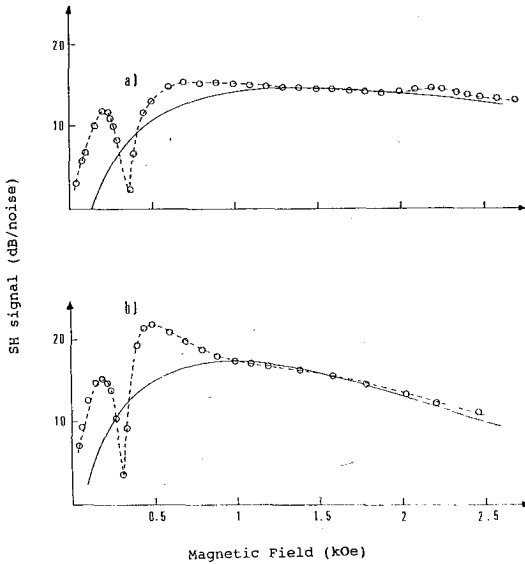


Fig.2 SH signal intensity in a sample of non-stoichiometric a-SiO₂ as a function of H⁰: a) θ=54°, b) θ=0°. T=4.2 K; input peak power ~300 W. Dashed lines are the ones which best fit the experimental points. Continuous lines are plots of eq.(3) with τ=0.7x10⁻¹¹s and m*=0.4m_e.

different values of θ: θ=0° and θ=54°. Fig.3 shows the SH signal intensity as a function of θ for H⁰ =1000 Oe and H⁰ =2000 Oe. We remark that the SH signals of Figs 2 and 3 are not related to similar ESR signals, except for the "bump" at about 2000 Oe. The bump is clearly due to magnetic defects, probably the same defects as the ones observed by Fritsch and Calas /9/ in silica melted in strongly reducing conditions and ascribed to small iron clusters originating from iron diffusion in the melt.

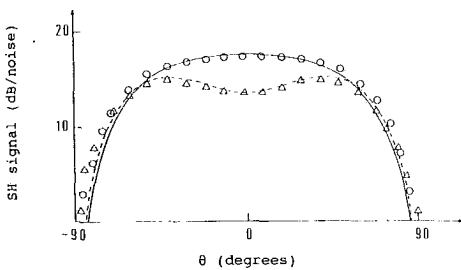


Fig.3 SH signal in a sample of non-stoichiometric a-SiO₂ as a function of θ for H⁰=1000 Oe (circles) and H⁰=2000 Oe (triangles). Continuous and dashed lines are the expected results.

content of OH⁻ ions, we argue that the concentration of D⁺ and D⁻ defects should be low. Mott /8/ suggests that a higher concentration of D⁺ and D⁻ defects is expected in non-stoichiometric a-SiO₂. This is so since a non-bridging oxygen, which gives rise to a pair of charged defects, is compensated by a Si-Si bond. We prepared samples of non-stoichiometric SiO₂, by melting fine powder of pure SiO₂ in reducing conditions in a vacuum of 10⁻³ Torr.

Charged defects are also expected in "strained" a-SiO₂. When silica glass is crushed, or heavily strained, in inert atmosphere, on the fresh surfaces are created D⁰ centres which lower their energy by forming D⁺ and D⁻ defects. We prepared samples of strained a-SiO₂ by reducing a rod of pure SiO₂ in fine powder in inert atmosphere at room temperature.

Fig.2 shows the SH signal intensity of non-stoichiometric a-SiO₂ as a function of H⁰ for two different values of θ: θ=0° and θ=54°. Fig.3 shows the SH signal intensity as a function of θ for H⁰ =1000 Oe and H⁰ =2000 Oe. We remark that the SH signals of Figs 2 and 3 are not related to similar ESR signals, except for the "bump" at about 2000 Oe. The bump is clearly due to magnetic defects, probably the same defects as the ones observed by Fritsch and Calas /9/ in silica melted in strongly reducing conditions and ascribed to small iron clusters originating from iron diffusion in the melt.

Fig.4 shows the SH signal intensity of strained a-SiO₂ as a function of H⁰ for θ =0° and θ =54°. Again, the broad line of Fig.4 is not related to a similar ESR signal. Only the "bump" at ~2000 Oe is due to paramagnetic centres, very probably the same E_s' surface centres observed by Hochstrasser and

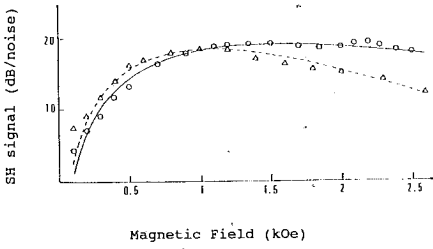


Fig.4 SH signal intensity in a sample of strained a-SiO₂ as a function of H⁰ for θ=54° (circles) and θ=0° (triangles). T=4.2 K; input peak power ~300 W. The lines are plots of eq.(3) with τ=0.8x10⁻¹¹s and m*=0.5m_e

paired electrons will be:

$$m^* \ddot{\mathbf{r}} = -2e \left[\mathbf{E} + \frac{(\dot{\mathbf{r}} \times \mathbf{H})}{c} \right] - m^* \frac{\dot{\mathbf{r}}}{\tau} \quad (1)$$

where m* is the composite effective mass of the two electrons and -2e is their electric charge;

$$\begin{aligned} \mathbf{E} &= \mathbf{z} E_1 \cos \omega t \cos \theta + \mathbf{z} E_1 \cos \omega t \sin \theta \\ \mathbf{H} &= \mathbf{x} H_1 \sin \omega t \sin \theta + \mathbf{z} (H^0 - H_1 \sin \omega t \cos \theta) \end{aligned}$$

E₁ and H₁ are the amplitudes of the electric and magnetic microwave fields, respectively. The relaxation time τ is the time the two electrons spend to move from D⁻ to D⁺ and is expected to be smaller than the half period of the microwave field. Eq. (1) has been solved by carrying out a harmonic expansion of the components x, y and z of **r**:

$$\begin{aligned} x &= a_0 + a_1 e^{i\omega t} + b_1 e^{-i\omega t} + a_2 e^{2i\omega t} + b_2 e^{-2i\omega t} + \dots \\ y &= A_0 + A_1 e^{i\omega t} + B_1 e^{-i\omega t} + A_2 e^{2i\omega t} + B_2 e^{-2i\omega t} + \dots \\ z &= \alpha_0 + \alpha_1 e^{i\omega t} + \beta_1 e^{-i\omega t} + \alpha_2 e^{2i\omega t} + \beta_2 e^{-2i\omega t} + \dots \end{aligned} \quad (2)$$

On inserting these equations into eq.(1) and equating the coefficients of terms varying at the same frequency an infinite set of equations results, which we solve in two steps. First, we neglect all terms varying as exp(±2iωt) and of higher order and we calculate the coefficients a₀, a₁, b₁, A₀, A₁, B₁, α₀, α₁ and β₁. In the second step, we neglect terms of order higher than exp(±2iωt) and calculate the coefficients a₂, b₂, α₂ and β₂ in which we are interested. In this way we have obtained the analytical expression of P_x^{2ω} = 2ex(2ω) and P_z^{2ω} = 2ez(2ω). The SH power radiated by the sample, in the field geometry of Fig.1, is given by:

$$SH \propto (P_x^{2\omega} \cos\theta + P_y^{2\omega} \sin\theta)^2 =$$

$$\frac{e^6 E_1^2 H_1^2 v_c^2 \tau^4}{\omega^2 m^{*4} c^2} \cos^2\theta \{ [d_1 \cos^2\theta + (d_3 + d_5) \sin^2\theta]^2 +$$

$$[d_2 \cos^2\theta + (d_4 + d_6) \sin^2\theta]^2 \} \cos^2(2\omega t + \phi) \quad (3)$$

ϕ is given by

$$\phi = \arctan \frac{d_2 \cos^2\theta + (d_4 + d_6) \sin^2\theta}{d_1 \cos^2\theta + (d_3 + d_5) \sin^2\theta} \quad (4)$$

where:

$$d_1 = 2(14v^4 + 4v^2 - 4v^2 v_c^2 - 2v_c^2 - v_c^4 - 1) / D_1 D_2$$

$$d_2 = -(12v^5 - 15v^3 - 9v - 6v v_c^2 - 15v^3 v_c^2 + 3v v_c^4) / D_1 D_2$$

$$d_3 = (8v^2 - 1 - v_c^2) / [D_2 (1 + v^2)]$$

$$d_4 = (5v - 4v^3 + v v_c^2) / [D_2 (1 + v^2)]$$

$$d_5 = (5v^2 - 1 - v_c^2) / [D_1 (1 + 4v^2)]$$

$$d_6 = (4v - 2v^3 + 2v v_c^2) / [D_1 (1 + 4v^2)]$$

and

$$D_1 = (v^2 - 1 - v_c^2)^2 + 4v^2$$

$$D_2 = (4v^2 - 1 - v_c^2)^2 + 16v^2$$

$$v = \omega \tau, \quad v_c = \omega_c \tau = 2eH^0 \tau / m^* c;$$

ω_c is the cyclotron angular frequency.

5. Discussion

Eq. (3) accounts satisfactorily well for the experimental data. The continuous and dashed lines of Fig.4 are plots of eq. (3) with $\tau = 0.8 \cdot 10^{-11}$ sec and $m^* = 0.5 m_e$, where m_e is the electron mass. Similarly, the expected SH signals of non-stoichiometric SiO_2 are given by the continuous lines of Fig.2 and the continuous and dashed lines of Fig.3 with $\tau = 0.7 \cdot 10^{-11}$ sec and $m^* = 0.4 m_e$. Both the θ - and H^0 -dependence of the SH signal are well reproduced by eq.(3), except for the dips of Fig.2 at about 300 Oe. The broad maxima of Figs 2 and 4 are a

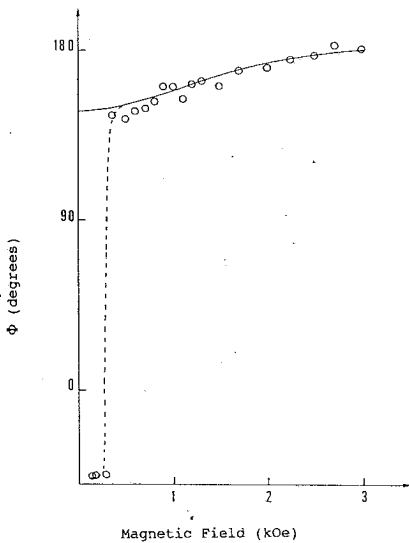


Fig.5 Phase of the SH signal in a sample of non-stoichiometric a-SiO₂ as a function of the external magnetic field H°. $\theta=0^\circ$. The continuous line is a plot of eq.(4) with $\tau=0.7 \times 10^{-11}$ s and $m^*=0.4 m_e$.

consequence of the short values of τ . For longer relaxation times the plots show two resolved lines at $\omega = \omega_c$ and $\omega = \omega_c/2$.

We remark that τ is the time the paired electrons spend to transfer from D⁻ to D⁺; it is expected to be shorter than the half period of the microwave field and limited by the distance between D⁻ and D⁺ rather than by the temperature. Therefore, we do not expect noticeable variations of the SH spectra on varying the temperature. Indeed, the SH spectra of non-stoichiometric SiO₂ at 1.5 K showed essentially the same behavior as the one of Fig.2.

SH signals radiated by the samples are phase-coherent. The phase angle Φ is a function of the external field H° according to eq.(4). For non-stoichiometric SiO₂ when H° is varied from zero to 3000 Oe the phase angle is expected to undergo the variations: $\Delta\Phi=18.5^\circ$ at $\theta=54^\circ$ and $\Delta\Phi=33.3^\circ$ at $\theta=0^\circ$.

Phase measurements of the SH signal have been performed by taking the SH content of the oscillator as a reference signal. Fig.5 shows the phase angle of the SH signal of non-stoichiometric SiO₂ as a function of the external field H°. The continuous line is a plot of eq.(4) with $\tau = 0.7 \cdot 10^{-11}$ sec and $m^* = 0.4 m_e$; it fits quite well the experimental points, except for the sharp variation of 180° near H° = 300 Oe. This variation is clearly related to the dip of Fig.2

which occurs at the same field. Both the phase variation and the field dependence of the dip are not accounted for by our model: clearly, the dip is not due to cyclotron resonance.

In conclusion, we report an effect of SH emission in dielectric glasses which gives an indirect evidence of charged defects in these materials. Our results suggest that the concentration of charged defects is low in pure a-SiO₂. A higher concentration is present in a-SiO₂ strained in inert atmosphere at room temperature as well as in non-stoichiometric a-SiO₂. Charged defects have been observed also in borate glasses containing Al₂O₃ and Li₂O or Na₂O.

References

- /1/ P. W. Anderson, Phys. Rev. Lett. **34**, 953 (1975).
- /2/ R. A. Street and N. F. Mott, Phys. Rev. Lett. **35**, 1293 (1975).
- /3/ N. F. Mott, E. A. Davis and R. A. Street, Phil. Mag. **32**, 961 (1975).
- /4/ I. Ciccarello, M. Guccione and M. Li Vigni, J. Phys. **C21**, 1631 (1988).
- /5/ G. N. Greaves, Phil. Mag. **B37**, 447 (1978).
- /6/ G. Lucovsky, Phil. Mag. **B41**, 457 (1980).
- /7/ N. F. Mott, J. Non-Cryst. Solids **40**, 1 (1980).
- /8/ N. F. Mott, Adv. Phys. **26**, 363 (1977).
- /9/ E. Fritsch and G. Calas, J. Non-Cryst. Solids **72**, 175 (1985).
- /10/ G. Hochstrasser and J. F. Antonini, Surf. Sci. **32**, 644 (1972).

HIGH QUALITY POLYSILICON FILMS FOR FLAT PANEL DISPLAYS FORMED ON GLASS ABOVE THE STRAIN POINT

J. Stoemenos, B. Kalaitzidis and N. A. Economou

Aristotle University of Thessaloniki, Physics Department
54006 Thessaloniki, Greece

Abstract

Amorphous polycrystalline silicon films deposited on borosilicate glasses were annealed at temperatures above the strain point of the glass. Conditions which ensure avoidance of glass deformation are established.

The structural characteristics of the crystallized poly-Si films and the quality of the poly-Si/glass interface were studied by combined plane view and cross-section transmission electron microscopy observations. The microroughness of the glass panel before and after the high temperature annealing was measured by Atomic Force Microscope (AFM).

A two step annealing gives the best quality of poly-Si films. At the first step amorphous Si films were crystallized at a temperature just below the strain point of the glass. The second step is a high temperature annealing above 780°C which results in the elimination of the defects inside the grains. The adherence between the borosilicate glass and the poly-Si film after the high temperature annealing was surprisingly good.

1. Introduction

Polycrystalline silicon films deposited on a soft glass substrate have attracted more and more attention in large-area electronic devices, as drivers of active matrix liquid crystal displays for flat panel TV and office systems (1,2). By the end of this century a market of 17.5 Bil.\$ is expected in this field (3). Glass is also extremely attractive material for supporting thin film silicon solar cells due to its very effective role as the superstrate in present generations of solar modules (4,5).

Direct deposition of thin polycrystalline silicon films onto glass would ultimately result in very little additional module cost above the cost of glass with a significant improvement of the efficiency of the photovoltaic cells compared with amorphous Si solar cells deposited on glass. However the realization of large-area electronics and solar cells on low cost glass is impeded by temperature limitation of polysilicon deposition because the borosilicate glass substrate degrades above 600°C, the strain point of this glass.

For this purpose a special experimental furnace was designed which permits deposition and crystallization of amorphous Si on glass at temperature above the strain point of borosilicate glasses to a temperature 850°C. The structural characteristics of the annealed poly-Si and their interface with the glass was studied by plane view and cross-section transmission electron microscopy (TEM).

2. Experimental

Amorphous Si (α -Si) films about 200nm thick were deposited at 550°C by the Low Pressure Chemical Vapour Deposition (LPCVD) method on Hoya NA40 or on Corning 7059 glasses. Prior the deposition of the α -Si a SiO₂ buffer layer 500nm thick was deposited on the glass. After the α -Si deposition a SiO₂ capping layer 500nm thick was deposited in order to protect the film from contamination.

The α -Si films were subjected to an anneal above the strain point of the glass using a tin bath as diagrammatically shown in fig.1. The tin is on a graphite crucible and

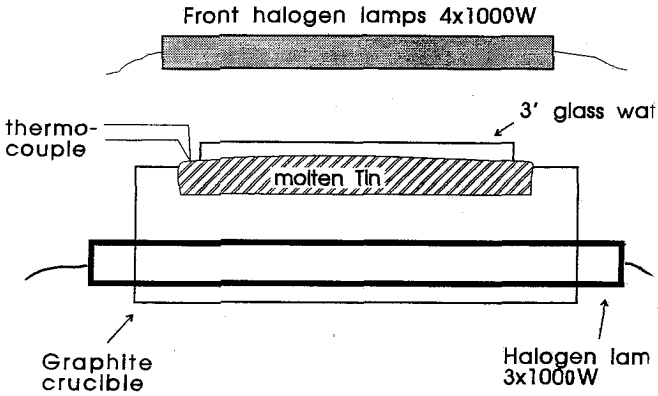


Fig.1. Schematic diagram of the furnace.

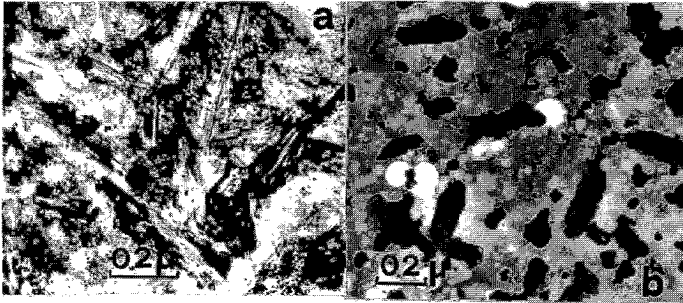


Fig.2. a) The α -Si films was deposited at 550°C by LPCVD, then was annealed at 590°C for 4h. In the plane view micrograph elongated grains are clearly evident. In the core of the crystallites (111) type twins run along the long axis of the grain.

b) Plane view micrograph from the same film annealed for 2h. Only 25% of the film was crystallized.

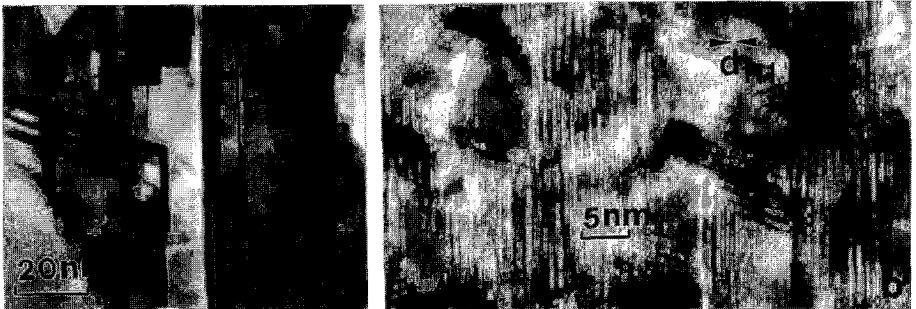


Fig.3. a) A high magnification micrograph from an elliptical crystallite. Long twins at the center of the grain, are evident. Microtwins also run at the side bands of the long central twins resulting in a tweed like appearance.

b) High resolution micrograph. Very regular lattice fringes with d_{111} spacing are clearly evident. The main defects inside the grains are the microtwins.

is heated by halogen lamps under vacuum. The base vacuum in the chamber is better than 5×10^{-5} torr.

The advantages of this method are the following:

i Glass floats on tin

ii No temperature gradient at the glass surface due to the very good thermal contact between liquid tin and glass.

iii Uniform temperature at glass wafers in vacuum without limitations on the shape and the size of the glass plates.

iv Tin doesn't wet glass and consequently it is very easy to remove the glass plates from the tin bath.

v Insignificant contamination due to tin, because the vapour pressure of tin at 800°C is only 10^{-6} torr.

3. Results and Discussion

Amorphous Si deposited on glass by LPCVD is completely crystallized after annealing at 590°C for 4 hours. Most of the crystallites exhibit a three dimensional ellipsoidal shape. In the core of the crystallites, multiple (111) type twins are formed along the $\langle 112 \rangle$ direction, fig.2a. The ellipsoid shape of the crystallites is clearly evident when the crystallization of the film is not completed as is shown in fig.2b.

The morphology of the individual crystallites is shown by the high magnification micrograph of fig.3a. Very often branches of twins are formed in other coplanar $\langle 112 \rangle$ directions resulting in a dendritic crystal. The growth along the $\langle 111 \rangle$ direction solely proceeds by the formation of very small twins resulting in a tweed like structure as it is shown in fig.3a. The defected structure within the crystallites is also revealed in detail by the high resolution micrograph in fig.3b. Lattice fringes of (111) type are clearly evident. The mean size of the grains is about 250nm while the mean size of the microtwins inside the grains is about 30nm only.

Due to the very small size of the microtwins inside the grain we considered them as unstable. In order to test the stability of the microtwins an in situ annealing experiment was performed in the electron microscope. We started with an α -Si film already crystallized in a conventional furnace at 600°C for 3h shown in the micrograph of fig.4a. Using a TEM heating stage the temperature was progressively increased. However the structure of the film was unaffected up to 750°C as it is shown in fig.4b. Above this temperature one observes a reorganization of the microtwins. After the temperature was stabilized at 780°C for 30min most of the microtwins were absorbed by the larger twins as it is shown in the micrograph of fig.4c.

Due to instability of microtwins a two step process involving a low temperature furnace annealing at 600°C in order to grow large but highly defected grains followed by an anneal using a tin bath above 780°C for 30min in order to eliminate the microtwins inside the grains can result in a significant improvement of the quality of the films. Notice that a direct annealing at the 780°C always results in poly-Si film with small grain size because at high temperatures a higher number of nucleation centers is activated.

The results of the two step annealing are presented in fig.5a which is a plane view micrograph from an α -Si film annealed first at 600°C for 3h and then subjected to a second anneal at 850°C for 1h. Figure 5b is a micrograph from the same film subjected only to the first anneal at 600°C . The defect density inside the grains was reduced substantially in the case of two step annealing. Notice that in both cases the size of the grains remains the same because the temperature for secondary recrystallization of Si is above 1150°C (6). The quality of the Si/glass interface is revealed by the cross-section micrograph in fig.6. The adherence between the poly-Si overgrown and the glass substrate is excellent.

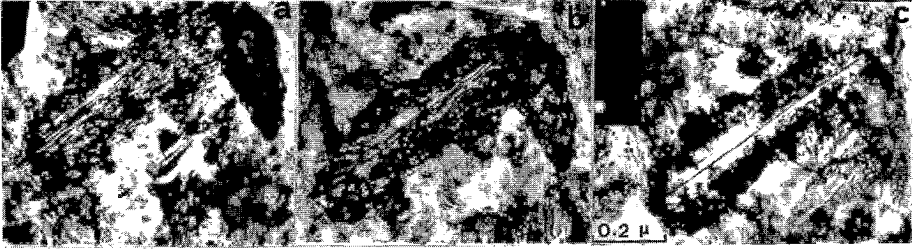


Fig.4. Plane view micrographs from an in situ annealing experiment in the electron microscope.

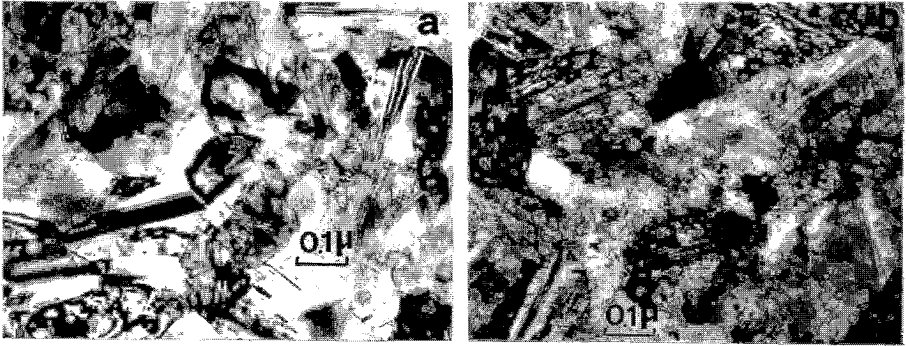


Fig.5. α -Si films deposited on Hoya glass a) First annealed at 600°C for 3h and then subjected to an annealing at 850°C for 1h. b) The same film annealed at 600°C for 3h only.

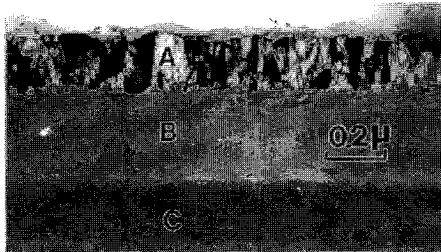


Fig.6. Cross-section micrograph from a poly-Si film annealed at 850°C for 1h. The poly-Si film, the SiO_2 buffer layer and the glass substrate are denoted by the letters A, B and C respectively.

The microroughness before and after high temperature annealing was studied by AFM (2). Three different areas $0.2\mu\text{x}0.2\mu$ were scanned in each case. The surfaces of both specimens exhibit fine corrugations as is shown in fig.7a and 7b respectively. Roughness measurements were performed along two mutually perpendicular directions in order to reveal possible surface textures, no such texture was observed. For the non annealed specimen the mean roughness value was 4.2nm while for the annealed was 3.9nm. Consequently no microroughness was induced during the two step annealing.

The profile of the heat treatment of a Hoya glass is shown in fig.8. The period AB describes the first low temperature annealing, after that the temperature increases with a rate $1^\circ\text{C}/\text{min}$ up to the point C at 850°C where the second annealing CD occurs. In order to avoid glass deformation the temperature decreases with a very low rate $0.6^\circ\text{C}/\text{min}$ up to the strain point of the glass at 650°C , denoted by the letter E in fig.8. Below this temperature the glass wafer was cooled with a higher rate of the order $5^\circ\text{C}/\text{min}$. It is expected that during this process a significant compaction of the glass will occur. However the very low cooling rate results in a structural relaxation of the glass which in turn increases the thermal dimensional stability of the glass during the fabrication of the plate panel liquid crystal display, which occurs at lower temperatures than those of the annealing process (7,8).

In spite of the very low cooling rate some times the glass wafers are slightly distorted after the two step annealing process. The distortion is attributed to instabilities of the heating elements as well as to capillarity effects of the tin surface because the diameter of the crucible is comparable with the size of the glass wafer.

The electrical characteristics of the poly-Si films are not affected by the tin because Sn is in general electrically inactive in Si. In addition, the SiO_2 capping layer acts a diffusion barrier for tin. A similar tin bath was applied in the case of high temperature implantation of Si-wafers, and no contamination due to tin bath was observed (9).

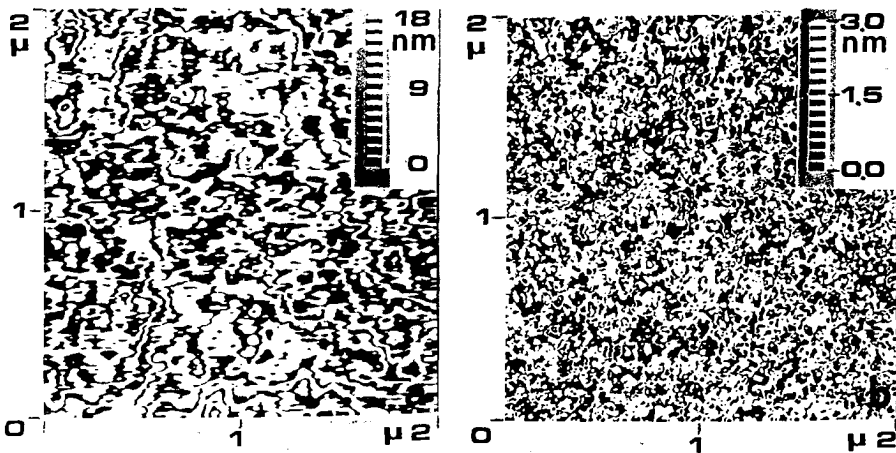


Fig.7. Atomic Force Microscope scan of Hoya glass surface a) After a $600^\circ\text{C}/3\text{h}$ annealing b) The same specimen subjected to additional anneal at 850°C for 1h.

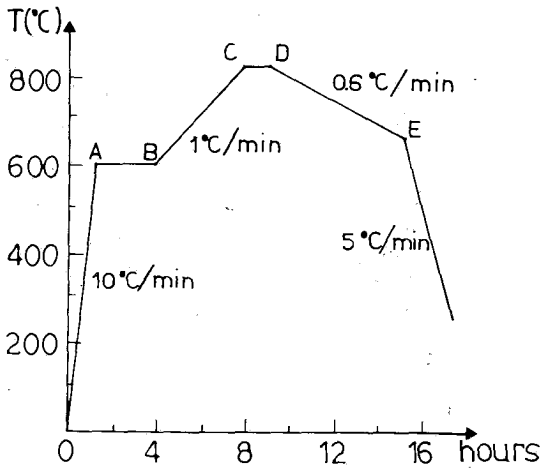


Fig.8. Thermal cycle annealing.

4. Conclusions

The quality of poly-Si films deposited on glass substrate was significantly improved by a two step annealing the second being above the strain point of the glass. Conditions for such a process are presented. However further work is needed for the optimization of these conditions. It is also evident that the insitu deposition of good quality poly-Si films during glass panel fabrication is feasible from a technological point of view.

References

1. C.Hilsum, N. Bryer, D. Meakin, P. Migliorato, J. Magarino, W. Senske, M. Anderson, F. Morin, N. Economou and J. Stoemenos. ESPRIT 86: Results and Achievements. Ed. Directorate General XIII, Elsevier Science Publishers B.V. (1987) p.241.
2. P. Migliorato *Microelectronic Engineering* 19 (1992) 89.
3. G.H. van Leeuwen and R.A. Hartman 23rd European Solid State Device Research Conference 13-16 Sep. 1993 Grenoble France.
4. S. Martinuzzi Conference on Polycrystalline Semiconductors, Physics and Technology 5-10 Sept. 1993 St Malo, France.
5. Z. Shi and M.A. Green, *Ibit*.
6. B.Y. Tsaur and L.S. Hung *Appl. Phys. Lett.* 37, (1980) 648.
7. F. Okamoto, T. Hayashi, T. Inuzuka, M. Anma and T. Araki *SID 91 DIGEST* (1991), 663.
8. J. Makino, K. Veno, K. Sagara and S. Sakamoto *SID 91 DIGEST* (1991), 671.
9. M. Bruel, J. Margail, J. Stoemenos, P. Martin and C. Jaussaud. *Vacuum* 35 (1985) 489.

ELECTROCHROMIC PROPERTIES OF CHEMICALLY VAPOUR DEPOSITED (CVD) WO_3 POLYCRYSTALLINE THIN FILMS.

D. Davazoglou.

NCSR "Demokritos" Ins. of Microelectronics POB 60228, 153 10 Ag. Paraskevi Attiki, Greece.

ABSTRACT.

Electrochromic configurations were formed by depositing WO_3 films on transparent SnO_2 conducting electrodes by pyrolysis of $W(CO)_6$ at $400^\circ C$ and under atmospheric pressure. The configurations were stable in acid environment and present reversible electrochromic effect. Measurements of the electrochromic properties of these devices have been made, using protons and lithium as inserting ions and under DC and AC bias. The coloration efficiencies measured were of the order of $35 \text{ cm}^2/\text{Cb}$ and $25 \text{ cm}^2/\text{Cb}$ for H^+ and Li^+ respectively while the corresponding coloration times (defined as the time intervals required to achieve an optical density equal to 0.3) were 0.3 and 2 sec. Bleaching times for DC bias were found to be of the order of 10 sec, while for AC bias coloration and bleaching times were comparable and of the order of 500 ms.

I. INTRODUCTION

Electrochromism has been termed the effect of coloration exhibited by some materials, called electrochromic (EC), when in contact with an electrolyte and under bias. Possible applications of this effect include the control of radiative energy (1,2) and the fabrication of displays (3,4). The coloration can be observed on configurations of the form:

Substrate / Transparent Electrode / EC Material / Electrolyte / Counter Electrode.

Among EC materials WO_3 thin films are of great interest because of their stability in acid environments, present a good electrochromic effect and their deposition is relatively feasible. Since the observation of the electrochromic effect on these films (5) many methods have been used for their deposition (for a review see ref. 1) and many studies have been published dealing with their electrochromic properties.

In this work we present some electrochromic properties of WO_3 films deposited by Chemical Vapour Deposition (CVD). The second part of this work is dealing with the presentation of the formation method of the electrochromic (EC) configurations and the measurements used to evaluate their properties. In the third part of this work are presented some properties of our EC configurations such as their coloration efficiency and their coloration and bleaching time. It is also discussed the influence on these properties of the injected ion and of the WO_3 film thickness. In the last part of this work are exposed the conclusions drawn from it.

II. EXPERIMENTAL.

The substrates used in this study were pyrex coated by fluorine

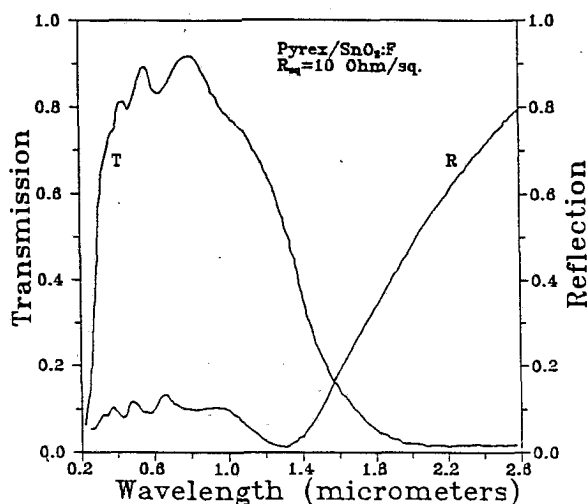


Fig. 1 Typical reflection-transmission spectra taken on an SnO₂:F film deposited on pyrex.

different modes: at 600°C and 500°C in air (modes 1 and 2 respectively) and at 500°C in a stream of a 10% mixture nitrogen-oxygen (mode 3).

The sandwiches pyrex/SnO₂/WO₃ were coloured in a two electrode electrochemical cell using a normal aqueous solution of H₂SO₄ as injected ion source and a platinum counter electrode. Optical transmission spectra within the range 0.2 to 1.5 micrometers, have been taken on such sandwiches in their initial (uncoloured) and in coloured states, with a Beckmann spectrophotometer. Various degrees of coloration were induced applying different voltages between the SnO₂ film and the platinum counter electrode in permanence during recording (approximately 2 minutes).

A three electrode electrochemical cell using a saturated sulphate electrode (SSE) as reference and a platinum disc as counter electrode, was used for the determination of properties such as the coloration efficiency, the coloration and the bleaching times. The solutions used were normal aqueous H₂SO₄ solution and an organic electrolyte made of 1M LiClO₄ dissolved in a hydroorganic solvent: propylene carbonate and 1 wt% distilled water. The coloration efficiency is the parameter correlating the variation of the optical density (decimal logarithm of the ratio initial to final transmission) of the coloured sandwich, with the charge injected in it. Coloration time is defined as the time interval that the electrochromic configuration must be polarized

doped SnO₂ thin films. The SnO₂ films were deposited by spray pyrolysis and are transparent electrodes. Typical reflection and transmission spectra taken on such films deposited on pyrex are shown in fig. 1 having square resistance of the order of 10 Ohms/sq. The deposition of the WO₃ films has been made in two steps. The first one was the pyrolysis of W(CO)₆ in presence of oxygen at 400°C and atmospheric pressure. This process results in the deposition of a film composed by a mixture of tungsten oxides that we have called "black" tungsten, referred to as BW hereafter. The second step was the complete oxidation of the BW film to WO₃. This step has been made in three

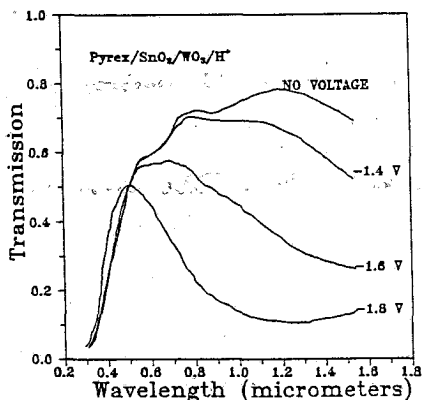


Fig. 2 Transmission spectra of an EC configuration uncolored and colored in various degrees.

approximately 500 nm, depending on film thickness. The films were very stable in acid environment and present reversible electrochromic effect.

In fig. 2 are shown the transmission spectra of an electrochromic configuration formed as described in the previous section using a WO_3 film oxidized by the first mode, coloured in various degrees with protons as injecting ions. It is observed that the coloration can be obtained with small polarizations and that it is easy to obtain large variations of the transmission.

Fig. 3 shows a typical relationship between the optical density of an electrochromic configuration using a WO_3 film made by the second mode and the injected charge, for protons and lithium ions. The slope of the obtained straight lines gives the colouring efficiency of the film. It is found to be of the order of 37 and $25 \text{ cm}^2/\text{C}$ for H^+ and Li^+ respectively. These small values compared with amorphous WO_3 films, i.e. $120 \text{ cm}^2/\text{C}$ for anodic oxidized films (6), $60 \text{ cm}^2/\text{C}$ for evaporated films (7) and $70 \text{ cm}^2/\text{C}$ for anodic oxidized films obtained under pulsed currents (8) may be attributed to the

to reach an optical density and bleaching time as the time interval that the sandwich, initially coloured at a certain optical density, must be inversely polarized to return to its initial transmission. The measurement of the above quantities in our electrochromic configurations, has been made in transmissive mode at wavelength 632.8 nm with the aid of a He-Ne laser, colouring them by injecting protons and lithium ions.

III. RESULTS AND DISCUSSION.

X-ray diffraction and scanning electron microscope measurements have shown that our WO_3 films were polycrystalline with grain sizes varying from 20 to

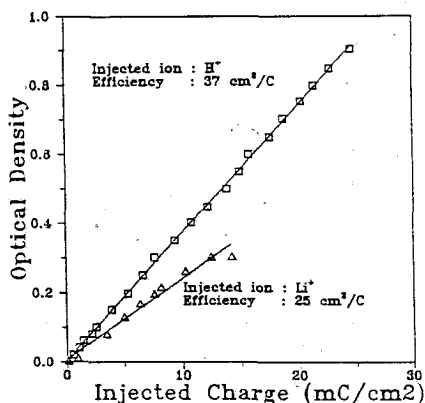


Fig. 3 Optical density vs injected charge for a typical EC configuration. The slope of the curve is defined as the coloration efficiency.

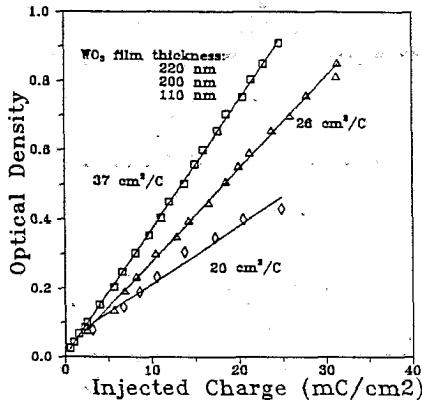


Fig. 4 Optical density vs injected charge for three EC devices formed with WO_3 films of different thickness.

capacity of the electrochromic films to absorb the charge injected.

The variation of the optical density with coloration time is shown in fig. 5 for three electrochemical configurations formed using WO_3 films of comparable thickness (approximately 320 nm) made by the three modes. It is observed that films made by the first mode are coloured faster than those by the second, followed by those made by the third. In a recent publication (10), we have shown that in WO_3 films prepared by a different method, the volume fraction occupied by crystalline and amorphous material and voids depends on film thickness and annealing mode. This variation of the volume fractions of the phases into the films (crystalline and amorphous material and voids) is probably related to the observed differences of the coloration times. Further research is necessary to conclude about the validity of this hypothesis. It must be pointed out that the time interval necessary to colour a film to the half of its initial transmission, i.e. to obtain an optical density of 0.3 which is the significant feature for the

polycrystalline nature of our CVD films. Indeed, crystallized anodic oxidized films show an efficiency of 34 cm^2/C (9) instead of 120 cm^2/C as mentioned above. The smaller value of the colouring efficiency obtained in the organic solution can be attributed to its larger resistance relative to the inorganic one and to the fact that the lithium ions are larger in size and heavier than protons. The colouring efficiency depends on WO_3 film thickness and increases with it. This is depicted in fig. 4 where the variation of the optical density versus injected charge is plotted for three films of various thickness prepared by the second mode. This can be attributed to the limited

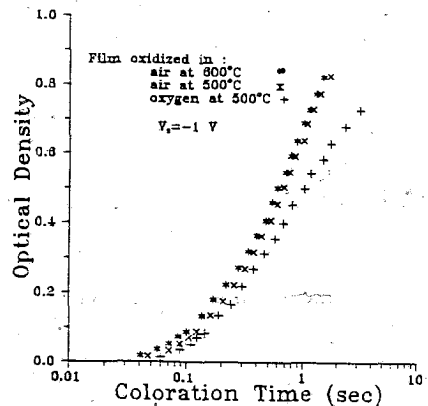


Fig. 5 Coloration times for three EC configurations made using WO_3 films oxidized by the three modes.

industry, is approximately 500 ms.

Optical densities versus bleaching time are shown in fig. 6. It can be observed that the bleaching times are at least one order of magnitude longer than those of coloration. This difference can

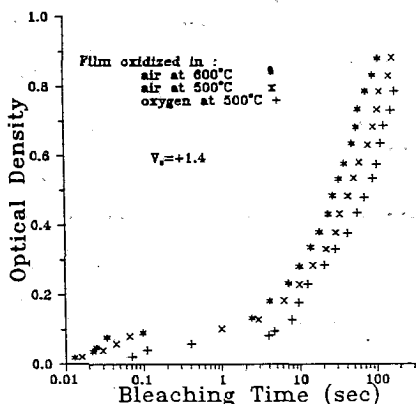


Fig. 6 Optical density vs bleaching time for the same as in the previous fig. EC configurations.

be associated with a memory effect that the EC devices present in coloration. This effect can be explained supposing that the electrochromic effect can be separated in two parts: an electronic fast one and an electrochemical slower, related to the ionic diffusion in the electrochromic film. Thus low colorations can be obtained injecting only electrons into the electrochromic film, so the coloration and bleaching times are comparable for small optical densities, that are obtained in time intervals of about 300 ms. Instead, if the polarization for the coloration lasts for a time intervals more than this limit, ionic injection takes place that results in longer bleaching times since now the

bleaching is also related to slow electrochemical reactions. In previous works (11,12) we have attempted to isolate the two mechanisms applying AC polarizations. It seems that the results justify our assumption, since for low frequencies the bleaching times are much longer than the coloration ones, the differences become smaller as the frequency raises and after a certain frequency the coloration and bleaching times are comparable.

IV. CONCLUSIONS.

The study of the electrochromic properties of CVD WO_3 films have shown their stability and their ability for coloration. Parameters such as coloring efficiency and time response are inferior than those observed on liquid crystals. However, taking into account the memory effect that these films present, their overall consumption when used in electrochromic configurations becomes smaller than that of liquid crystals. On the other hand the feasibility with which WO_3 films can be deposited on large surfaces and their ability for blue coloration, makes them suitable for applications such as publicity panels or "smart windows" under the condition that "good" a solid electrolyte will be found in the near future.

REFERENCES.

1. C. Lambert Sol. En. Mat. 11 (1984) 1
2. J. Svenson and C. Granqvist Appl. Phys. Lett. 45 (1984) 828
3. B. Faughnan and R. Crandal in Topics in Applied Physics,

- edited by J. Pancove (Springer, Berlin 1980) Chap. 5.
4. W. Dautremont-Smith, *Displays* 3 (1982) 3.
 5. S. Deb *Phil. Mag.* 27 (1973) 801.
 6. D. Davazoglou and A. Donnadiou *Thin Sol. Films* 147 (1987) 131.
 7. D. Davazoglou, A. Donnadiou and O. Bohnke *Sol. En. Mat.* 16 (1987) 55.
 8. D. Davazoglou, G. Leveque and A. Donnadiou *Sol. En. Mat.* 17 (1988) 379.
 9. D. Davazoglou and A. Donnadiou *Proc. of the SPIE Vol. 653* (1986) 36
 10. P. Falaras Thesis, Paris VI (June 1986)
 11. O. Bohnke Thesis, Besancon (June 1984)
 12. M. Resrazi, O. Bohnke and J. Pagetti, *Displays* (1987)
 13. D. Davazoglou and A. Donnadiou *J. Appl. Phys.* 72 (1992) 1511.
 14. D. Davazoglou, Thesis Montpellier (1987)
 15. D. Davazoglou and A. Donnadiou *Thin Sol. Films* 164 (1988) 369.

AUTHOR INDEX

- J. Allegre.....163
 W. P. Allen.....251
 C. A. Angell.....211
 A. Aronne.....199
 D. Bain.....315
 C. Bessada.....351
 R. Boekenhauer.....315
 M. Bouchnafa.....187
 L. Boudes.....163
 P. J. Bray.....309
 K. Budhwani.....315
 A. Bunde.....221
 M. Cable.....53
 M. Catauro.....199
 G. D. Chryssikos.....
245, 271, 309, 341
 I. Ciccarello.....411
 M. R. P. Correia.....323
 G. J. Copley.....45
 B. Cote.....351
 M. Cuccione.....411
 A. Dauger.....187
 D. Davazoglou.....423
 J. E. Dickinson.....355
 Y. Dimitriev.....361
 V. Dimitrov.....367
 G. S. Dixon.....251
 P. G. Dixon.....251
 A. Dobрева.....373, 379
 I. Dounis.....205
 T. Doyle.....251
 O. Dushkin.....181
 N. A. Economou.....417
 D. Ehrt.....347
 D. Feil.....315
 S. Feller.....309, 315
 G. H. Frischat.....157
 J. Fukunaga.....385
 K. Fröberg.....289
 Fuxi Gan.....295
 B. D. Gault.....251
 F. Gervais.....351
 S. Ghosh.....315
 K. Golematis.....193
 W. Granier.....163
 R. Guinebretiere.....187
 M. Guglielmi.....181
 I. Gutzow.....373, 379
 G. Hauret.....329
 L. Hou.....175
 C. H. Hsieh.....335
 F. Hubert.....119
 M. D. Ingram.....221
 P. Innocenzi.....181
 H. Jain.....335
 C. Jäger.....347
 B. Kalaitzidis.....417
 E.I. Kamitsos.....
245, 271, 309, 335, 341
 J.A. Kapoutsis 245, 271, 335, 341
 M. A. Karakassides.....193, 205
 K. H. Karlsson.....289
 S. Kasa.....81
 E. T. Knobbe.....251
 M. Kodama.....303
 L. L. Konstantinov.....277, 283
 A. Koufoudakis.....205
 G. Kordas.....193, 205
 H. Kozuka.....137
 G. Kunath.....347
 A. Lecomte.....187
 P. Lefebvre.....163
 P. Lianos.....169
 A. Lisý.....81
 C. Liu.....211
 M. Li Vigni.....411
 Y. Luspín.....329
 P. Maass.....221
 N. Machida.....227
 J. Mackenzie.....309, 315
 N. Maliavski.....181
 J. L. Marc.....163
 M. S. Marinov.....277, 283
 A. Marotta.....199
 M. Maryska.....107
 D. Massiot.....351
 J. Matousek.....107
 T. Matsushita.....303
 S. K. Mendiratta.....323
 M. Mennig.....175
 G. Mezinskis.....157
 B. D. Mihailova.....277, 283
 M. Mika.....113, 239
 T. Minami.....227

| | | | |
|------------------------|--------------------|--------------------------|----------|
| N. Mishima | 385 | R. Sims | 63 |
| M. Mochev | 131 | R. Snider | 251 |
| H. Moser | 39 | B. Soulestin | 187 |
| S. Nijhawan | 309, 315 | P. E. Stallworth | 309 |
| M. Oran | 101 | Yu. K. Startsev | 125 |
| R. Ota | 385 | L. Stoch | 391, 397 |
| C. Parameswar | 315 | J. Stoemenos | 417 |
| T. Parot-Rajaona | 329, 351 | I. Szabó | 403 |
| A. P. Patsis ... | 245, 271, 309, 341 | M. Tatsumisago | 227 |
| E. A. Pavlatou | 257, 265 | J. Taylor | 309 |
| P. Pernice | 199 | E. Tchekounova | 181 |
| H. Pieper | 71 | C. C. Trapalis | 193, 205 |
| A. Pradel | 163 | Y. Vails | 329 |
| M. Prassas | 341 | N. Vanandruel | 89, 95 |
| M. Rada | 113, 239 | P. A. Watson | 251 |
| M. Rappensberger | 403 | T. Wakasugi | 385 |
| M. Ribes | 163 | I. Waclawska | 397 |
| J. Rosenthal | 31 | K. Yamakawa | 303 |
| M. Royle | 309 | S. N. Yannopoulos | 257 |
| S. Sakka | 137 | Y. D. Yiannopoulos | 341 |
| E. Sanchez | 211 | B. E. Yoldas | 147 |
| L. Sasek | 113, 239 | E. D. Zanutto | 3 |
| G. Scarcini | 181 | H. Zhang | 315 |
| H. Schaeffer | 21 | N. S. Zotov | 277, 283 |
| M. Sharma | 309 | | |
| H. Schmidt | 175 | | |
| S. Shi | 251 | | |

LIST OF PARTICIPANTS

Mr. P. Agorastos
E. Tsantalís S.A.
Agiós Paylós 63080
Chalkídiki, GREECE

Mr. J. Allcock
Electroglass Ltd.
4, Brunel Road, Benfleet
Essex SS7 4PS, England, UK

Dr. G. André
GLAVERBEC
166 Chaussée de la Halpe
1175 Brussels, BELGIUM

Prof. C. A. Angell
Department of Chemistry
Arizona State University
Tempe, AZ 85287, USA

Dr. N. Araki
Nippon Sheet Glass Co
5-11-3, Shimbashu, Minatoku
Tokyo, JAPAN

Mr. S. Barna
National Institut of Glass
Bul. Th. Pallady Nr. 47
Bucarest 74584, ROMANIA

Prof. H. A. El Batal
Glass Research Department
National Research Centre
Dokki, Cairo, EGYPT

Ir. A. Bergstein
Burg. Meslaan 75
4003 CA Tiel
THE NETHERLANDS

Mr. A. Berlanda
Rombos Glass
Kifissou 8
12241 Egaleo, Athens, GREECE

Prof. M. Cable
Engineering Materials, Hadfield Bldg
University of Sheffield
Sheffield S1 4DU, UK

Dr. M. Catauro
Dept. of Materials and Production Eng.
Piazzale Tecchio
80125, Naples, ITALY

Mr. J.-P. Causse
25, Rue de l'Ouest
75014 Paris
FRANCE

Mr. J. Chatzis
Cali Hellas Ltd.
4, Gordiou Str.
N. Smirni 171 21, GREECE

Dr. G. D. Chryssikos
Theor. & Phys. Chem. Inst., NHRF
48, Vass. Constantinou Ave.
Athens 11635, GREECE

Dr. I. Ciccarello
Istituto di Fisica dell'Università,
via Archirafi 36,
90123 Palermo, ITALY

Dipl.-Ing. G.-A. Clasen
ICC Clasen Consulting
Bernhard-Hahn-Str. 11-15
41812 Erkelenz, GERMANY

Mr. B. Copet
S.E.P.R. - B.P. 25
84131 Le Pontet Cedex
FRANCE

Dr. G. J. Copley
British Glass
Northumberland Road
Sheffield S10 2UA, UK

Dr. Maria do Rosario P. Correia
Dep. de Física da Universidade de Aveiro
3800 Aveiro
PORTUGAL

Dr. D. Davazoglou
Institute of Microelectronics
NCSR 'Demokritos', P.O. Box 60228
Ag. Paraskevi, 15310 Attiki, GREECE

Mr. S. Devetzoglou
Foseco Hellas S.A.
Themistocleous 42
10678 Athens, GREECE

Dr. J. E. Dickinson
Corning Inc.,
SP-FR-5, Corning,
NY 14831, USA

Prof. Y. Dimitriev
Higher Inst. of Chemical Techn.
Dept. of Silicate Techn
8 Kl. Ohrydski Sofia 1756, BULGARIA

Dr. V. Dimitrov
Higher Inst. of Chemical Techn.
Dept. of Silicate Techn
8 Kl. Ohrydski Sofia 1756, BULGARIA

Mr. S. Dimoulas
26, Kritis str.
Athens, 10439
GREECE

Prof. G. Dixon
Department of Physics,
Oklahoma State University,
Stillwater, OK 74078, USA

Dr. P. J. Dornbusch
Dornbusch GmbH
Am Selder 31
4152 Kempen, GERMANY

Prof. N. Economou
Department of Physics
University of Thessaloniki
54006 Thessaloniki, GREECE

Dr. O. Elbayoumi *
US Air Force
223/231 Old Marylebone Road
London NW1 5TH, U.K.

Prof. S. Feller
Coe College
Physics Department
Cedar Rapids, IA52402, USA

Mr. L. Fontaine
Glaverbel S.A.
Rue d'Aurore
B - 6040 Jumet, BELGIUM

Prof. Dr. G. H. Frischat
Inst. f. Nichtmetallische Werkstoffe
Techn. Univ. Clausthal, Zehntnerstr. 2A
38678 Clausthal-Zellerfeld, GERMANY

Prof. Fuxi Gan
Shanghai Inst. of Optics and Fine Mechanics
P.O. Box 800-211,
Shanghai 201800, P. R. CHINA

Mr. N. Georgopoulos
Gryparis-Amelka E.P.E.
Aristippou 10
Athens 10675, GREECE

Mr. A. Geppard
Calumite S.A., Z.I. d' Esch-Schiffange
L-4149 Esch-sur-Alzette
LUXEMBOURG

Prof. G. N. Greaves
SERC Daresbury Laboratory,
Warrington WA4 4AD,
UK

Dr. R. Guinebretiere
Lab. de Materiaux et Trait. de Surface
ENSCI 45-67 Av. A. Thomas
87065- Limoges, FRANCE

Prof. I. Gutzow
Institute of Physical Chemistry
Bulgarian Academy of Sciences
Sofia 1040, BULGARIA

Mr. D. Hadjis
CALI ITALIA SRL
Via Roma 22
Ronciglione (VT) 01037, ITALY

Prof. Dr. W. Hoeland
c/o IVOCLAR AG
Bendererstrasse 2
FL 9494 Schaan, LIECHTENSTEIN

Dr. L. Hou
Inst. f. Neue Materialien,
Uni-campus, Geb. 43, Im Stadtwald
W-6600, Saarbruecken, GERMANY

Dr. F. Hubert
LUMSONRY
2e Ave 267
B-5651, Tarcienne, BELGIUM

Prof. M. D. Ingram
University of Aberdeen/Chemistry
Meston Walk, Aberdeen AB9 2UE
Scotland, U.K.

Dr. C. Jaeger
Max-Planck-Inst. f. Polymerforschung
Postfach 3148,
55021 Mainz, GERMANY

Mr. Th. Kakkos
Viokef N. Kakkos S.A.
26th Km Varis Ave, P.O. Box 28
19400 Koropi, GREECE

Mr. G. Kallergis
Yioula Glassworks Ltd
Orizomilon 5
Egaleo 12244, Athens, GREECE

Dr. E. I. Kamitsos
Theor. & Phys. Chem. Inst., NHRF
48, Vass. Constantinou Ave.
Athens 11635, GREECE

Mr. C. Kampitsis
1. Vass. Alexandrou Str.
14561 Kifissia
GREECE

Mr. J. A. Kapoutsis
Theor. & Phys. Chem. Inst., NHRF
48, Vass. Constantinou Ave.
Athens 11635, GREECE

Dr. M. A. Karakassides
Inst. Mat. Science, NCSR Demokritos
15310, Aghia Paraskevi
Attiki, GREECE

Prof. K. H. Karlsson
Department of Chemical Engineering,
Abo Akademi,
20500 Abo, FINLAND

Mr. N. Kartis
Yioula Glassworks Ltd
Orizomilon 5
Egaleo 12244, Athens, GREECE

Dr. S. Kasa
Institute of Chemical Technology,
Dept. Glass & Ceram., Technicka 5
16628 Prague 6, CZECH REPUBLIC

Mrs. V. Kastania
31, Navarinou Str.
A. Holargos
Athens 155 62, GREECE

Mr. H. Kiussopoulos
25, Lykavittou Str.
10672 Athens, GREECE

Dr. M. Kodama
Dept. of Industrial Chemistry
Kumamoto Institute of Technology
Ikeda, Kumamoto 860, JAPAN

Dr. G. Kordas
Inst. Mat. Science, NCSR Demokritos
15310, Aghia Paraskevi
Attiki, GREECE

Dr. A. Koufoudakis
Inst. Mat. Science, NCSR Demokritos
15310, Aghia Paraskevi
Attiki, GREECE

Dr. A. Kut
T. Sise ve cam Fabrikalari A.S.
Barbaros Bulvari No. 125
80706 Besiktas, Istanbul, TURKEY

Mr. J.- H. Lee
Hankuk Glass Industries Inc.
San 14-5, Tongchun-Dong, Nam-Ku
Inchon, KOREA

Mrs. R. Li
Univ. of Sheffield, Dept. Engin: Mat.
P.O. BOX 600, Sir R. Hadfield Building
Sheffield S1 4DU, UK

Dr. P. Lianos
University of Patras,
School of Engineering, Physics Section
26500 Patras, GREECE

Mr. G. Liptak
H 1340 Budapest
IV Vaci Ut 77
HUNGARY

Dr. A. Lisy
Inst. Chem. Tech-Dept. Glass & Ceram.
Technicka 1905/5, 16628 Prague 6
CZECH REPUBLIC

Dr. N. Maliavski
Dept. of General Chemistry
Moskow Inst. Civil Eng, Yaroslavskoe sh. 26
129337 Moskow, RUSSIA

Mr. M. Marinov
Bulgarian Academy of Sciences,
Inst. of Appl. Mineral, Rakovski Str. 92
1000-Sofia, BULGARIA

Prof. A. Marotta
Dept. of Materials and Production Eng.
Piazzale Tecchio
80125, Naples, ITALY

Dr. M. Marti
Societa Veneziana Vetro S.A.
Via delle Industrie 46
30175 P. Marghera, Venice, ITALY

Dr. D. Martlew
Pilkington Technology MGMT Ltd
Hall Lane, Lathom, Lancashire
L40 54F England, UK

Mr. Y. Mathios
Mathios Refractories
Epidaurou 5
18233 Rentis Piraeus, GREECE

Prof. Dr. J. Matousek
Institute of Chemical Technology,
Dept of Glass & Ceram, Technicka 5
16628 Prague 6, CZECH REPUBLIC

Mr. N. McDonnel
Society of Glass Technology
20 Hallam Gate Rd.
Sheffield S10 5BT, England, UK

Dr. M. Mennig
Inst.f. N. Mater., Universitaetscampus,
Gebaeude 43, Im Stadtwald
W-66123, Saarbruecken, GERMANY

Ms. B. Mihailova
Bulgarian Academy of Sciences,
Inst. of Appl. Mineral, Rakovski Str. 92
1000-Sofia, BULGARIA

Dr. M. Mika
Institute of Chemical Technology,
Dept of Glass & Ceram, Technicka 5
16628 Prague 6, CZECH REPUBLIC

Mr. S. Minaldi
CALI ITALIA SRL
Via Roma 22
Ronciglione (VT) 01037, ITALY

Prof. T. Minami
Dept. of Applied Materials Science
Osaka Prefecture University
Sakai, Osaka 593, JAPAN

Mrs. E. Mirtsou
Archaeol. Museum of Thessaloniki
54621 Thessaloniki
GREECE

Mr. M. Mochev
Kaolin plc
7272 Senovo, Rousse region
BULGARIA

Mr. I. Molnar
Mosommagyarovar
Hold u 3
HUNGARY

Prof. M. M. Morsi
Glass Research Department,
National Research Centre,
Dokki, Cairo, EGYPT

Dipl.-Ing. H. Moser
ZIPPE Industrieanlagen GmbH,
Alfred-Zippe-Str.
97877 Wertheim / Main, GERMANY

Dr. G. Mousdis
Inst. Mat. Science, NCSR Demokritos
15310, Aghia Paraskevi
Attiki, GREECE

Dr. W. Muschick
Shott Glaswerke
Hattenberg Strasse 10
D 55014 Mainz, GERMANY

Prof. J. M^a. Fernandez Navarro
CSIC - Instituto de Ceramica y Vidrio
Ctra. de Valencia, km 24.300
28500 Arg. del Ray, Madrid, SPAIN.

Dr. F. Nicoletti
Stazione Sperimentale del Vetro
Via Briati 10
30121 Murano, Venezia, ITALY

Mrs. L. Onsel
SISECAM
Camhan, Barbaros Bul. No.125
80706 Besiktas, Istanbul, TURKEY

Dr. M. Oran
Research Center,
Turkiye Sise ve Cam fabricalari A.S.
Istanbul, TURKEY

Mr. S. Orphanos
Yioula Glassworks Ltd
Orizomilon 5
Egaleo 12244, Athens, GREECE

Prof. R. Ota
Dept. of Chem. & Mater. Technology
Kyoto Institute of Technology
Matsugasaki, Sakyoku, Kyoto 606, JAPAN

Mr. A. Panagiotopoulos
ICE / HT
P.O. Box 1414
GR-26500 Patras, GREECE

Mr. N. Papadopoulos
Yioula Glassworks Ltd
Orizomilon 5
Egaleo 12244, Athens, GREECE

Prof. G. Papatheodorou
ICE/HT
P.O. Box 1414
GR-26500, Patras, GREECE

Ms. Parot-Rajaona
CNRS / CRPHT
Av. de la Recherche Scientifique
45071 Orleans. Cedex 2. FRANCE

Mr. A. Patsis
Theor. & Phys. Chem. Inst., NHRF
48, Vass. Constantinou Ave.
Athens 11635, GREECE

Mrs. E. A. Pavlatou
Inst. Chem. Eng. & High Temp. Proc.
Dept. of Chem. Eng., Univ. of Patras
P.O. Box 1414, 26500 Patras, GREECE

Mr. G. Perakakis
Viokef N. Kakkos S.A.
26th Km Varis Ave, P.O. Box 28
19400 Koropi, GREECE

Mr. S. Persson
The Glass Research Institute
Box 3093
S-350 33 Vaxjo, SWEDEN

Mrs. B. Kráznai Peterne
1064 Budapest
Izabella u 92
HUNGARY

Dr. J. Petzold
Schott Glaswerke
Hattenbergstrasse 10
D-55122 Mainz, GERMANY

Dipl.-Ing. H. Pieper
Nikolaus Sorg GmbH & Co. KG
P.O.Box 520, 97805 Lohr/Main
GERMANY

Dr. M. Prassas
Corning Europe
7bis Av. des Valvins
77210 - Avon, FRANCE

Dr. G. Priftis
Moretco S.A.
1, G. Lambraki Str., P.O. Box 80046
18510 Piraeus, GREECE

Mr. J. Protopapas
Interactive Ltd.
9, Kodrou Str.
Athens 10558, GREECE

Dr. P. Van de Putte
c/o Federation de l'Industrie du Verre
rue Montoyer 47
B-1040, Brussels, BELGIUM

Prof. L.D. Pye
N.Y. State College of of Ceramics
Alfred University
Alfred, N.Y. 14802, USA

Mr. D.-S. Pyun
Samsung Corning Co. Ltd.
472 Sin-Ri Taeam-Eup Hwasung-Gun
Kyeonggi-Do, 445-970. S. KOREA

Dr. M. Rada
Institute of Chemical Technology,
Dept of Glass & Ceram, Technicka 5
16628 Prague 6, CZECH REPUBLIC

Dr. H. Raedisch
VEGLA Vereinigte Glaswerke GmbH
Glasstrasse 1
D-52134 Herzogenrath, GERMANY

Miss M. Rappensberger
Univ. of Veszprem, Dept. Silic. Chem. Techn.
Egyetem Str. 10 H-8200 Veszprem,
HUNGARY

Dr. A. K. Rastogi
Batelle Ing. Tech. GmbH
Am Romerhof 35
60486 Frankfurt, GERMANY

Dr. V. Rheinberger
c/o IVOCLAR AG
Bendererstrasse 2,
FL- 9494 Schaan, LIECHTENSTEIN

Prof. M. Ribes
LPMS URA D0407 CNRS CC003
Universite de Montpellier II,
34095 Montpellier Cedex 05, FRANCE

Dipl.-Ing. J. Rosenthal
EME MASCHINENFABRIK CLASEN
Bernhard Hahn Str. 11-15
41812 Erkelenz, GERMANY

Prof. S. Sakka
Institute for Chemical Research
Kyoto University
Uji, Kyoto-Fu 611, JAPAN

Mr. F. Scarfe
Electroglass Ltd
4 Brunel Road, Benfleet,
Essex SS7 4PS, ENGLAND, UK

Prof. Dr. H. Schaeffer
HVG/DGG
Mendelssohnstrasse 75-77
60325 Frankfurt/Main, GERMANY

Dr. J. Scherg
NIKOLAUS SORG GmbH & CO. KG
Stoltestrasse 23
97816 Lohr/Main, GERMANY

Mr. Schmitt
Tranos Themis & Sons S.A.
31 Akadimias str.
Athens, GREECE

Mr. P. Sevastos
45, Fokionos Negri Str.
Athens 11361
GREECE

Dr. T. Seward
Corning Inc.
SP-FR-03-1
Corning, NY 14831, USA

Dr. P. Sewell
Pilkington Technol. Management Ltd.
Group Research, Hall Lane, Lathom,
Ormskirk, Lancashire L40 5UF, U.K.

Ir. F. Simonis
TNO-TPD Endhoven
Postbus 595,5600 AN Eindhoven
THE NETHERLANDS

Dr. W. Simpson
Society of Glass Technology
20 Hallam Gate Road
Sheffield S10 5BT, ENGLAND, U.K.

Dr. R. Sims
Nikolaus Sorg GmbH & CO. KG
Stoltenstrasse 23
97805 Lohr a. Main, GERMANY

Prof. N. Soga
Dept. of Materials Chem./Engineering
Kyoto University
Sakyo-ku, Kyoto 606, JAPAN

Dipl. Ing. K.-H. Sorg
NIKOLAUS SORG GmbH & Co. Kg
Stoltestrasse 23
97816, Lohr/Main, GERMANY

Mr. B. Stamelos
5, Aglaonikis Str.
Athens 117 43
GREECE

Prof. Yu. K. Startsev
Russian Academy of Sciences,
Inst. Silicate Chem., Odoevskogo 24/2,
199 155 St. Petersburg, RUSSIA

Dr. Z. Stoch
Institute of glass and Ceramics,
30-702 Krakow,
POLAND

Prof. Dr. L. Stoch
University of Mining and Metallurgy
30-059 Cracow
POLAND

Prof. J. Stoemenos
Department of Physics
University of Thessaloniki
54006 Thessaloniki, GREECE

Dr. I. Szabo
Univ. of Veszprem, Dept of Sil. Chem. Techn.
Egyetem str. 10,
H-8200 Veszprem, HUNGARY

Dr. K. Tajima
Asahi Glass Co Ltd.
2-1-2 Marounouchi Chiyoda-ku
Tokyo 100, JAPAN

Mr. S. Tranos-Karalis
Tranos Themis & Sons S.A.
31 Akadimias Str.
Athens, GREECE

Dr. C. Trapalis
Inst. Mat. Science, NCSR Demokritos
15310, Aghia Paraskevi
Attiki, GREECE

Prof. A. Tsatsas
University of Athens
Department of Chemistry
Panepistimiopolis, Athens, GREECE

Dr. P. Tsaussoglou
44, Tinou Str.
Athens 11361
GREECE

Prof. D. Uhlmann
Arizona Materials Laboratories
The University of Arizona
Tucson, AZ 85712, USA

Dr. P. Uva
Societa Veneziana Vetro S.A
Via delle Industrie 46
30 175 p. Marghera, Venice, ITALY

Mr. N. Valavanis
Valavanis Bros. Glassworks S.A.
109 Farsalon Str.
41335 Larisa, GREECE

Dr. K. Vamvakas
Mantzarou 1-3
Neo Psychiko
Athens, GREECE

Dr. N. Vanadruel
Catholic University of Louvain
Batiment Euler, Av. G.Lemaitre, 4 6
B-1348 Louvain-la-Neuve, BELGIUM

Dr. Z. Varga
IV Vaci Ut 77
H-1340 Budapest
HUNGARY

Dr. V. Veiko
Institute of Fine Mechanics and Optics
Sablenskaja Str. 14
Saint-Petersburg 197101, RUSSIA

Mr. N. Voulgarakis
Yioula Glassworks Ltd
Orizomilon 5
Egaleo 12244, Athens, GREECE

Prof. Dr. H. De Waal
TNO Institute of Applied Physics
Stietjesweg 1, NL 2628 CK Delft
THE NETHERLANDS

Prof. M. C. Weinberg
Dept. of Mater. nce and Engin.
University of Arizona
Tucson, AZ. 85721, USA

Mr. M. Werner
Vegla GmbH
Viktoriaallee 3-5
D 52066 Aachen, GERMANY

Dr. H. Yamamoto
Asahi Glass Europe BV, World Trade Centre
Strawinskylaan 1525 1077 xx
Amsterdam, THE NETHERLANDS

Mr. S. Yannopoulos
Inst. Chem. Eng. & High Temp. Proc.
Dept. of Chem. Eng., Univ. of Patras
P.O Box 1414, 26500 Patras, GREECE

Mrs. A. Yaraman
SISECAM
Camhan, Barbaros Bul. No.125
80706 Besiktas, Istanbul, TURKEY

Mr. Y. Yiannopoulos
Theor. & Phys. Chem. Inst, NHRF
48, Vass. Constantinou Ave.
Athens 11635, GREECE

Prof. B. Yoldas
PPG Industries Inc., Chemical Techn. Center
440 College Park Dr.
Monroville, PA 15146, USA

Prof. E. D. Zanotto
DEMA - UFSCAR
Via Washington Luiz-Km. 235
13565-905, Sao Carlos-SP-BRAZIL

Prof. B. Zelinski *
Arizona Materials Laboratories
University of Arizona
Tucson, AZ 85712, USA

Mr. C. Ziogas
Kronos Glassworks S.A.
25th km New Natl Rd Athens-Korinthos
P.O. BOX 7, 19200 Elefsis, GREECE

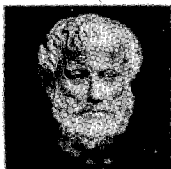
** participations sponsored by USAF/EOART*

*This year visit
Macedonia*

Macedonia

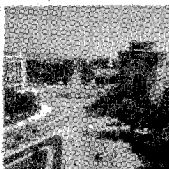
For 4,000 years steeped in the history of Greece*

Statue of Aristotle, Stagira.



Aristotle, the tutor of Alexander the Great, was born in Stagira in Macedonia in 384 BC. Together with Plato, he is regarded as one of the greatest philosophers the world has known. Aristotle was a true academic, concerned with Physics, Astronomy, Rhetoric, Literature, Political Science and History. His teachings laid the foundation for modern scientific thought.

The White Tower of Thessaloniki.



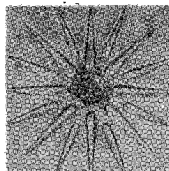
Thessaloniki, the heart of Macedonia, is a modern city with 1,000,000 inhabitants. It is strategically located at the crossroads of Europe with Asia. Having spread the Word at Philippi, the Apostle Paul continued his teachings in Thessaloniki. Its important monuments from antiquity and byzantium up to the present, provide testimony to the role that the city has played as the second capital of Hellenism.

The Bust of Alexander the Great. Acropolis Museum, Athens.



Alexander was born in 356 BC in Pella, Macedonia, established by his father Philip II, as the centre of Hellenism. Nurtured on the thoughts of his tutor, Aristotle, he rose to fame as a brilliant military leader. He influenced the course of history, rightfully earning his title as Alexander the Great. In 335 BC he became Commander in Chief of all the Greeks. By the time of his death in 323 BC he had created an enormous empire, stretching from the shores of the Adriatic to India, and from the Caucasus Mountains to Egypt. He spread the Greek spirit far and wide among nations who worshipped him as a god.

Symbol of the Greek Macedonian Dynasty from the tomb of Philip II. Archaeological Museum, Thessaloniki.



This 16-pointed star of Vergina was uncovered during the archaeological excavations at Vergina. This symbol of the Greek Macedonian Dynasty decorated the golden tomb of Philip II. The Star of Vergina, extracted from the soil of Macedonia, has since become the symbol of Hellenism.

The Olympian Aphrodite (3rd Century BC) Museum of Dion.



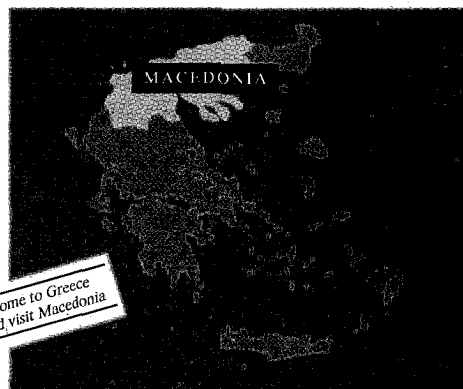
This statue of Aphrodite came to light during archaeological digs at the ancient sacred city of Dion. Dion, at the foot of Mt Olympus, was the most important spiritual site for the Northern Greeks, playing the same role in their lives as that of the oracle at Delphi.

St Dimitrios, detail of 7th Century Mosaic. Church of St. Dimitrios, Thessaloniki.



St Dimitrios, Protector of the city of Thessaloniki, was martyred in 305 AD defending Christianity. He is regarded as the Patron Saint of Thessaloniki and its saviour during difficult moments.

4,000 years: Post-Mycenaean ceramic relics found in Assiros and Mycenaean swords found in Grevena date back 4,000 years, evidence of Macedonia's role at the vortex of Greek history. Even in mythology Macedon, mythical founder of the Macedonian race, is the son of Aeolus (god of the winds). Throughout the years Macedonia contributed to the fountain of knowledge of the Ancient Greeks. In the 5th century BC Demokritos, father of Atomic Theory, lived and worked in Avdtra.*



G R E E C E
Chosen by the Gods